A Thermotectonic Framework for the Growth and Stabilization of the Eastern Kaapvaal Craton, Southern Africa

Robert Blair Schoene

B.A. Geology
Colorado College, 1999

SUBMITTED TO THE DEPARTMENT OF EARTH, ATMOSPHERIC AND PLANETARY SCIENCES IN PARTIAL FULFILLMENT OF THE REQUIREMENTS FOR THE DEGREE OF

DOCTOR OF PHILOSOPHY IN GEOLOGY
AT THE
MASSACHUSETTS INSTITUTE OF TECHNOLOGY

SEPTEMBER 2006

Signature of Author: _____
Department of Earth, Atmospheric and Planetary sciences
June 2006

Certified by: _____
Samuel A. Bowring
Professor of Geology
Thesis Supervisor

Accepted by: _____
Maria T. Zuber
E.A. Griswold Professor of Geophysics and Planetary Science
Department Head

A thermotectonic framework for the growth and stabilization of the eastern Kaapvaal craton, southern Africa

Robert Blair Schoene

Submitted to the Department of Earth Atmospheric and Planetary Sciences at the Massachusetts Institute of Technology in 2006 in partial fulfillment of the requirements for the degree of Doctor of Philosophy in Geology

ABSTRACT

Continents are an amalgamation of crust and mantle lithosphere assembled over ~4 Gyr and are therefore our best record of the early Earth. Exposures of rocks ~3.0-3.7 Ga cover ~20,000 km^2 of eastern S. Africa and Swaziland, and provide a record of the continental assembly and subsequent stabilization of the eastern Kaapvaal craton. This thesis uses structural, geochronological, thermochronological and isotopic constraints to examine the tectonothermal processes responsible for the growth and stabilization of this portion of Mesoarchean lithosphere. Field mapping was focused on terrane-bounding shear zones and syntectonic plutons, and in combination with ID-TIMS U-Pb zircon geochronology and Sm-Nd analysis, places sub-Myr constraints on the timing, distribution, and kinematics of magmatism and deformation during growth and modification of continental lithosphere. Detailed U-Pb apatite and titanite thermochronological datasets are used in combination with finite difference numerical modeling to determine non-linear temperature-time paths for rocks between ~650-300 °C from 3.45-3.08 Ga – providing a sensitive indicator of tectonic and magmatic processes in the middle to lower crust.

From 3.2 to 3.3 Ga, multiple microcontinental fragments with distinct age and Nd isotopic characteristics were assembled along an oblique subduction zone boundary, with the Barberton Greenstone belt representing a lithospheric suture zone. During continental assembly and orogeny, strain was partitioned into 3236-3220 Ma syntectonic plutons and terrane-bounding transcurrent shear zones bordering the margins of the previously stabilized ca. 3.66-3.45 Ga Ancient Gneiss Complex. Subsequent 3.2-3.1 Ga reactivation of crustal anisotropies within the lithospheric suture zone – represented broadly by the Barberton Greenstone Belt – controlled the thermal and compositional reorganization of the crust through transtensional tectonics, exhumation of deep-crustal gneiss terranes, and upward migration of granitic batholiths. This final period of crustal modification was responsible for juxtaposing low-grade greenstone supracrustal rocks against middle- to lower-crustal gneiss terranes, and ultimately led to crustal stabilization in the greenstone belt and vicinity. These results support a model in which the stabilization of the Kaapvaal craton was a piece-wise transition resulting from lithospheric thickening and crustal thinning over hundreds of Myr.

Thesis Supervisor: Samuel A. Bowring
Title: Professor of Geology

ACKNOWLEDGEMENTS

This thesis is a product of more than just myself – from co-authors to those behind the scenes. One of the most rewarding parts of my time at MIT is the daily interaction with professors, post-docs, research scientists, and fellow students on a personal and academic level – I should hope to always reside in such an intellectual incubator. Of special note is my advisor Sam, who is a bottomless pit of ideas, a strangely efficient motivator, and emanates a scientific integrity that I hope to carry with me in the future. I thank him for the support and freedom he has provided during my time at MIT.

Additionally, the MIT TIMS lab and all its members have been a constant source of inspiration and fatigue over the past six years. The quality of work, constant feedback, excessive banter, and enthusiasm for good science provided by all its members, past and present, made the analytical work of this thesis possible.

There are innumerable people in southern Africa who deserve my thanks. From colleagues to farmers, I was constantly impressed by the kindness, openness, and hilarity of the Swazis and South Africans. I will always be grateful for my time there on a scientific, cultural and personal level. In particular, Maarten de Wit, in addition to making available his bountiful knowledge of the Kaapvaal craton through collaboration and guidance, also provided unconditional support during field work. His enthusiasm for my intellectual growth and independence will not be forgotten.

Finally, it is no small task to thank my family and friends in Boston and afar for their steadfast support, love and resolve. I can't possibly do them justice here. Especially my wife and friend Colby whose love, wisdom and inspiration have helped guide and educate me. Thanks.

TABLE OF CONTENTS

INTRODUCTION

Many early studies of tectonic and thermal histories of Archean terranes described processes that differ from modern plate tectonics, attributed to possible incongruencies in the physical structure or amount of continental crust compared to the present day or higher geothermal gradients in the Archean (Anhaeusser et al., 1969; Glikson, 1970; Green, 1975; Hamilton, 1998). Most investigations, however, appeal to more actualistic plate tectonic interactions that hinge on our understanding of younger orogenic belts, though acknowledge the potential bias in the geologic record introduced by preferential preservation of continental lithosphere that has unique physical or geochemical characteristics (Burke et al., 1976; de Wit, 1998; Jordan, 1988; Parman et al., 2004; Schmitz et al., 2004; Tarney et al., 1976). Ongoing multidisciplinary investigations in continental lithospheric evolution explore the conditions necessary for the accretion and long-term preservation of lithosphere versus the periodic structural and thermal reactivation that may result in its recycling back into the asthenosphere (e.g. Carlson et al., 2000; Karlstrom and Keller, 2005). Because Archean cratons are the best examples of stable continental lithosphere, a detailed understanding of their tectonic evolution is essential for building models for continental growth throughout Earth history. This thesis summarizes my efforts to understand the processes of assembly, reactivation and differentiation of a Mesoarchean lithospheric block in the eastern Kaapvaal craton, Southern Africa (Figs. 1, 2.). The chosen field area is, in fact, one of the best examples of preserved Archean lithosphere in that it contains well-exposed remnants of Mesoarchean crustal rocks that have remained undisturbed structurally and thermally

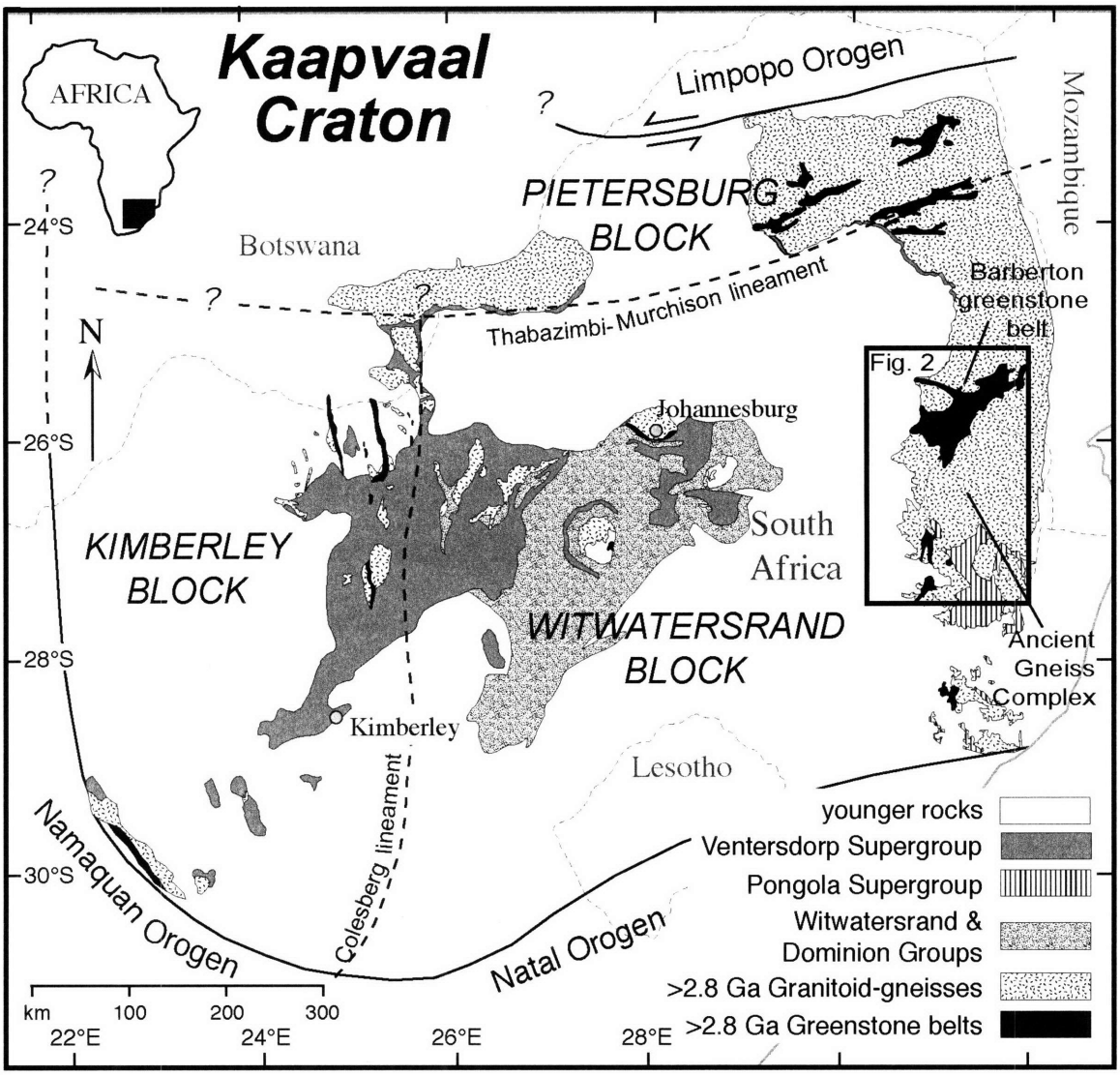

Fig. 1 Geologic map of exposed Archean rocks in the Kaapvaal craton, modified from Schmitz et al. (2004). Included are the major terrane subdivisions of the craton, and the distribution of the major Neoarchean depositional basins. Position of Fig. 2 is outlined in black box.

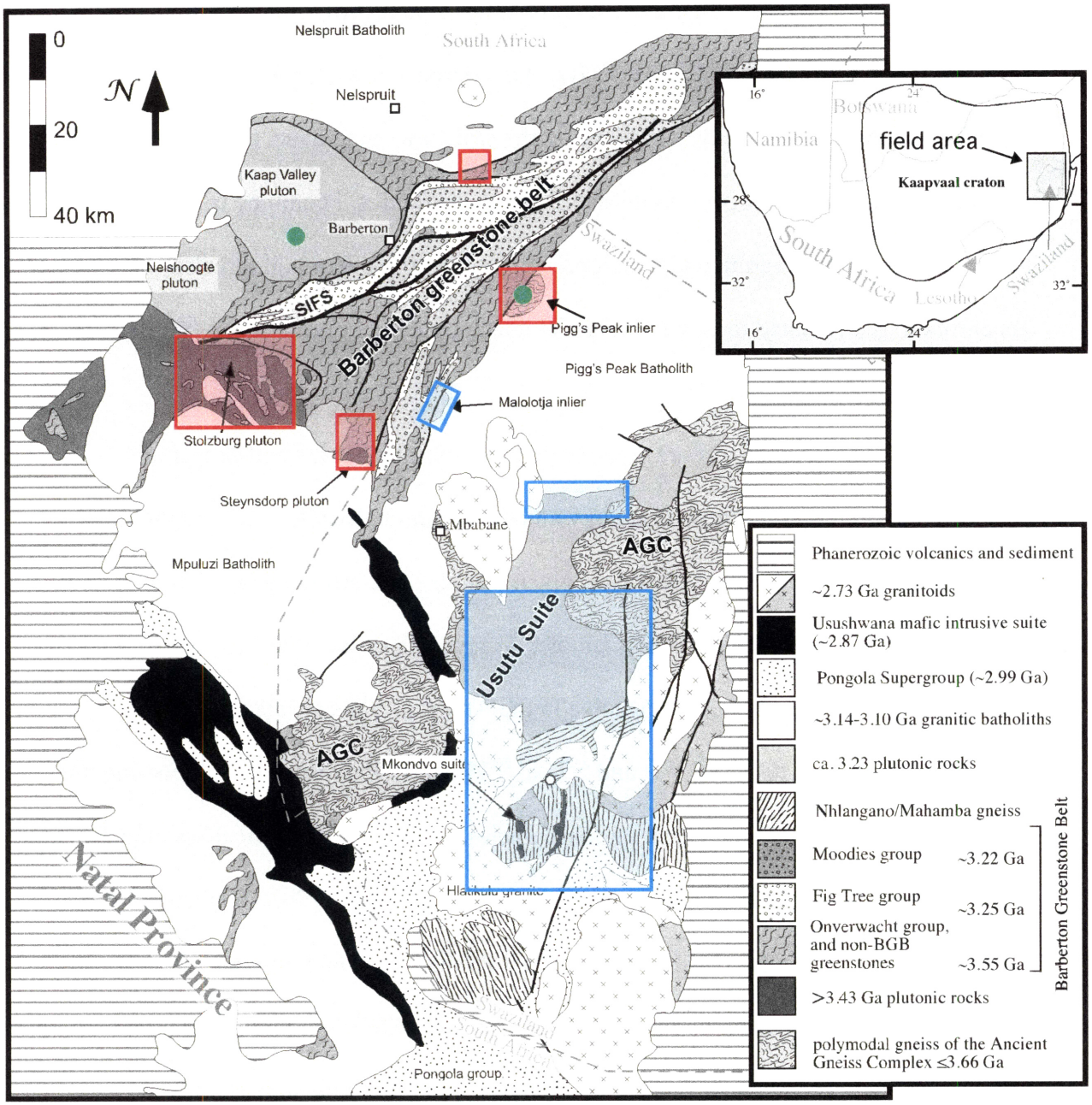

Fig. 2: Geologic map of the eastern Kaapvaal craton. Areas studied in chapters 1-3 are highlighted (green circles: Ch. 1; red rectangles: Ch. 2; blue rectangles: Ch. 3). See text for details.

since the Archean, and in places for > 3 Gyr. This apparent stabilization is even more striking because the eastern craton abuts directly against the edge of the African plate and, to give the most recent example, contains little or no record of the assembly and breakup of Gondwanaland in the last 1 Gyr. My approach to understanding this remarkable long-term stability is to focus on the structural, magmatic, and thermal events that occurred immediately prior to its stabilization. To do this, I combine traditional methods of field observation and structural mapping with modern high-precision U-Pb geochronology dedicated to constraining tectonic and thermal events at sub-million year timescales.

Geologic terranes that are complicated by multiple thermal and/or tectonic episodes require the use of geochronology and thermochronology to work out the relative and absolute timing of events. However, given that absolute errors by any dating method generally increase with the age of the sample, orogenic processes that occur on timescales of millions of years are difficult to resolve in the Archean. This problem is partly overcome by the dual decay of ^{238}U and ^{235}U to ^{206}Pb and ^{207}Pb, respectively. For one, this system allows for an internal check on inaccuracies arising from analytical assumptions or problems and open-system behavior in minerals (Davis et al., 2003; Wetherill, 1956). Second is that it allows for dating by the $^{207}Pb/^{206}Pb$ method, which provides dramatically higher precision than any other geochronological tool in Archean rocks (Mattinson, 1987), such that individual dates on single zircon crystals is achievable at <1 Myr. Wielding this power towards determining crystallization ages that constrain rates of magmatic processes or date dikes that cross-cut important structures requires resolving and eliminating zones of minerals (most importantly zircon) that experienced open

system behavior such that dates are as accurate as they are precise. This has been one of the major deterrents from attaining high-precision dates in old zircons whose crystal lattices have become metamict through the time-integrated effects of radioactive decay of U. During the course of my thesis work, advances in the preferential dissolution of discordant domains of highly metamict zircon (Mattinson, 2003, 2005) have allowed for the determination of crystallization dates of Archean zircons with unprecedented precision. Their application towards problems in the eastern Kaapvaal craton allows calibration of the timescales of arc formation and the development and distribution of deformation patterns with similar absolute precision as is routinely achieved in Phanerozoic orogenic belts.

The Kaapvaal craton has been the focus of innumerable seismic, geologic, petrologic, geochronologic and xenolith studies which have aided in the generation of robust 4-D models for the evolution of cratonic lithosphere and have also provided key constraints on early earth processes such as the appearance of life and asthenospheric mantle evolution. Excellent exposures of ca. 3.6-3.2 Ga gneissic basement and ca. 3.45-3.2 Ga volcano-sedimentary cover sequences outcrop in eastern South Africa and Swaziland in the Ancient Gneiss Complex (AGC) and Barberton Greenstone Belt (BGB), respectively (Figs. 1, 2; see references from the individual chapters that follow). These rocks, when combined with associated granitoids and ortho- and paragneisses, exhibit a spectrum of metamorphic grades from greenschist to granulite, suggesting that these rocks were equilibrated and exhumed from very different levels of the crust. Previous tectonic models derived from structural, sedimentilogical, geochronological and petrological studies suggest that the imbrication, metamorphism, and exhumation of

rocks from different crustal levels may all be related to a short ca. 3230-3215 Ma continent-continent collision. However, models have primarily been generated based on restricted evidence from relatively few geologic areas. For example, numerous published models for ca. 3.2 Ga assembly require deformation, uplift and exhumation of the AGC in Swaziland, though not a single structural study on the AGC has been published in 20 years and there is no thermochronological data published. Several papers suggest that ca. 3.2 Ga magmatism associated with subduction is restricted to north of the BGB, but no detailed geochronological or field study has been focused on the large swaths of apparently ca. 3.2 Ga plutonic rocks south of the BGB in the AGC. Finally, most structural studies from the BGB acknowledge strike-slip kinematics on what are interpreted to be small-scale faults post-dating major contractional structures. However, some workers have speculated that these structures may be important in accommodating post-assembly transtensional faulting and related granitic batholith generation ca. 3.1 Ga. If true, it suggests that reworking ~100 Myr after assembly was an important modifier of crustal architecture and potentially important the stabilization of the eastern craton. These observations and apparent holes in our knowledge of the evolution of the eastern Kaapvaal craton form the major driving questions in this thesis, and their investigation are laid out by chapter below.

A reoccurring theme in the research of greenstone belts around the world lies in understanding the relationship between high-grade basement orthogneiss complexes and low-grade metavolanic and siliciclastic deposits within the belt – a relationship often called "dome-keel" structure (e.g. de Wit and Ashwal, 1997). An underlying constraint or assumption in these models is that structures or fabrics observed at the contacts

between these very different terranes formed simultaneously. I approach this problem in Chapter 1 by conducting a detailed U-Pb thermochronlogical study using apatite and sphene from two ca. 3227 Ma samples on opposite sides of the BGB. Accurately interpreting thermochronological dates requires understanding and manipulating predictable open-system behavior of daughter isotopes, such that one can translate mineral-isotope dates into accurate temperature-time paths for rocks. This involves documenting the variable effects of the metamorphic growth versus diffusion of Pb within the apatite and sphene, and can be accomplished both by grain imaging and microsampling and by examining closure date versus grain-size relationships. Perhaps more difficult is to resolve the variable effects of primary mid-crustal cooling from thermal reheating due to nearby magmatic intrusions, given than both are recorded by volume diffusion of Pb within the mineral. This is overcome by generating robust grain size versus date curves for apatite and sphene that span >100 Myr and using finite-difference numerical modeling to generate a unique temperature-time curve for the rock. The results show that rocks north and south of the BGB experienced drastically different cooling histories: the sample to the north intruded and cooled rapidly to below 400 °C within a few Myr, whereas the sample south, within the AGC, resided in the lower crust for 80 Myr prior to rapid exhumation to the middle or upper crust during granite intrusion ca. 3140 Ma. These results indicate that major post-assembly crustal restructuring was important in the generation of widespread granitic magmatism and that the BGB need be viewed as a dynamic tectonic terrane from 3.2-3.1 Ga prior to its stabilization.

In an effort to further characterize the "dome-keel" formation in the BGB from 3.2-3.1 Ga, and to place the thermal constraints from Chapter 1 into a structural context,

Chapter 2 involves structural mapping and kinematic description of important localities that expose the contacts between supracrustal rocks and the basement gneisses. These contacts are primarily characterized by extensional to transtensional shear zones and brittle faults, which contrasts with the primarily contractional tectonic models for the BGB dominating the literature. Two exposures of ductile shear zones on the NW and SE margins of the belt have strikes parallel to the overall NE-SW regional fabric and record right-lateral transtensional kinematics. The dome-shaped ca. 3.5 Ga Steynsdorp pluton along the SW margin of the greenstone belt is shown to represent a NE verging core-complex. U-Pb zircon dating of syn- to post-tectonic dikes within the mapped structures in the three localities reveal that movement along these structures took place during at least two periods of time, ca. 3.2 and 3.1 Ga. This data suggests that while early phases of ca. 3.2 Ga deformation may have involved a significant contractional component, the later structural evolution along the margins of the of the belt was characterized by transtension to strike-slip kinematics during multiple episodes over 100 Myr. Constraints on the timing and magnitude of exhumation on these structures is also provided U-Pb apatite thermochronology, which records a heterogeneous thermal structure during restructuring of the crust from 3.2-3.1 Ga, and is consistent with the juxtaposition of high- and low-grade terranes along transtensional to extensional structures synchronous with granite intrusion. Thus, the development of the characteristic dome-keel structure in the BGB was a protracted event resulting from the periodic reactivation of crustal to lithospheric anisotropies. It was likely this period of crustal extension and differentiation that resulted in the stabilization of the BGB and adjacent terranes.

Chapter 3 explores the role of the AGC and associated orthogneisses in ca. 3.23 continental assembly. But instead of a detailed investigation of the AGC itself, I describe the magmatic, structural, and geochronological history of plutonic rocks from the cross-cutting Usutu intrusive suite and lower crustal Nhlangano orthogneiss (NG), which this chapter determines to be ca. 3.2-3.3 Ga and therefore critical in building regional tectonic models for the assembly of the craton. Magmatic and subsolidus fabrics in Usutu suite record their syntectonic intrusion into a NW-SE compressional stress field, consistent with documented compression in the BGB. Therefore, combining these field observations with high-precision U-Pb zircon geochronology describes not only the timing of emplacement of the Usutu intrusive suite, but to inform a larger tectonic model. U-Pb zircon crystallization ages from >15 samples from the Usutu suite show that it intruded over a period between 3236-3220, with the majority of the magmatism between ca. 3232 and 3227 Ma. Subsolidus strain in the Usutu suite is partitioned near the boundaries of the AGC, along the margin of the BGB and the NG, suggesting the AGC behaved as a rigid crustal block during continental assembly and testimony to a pre-3.2 Ga structural stability of the AGC. Coeval magmatism and deformation north and south of the BGB lead to a model of a doubly verging subduction zone ca. 3.2-3.3 Ga, in which the NG formed the deep magmatic core of a continental arc.

The implication that the NG was built upon older AGC lithosphere is suggested in the surface geology and >3.5 Ga inherited zircons, whereas the orthogneisses north of the BGB may represent a younger, island arc type continental fragment. Chapter 4 explores this assertion using the Sm-Nd isotopic systematics from a transect of 79 plutonic and orthogneiss samples from north of the BGB southward into the NG. Coeval magmas

across the transect are used to compare the time-integrated Nd isotopic signature of sources of Nd contributing to their petrogenesis. The results confirm the existence of at least two distinct lithospheric boundaries near the BGB and that enriched rocks similar if not identical to the AGC contributed to the Nd budget of the NG and associated 3.2-3.3 Ga magmas south of the BGB. A simple Nd mass balance through the old (>3.45 Ga) lithospheric blocks shows that after 3.2 Ga, crustal evolution was dominated by intracrustal differentiation rather than crustal growth. This conclusion is consistent with the geologically and geochronologically derived models suggesting that arc magmatism and crustal growth occurred ca. 3.2-3.3 Ga (Chapter 3) followed by melting of the lower crust during extension ca. 3.1 Ga (Chapter 2) with little mantle input.

The final two chapters, though primarily analytical in scope, are in many ways outgrowths of the work within the first four chapters. Chapter 5 (Schoene et al., 2006) serves as a detailed analysis of numerous zircon and xenotime samples in conjunction with a high-precision recalibration of the MIT U-Pb tracer solution that achieves the level of precision of weighted mean datasets required to test the relative accuracy of the uranium decay constants. This work was partially the result of testing and refinement of the chemical abrasion technique within the MIT laboratory, which was essential for attaining accurate, concordant data from the Archean zircons analyzed in the rest of the thesis. Several of the samples from this study can be used as a direct comparison with $^{40}Ar/^{39}Ar$ dates on the same rocks, and thus are important for the intercalibration of the two radiometric dating schemes. Chapter 6 (Schoene and Bowring, 2006) is a more in depth study of a single sample that contains the hornblende MMhb, used as a popular secondary standard in $^{40}Ar/^{39}Ar$ dating. Comparing $^{40}Ar/^{39}Ar$ and U-Pb dates is difficult

in part because the differing closure temperatures of zircon and $^{40}Ar/^{39}Ar$ geochronometers. Therefore, this study requires a critical assessment of the uncertainties involved in U-Pb thermochronology, such as the correction for initial Pb in apatite and sphene, such that comparison with $^{40}Ar/^{39}Ar$ hornblende dates can made within an accurate and precise time-frame in the U-Pb system. Both chapters highlight the difficulty and importance of making rigorous comparisons between different geochronometric systems, which is especially important in thermochronologic studies that take advantage of the broad temperature range accessible by multiple thermochronometric methods. Method development in these chapters therefore contribute to future work in both Archean and younger geologic terranes in a wide-variety of tectonic settings.

In summary, stabilization of the eastern Kaapvaal craton is hallmarked by complex crustal scale strain partitioning during assembly and the subsequent reactivation of lithospheric anisotropies that accommodated post amalgamation transtensional crustal restructuring and geochemical differentiation. Comparison with other parts of the craton indicate that construction of the Kaapvaal craton was a piece-wise process rather than a single event, though the processes that stabilized different craton blocks were likely similar. I show that integrating traditional methods of field mapping and structural geology with modern, high-precision U-Pb ID-TIMS geochronology and thermochronology allows for the characterization of a rich and complicated tectonic evolution in the Archean at timescales similar to those normally restricted to Proterozoic and Phanerozoic orogens. Similar studies in other crustal exposures across the Kaapvaal

craton and in other areas around the world will aid in describing fundamental processes in lithosphere evolution.

REFERENCES

Anhaeusser, C. R., R. Mason, M. J. Viljoen, and R. P. Viljoen, 1969, A reappraisal of some aspects of Precambrian shield geology: GSA Bull., v. 80, p. 2175-2200.

Burke, K., J. F. Dewey, and W. S. F. Kidd, 1976, Dominance of horizontal movements, arc and microcontinental collisions during the later premobile regime, *in* B. F. Windley, ed., The Early History of the Earch: New York, John Wiley and Sons, p. 113-130.

Carlson, R. W., F. R. Boyd, S. B. Shirey, P. E. Janney, T. L. Grove, S. A. Bowring, M. D. Schmitz, J. C. Dann, D. R. Bell, J. J. Gurney, S. H. Richardson, M. Tredoux, A. H. Menzies, D. G. Pearson, R. A. Hart, A. C. Wilson, and D. E. Moser, 2000, Continental growth, preservation, and modification in Southern Africa: GSA Today, v. 10, p. 1-8.

Davis, D. W., I. S. Williams, and T. E. Krogh, 2003, Historical development of zircon geochronology, *in* J. M. Hanchar, and P. W. O. Hoskin, eds., Zircon: Reviews in Mineralogy and Geochemistry, v. 53: Washington, D.C., Mineralogical Society of America, p. 145-181.

de Wit, M. J., 1998, On Archean granites, greenstones, cratons and tectonics: does the evidence demand a verdict? Precam. Res., v. 91, p. 181-226.

de Wit, M. J., and L. D. Ashwal, eds., 1997, Greenstone Belts: Oxford Monographs on Geology and Geophysics, v. 35: Oxford, Clarendon Press, 809 p.

Glikson, A. Y., 1970, Geosynclinal evolution and geochrmical affinities of early Precambrian systems: Tectonophysics, v. 9, p. 397-433.

Green, D. H., 1975, Genesis of Archean peridotitic magmas and constraints on Archean geothermal gradients and tectonics: Geology, v. 3, p. 15-18.

Hamilton, W. B., 1998, Archean magmatism and deformation were not products of plate tectonics: Precambrian Research, v. 91, p. 143-179.

Jordan, T. H., 1988, Structure and formation of the continental tectosphere, *in* M. A. Menzies, and K. G. Cox, eds., Oceanic and Continental Lithosphere: Similarities and Differences: London, Oxford University Press, p. 11-37.

Karlstrom, K. E., and G. R. Keller, eds., 2005, The Rocky Mountain Region -- An Evolving Lithosphere: Tectonics, Geochemistry, and geophysics: AGU Geophys. Mono., v. 154: Washington, D.C., Amer. Geophys. Union.

Mattinson, J. M., 1987, U-Pb ages of zircons: a basic examination of error propagation: Chemical Geology, v. 66, p. 151-162.

Mattinson, J. M., 2003, CA (chemical abrasion)-TIMS: high-resolution U-Pb zircon geochronology combining high-temperature annealing of radiation damage and

multi-step partial dissolution analysis: Eos Trans. AGU, Fall Meet. Suppl., Abstract V22E-06.

Mattinson, J. M., 2005, Zircon U-Pb chemical-abrasion ("CA-TIMS") method: combined annealing and multi-step dissolution analysis for improved precision and accuracy of zircon ages: Chem. Geol., v. 220, p. 47-56.

Parman, S. W., T. L. Grove, J. C. Dann, and M. J. de Wit, 2004, A subduction origin for komatiites and cratonic lithospheric mantle: S. Afr. J. Geol., v. 107, p. 107-118.

Schmitz, M. D., S. A. Bowring, M. J. de Wit, and V. Gartz, 2004, Subduction and terrane collision stabilized the western Kaapvaal craton tectosphere 2.9 billion years ago: Earth Planet. Sci. Lett., v. 222, p. 363-376.

Schoene, B., and S. A. Bowring, 2006, U-Pb systematics of the McClure Mountain syenite: thermochronological constraints on the age of the $^{40}Ar/^{39}Ar$ standard MMhb: Contrib. Miner. Petrol., v. 151, p. 615-630.

Schoene, B., J. L. Crowley, D. C. Condon, M. D. Schmitz, and S. A. Bowring, 2006, Reassessing the uranium decay constants for geochronology using ID-TIMS U-Pb data: Geochim. Cosmochim. Acta, v. 70, p. 426-445.

Tarney, J., I. W. D. Dalziel, and M. J. de Wit, 1976, Marginal basin 'Rocas Verdes' complex from S. Chile: A model for Archaean greenstone belt formation, *in* B. F. Windley, ed., The Early History of the Earch: New York, John Wiley and Sons, p. 131-146.

Wetherill, G. W., 1956, Discordant uranium-lead ages: Trans. Amer. Geophys. Union, v. 37, p. 320-326.

CHAPTER 1

Determining accurate temperature-time paths from U-Pb thermochronology: An example from the Kaapvaal craton, southern Africa

Blair Schoene* and Samuel A. Bowring

Department of Earth, Atmospheric and Planetary Sciences; Room 54-1116; 77 Massachusetts Ave., Massachusetts Institute of Technology, Cambridge, MA 02139, USA.

**schoene@mit.edu*

accepted for publication in *Geochimica et Cosmochimica Acta*

ABSTRACT

Thermochronology has revolutionized our understanding of the establishment and evolution of lithospheric thermal structure. However, many potential benefits provided by the application of diffusion theory to thermochronology have yet to be fully exploited. This study uses apatite (T_c = 450-550 °C) and titanite (T_c = 550-650 °C) U-Pb ID-TIMS thermochronology at the single- to sub-grain scale to separate the variable effects of volume diffusion of Pb from metamorphic (over)growth above and below the T_c of a mineral. Data are presented from two ca. 3227 Ma tonalite samples from north and south of the Barberton Greenstone Belt (BGB), southern Africa. Two distinct populations of apatite from a sample north of the BGB record fast cooling followed by metamorphic growth ~10 Myr later. Both apatite and titanite dates from south of the BGB show a strong correlation with the grain size and record 100 Myr of post-emplacement cooling. Complex core-rim zoning observed in cathodoluminesence images of apatite is interpreted to reflect metamorphic overgrowth above the T_c. The age and topology of grain size versus date curves from titanite and apatite are used in combination with a finite-difference numerical model to show that slow, non-linear, cooling and not thermal resetting is responsible for the observed distribution. The thermal histories from either side of the BGB are very different and provide unique insight into the BGB's tectonic evolution: a ~70 Myr period of apparent stability after ca. 3.2 Ga terrane assembly was followed by fast exhumation south of the BGB that led to lower-crustal melting and intrusion of granitic batholiths ca. 3.14-3.10 Ga.

1. INTRODUCTION

The integration of radiogenic isotope geo- and thermochronology with petrologic and tectonic studies is the only way to directly quantify lithospheric thermal structure as a function of time. Typically, a cooling date in a mineral is described by the closure temperature (T_c) concept of Dodson (1973, 1986). This model is based on the assumption that an isotopic date is the result of volume diffusion of the daughter product through the crystal lattice over time (t), and is therefore fundamentally a function of temperature (T). Interpreting mineral isotopic dates using Dodson's equation for T_c is subject to experimentally determining the physical diffusivity characteristics of an element in a crystal lattice (D_o and E), assuming that diffusion operates over a specified cooling rate (dT/dt) and within some idealized geometric shape with an effective diffusion dimension, a, ideally corresponding to the grain radius (see also reviews in Ganguly and Tirone, 1999, Hodges, 2003, and McDougall and Harrison, 1999). Most studies use Dodson's theory as a qualitative construct and assume a nominal closure temperature for a given system, which proves to be valid on a semi-quantative level, in that cooling dates are often consistent with well-understood geology and maintain relative consistency in ages among different thermochronometers. Empirical estimates of closure temperatures for a variety of U-Pb, $^{40}Ar/^{39}Ar$, (U-Th)/He, and Sm- Nd, and fission track thermochronometers from natural settings are broadly consistent with predictions based on experimental determination of physical diffusion parameters (e.g. Cherniak, 1993; Cherniak et al., 1991; Cherniak and Watson, 2001; Ducea et al., 2003; Ganguly et al., 1998; Harrison, 1981; Harrison et al., 1985; Reiners and Ehlers, 2005) and theoretical

estimates based on ionic porosity (Dahl, 1997). In reality, many of the assumptions that go into Dodson's formulation are likely to be compromised in real geologic scenarios, and the result is that distributions of cooling dates are often much more precise than our ability to interpret them. For example, application of Dodson's (1973, 1986) formulation becomes limited for large grain sizes with fast cooling (Ganguly and Tirone, 1999) and in conditions of nonmonotonic cooling or isothermal holding (Dodson, 1973), or in rocks where thermal resetting of dates is important (Dodson, 1975).

Furthermore, microanalytical $^{40}Ar/^{39}Ar$ studies have shown that the assumption of volume diffusion is not always valid, in that dates may be controlled by, for example, deformation-related microsctructure or solid-state recrystallization (Dunlap and Kronenberg, 2001; Mulch et al., 2002; Wartho, 1995). Comparable studies within the U-Pb system are relatively few, though it is well known that titanite can be involved in a host of metamorphic reactions from granulite to greenschist grade conditions (Frost et al., 2000; Lucassen and Becchio, 2003; Spear, 1993) – well below its T_c of 550-650 °C (Cherniak, 1993; Corfu, 1988; Hawkins and Bowring, 1999). Multiple generations of titanite in single rocks have been identified based on optical microscopy, back-scattered electron imaging, petrography, and both ID-TIMS and SIMS U-Pb geochronology (Aleinikoff et al., 2002; Corfu and Stone, 1998; Franz and Spear, 1985; Gromet, 1991; Verts et al., 1996). Apatite ($T_c \approx$ 450-550 °C; Cherniak et al., 1991; Chamberlain and Bowring, 2000) is also stable in a wide range of metamorphic conditions (Bea and Montero, 1999; Bingen et al., 1996; Pan and Fleet, 1996), as well as in low-T fluid-rich environments (Smith and Yardley, 1999; Spear and Pyle, 2002). Metamorphic

reequilibration below the T_c of thermochronometers jeopardizes closed-system behavior and therefore may lead to erroneous interpretations of mineral dates.

An independent constraint on whether volume diffusion is controlling a recorded date resides in that Dodson's (1973) theory predicts a distribution in closure dates as a function of grain size (here called the *a-t* curve). Though both metamorphic overgrowth and volume diffusion predict a younging in age towards the outside of a grain (Fig. 1), volume diffusion alone predicts a correlation with grain size. Wright et al. (1991) documented a relationship between $^{40}Ar/^{39}Ar$ closure dates in biotite and grain diameter and used manipulations of Dodson's equation to calculate *dT/dt* over its closure interval. Hawkins and Bowring (1999) use the *a-t* curve to calculate *T-t* curves for a suite of titanite grains from a slowly-cooled Proterozoic terrane. Several U-Pb studies have documented crude *a-t* curves for rutile (Mezger et al., 1989; Schmitz and Bowring, 2003), suggesting its grain size may also act as the effective diffusion dimension.

Perhaps a more difficult problem arises from the fact that both slow cooling and thermal resetting in U-Pb, $^{40}Ar/^{39}Ar$ and other thermochronometers should result in robust *a-t* curves. Because of the assumption that *T* varies with *1/t* in Dodson's (1973) formulation, quantitatively testing the effect of partial thermal resetting is not possible with that model (Dodson, 1973, 1975). Therefore, most studies approach the problem of resetting by qualitatively weighing the importance of previously documented local or regional geologic thermal anomalies (e.g. Ketchum et al., 1998; Layer et al., 1992; Pidgeon et al., 1996). Some studies have shown, however, that thermal modeling with reasonable geologic constraints is useful in testing the likelihood and the effect of

resetting in the U-Pb system (Schmitz and Bowring, 2003; Verts et al., 1996), though none of these studies incorporate complicated, non-linear *T-t* paths.

In this study, we use U-Pb ID-TIMS thermochronology to investigate the competing processes controlling U-Pb closure dates in apatite and titanite. We utilize two ca. 3227 Ma tonalites with contrasting thermal histories from north and south of the Barberton greenstone belt (BGB), SE Kaapvaal craton, southern Africa. The minerals' growth history are inferred from petrographic characterization and by back-scattered electron (BSE) and cathodoluminesence (CL) imaging. A combination of whole grain and microsampled apatite are used to document age gradients as a function of grain size and zoning characteristics. Air-abraded and unabraded single grains of titanite were also analyzed to investigate *a-t* relationships and intragrain date gradients. Finally, we use a finite-difference numerical model that calculates *a-t* curves for different thermal histories to test whether the observed *a-t* curves are a result of slow cooling or resetting. Though previously hypothesized (e.g. Watson and Harrison, 1984), we show for the first time that *a-t* curves from multiple thermochronometers with different nominal T_c can be used together to constrain unique thermal histories for rocks.

2. MESOARCHEAN EVOLUTION OF THE KAAPVAAL CRATON

The southeast portion of the Kaapvaal craton is characterized by a protracted evolution during the Mesoarchean that culminated in a period of orogenesis and continental assembly *ca.* 3.2 Ga (Fig. 2). The study area has traditionally been divided into several terranes, including the Barberton Greenstone Belt (BGB; Anhaeusser, 1969; Lowe and

Byerly, 1999; Viljoen and Viljoen, 1969) and the Ancient Gneiss Complex (AGC; Compston, 1988; Hunter et al., 1978; Jackson, 1984). The AGC is composed primarily of banded felsic to mafic orthogneisses which intruded and were metamorphosed and deformed during several distinct periods at 3.55-3.50 Ga, *ca.* 3.45 Ga, and *ca.* 3.23 Ga (Compston, 1988; Hunter et al., 1978; Jackson, 1979, 1984; Kröner et al., 1989; Schoene and Bowring, 2004). The BGB was erupted, intruded, and deposited over roughly the same period of time, but is composed of dominantly supracrustal rocks including mafic to ultramafic lavas, cherts, banded iron formations, and a heterogeneous sequence of siliciclastics (Anhaeusser, 1969, 1976; Condie et al., 1970; de Wit, 1982; de Wit et al., 1987; Eriksson, 1980; Lowe and Byerly, 1999; Viljoen and Viljoen, 1969). Also present along the margins of the BGB are plutonic rocks, ranging in composition from tonalitic to granitic, which give ages that fall roughly into four age groups: ca. 3.51, 3.45, 3.23 and 3.11 Ga (Anhaeusser et al., 1981; Armstrong et al., 1990; de Ronde and Kamo, 2000; Kamo and Davis, 1994; Kisters and Anhaeusser, 1995; Westraat et al., 2005).

An important aspect of the thermotectonic history of the region involves the juxtaposition of lower-grade rocks of the BGB and the higher-grade plutonic complexes that surround them. P-T estimates and $^{40}Ar/^{39}Ar$ hornblende data show that portions of the BGB were never subjected to metamorphic grades above greenschist to lower-amphibolite (Cloete, 1991; Lopez Martinez et al., 1992; Xie et al., 1997). To the south of the BGB, slivers of mafic semipelites within the plutonic complexes yield P-T estimates from upper-amphibolite to granulite grade conditions (Diener et al., 2005; Dziggel et al., 2002; Kisters et al., 2003; Stevens et al., 2002). A period of major convergent tectonism and inferred terrane accretion ca. 3.23 Ga imposed the dominant NE-SW structural trend

of the belt (de Ronde and de Wit, 1994; de Ronde and Kamo, 2000; Heubeck and Lowe, 1994; Jackson et al., 1987; Kamo and Davis, 1994; Lowe, 1999), and may be responsible for the high-grade metamorphism in the plutonic complexes at the south of the belt (Diener et al., 2005; Dziggel et al., 2002; Kisters et al., 2003; Stevens et al., 2002). Following NW-SE convergent tectonism, there was a transition towards NE-SW strike-slip to transtensional faulting through at least the central belt (de Ronde and de Wit, 1994; de Ronde and Kamo, 2000; Jackson et al., 1987). Extensional kinematics are inferred to be either the result of a gravitational collapse immediately following ca. 3.23 Ga orogenesis (Kisters et al., 2003) or ~100 Myr later contemporaneous with ca. 3.11 Ga granitic intrusions (de Ronde and de Wit, 1994; Jackson et al., 1987; Kamo and Davis, 1994; Westraat et al., 2005). Our objective in this study is to use U-Pb thermochronology on apatite and titanite to calculate thermal histories of rocks both N and S of the BGB that can then be used in concert with structural studies and existing thermochronology to construct robust thermotectonic models that help explain the differential exhumation of rocks evidenced in the surface geology.

3. ANALYTICAL METHODS

3.1. Electron microprobe analysis

The MIT JEOL 733 Superprobe electron microprobe (EMP) facility was used for making cathodoluminescence (CL) and backscatter-electron (BSE) images of zircon, titanite and apatite. Minerals were hand-picked based on varying morphology, color, and clarity, were mounted in epoxy resin, and were polished, cleaned, and carbon-coated. BSE and

CL images were collected using a 15 keV accelerating voltage and the beam current was varied between 4 and 80 nA depending on the intensity of the luminescence.

3.2. U-Pb analytical procedure

Minerals were extracted from rock samples by standard crushing, Wilfley table, heavy-liquid and magnetic separation. Zircon fractions were pre-treated with either the air-abrasion (Krogh, 1982) or chemical-abrasion (Mattinson, 2003, 2005) technique. Air-abraded zircons and both air-abraded and unabraded titanite fractions were ultrasonicated in 30% HNO_3 for an hour, fluxed in 30% HNO_3 at ~80°C for an hour, and rinsed in ultrapure acetone and H_2O before being loaded into 300 μl Teflon FEP microcapsules and spiked with a mixed ^{233}U-^{235}U-^{205}Pb tracer. Zircon and titanite were dissolved in Parr bombs in ~120 μl 29M HF with ~25 μl 30% HNO_3 at ~210°C for 48 hours, dried, and re-dissolved in 6M HCl at ~180°C overnight. For the chemical-abrasion technique, zircons were placed in a muffle furnace at 900 ± 20°C for ~60 hours in quartz beakers before being transferred to 300 μl Teflon FEP microcapsules and leached in ~120 μl 29M HF + ~25 μl 30% HNO_3 for 12-14 hours at ~180 °C. The acid was removed from the capsules and the fractions were then rinsed in ultrapure H_2O, fluxed on a hotplate at ~80 °C for an hour in 6M HCl, and rinsed in ultrapure H_2O and 30% HNO_3. Fractions were then spiked and fully dissolved using the procedure described above.

Imaged apatite grains were broken and removed from epoxy resin by pushing a stainless steel tool into the epoxy next to the desired grain. All apatite fractions were hand-picked, rinsed and ultrasonicated in ultrapure H_2O and acetone prior to loading into single 300 μl FEP teflon microcapsules. Apatite was then spiked with the mixed ^{233}U-

^{235}U-^{205}Pb tracer and dissolved in 12N HCl overnight in a Parr bomb at 180 °C, dried down and redissolved in 6N HCl overnight.

Clear, non-metamict, and inclusion-free feldspar grains, handpicked from non-magnetic separates, were ultrasonicated in ultrapure H_2O. Step-wise leaching of feldspar followed the procedure of Housh and Bowring (1991), modified to account for smaller sample size.

U and Pb were separated using an HCl-based single-column (zircon) or an HBr-based two-column (titanite, apatite, and feldspar leachates) anion exchange chemistry modified after Krogh (1973). Isotopic measurements were performed on a VG Sector-54 multi-collector thermal-ionization mass spectrometer at MIT. Pb and U were either loaded together (HCl-based chemistry) or on separate (HBr-based chemistry) Re filaments in a silica-gel/phosphoric acid mixture (Gerstenberger and Haase, 1997). Pb was measured by either 1) peak-hopping on a single Daly detector (for smaller beams), 2) a dynamic Faraday-Daly routine (F-D), or 3) for feldspar analyses with large 204 peaks, in static Faraday mode. U isotopic measurements were made in static Faraday mode. Mass fractionation on the Daly detector was determined to be 0.25 ± 0.04 %/a.m.u. over a wide temperature range based on analysis of the NBS-981 common Pb standard and spiked aliquots of NBS-983. Mass fractionation and detector bias on the F-D and static Faraday routines was determined to be 0.07 ± 0.04 %/a.m.u. U mass fractionation is monitored using a double spike. All common Pb for the zircon analyses was attributed to procedural blank. Total procedural Pb blanks for the HBr-based chemistry (apatite and titanite) were determined to be 1.5 ± 0.4 pg. K-feldspar leachates were assigned a Pb blank of 10 pg based on the amount of reagent used in the procedure, though the blank is

a negligible proportion of the total Pb in those analyses. U blanks are assigned a value of 0.10 ± 0.05 pg. All samples were spiked with a ^{205}Pb-^{233}U-^{235}U tracer, whose calibration is detailed in Schoene et al. (2006), in which an error of ± 0.015% is assigned to the $^{205}Pb/^{235}U$ of the tracer. U-Pb data reduction was performed using the algorithms of Ludwig (1980).

4. SAMPLE DESCRIPTIONS AND U-PB RESULTS

4.1. EKC02-51 (Kaap valley pluton)

EKC02-51 comes from the Kaap Valley pluton, a multiphase intrusion located north of the Barberton Greenstone Belt (Fig. 2). Several previous geochronologic studies have reported U-Pb and $^{40}Ar/^{39}Ar$ dates for the pluton (Armstrong et al., 1990; Kamo and Davis, 1994; Layer et al., 1992; Schoene et al., 2006). Kamo and Davis (1994) and Schoene et al. (2006) report identical $^{207}Pb/^{206}Pb$ dates of 3227 ± 1 and 3227.2 ± 0.2 Ma, respectively, which are interpreted to be the time of igneous crystallization (this study uses the same sample as in Schoene et al., 2006). The date from Kamo and Davis (1994) included both zircon and titanite fractions, indicating fast post-crystallization cooling through ~600 °C. $^{40}Ar/^{39}Ar$ hornblende dates of ca. 3212 Ma also support fast post-intrusion cooling (Layer et al., 1992).

Our sample of the Kaap Valley pluton was collected from a fresh roadcut several kilometers east of the pass on R61 between Badplaas and Barberton. EKC02-51 is a weakly-foliated fine-grained biotite tonalite containing abundant pristine zircon and apatite, but no titanite or hornblende. Thin-section analysis reveals significant low-grade

metamorphism in this rock, including chloritization of biotite and secondary epidote, clinozoisite and sericite. Mineral separates reveal two end-member populations of apatite that differ according to magnetic susceptibility, habit, and color. One end-member group is non-magnetic, clear, and of variable habit. The second end-member is primarily found in the more magnetic separates, is light blue and translucent, and form both stubby euhedral hexagonal prisms and subhedral grains. BSE images of both populations reveal no internal zonation, while CL images show patchy zoning of unclear origin (Fig. 3). There is a gradient between the two end-member populations, and so a range of grains was chosen for analysis. The different populations are difficult to distinguish in thin-section, though large (>250 μm in diameter) and/or euhedral grains are only found along grain boundaries and/or associated with biotite. Subhedral cylinders and barrels are found as inclusions in plagioclase and quartz.

Apatite from this sample was analyzed for U-Pb systematics (Table 1), including seven whole single-grains, two multi-grain fractions (a1 and a2 each had two grains), and four grains that were removed from grain mount. Three grains from grain mount were broken in half prior to analysis. The $^{207}Pb/^{206}Pb$ dates form two distinct populations (Figs. 3, 4). Fig. 5 shows the $^{207}Pb/^{206}Pb$ dates as a function of grain size. The older, ca. 3225-3220 Ma population shows a slight trend towards younger $^{207}Pb/^{206}Pb$ dates with smaller grain size, such that the MSWD of equivalence is 8.0 (Ludwig, 1998), though it is unclear whether this trend reflects cooling. The younger population gives a weighted mean $^{207}Pb/^{206}Pb$ date of 3213.0 ± 0.5 Ma (MSWD = 0.8; excluding one negatively discordant analysis, a1.29a). Of the two grains that were successfully halved and analyzed, two shards from one grain gave identical results, while one of the shards from

the other broken grain (a1.29a) was negatively discordant and yielded a much younger $^{207}Pb/^{206}Pb$ date. One other grain (a1.30) was -0.7% discordant, but gave an identical $^{207}Pb/^{206}Pb$ date to the younger population. All of the other analyses plot between ~0.0 and ~0.3% discordant and have radiogenic Pb to common Pb (Pb^*/Pb_c) ratios between ~3 and ~14 (Table 1).

4.2. AGC01-4

This sample is a biotite tonalite from an inlier of highly deformed plutonic basement rocks adjacent to the southeast margin of the BGB (Fig. 2). From near this locality, Compston (1988) and Kröner et al. (1989) reported ion-microprobe U-Pb dates of zircon from multiple samples that show a complex and enigmatic growth history between ca. 3.6 and 3.1 Ga. Our sample comes from an outcrop on the Phophonyane river, approximately one kilometer north of the main highway, from a unit that clearly cross-cuts the oldest phases of bimodal gneiss in the area, but is foliated parallel to the local fabric in those rocks. This sample yielded abundant zircon, titanite and apatite, which were analyzed for U-Pb systematics.

4.2.1. Zircon

Zircon grains from this sample are stubby to elongate dully-faceted prisms ranging in length from ~30 to 200 μm. The least magnetic separate yielded abundant cloudy to translucent grains, which reveal oscillatory zoning in BSE images, typical of magmatic zircons (see Corfu et al., 2003; Fig. 6). Fifteen air-abraded grains and nine chemical-abraded grains were analyzed for U-Pb isotope systematics. Three chemical-abraded

grains are within error of concordia and these analyses give a weighted mean $^{207}Pb/^{206}Pb$ date of 3226.1 ± 0.7 Ma (MSWD = 0.2; Fig.7).

4.2.2. Titanite

Titanite is light to dark brown in color and ranges in size from <50 μm to 250 μm (diameters measured as the average of the 3 principle axes) and is subhedral to anhedral in mineral separates. BSE images of titanite grains show faint oscillatory zoning in subhedral fragments (Fig. 6). Thin-section analysis reveals that titanite is primarily euhedral and can be as large as 500 μm, suggesting that many grains were broken during the crushing process. For this reason, only the most euhedral grains were selected, though this is an imperfect process. Eleven single grain fractions and two fractions consisting of two grains each (s4 and s7) were analyzed for U-Pb isotopes (Table 1, Fig. 8). All fractions but one (s7) are within error of concordia, and that fraction is about -6% discordant and will not be discussed further. Three of those twelve (s1, s4, and s6) were air-abraded until they had a distinctly spherical shape. The air-abraded fractions yield consistently old $^{207}Pb/^{206}Pb$ dates from about 3168-3171 Ma, while all but two of the remaining unabraded fractions show a trend between grain size and $^{207}Pb/^{206}Pb$ date from about 3140-3170 Ma (Fig. 9).

4.2.3. Apatite

Apatite picked from AGC01-4 is clear, non-magnetic and ranges from elongate cylindrical prisms to stubby cylindrical barrels. Larger grain sizes (>150 μm diameter) lack an elongate habit, with typical aspect ratios of ~2, and this distinction appears

texturally to be a primary feature, not a result of rock processing. BSE images show no zoning features, but CL images reveal oscillatory zoning in the cores with overgrowths of variable thickness (Fig. 10). Overgrowths are both bright and dark in CL and cut the internal zoning in places and are concordant to the zoning in others.

Twenty-eight apatite fractions were analyzed for U-Pb systematics (Table 1, Fig. 8). Ten grains were removed from grain mount after imaging (Fig. 8, 10). In addition, three multi-grain and nine single-grain apatite fractions were analyzed without imaging. All of the analyses are nearly concordant (except for one that is -3% discordant) and give $^{207}Pb/^{206}Pb$ dates that span over 100 Myr from about 3060 to 3170 Ma (Fig. 8). In addition, the analyses show a strong correlation between grain size and $^{207}Pb/^{206}Pb$ date (Fig. 9). Grain size was measured as 1) the width of the cylinder or barrel for single, whole grain analyses (i.e. perpendicular to the c-axis), 2) the original width of the cylinder or barrel as the grain appeared in the EMP image prior to their removal or breaking in grain mount, or 3) the average cylinder width for multi-grain analyses (which were grouped to be roughly the same grain size).

4.3. BSO4-5

This is a sample of the Pigg's Peak granite that intrudes the inlier of ca. 3.2-3.6 Ga basement rocks where AGC01-4 was sampled (Fig. 2). Our sample was collected at the SE margin of the basement inlier near the "falls" outcrop (Compston, 1988; Kröner et al., 1989), within several hundred meters from the contact with AGC rocks. It is a medium-grained undeformed biotite granite that clearly post-dates all deformation in the adjacent polymodal gneisses. Zircon from this sample is clear to pink and euhedral with sharp

crystal terminations. Five grains were chosen for U-Pb analysis by the chemical-abrasion method (Table 1, Fig. 11). Four of the five grains yield a $^{207}Pb/^{206}Pb$ date of 3140.3 ± 0.3 Ma (MSWD = 0.4), and we interpret this to reflect the local crystallization age of the Pigg's Peak batholith. One grain (za1) falls outside this cluster, and including it in the weighted mean does not effect the age beyond error, but raises the MSWD to 3.2. The outlier may be a result of an older, inherited domain in the grain.

5. DISCUSSION and ANALYSIS

5.1. U-Pb thermochronology in an absolute time-frame

Interpreting our U-Pb apatite and titanite data in an absolute time-frame is hampered by potential inaccuracies in the U decay constants and uncertainties in the composition of non-radiogenic Pb (Pb_c). Inaccuracies in the U decay constants are discussed elsewhere (Mattinson, 1994, 2000; Schoene et al., 2006), and introduce a bias of <0.3% between $^{206}Pb/^{238}U$ and $^{207}Pb/^{206}Pb$ dates for rocks ~3 Ga. In this study we choose to report and compare data within the $^{207}Pb/^{206}Pb$ system alone, using the ^{238}U-^{206}Pb and ^{235}U-^{207}Pb systems only to evaluate open system behavior. Therefore, any absolute inaccuracy introduced by the U decay constants is systematic and does not jeopardize our ability to quantitatively compare $^{207}Pb/^{206}Pb$ dates. Studies wishing to compare these dates with non-$^{207}Pb/^{206}Pb$ dates need to incorporate decay constant errors (see also Begemann et al., 2001; Min et al., 2000; Renne et al., 1998).

The correction for Pb_c in minerals with low Pb^*/Pb_c is the biggest source of inaccuracy in calculated U-Pb dates. Making the correction to measured ratios can be

done in three ways: 1) using a bulk-earth Pb evolution model, such as Stacey and Kramers (1975), 2) using the Pb isotopic composition from cogenetic low-μ phases, such as K-feldspar, and 3) using traditional ^{238}U-^{206}Pb and ^{235}U-^{207}Pb isochron regressions or the more powerful 3-D total Pb-U isochron (Ludwig, 1998). Isochron methods are not applicable here, given that these data obviously do not meet the required assumption that all the minerals record the same date. We have chosen instead to reduce the data using the K-feldspar step-leaching techniques of Housh and Bowring (1991), taking the values determined from the leach step with the least radiogenic Pb composition as the best estimate of initial Pb (these data are reported in the caption of Table 1). In the case of apatite from EKC02-51 and titanite from AGC01-4 (because of the relatively high Pb^*/Pb_c ratios) the difference in calculated dates between using K-feldspar Pb_c and the Stacey and Kramers (1975) estimate is on average only different by 0.3 and 1.5 Myr, respectively (Figs. 5, 9). Apatite data from AGC01-4, however, is quite dependent on the choice of Pb_c, and the data are on average ~11 Myr younger with the K-feldspar Pb_c values (Fig. 9). Though numerous studies have shown that this is probably more accurate than using the ad-hoc correction provided by the Stacey and Kramers (1975) Pb curve (Chamberlain and Bowring, 2000; Corfu, 1988; Mezger and Cosca, 1999; Schmitz and Bowring, 2001; Verts et al., 1996), the accuracy of the K-feldspar Pb correction is difficult to verify. For example, Schoene and Bowring (2006) show that U-Pb thermochronometers and K-feldspar in a quickly cooled syenite do not share the same Pb_c composition, and hypothesize that this is due to the exchange of Pb with an isotopically heterogeneous magmatic fluid over their differing closure intervals. The potential for heterogeneous Pb_c compositions within thermochronometers is even more substantial in

slowly cooled rocks, simply because of the heightened probability of complicated rock/fluid interactions over longer time-scales. Therefore, demonstration of the accuracy of the Pb_c correction in slowly cooled U-Pb thermochronometers remains a problem to be solved. What is important for this study, however, is that no correlation exists between $^{207}Pb/^{206}Pb$ date and Pb^*/Pb_c but instead between apparent age and grain size, and that the topology of this curve does not change with differing Pb_c estimates (Fig. 9). Therefore, the thermal history defined by apatite is robust, though we must be careful when comparing the absolute timing of this history relative to other data.

5.2. Volume diffusion vs. metamorphic growth

Apatite and titanite from two samples examined in this study can be interpreted to record very different thermal histories. AGC01-4 apatite and titanite show a distribution of dates versus grain size that spans over 100 Myr (Fig. 8, 9), while EKC02-51 apatite from the Kaap Valley pluton fall into two distinct clusters of dates within 15 Myr after crystallization of the pluton (Figs. 4, 5). Each sample can be used to illustrate fundamental processes controlling U-Pb systematics in these minerals, and will be discussed below.

5.2.1. EKC02-51

Apatite from the Kaap Valley pluton form two populations with distinct $^{207}Pb/^{206}Pb$ dates (Figs. 4,5), suggesting two different processes are recorded and can be interpreted in the context of two models: 1) that the older population represents primary igneous apatite that records cooling and the younger one records a period of metamorphic/hydrothermal

growth below the T_c of apatite, or 2) that the two populations, because of compositional heterogeneities, have different T_c. Experiments have been published on the diffusion of O (Farver and Giletti, 1989), Sr (Cherniak and Ryerson, 1993; Watson et al., 1985), REE (Cherniak, 2000; Watson et al., 1985), U and Mn (Cherniak, 2005), anionic halogens such as F, Cl, and OH (Brenan, 1993), and Pb (Cherniak et al., 1991; Watson et al., 1985). We know of no study that looks at compositional effects on the diffusion of Pb in apatite. Cherniak (2000) documented the dependence of trivalent REE diffusion on the method of cation substitution (coupled or non-coupled) in fluorapatite, which in turn depends on the concentration of other mono- to pentavalent cations in the crystal lattice (see summary in Pan and Fleet, 2002). Because Pb^{2+} substitutes directly for Ca^{2+} in the apatite structure, intralattice cation distribution is less likely to affect Pb diffusion, and one may expect any compositional effect on Pb diffusion to be minimal. If the closure temperature of a compositionally distinct generation of apatite was more than ~100 °C lower than the older population, then the apatite dates would reflect a complex history of slow-cooling or reheating, similar to ~3.03-3.14 Ga $^{40}Ar/^{39}Ar$ dates from biotite ($T_c \approx$ 300-350 °C; (Grove and Harrison, 1996; Harrison et al., 1985) in this pluton (Layer et al., 1992). Whether compositionally variable closure temperatures are represented in these data or not, both options 1 and 2 require the generation of multiple populations of apatite and this deserves discussion.

Numerous natural and experimental studies have documented that apatite is sensitive to variable metamorphic conditions and/or fluid compositions (Fleet et al., 2000; Fleet and Pan, 1997; Korzhinskiy, 1981; Yardley, 1985; Zhu and Sverjensky, 1991), such that intragrain variations in apatite composition can act as a robust indicator

of changing metamorphic conditions and/or fluid composition as a function of time. Krenn and Finger (2004) reported both Sr-rich (>33 wgt.%) apatite armored by garnets and Ca-rich compositions elsewhere in the rock and conclude the Sr-rich varieties preserve apatite equilibrated during high-pressure metamorphism. Grain armoring was also inferred by Loferski and Ayuso (1995), who showed that apatite occurring as multiphase inclusions in clinopyroxene have distinct Cl/(F+Cl+OH) ratios from apatite located within the groundmass. Meurer and Boudreau (1996) and Willmore et al. (2000) investigated apatite halogen composition within the Stillwater and Bushveld layered mafic intrusions, respectively. Each found distinct differences in Cl mole fraction in fluorapatite as a function of stratigraphic height and conclude that this is because the composition of fluids in the rock evolved over time and space during the late-stage magmatic history. These studies exemplify that the composition of apatite within a rock can change as a function of time depending on the degree of rock-fluid interaction; the textural setting of apatite (e.g. degree of armoring) may help determine whether or not it preserves early compositional variations.

Grain armoring may have been important in preserving the two different populations of U-Pb apatite dates recorded in EKC02-51 (Figs. 4, 5). Petrographic evidence shows that large euhedral apatite exists only along grain boundaries and as inclusions in biotite, and we infer that this population is the euhedral blue colored population in mineral separates. Secondary chlorite, epidote, clinozoisite, and white mica are also associated with euhedral apatite. Only subhedral cylinder to barrel shaped apatite is found as inclusions in quartz and plagioclase. It therefore seems plausible that the older population is represented by grains that are armored by quartz or feldspar and

the younger population is associated with metamorphic/hydrothermal processes. Igneous apatite originally located on grain boundaries or otherwise accessible by fluid flow must have been dissolved or recrystallized during secondary apatite growth because there is no evidence of mixing between the two populations. Therefore, chemical equilibration of apatite during metamoprhism would have occurred by dissolution/reprecipitation and not diffusion or mineral overgrowth.

5.2.2. AGC01-4

Apatite from AGC01-4 gives $^{207}Pb/^{206}Pb$ dates that span over 100 Myr (Figs. 8, 9). Such a spread in dates could be the result of mixing portions of grains with different ages, which is supported by CL images that reveal fine-scale oscillatory zoning in cores typically overgrown and/or truncated by rims with broad to patchy zoning (Fig. 10). To test this hypothesis, grains a1.5 and a2.5 were imaged, broken, and removed from grain mount and analyzed for U and Pb in order to isolate portions of the grains near the edge (Fig. 10). Fragments with a proportionally larger amount of material near the grain edge are distinctly younger (i.e. a1.5b is younger than a1.5a and a2.5a is younger than a2.5b; Fig. 10), which is consistent with isotopic zonation from core to rim. In addition, grain a1.2 was microsampled to isolate one of the overgrowths in three dimensions by removing a thin slice of material parallel to the imaged surface (a1.2b; Fig. 10). One would expect that fragment to be distinctly younger than a1.2c if the apparent metamorphic overgrowth occurred after the rock passed below the T_c of apatite. Instead, dates for a1.2b and a1.2c are within error. These observations suggest that there is a gradient in $^{207}Pb/^{206}Pb$ date within the apatites, but that it is not resulting from metamorphic overgrowth. Also, the

strong correlation of date with grain size would not be expected from mixing igneous and metamorphic growth zones. We should note that on the *a-t* curve in Fig. 9, the grains which were removed from grain mount all plot slightly below the whole-grain analyses, such that they are slightly younger for a given grain size. This is because when the grains were removed from the mounts, it became apparent that more than 50% of the material was removed during polishing, thereby increasing the proportion of material near the grain edge. These data are best explained by volume diffusion of Pb through the crystal lattice with the grain size as the effective diffusion dimension, as predicted by Dodson (1973, 1986). Because these apatite retain that information, it suggests not only that the grain size is a good proxy for the effective diffusion dimension, but also that the metamorphic rims observed in CL images grew above the closure temperature of apatite at an unrecorded time.

Titanite from AGC01-4 also show a correlation between $^{207}Pb/^{206}Pb$ date and grain size (Fig. 9). Two of the larger fractions (s5 and s14) deviate from this trend, yielding both older and younger dates and this anomalous behavior may be explained by 1) unrecognized zircon inclusions in the grain, 2) if the picked fractions were not, in fact, whole grains but instead broken shards of once larger grains, or 3) if cracks or metamictization in the grains produced fast-diffusion pathways for Pb-loss. In any case, we regard the *a-t* relationship as robust despite the two outliers. The three grains that were air-abraded to isolate their cores give nearly identical $^{207}Pb/^{206}Pb$ dates of ~3170 Ma regardless of the grain size (grain sizes were measured post-abrasion). As with the apatite, these observations are consistent with titanite that have the grain size acting as the effective diffusion dimension.

5.3. Testing for slow-cooling or reheating with numerical modeling

The interpretation that volume diffusion is the primary control on the measured dates in both apatite and titanite from AGC01-4 implies that significant information about the thermal history of the rock is recorded in these minerals. In the analysis that follows, we use a finite-difference numerical model to explore the predicted closure-times (t) of apatite and titanite as a function of grain size (a) for varying T-t paths to test whether or not a-t curves from multiple thermochronometers are unique indicators of thermal history recorded in AGC01-4. The setup and inputs for our model are presented in the Appendix; only discussions of the particularly important input variables and the results are presented below.

We use the model to test the two ways of generating the observed a-t curves for apatite and titanite: 1) slow-cooling after crystallization of AGC01-4, and 2) fast cooling followed by thermal perturbation. These differing scenarios are shown in Figs. 12-14, with both the model T-t paths and the resulting a-t curves for apatite and titanite. The data from AGC01-4 is plotted for comparison; only whole-grain data is plotted (i.e. non-abraded titanite, non-polished apatite), as the U-Pb systematics in those grains should best approximate volume diffusion.

In the case of slow cooling, it can be shown that a single cooling rate following intrusion can explain both the apatite and the titanite data exclusively, but not both data sets together. Fig. 12 illustrates this point by showing 0.7 °C/Myr (curve 1) and 1.5 °C/Myr (curve 3) linear cooling trajectories, which can fit the a-t curve for titanite and apatite, respectively; neither curve fits both datasets. In order to produce the observed

combination of trends, a model that combines slow and fast cooling is necessary, and the best combination is shown in Fig. 12, curve 2. A *T-t* curve with such topology is necessary not only to explain the nearly overlapping closure times for titanite and apatite, but also to replicate the topology of the apatite data: relatively flat in larger grain sizes, and steepening in smaller grain sizes.

We also tested the possibility that resetting by known magmatic intrusions could have created the observed titanite and apatite *a-t* curves. We subjected the model grains to *T-t* paths that initially approximate that of EKC02-51 such that apatite closes several Myr after intrusion, and we then insert a period of reheating at either ~3110 Ma to approximate the intrusion of widespread ca. 3.1 Ga granites into the SE Kaapvaal craton (Fig. 13) or at ~3140 Ma to approximate the effect of the Pigg's Peak granite intrusion dated in this study (Fig. 14). For the ca. 3.1 Ga intrusion, a series of *T-t* paths were chosen ranging from a lower-temperature thermal perturbation of long duration (curve 1, Fig. 13) to one of higher-temperature but shorter duration (curve 3, Fig. 13). Two scenarios, illustrated by curves 1 and 2 in Fig. 13 can reproduce the titanite and apatite data, respectively, but neither can reproduce both. A high temperature, short duration thermal anomaly can produce model ages similar to both titanite and apatite, but the topology of the model *a-t* curve for apatite is convex up - opposite of the observed trend. We note that in this analysis the characteristics of the intrusion (i.e. temperature, size, and distance from the sample) are unimportant – no thermal perturbation can reproduce the mineral *a-t* data.

For a thermal perturbation at ~3140 Ma, the analysis is more sensitive to the duration and magnitude of heating. Fortunately, we know the necessary model inputs

from the local geology: the distance from the intrusion margin is known (2 km), the intrusion has been suggested to be tabular and horizontally expansive but only 1-2 kilometers thick (Jackson and Robertson, 1983), and the chemistry of the magma gives a constraint on the temperature. For an ~750 °C granite, it is necessary for the intrusion to be about 75 km wide to reset the modeled titanite to fit the data, and this results in apatite ages that are far too young (Fig. 14, curve 1). The apatite data can be reproduced with a 15 km wide intrusion, but the titanite is not reset at all (Fig. 14, curve 2). To reproduce both apatite and titanite, a short-duration, very high-temperature intrusion is necessary. For example, curve 3 in Fig. 14 corresponds to a 12 km wide, 1100 °C intrusion and curve 4 corresponds to a 4 km wide, 1360 °C intrusion; the latter of which reproduces the data but is an unrealistically high temperature for a granite. Therefore, we conclude that the cooling curve 2 in Fig. 12, which shows two periods of slow cooling interrupted by a period of fast cooling, to be the best fit to our data. The implications of this path for the geology of the Kaapvaal craton will be discussed later in the text.

5.3.2. Model uncertainties

The analysis above focuses on the mean values of the experimental data for Pb diffusion in titanite and apatite of Cherniak (1993) and Cherniak et al. (1991), respectively, though the uncertainties in D_o and E_a are important. Consideration of the uncertainties in D_o and E_a (titanite: D_o is +106/-51% and E_a is ±3.4%; apatite: errors for D_o are not reported and E_a is ±2.6%) results in considerable uncertainty in the predicted closure times of the modeled grains. These were propagated by reproducing the model run using the maximum error-bounds for D_o and E_a. The results are illustrated by the shaded gray

regions in Figs. 12-14 for a single predicted *a-t* curve. The magnitude of the errors in the predicted *t* decrease with increasing cooling rate, and therefore for non-linear *T-t* paths, these errors can affect the topology of the resulting model *a-t* curve (which is partly responsible for the asymmetry of the error envelopes). Despite the large errors in the predicted titanite closure time, the broad conclusions of the model do not change. For example, in the case of resetting, *T-t* curve 2 in Fig. 12 is the best estimate for mimicking the *a-t* curve for apatite data. The predicted *a-t* curve for titanite plots outside of the field of view in Fig. 12C and the actual data are still far outside the error envelope. Similarly, *T-t* curve 3 in Fig. 13 can reproduce the titanite data, but the errors in apatite diffusion parameters cannot account for the bad fit of the topology of the predicted *a-t* curve for apatite. Clearly, our understanding of diffusion of Pb in accessory minerals, and the uncertainties in those values, can only be aided by further experimentation under variably hydrous conditions.

5.4. Future considerations

Because our data show a clear correlation between grain size and closure date, it can be inferred that volume diffusion over the grain diameter is an important process in the transfer of Pb. Despite this observation, our data show scatter beyond the analytical error from an expected idealized *a-t* curve, suggesting that certain assumptions of the model may not have been fully met in reality. The following sections discuss the relevance of several possible sources of scatter in *a-t* curves.

5.4.1. Crystal geometry and anisotropy

The preferred *T-t* path determined above is slightly affected by the choice of diffusion geometry in the minerals. Clearly titanite is not spherical, though it was modeled as such. We regard this assumption to be of minimal importance because as long as the analyzed grains for a given phase are of similar morphology, then the topology of the *a-t* curve doesn't change and this can be more important than assumptions of diffusion geometry and therefore the absolute T_c. For example, titanite picked for analysis was as euhedral as possible, and in reality is more ellipsoidal than spherical. Picking small euhedral apatite is trivial because they closely approximate that of perfect cylinders, though larger grains (> 150 μm diameter) more closely approximate a barrel or sphere. Deviation from an ideal cylindrical shape in larger grain sizes could affect the topology of the *a-t* curve (Fig. 15).

A similar concern is that due to the crystal structures of titanite and apatite (monoclinic and hexagonal, respecitvely), one may expect diffusion of Pb to be anisotropic. In the case of apatite, the diffusion data of Cherniak et al. (1991) was measured perpendicular to the c-axis, which is identical to the modeled diffusion direction in a hexagonal crystal. The reported titanite data (Cherniak, 1993) was measured in two crystallographic directions and found to be very similar in each case, suggesting that titanite can be adequately modeled as an isotropic sphere for diffusion of Pb. These points, though probably of minor importance here, stress the need to carefully choose grains analyzed in studies such as this one.

5.4.2. Zoning and diffusion of the parent isotope

The mathematical formulation of Dodson (1973, 1986) and the model above assume that the parent isotope (in this case U) is distributed homogeneously throughout the grain and is immobile. The latter assumption is supported by diffusion experiments of uranium in apatite (Cherniak, 2005), which show that uranium diffuses much slower than both Pb and the REE. Because the apatite from AGC01-4 preserve zoning in CL images that is likely the result of REE zoning (e.g. Waychunas, 2002), uranium diffusion is likely unimportant in these grains. More important is that chemical zonation of the parent can affect the closure date of a mineral, which has been acknowledged in U-Th/He dating (Boyce and Hodges, 2005), but thus far has not been treated in the U-Pb system. Complex zonation in apatite with respect to REE, Y, Si and the halogens have been documented (Bea and Montero, 1999; Bingen et al., 1996; Jolliff et al., 1989; Rakovan et al., 1997; Rakovan and Reeder, 1994), and zonation with respect to U and Th have also been reported (Boyce and Hodges, 2005). Such zonation is most important for whole-grain Pb/U analysis if high-U zones exist near the grain edge. Fig. 15 illustrates this point using results from our model in which high U concentrations were placed in the outer 10% of the grain radius, and these models yield anomalously low calculated ages (Fig. 15). Because high-U rims in accessory minerals are commonplace, this effect may help explain the observed scatter in *a-t* curve in AGC01-4 (Fig. 9).

5.4.3. Boundary conditions

Our model imposes a zero concentration boundary condition for Pb* on the grain margins (see Appendix), which in reality assumes that the grains are encased in an infinite

reservoir of constant Pb concentration and isotopic composition. In reality, diffusion across the boundary of the thermochronometer will be dictated by the partition coefficient for Pb (as a function of temperature) between the grain (e.g. titanite or apatite) and the adjacent phase(s), which cannot be inferred using bulk sample crushing. In the worst-case scenario, the mineral would be entirely encased in a phase with very slow diffusion of Pb, such as garnet or zircon, and therefore prevent escape of Pb and raise the effective T_c. Remedying this problem by establishing petrographic context prior to ID-TIMS U-Pb analysis is not likely to be useful given the difficult necessity of recovering whole or half grains for quantitative thermochronology. In situ U-Pb analysis of apatite, for example by SIMS, is not likely to be useful for establishing *a-t* curves or characterizing intragrain age gradients because of large errors on individual $^{207}Pb/^{206}Pb$ dates (e.g. ± 30-100 Myr in Paleoproterozoic grains; Sano et al., 1999). Given the composition of AGC01-4 (tonalitic), it is likely that all the minerals analyzed were either located along grain boundaries or included in feldspar or quartz. No diffusion studies of Pb in quartz have been published, but the T_c of Pb in feldspar is likely similar to that of apatite (Cherniak, 1995) and would not restrain diffusion of Pb* across its grain boundary. Therefore, while this may affect closure dates of some of the minerals, the robustness of the *a-t* curves suggests it is of minimal concern. The more important effect of matrix composition is in the Pb_c correction, as discussed above.

5.5. Implications for the geology of the SE Kaapvaal craton

The precisely constrained cooling histories from NW and SE of the Barberton Greenstone Belt (BGB), represented by samples EKC02-51 and AGC01-4, respectively, show that

rocks on either side of the belt experienced drastically different cooling histories between ca. 3.2 and 3.1 Ga (Figs. 2, 16). Layer et al. (1992) documented fast cooling in the Kaap valley pluton in the $^{40}Ar/^{39}Ar$ systematics of hornblende and biotite (Fig. 16), and interpreted those data to represent emplacement of the pluton to mid-crustal depths, followed by a variable thermal effect of ca. 3.1 Ga granites depending on sample locality. Our U-Pb apatite data from the Kaap Valley pluton are consistent with those data.

The model cooling path determined above for AGC01-4 (Fig. 12, 16) can be interpreted as follows: 1) emplacement of granodiorite into the middle- to lower-crust, where it resided for ~80 Myr, 2) exhumation to the middle to upper crust coincident with intrusion of the Pigg's Peak batholith ca. 3140 Ma, and 3) slow-cooling during thermal equilibration of the BGB after the period of 3.1 Ga granitic intrusion. Modeling studies have shown that differential cooling paths in adjacent terranes can be strongly controlled by differential heat production by varying concentrations of U, Th, and K (Flowers et al., 2004, 2005; Huerta et al., 1996; Royden, 1993). However, such models cannot account for the period of rapid cooling evident in AGC01-4. The sharp changes in the cooling rates must be due to some combination of tectonic and erosional processes. In this case, assuming a linear geotherm between 15 and 35 °C/km gives exhumation rates between 1.3 and 0.6 mm/yr for the 12 Myr period of ~20 °C/Myr cooling in AGC01-4. If exhumation were due entirely to erosion (and the geotherm was constant over time), these rates would be reasonable for areas of moderate topography (e.g. Burbank, 2002). This translates into 7-16 km of vertical exhumation over 12 Myr of rapid cooling for the stated geotherms, and requires a major modification of crustal structure.

Attaching a tectonic impetus to the observed exhumation is difficult because geochronologic constraints on tectonic activity after ~3.2 Ga are rare. The necessary period of exhumation along the eastern margin of the BGB begins at the time of the intrusion of the Pigg's Peak batholith ca. 3140 Ma and prior to the intrusion of the ca. 3107 Ga Mpuluzi and Nelspruit batholiths to the south and north of the BGB (Fig. 2). It is widely documented that following ca. 3.23 Ga convergence and thrust-faulting within the greenstone belt, the primary kinematics of the area switched to transtension and extension (de Ronde and de Wit, 1994; de Ronde and Kamo, 2000; Jackson et al., 1987). A proposed mechanism for this transition is extensional collapse of the ca. 3.23 Ga orogen (de Ronde and de Wit, 1994; Jackson et al., 1987; Kamo and Davis, 1994; Kisters et al., 2003), though the timing is poorly constrained. De Ronde et al. (1991) document movement on one such shear zone in BGB near the Kaap Valley pluton to have occurred between 3126±21 and 3084±18 Ma by dating zircon and rutile from a syntectonic porphyry. It seems likely then, given the current geologic constraints, that the exhumation inferred from our data and modelling is connected to the observed transtension of the crust. The resulting crustal thinning may be responsible for induced heating and melting in the lower crust and the production of the Pigg's Peak batholith to the SE and the ca. 3.1 Ga granites elsewhere. Detailed mapping has revealed that along the borders of the Mpuluzi batholith, the rocks intruded into transcurrent shear zones (Westraat et al., 2005), consistent with this interpretation. When movement on these shear zones stopped is unclear, though our data suggest that significant horizontal thermal gradients existed across the BGB for at least 50 Myr after granitoid intrusion, indicated by the youngest apatite age in AGC01-4 compared to that in the Kaap valley pluton.

Thus, the U-Pb thermochronology reported in this study record both differential exhumation across the BGB ca. 3.2-3.1 Ga and also track the thermal imprint left by granitic intrusion during cratonization ca. 3.1-3.0 Ga.

APPENDIX: FINITE-DIFFERENCE MODEL SETUP

To model the diffusion of Pb within apatite and titanite, we use a one-dimensional forward-time center-space finite difference code based on the 1D diffusion equation:

$$\frac{\partial C}{\partial t} = D(T,t)\frac{\partial^2 C}{\partial x^2},$$

in which C is the concentration of Pb [moles/m], t is time [sec] and, x is the radial distance from the grain's center [m]. D, the diffusion coefficient [m^2/sec], is subject to the Arhenius relationship:

$$D = D_o \exp\left[\frac{-E_a}{RT(t)}\right].$$

Values for D_o and E_a for titanite and apatite were measured experimentally by Cherniak (1993) and Cherniak et al. (1991), respectively, R is the gas constant [J/mole/K], and $T(t)$ is temperature [K] as a function of time [sec]. T-t curves were constructed by (1) using conjoined segments of linear dT/dt of various durations, or (2) a combination of linear cooling and exponential cooling/reheating that was approximated using the error function solution to the diffusion equation for intrusions of various widths (Carslaw and Jaeger, 1959; Royden, 1993; Turcotte and Schubert, 1982).

Modeled minerals were generated over varying grain radii with a set number of nodes across the radius of each grain. The parent isotope was assigned a concentration for each node along the radius of the grain and allowed to generate daughter product as a function of time. The parent was not allowed to diffuse, and the daughter was allowed to diffuse according the above equations. The concentration of daughter at the grain edge was held constant at zero, mimicking a homogeneous infinite reservoir. Closure ages for minerals are determined by calculating the apparent age at each node based on the ratio

of parent to daughter, and to approximate the 3D nature of the problem, each node age was integrated over the appropriate volume depending on the diffusion geometry assumed (i.e. sphere for titanite or cylinder for apatite). Stability of the model was maintained by adjusting the length of a time step based on the T of that time step for a given node spacing, based on the relationship $dt = stability * dx^2 / D$. The relationship between the predicted T_c and the variables dx (as determined by the # of nodes) and stability is shown in Fig. A1; also shown is the T_c predicted analytically by Dodson (1986). Based on these curves, stability was held at 0.2 for the model runs and 100 nodes were used in each grain. The results from the modeled titanite agree very well with that predicted by Dodson (1986) in that T_c from our model agree to within 8 °C for cooling rates of <1 °C/Myr and ~5 °C for cooling rates of 10 °C/Myr (Fig. A2) using a spherical geometry. Agreement is even better for cylindrical geometries. The discrepancy between the apparent T_c likely resides in the fact that the Dodson formulation becomes inaccurate at low cooling rates (Dodson, 1973, 1986). Note that in the example here, the grain size and cooling rate are small enough such that the Dodson (1986) formulation is not restricted by diffusive isolation of grain cores (see Ganguly and Tirone, 1999). Therefore, we regard the strong agreement between the analytical and numerical approaches to indicate that our results are robust within the stated assumptions.

Acknowledgements – The authors would like to thank J. Ganguly, S. Kamo, and W.E. Hames for helpful reviews of the manuscript. Comments on an early version of the manuscript by J.P. Matzel, and general insight as well as assistance with the numerical modeling from J.W. Boyce are also gratefully acknowledged. Comments on the manuscript, prolonged discussions about the geology of the SE Kaapvaal craton, and invaluable logistical support in the field from M.J. de Wit are continually appreciated.

REFERENCES CITED

Aleinikoff, J. N., R. P. Wintsch, C. M. Fanning, and M. J. Dorais, 2002, U-Pb geochronology of zircon and polygenetic titanite from the Glastonbury Complex, Connecticut, USA: an integrated SEM, EMPA, TIMS, and SHRIMP study: Chemical Geology, v. 188, p. 125-147.

Anhaeusser, C. R., 1969, The stratigraphy, structure, and gold mineralization of the Jamestown and Sheba Hills areas of the Barberton Mountain Land, University of Witwatersrand, Johannesburg, 332 p.

Anhaeusser, C. R., 1976, The geology of the Sheba HIlls area of the Barberton Mountain Land, South Africa, with particular references to the Eureka syncline: Geological Society of South Africa Transactions, v. 79.

Anhaeusser, C. R., L. J. Robb, and M. J. Viljoen, 1981, Provisional geological map of the Barberton Greenstone Belt and surrounding granitic terrane, Eastern Transvaal and Swaziland. Scale 1:125,000: Geological Society of South Africa.

Armstrong, R. A., W. Compston, M. J. de Wit, and I. S. William, 1990, The stratigraphy of the 3.5-3.2 Ga Barberton Greenstone Belt revisited: a single zircon ion microprobe study: EPSL, v. 101, p. 90-106.

Bea, F., and P. Montero, 1999, Behavior of accessory phases and redistribution of Zr, REE, Y, Th, and U during metamorphism and partial melting of metapelites in the lower crust: An example from the Kinzigite Formation of Ivrea-Verbano, NW Italy: Geo. and Cosmo. Acta, v. 63, p. 1133-1153.

Begemann, F., K. R. Ludwig, G. W. Lugmair, K. Min, L. E. Nyquist, P. J. Patchett, P. R. Renne, C.-Y. Shih, I. M. Villa, and R. J. Walker, 2001, Call for an improved set of decay constants for geochronological use: Geochim. Cosmochim. Acta, v. 65, p. 111-121.

Bingen, B., D. Demaiffe, and J. Hertogen, 1996, Redistribution of rare earth elements, thorium, and uranium over accessory minerals in the course of amphiblite to granulite facies metamorphism: The role of apatite and monazite in orthogneiss from wouthwestern Norway: Geo. and Cosmo. Acta, v. 60, p. 1342-1354.

Boyce, J. W., and K. V. Hodges, 2005, U and Th zoning in Cerro de Mercado (Durango, Mexico) fluorapatite: Insights regarding the impact of recoil distribution of radiogenic ^{4}He on (U-Th)/He thermochronology: Chemical Geology, v. 219, p. 261-274.

Brenan, J., 1993, Kinetics of fluorine, chlorine, and hydroxyl exchange in fluorapatite: Chemical Geology, v. 110, p. 195-210.

Burbank, D. W., 2002, Rates of erosion and their implications for exhumation: Mineral. Mag., v. 66, p. 25-52.

Byerly, G. R., A. Kröner, D. R. Lowe, W. Todt, and M. M. Walsh, 1996, Prolonged magmatism and time sontraints for sediment deposition in the early Archean Barberton greenstone belt: evidence from the Upper Onverwacht and Fig Tree groups: Precambrian Research, v. 78, p. 125-138.

Carslaw, H. S., and J. C. Jaeger, 1959, Conduction of heat in solids: Oxford, Oxford Univ. Press, 510 p.

Chamberlain, K. R., and S. A. Bowring, 2000, Apatite-feldspar U-Pb thermochronometer: a reliable mid-range (~450°C), diffusion controlled system: Chem. Geol., v. 172, p. 173-200.

Cherniak, D. J., 1993, Lead diffusion in titanite and preliminary results on the effects of radiation damage on Pb transport.: Chem. Geol., v. 110, p. 177-194.

Cherniak, D. J., 1995, diffusion of Pb in plagioclase and K-feldspar investigated using Rutherford backscatter and resonant nuclear reaction analysis: Contrib. Miner. Petrol., v. 120, p. 358-371.

Cherniak, D. J., 2000, Rare earth element diffusion in apatite: Geochim. Cosmochim. Acta, v. 22, p. 3871-3885.

Cherniak, D. J., 2005, Uranium and manganese diffusion in apatite: Chem. Geol., v. 219, p. 297-308.

Cherniak, D. J., W. A. Lanford, and F. J. Ryerson, 1991, Lead diffusion in apatite and zircon using ion implantation and Rutherford Backscattering techniques: Geochim. Cosmochim. Acta, v. 55, p. 1663-1673.

Cherniak, D. J., and F. J. Ryerson, 1993, A study of strontium diffusion in apatite using Rutherford backscattering spectroscopy and ion implantation: Geochim. Cosmochim. Acta, v. 57, p. 4653-4662.

Cherniak, D. J., and E. B. Watson, 2001, Pb diffusion in zircon: Chem. Geol., v. 172, p. 5-24.

Cloete, M., 1991, An overview of metamorphism in the Barberton greenstone belt, *in* L. D. Ashwal, ed., Two Cratons and an Orogen - Excursion Guidebook and Review Articles for a Field Workshop through Selevted Archean Terranes of Swaziland, South Africa and Zimbabwe: Johannesburg, IGCP project 280, Dept. of Geology, Univ. Witwatersrand.

Compston, W., Kröner, A., 1988, Multiple zircon growth within early Archean tonalitic gneiss from the Ancient Gneiss Complex, Swaziland: EPSL, v. 87, p. 13-28.

Condie, K. C., J. E. Macke, and T. O. Reimer, 1970, Petrology and geochemistry of early Precambrian graywackes from the Fig Tree Group, South Africa: Geological Society of America Bulletin, v. 81, p. 2759-2776.

Corfu, F., 1988, Differential response of U-Pb systems in coexisting accessory minerals, Winnepeg River Subprovince, Canadian Shield: implications for Archean crustal growth and stabilization: Contrib. Mineral. Petrol., v. 98, p. 312-325.

Corfu, F., J. M. Hanchar, P. W. O. Hoskin, and P. Kinny, 2003, Atlas of zircon textures, *in* J. M. Hanchar, and P. W. O. Hoskin, eds., Zircon: Reviews in Mineralogy and Geochemistry, v. 53: Washington, D.C., Mineralogical Society of America, p. 468-500.

Corfu, F., and D. Stone, 1998, The significance of titanite and apatite U-Pb ages: Constraints for the post-magmatic thermal-hydrothermal evolution of a batholithic complex, Berens River area, northwestern Superior Province, Canada.: Geochim. Cosmochim. Acta, v. 62, p. 2979-2995.

Dahl, P. S., 1997, A crystal-chemical basis for Pb retention and fission-track annealing systematics in U-bearing minerals, with implications for geochronology: Earth Planet. Sci. Lett., v. 150, p. 277-290.

de Ronde, C. E. J., and M. J. de Wit, 1994, Tectonic history of the Barberton Greenstone Belt, South Africa: 490 million years of Archean crustal evolution: Tectonics, v. 13, p. 983-1005.

de Ronde, C. E. J., and S. Kamo, 2000, An Archean arc-arc collisional event: a short-lived (*ca.* 3 Myr) episode, Weltevreden area, Barberton greenstone belt, South Africa: Jour. Afr. Earth Sci., v. 30, p. 219-248.

de Ronde, C. E. J., S. Kamo, D. W. Davis, M. J. de Wit, and E. T. C. Spooner, 1991, Field, geochemical and U-Pb isotopic constraints from hypabyssal felsic intrusions within the Barberton greenstone belt, South Africa: Implications for tectonics and the timing of gold mineralization: Precambrian Research, v. 1991, p. 261-280.

de Wit, M. J., 1982, Gliding and overthrust nappe tectonics in the Barberton greenstone belt: Jour. Struc. Geol., v. 4, p. 117-136.

de Wit, M. J., R. A. Hart, and R. J. Hart, 1987, The Jamestown ophiolite complex, Barberton mountain belt; a section through 3.5 Ga oceanic crust.: J. African Earth Science, v. 6, p. 681-730.

Diener, J. F. A., G. Stevens, A. F. M. Kisters, and M. Poujol, 2005, Metamorphism and exhumation of the basal parts of the Barberton greenstone belt, South Africa: Constraining the rates of Mesoarchean tectonism: Precambrian Research, v. 143, p. 87-112.

Dodson, M. H., 1973, Closure temperature in cooling geochronological and petrological systems: Contrib. Mineral. Petrol., v. 40, p. 259-274.

Dodson, M. H., 1975, Kinetic processes and thermal history of rocks: Carnegie Inst. Yearbook, v. 74, p. 210-217.

Dodson, M. H., 1986, Closure profiles in cooling systems: Materials Science Forum, v. 7, p. 145-154.

Ducea, M. N., J. Ganguly, E. J. Rosenburg, P. J. Patchett, W. Cheng, and C. Isachsen, 2003, Sm-Nd dating of spatially controlled domains of garnet single crystals: a new method of high-temperature thermochronology: Earth Planet. Sci. Lett., v. 213, p. 31-42.

Dunlap, W. J., and A. K. Kronenberg, 2001, Argon loss during deformation of micas: constraints from laboratory deformation experiments: Contrib. Miner. Petrol., v. 141, p. 174-185.

Dziggel, A., G. Stevens, M. Poujol, C. R. Anhaeusser, and R. A. Armstrong, 2002, Metamorphism of the granite-greenstone terrane south of the Barberton Greenstone Belt, South Africa: an insight into the tectono-thermal evolution of the 'lower' portions of the Onverwacht Group: Precambrian Research, v. 114, p. 221-247.

Eriksson, K. A., 1980, Transitional sedimentation stules in the Moodies and Fig Tree Groups, Barberton Mountain Land, South Africa: evidence favouring an Archean continental margin: Precambrian Research, v. 12, p. 141-160.

Farver, J. R., and J. Giletti, 1989, Oxygen and strontium diffusion kinetics in apatite and potential applications to thermal history determinations: Geo. and Cosmo. Acta, v. 53, p. 1621-1631.

Fleet, M. E., X. Liu, and Y. Pan, 2000, Rare-earth elements in chlorapatite [$Ca_{10}(PO_4)_6Cl_2$: Uptake, site preference, and degredation of monoclinic structure: Amer. Mineral., v. 85, p. 1437-1446.

Fleet, M. E., and Y. Pan, 1997, Site preference of rare earth elements in fluorapatite: Binary (LREE+HREE)-substituted crystals: Amer. Mineral., v. 82, p. 870-877.

Flowers, R. M., L. H. Royden, and S. A. Bowring, 2004, Isostatic constraints on the assembly, stabilization, and preservation of cratonic lithosphere: Geology, v. 32, p. 321-324.

Flowers, R. M., L. H. Royden, and S. A. Bowring, 2005, Isostatic constraints on lithospheric thermal evolution: Application to the Proterozoic orogen of the southwestern, U.S., *in* K. E. Karlstrom, and G. R. Keller, eds., Geophysical Monograph Series: Lithospheric structure and evolution of the Rocky Mountain region, v. 154.

Franz, G., and F. S. Spear, 1985, Aluminous titanite (sphene) from the eclogite zone, South-central Tauern Window, Austria: Chemical Geology, v. 50, p. 33-46.

Frost, B. R., K. R. Chamberlain, and J. C. Schumacher, 2000, Sphene (titanite): phase relations and role as a geochronometer: Chemical Geology, v. 172, p. 131-148.

Ganguly, J., and M. Tirone, 1999, Diffusion closure temperature and age of a mineral with arbitrary extent of diffusion: theoretical formulation and applications: Earth Planet. Sci. Lett., v. 170, p. 131-140.

Ganguly, J., M. Tirone, and R. Hervig, 1998, Diffusion kinetics of samarium and neodymuim in garnet, and a method of determining cooling rates of rocks: Science, v. 281, p. 805-807.

Gerstenberger, H., and G. Haase, 1997, A highly effective emitter substance for mass spectrometric Pb isotope ratio determinations: Chem. Geol., v. 136, p. 309-312.

Gromet, L. P., 1991, Direct dating of deformational fabrics, Short Course Handbook on Applications of Radiogenic Isotope Systems to Problems in Geology, Mineralogical Association of Canada, p. 167-189.

Grove, M., and T. M. Harrison, 1996, $^{40}Ar^*$ diffusion in Fe-rich biotite: Amer. Mineral., v. 81, p. 940-951.

Harrison, T. M., 1981, Diffusion of ^{40}Ar in hornblende: Contrib. Miner. Petrol., v. 78, p. 324-331.

Harrison, T. M., I. Duncan, and I. McDougall, 1985, Diffusion of ^{40}Ar in biotite; temperature, pressure and compositional effects: Geochim. Cosmochim. Acta, v. 49, p. 2461-2468.

Hawkins, D. P., and S. A. Bowring, 1999, U-Pb monzaite, xenotime and titanite geochronological constraints on the prograde to post-peak metamorphic thermal history of Paleoproterozoic migmatites from the Grand Canyon, Arizona: Contrib. Mineral. Petrol., v. 134, p. 150-169.

Heubeck, C., and D. R. Lowe, 1994, Late syndepositional deformation and detachment tectonics in the barberton Greenstone Belt, South Africa.: Tectonics, v. 13, p. 1514-1536.

Hodges, K. V., 2003, Geochronology and thermochronology in orogenic systems: Treatise on Geochemistry, v. 3, p. 263-292.

Housh, T., and S. A. Bowring, 1991, Lead isotopic heterogeneities within alkali feldspars: implications for the determination of initial lead isotopic compositions: Geochim. Cosmochim. Acta, v. 55, p. 2309-2316.

Huerta, A. D., L. H. Royden, and K. V. Hodges, 1996, The interdependence of deformational and thermal processes in mountain belts: Science, v. 273, p. 637-639.

Hunter, D. R., F. Barker, and H. T. Millard, 1978, The geochemical nature of the Archean Ancient Gneiss Complex and granodiorite suite, Swaziland: a preliminary study: Precambrian Research, v. 7, p. 105-127.

Jackson, M. P. A., 1979, High-strain deformation of the Ancient Gneiss Complex in the Mankayane area, Swaziland: a preliminary account (abstr.): Geological Society of South Africa - 18th congress, v. 1, p. 210-216.

Jackson, M. P. A., 1984, Archean structural styles in the Ancient Gneiss Complex of Swaziland, southern Africa, *in* A. Kröner, and R. Greiling, eds., Precambrian Tectonics Illustrated: Stuttgart, Schweizerbart'sche Verlagsbuchhandlung, p. 1-18.

Jackson, M. P. A., K. A. Eriksson, and C. W. Harris, 1987, Early Archean foredeep sedimentation related to crustal shortening: a reinterpretation of the Barberton Sequence, southern Africa: Tectonophysics, v. 136, p. 197-221.

Jackson, M. P. A., and D. I. Robertson, 1983, Regional implications of early-Precambrian strains in the Onverwacht Group adjacent to the Lochiel Granite, northwest Swaziland, *in* C. R. Anhaeusser, ed., Contributions to the geology of the Barberton Mountain Land, v. 9, Geol. Soc. S. Africa Spec. Publ., p. 45-62.

Jolliff, B. L., J. J. Papike, C. K. Shearer, and N. Shimizu, 1989, Inter- and intra-crystal REE variations in apatite from the Bob Ingersoll Pegmatite, Black Hills, South Dakota: Geo. and Cosmo. Acta, v. 53, p. 429-441.

Kamo, S., and D. W. Davis, 1994, Reassessment of Archean crustal development in the Barberton Mountain Land, South Africa, based on U-Pb dating: Tectonics, v. 13, p. 167-192.

Ketchum, J. W. F., L. M. Heaman, T. E. Krogh, N. G. Culshaw, and R. A. Jamieson, 1998, Timing and thermal influence of late orogenic extension in the lower crust: a U-Pb geochronological study from the southwest Grenville orogen, Canada: Precambrian Research, v. 89, p. 25-45.

Kisters, A. F. M., and C. R. Anhaeusser, 1995, Emplacement features of Archean TTG plutons along the southern margin of the Barberton greenstone belt, South Africa: Precambrian Research, v. 75, p. 1-15.

Kisters, A. F. M., G. Stevens, A. Dziggel, and R. A. Armstrong, 2003, Extensional detachment faulting and core-complex formation in the southern Barberton granite-greenstone terrain, South Africa: evidence for a 3.2 Ga orogenic collapse: Precambrian Research, v. 127, p. 335-378.

Korzhinskiy, M. A., 1981, Apatite solid solutions as indicators of the fugacity of HCl and HF in hydrothermal fluids: Geochem. Intl., v. 3, p. 45-60.

Krenn, E., and F. Finger, 2004, Metamorphic formation of Sr-apatite and Sr-bearing monazite in a high-pressure rock from teh Bohemian Massif: Amer. Mineral., v. 89, p. 1323-1329.

Krogh, T. E., 1973, A low contamination method for hydrothermal decomposition of zircon and extraction of U and Pb for isotopic age determination: Geochim. Cosmochim. Acta, v. 37, p. 485-494.

Krogh, T. E., 1982, Improved accuracy of U-Pb zircon ages by the creation of more concordant systems using an air abrasion technique: Geochim. Cosmochim. Acta, v. 46, p. 637-649.

Kröner, A., W. Compston, and I. S. William, 1989, Growth of early Archean crust in the Ancient Gneiss Complex of Swaziland as revealed by single zircon dating: Tectonophysics, v. 161, p. 271-298.

Kröner, A., E. Hegner, J. I. Wendt, and G. R. Byerly, 1996, The oldest part of the Barberton granitoid-greenstone terrain, South Africa: evidence for crust formation between 3.5 and 3.7 Ga: Precam. Res., v. 78, p. 105-124.

Layer, P. W., A. Kröner, and D. York, 1992, Pre-3000 Ma thermal history of the Archean Kaap Valley pluton, South Africa: Geology, v. 20, p. 717-720.

Loferski, P. J., and R. A. Ayuso, 1995, Petrography and mineral chemistry of the composite Deboullie pluton, northern Maine, U.S.A.: Implications for the genesis of Cu-Mo mineralization: Chem. Geol., v. 123, p. 89-105.

Lopez Martinez, M., D. York, and J. A. Hanes, 1992, A $^{40}Ar/^{39}Ar$ geochronological study of komatiites and komatiitic basalts from the Lower Onverwacht Volcanics: Barberton Mountain Land, South Africa: Precambrian Research, v. 57, p. 91-119.

Lowe, D. R., 1999, Geologic evolution of the Barberton Greenstone Belt and vicinity, *in* D. R. Lowe, and G. R. Byerly, eds., Geologic evolution of the Barberton Greenstone Belt, South Africa, v. Special Paper 329: Boulder, Geol. Soc. Amer., p. 287-312.

Lowe, D. R., and G. R. Byerly, 1999, Geologic evolution of the Barberton Greenstone Belt, South Africa, v. Special Paper 329: Boulder, CO, Geol. Soc. Amer.

Lucassen, F., and R. Becchio, 2003, Timing of high-grade metamorphism: Early Paleozoic U-Pb formation ages of titanite indicate long-standing high-T conditions at the western margin of Gondwana (Argetina, 26-29°): Jour. Met. Geol., v. 21.

Ludwig, K. R., 1980, Calculation of uncertainties of U-Pb isotope data: Earth Planet. Sci. Lett., v. 46, p. 212-220.

Ludwig, K. R., 1998, On the treatment of concordant uranium-lead ages: Geochim. Cosmochim. Acta, v. 62, p. 665-676.

Mattinson, J. M., 1994, Real and apparent concordance and discordance in the U-Pb systematics of zircons: limitations of "high-precision" U/Pb and Pb/Pb ages: Eos, v. 75, p. 691.

Mattinson, J. M., 2000, Revising the "gold standard" – the uranium decay constants of Jaffey et al., 1971: Eos Trans. AGU, Spring Meet. Suppl., Abstract V61A-02.

Mattinson, J. M., 2003, CA (chemical abrasion)-TIMS: high-resolution U-Pb zircon geochronology combining high-temperature annealing of radiation damage and multi-step partial dissolution analysis: Eos Trans. AGU, Fall Meet. Suppl., Abstract V22E-06.

Mattinson, J. M., 2005, Zircon U-Pb chemical-abrasion ("CA-TIMS") method: combined annealing and multi-step dissolution analysis for improved precision and accuracy of zircon ages: Chem. Geol., v. 220, p. 47-56.

McDougall, I., and T. M. Harrison, 1999, Geochronology and Thermochronology by the $^{40}Ar/^{39}Ar$ method: New York, NY, Oxford University Press.

Meurer, W. P., and A. E. Boudreau, 1996, An evaluation of models of apatite compositional variability using apatite from the Middle Banded series of the Stillwater Complex, Montana: Contrib. Miner. Petrol., v. 125, p. 225-236.

Mezger, K., and M. A. Cosca, 1999, The thermal history of the Eastern Ghats Belt (India) as revealed by U-Pb and $^{40}Ar/^{39}Ar$ dating of metamorphic and magmatic minerals: implications for the SWEAT correlation: Precam. Res., v. 1999, p. 251-271.

Mezger, K., G. N. Hanson, and S. R. Bohlen, 1989, High-precision U-Pb ages of metamorphic rutile: application to the cooling history of high-grade terranes: Earth Planet. Sci. Lett., v. 96, p. 106-118.

Min, K., R. Mundil, P. R. Renne, and K. R. Ludwig, 2000, A test for systematic errors in $^{40}Ar/^{39}Ar$ geochronology through comparison with U-Pb analysis of a 1.1 Ga rhyolite: Geochim. Cosmochim. Acta, v. 64, p. 73-98.

Mulch, A., M. A. Cosca, and M. R. Handy, 2002, *In-situ* UV-laser $^{40}Ar/^{39}Ar$ geochronology of a micaceous mylonite; an example of defect-enhanced argon loss: Contrib. Miner. Petrol., v. 142, p. 738-752.

Pan, Y., and M. E. Fleet, 1996, Rare earth mobility during prograde granulite facies metamorphism: significance of flourine: Contrib. Miner. Petrol., v. 123, p. 251-262.

Pan, Y., and M. E. Fleet, 2002, Compositions of the Apatite-Group minerals: substitution mechanisms and controlling factors, *in* M. J. Kohn, J. Rakovan, and J. M. Hughes, eds., Phosphates: Geochemical, Geobiological, and Materials Importance, v. Reviews in Mineralogy and Geochemistry 48: Washington, D.C., Mineralogical Society of America, p. 13-49.

Pidgeon, R. T., D. Bosch, and O. Bruguier, 1996, Inherited zircon and titanite U-Pb systems in an Archean syenite from southwestern Australia: implications for U-Pb stability of titanite: EPSL, v. 141, p. 187-198.

Rakovan, J., D. K. McDaniel, and R. J. Reeder, 1997, Use of surface-controlled REE sectoral zoning in apatite from Llallagua, Bolivia, to determine a single-crystal Sm-Nd age.: Earth and Planetary Science Letters, v. 146, p. 329-336.

Rakovan, J., and R. J. Reeder, 1994, Differential incorporation of trace-elements and dissymmetrization in apatite – the role of surface-structure during growth: American Mineralogist, v. 79, p. 892-903.

Reiners, P. W., and T. A. Ehlers, eds., 2005, Low-Temperature Thermochrology: Techniques, Interpretations, and Applications: Reviews in Mineralogy and Geochemistry, v. 58: Chantilly, VA, The Mineralogy Society of America.

Renne, P. R., D. B. Karner, and K. R. Ludwig, 1998, Absolute ages aren't exactly: Science, v. 282, p. 1840-1841.

Royden, L. H., 1993, The steady-state thermal structure of eroding orogenic belts and accretionary prisms: Jour. Geophys. Res., v. 98, p. 4487-4507.

Sano, Y., K. Terada, H. Hidaka, K. Yokoyama, and A. P. Nutman, 1999, Paleoproterozoic thermal events recorded in the ~4.0 Ga Acasta gneiss, Canada: Evidence from SHRIMP U-Pb dating of apatite and zircon: Geo. and Cosmo. Acta, v. 63, p. 899-905.

Schmitz, M. D., and S. A. Bowring, 2001, U-Pb zircon and titanite sytematics of the Fish Canyon Tuff: an assessment of high-precision U-Pb geochronology and its application to young volcanic rocks: Geochim. Cosmochim. Acta, v. 65, p. 2571-2587.

Schmitz, M. D., and S. A. Bowring, 2003, constraints on the thermal evolution of continental lithosphere from U-Pb accessory mineral thermochronometry of lower crustal xenoliths, southern Africa: Contrib. Miner. Petrol., v. 144, p. 592-618.

Schoene, B., and S. A. Bowring, 2004, Rates and mechanisms of magma emplacement in the Usutu intrusive suite: implications for ca. 3.2 Ga assembly of the Kaapvaal craton: G.S.A. abstracts with programs, v. 36, p. 46.

Schoene, B., and S. A. Bowring, 2006, U-Pb systematics of the McClure Mountain syenite: thermochronological constraints on the age of the $^{40}Ar/^{39}Ar$ standard MMhb: Contrib. Miner. Petrol., v. 151, p. 615-630.

Schoene, B., J. L. Crowley, D. C. Condon, M. D. Schmitz, and S. A. Bowring, 2006, Reassessing the uranium decay constants for geochronology using ID-TIMS U-Pb data: Geochim. Cosmochim. Acta, v. 70, p. 426-445.

Smith, M. P., and W. D. Yardley, 1999, Fluid evolution during metamoprhism of the Otago Schist, New Zealand: (II) Influence of detrital apatite on fluid salinity: J. Metamorphic. Geol., v. 17, p. 187-193.

Spear, F. S., 1993, Metamorphic Phase Equilibria and Pressure-Temperature-Time Paths: MSA monograph: Washington, D.C., Min. Soc. Amer., 799 p.

Spear, F. S., and J. M. Pyle, 2002, Apatite, Monazite, and Xenotime in Metamorphic Rocks, *in* M. J. Kohn, J. Rakovan, and J. M. Hughes, eds., Phosphates: Geochemical, Geobiological, and Materials Importance: Reviews in Mineralogy and Geochemistry, v. 48: Washington, D.C., Min. Soc. Amer.

Stacey, J. C., and J. D. Kramers, 1975, Approximation of terrestrial lead isotope evolution by a two-stage model: Earth Planet. Sci. Lett., v. 26, p. 207-221.

Stevens, G., G. T. R. Droop, R. A. Armstrong, and C. R. Anhaeusser, 2002, Amphibolite facies metamorphism in the Schapenburg schist belt: A record of the mid-crustal response to ~3.23 Ga terrane accretion in the Barberton greenstone belt: South African Journal of Geology, v. 105, p. 271-284.

Turcotte, D. L., and G. Schubert, 1982, Geodynamics: New York, John Wiley & Sons, 450 p.

Verts, L. A., K. R. Chamberlain, and C. D. Frost, 1996, U-Pb sphene dating of metamorphism: the importance of sphene growth in the contact aureole of the Red Mountain pluton, Laramie Mountains, Wyoming: Contrib. Miner. Petrol., v. 125, p. 186-199.

Viljoen, M. J., and R. P. Viljoen, 1969, An introduction to the geology of the Barberton, granite-greenstone terrain: Geol. Soc. S. Afr., Spec. Pub., v. 9, p. 1-20.

Wartho, J.-A., 1995, Apparent argon diffusive loss $^{40}Ar/^{39}Ar$ age spectra in amphiboles: Earth and Planetary Science Letters, v. 134, p. 393-407.

Watson, E. B., and T. M. Harrison, 1984, Accessory minerals and the geochemical evolution of crustal magmatic systems: a summary and prospectus of experimental approaches: Phys. Earth Planet. Int., v. 35, p. 19-30.

Watson, E. B., T. M. Harrison, and F. J. Ryerson, 1985, Diffusion of Sm, Sr, and Pb in fluorapatite: Geo. and Cosmo. Acta, v. 49, p. 1813-1823.

Waychunas, G. A., 2002, Apatite Luminescence, *in* M. J. Kohn, J. Rakovan, and J. M. Hughes, eds., Phosphates - Geochemical, geobiological, and materials importance, v. 48: Washington, D.C., The Mineralogical Society of America, p. 701-742.

Westraat, J. D., A. F. M. Kisters, M. Poujol, and G. Stevens, 2005, Transcurrent shearing, granite sheeting and the incremental construction of the tabular 3.1 Ga Mpuluzi batholith, Barberton granite-greenstone terrane, South Africa: Jour. Geol. Soc. London, v. 162, p. 373-388.

Willmore, C. C., A. E. Boudreau, and F. J. Kruger, 2000, The halogen geochemistry of the Bushveld Complex, Republic of South Africa: Implications for chalcophile element distribution in the lower and critical zones: Jour. Petrol., v. 41, p. 1517-1539.

Wilson, A. C., 1982, 1:250,000 Geological map of Swaziland: Geological Survey Mines Department.

Wright, N., P. W. Layer, and D. York, 1991, New insights into thermal history from single grain $^{40}Ar/^{39}Ar$ analysis of biotite: EPSL, v. 104, p. 70-79.

Xie, X., G. R. Byerly, and R. E. Ferrell, 1997, IIb trioctehedral chlorite from the Barberton greenstone belt; crystal structure and rock composition constraints with implications to geothermometry: Contrib. Miner. Petrol., v. 126, p. 275-291.

Yardley, B. W. D., 1985, Apatite composition and fugacities of HF and FCl in metamorphic fluids: Mineral. Mag., v. 49, p. 77-79.

Zhu, C., and D. A. Sverjensky, 1991, Partitioning of F-Cl-OH between minerals and hydrothermal fluids: Geochim. Cosmochim. Acta, v. 55, p. 1837-1858.

Figure captions:

Fig. 1: 1-D depiction of age distributions within thermochronometers as a function of radius resulting from different thermal and metamorphic histories.

Fig. 2: Location map of the eastern Kaapvaal craton. Sample locations are shown; see text for discussion. Outlined box in inset shows enlarged area. Geology compiled from Kröner et al. (1989), Lowe and Byerly (1999), and Wilson (1982). Age information from Armstrong et al. (1990), Byerly et al. (1996), de Ronde and Kamo (2000), de Ronde et al. (1991), Kamo and Davis (1994), Kröner et al. (1989), Kröner et al. (1996), and Schoene and Bowring (2004).

Fig. 3: Cathodoluminescence images of apatite from EKC02-51 (Kaap valley pluton), with fraction number in top corner. White lines are where grains were broken prior to removal from grain mount, and the corresponding $^{207}Pb/^{206}Pb$ dates are shown (*this analysis is very negatively discordant). U-Pb data are in table 1. Scale bars are 100 μm. Errors are at the 95% confidence interval.

Fig. 4: Concordia diagram for apatite from EKC02-51 (Kaap valley pluton). Also shown is the weighted mean zircon ellipse from Schoene et al. (2006), reported from the same sample. Gray band is the error envelope for the concordia curve. Errors are at the 95% confidence interval.

Fig. 5: *a-t* plot for apatite from EKC02-51. Errors on the grain diameter are estimated to be uniformly ±10 μm. Diameter is measured perpendicular to the c-axis. Errors are at the 95% confidence interval.

Fig. 6: Back-scattered electron images of typical zircon (A) and titanite (B, C) from AGC01-4. Scale bar in A is 50 μm, and in B and C is 100 μm. Note the concentric oscillatory zoning in the zircon, indicating a magmatic origin. Also note that titanite grains display weak oscillatory zoning and are subhedral, but likely broken during processing.

Fig. 7: Concordia diagram for zircon from AGC01-4 depicting both air-abraded and chemical-abraded zircon grains. (B) is blow-up of shaded region in (A). Shaded gray envelope is the error-bounds of the concordia curve. Errors are at the 95% confidence interval.

Fig. 8: Concordia diagram for titanite and apatite from AGC01-4. Shaded gray envelope is the error-bounds of the concordia curve. Errors are at the 95% confidence interval.

Fig. 9: *a-t* curves for apatite and titanite from AGC01-4. Light gray points (without error bars) represent the data reduced with the Stacey and Kramers (1975) estimate for common Pb (S&K Pbc), to show the affect of Pb_c choice. See text for further discussion, and see Table 1 caption for Pb_c from feldspar leachine. Errors on grain diameters are uniformly chosen to be ±10 μm. Diameter for apatite was measured perpendicular to the

c-axis and for titanite is the average of the 3 principle axes. Errors are at the 95% confidence interval.

Fig. 10: Cathodoluminesence images of apatite from AGC01-4, with fraction number in top corner. White lines are where grains were broken prior to removal from grain mount, and the corresponding $^{207}Pb/^{206}Pb$ dates are shown. U-Pb data is in table 1. Note that the lower a1.2 grain is meant to be a 3D depiction of how the grain was fragmented. See text for further discussion. Scale bars are 100 μm. Errors are at the 95% confidence interval.

Fig. 11: Concordia diagram for zircon from BS04-5, a granitic sample from the Pigg's Peak batholith. Shaded gray envelope is the error-bounds of the concordia curve. Errors are at the 95% confidence interval.

Fig. 12: Results from finite-difference numerical model to test whether slow cooling can explain the observed data from AGC01-4. *T-t* paths labeled 1, 2, and 3 in (A) correspond to the resulting *a-t* curves in (B) and (C) for apatite and titanite, respectively. Dates at the top of (A) are when changes in cooling rate occur in curve 2. Note that curve 2 is the optimized scenario, which fits the U-Pb data the best. Shaded regions in (B) and (C) are the error-bounds for the synthetic *a-t* curve 2. See text for discussion. Errors are at the 95% confidence interval.

Fig. 13: Results from finite-difference numerical model to test whether thermal resetting of apatite and titanite at 3110 Ma can explain the observed data from AGC01-4. *T-t*

paths labeled 1, 2, and 3 in (A) correspond to the resulting *a-t* curves in (B) and (C) for apatite and titanite, respectively. Dates at top of (A) are the dates of crystallization and intrusion of magma that causes the thermal anomaly. Shaded regions in (B) and (C) are the error-bounds for the synthetic *a-t* curves 2 and 1, respectively. See text for discussion. Errors are at the 95% confidence interval.

Fig. 14: Results from finite-difference numerical model to test whether thermal resetting of titanite and apatite at 3140 Ma can explain the observed data from AGC01-4. *T-t* paths labeled 1, 2, 3, and 4 in (A) correspond to the resulting *a-t* curves in (B) and (C) for apatite and titanite, respectively. Curves in A correspond to intrusions of the following characteristics: 1 = 75 km wide, 750 °C; 2 = 15 km wide, 750 °C; 3 = 12 km wide, 1100 °C; 4 = 4.5 km wide, 1360 °C. Gray bands in (B) and (C) are error-bounds for synthetic *a-t* curve 4. See text for discussion. Errors are at the 95% confidence interval.

Fig. 15: Results from finite-difference numerical model depicting the affects of the assumed grain geometry and U zonation. Model is run for titanite, which started cooling at 650 °C at 3224 Ma, though it is applicable to any mineral-isotope system. Note that having high U rims on a grain can result in younger ages than with uniform zonation, and can therefore result in scatter in *a-t* curves. See text for further discussion.

Fig. 16: *T-t* curves from the Kaap valley pluton (north of the BGB) and from the Ancient Gneiss Complex inlier (south of the BGB). See Fig. 2 for sample localities. South of the BGB curve is that determined from titanite and apatite data from this study in conjunction

with numerical modeling (see Figs. 12-14 and the text for discussion). Zircon dates for the Kaap Valley pluton come from Kamo and Davis (1994) and Schoene et al. (2006). ***data from de Ronde et al. (1991). **data from Kamo and Davis (1994). *data from Layer et al. (1992).

Fig. A1: Stability test of numerical model, comparing results from this model the analytical solution of Dodson (1986) for spherical titanite. See text for discussion.

Fig. A2: Quantitative comparison of spherical titanite T_c estimates from the numerical model used in this study to that of Dodson (1986) for a given cooling scenario. See text for discussion.

Table 1. U-Pb isotopic data

Sample (a)	# grains	grain diameter (b)	Pb* / Pb_c (c)	Pb_c (pg) (d)	Th / U (e)	Isotopic ratios: $^{206}Pb/^{204}Pb$ (f)	$^{208}Pb/^{206}Pb$ (g)	$^{206}Pb/^{238}U$ (g)	% err (h)	$^{207}Pb/^{235}U$ (g)	% err (h)	$^{207}Pb/^{206}Pb$ (g)	% err (h)	corr. coef.	Dates (Ma): $^{206}Pb/^{238}U$ (i)	$^{207}Pb/^{235}U$ (i)	$^{207}Pb/^{206}Pb$ (i)	% disc. (j)
EKC02-51 (Kaap valley pluton)																		
apatite																		
a1	3	90	3.8	14.5	0.04	198	0.011	0.645753	0.16	22.67103	0.22	0.25463	0.12	0.839	3211.6	3212.9	3213.8	0.09
a2	2	110	3.2	32.3	0.04	165	0.010	0.648107	0.17	22.90351	0.19	0.25630	0.08	0.904	3220.8	3222.9	3224.1	0.13
a4	1	170	5.1	29.7	0.09	254	0.023	0.646260	0.15	22.68531	0.17	0.25459	0.08	0.893	3213.6	3213.5	3213.5	0.00
a5	1	240	5.4	43.2	0.03	273	0.007	0.644832	0.09	22.62546	0.11	0.25448	0.06	0.827	3208.0	3211.0	3212.8	0.19
a6	1	110	5.2	14.9	0.02	268	0.006	0.648154	0.11	22.89598	0.13	0.25620	0.06	0.880	3221.0	3222.5	3223.5	0.10
a7	1	100	13.9	22.9	0.07	677	0.020	0.647802	0.08	22.87322	0.09	0.25608	0.05	0.852	3219.6	3221.6	3222.8	0.12
a8	1	200	7.8	66.2	0.03	386	0.009	0.647884	0.05	22.91164	0.07	0.25648	0.05	0.744	3219.9	3223.2	3225.2	0.21
a9	1	225	6.6	71.0	0.00	337	0.001	0.648811	0.08	22.94491	0.10	0.25649	0.05	0.856	3223.6	3224.6	3225.3	0.07
a10	1	275	8.7	113.3	0.03	427	0.007	0.646082	0.07	22.78394	0.08	0.25576	0.05	0.814	3212.9	3217.8	3220.8	0.31
a1.29a	<1	250	5.1	5.8	0.03	268	0.009	0.654559	0.23	22.74551	0.26	0.25203	0.10	0.918	3246.0	3216.1	3197.5	-1.93
a1.29b	<1	250	9.4	13.9	0.01	473	0.004	0.645059	0.09	22.63267	0.11	0.25447	0.06	0.856	3208.9	3211.3	3212.8	0.15
a1.30a	<1	120	3.1	10.0	0.02	164	0.005	0.650454	0.34	22.80895	0.36	0.25432	0.12	0.944	3230.0	3218.8	3211.9	-0.72
a1.33	<1	90	6.8	22.6	0.02	341	0.005	0.646313	0.06	22.80567	0.08	0.25592	0.05	0.741	3213.8	3218.7	3221.7	0.31
a1.35a	<1	150	7.5	22.7	0.01	374	0.003	0.647730	0.07	22.89238	0.11	0.25633	0.09	0.625	3219.3	3222.4	3224.3	0.20
a1.35b	<1	150	7.3	21.9	0.01	366	0.003	0.646910	0.09	22.86110	0.11	0.25630	0.07	0.790	3216.1	3221.0	3224.1	0.31
AGC01-4																		
zircon																		
z1	1	-	47.9	2.6	0.22	2453	0.071	0.528134	0.23	18.06069	0.29	0.24802	0.17	0.816	2733.6	2993.0	3172.2	16.92
z2	1	-	180.5	1.4	0.18	10143	0.068	0.437855	0.12	14.41993	0.14	0.23885	0.06	0.905	2341.0	2777.7	3112.4	29.45
z4	1	-	79.4	4.2	0.23	3885	0.073	0.523614	0.16	17.68981	0.17	0.24502	0.08	0.900	2714.5	2973.0	3152.9	17.00
z5	1	-	13.6	11.3	0.22	645	0.079	0.482140	0.14	16.03199	0.16	0.24116	0.06	0.918	2536.6	2878.7	3127.7	22.79
z6	1	-	19.3	5.0	0.17	953	0.054	0.537140	0.15	18.29210	0.17	0.24699	0.06	0.929	2771.5	3005.2	3165.6	15.28
z7	1	-	4.7	20.8	0.24	231	0.079	0.523837	0.21	17.74783	0.23	0.24572	0.08	0.931	2715.4	2976.2	3157.4	17.11
z9	1	-	1.6	12.8	0.44	81	0.174	0.411169	0.73	12.91834	0.76	0.22787	0.15	0.981	2220.3	2673.7	3037.1	31.68
z10	1	-	2.7	12.2	0.44	133	0.120	0.632324	0.39	22.25520	0.42	0.25526	0.15	0.935	3158.8	3194.9	3217.7	2.32
z11	1	-	7.2	11.3	0.26	349	0.094	0.452246	0.25	14.22166	0.30	0.22807	0.16	0.851	2405.2	2764.6	3038.6	24.90
z12	1	-	2.2	4.7	0.33	118	0.091	0.636983	0.79	22.51567	0.81	0.25636	0.15	0.982	3177.1	3206.2	3224.5	1.86
z13	1	-	21.0	3.2	0.39	980	0.147	0.442169	0.23	14.49386	0.24	0.23774	0.07	0.953	2360.3	2782.6	3104.9	28.54
z14	1	-	14.5	1.1	0.03	847	0.014	0.334743	0.54	11.35342	0.55	0.24599	0.07	0.992	1861.3	2552.6	3159.1	47.07
z15	1	-	8.3	7.7	0.31	393	0.093	0.577756	0.16	19.68108	0.20	0.24706	0.11	0.837	2939.6	3075.8	3166.0	8.89
z18	1	-	0.5	25.1	0.85	30	0.357	0.389799	0.99	12.34292	1.11	0.22965	0.41	0.929	2121.9	2630.8	3049.6	35.56
z19	1	-	1.2	5.9	0.48	68	0.160	0.503230	1.11	16.42092	1.23	0.23666	0.44	0.935	2627.7	2901.6	3097.7	18.43
za1	1	-	18.0	8.8	0.20	845	0.059	0.590673	0.10	21.67507	0.11	0.26614	0.05	0.892	2992.2	3169.3	3283.4	11.07
za2	1	-	15.7	2.2	0.23	795	0.063	0.649166	0.32	22.97418	0.32	0.25667	0.05	0.986	3224.9	3225.8	3226.4	0.06
za5	1	-	36.0	1.1	0.12	2013	0.040	0.519119	0.25	18.24451	0.26	0.25490	0.06	0.973	2695.4	3002.7	3215.4	19.73
za6	1	-	82.2	0.6	0.21	4594	0.060	0.602185	0.07	21.16657	0.09	0.25493	0.05	0.827	3038.6	3146.3	3215.6	6.90
za7	1	-	61.0	0.7	0.21	3415	0.059	0.615876	0.11	21.64515	0.12	0.25490	0.06	0.887	3093.5	3167.9	3215.4	4.77
za10	1	-	32.9	1.9	0.18	1866	0.050	0.639734	0.13	22.65198	0.14	0.25681	0.05	0.926	3188.0	3212.1	3227.2	1.54
za12	1	-	9.7	0.3	0.13	565	0.035	0.646799	0.55	22.88202	0.60	0.25658	0.21	0.939	3215.7	3221.9	3225.8	0.40
za13	1	-	19.7	0.2	0.20	1119	0.053	0.648283	0.27	22.93540	0.29	0.25659	0.09	0.953	3221.5	3224.2	3225.9	0.17
za17	1	-	8.9	0.6	0.16	520	0.042	0.638487	0.46	22.57750	0.50	0.25646	0.17	0.940	3183.1	3208.9	3225.1	1.65
titanite																		
s1	1	185	13.1	27.8	0.52	582	0.141	0.632054	0.12	21.58132	0.13	0.24764	0.06	0.896	3157.7	3165.1	3169.8	0.48
s2	1	180	6.9	120.0	0.23	332	0.063	0.629620	0.07	21.31665	0.11	0.24555	0.09	0.642	3148.1	3153.1	3156.3	0.33
s4	2	120	26.2	18.6	0.16	1247	0.044	0.632319	0.08	21.56202	0.10	0.24732	0.05	0.876	3158.8	3164.2	3167.7	0.36
s5	1	220	6.0	82.4	0.40	278	0.107	0.636272	0.13	21.90596	0.16	0.24970	0.08	0.876	3174.3	3179.6	3182.9	0.34
s6	1	210	14.8	41.8	0.36	680	0.096	0.633222	0.09	21.63886	0.10	0.24784	0.05	0.887	3162.3	3167.7	3171.0	0.35
s7	2	140	2.1	207.7	0.72	100	0.183	0.672447	0.11	23.00599	0.14	0.24813	0.08	0.809	3315.3	3227.2	3172.9	-5.75
s8	1	120	3.3	7.2	0.19	171	0.051	0.626553	0.15	20.96218	0.18	0.24265	0.08	0.889	3135.9	3136.8	3137.4	0.06
s9	1	130	4.5	7.0	0.14	233	0.038	0.627574	0.23	21.03517	0.26	0.24310	0.10	0.914	3140.0	3140.2	3140.4	0.02
s10	1	200	26.5	6.5	0.17	1285	0.045	0.630283	0.11	21.36701	0.12	0.24587	0.05	0.910	3150.7	3155.4	3158.4	0.31
s11	1	170	7.0	12.4	0.25	337	0.068	0.628332	0.14	21.22956	0.21	0.24505	0.13	0.789	3143.0	3149.1	3153.0	0.40
s12	1	190	4.7	21.6	0.31	227	0.083	0.631037	0.10	21.33124	0.12	0.24517	0.07	0.825	3153.7	3153.8	3153.8	0.01
s13	1	220	22.4	21.1	0.34	1027	0.091	0.633599	0.13	21.61638	0.14	0.24744	0.05	0.941	3163.8	3166.6	3168.4	0.19
s14	1	220	3.9	27.9	0.20	193	0.054	0.627092	0.22	21.03899	0.23	0.24333	0.08	0.939	3138.1	3140.4	3141.9	0.15

Table 1. U-Pb isotopic data (cont.)

Sample (a)	# grains	grain diameter (b)	Pb* / Pb$_c$ (c)	Pb$_c$ (pg) (d)	Th / U (e)	Isotopic ratios: $^{206}Pb/^{204}Pb$ (f)	$^{208}Pb/^{206}Pb$ (g)	$^{206}Pb/^{238}U$ (g)	% err (h)	$^{207}Pb/^{235}U$ (g)	% err (h)	$^{207}Pb/^{206}Pb$ (g)	% err (h)	corr. coef.	Dates (Ma): $^{206}Pb/^{238}U$ (i)	$^{207}Pb/^{235}U$ (i)	$^{207}Pb/^{206}Pb$ (i)	% disc. (j)
AGC01-4																		
apatite																		
a1	5	70	4.1	24.2	0.29	207	0.078	0.619091	0.19	20.37702	0.25	0.23872	0.16	0.782	3106.3	3109.4	3111.4	0.21
a2	5	55	4.3	30.1	0.26	218	0.071	0.616424	0.19	20.20308	0.21	0.23770	0.08	0.919	3095.7	3101.1	3104.7	0.36
a3	1	170	3.6	62.0	0.18	184	0.050	0.621628	0.16	20.62574	0.18	0.24065	0.08	0.892	3116.4	3121.2	3124.2	0.32
a5	1	90	3.4	71.3	0.26	170	0.070	0.616814	0.11	20.23397	0.15	0.23792	0.09	0.802	3097.2	3102.6	3106.1	0.36
a6	1	235	3.0	66.6	0.29	152	0.078	0.623436	0.10	20.75546	0.14	0.24146	0.09	0.783	3123.6	3127.2	3129.6	0.24
a7	3	60	4.3	20.2	0.23	217	0.062	0.618845	0.20	20.31393	0.22	0.23807	0.10	0.889	3105.3	3106.4	3107.1	0.07
a8	1	40	1.4	3.7	0.35	88	0.095	0.613951	0.78	19.92355	0.87	0.23536	0.38	0.897	3085.8	3087.7	3088.9	0.12
a10	1	35	3.2	7.3	0.27	181	0.074	0.608771	0.29	19.52679	0.33	0.23264	0.16	0.877	3065.1	3068.2	3070.3	0.21
a11	1	90	3.9	9.6	0.29	202	0.077	0.623017	0.11	20.69392	0.19	0.24090	0.14	0.695	3121.9	3124.4	3125.9	0.16
a12	1	120	2.6	36.6	0.21	144	0.056	0.624977	0.25	20.86188	0.28	0.24210	0.12	0.895	3129.7	3132.2	3133.8	0.17
a13	1	180	2.3	45.6	0.21	123	0.056	0.629058	0.14	20.89147	0.21	0.24087	0.14	0.747	3145.9	3133.6	3125.7	-0.81
a14	1	240	3.1	109.4	0.27	159	0.073	0.624029	0.06	20.78611	0.09	0.24158	0.06	0.688	3125.9	3128.7	3130.4	0.18
a1.2a	<1	200	2.6	7.7	0.21	146	0.058	0.623147	0.49	20.73630	0.52	0.24135	0.16	0.951	3122.4	3126.3	3128.9	0.26
a1.2b	<1	200	2.5	6.3	0.19	151	0.050	0.625954	0.97	20.92664	0.99	0.24247	0.23	0.973	3133.6	3135.2	3136.3	0.11
a1.2c	<1	200	3.2	4.5	0.23	180	0.063	0.624124	0.62	20.79129	0.64	0.24161	0.16	0.969	3126.3	3128.9	3130.6	0.17
a1.2d	<1	200	3.6	11.8	0.25	189	0.067	0.622832	0.22	20.66060	0.25	0.24059	0.11	0.897	3121.2	3122.8	3123.8	0.11
a1.5a	<1	115	2.0	29.2	0.30	109	0.082	0.622059	0.18	20.61508	0.23	0.24035	0.14	0.815	3118.1	3120.7	3122.3	0.17
a1.5b	<1	115	2.5	21.8	0.29	134	0.079	0.618046	0.11	20.25586	0.16	0.23770	0.10	0.747	3102.1	3103.7	3104.6	0.10
a1.8	<1	250	3.2	63.1	0.19	165	0.053	0.627909	0.08	21.17324	0.10	0.24456	0.07	0.774	3141.3	3146.6	3149.9	0.34
a1.11	<1	200	2.4	30.1	0.28	127	0.076	0.618502	0.13	20.32761	0.27	0.23837	0.20	0.702	3104.0	3107.1	3109.1	0.21
a1.12	<1	180	2.0	40.5	0.30	109	0.081	0.616764	0.21	20.15648	0.23	0.23703	0.10	0.906	3097.0	3098.9	3100.1	0.13
a2.2	<1	120	2.4	19.5	0.32	125	0.087	0.621540	0.18	20.58156	0.23	0.24016	0.13	0.829	3116.0	3119.1	3121.1	0.20
a2.5a	<1	122	2.3	13.0	0.19	126	0.053	0.622345	0.14	20.64705	0.18	0.24062	0.11	0.789	3119.2	3122.2	3124.1	0.19
a2.5b	<1	122	1.3	4.7	0.36	79	0.098	0.618700	1.41	20.34661	1.43	0.23851	0.36	0.967	3104.7	3108.0	3110.1	0.22
a2.6	<1	65	3.3	11.20	0.30	170	0.082	0.616637	0.17	20.14140	0.21	0.23690	0.10	0.864	3096.5	3098.2	3099.2	0.11
a2.10	<1	130	1.2	14.67	0.40	73	0.105	0.643566	0.90	21.25535	0.92	0.23954	0.25	0.963	3203.0	3150.3	3116.9	-3.51
a2.14a	<1	50	1.6	6.67	0.48	92	0.129	0.606740	0.72	19.36093	0.78	0.23143	0.29	0.928	3056.9	3060.0	3062.0	0.21
a2.14b	<1	50	1.3	6.11	0.57	79	0.154	0.605331	1.27	19.28529	1.31	0.23106	0.36	0.962	3051.3	3056.2	3059.4	0.33
BSO4-5 (Pigg's Peak batholith)																		
zircon																		
za1	1	-	520	0.23	0.49	20711	0.134	0.626060	0.11	21.00242	0.12	0.24331	0.05	0.918	3134.0	3138.7	3141.7	0.31
za2	1	-	1620	0.22	0.41	66197	0.110	0.625793	0.07	20.97847	0.08	0.24313	0.04	0.834	3132.9	3137.6	3140.6	0.31
za3	1	-	849	0.20	0.46	33785	0.124	0.624259	0.11	20.92089	0.12	0.24306	0.04	0.925	3126.8	3134.9	3140.1	0.53
za4	1	-	10907	0.16	0.41	405376	0.110	0.625586	0.05	20.96650	0.06	0.24307	0.04	0.772	3132.1	3137.0	3140.2	0.33
za5	1	-	15791	0.20	0.49	573023	0.134	0.624828	0.12	20.94386	0.12	0.24311	0.04	0.945	3129.1	3136.0	3140.4	0.45

(a) z1, z2, etc. are air-abraded zircons, za1, za2, etc. are chemical-abraded zircons
a1, a2, etc. are whole single grains or multiple grains; a1.xx, a2.xx are grains or grain fragments that were removed from grain-mount
s1, s2, etc. are whole grains or abraded grains
(b) Apatite diameter is that of a cylinder. Titanite diameter is average of 3 axes. Multi-grain fraction diameter is average of all grains
(c) Ratio of radiogenic Pb (including 208Pb) to common Pb.
(d) Total weight of common Pb.
(e) Model Th/U ratio calculated from radiogenic 208Pb/206Pb ratio and 207Pb/206Pb age.
(f) Measured ratio corrected for spike and fractionation only. Mass fractionation corrections were based on analysis of NBS-981 and NBS-983. Corrections of 0.25 ± 0.04%/amu (atomic mass unit) and 0.07 ± 0.04%/amu were applied to single-collector Daly analyses and dynamic Faraday-Daly analyses, respectively.
(g) Corrected for fractionation, spike, blank, and common Pb. Errors below are 2-sigma.
blank Pb: 206Pb/204Pb = 18.271±0.039; 207Pb/204Pb = 15.587±0.095; 208Pb/204Pb = 38.119±0.024.
Common Pb values used are from feldspar leaching (Housh and Bowring 1991; see text).
EKC02-51: 206Pb/204Pb = 12.576±0.064; 207Pb/204Pb = 14.042±0.063; 208Pb/204Pb = 32.269±0.060
AGC01-4: 206Pb/204Pb = 12.885±0.001; 207Pb/204Pb = 14.419±0.001; 208Pb/204Pb = 32.572±0.002
(h) Errors are 2 sigma, propagated using the algorithms of Ludwig (1980).
(i) Calculations are based on the decay constants of Jaffey et al. (1971).
(j) % discordance = 100 - (100 x 206Pb/238U date / 207Pb/206Pb date).

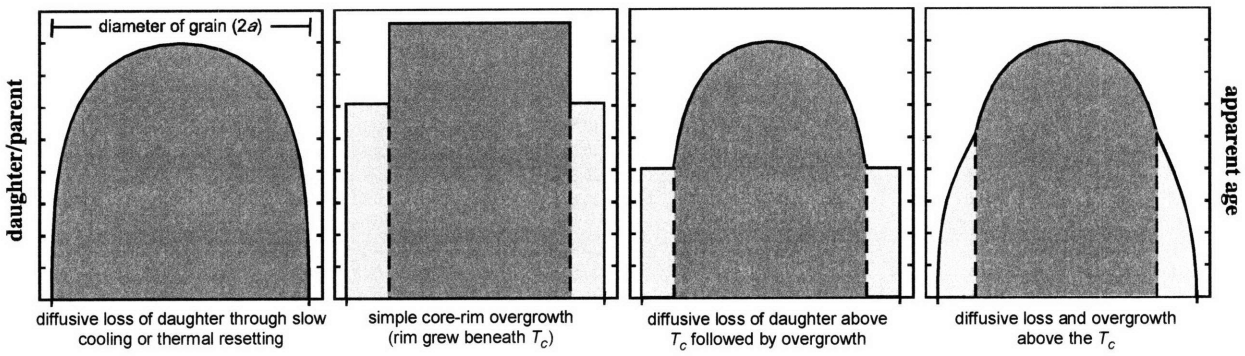

Schoene&Bowring Fig. 1

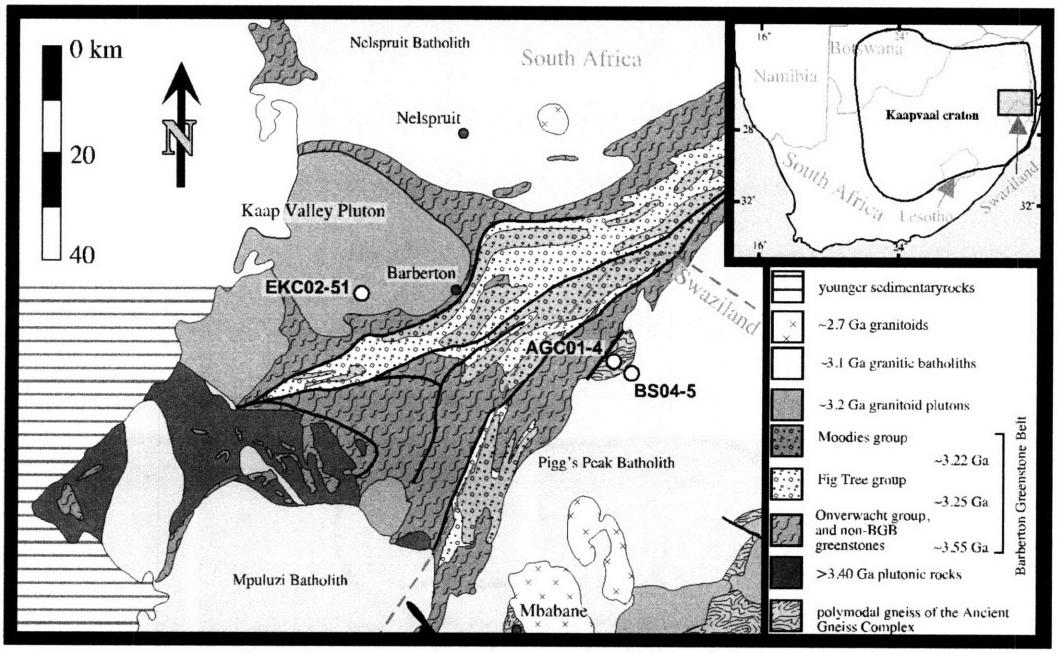

Schoene&Bowring Fig. 2

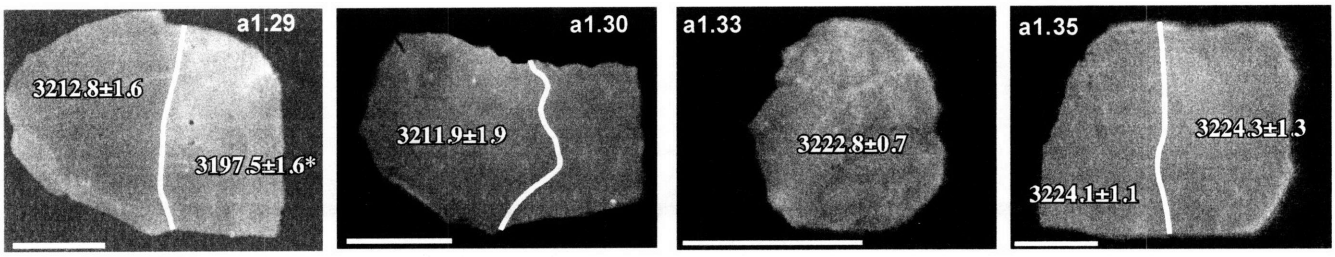

Schoene&Bowring Fig. 3

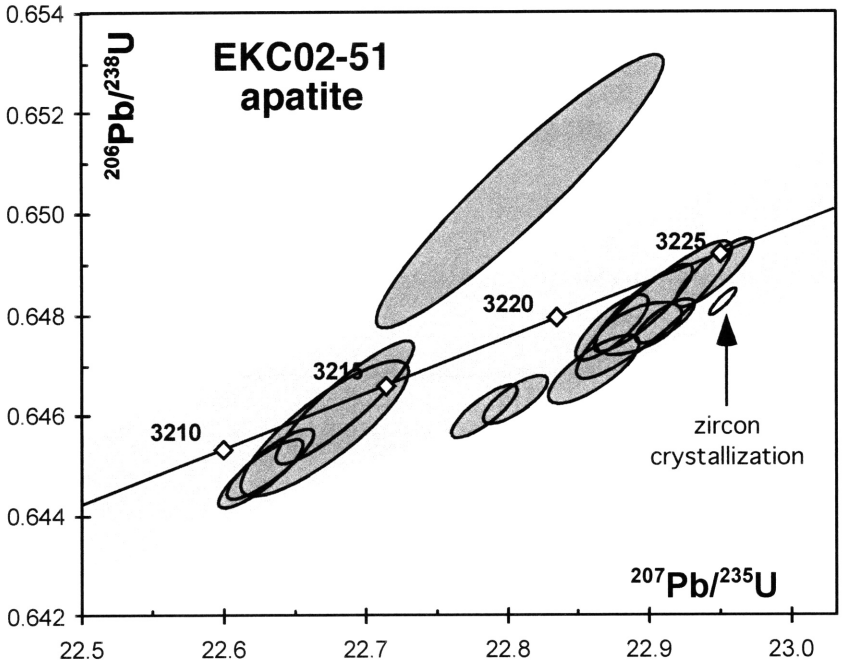

Schoene&Bowring Fig. 4

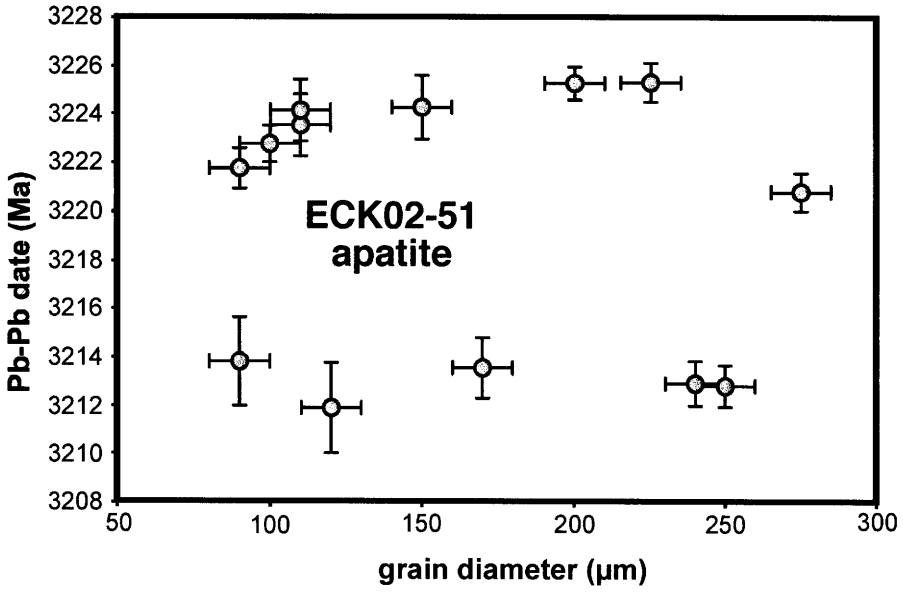

Schoene&Bowring Fig. 5

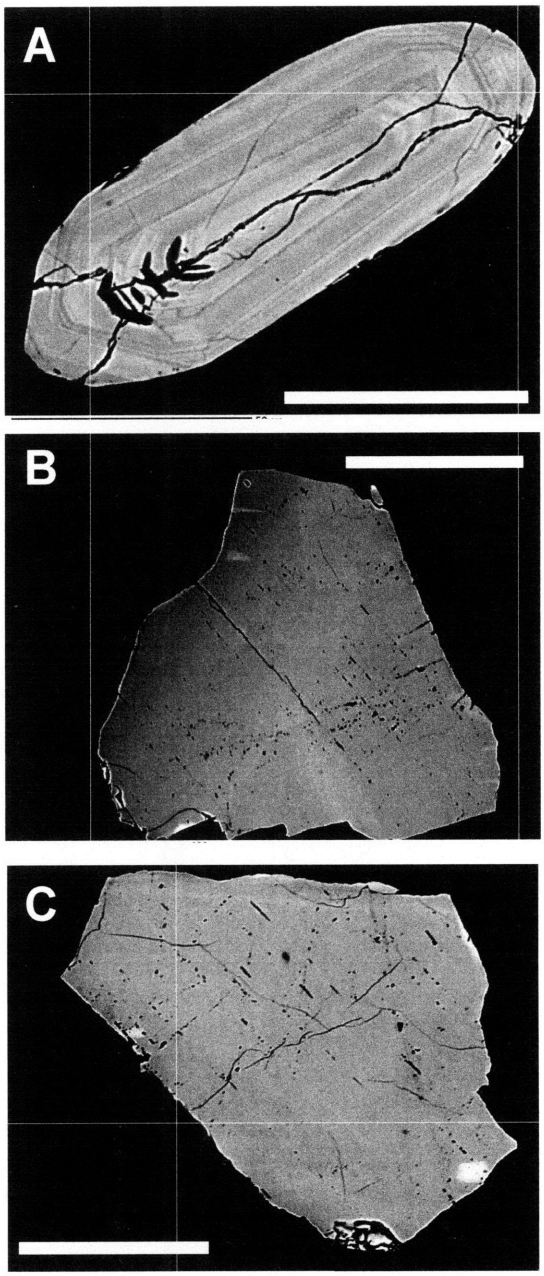

Schoene&Bowring Fig. 6

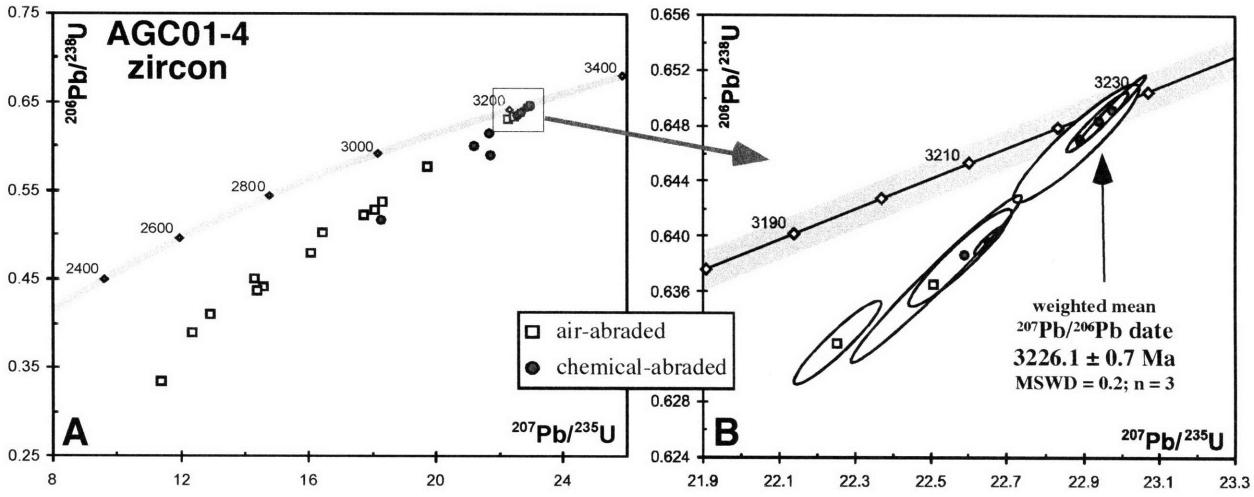

Schoene&Bowring Fig. 7

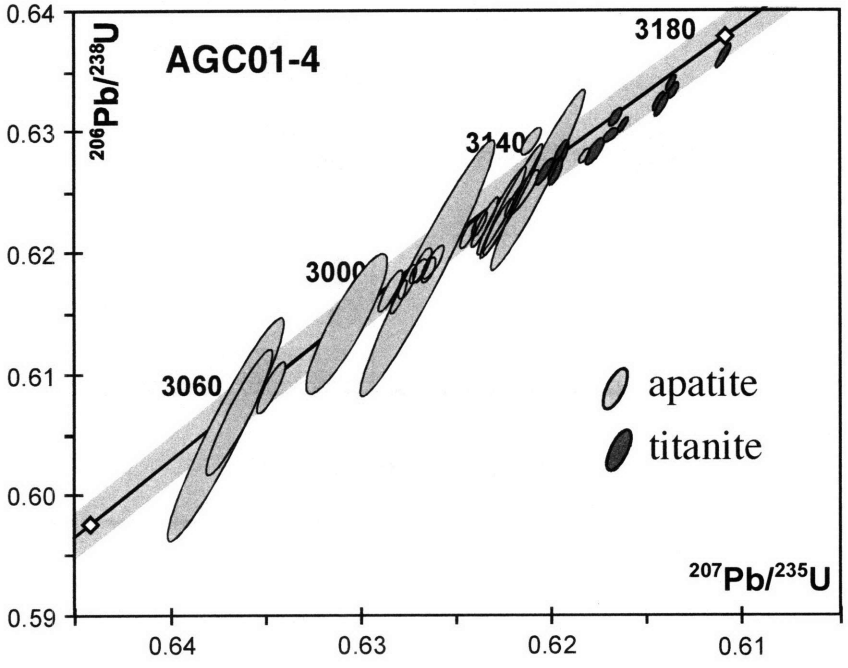

Schoene&Bowring Fig. 8

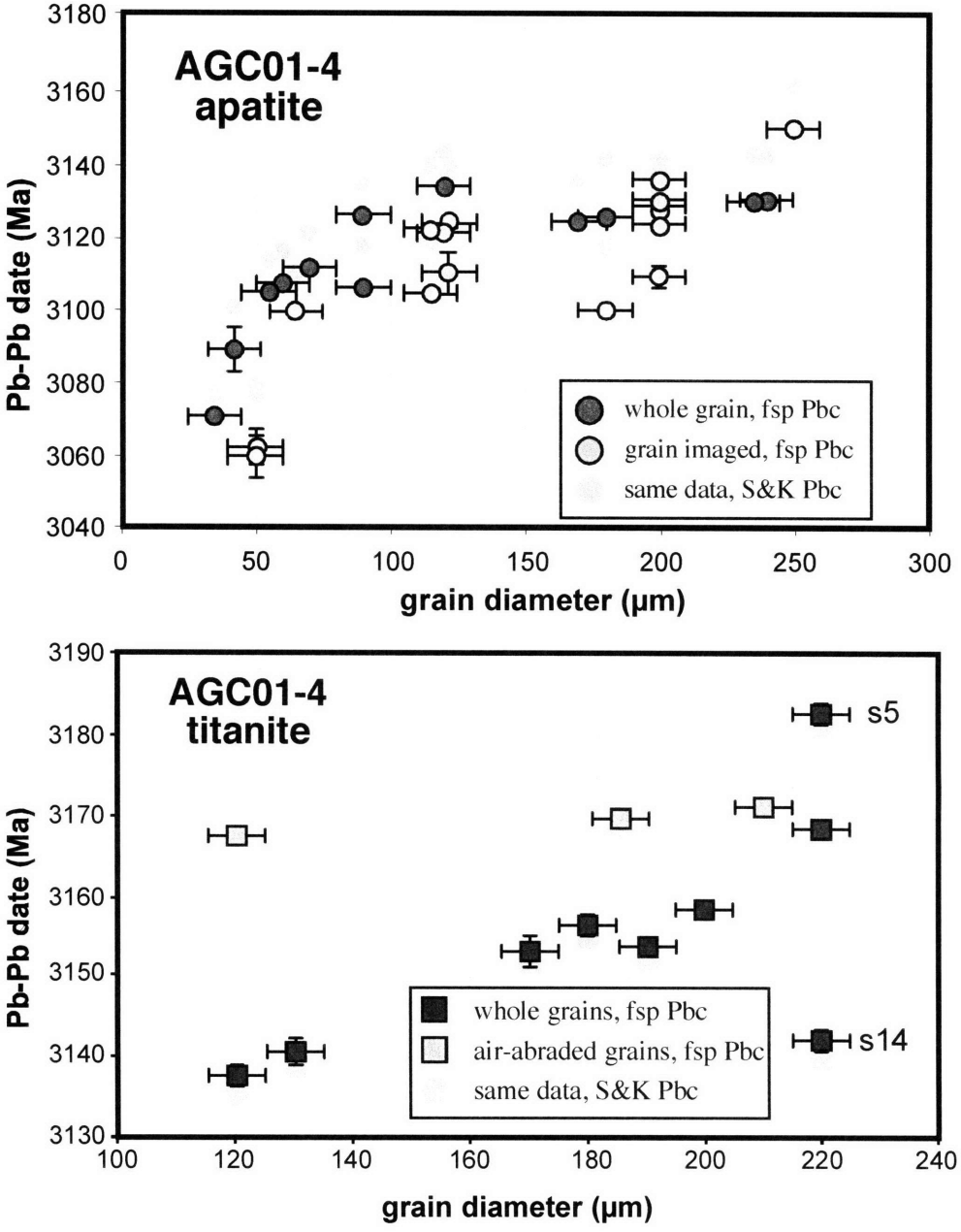

Schoene&Bowring Fig. 9

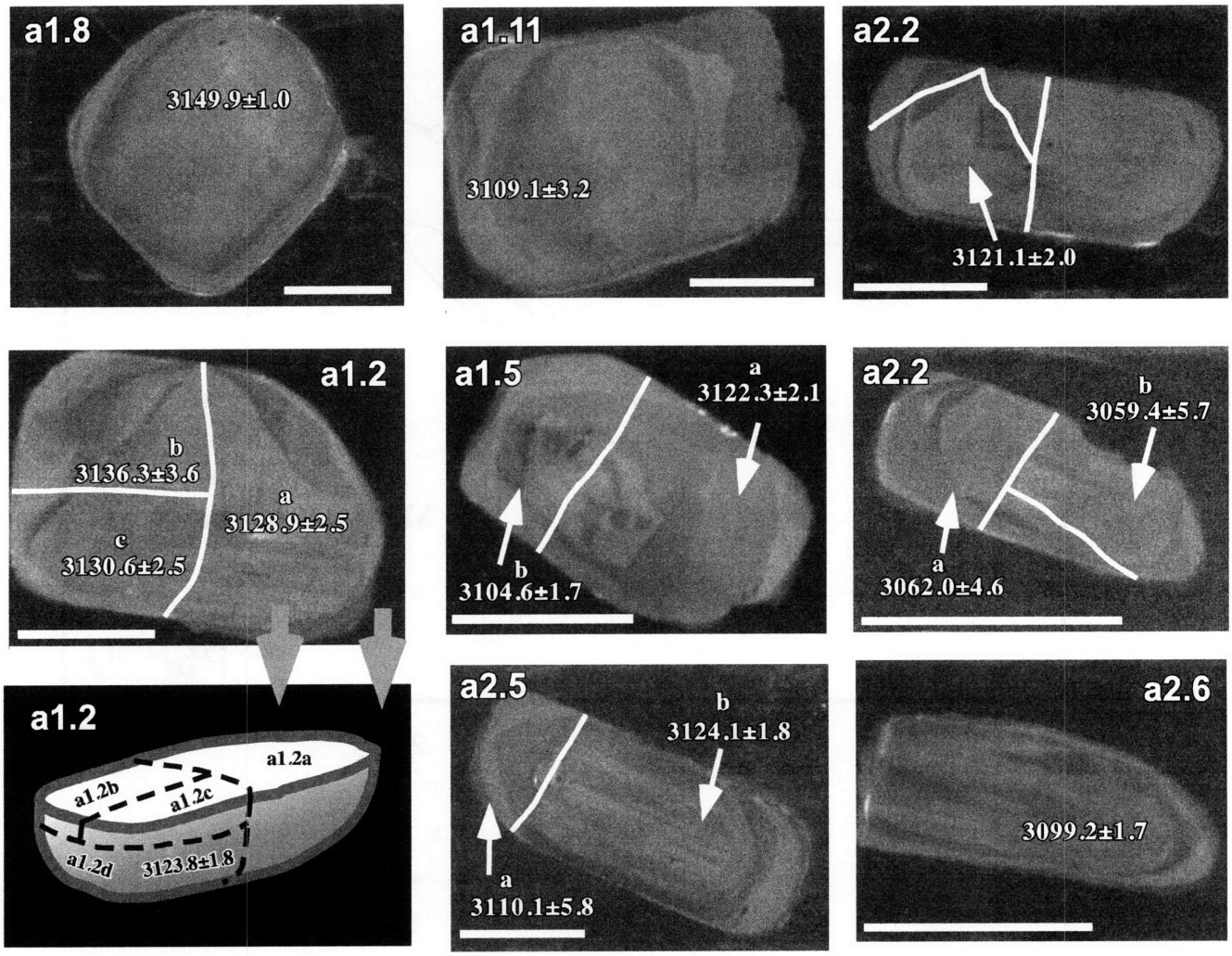

Schoene&Bowring Fig. 10

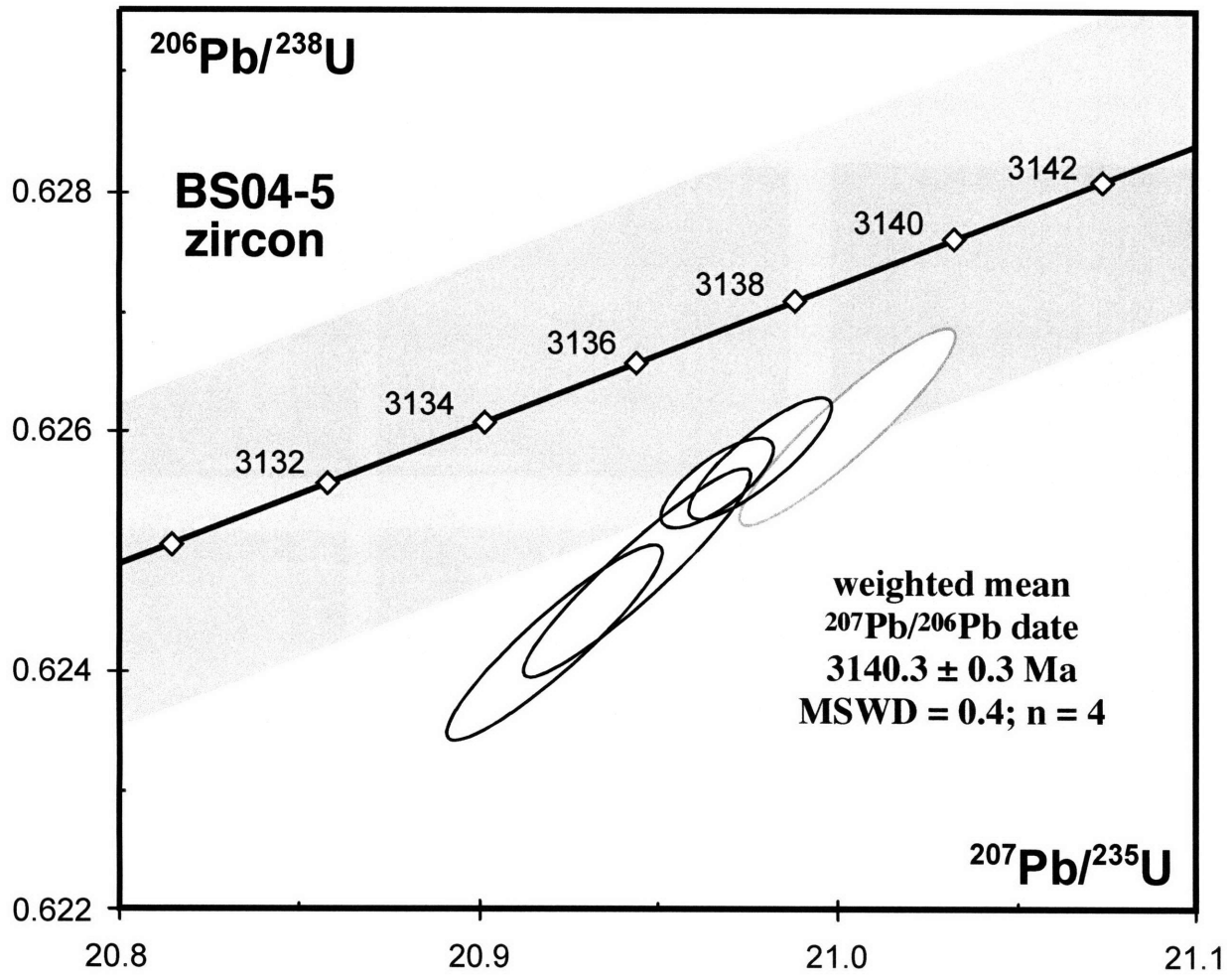

Schoene&Bowring Fig. 11

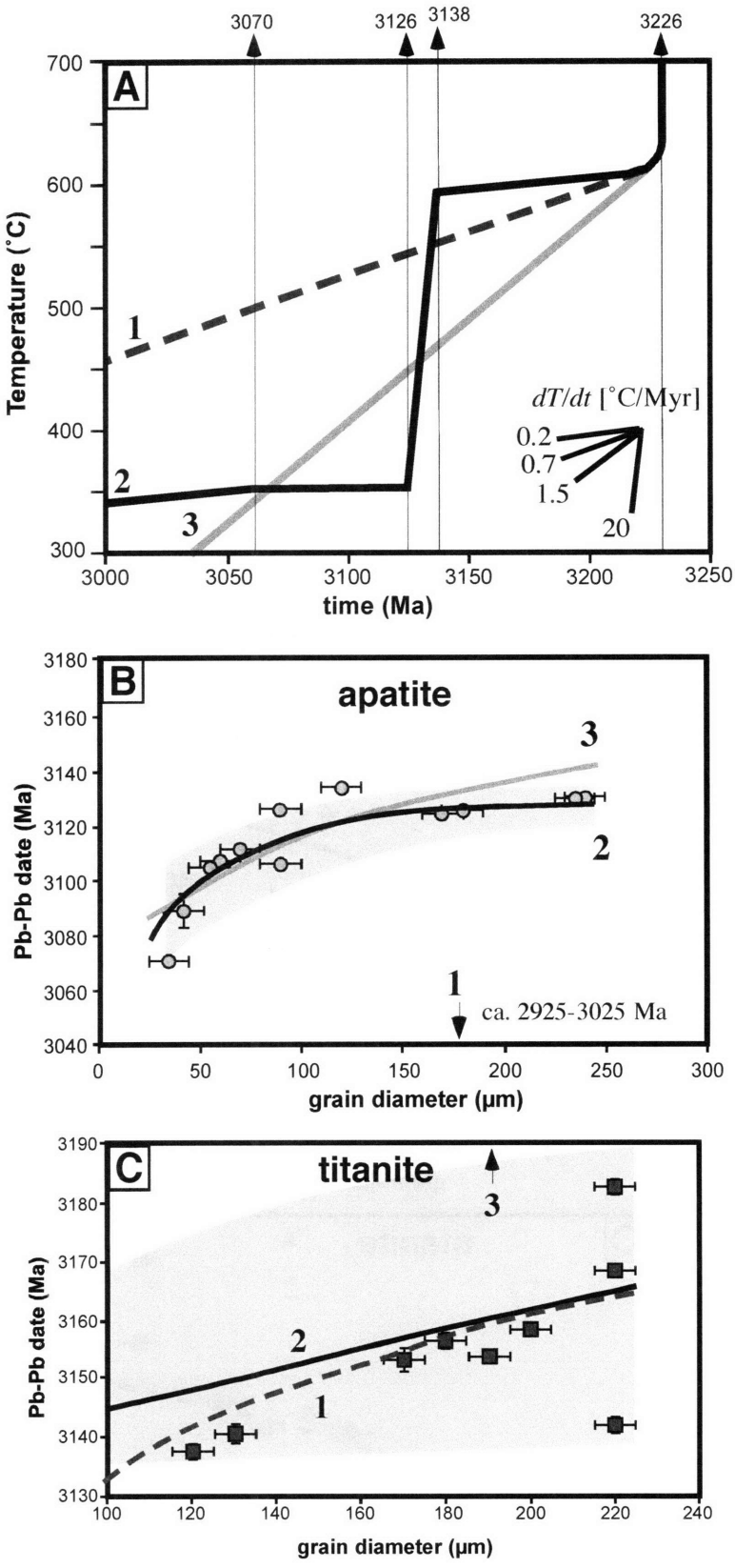

Schoene&Bowring Fig. 12

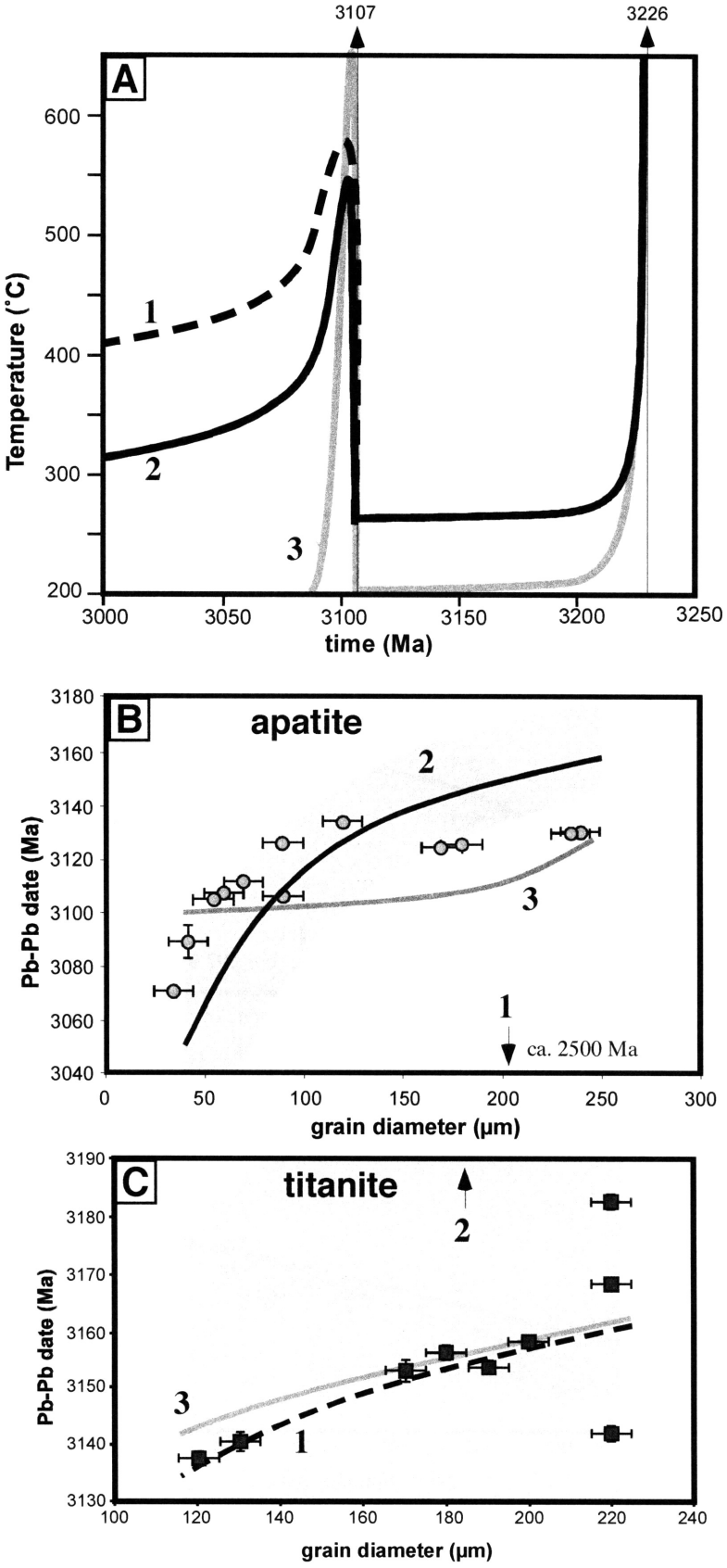

Schoene&Bowring Fig. 13

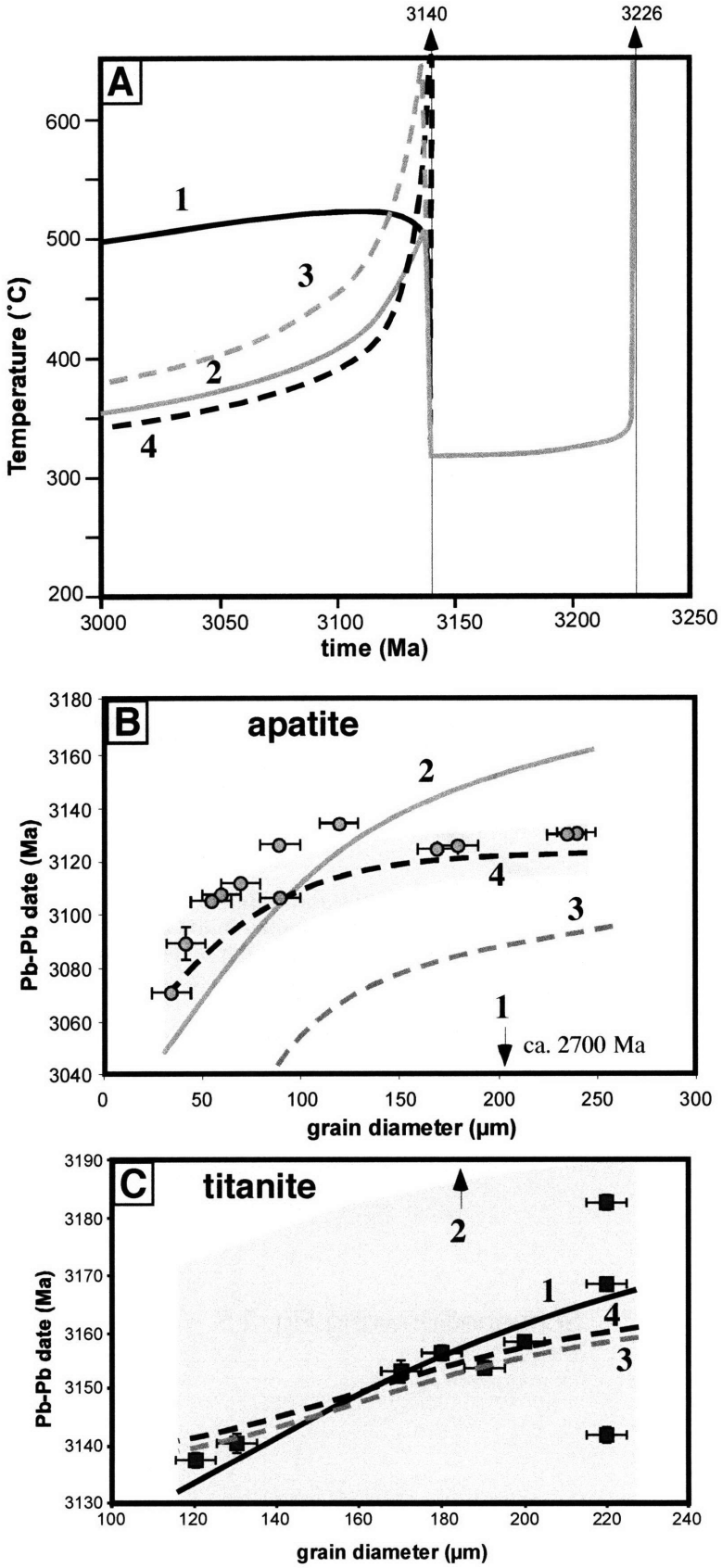

Schoene&Bowring Fig. 14

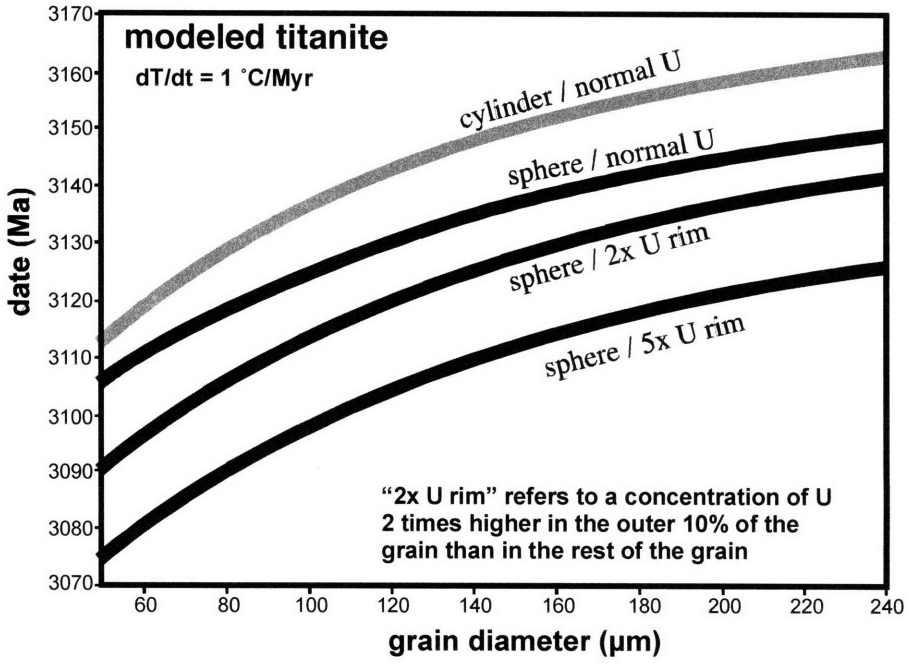

Schoene&Bowring Fig. 15

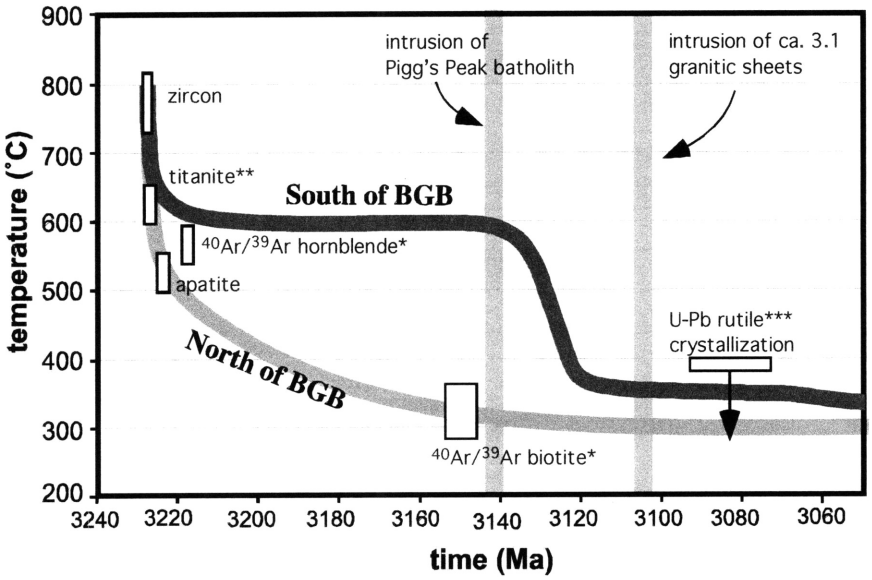

Schoene&Bowring Fig. 16

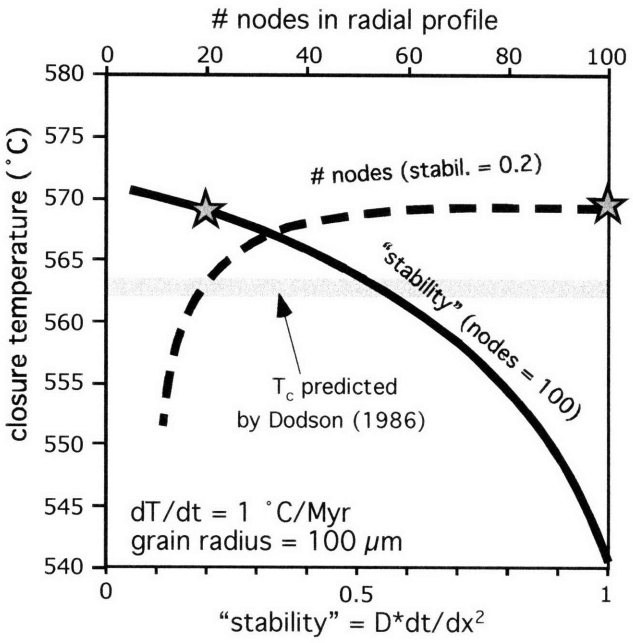

Schoene&Bowring Fig. A1

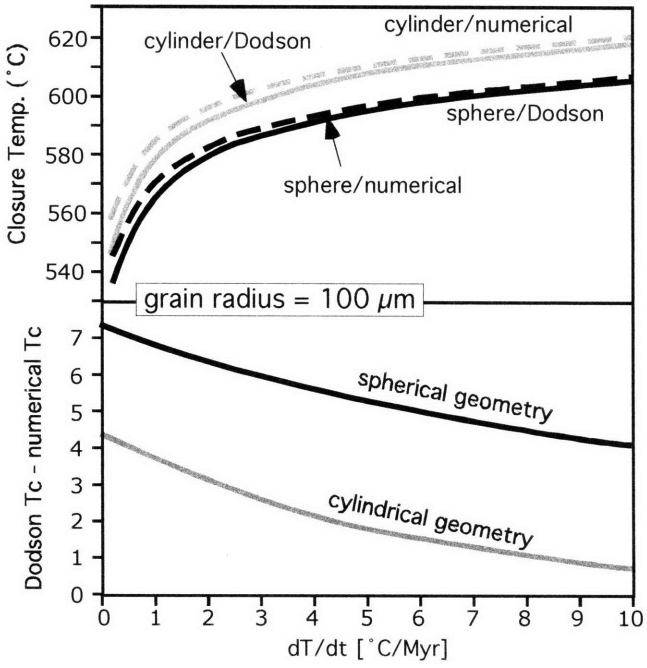

Schoene&Bowring Fig. A2

CHAPTER 2

The 3.2-3.1 Ga tectonothermal history of the Barberton greenstone belt: the importance of crustal extension in cratonization

Blair Schoene[1], Samuel A. Bowring[1] and Maarten J. de Wit[2],

1. Department of Earth, Atmospheric and Planetary Sciences, Massachusetts Institute of Technology, Cambridge, MA 02139, USA.

2. AEON, and Department of Geological Sciences, University of Cape Town, Rondebosch, 7701, South Africa.

submitted to *Tectonics*

ABSTRACT

Processes that lead to stabilization of the earliest Archean cratons are not well understood, especially how and when the crust attained its early stabilization. We report on structural and thermal events leading to the stabilization of the eastern Kaapvaal craton, in the vicinity of the Barberton greenstone belt (BGB), ca. 3.23-3.10 Ga. U-Pb geochronology and thermochronology are used in conjunction with field mapping and structural analysis to place time constraints on important tectonic events, for example to describe the timing and kinematics of movement on major shear zones and to relate these offsets to the exhumation histories of distinct crustal blocks. We find that during and following continental assembly ca. 3.23 Ga, widespread transtension on reactivated faults throughout the BGB over a period of >100 Myr led to crustal thinning, episodic emplacement of granitic batholiths, and juxtaposition of middle- to lower-crustal basement orthogneiss complexes against upper-crustal basement-greenstone sequences. Near coeval compression and extension during ca. 3.23 Ga orogenesis is most consistent with the BGB as a long-lived transform plate boundary with an assymetric flower-like structural geometry. The timing of post-orogenic extensional tectonics shows that it was not due to a gravitational collapse of the crust, but instead was a result of rigid plate interactions and/or long-term thermal and structural settling accommodated by pre-existing crustal to lithospheric scale anisotropies. This period of extension and upward granite migration resulted in a crust that is more resistant to deformation both by removing a weak lower crust and redistributing heat-producing elements to the upper crust followed by removal of a significant portion of the radiogenic-rich upper crust. Therefore, stabilization of this portion of Archean lithosphere likely involved a three-stage process: generation of a thick and rigid lithospheric root during subduction and terrane assembly ca. 3.23 Ga followed by generation of a thin and rigid crust by extensional tectonics ca. 3.2-3.1 Ga, and finally by erosion of the upper most crust. The early stabilization of the eastern craton compared to the rest of the Kaapvaal craton suggests that craton stabilization was not a single event, but rather a piece-wise transition resulting from a common set of processes.

1. INTRODUCTION

Archean cratons are characterized by their resistance to lithosphere recycling processes. Whether or not their preservation is more a function of their isolation from plate-boundary processes that enhance recycling or whether it is the result of a unique set of protective parameters remains a subject of active debate. Support for the latter comes from the fact that numerous physical characteristics of Archean cratons are different from adjacent younger lithosphere. The most prominent example is that cratonic lithosphere has been shown by numerous tomographic studies to have a thick and relatively high-velocity mantle root (Fouch et al., 2004; James et al., 2001; Jordan, 1978, 1988; Ritsema et al., 1998; Rudnick and Nyblade, 1999; Simons et al., 1999). Jordan (1978) suggested that retaining a thick and 'cold' buoyant lithosphere requires that it is depleted in heavy elements, possibly by the removal of basaltic melt in a subduction zone setting, creating a physically thick and rigid tectosphere that will not sink into the underlying asthenospheric mantle (also see Jordan, 1988). This so-called isopycnic theory is convenient in that is also explains the observed lower surface heat flow of some cratons compared to adjacent terranes (Morgan, 1985; Perry et al., 2006) and predicts a mantle that is capable of preserving ancient diamonds (Richardson et al., 1984; Richardson et al., 2001).

However, if tectonically stable lithosphere is generated in convergent regimes concurrent with terrane amalgamation, this should usually result in an overthickened continental crust relative to adjacent terranes. In reality, cratonic crustal thickness is characterized by highly variable thickness (Doucouré and de Wit, 2002; Durrheim and Mooney, 1994; Gupta et al., 2003; James and Fouch, 2002; Nguuri et al., 2001), which in

some cases is actually on average thinner than adjacent younger terranes (Assumpção et al., 2002; Clitheroe et al., 2000; Perry et al., 2002). If cratonic lithosphere is generated by depletion during subduction zone magmatism, then thinner crust can be explained by surface erosion to maintain isostatic equilibrium with a positively buoyant mantle lithosphere (Perry et al., 2002). An importance piece of this argument is the juxtaposition of low-grade supracrustal rocks against middle- to lower-crustal basement orthogneiss terranes – a feature that is common in many cratonic settings (de Wit and Ashwal, 1997) – and this architecture is inconsistent with crustal thinning by isostatic forces and erosion alone. This observation in concert with the heterogeneity of crustal thickness observed in some cratons suggests that post-assembly modification of the crust is an important tool for its stabilization, and that the processes and timing of stabilization may vary widely. Furthermore, it is apparent that determining a high-resolution time-scale for the tectonic and thermal evolution of cratonic crust is essential for determining their importance in litospheric stabilization.

The Kaapvaal craton in southern Africa (Fig. 1) is ideal for the study of Archean lithospheric evolution, in part because many aspects of its growth and stabilization are well understood from seismic (Fouch et al., 2004; James et al., 2001; Nguuri et al., 2001) and xenolith (Bell and Moore, 2004; Carlson et al., 2000; Pearson et al., 1995; Schmitz and Bowring, 2003a; Shirey et al., 2001) studies. These studies have shown that there is a ~250-300 km thick chemically depleted mantle root beneath continental crust that varies from 34-50 km thick within the craton, adjacent to a Proterozoic lithosphere with significantly thinner mantle and >40 km of crust. The oldest and best-exposed basement rocks in the craton are located in eastern South Africa and Swaziland, in the vicinity of

the Barberton greenstone belt (BGB; Figs. 1, 2). In addition to hosting some of the largest gold mines in the world, this area has become a classic locality for understanding Archean tectonics, sedimentology and biology since the landmark studies of (Viljoen and Viljoen, 1969). Furthermore, its apparent resistance to deformation for over 3 Gyr marks it as a prime target for understanding the characteristics of stable cratonic lithosphere. The growth and stabilization of the eastern Kaapvaal craton occurred from about 3.6-3.1 Ga, culminating at ca. 3.23 Ga during the collision and amalgamation of two or more microcontinents (de Ronde and de Wit, 1994; de Ronde and Kamo, 2000; de Wit, 1982; Kamo and Davis, 1994; Lowe, 1994). Stabilization of the crust is thought to have occurred at ca. 3.1 Ga following the intrusion of large subhorizontal granitic batholiths and a transition towards dominantly transcurrent tectonics (Anhaeusser, 1983; de Ronde et al., 1994; de Wit et al., 1992; Jackson et al., 1987; Lowe and Byerly, 1999a; Westraat et al., 2005). However, the period between 3.2 and 3.1 Ga is poorly understood, despite its importance in defining the stability of this portion of craton. In particular, the timing and genetic relationship between granitic magmatism and strike-slip tectonics and their importance in modifying ca. 3.23 Ga crustal architecture remain speculative.

This paper summarizes a detailed structural, geochronological, and thermochronological study focused at three different margins of the BGB aimed at constructing a high-precision thermotectonic timeframe for the evolution of the supracrustal sequences and granitoid complexes near the margins of the BGB immediately prior to cratonization. We have used structural analysis on several key shear zones that separate high-grade orthogneisses from lower-grade greenstone sequence rocks in order to characterize the kinematics of the final period of deformation in this

area. High-precision ID-TIMS U-Pb zircon geochronology of orthogneisses and cross-cutting syntectonic intrusions in these shear zones allows us to bracket the timing of deformation and determine crystallization ages with sub-million year precision. New U-Pb apatite thermochronology in combination with existing thermochronological data constrain the relative exhumation history of different crustal blocks between ca. 3.45-3.1 Ga within the tectonic framework established by structural geology and geochronology. This study allows for detailed testing of existing tectonic models and provides insight on craton formation and the modification and stabilization of continental fragments during the Mesoarchean.

2. HIGH PRECISION GEOCHRONOLOGY IN ARCHEAN STUDIES

U-Pb ID-TIMS geochronology is one of the most precise methods for dating the rates and durations of geologic events. The beneficial test of open-system behavior that is afforded by the dual decay of ^{235}U and ^{238}U to ^{207}Pb and ^{206}Pb, respectively, also makes this system one of the most accurate (Wetherill, 1956). In Archean rocks, open-system behavior due to Pb-loss is easy to recognize because it results in a spread of dates that is at high angles to the concordia curve. Such Pb-loss arrays are commonly modeled or assumed to be the result of Pb-loss at a single moment in time, for example as the result of a metamorphic event. Diffusion studies of Pb in zircon, however, suggest that at most metamorphic conditions (e.g. T<1000 °C), Pb-loss by volume diffusion is unimportant (Cherniak et al., 1991; Cherniak and Watson, 2001; Lee, 1997). Therefore, it seems more reasonable to suggest that statistically significant discordia lines represent a mixture of two domains of zircon with different growth ages. More common is that discordant

zircons do not define a linear array, but instead scatter below the concordia curve. In such cases, either the data represent a mixture of growth ages or are the result of Pb-loss made possible by enhanced Pb diffusivity through metamictization of zircon by uranium decay. Lower-intercepts of scattered discordia lines are often meaningless and upper intercepts are difficult to interpret. Furthermore, due to tangible inaccuracies in the uranium decay constants, it is essential to propagate their uncertainties into intercept ages unless the time of Pb-loss is reasonably zero (Begemann et al., 2001; Mattinson, 1994, 2000; Schoene et al., 2006). Attaining accurate and precise crystallization ages is therefore greatly benefited by obtaining concordant analyses with internal analytical errors comparable to the uncertainties of the decay constants of uranium (0.11 and 0.14% for ^{238}U and ^{235}U, respectively; Jaffey et al., 1971). The benefit of providing high-resolution in situ analysis of minerals provided by the SIMS or LA-ICPMS U-Pb methods is unfortunately coupled with large errors in calculated Pb/U ratios (e.g. ≥1-2%), which can in some cases make discordant analyses appear concordant and yield potentially misleading ages. Such misinterpretation can be avoided by obtaining numerous equivalent analyses (see review in Ireland and Williams, 2003). Pb-Pb dates produced by the zircon evaporation method (Kober, 1986, 1987), because they lack the internal check for concordancy afforded by U-Pb methods, are often much more precise than they are accurate and therefore difficult to verify without ID-TIMS, SIMS, or LA-ICP-MS U-Pb analysis.

Because of the importance of obtaining concordant analyses, one of the primary goals in modern U-Pb ID-TIMS zircon geochronology is to both recognize and eliminate the effects of Pb-loss, and this has been largely realized through modern sample

preparation techniques. Air-abrasion (Krogh, 1982) of carefully selected zircons to remove high-U rims has until recently been the primary method of removing the effects of Pb-loss in zircons. The chemical-abrasion method (CA-TIMS; Mattinson, 2003, 2005; see analytical procedure in the Appendix) has now vastly improved our ability to resolve Pb-loss in otherwise terminally discordant zircons in that this method preferentially removes high-U discordant domains that may or may not reside within the outer rim of a grain. The benefits of this technique are most readily recognized in Archean zircons, such as those in this study, because the Pb-loss trajectories of these grains are obvious in concordia space and also because in many such samples attaining concordant analyses by air-abrasion has proved inefficient or impossible. HF leaching of such grains frequently removes >90% of the original zircon, leaving <5 μm fragments of low-U zircon. Analytical precision on low-U residues is on average 0.1-0.2%, compared to <0.1% precision of younger, higher-U zircon with greater intensity ion beams. This level of precision is not ideal for age determination but is adequate to resolve concordancy in single grains. Working primarily with clusters of U-Pb analyses that are within error of concordia allows for the use of the $^{207}Pb/^{206}Pb$ date with confidence in its accuracy, and this is by far the most precise date available for Archean rocks. Relatively high amounts of $^{206}Pb^*$ and $^{207}Pb^*$ in old zircons coupled with modern sub-picogram Pb-blanks allows for precision in weighted mean $^{207}Pb/^{206}Pb$ dates of ≤0.01%. Also, by exploiting the $^{207}Pb/^{206}Pb$ system and using U for evaluation of concordance only, it is not necessary to propagate inaccuracies in the U decay constants, in that they can be ignored when looking at the durations of time using a single decay scheme (Begemann et al., 2001; Min et al., 2000; Renne et al., 1998). Therefore, when analyzing zircons with relatively

simple growth histories (i.e. single-stage growth), CA-TIMS analysis has the potential to resolve Archean events within 1 Myr of each other – essential when addressing typical, short-duration tectonic episodes or magmatic events.

3. MESOARCHEAN EVOLUTION OF THE EASTERN KAAPVAAL CRATON

The present-day character of the eastern Kaapvaal craton is primarily the result of a complex and protracted evolution during the Mesoarchean, followed by ~3 Ga of relative stability. Therefore, of primary importance for this study is the tectonic development ca. 3.23-3.10 Ga, which began with a period of terrane assembly that is inferred to have produced most of the observed structures (Fig. 2).

This study is primarily concerned with the Barberton Greenstone Belt (BGB), and the surrounding basement orthogneisses. The stratigraphy of the BGB is locally variable and characterized by a diverse set of unconformities, structural repetitions and deformation patterns. It is composed of mafic to ultramafic metavolcanics, cherts, banded iron formations, and a heterogeneous sequence of siliciclastics, that are broadly subdivided into three main lithofacies: The Onverwacht Group, the Fig Tree Group, and the Moodies Group (Anhaeusser, 1969, 1976; Anhaeusser, 1983; Condie et al., 1970; de Wit, 1982; de Wit et al., 1987b; Eriksson, 1980; Heubeck and Lowe, 1994a, 1994b; Lowe and Byerly, 1999a; Viljoen and Viljoen, 1969; Fig. 2). The Sandspruit and Theespruit formations structurally make up the lower-most units of the Onverwacht Group, and these comprise mafic to silicic fine-grained metasediments and volcaniclastics. The Theespruit Formation is, at least in places, younger than the overlying Komati Formation (see below), and is separated from it by a major shear zone (Armstrong et al., 1990; de

Ronde and de Wit, 1994). The upper Onverwacht Group consists of komatiitic to basaltic metavolcanics and interlayered siliciclastics, cherts, banded-iron formations, and tuffs, which are divided into the (from bottom to top) Komati, Hooggenoeg, Kromberg, Mendon, and Weltevreden Formations. The overlying Fig Tree Group consists of fine-grained shales, siltstones, cherts and silicic volcanics that coarsen upward into chert conglomerates that lie below the coarser-grained sandstones and conglomerates of the Moodies Group. The source and depositional setting of the Moodies Group likely differs across the greenstone belt (Lamb and Paris, 1988) and even within single stratigraphic sequences (Heubeck and Lowe, 1994a, 1994b; Lowe and Byerly, 1999b)

The BGB is bordered on all sides by gneisses and plutonic rocks that span ca. 500 Myr in age (Fig. 2). The Ancient Gneiss Complex (AGC), exposed mostly in Swaziland, flanks the SE margin of the belt and contains the oldest rocks in the Kaapvaal craton yet identified. It is composed primarily of banded felsic to mafic gneisses that were metamorphosed and deformed during several distinct periods at >3.6 Ga, 3.55-3.50 Ga, and ca. 3.45 Ga (Compston, 1988; Hunter et al., 1978; Jackson, 1979, 1984; Kröner et al., 1989). These older rocks were intruded by a series of tonalites and granodiorites ca. 3.23 Ga (Kröner et al., 1989, Schoene, 2004; Schoene and Bowring, in prep; Wilson, 1982). Orthogneiss complexes are also juxtaposed against the southern and northwestern margins of the BGB, namely the ca. 3.51 Ga Steynsdorp pluton, the ca. 3.45 Ga Stolzburg, Theespruit, and Doornhoek plutons and the ca. 3.23 Kaap Valley and Nelshoogte plutons (Fig. 2). These rocks are all intruded by a series of ca. 3.107 Ga subhorizontal granitic batholiths and syenogranitic intrusions along all margins of the BGB (Anhaeusser, 1983; Kamo and Davis, 1994; Westraat et al., 2005) except the SE

margin, where the ca. 3.14 Ga Pigg's Peak batholith intruded (Schoene and Bowring, submitted).

The relationship between the orthogneiss basement complexes and the BGB is often described as a dome-keel structural geometry: greenschist- or lower-grade supracrustal rocks juxtaposed against higher-grade basement rocks in a series of upright tight to isoclinal anticline/syncline pairs. $^{40}Ar/^{39}Ar$ hornblende data combined with P-T estimates show that most mafic to ultramafic units in the BGB were never above greenschist to lower-amphibolite grade conditions (Cloete, 1991; Lopez Martinez et al., 1992; Xie et al., 1997). This is inferred to have occurred immediately following their formation and burial on the sea-floor (de Ronde and de Wit, 1994; de Wit, 1982; de Wit et al., 1987b; de Wit et al., 1992; Lowe, 1999; Williams and Furnell, 1979). SW of the BGB, slivers of amphibolites and mafic semipelites within the ca. 3.45 Ga orthogneiss complexes yield P-T estimates from upper-amphibolite to granulite grade conditions (Diener et al., 2005; Dziggel et al., 2002; Kisters et al., 2003; Stevens et al., 2002). Constraints on the timing of metamorphism and deformation in these rocks are provided by a U-Pb date of ca. 3.23 Ga on a synkinematic intrusion (Dziggel et al., 2005), and by U-Pb sphene dates of ca. 3.23 Ga, which provide a minimum estimate on the timing of metamorphism (Diener et al., 2005; Dziggel et al., 2005). These data are consistent with previous investigations that infer a major period of compression associated with terrane accretion occurred ca. 3.23 Ga.

The ca. 3.23 Ga period of convergent tectonism is suggested to have formed the dominant NE-SW structural trend of the belt during terrane collision and lithospheric suturing along the Saddleback-Inyoka fault system (SIFS; Fig. 2; de Ronde and de Wit,

1994; de Wit et al., 1992). NW-SE directed thrusting and syntectonic sedimentation of the Moodies Group lithologies has been widely documented throughout the belt (de Ronde and de Wit, 1994; de Ronde and Kamo, 2000; de Wit et al., 1992; Heubeck and Lowe, 1994b; Jackson et al., 1987; Lamb, 1984; Lowe, 1999), and overprints an earlier phase of deformation that is potentially responsible for placing the oldest portions of the Onverwacht Group, in places overturned, onto plutonic basement rocks (de Ronde and de Wit, 1994; de Wit, 1982; de Wit et al., 1987a; de Wit et al., 1983; Kisters and Anhaeusser, 1995b). Constraints on the timing of NW-SE thrusting are provided by U-Pb dating of ca. 3.23 Ga intrusions and volcanic rocks that place brackets on folds and unconformities in the Fig Tree and Moodies Groups that developed during compression in the central and SW portion of the BGB (de Ronde and de Wit, 1994; Kamo and Davis, 1994, de Ronde, 2000 #65).

Following NW-SE convergent tectonism, there was a transition towards NE-SW strike-slip to transtensional faulting and sedimentary deposition through at least the central and NW belt (de Ronde and de Wit, 1994; de Ronde and Kamo, 2000; de Ronde et al., 1991; Heubeck and Lowe, 1994a, 1994b; Jackson et al., 1987; Lowe, 1999). Translational and extensional kinematics are inferred to be either the result of a gravitational collapse immediately following ca. 3.23 Ga orogenesis (Kisters et al., 2003) or ~100 Myr later contemporaneous with ca. 3.11 Ga granitic intrusions (de Ronde and de Wit, 1994; Jackson et al., 1987; Kamo and Davis, 1994; Westraat et al., 2005), though few temporal constraints exist for this event. De Ronde et al. (1991) bracket movement on one translational fault to have occurred between 3126 ± 21 and 3080 ± 18 Ma by U-Pb dating of a synkinematic porphyry and post-kinematic rutile growth. Rocks inferred to be

ca. 3.11 Ga associated with the Mpuluzi batholith intruded synkinematically into transcurrent shear zones (Westraat et al., 2005). Schoene and Bowring (submitted) use U-Pb apatite and sphene thermochronology to show that ca. 3227 Ma orthogneisses NW and SE of the BGB experienced dramatically different cooling histories, and that the basement to the SE in Swaziland experienced rapid cooling from ~3140-3130 Ma concomitant with intrusion of the Pigg's Peak batholith. (Schoene and Bowring, submitted) infer that rapid cooling SE of the BGB may be related to exhumation as a result of local or regional transtension. These data suggest that the scale and effect of transtension throughout the belt may be larger than previously inferred from structural observations. Therefore, further calibration of the kinematics and timing of this episode along all margins of the belt is crucial in understanding the final structural and thermal stabilization of this portion of the Kaapvaal craton. Here, we report on such work along four of these margins in detail.

4. FIELD LOCALES, KINEMATIC ANALYSIS AND GEOCHRONOLOGY

4.1. Southeast margin: Pigg's Peak inlier

4.1.1. previous work

The Pigg's Peak inlier (Fig. 3) is the only exposure in the region where the AGC is in direct contact with any portion of the BGB. This contact is here termed the Phophonyane Shear Zone, PSZ. Preliminary mapping of the inlier is published by the Geological Survey of Swaziland (Wilson, 1979, 1982). Compston (1988) present a complex U-Pb SHRIMP dataset on zircons from a sample of lithologically complex gneiss sample from

the inlier. Apparently concordant U-Pb dates ranging from ca. 3.6 to 3.0 Ga are found in the zircons, but complex Pb-loss and negative discordance in the analyses prevent a straightforward interpretation of the results. One $^{207}Pb/^{206}Pb$ date of 3644 ± 4 Ma from that study is the oldest date is the oldest date that has been published from the Kaapvaal craton. Kröner et al. (1989) present further U-Pb SHRIMP dates on two leucocratic granitic gneiss samples from this inlier. These analyses are generally discordant with an upper-intercept age of 3179 ± 11 Ma. Schoene and Bowring (submitted) report U-Pb zircon, sphene, and apatite data from a granodioritic gneiss sample within the inlier (AGC01-4; Fig. 3). They conclude that the rock, which gives a $^{207}Pb/^{206}Pb$ age of 3226.1 ± 0.7 Ma, had a protracted cooling history between 3.23 and 3.05 Ma, which is likely due to post-3.2 Ga exhumation along the PSZ.

4.1.2. Mapping and structural analysis

Mapping, structural analysis, and geochronology from the Pigg's Peak inlier are directed towards understanding the timing of movement along the PSZ and relating that to the regional thermal structure in the Mesoarchean. Fig. 3 shows a lithologic and structural map of the Pigg's Peak inlier. Rocks of the inlier consist of mafic-felsic banded gneisses typical of the AGC (Fig. 4), but also present are several younger generations of metaigneous rocks including a distinct fine-grained foliated granite and a series of undifferentiated granites, granodiorites, and monzogranites that cross-cut the fine-grained granite and the bimodal gneisses, and are variably foliated themselves. These three lithologic packages are all cut by a series of quartz-feldspar pegmatitic and aplitic dikes. The medium- to coarse-grained, undeformed Pigg's Peak granite, gives a

$^{207}Pb/^{206}Pb$ date of 3140.3 ± 0.3 Ma (Schoene and Bowring, submitted). This is the youngest intrusion in the area and defines the eastern margin of the inlier. The eastern portion of the inlier, to the west of the Pigg's Peak granite, forms an open upright antiform that trends E to ESE and is several km in wavelength. The formation of this structure post-dates the intrusion of all three lithologies of the AGC and is superimposed upon older small-scale folding within the bimodal gneisses that is not apparent in the younger AGC units. This early folding in the N and S limbs of the anticline is defined by mafic and felsic banding that forms tight to isoclinal folds that in places are transposed in moderately developed sheath folds that define an irregular fold-hinge pattern on a stereographic projection (Fig. 3C). These structures are well-exposed in road-cuts within the bimodal gneisses near "the falls" on Fig. 3.

Structures in the NW portion of the inlier are dominated by kinematics associated with movement in the NW-dipping PSZ. Within 1 km of the contact with the BGB, the rocks become strongly mylonitic such that foliation, fold hinges and stretching lineations are subparallel, and together define a NE-SW direction of transport (Figs. 3B, 4). Amphibolite lenses within this zone are frequently folded and/or boudinaged. The cross-cutting pegmatitic and aplitic dikes present in the SE are also present in the proximity of the PSZ but locally contain foliation parallel to the host rocks and are variably sheared with consistent offset direction (Fig. 5). These observations are interpreted to illustrate that the dikes intruded synchronously with shearing and they also provide a ubiquitous right-lateral/normal sense of displacement. The PSZ is therefore a dextral transtensional structure with hanging-wall down to the NE. This interpretation is consistent with the observation that the BGB NW of the PSZ consists of low-grade sandstones and siltstones

containing chlorite and actinolite – contrasting to the amphibolite grade rocks within the AGC. Nowhere in the field area is the contact between the AGC and BGB exposed.

4.1.3. Sampling strategy and geochronology

Samples were collected for U-Pb zircon analysis in order to 1) place temporal constraints on the crystallization ages of the various rocks in the field area, and 2) to bracket the timing of dextral transtension in the PSZ. Sample locations are shown in Fig. 3, the data is presented in Table 1, and concordia diagrams are included in Figs. 4, and 5. Geochronology of the Pigg's Peak granite and a ca. 3.226 Ga intrusion from within the banded gneiss (marked on the map in Fig. 3 as samples BS04-5 and AGC01-4, respectively), in addition to U-Pb apatite and sphene thermochronology, are reported in Schoene and Bowring (submitted).

AGC01-5

This is a sample of porphyritic granodioritic gneiss, collected on the Phophonyane river near a road crossing of R570 (Fig. 3). Mafic banding in this unit is less abundant than what was mapped as the bimodal gneiss in Fig. 3, though some lithologic variation does occur, for example variance in the abundance of K-feldspar megacrysts. Mineral separates yielded abundant zircon with varying morphology and color; most grains are nearly euhedral with slightly rounded crystal terminations. Some rounded anhedral zircons were observed, but these were avoided for analysis. It is inferred that much of the color variation in euhedral crystals is a result of varying degrees of metamictization, such as the observation that white, cloudy rims of zircons often encase purple cores. Only the

clearest, most euhedral grains were selected for imaging and analysis. Initial attempts at dating these zircons treated with the air-abrasion method were unsuccessful due to persistent Pb-loss from both single grains and grain-fragments (Fig. 4). Chemical abrasion drastically improved the results, and yielded several analyses near concordia. Overall, twelve air-abraded grains and ten chemical abraded grains were analyzed, and the three with the oldest $^{207}Pb/^{206}Pb$ dates yield a weighted mean $^{207}Pb/^{206}Pb$ date of 3662.8 ± 0.5 (MSWD = 0.3), which is interpreted to date the crystallization of this rock (Fig. 4). This is the oldest rock in the Kaapvaal craton so far dated, and is ca. 20 Ma older than the zircon SHRIMP analysis of Compston (1988). It is possible, however, that the two dates are approximately the same and that the large errors in the SHRIMP analysis mask Pb-loss in that grain which therefore appears concordant at ca. 3644 Ma.

EKC02-20

This sample was collected from within the fine-grained granitic gneiss unit that we group with the AGC. In places, this unit clearly cuts the older bimodal gneiss and is in turn cut by multiple younger dikes and intrusions, including the Pigg's Peak granite. Zircon picked for analysis were sub- to euhedral stubby prisms <100 μm in length. Seven analyses give $^{207}Pb/^{206}Pb$ dates between ca. 3.49 and 3.55 Ga. The youngest grain and one other zircon are negatively discordant and the three oldest are near concordant with a weighted-mean $^{207}Pb/^{206}Pb$ date of 3545.6 ± 0.5 Ma (MSWD = 0.9), interpreted to date crystallization of this granite (Fig. 4).

EKC02-8 and EKC02-10

These are samples of syntectonic dikes from a river section across the PSZ. EKC02-10 is an example of one of the granitic pegmatite dikes that are widespread in this area. This dike cross-cuts gneiss of the AGC, and is sheared itself to contain the local foliation, and in places strikes parallel to the foliation (Fig. 5). ECK02-8 is an aplitic dike that cross-cuts EKC02-10, contains a weak planar fabric parallel to the local foliation, and is ductilely offset in places, giving a dextral sense of shear (Fig. 5). About five kilograms of the samples were processed and each yielded <20 zircons. Attempts to analyze the grains that were pre-treated with air-abrasion were unsuccessful, yielding only very discordant results (Fig. 5). Chemical abrasion of zircon from EKC02-10 also yielded discordant results with little useful age information. Several near concordant chemical abrasion analyses from EKC02-8 were attained, and two grains that overlap concordia yield a weighted mean $^{207}Pb/^{206}Pb$ date of 3223.4 ± 1.9 Ma (MSWD = 1.0; Fig. 5). We interpret this date to represent the intrusion of the aplitic dike and because this dike is only weakly deformed, this date represents a lower-limit on major movement along the PSZ at this location.

4.2. Southern margin: Steynsdorp antiform

4.2.1. Previous work

The Steynsdorp complex, along the southern margin of the BGB (Fig. 2), consists of the dome-shaped tonalite-trondhjemite-granodiorite Steynsdorp pluton and the structurally overlying lower-most units of the BGB – the Sandspruit Formation, the Theespruit Formation, and the the lower portions of the Onverwacht Group (Anhaeusser, 1983;

Kröner et al., 1996; Viljoen and Viljoen, 1969); Fig. 6). The southern margin of the complex is bordered by the cross-cutting Mpuluzi granite, which has been dated by U-Pb ID-TIMS on zircon and sphene at 3107 +4/-2 Ma (Kamo and Davis, 1994). The Steynsdorp pluton itself has been dated by U-Pb in zircon both by ID-TIMS, giving an upper-intercept of 3509 +8/-7 (Kamo and Davis, 1994) Ma, and by SHRIMP, giving an upper-intercept at 3509 ± 4 Ma (Kröner et al., 1996). Zircons from a felsic mylonitic tuff within the Theespruit Formation were dated by U-Pb SHRIMP, and these analyses form a discordia with an upper intercept of 3544 ± 3 Ma (Kröner et al., 1996).

The structural history of the Steynsdorp complex was studied in detail by Kisters and Anhaeusser (1995b), in which those authors interpreted the Steynsdorp antiform to be the result of subhorizontal E-W shortening. Broad hemispherical foliation patterns within the Steynsdorp pluton and in the adjacent paragneisses (Fig. 6) make up the core of the antiform. Further north, this fold pattern tightens, interpreted to be the result of preferential shortening within the rheologically weak mafic metavolcanics of the lower Onverwacht Group compared to the structurally rigid Steynsdorp pluton. Mineral stretching lineations within the entire antiform trend and plunge NE and are coaxial with mesoscale isoclinal folds within the Theespruit Formation. The development of lineations and the antiformal structure are interpreted to post-date or be synchronous with the Formation of the Steynsdorp dome, which is interpreted to have risen buoyantly during ~E-W compression (Kisters and Anhaeusser, 1995b). The timing of the Formation of the Steynsdorp antiform is bracketed by the intrusion of the 3216 +2/-1 Ma Dalmein pluton (Kamo and Davis, 1994), located immediately to the west. However, $^{207}Pb/^{206}Pb$ zircon evaporation dates of the Vlakplaats granodiorite (sample WKC00-88), which cross-cuts

the lower Onverwacht Group and its foliation within the antiform (Fig. 6), give a mean of 3450 ± 3 Ma, and this is interpreted to place a minimum age on development of the antiform and the foliation/folds it contains (Kröner et al., 1996).

4.2.2. Mapping and structural analysis

Field mapping and sample collection focused mainly on the Steynsdorp pluton and the contact between it and the Theespruit Formation. A compilation of mapping efforts with previous maps is presented in Fig. 6. Overall, our observations agree with those reported in previous studies (Kisters and Anhaeusser, 1995b; Kröner et al., 1996; Viljoen and Viljoen, 1969), though several observations not reported or emphasized in those studies will receive focus here. Firstly, contact-parallel, concentric foliation in the pluton becomes less evident towards its center, where foliation is weak to non-existent. As noted also in Kisters and Anhaeusser (1995b), flattening strains decrease structurally above the pluton-supracrustal contact as well. The NE trending stretching lineation is apparent in the pluton even where the foliation is not (Fig. 6).

An important characteristic of the sheared contact between the Steynsdorp pluton and the overlying Theespruit Formation is that kinematic indicators show that the major sense of offset is Theespruit Formation to the NE. Evidence for this sense of shear is sparse but consistent within several meters of the contact and is manifested in sigmoidal garnet porphyroblasts in the Theespruit Formation (Fig. 7), sigmoidal feldspar megacrysts in the orthogneiss, and sheared and offset granitic dikes. Along the northern margin of the pluton this offset corresponds to a normal sense of shear and on the western margin it corresponds predominantly dextral strike-slip motion. The contact on the

eastern margin of the pluton is not as well exposed, though lineations are parallel to those throughout the antiform. To maintain structural continuity across the antiform, a sinistral sense of shear is inferred for the Steynsdorp pluton/Theespruit Formation contact here.

Along the southern margin of the Steynsdorp pluton, the Mpuluzi batholith is well exposed. This portion of the batholith is fine-grained and in places contains shallowly dipping foliation defined by biotite alignment (Fig. 6). Some localities contain strongly to moderately developed quartz stretching lineations that are subparallel to the lineations observed in the Steynsdorp antiform.

The field observations of Kisters and Anhaeusser (1995b) and ourselves are consistent with the Steynsdorp antiform representing a structure similar to a core-complex, where the contact between the Steynsdorp pluton and the Theespruit Formation forms the primary extensional shear zone. This interpretation is substantially different from that of Kisters and Anhaeusser (1995b), and this will be discussed later in the paper.

4.2.3. Sample collection and geochronology

Five samples were collected for geo- and thermochronology from the Steynsdorp anticline in an effort to constrain crystallization ages of the major lithologies and to bracket deformation associated with the formation of the Steynsdorp antiform. Data are presented in Table 1 and in Fig. 7.

EKC02-40

This sample of Steynsdorp pluton is a thinly banded tonalite to granodiorite from a deeply incised valley near its western margin (Fig. 6); it is a typical sample of the pluton

near its sheared boundaries. Approximately 5 kg of crushed sample yielded abundant zircon and apatite. The zircon population consisted of a number of grain morphologies: small, rounded grains, subhedral, rounded elongate prisms, and euhedral, sharply terminated elongate prisms. We picked only euhedral elongate grains, which are interpreted to be magmatic. Four chemical-abraded grains yield an equivalent cluster, though one analysis is very imprecise because it nearly dissolved during chemical abrasion and contains <0.2 pg of Pb*. These four analyses yield a weighted mean $^{207}Pb/^{206}Pb$ date of 3517.6±0.7 Ma (MSWD = 0.6), interpreted to date crystallization of this phase of the granitoids. Apatite from the sample ranged from stubby subrounded hexagonal prisms to elongate euhedral hexagonal prisms. Nine single grain fractions are within ±1% concordant, and give $^{207}Pb/^{206}Pb$ dates that range primarily from ~3160 to 3190 Ma. One fraction is ~-3% discordant, and one grain 0.6% discordant is ~3109 Ma (Fig. 7).

EKC02-38, EKC02-46, EKC02-47

Three dikes interpreted to be syntectonic in origin were collected from within ± 10 m of the contact between the Steynsdorp pluton and the Theespruit Formation (Fig. 6). EKC02-46 and EKC02-47 are granitic pegmatites <10 cm in width, cross-cut foliation of the host rock (EKC02-46 cuts the footwall, and EKC02-47 cuts the hanging wall), but also contain open to tight isoclinal folds that are axial planar to the local foliation and have hinge lines that are parallel to the regional stretching lineations (Figs. 6, 7). EKC02-38 is an aplitic dike ~20 cm wide that cross-cuts the pegmatitic dikes in the area but is foliated parallel to the local foliation. About 2-3 kg of the dikes yielded only a

dozen zircons each, which were all sub- to euhedral and elongate, with fresh crystal terminations. The grains ranged in size from <100 to >200 μm in length and were clear to cloudy to brown in appearance. Many of these zircons dissolved during chemical-abrasion, though 5-6 analyses were successfully recovered. Each dike yielded inherited zircons that ranged in age from 3510-3518 Ma, presumably derived from the Steynsdorp gneisses. EKC02-47 also contained a population of four zircons that were ~3212 Ma, that are also interpreted to be inherited. EKC02-38 and EKC02-46 yielded one concordant grain each, and both grains have a $^{207}Pb/^{206}Pb$ date of 3103.7 ± 0.8 Ma. One grain from EKC02-47 yielded a $^{207}Pb/^{206}Pb$ date of 3102.4 ± 0.8 Ma (Fig. 7).

WKC00-88

This is a coarse-grained, undeformed sample of Vlakplaats granodiorite, sampled about 1.5 km north of the Steynsdorp pluton (Fig. 6). Because this body cross-cuts the Theespruit Formation, the primary folding and foliation within the Steynsdorp antiform predate this intrusion. An ~5 kg sample of this rock yielded about 20 zircons that were acceptable for analysis. Many of these zircons dissolved during chemical-abrasion, though seven grains were successfully analyzed. Four discordant inherited grains yield $^{207}Pb/^{206}Pb$ dates between ~3300 and 3400 Ma. A population of three younger grains have $^{207}Pb/^{206}Pb$ dates of ~3230 Ma, and two of these are concordant and yield a weighted mean $^{207}Pb/^{206}Pb$ date of 3229.8 ± 0.6 Ma (MSWD = 1.7), interpreted to be the crystallization age of the rock (Fig. 7). Six single apatite grains were also dated, and the analyses are variably discordant, though all but one give $^{207}Pb/^{206}Pb$ dates ≥3200 Ma, consistent with their recording cooling after intrusion.

4.3. Northwest margin: Honeybird Shear Zone

4.3.1. Previous work

A series of exposures located along the Kaap river NE of Barberton show clearly the shear zone separating quartzites and metaconglomerates of the Moodies Group from plutonic basement rocks (here called the Honeybird Shear Zone, HSZ, Fig. 2). Several studies detail the sedimentology and structural geology of this portion of the Moodies Group and nearby localities (Anhaeusser, 1976; de Ronde and de Wit, 1994; Fripp et al., 1980; Gay, 1969; Heubeck and Lowe, 1994b; Lowe and Byerly, 1999a). Fripp et al. (1980) interpreted the contact to be a ductile, south dipping thrust fault. However, de Ronde and de Wit (1994) noted that the footwall of this south-dipping shear zone is part of the Stentor pluton, which was dated at 3107 ± 5 Ma ~10 km away from the Honeybird locality (Kamo and Davis, 1994), and suggest the fabrics in the HSZ record late transtension in the area. The orthogneisses in the footwall of the HSZ clearly contain multiple phases of intrusions within distinct cross-cutting relationships, and our purpose for studying the area is to work out the relative sequence of intrusions and to resolve the kinematics and timing of movement on the HSZ.

4.3.2. Structural analysis

Our investigation of the HSZ focuses on where the rocks are clearly exposed in a gorge along the Kaap river, off of R38 NE of Barberton, on the dirt road to the old Honeybird rail depot. The footwall of the Honeybird Shear Zone is composed of two main rock types. The older is a banded gneiss with alternating tonalitic to granodioritic lithologies and also sparse mafic layers. This unit is cut by a more homogeneous intrusion of

granodioritic to granitic composition. About 1 km north of the road crossing, only the homogeneous granitic gneiss is present, and it strikes ~E-W and dips 30-60° to the south (Fig. 8), and this rock is cut by late pegamtitic dikes. In several locations, these dikes have a weak foliation and are offset in a normal sense (top to the south). Further towards the south, the older banded gneiss is present and both rock types develop a strongly pronounced foliation with a strong stretching lineation that trends and plunges to the SW (Fig. 8). Also present are amphibolite bands and boudins. On the south side of the river crossing, rocks are highly mylonitized, rock types are difficult to distinguish, and several generations of pegmatitic dikes cross-cut the foliation. The older generations are variably sheared into parallelism with the host rock and have parallel lineation patterns as well. Younger generations of dikes cross-cut foliation, and are foliated yet unlineated, and are offset semi-ductilely with a normal shear sense (top to the south) along foliation planes. The contact with the Moodies Group in the hanging wall of the HSZ is several hundred meters to the south, but is not exposed. Moodies conglomerates are exposed ~1 km to the SW, where the bedding/foliation is parallel to the orthogneisses in the HSZ and a strong SW-dipping stretching fabric is recorded by elongate pebbles (Gay, 1969).

4.3.3. Sample collection and geochronology

Four samples from the HSZ were collected for U-Pb zircon geochronology. The main goals were to date crystallization of the main rock-types in the basement rocks and to place constraints on the timing of movement in the shear zone. Data are presented in Table 1 and Fig. 8.

KPV99-90

This is a sample of a tonalitic phase of the older, banded gneiss from the footwall of the HSZ. KPV99-90 was collected near the river crossing, where the younger granitic gneiss clearly cross-cuts it. This sample yielded abundant euhedral prismatic zircons up to 300 μm in length. Nine chemical-abraded single zircons were analyzed, and five yield a cluster near concordia with weighted mean $^{207}Pb/^{206}Pb$ date of 3258.3 ± 0.3 Ma (MSWD = 1.0), while the other four grains are excessively discordant.

KPV99-89

This sample was collected from within the homogeneous granitic gneiss that cross cuts KPV99-90. It yielded abundant clear, euhedral prismatic zircons, and seven were chosen for analysis. Three of these grains yield a weighted mean $^{207}Pb/^{206}Pb$ date of 3106.0 ± 0.5 Ma (MSWD = 1.2; Fig. 8). One other grain also has a $^{207}Pb/^{206}Pb$ date of ~3100, but is discordant, and three nearly concordant inherited grains have dates that range from 3224-3227 Ma.

BSO4-1, BS04-2

Two pegmatitic dikes from the highly mylonitized zone south of the river crossing were sampled. BS04-1 is sheared into parallelism with the host-rock foliation and is strongly lineated. BS04-2 cross-cuts BS04-1 and is foliated but not strongly sheared, though in places is ductilely offset along foliation planes. Each sample yielded <10 zircons that were acceptable for analysis. Five of six grains analyzed from BS04-1 are concordant and have $^{207}Pb/^{206}Pb$ dates from 3223-3226 Ma. Because these grains do not form a

coherent cluster, it suggests that they do not represent a crystallization age, but may instead be inherited. One analysis from BS04-2 is concordant with a $^{207}Pb/^{206}Pb$ date of 3104.6 ± 1.3 Ma, and this is our best estimate of the crystallization age. Two concordant analyses from BS04-2 were ~3254 and 3226 Ma, and two more discordant zircons were ~3100 and 3250 Ma.

4.4. Southwest margin: Stolzburg pluton

4.4.1. Previous work

Most of the recent published work on the BGB is has been focused along the SW margin of the belt, particularly within the Stolzburg Pluton and surroundings (Diener et al., 2005; Dziggel et al., 2005; Dziggel et al., 2002; Kisters et al., 2003; Stevens et al., 2002; Westraat et al., 2005; Fig. 9). Kamo and Davis (1994) reported an age of 3460 +5/-4 Ma for the oldest phase of the Stolzburg pluton, and also dated two near-concordant zircons with $^{207}Pb/^{206}Pb$ dates of ca. 3237 and 3255 Ma in a younger foliated phase. One concordant sphene analysis from that sample gave a $^{207}Pb/^{206}Pb$ date of ca. 3201 Ma. U-Pb zircon dating of a syntectonic dike intruding one of the paragneiss units included in the Stolzburg pluton suggest that deformation associated with amphibolite to granulite grade metamorphism occurred at ~3230 Ma (Dziggel et al., 2005), while U-Pb dates of sphene place a minimum date on metamorphism, also at ca. 3230 Ma (Diener et al., 2005; Dziggel et al., 2005). Kisters et al. (2003) suggest exhumation of these rocks occurred along a mid-crustal detachment that runs within the BGB directly north of the northern margin of the Stolzburg pluton, thereby juxtaposing those rocks against the lower-grade rocks of the greestone belt, but no constraints on the timing of movement were reported.

Our sampling effort in this area was geared towards placing constraints on the <600 °C exhumation history of the footwall rocks of the proposed detachment, in order to help constrain the timing of juxtaposition of the BGB with the higher-grade rocks to the south.

4.4.2. Sample collection and geochronology

EKC03-3

This sample was collected at the NE margin of the Stolzburg pluton along the Komati river, below the proposed detachment zone of Kisters et al. (2003), approximately 200 m NW of the location of sample 61406 in Fig. 2 of Diener et al. (2005). Here, outcrops are well-exposed by the Komati river, where undeformed rocks of the Stolzburg pluton intrude into amphibolites that are in contact with garnet sericite schists of the Theespruit Formation. Where the Stolzburg pluton intrudes the amphibolites, it becomes fine-grained and the amphibolites have a flattening fabric defined by amphibole elongation and flattened spherical ocelli. Sample EKC03-3 yielded abundant stubby euhedral zircon prisms and euhedral apatite. Six single grain zircon analyses all give $^{207}Pb/^{206}Pb$ dates of ca. 3.45 Ga, of which two are concordant and yield a weighted mean $^{207}Pb/^{206}Pb$ date of 3455.9 ± 0.5 Ma (MSWD = 0.1; Fig. 10). Eight single-grain apatite analyses yield $^{207}Pb/^{206}Pb$ dates between ca. 3263 and 3401 Ma, and all are variably discordant (Fig. 10). There is no correlation between the $^{207}Pb/^{206}Pb$ date of the grains and their cylindrical diameter, suggesting that the spread in dates did not result from simple volume diffusion, but instead may be a product of a complex series of metamorphic growth and Pb-loss. The $^{207}Pb/^{206}Pb$ dates therefore place a lower limit on the passage of

the rock through the closure temperature of apatite (T_c ~ 400-500 °C; Chamberlain and Bowring, 2000; Cherniak et al., 1991).

KPV99-96 and EKC03-11

These samples were collected along the Theespruit river near the center of the Stolzburg pluton (Fig.9). This outcrop contains numerous lithologies including banded tonalitic gneiss that is cross-cut by younger granodioritic gneiss, and several younger phases of cross-cutting and heterogeneously deformed dikes. There are large (≤ 50 m in diameter) greenstone xenoliths that are cut by the younger dikes both parallel and discordant to foliation. These are the same outcrops that were sampled by Kamo and Davis (1994), and were described in some detail by Robb and Anhaeusser (1983).

Sample KPV99-96 is a representative sample of the oldest banded gneiss (Fig. 11). It contains abundant euhedral stubby zircons from which four grains were picked for analysis. Three of these grains form a concordant cluster with a weighted mean $^{207}Pb/^{206}Pb$ date of 3455.5 ± 0.6 Ma (MSWD = 0.6; Fig. 11), which we interpret to be the timing of crystallization. One older grain is also concordant and has a $^{207}Pb/^{206}Pb$ date of ca. 3467 Ma, and is likely inherited. EKC03-11 is a sample of a granodioritic dike that cross-cuts one of the larger mafic xenoliths, and is itself locally folded and contains a weak foliation parallel to its host (Fig. 11). Three concordant zircon analyses yield a weighted-mean $^{207}Pb/^{206}Pb$ date of 3212.5 ± 0.8 Ma, interpreted to be the crystallization age. U-Pb systematics of apatite from both samples are similar, in that nine of eleven analyses give $^{207}Pb/^{206}Pb$ dates between 3080 and 3100 Ma, and are between ~0 and 35% discordant (Fig. 11).

EKC03-9 and KPV99-94

The contact between this pluton and the Stolzburg areas sampled above is not well exposed and has not been previously described. We note, however, that it lies to the north of the Saddleback-Inyoka fault system, which has been interpreted to be the major transcurrent shear zone representing the surface exposure of a continental suture (de Ronde and de Wit, 1994; de Wit et al., 1992; Heubeck and Lowe, 1994a). Two samples of variably foliated granodioritic gneiss from the central portion of the Nelshoogte pluton were collected from quarried outcrops at the Vygeboom dam on the Komati river (Fig. 9). Both samples yielded abundant zircon and apatite. Four zircons from each sample are near concordant and yield a weighted mean $^{207}Pb/^{206}Pb$ date of 3236.2 ± 0.3 Ma (MSWD = 0.6; Fig. 10), which is identical to the zircon and sphene $^{207}Pb/^{206}Pb$ date reported in de Ronde and Kamo (2000) of 3236 ± 1 Ma. Two apatites from KPV99-94 and six apatites from EKC03-9 were analyzed. Two of the six analyses from EKC03-9 were negatively discordant, though the other four are near concordant and have $^{207}Pb/^{206}Pb$ dates between ca. 3225 and 3201 Ma, and the spread in dates show a positive correlation with grain size, consistent with their representing cooling dates (Fig. 10). The two analyses from KPV99-94 are younger and discordant, with dates of ca. 3122 and 3166 Ma (Fig. 10).

5. SYNTHESIS AND DISCUSSION

5.1. Timing and kinematics of deformation ca. 3.2-3.1 Ga

One of the key characteristics of both Archean and younger greenstone belts is the juxtaposition of high-grade orthogneisses and metasediments against lower grade supracrustal metasediments and metavolcanics. We describe several of the particularly well-exposed shear zones that separate the low-grade supracrustal rocks of the Barberton greenstone belt (BGB) from the generally higher-grade orthogneiss bodies that surround the belt. This section will summarize the kinematics of shear zones examined and the time-constraints placed on transtension and differential exhumation by zircon U-Pb geochronology and new and published U-Pb and $^{40}Ar/^{39}Ar$ thermochronology.

The Pigg's Peak inlier in NW Swaziland (Figs. 2, 3) records complicated early intrusion and deformation that was overprinted within the NE-striking, NW- dipping Phonphonyane Shear Zone (PSZ), which separates the upper amphibolite-grade basement orthogneisses of the Ancient Gneiss Complex (AGC) from lower greenschist grade sandstones and siltstones of the BGB to the NW. The oldest sampled unit, a porphyritic tonalite gneiss (Fig. 4) also gives the oldest age in the Kaapvaal craton, with a $^{207}Pb/^{206}Pb$ date of 3662.8 ± 0.5 Ma. The fine-grained foliated granite (Fig. 3), originally mapped as Pigg's Peak granite (Wilson, 1979, 1982), is in fact distinct texturally from the ca. 3140 Ma Pigg's Peak granite (Schoene and Bowring, submitted) and is also considerably older, dated at 3545.6 ± 0.5 Ma (Fig. 4). These dates from the AGC are consistent with zircon ion-microprobe dates reported in Compston (1988) and Kröner et al. (1989), though our samples show a less heterogeneous spread in dates that may be due to actual differences

in zircon growth, a bias introduced by the chemical-abrasion method (i.e. preferentially dissolved younger high-U metamorphic rims), or that Pb-loss in the previous studies was masked by the relatively large errors associated with ion-microprobe U-Pb analysis. Timing of north-directed transtension in the PSZ is bracketed locally by the crystallization age of a late syntectonic dike (sample EKC02-8) of 3223.4 ± 1.9 Ma (Fig. 5). This date needs to be reconciled with the results of Schoene and Bowring (submitted), who conclude based on U-Pb titanite and apatite thermochronology that a period of rapid cooling and 7-15 km of exhumation associated with the intrusion of the Pigg's Peak granite ca. 3140 Ma affected these rocks. Our data show that this period of exhumation was not accommodated by penetrative shear in the PSZ, but instead was accommodated along a reactivated portion of the fault within the one kilometer between our sampled dike and the contact with the BGB, where outcrop is sparse (Fig. 3). The rock unit exposed closest to the fault in the footwall is in the northern portion of the mapping area and is fine-grained foliated granite, identical in appearance to the ca. 3545 Ma granite from the center of the mapping area. Those few outcrops are densely invaded by quartz veins and brittle fractures, possibly related to late brittle movement on the PSZ. We note that if the Pigg's Peak granite were sheared, it would be difficult to distinguish from the older granite, and such material may crop out close to a reactivated portion of the PSZ. Also, the recognition of a foliated homogeneous ca. 3.545 Ga granite within the AGC that is easily misidentified as ca. 3.1 Ga granite means that there may be much more pre-3.5 Ga bedrock exposed in NW Swaziland than previously recognized.

The predominant foliation and lineation pattern in the Steynsdorp antiform is attributed to NE-SW extension that resulted in doming and exhumation of the Steynsdorp

pluton during core-complex formation, in which the contact between the Steynsdorp pluton and the overlying Theespruit Formation is the bounding extensional shear zone (here called the Steynsdorp shear zone; SSZ). The primary evidence for this is the decreasing plane strain away from that contact, the parallel stretching lineations and isoclinal fold hinges throughout the anticline, and the strike-slip to normal shear sense indicators along the western margin of the pluton, similar to descriptions of core-complexes in other localities (e.g. Davis et al., 1988; Lister et al., 1984; Saltzer and Hodges, 1988; Whitney et al., 2004). Kisters and Anhaeusser (1995b) suggest the present structural pattern is a result of NW-SE directed compression superimposed on a dome geometry. Both models require that the maximum compressional stress be roughly NW-SE, though the model of Kisters and Anhaeusser (1995b) does not involve any offset along the SSZ, and implies a pre-existing domal pluton. The observation that stretching lineations remain oriented in the same direction throughout the radial plane of foliation along that contact in addition to simple shear indicated by offset dikes and sigmoidal porphyroclasts suggests offset along that contact was important. The timing of formation of the Steynsdorp antiform is in part bracketed by the intrusion of the undeformed Vlakplaats granodiorite (sample WKC00-88; Fig. 7), dated here to be 3229.8±0.6 Ma. However, the SSZ was clearly locally reactivated with a similar kinematic sense, constrained by the intrusion of a series of syntectonic dikes (samples EKC02-38, EKC02-46 and EKC02-47) ca. 3104 Ma (Fig. 7). Moderate foliation and locally strong lineations within the ca. 3107 Ma Mpuluzi batholith at the southern contact with the Steynsdorp pluton is consistent with its intrusion into an extensional setting. The timing of major movement along the SSZ is bracketed by U-Pb apatite thermochronology. U-Pb apatite

dates from the Vlakplaats granodiorite in the hanging wall of the decollment are 3200-3230 Ma while those from the footwall in the Steynsdorp gneisses (sample EKC02-40; Fig. 7) are ca. 3160-3185 Ma. Younger apatite dates from the Steynsdorp pluton are therefore either a result of continued localized extensional exhumation along the SSZ, slow thermal equilibration following exhumation, or from slight resetting by the Mpuluzi batholith, which is ~1.5 km from the sample locality. What is clear from these data are that the timing of juxtaposition of the low-grade rocks in the hanging wall of the SSZ with the amphibolite grade Steynsdorp pluton occurred not long before the intrusion of the Vlakplaats granodiorite ca. 3.23 Ga. If the juxtaposition had occurred earlier than that, the apatite cooling dates from the Steynsdorp pluton would have to be older to be in equilibrium with the low-grade conditions of the lower Onverwacht Group rocks in the hanging wall of the SSZ.

The SW margin of the BGB in the area of the Stolzburg pluton exposes the highest-grade rocks near the BGB (Diener et al., 2005; Dziggel et al., 2002; Kisters et al., 2003; Stevens et al., 2002). Our two samples of the Stolzburg pluton record very different histories. In particular, one sample from the interior of the pluton (sample KPV99-96) is part of highly deformed gneisses whereas that from the NE margin of the pluton (sample EKC03-3) is undeformed and preserves intrusive contacts into the base of the Theespruit Formation of the BGB. Both samples give identical crystallization ages of 3455.5 ± 0.6 and 3455.9 ± 0.5 Ma for the deformed and undeformed samples, respectively (Figs. 9, 10, 11). Ductile deformation of KPV99-96 in the central portion of the Stolzburg pluton is bracketed by the age of a cross-cutting dike (sample EKC03-11, Fig. 11), to have occurred largely before 3212.5 ± 0.8 Ma. The fact that the central

Stolzburg pluton was deformed, whereas the northern boundary of the pluton was not, suggests that either there is a significant structural break between these two locales or that they responded differently to ca. 3.2 Ga regional deformation. This question is further clarified by the U-Pb apatite thermochronology, as follows.

Moderately discordant U/Pb apatite dates of 3260-3400 in the undeformed northern margin of the Stolzburg pluton (sample EKC03-3) are a minimum cooling time for the rock through ~400-500 °C. Retrograde P-T conditions for metasediments <100 m from the sample locality are 6.1 ± 2.7 kbar and 569 ± 42 °C and peak conditions in rocks nearby are ~7.5 kbar and 550 °C (Diener et al., 2005). Reconciling our thermochronological data and the field relations with these P-T estimates is easiest if peak metamorphism occurred at >3400 Ma, and that the apatite data record cooling and/or cooling and low-T metamorphic overgrowth or Pb-loss. However, U-Pb sphene data reported in Diener et al. (2005) give an upper intercept date of 3229 ± 25 Ma on twelve LA-ICPMS U-Pb analyses which they suggest dates peak metamorphism. It is difficult to reconcile those conclusions with our data because apatite would be completely reset at 3230 Ma under the reported metamorphic conditions. Application of the simple diffusion model of Schoene and Bowring (submitted) shows that for apatite dates to fall roughly between 3.40 and 3.26 Ga by resetting at 3.23 Ga, the rock would have to be heated, for example, from <400 to 560 °C (the lower end of peak temperatures) and cooled again in less than 1.5 Myr. Given the P-T path calculated for these rocks by Diener et al. (2005), it implies an average burial-exhumation rate of ~2.4 cm/yr. This is unlikely, as it is among the highest exhumation rates observed in modern orogenic belts (e.g. Burbank, 2002), and to achieve this without deforming this portion of the Stolzburg

pluton seems unlikely. Therefore it seems that the sphene dated by Diener et al. (2005) grew below its closure temperature and that this portion of the BGB actually maintains a signature of ca. 3.45 Ga metamorphism synchronous with intrusion of the Stolzburg, Theespruit and Doornhoek plutons, as was previously inferred (de Wit et al., 1983; de Wit et al., 1987b; Kisters and Anhaeusser, 1995a). Metamorphism of this age is reflected by $^{40}Ar/^{39}Ar$ dates of metamorphic amphiboles of >3.4 Ga from within the Komati Formation (Lopez Martinez et al., 1992). U/Pb zircon ages of the Theespruit and Doornhoek plutons are identical to those of the Stolzburg pluton (Kamo and Davis, 1994), and a sphene date of ca. 3.45 Ga was reported from the Theespruit pluton (Kamo and Davis, 1994), which is consistent with it having resided below the closure temperature of sphene since its intrusion.

By contrast, U/Pb apatite dates from the central Stolzburg pluton (samples KPV99-96 and EKC03-11; Fig. 11) of ca. 3080-3100 Ma likely record exhumation and cooling of these rocks synchronous with granitoid intrusion ca. 3.1 Ga. The ca. 3107 Ma Boemanskop syenite and Mpuluzi batholith are >5 km from the sample locality (Fig. 9), and it is unlikely that they are responsible for resetting the ca. 3.1 Ga apatite dates from initial 3.2 Ga cooling. By comparison, the apatite from the Steynsdorp samples (EKC02-40 and WKC0088) are <2 km from the Mpuluzi batholith and still largely retain the 3.2 Ga cooling signature in the U-Pb systematics. The interpretation that cooling and unroofing coeval with granite intrusion here is similar to that for the rocks in the PSZ, which cooled rapidly during intrusion of the Pigg's Peak granite ca. 3140 Ma following ~80 Myr of middle to lower crustal residence (Schoene and Bowring, submitted). Because we have documented extension to have occurred synchronous with granite

intrusion ca. 3.1 Ga elsewhere in the belt, and because Westraat et al. (2005) show that the Boesmanskop and nearby Mpuluzi granites intruded in an extensional setting also, it seems likely that extension affected the central portion of the Stolzburg pluton as well. This hypothesis reconciles the disparate cooling histories observed in the central and northern portions of the pluton, but also requires that a major decollment zone runs through the interior of the Stolzburg pluton, and not within the BGB as suggested by Kisters et al. (2003) (Fig. 9).

Along the northern margin of the BGB, the south-dipping Honeybird Shear Zone (HSZ) that separates low-grade sandstones and conglomerates of the Moodies Group in the hanging wall from amphibolite grade orthogneisses (Fig. 2) also records dominantly NE-SW directed extension ca. 3.1 Ga (Fig. 8). A banded gneiss in the footwall (sample KPV99-90; Fig. 8) crystallized at 3258.3 ± 0.3 Ma, and is the oldest example of bedrock dated immediately north of the BGB, though xenoliths from the Nelspruit batholith gave U-Pb zircon dates of ca. 3.3 Ga (Kamo and Davis, 1994). This may be the plutonic equivalent of felsic tuffs from within the Fig Tree Group, which contain zircons that give a weighted mean U-Pb date of 3258 ± 3 Ma (Byerly et al., 1996). Movement in the HSZ is constrained by the intrusion of the 3106.0 ± 0.5 Ma granitic gneiss of the Stentor pluton (sample KPV99-89; Fig. 8). A late synkinematic dike (sample BS04-2; Fig. 8) from this outcrop contained a single non-inherited concordant zircon with an age of 3104.6 ± 1.3 Ma, consistent with movement in the shear zone ca. 3110-3100 Ma.

Thermchronology from the Kaap Valley and Nelshoogte plutons, also along the northern margin of the BGB (Fig. 2), are consistent with their intrusion into the middle or upper crust. U-Pb sphene and apatite data (Kamo and Davis, 1994; Schoene and

Bowring, submitted) and $^{40}Ar/^{39}Ar$ hornblende data (Layer et al., 1992) from the Kaap Valley pluton document rapid cooling after intrusion ca. 3227 Ma (Kamo and Davis, 1994; Schoene et al., 2006) (Fig. 10). To the SW, our U-Pb apatite data from the 3236.2 ± 0.3 Ma Nelshoogte pluton (sample EKC03-9) range between 3225 and 3200 Ma, consistent with slightly slower post-intrusion cooling compared to the Kaap Valley pluton. Layer et al. (1998) report $^{40}Ar/^{39}Ar$ hornblende dates of 3179 ± 18 Ma from a gabbroic dike cross-cutting the Nelshoogte pluton. Updated ages for reference monitors and potentially inaccurate ^{40}K decay constants make the $^{40}Ar/^{39}Ar$ dates difficult to compare to the U-Pb dates (Min et al., 2000; Renne et al., 1998; Schoene et al., 2006), but they are broadly consistent with a rapid high-temperature cooling history nonetheless for both the Kaap Valley and Nelshoogte plutons. $^{40}Ar/^{39}Ar$ biotite and muscovite from those plutons give dates from 3.1-3.0 Ga that are interpreted to reflect a combination of slow-cooling and partial resetting by the ca. 3.107 Ga Mpuluzi batholith (Layer et al., 1992, 1998). In light of the data presented in this study, the $^{40}Ar/^{39}Ar$ may also represent middle to upper crustal residence and slow cooling of these rocks during relaxation of isotherms following crustal extension ca. 3.1 Ga. The development of the ubiquitous gneissose fabric in both plutons must therefore have either occurred immediately after crystallization at high temperatures, or from ~3.2-3.1 Ga within the closure temperature range of biotite and muscovite.

5.2. Reconciling tectonic models for the evolution of the Barberton greenstone belt

The field mapping, kinematic analysis and geo- and thermochronology from this study place tight constraints on the post-3.2 Ga tectonic history of the BGB and also have

significant bearing on the nature of the tectonic setting for deformation and inferred terrane accretion ca. 3.23 Ga (Fig. 12). Field mapping and geochronology reveal that extensional to transtensional deformation along the margins of the BGB occurred widely between ca. 3.23-3.1 Ga, either as discrete episodes focused at ca. 3.23, 3.14 and 3.10 Ga or more continuously over that period of time (Fig. 12). Our inability to date movement on these faults beyond the simultaneous occurrence of syntectonic intrusions results in a correlative relationship between deformation and magmatism. However, thermochronology alone was used to determine fault offset along the PSZ, which does not rely on magmatism but still shows a correlation between exhumation on the PSZ and granite emplacement ca. 3.14 Ga. Thermochronology also indicates that transtension was likely responsible for exhuming and juxtaposing rocks from different crustal levels at ca. 3.23-3.19 Ga in the SSZ and ca. 3.1 Ga in the Stolzburg area (Dziggel et al., 2005; Kamo and Davis, 1994; Lopez Martinez et al., 1992; Schoene and Bowring, submitted).

A precise time-frame for the distribution of transtension is important in understanding the dynamics and tectonic setting of the proposed ca. 3.23 Ga orogenic event. For example, our data show that crustal extension and core-complex formation in the Steynsdorp area occurred immediately before or contemporaneously with compression documented in the SW portion of the BGB (de Ronde and de Wit, 1994; de Ronde and Kamo, 2000; Kamo and Davis, 1994; Fig. 12). In addition, transtension recorded on the PSZ occurred soon before 3223.4±1.9 Ma (Figs. 4, 5), post-dating compression documented to have occurred between 3229 and 3227 Ma within Onverwacth and Fig Tree Group rocks throughout the Weltevreden area in the SW BGB (de Ronde and Kamo, 2000), which can likely be extended to other NW-verging thrust

faults in western BGB. These observations possibly point to a partitioning of extension in the southern BGB and compression in the northern BGB ca. 3.23 Ga, or perhaps the relationship is much more complicated and biased by the structures we have sampled (Fig. 12). In any case, a comprehensive ca. 3.23 Ga tectonic model for the BGB must account for the contemporaneous existence of compression and extension along these structures. Sedimentology in the Moodies Group is consistent with the deposition of clastic conglomerates into a wide array of depositional settings contemporaneous with the NW-directed thrusting in the belt (Heubeck and Lowe, 1994a, 1994b; Lamb, 1984; Lamb and Paris, 1988; Lowe and Byerly, 1999b), though the timing of deposition of the Moodies Group sediment remain poorly constrained, and is probably highly variable across the belt (de Ronde and de Wit, 1994; de Wit, 1991; Heubeck and Lowe, 1994a; Lamb, 1984). For example, Heubeck and Lowe (1994b) showed that Moodies deposition in the western BGB, north of the Saddleback-Inyoka fault system (Figs. 2, 9), was initiated in extensional basins, some of which were then converted to contractional depositional settings in intermontane basins. Additionally, clast composition and paleocurrent directions are variable within the Moodies Groups across the belt (Heubeck and Lowe, 1994a, 1999; Jackson et al., 1987; Kröner and Compston, 1988), indicating a potentially complicated tectonic setting for their deposition.

Because we have constrained the timing of transtension in the BGB, we can further distinguish between different models for ca. 3.23 Ga tectonism. For example, Kisters et al. (2003), following a model of Marshak et al. (1992), suggests that following terrane collision and crustal thickening ca. 3.23 Ga, a gravitational instability led to an extensional collapse of the orogen along a basal mid-crustal detachment, in turn followed

by diapiric rise of the bounding orthogneiss terranes. The intrusion and thermal histories of the Kaap Valley and Nelshoogte plutons are not inconsistent with this model, in that these plutons intruded and cooled quickly, but contain a broadly domal geometry and were deformed plastically. Data from the PSZ are at first glance consistent with this model also, in that NE-SW transtension is bracketed to have nearly terminated ca. 3224 Ma – immediately after the compression documented in the SW BGB. However, the PSZ at that time was a middle- to lower-crustal shear zone, and these rocks were not exhumed to below 500 °C until < 3.14 Ga (Schoene and Bowring, submitted), ruling out a genetically linked diapiric episode. Core-complex formation in the Steynsdorp antiform, having predated compression in at least part of the belt, does not support an extensional collapse model.

Thermochronological constraints from the Stolzburg pluton are also inconsistent with the orogenic collapse model, in that rocks from the northern portion of the Stolzburg pluton preserve metamorphism from ca. 3.45 Ga (Fig. 10), despite the fact that position of the mid-crustal detachment proposed by Kisters et al. (2003) as responsible for accommodating gravitational collapse places these rocks in its footwall (Fig. 9). Therefore, either the structure mapped by Kisters et al. (2003) is actually older than 3.23 Ga (de Ronde and de Wit, 1994), or in reality it cuts structurally below the NE portion of the Stolzburg pluton and possibly the Theespruit and Doornhoek plutons and the Tjakastad schist belt (Fig. 9). In any case, because the central portion of the Stolzburg pluton was not exhumed to below 400 °C until ca. 3.1 Ga, its juxtaposition against the upper crustal rocks to the north was not likely a result of orogenic collapse. We suggest instead that it relates to the ca. 3.1 Ga extensional unroofing driven by other forces.

The contemporaneous existence of deformation and widespread magmatisn ca. 3.23 Ga as summarized above is most consistent with a model involving oblique collision and terrane accretion in which the BGB accommodated strain with a flower-structure geometry. Because the structures in the western BGB all verge to the NW, the flower-structure is assymetric, and thus possibly linked to a single fault at depth. This mechanism is convenient in that it allows for the potentially simultaneous occurrence of compression, extension and translation without appealing to major changes in tectonic stresses. In such a scenario, the specific kinematics on a fault plane would be dictated by the local stresses imposed by rigid blocks such as plutons or gneiss domes and the preexisting orientation of reactivated fault surfaces (Fig. 12). This interpretation does not affect previous models regarding the localized timing of compression or inferred terrane accretion, and in fact oblique convergence was suggested by de Ronde and de Wit (1994). Subsequent slight changes in the magnitude and direction of the maximum compressive stress resulted in a regional scale transition towards primarily transtensional tectonics along reactivated faults between 3.2 and 3.1 Ga. Reactivation of older structures partitioned strain into localized zones and acted to help preserve the older geologic histories of individual tectonic blocks, for example sedimentary packages throughout the BGB that still record ca. 3.23 Ga compression, the Steynsdorp antiform that records pre-3.23 Ga extension, and numerous blocks of crust that preserve distinct thermal and structural histories spanning 3.45-3.10 Ga. In fact, all cases of reported 3.23 Ga thrust faults are interpreted to be later reactivated as strike-slip faults, with crustal shortening preserved within fault-bounded individual packages of shortened Onverwacht, Fig Tree and Moodies Group rocks (de Ronde and de Wit, 1994; de Ronde and Kamo,

2000; de Ronde et al., 1991; Heubeck and Lowe, 1994a, 1994b; Lowe et al., 1999). An important corollary to this is that undeformed intrusions that cross-cut certain structures may locally constrain deformation, but correlating that timing elsewhere in the region may not be appropriate. For example, the intrusion of the Dalmein pluton at 3216 +2/-1 Ma (Kamo and Davis, 1994) has been cited to mark the end of deformation in the BGB (Diener et al., 2005; Kamo and Davis, 1994; Kisters et al., 2003). This inference may be locally applicable but is clearly inaccurate elsewhere in the belt where transtensional deformation occurred during intrusion of the ca. 3140 Ma Pigg's Peak batholith (Schoene and Bowring, submitted), the ca. 3107 Ma Mpulizi batholith (Westraat et al., 2005, and this study), and the Stentor pluton. Indeed, the northern margin of the ca. 3445 Ma Stolzburg pluton avoided penetrative strain during ca. 3.23 Ga deformation, though the central pluton was exhumed from the middle or lower crust ca. 3.1 Ga.

In summary, our new structural observations and geochronology, when combined with new and existing thermochronology show that the BGB can be envisioned as a tectonic melánge that preserves the geologic histories of numerous lithotectonic terranes through prolonged transform boundary deformation localized on reactivated faults. Thus, Moodies Group deposition likely occurred between 3.23-3.10 Ga in a series of compressional and extenional basins that were subsequently deformed and modified during lower- to mid-crustal exhumation. The amount of offset during strike-slip faulting over this period is unknown, but had potential to translate different blocks large distances. Further constraining the original geometry of the crust during ca. 3.23 Ga terrane assembly would be benefited by further work north and south of the BGB in the Nelspruit migmatite terranes described by (Viljoen and Viljoen, 1969) and in the AGC

and southern Swaziland. In fact, our date of the basement gneiss from the HSZ of ca. 3258 Ma may represent juvenile continental crust that was accreted along the Saddleback-Inyoka fault synchronous with widespread magmatism and localized high-grade metamorphism ca. 3.23 Ga (Armstrong et al., 1990; de Ronde and de Wit, 1994; de Ronde and Kamo, 2000; Dziggel et al., 2005; Kamo and Davis, 1994; Stevens et al., 2002). Correlating this date with deformation and magmatism south of the BGB would undoubtedly help constrain the history of this potentially complicated plate margin during subduction and amalgamation.

5.3. Implications for stabilization of the eastern Kaapvaal craton

The period of transtensional tectonics ca. 3.2-3.1 Ga is the last regionally extensive deformational event documented in the vicinity of the BGB and is therefore somehow related to the final stabilization of this segment of lithosphere. Two major modifications of the compositional and structural architecture of the crust occurred during this period: crustal extension may have led to an overall thinner crust, and granitic magma generated in the lower crust intruded as subhorizontal planar sheets in the middle to upper crust, and subsequent peniplaination through an unknown thickness of these granites occurred prior to the deposition of the Transvaal supergroup at ca. 2.6 Ga. It has previously been hypothesized that the generation of ca. 3.1 Ga granites and translational faulting led to the stabilization BGB and AGC (de Ronde and de Wit, 1994; de Wit et al., 1992; Heubeck and Lowe, 1994b; Jackson et al., 1987; Kamo and Davis, 1994; Lowe and Byerly, 1999a). However, little geochronological, thermochronological or structural data for this

event have existed until now, and the causes of transtension and magma generation remain unclear.

Transtension and lower-crustal melting could have been generated by a number of processes, including post-orogenic collapse with extension occurring during or immediately after orogenic crustal thickening (e.g. Bott, 1982; Dewey, 1988; England and McKenzie, 1982). Though extension and transtension did occur during orogency ca. 3.23 Ga, an extensional collapse driven by gravitational forces alone was not likely responsible the observed extension ca. 3.14 or 3.11 Ga (see discussion above). Another process that has been invoked to cause extension and heating of the lower crust is that of lithospheric and/or lower crustal delamination (Bird, 1979; Meissner and Mooney, 1998). Lithospheric delamination ca. 3.14 or 3.1 Ga beneath the BGB is difficult because in this model, upwelling of fertile asthenosphere would occur, whereas the observed cratonic lithosphere beneath this area was likely derived during ca. 3.23 Ga subduction and arc magmatism by the model of Jordan (1978, 1988). The lack of kimberlites bearing fresh xenoliths in the eastern Kaapvaal craton prevents a better understanding of the timing of lithosphere formation. Episodic lower crustal delamination as a driving mechanism for extension and magmatism beneath the BGB may be more plausible. A mafic residue left in the lower crust during arc magmatism or from basaltic underplating ca. 3.23 Ga may have cooled over a period of 90-120 Myr during post-orogenic erosion and isostatic rebound, resulting in a lower crust that is more dense than the buoyant cratonic mantle. Alternatively, numerical modeling mimicking the crustal structure of the Pilbara craton in the Mesoarchean showed that extended residence of heat producing elements (U, Th, K; HPEs) in the lower crust beneath a thermal blanket of mafic material may have lead to

temperature increases of up to 230 °C in the middle to lower crust over periods of 10-100 Myr (Sandiford et al., 2004). These authors suggested that this triggered diapiric upwelling and dome-keel formation there. While our structural observations and geochronology are inconsistent with large-scale diapirism in the BGB, a similar mechanism may have led to melting in the lower crust or made it easier for melting to occur 90-120 Myr after compression and crustal thickening ca. 3230 Ma. Increasing temperatures in the lower crust could also lead to a long-term rheological weakening of those rocks, which may result in lateral extrusion of material, extension in the upper crust, and lower crustal melting (Bird, 1991; Kusznir and Matthews, 1988; Zhao and Morgan, 1987). Equally viable is that far-field stresses on the BGB resulted in crustal extension ca. 3.2-3.1 Ga. Unfortunately, far-field stresses are difficult to evaluate because very little research in the eastern Kaapvaal craton has been directed south in the AGC (Compston, 1988; Hunter et al., 1978, 1984; Jackson, 1984; Jackson et al., 1987; Kröner et al., 1989) or within the basement rocks and migmatite terranes within the Nelspruit granite north of the BGB (Anhaeusser, 1973; Viljoen and Viljoen, 1969). However, similar ca. 3.10-3.08 Ga magmatism reported in crust exposed by the Vredefort impact structure (Flowers et al., 2003; Hart et al., 1999; Moser et al., 2001; Robb et al., 1992), which closely predates eruption of the rift-related Dominion volcanics ca. 3.09-3.07 Ga (Armstrong et al., 1991; Robb et al., 1992), may not only provide far-field correlations for extensional tectonics, but may also suggest that the entire eastern and central portion of the craton was assembled by that time (de Wit et al., 1992).

Regardless of the driving mechanism of crustal extension and granite intrusion, it is difficult to avoid that these events led to the stabilization of the lithosphere, which it

turns out is a predictable result. For example, extension and thinning of the crust will result in a lithosphere that is structurally stable over long time-periods (Fig. 13). This statement is based on rheological profiles of materials as a function of pressure and temperature, in which a material's intrinsic strength generally increases as a function of depth until it passes from the brittle into the ductile flow regime, at which point the strength decreases dramatically with depth (Brace and Kohlstedt, 1980; Kusznir and Karner, 1985; Ranalli, 1995; Ranalli and Murphy, 1987). In their most simple form, these diagrams predict that a crust of any material will be stronger if its thickness is near the brittle-ductile transition, which is usually in the middle to lower crust, depending on the composition of the crust and geotherm. If the present day lower-crust was composed of mafic residue, perhaps left behind by granitic melt generation and extraction ca. 3.2-3.1 Ga, then one would predict an even stronger crustal profile (Ranalli, 1995). The transport of granitic magma into the upper crust can help stabilize the crust in several ways in addition to generating a strong rheological stratigraphy. Firstly, the placement of horizontally extensive sheets of granitic material can mechanically strengthen the crust, perhaps by cross-cutting pre-existing weaknesses with rigid material (Davidson et al., 1994; Karlstrom and Williams, 1998; Pavlis, 1996). Perhaps more important is the redistribution of the radiogenic HPEs from the lower crust into higher crustal levels. This mechanism can act to stabilize lower crust by lowering its long-term heat production, and also by creating opportunity to remove HPEs from the crustal column entirely through erosion of the upper crust (Sandiford and McLaren, 2002; Sandiford et al., 2002). In the central Kaapvaal craton, exhumation and peniplaination of ca. 3.1 Ga granites and their subsequent burial beneath the Witswatersrand basin occurred in a relatively short amount

of time, bracketed by the deposition of Dominion Group volcanics ca. 3.09-3.07 Ga (Armstrong et al., 1991; Robb et al., 1992). This process acted to remobilize HPEs, which in turn had an important affect on the final distribution of heat in the crust there (Hart et al., 1981; Nicolaysen et al., 1981). Timing of upper-crustal exhumation is less-well constrained in the eastern craton, but clearly the removal of the HPE rich upper crust was an important process there as well. Thus, there are a number of positive feedbacks between extension and granitic magmatism that could have resulted in a stable cratonic crust that is separate from the generation of a cratonic lithospheric mantle through subduction and accretion (Jordan, 1988; Schmitz et al., 2004).

Our observations in concert with previous investigations allow us to pose a three-stage model for stabilization of the eastern Kaapvaal craton: 1) subduction, mantle melting and terrane collision ca. 3.23 Ga led to depletion and stabilization of the mantle lithosphere (de Wit et al., 1992; Jordan, 1988; Parman et al., 2004), 2) extension, crustal thinning, and lower crustal melting ca. 3.14-3.10 Ga led to a more stable crustal rheological structures, which was further induced by 3) erosion and removal of HPE-rich upper crust. This sequence of processes gave it an inherent strength that has isolated it from deformation for ca. 3.1 Ga, despite its recent proximity to the margin of the African plate. The timing of stabilization is apparently different between the eastern and western Kaapvaal craton, in that most of the craton experienced several episodes of compression and extension between 3.1 and 2.7 Ga (see summaries in de Wit et al., 1992; Schmitz et al., 2004; Thomas et al., 1993). Generation and apparent stabilization of the mantle lithosphere in the vicinity of Kimberly (Fig. 1) is constrained by ca. 2.9 Ga Re-Os model ages from kimberlite-borne mantle peridotite xenoliths and diamond inclusions (Carlson

et al., 1999; Richardson et al., 1984; Richardson et al., 2001), which Schmitz et al. (2004) argued was the result of mantle growth during convergence and terrane accretion ca. 2.9 Ga between the Witswatersrand and Kimberly blocks (Fig. 1). However, significant crustal modification occurred after ca. 2.9 Ga terrane collision across large portions of the central craton, most notably that of the ca. 2.71 Ga Ventersdorp extensional episode. The effects of this event are evidenced as bimodal flood volcanism, generation of vast depositional basins (Fig. 1) and also as ultrahigh temperature metamorphism of the lower crust (Armstrong et al., 1991; Burke et al., 1985; de la Winter, 1976; de Wit and Tinker, 2004, Schmitz, 2003 #752; Tinker et al., 2002). This final reactivation of the crust brings up several important points. The first is that the BGB and northern AGC were largely unaffected by these events, illustrating that craton stabilization is at least partly a piecewise transition, or diachronous, effecting different portions of lithosphere at different times. Second, it is an interesting observation that rifting associated with the Ventersdorp event, not compression, was the final event to modify substantial portions of cratonic crust to the west of the areas described in this paper. Third, the preservation of peridotic diamond ages of ca. 2.9-3.2 Ga from mantle lithosphere may imply a decoupling between mantle and crust ca. 2.7 Ga (Doucouré and de Wit, 2002; Schmitz and Bowring, 2003b). This striking similarity between the relative sequence of events in the eastern and the west-central parts of the Kaapvaal craton that potentially led to their temporally distinct stabilizations tempts the application of this model towards a more general case for cratonic lithosphere growth and preservation.

APPENDIX: U-Pb ANALYTICAL PROCEDURE

Zircon and apatite were concentrated by standard crushing, Wilfley table, heavy-liquid and magnetic separation. Zircon was pre-treated with either the air-abrasion (Krogh, 1982) or chemical-abrasion (Mattinson, 2003, 2005) technique. Air-abraded zircons were ultrasonicatelly cleaned in 30% HNO_3 for an hour, fluxed in 30% HNO_3 at ~80°C for an hour, and rinsed in ultrapure acetone and H_2O before being loaded into 300 µl Teflon FEP microcapsules and spiked with a mixed ^{233}U-^{235}U-^{205}Pb tracer. Zircon was dissolved in ~120 µl 29M HF with ~25 µl 30% HNO_3 at ~210°C for 48 hours, dried to fluorides, and then re-dissolved in 6M HCl at ~180°C overnight. For the chemical-abrasion technique, zircons were placed in a muffle furnace at 900 ± 20°C for ~60 hours in quartz beakers before being transferred to 300 µl Teflon FEP microcapsules and leached in ~120 µl 29M HF + ~25 µl 30% HNO_3 for 12-14 hours at ~180 °C. The acid was removed from the capsules and the fractions were then rinsed in ultrapure H_2O, fluxed on a hotplate at ~80 °C for an hour in 6M HCl, ultrasonically cleaned for an hour, placed back on the hotplate for an additional 30 minutes, and rinsed in the capsults in ultrapure H_2O and 30% HNO_3. Fractions were then spiked and fully dissolved using the procedure described above. Single grains of apatite were hand-picked from non-magnetic separates, rinsed and ultrasonically cleaned in ultrapure H_2O and acetone prior to loading into single 300 µl FEP teflon microcapsules. Apatite was then spiked with the mixed ^{233}U-^{235}U-^{205}Pb tracer and dissolved in 12N HCl overnight, dried down and redissolved in 6N HCl overnight.

U and Pb were separated using an HCl-based single-column (zircon) or an HBr-based two-column (apatite) anion exchange chemistry modified after Krogh (1973). U

and Pb isotopic measurements were performed on a VG Sector-54 multi-collector thermal-ionization mass spectrometer at MIT. Pb and U were either loaded together (HCl-based chemistry) or on separate (HBr-based chemistry) Re filaments in a silica-gel/phosphoric acid mixture (Gerstenberger and Haase, 1997). Pb was measured by either 1) peak-hopping on a single Daly detector (for smaller beams), or 2) a dynamic Faraday-Daly routine (F-D) that cycles between placing mass 204 in the axial Daly collector and masses 205-208 on the H1-H4 Faraday detectors to placing mass 205 in the axial Daly and masses 206-208 in the H1-H3 Faradays, providing real-time Daly gain correction. U isotopic measurements were made in static Faraday mode. Mass fractionation on the Daly detector was determined to be 0.25 ± 0.04 %/a.m.u. over a wide temperature range based on analysis of the NBS-981 common Pb standard and spiked aliquots of NBS-983. Mass fractionation and detector bias on the F-D routine was determined to be 0.07 ± 0.04 %/a.m.u. U mass fractionation is calculated in real-time using the ^{233}U-^{235}U tracer. All common Pb for the zircon analyses was attributed to procedural blank. Total procedural Pb blanks for the HBr-based chemistry were determined to be 1.2 ± 0.4 pg, which was used in the reduction of apatite data. U blanks are assigned a value of 0.10 ± 0.05 pg. All samples were spiked with a ^{205}Pb-^{233}U-^{235}U tracer, whose calibration is detailed in Schoene et al. (2006), in which an error of ± 0.015% is assigned to the $^{205}Pb/^{235}U$ of the tracer.

REFERENCES CITED

Anhaeusser, C. R., 1969, The stratigraphy, structure, and gold mineralization of the Jamestown and Sheba Hills areas of the Barberton Mountain Land, University of Witwatersrand, Johannesburg, 332 p.

Anhaeusser, C. R., 1973, The evolution of the early Precambrian crust of southern Africa: Philos. Trans. R. Soc. London, v. A273, p. 359-388.

Anhaeusser, C. R., 1976, The geology of the Sheba HIlls area of the Barberton Mountain Land, South Africa, with particular references to the Eureka syncline: Geological Society of South Africa Transactions, v. 79.

Anhaeusser, C. R., 1983, Contributions to the geology of the Barberton Mountain Land: Geol. Soc. S. Afr., Spec. Pub., v. 9, 223 p.

Armstrong, R. A., W. Compston, M. J. de Wit, and I. S. William, 1990, The stratigraphy of the 3.5-3.2 Ga Barberton Greenstone Belt revisited: a single zircon ion microprobe study: EPSL, v. 101, p. 90-106.

Armstrong, R. A., W. Compston, E. A. Retief, I. S. Williams, and H. J. Welke, 1991, Zircon ion microprobe studies bearing on the age and evolution of the Witwatersrand triad: Precambrian Research, v. 53, p. 243-266.

Assumpção, M., D. James, and A. Snoke, 2002, Crustal thickness in the SE Brazilian Shield by receiver function analysis: Implications for isostatic compensation: J. Geophys. Res., v. 107, p. 10.1029/2001JB000422.

Begemann, F., K. R. Ludwig, G. W. Lugmair, K. Min, L. E. Nyquist, P. J. Patchett, P. R. Renne, C.-Y. Shih, I. M. Villa, and R. J. Walker, 2001, Call for an improved set of decay constants for geochronological use: Geochim. Cosmochim. Acta, v. 65, p. 111-121.

Bell, D. R., and R. O. Moore, 2004, Deep chemical structure of the southern African mantle from kimberlite megacrysts: S. Afr. J. Geol., v. 107, p. 59-80.

Bird, P., 1979, Continental delamination and the Colorado Plateau: Jour. Geophys. Res., v. 84.

Bird, P., 1991, Lateral extrusion of lower crust from under high topography, in the isostatic limit: Jour. Geophys. Res., v. 96, p. 10275-10286.

Bott, M. H. P., 1982, Origin of lithospheric tension causing basin formation: Philos. Trans. R. Soc. London, v. 305, p. 319-324.

Brace, W. F., and D. L. Kohlstedt, 1980, Limits on lithospheric strength imposed by laboratory experiments: Jour. Geophys. Res., v. 85, p. 6248-6252.

Burbank, D. W., 2002, Rates of erosion and their implications for exhumation: Mineral. Mag., v. 66, p. 25-52.

Burke, K., W. S. F. Kidd, and T. Kusky, 1985, Is the Ventersdorp rift system of southern Africa related to a continental collision between teh Kaapvaal and Zimbabwe Cratons at 2.64 Ga ago? Tectonophysics, v. 115, p. 1-24.

Byerly, G. R., A. Kröner, D. R. Lowe, W. Todt, and M. M. Walsh, 1996, Prolonged magmatism and time sontraints for sediment deposition in the early Archean Barberton greenstone belt: evidence from the Upper Onverwacht and Fig Tree groups: Precambrian Research, v. 78, p. 125-138.

Carlson, R. W., F. R. Boyd, S. B. Shirey, P. E. Janney, T. L. Grove, S. A. Bowring, M. D. Schmitz, J. C. Dann, D. R. Bell, J. J. Gurney, S. H. Richardson, M. Tredoux, A. H. Menzies, D. G. Pearson, R. A. Hart, A. C. Wilson, and D. E. Moser, 2000, Continental growth, preservation, and modification in Southern Africa: GSA Today, v. 10, p. 1-8.

Carlson, R. W., D. G. Pearson, F. R. Boyd, S. B. Shirey, G. Irvine, A. H. Menzies, and J. J. Gurney, 1999, Re-Os systematics of lithospheric peridotites: implications for lithosphere formation and preservation, *in* J. J. Gurney, J. L. Gurney, M. D. Pascoe, and S. H. Richardson, eds., proc. of the 7th int. kimberlite. conf.: Cape Town, Red Roof Design.

Chamberlain, K. R., and S. A. Bowring, 2000, Apatite-feldspar U-Pb thermochronometer: a reliable mid-range (~450°C), diffusion controlled system: Chem. Geol., v. 172, p. 173-200.

Cherniak, D. J., W. A. Lanford, and F. J. Ryerson, 1991, Lead diffusion in apatite and zircon using ion implantation and Rutherford Backscattering techniques: Geochim. Cosmochim. Acta, v. 55, p. 1663-1673.

Cherniak, D. J., and E. B. Watson, 2001, Pb diffusion in zircon: Chem. Geol., v. 172, p. 5-24.

Clitheroe, G., O. Gudmundsson, and B. L. N. Kennett, 2000, The crustal thickness of Australia: J. Geophys. Res., v. 103, p. 13,697-13,713.

Cloete, M., 1991, An overview of metamorphism in the Barberton greenstone belt, *in* L. D. Ashwal, ed., Two Cratons and an Orogen - Excursion Guidebook and Review Articles for a Field Workshop through Selevted Archean Terranes of Swaziland, South Africa and Zimbabwe: Johannesburg, IGCP project 280, Dept. of Geology, Univ. Witwatersrand.

Compston, W., Kröner, A., 1988, Multiple zircon growth within early Archean tonalitic gneiss from the Ancient Gneiss Complex, Swaziland: EPSL, v. 87, p. 13-28.

Condie, K. C., J. E. Macke, and T. O. Reimer, 1970, Petrology and geochemistry of early Precambrian graywackes from the Fig Tree Group, South Africa: Geological Society of America Bulletin, v. 81, p. 2759-2776.

Davidson, C., S. M. Schmidt, and L. S. Hollister, 1994, Role of melt during deformation in the deep crust: Terra Nova, v. 6, p. 133-142.

Davis, G. A., G. S. Lister, S. P. Clark, Jr. (editor), B. C. e. Burchfiel, and J. e. Suppe, 1988, Detachment faulting in continental extension; perspectives from the Southwestern U.S. Cordillera: Special Paper - Geological Society of America, v. 218, p. 133-159.

de la Winter, H. R., 1976, A lithostratigraphic classification of the Ventersdorp succession: Trans. Proc. Geol. Soc. S. Afr., v. 79, p. 31-48.

de Ronde, C. E. J., and M. J. de Wit, 1994, Tectonic history of the Barberton Greenstone Belt, South Africa: 490 million years of Archean crustal evolution: Tectonics, v. 13, p. 983-1005.

de Ronde, C. E. J., M. J. de Wit, and E. T. C. Spooner, 1994, Early Archean (>3.2 Ga) Fe-oxide-rich, hydrothermal discharge veins in the barberton greenstone belt, South Africa: GSA Bull., v. 106, p. 86-104.

de Ronde, C. E. J., and S. Kamo, 2000, An Archean arc-arc collisional event: a short-lived (*ca.* 3 Myr) episode, Weltevreden area, Barberton greenstone belt, South Africa: Jour. Afr. Earth Sci., v. 30, p. 219-248.

de Ronde, C. E. J., S. Kamo, D. W. Davis, M. J. de Wit, and E. T. C. Spooner, 1991, Field, geochemical and U-Pb isotopic constraints from hypabyssal felsic intrusions within the Barberton greenstone belt, South Africa: Implications for tectonics and the timing of gold mineralization: Precambrian Research, v. 1991, p. 261-280.

de Wit, M. J., 1982, Gliding and overthrust nappe tectonics in the Barberton greenstone belt: Jour. Struc. Geol., v. 4, p. 117-136.

de Wit, M. J., 1991, Archean greenstone belt tectonism and basin development: Some insights from the Barberton and Pietersburg greenstone belts, Kaapvaal Craton, South Africa.: J. Afr. Earth Sci., v. 13, p. 45-63.

de Wit, M. J., R. A. Armstrong, R. J. Hart, and A. H. Wilson, 1987a, Felsic igneous rocks within the 3.3-3.5 Ga Barberton greenstone belt: high crustal level equivalents of the surrounding tonalite-trondhjemite terrain, emplaced during thrusting: Tectonics, v. 5, p. 529-549.

de Wit, M. J., and L. D. Ashwal, eds., 1997, Greenstone Belts: Oxford Monographs on Geology and Geophysics, v. 35: Oxford, Clarendon Press, 809 p.

de Wit, M. J., R. E. P. Fripp, and I. G. Sainstreet, 1983, Tectonic and stratigraphic implications of new field observations along the southern part of the Barberton greenstone belt.: Spec. Publ. Geol. Soc. S. Afr., v. 9, p. 21-29.

de Wit, M. J., R. A. Hart, and R. J. Hart, 1987b, The Jamestown ophiolite complex, Barberton mountain belt; a section through 3.5 Ga oceanic crust.: J. African Earth Science, v. 6, p. 681-730.

de Wit, M. J., C. Roering, R. J. Hart, R. A. Armstrong, C. E. J. de Ronde, R. W. E. Green, M. Tredoux, E. Peberdy, and R. A. Hart, 1992, Formation of an Archean continent: Nature, v. 357, p. 553-562.

de Wit, M. J., and J. Tinker, 2004, Crustal structures across the central Kaapvaal craton from deep-seismic reflection data: S. Afr. J. Geol., v. 107, p. 185-206.

Dewey, J. F., 1988, Extensional collapse of orogens: Tectonics, v. 7, p. 1123-1139.

Diener, J. F. A., G. Stevens, A. F. M. Kisters, and M. Poujol, 2005, Metamorphism and exhumation of the basal parts of the Barberton greenstone belt, South Africa: Constraining the rates of Mesoarchean tectonism: Precambrian Research, v. 143, p. 87-112.

Doucouré, C. M., and M. J. de Wit, 2002, Temporal variation in rigidity and mechanical behavior of old thick continental lithosphere: S. Afr. J. Geol., v. 105, p. 39-50.

Durrheim, R. J., and W. D. Mooney, 1994, Evolution of the Precambrian lithosphere: Seismological and geochemical constraints: Jour. Geophys. Res., v. 99, p. 15,359-15,374.

Dziggel, A., R. A. Armstrong, G. Stevens, and L. Nasdala, 2005, Growth of zircon and titanite during metamorphism in the granitoid-gneiss terrane south fo the Barberton greenstone belt, South Africa: Mineral. Mag., v. 69, p. 1019-1036.

Dziggel, A., G. Stevens, M. Poujol, C. R. Anhaeusser, and R. A. Armstrong, 2002, Metamorphism of the granite-greenstone terrane south of the Barberton Greenstone Belt, South Africa: an insight into the tectono-thermal evolution of the

'lower' portions of the Onverwacht Group: Precambrian Research, v. 114, p. 221-247.
England, P. C., and D. P. McKenzie, 1982, A thin viscous sheet model for continental deformation: Geophys. Jour. R. Astron. Soc., v. 70, p. 295-321.
Eriksson, K. A., 1980, Transitional sedimentation stules in the Moodies and Fig Tree Groups, Barberton Mountain Land, South Africa: evidence favouring an Archean continental margin: Precambrian Research, v. 12, p. 141-160.
Flowers, R. M., D. E. Moser, and R. J. Hart, 2003, Evolution of the amphibolite-granulite facies transition exposed by the Vredefort impact structure, Kaapvaal Craton, South Africa: J. Geol., v. 111, p. 455-470.
Fouch, M. J., D. E. James, J. C. VanDecar, S. van der Lee, and K. S. Group, 2004, Mantle seismic structure beneath the Kaapvaal and Zimbabwe Cratons: S. Afr. J. Geol., v. 107, p. 33-44.
Fripp, R. E. P., D. A. Van Nierop, M. J. Callow, P. A. Lilly, and L. U. de Plessis, 1980, Deformation in part of the Archaean Kaapvaal Craton, South Africa: Precambrian Research, v. 13, p. 241-251.
Gay, N. C., 1969, The analysis of strain in the Barberton Mountain Land, Eastern Transvaal, using deformed pebbles: J. Geol., v. 77, p. 377-396.
Gerstenberger, H., and G. Haase, 1997, A highly effective emitter substance for mass spectrometric Pb isotope ratio determinations: Chem. Geol., v. 136, p. 309-312.
Gupta, S., S. S. Rai, K. S. Prakasam, D. Srinagesh, B. K. Bansal, R. K. Chadha, K. Priestly, and V. K. Gaur, 2003, The nature of the crust in southern India: Implications for Precambrian crustal evolution: Geophys. Res. Lett., v. 30, p. 1419, doi: 10.1029/2002GL016770.
Hart, R. A., D. Moser, and M. Andreoli, 1999, Archean age for the granulite facies metamorphism near the center of the Vredfort structure, South Africa: Geology, v. 27.
Hart, R. J., L. O. Nicolaysen, and N. H. Gale, 1981, Radioelement concentrations in the deep profile through precambrian basement of the Vredefort structure: J. Geophys. Res., v. 86, p. 10,639-10,652.
Heubeck, C., and D. R. Lowe, 1994a, Depositional and tectonic setting of the Archean Moodies Group, Barberton Greenstone Belt, South Africa: Precam. Res., v. 68, p. 257-290.
Heubeck, C., and D. R. Lowe, 1994b, Late syndepositional deformation and detachment tectonics in the barberton Greenstone Belt, South Africa.: Tectonics, v. 13, p. 1514-1536.
Heubeck, C., and D. R. Lowe, 1999, Sedimentary petrography and provenance of the Archean Moodies Group, Barberton Greenstone Belt, *in* D. R. Lowe, and G. R. Byerly, eds., Geologic evolution of the Barberton Greenstone Belt, South Africa, v. 329: Boulder, Geological Society of America, p. 259-286.
Hunter, D. R., F. Barker, and H. T. Millard, 1978, The geochemical nature of the Archean Ancient Gneiss Complex and granodiorite suite, Swaziland: a preliminary study: Precambrian Research, v. 7, p. 105-127.
Hunter, D. R., F. Barker, and H. T. Millard, 1984, Geochemical investigations of Archean bimodal and Dwalile metamorphic suites, Ancient Gneiss Complex, Swaziland: Precambrian Research, v. 24, p. 131-155.

Ireland, T. R., and I. S. Williams, 2003, Considerations in zircon geochronology by SIMS, *in* J. M. Hanchar, and P. W. O. Hoskin, eds., Zircon: Reviews in Mineralogy and Geochemistry, v. 53: Washington, D.C., Mineralogical Society of America, p. 215-241.

Jackson, M. P. A., 1979, High-strain deformation of the Ancient Gneiss Complex in the Mankayane area, Swaziland: a preliminary account (abstr.): Geological Society of South Africa - 18th congress, v. 1, p. 210-216.

Jackson, M. P. A., 1984, Archean structural styles in the Ancient Gneiss Complex of Swaziland, southern Africa, *in* A. Kröner, and R. Greiling, eds., Precambrian Tectonics Illustrated: Stuttgart, Schweizerbart'sche Verlagsbuchhandlung, p. 1-18.

Jackson, M. P. A., K. A. Eriksson, and C. W. Harris, 1987, Early Archean foredeep sedimentation related to crustal shortening: a reinterpretation of the Barberton Sequence, southern Africa: Tectonophysics, v. 136, p. 197-221.

Jaffey, A. H., K. F. Flynn, L. E. Glendenin, W. C. Bentley, and A. M. Essling, 1971, Precision measurement of half-lives and specific activities of ^{235}U and ^{238}U: Phys. Rev., v. C4, p. 1889-1906.

James, D. E., and M. J. Fouch, 2002, Formation and evolution of Archean cratons: insights from Southern Africa, *in* C. Ebinger, M. Fowler, and C. J. Hawkesworth, eds., The Early Earth: Physical Chemical and biological Development, v. 199: London, Geo. Soc. London Spec. Pub., p. 1-26.

James, D. E., M. J. Fouch, J. C. VanDecar, S. van der Lee, and K. S. Group, 2001, Tectospheric structure beneath southern Africa: Geophys. Res. Lett., v. 28, p. 2485-2488.

Jordan, T. H., 1978, Composition and development of the continental tectosphere: Nature, v. 274, p. 544-548.

Jordan, T. H., 1988, Structure and formation of the continental tectosphere, *in* M. A. Menzies, and K. G. Cox, eds., Oceanic and Continental Lithosphere: Similarities and Differences: London, Oxford University Press, p. 11-37.

Kamo, S., and D. W. Davis, 1994, Reassessment of Archean crustal development in the Barberton Mountain Land, South Africa, based on U-Pb dating: Tectonics, v. 13, p. 167-192.

Karlstrom, K. E., and M. L. Williams, 1998, Heterogeneity of the middle crust: Implications for strength of continental lithosphere: Geology, v. 26, p. 815-818.

Kisters, A. F. M., and C. R. Anhaeusser, 1995a, Emplacement features of Archean TTG plutons along the southern margin of the Barberton greenstone belt, South Africa: Precambrian Research, v. 75, p. 1-15.

Kisters, A. F. M., and C. R. Anhaeusser, 1995b, The structural significance of the Steynsdorp pluton and anticline within the tectonomagmatic framework of the Barberton Mountain Land: S. Afr. J. Geol., v. 98, p. 43-51.

Kisters, A. F. M., G. Stevens, A. Dziggel, and R. A. Armstrong, 2003, Extensional detachment faulting and core-complex formation in the southern Barberton granite-greenstone terrain, South Africa: evidence for a 3.2 Ga orogenic collapse: Precambrian Research, v. 127, p. 335-378.

Kober, B., 1986, Whole-grain evaporation for $^{207}Pb/^{206}Pb$-age-investigations on single zircons using a double-filament thermal ion source: Contributions to Mineralogy and Petrology, v. 93, p. 482-490.

Kober, B., 1987, Single-zircon evaporation combined with Pb emitter-bedding for $^{207}Pb/^{206}Pb$-age investigations using thermal ion mass spectrometry, and implications to zirconology: Contributions to Mineralogy and Petrology, v. 96, p. 63-71.

Krogh, T. E., 1973, A low contamination method for hydrothermal decomposition of zircon and extraction of U and Pb for isotopic age determination: Geochim. Cosmochim. Acta, v. 37, p. 485-494.

Krogh, T. E., 1982, Improved accuracy of U-Pb zircon ages by the creation of more concordant systems using an air abrasion technique: Geochim. Cosmochim. Acta, v. 46, p. 637-649.

Kröner, A., and W. Compston, Kröner, A., 1988, Ion microprobe ages of zircons from early Archean granite pebbles and greywacke, Barberton Greenstone Belt, southern Africa: Precam. Res., v. 38, p. 367-380.

Kröner, A., W. Compston, and I. S. William, 1989, Growth of early Archean crust in the Ancient Gneiss Complex of Swaziland as revealed by single zircon dating: Tectonophysics, v. 161, p. 271-298.

Kröner, A., E. Hegner, J. I. Wendt, and G. R. Byerly, 1996, The oldest part of the Barberton granitoid-greenstone terrain, South Africa: evidence for crust formation between 3.5 and 3.7 Ga: Precam. Res., v. 78, p. 105-124.

Kusznir, N., and G. Karner, 1985, Dependence of the flexural rigidity of the continental lithosphere on rheology and temperature: Nature, v. 316, p. 138-142.

Kusznir, N., and D. H. Matthews, 1988, Deep seismic reflections and the deformational mechanics of the continental lithosphere: Jour. Pet. Spec. Lithosphere Issue, p. 63-87.

Lamb, S. H., 1984, Structures on the eastern margin of the Archaean Barberton greenstone belt, northwest Swaziland, *in* A. Kröner, and R. Greiling, eds., Precambrian Tectonics Illustrated: Stuttgart, Germany, E. Schweizerbart'sche Verlagbuchhandlung, p. 19-39.

Lamb, S. H., and I. Paris, 1988, Post-Onverwacth Group stratigraphy in the SE part of the Archean Barberton greenstone belt: J. Afr. Earth Sci., v. 7, p. 285-306.

Layer, P. W., A. Kröner, and D. York, 1992, Pre-3000 Ma thermal history of the Archean Kaap Valley pluton, South Africa: Geology, v. 20, p. 717-720.

Layer, P. W., M. Lopez-Martinez, A. Kröner, and D. York, 1998, Thermochronometry and paleomagnetism of the Archean Nelshoogte Pluton, South Africa: Geophys. Jour. Int., v. 135, p. 129-145.

Lee, J. K. W., 1997, Pb, U, and Th diffusion in natural zircon: Nature, v. 390, p. 159-162.

Lister, G. S., G. Banga, and A. Feenstra, 1984, Metamorphic core complexes of Cordilleran type in the Cyclades, Aegean Sea, Greece: Geology, v. 12, p. 221-225.

Lopez Martinez, M., D. York, and J. A. Hanes, 1992, A $^{40}Ar/^{39}Ar$ geochronological study of komatiites and komatiitic basalts from the Lower Onverwacht Volcanics: Barberton Mountain Land, South Africa: Precambrian Research, v. 57, p. 91-119.

Lowe, D. R., 1994, Accretionary history of the Archean Barberton greenstone belt (3.55-3.22 Ga), Southern Africa: Geology, v. 22, p. 1099-1102.

Lowe, D. R., 1999, Geologic evolution of the Barberton Greenstone Belt and vicinity, *in* D. R. Lowe, and G. R. Byerly, eds., Geologic evolution of the Barberton

Greenstone Belt, South Africa, v. Special Paper 329: Boulder, Geol. Soc. Amer., p. 287-312.
Lowe, D. R., and G. R. Byerly, 1999a, Geologic evolution of the Barberton Greenstone Belt, South Africa, v. Special Paper 329: Boulder, CO, Geol. Soc. Amer.
Lowe, D. R., and G. R. Byerly, 1999b, Stratigraphy of the west-central part of the Barberton Greenstone Belt, South Africa, *in* D. R. Lowe, and G. R. Byerly, eds., Geologic evolution of the Barberton Greenstone Belt, South Africa, v. 329: Boulder, Geological Society of America, p. 1-36.
Lowe, D. R., G. R. Byerly, and C. Heubeck, 1999, Structural divisions and development of the west-central part of the Barberton Greenstone Belt, *in* D. R. Lowe, and G. R. Byerly, eds., Geologic evolution of the Barberton Greenstone Belt, South Africa, v. 329: Boulder, Geological Society of America, p. 37-82.
Marshak, S., F. Alkmim, and H. Jordt-Evangelista, 1992, Proterozoic crustal extension and the generation of dome-and-keel structure in an Archaean granite-greenstone terrane: Nature, v. 357, p. 491-493.
Mattinson, J. M., 1994, Uranium decay constant uncertainties and their implications for high-resolution U-Pb geochronology: GSA Abst. with Prog., v. 77; A-221.
Mattinson, J. M., 2000, Revising the "gold standard" – the uranium decay constants of Jaffey et al., 1971: Eos Trans. AGU, Spring Meet. Suppl., Abstract V61A-02.
Mattinson, J. M., 2003, CA (chemical abrasion)-TIMS: high-resolution U-Pb zircon geochronology combining high-temperature annealing of radiation damage and multi-step partial dissolution analysis: Eos Trans. AGU, Fall Meet. Suppl., Abstract V22E-06.
Mattinson, J. M., 2005, Zircon U-Pb chemical-abrasion ("CA-TIMS") method: combined annealing and multi-step dissolution analysis for improved precision and accuracy of zircon ages: Chem. Geol., v. 220, p. 47-56.
Meissner, R., and W. D. Mooney, 1998, Weakness of the lower continental crust: a condition for delamination, uplift, and excape: Tectonophysics, v. 296, p. 47-60.
Min, K., R. Mundil, P. R. Renne, and K. R. Ludwig, 2000, A test for systematic errors in $^{40}Ar/^{39}Ar$ geochronology through comparison with U-Pb analysis of a 1.1 Ga rhyolite: Geochim. Cosmochim. Acta, v. 64, p. 73-98.
Morgan, P., 1985, Crustal radiogenic heat production and the selective survival of ancient continental crust: Jour. Geophys. Res., v. 90-supplement, p. C561-C570.
Moser, D. E., R. M. Flowers, and R. J. Hart, 2001, Birth of the Kaapvaal tectosphere 3.08 billion years ago: Science, v. 291, p. 465-468.
Nguuri, T. K., J. Gore, D. E. James, S. J. Webb, C. Wright, T. G. Zengeni, O. Gwavava, J. A. Snoke, and K. S. Group, 2001, Crustal structure beneath southern Africa and its implications for the formation and evolution of the Kaapvaal and Zimbabwe cratons: Geophys. Res. Lett., v. 28, p. 2501-2504.
Nicolaysen, L. O., R. J. Hart, and N. H. Gale, 1981, Vredefort radioelement profile extended to supracrustal strata at Carletonville, with implications for continental heat flow: J. Geophys. Res., v. 86, p. 10,653-10,662.
Parman, S. W., T. L. Grove, J. C. Dann, and M. J. de Wit, 2004, A subduction origin for komatiites and cratonic lithospheric mantle: S. Afr. J. Geol., v. 107, p. 107-118.

Pavlis, T. L., 1996, Fabric development in syn-tectonic intrusive sheets as a consequence fo melt-dominated flow and thermal softening of the crust: Tectonophysics, v. 253, p. 1-31.
Pearson, D. G., R. W. Carlson, S. B. Shirey, F. R. Boyd, and P. H. Nixon, 1995, Stabilization of Archean lithospheric mantle: A Re-Os isotope study of peridotite xenoliths from the Kaapvaal craton: EPSL, v. 134, p. 341-357.
Perry, H. K. C., D. W. S. Eaton, and A. M. Forte, 2002, LITH5.0: a revised crustal model for Canada based on Lithoprobe results: Geophys. Jour. Int., v. 150, p. 285-294.
Perry, H. K. C., C. Jaupart, J.-C. Mareschal, and G. Bienfait, 2006, Crustal heat production in the Superior Province, Canadian Shield, and in North America inferred from heat flow data: J. Geophys. Res., v. 111, p. doi:10.1029/2005JB003893.
Ranalli, G., 1995, Rheology of the Earth: New York, Chapman and Hall, 413 p.
Ranalli, G., and D. C. Murphy, 1987, Rheological stratification of the lithosphere: Tectonophysics, v. 132, p. 281-295.
Renne, P. R., D. B. Karner, and K. R. Ludwig, 1998, Absolute ages aren't exactly: Science, v. 282, p. 1840-1841.
Richardson, S. H., J. J. Gurney, A. J. Erlank, and J. W. Harris, 1984, Origin of diamonds in old enriched mantle: Nature, v. 310, p. 198-202.
Richardson, S. H., S. B. Shirey, J. W. Harris, and R. W. Carlson, 2001, Archean subduction recorded by Re-Os isotopes in eclogitic sulfide inclusions in Kimberly diamonds: Earth Planet. Sci. Lett., v. 191, p. 257-266.
Ritsema, J., A. A. Nyblade, T. J. Owens, C. A. Langston, and J. C. VanDecar, 1998, Upper mantle seismic velocity structure beneath Tanzania, east Africa: Implications for the stability of cratonic lithosphere: Jour. Geophys. Res., v. 102, p. 21,201-21,213.
Robb, L. J., and C. R. Anhaeusser, 1983, Chemical and petrogenetic characteristics of the Archaean tonalite-trondhjemite gneiss plutons in the Barberton Mountain Land, *in* C. R. Anhaeusser, ed., Contributions to the Geology of the Barberton Mountain Land, v. 9, Spec. Pub. Geol. Soc. S. Africa, p. 103-116.
Robb, L. J., D. W. Davis, S. L. Kamo, and F. M. Meyer, 1992, Ages of altered granites adjoining the Witwatersrand Basin with implications for the origin of gold and uranium: Nature, v. 357, p. 677-680.
Rudnick, R. L., and A. A. Nyblade, 1999, The thickness and heat production of Archean lithosphere: Constraints from xenolith thermobarometry and surface heat flow, *in* Y. Fei, C. Bertka, and B. O. Mysen, eds., Mantle Petrology: Field Observations and High Pressure Experimentation: A Tribute to Francis R. (Joe) Boyd, Geochem. Soc., p. 3-12.
Saltzer, S. D., and K. V. Hodges, 1988, The Middle Mountain shear zone, southern Idaho: kinematic analysis of an early Tertiary high-temperature detachment: GSA Bull., v. 100, p. 96-103.
Sandiford, M., and S. McLaren, 2002, Tectonic feedback and the ordering of heat producing elements within the continental lithosphere: Earth Planet. Sci. Lett., v. 204, p. 133-150.

Sandiford, M., S. McLaren, and N. Neumann, 2002, Long-term thermal consequences of the redistribution of heat-producing elements associated with large-scale granitic complexes: J. Metamorphic Geol., v. 20, p. 87-98.

Sandiford, M., M. J. Van Kranendonk, and S. Bodorkos, 2004, Conductive incubation and the origin of dome-and-keel structure in Archean granite-greenstone terrains: A model based on the eastern Pilbara Craton, Western Australia: Tectonics, v. 23, p. doi:10.1029/2002TC001452.

Schmitz, M. D., and S. A. Bowring, 2003a, constraints on the thermal evolution of continental lithosphere from U-Pb accessory mineral thermochronometry of lower crustal xenoliths, southern Africa: Contrib. Miner. Petrol., v. 144, p. 592-618.

Schmitz, M. D., and S. A. Bowring, 2003b, Ultrahigh-temperature metamorphism in the lower crust during Neoarchean Ventersdorp rifting and magmatism, Kaapvaal Craton, southern Africa: GSA Bull., v. 115, p. 533-548.

Schmitz, M. D., S. A. Bowring, M. J. de Wit, and V. Gartz, 2004, Subduction and terrane collision stabilized the western Kaapvaal craton tectosphere 2.9 billion years ago: Earth Planet. Sci. Lett., v. 222, p. 363-376.

Schoene, B., and S. A. Bowring, 2006, U-Pb systematics of the McClure Mountain syenite: thermochronological constraints on the age of the $^{40}Ar/^{39}Ar$ standard MMhb: Contrib. Miner. Petrol., v. 151, p. 615-630.

Schoene, B., and S. A. Bowring, in prep, The Usutu suite.

Schoene, B., and S. A. Bowring, submitted, Determining accurate T-t paths in U-Pb thermochronology: an example from the SE Kaapvaal craton, Southern Africa: Geo. and Cosmo. Acta.

Schoene, B., J. L. Crowley, D. C. Condon, M. D. Schmitz, and S. A. Bowring, 2006, Reassessing the uranium decay constants for geochronology using ID-TIMS U-Pb data: Geochim. Cosmochim. Acta, v. 70, p. 426-445.

Shirey, S. B., R. W. Carlson, S. H. Richardson, A. H. Menzies, J. J. Gurney, D. G. Pearson, J. W. Harris, and U. Wiechert, 2001, Archean emplacement of eclogitic components into the lithospheric mantle during formation of the Kaapvaal Craton: Geophys. Res. Lett., v. 28, p. 2509-2512.

Simons, F. J., A. Zielhuis, and R. D. van der Hilst, 1999, The deep structure of the Australian continent from surface wave tomography: Lithos, v. 48, p. 17-43.

Stevens, G., G. T. R. Droop, R. A. Armstrong, and C. R. Anhaeusser, 2002, Amphibolite facies metamorphism in the Schapenburg schist belt: A record of the mid-crustal response to ~3.23 Ga terrane accretion in the Barberton greenstone belt: South African Journal of Geology, v. 105, p. 271-284.

Thomas, R. J., M. W. von Veh, and S. McCourt, 1993, The tectonic evolution of southern Africa: an overview: Journal of African Earth Sciences, v. 16, p. 5-24.

Tinker, J., M. J. de Wit, and J. Grotzinger, 2002, Seismic stratigraphic constraints on Neoarchean-Paleoproterozoic evolution of the Western Margin of the Kaapvaal Craton, South Africa: S. Afr. J. Geol., v. 105, p. 107-134.

Viljoen, M. J., and R. P. Viljoen, 1969, An introduction to the geology of the Barberton, granite-greenstone terrain: Geol. Soc. S. Afr., Spec. Pub., v. 9, p. 1-20.

Westraat, J. D., A. F. M. Kisters, M. Poujol, and G. Stevens, 2005, Transcurrent shearing, granite sheeting and the incremental construction of the tabular 3.1 Ga Mpuluzi

batholith, Barberton granite-greenstone terrane, South Africa: Jour. Geol. Soc. London, v. 162, p. 373-388.
Wetherill, G. W., 1956, Discordant uranium-lead ages: Trans. Amer. Geophys. Union, v. 37, p. 320-326.
Whitney, D. L., C. Teyssier, C. S. Siddoway, and eds., eds., 2004, Gneiss domes in orogeny: GSA Spec. Paper 380: Boulder, CO, 378 p.
Williams, D. A. C., and R. G. Furnell, 1979, A reassessment of part of the Barberton area: Precambrian Research, v. 9, p. 325-347.
Wilson, A. C., 1979, 1:50,000 Geological series: Geological survey mines department.
Wilson, A. C., 1982, 1:250,000 Geological map of Swaziland: Geological Survey Mines Department.
Xie, X., G. R. Byerly, and R. E. Ferrell, 1997, IIb trioctehedral chlorite from the Barberton greenstone belt; crystal structure and rock composition constraints with implications to geothermometry: Contrib. Miner. Petrol., v. 126, p. 275-291.
Zhao, W., and W. J. P. Morgan, 1987, Injection of Indian crust into Tibetan lower crust; a two-dimensional finite element model study: Tectonics, v. 6, p. 489-504.

Figure captions:

Fig. 1: Geologic map of exposed Archean rocks in the Kaapvaal craton, modified from Schmitz et al. (2004). Included are the major terrane subdivisions of the craton, and the distribution of the major Neoarchean depositional basins. Position of Fig. 2 is outlined in black box.

Fig. 2: Geologic map of the Barberton greenstone belt and adjacent orthogneiss terranes, with important features from the text labeled. Position of maps from Figs. 3, 6 and 9 are outlined in black. PSZ = Phophonyane Shear Zone, HSZ = Honeybird Shear Zone, SSZ = Steynsdorp Shear Zone, SIFS = Saddleback-Inyoka fault system. Map compiled from this study, Anhaeusser (1983), de Ronde et al. (1994), de Wit (1982), Lowe and Byerly, (1999a), and Wilson (1982).

Fig. 3: (A) Geologic map of the Pigg's Peak inlier and the Phophonyane Shear Zone (PSZ). Sample locations from this study and (Schoene and Bowring, submitted) are shown; outcrop photos and concordia plots for U-Pb data are given in Figs. 4, 5. (B) Stereonet for structural data within the PSZ (within ~1 km from inferred lithologic contact). (C) Stereonet for structural data from outside the PSZ. See text for discussion. Mapping by B. Schoene 2002-2004.

Fig. 4: Field photos and concordia plots for the Ancient gneiss complex (AGC) in the Phophonyane shear zone. Photos are of typical mafic-silicic banded gneiss (mapped as undiff. banded gneiss in Fig. 3). AGC01-5 represents a more homogeneous, tonalitic unit of the AGC than pictured, and EKC02-20 is a homogeneous granite inlier (not pictured),

apparently cross-cutting the the banded AGC. Concordia plot for AGC01-5 contains data from both air-abraded (shaded circles) and chemical-abraded (open circles) zircons. Note Brunton compass for scale in both photos. Sample locations in Fig. 3.

Fig. 5: Field photos and concordia plot for syntectonic dikes from the Phophonyane Shear Zone, Pigg's Peak inlier. Field photos show dikes crosscutting foliation of banded orthogneiss of the Ancient gneiss complex. The dikes contain foliation parallel to the host rocks, and are sheared to indicate right-lateral dip-slip offset. EKC02-10 has NE trending stretching lineations as well. EKC02-8 cross-cuts EKC02-10, and only the latter has strong stretching lineations. Field notebook for scale in both photos. Sample locations in Fig. 3.

Fig. 6: (A) Geologic map of the Steynsdorp antiform, compiled from this study, Anhaeusser (1983), and Kröner et al. (1996). Sample locations are shown and concordia plots for U-Pb data are in Fig. 7. (B) Structural data from this study plotted on a stereonet.

Fig. 7: Field photos and concordia plots for U-Pb apatite and zircon data from the Steynsdorp antiform. See Fig. 6 for sample localities. (A) mantled garnet porphyroblasts from the western side of the Steynsdorp pluton indicating right-lateral shear in subvertical foliation. Taken within the Theespruit formation several meters from the contact with the pluton. Tip of pencil for scale. (B) Typical granitic dike cross-cutting foliation, but sheared and folded itself, with NE trending fold axes and stretching lineations (see Fig.

6). EKC02-46 was collected out of field of view, where dike was wider and more easily sampled.

Fig. 8: Concordia plots and structural data from the Honeybird Shear Zone. See Fig. 2 for location and text for discussion.

Fig. 9: Geologic map of the Stolzburg area. See Fig. 2 for location. Sample locations are shown, and concordia plots for U-Pb data are in Figs. 10 and 11. Light gray normal fault indicates the mid-crustal detachment of Kisters et al. (2003) and Diener et al. (2005). Thick dashed black line indicates an inferred exhumation zone based on field observation and U-Pb data from this study. Map compiled from Anhaeusser (1983), de Wit (1982), Kisters and Anhaeusser (1995a), and Westraat et al. (2005).

Fig. 10: Concordia diagrams from the northern margin of the Stolzburg pluton and the Nelshoogte pluton. See Fig. 9 for sample localities.

Fig. 11: Field photos and concordia plots for samples from the central Stolzburg pluton. See Fig. 9 for sample localities. (A) Sample location of orthogneiss KPV99-96. This sample was the oldest generation from this outcrop. Note field book for scale. (B) Sample location of late syntectonic dike EKC03-11. Dark rock is a large greenstone xenolith, and the aplitic dikes intrude along foliation and have slight foliation themselves. Hammer and tape roll for scale.

Fig. 12: Summary diagram of structural, geochronological and thermochronological data for the kinematics, distribution and timing of important tectonothermal events in the BGB between ca 3.23 and 3.10 Ga. BGB = Barberton greenstone belt; PSZ = Phophonyane Shear Zone; SSZ = Steynsdorp Shear Zone; HSZ = Honeybird Shear Zone. Numbers in parentheses represent data from the literature: (1: Lopez Martinez et al., 1992); (2: Kamo and Davis, 1994); (3: de Ronde et al., 1991); (4: Layer et al., 1998); (5: Layer et al., 1992); (6: de Ronde and Kamo, 2000); (7: Westraat et al., 2005); (8: Schoene and Bowring, submitted); all other data from this study.

Fig. 13: Cartoon illustrating how extension and lower crustal melting can result in a stronger lithospheric column, as occurred in the eastern Kaapvaal craton ca. 3.2-3.1 Ga. Black box is a histogram indicating the relative concentration of heat-producing elements (HPEs) U, Th and K within the crust before and after granite production and migration upwards in the crust, taken from Sandiford and McLaren (2002) and Sandiford et al. (2002). Uniteless σ_1-σ_3 represents the differential stress required for failure of a rock (i.e. higher σ_1-σ_3 corresponds to a stronger crust), plotted as a function of depth in the lithosphere, assuming a quartzofeldspathic crust and peridotitic mantle, both with homogeneous compositions, taken from Ranalli and Murphy (1987).

Table 1. U-Pb isotopic data

				Isotopic ratios									Dates (Ma)						
Sample	$^{Pb*}/_{Pb_c}$	Pb_c (pg)	$^{Th}/_{U}$	$^{206Pb}/_{204Pb}$	$^{208Pb}/_{206Pb}$	$^{206Pb}/_{238U}$	% err	$^{207Pb}/_{235U}$	% err	$^{207Pb}/_{206Pb}$	% err	corr. coef.	$^{206Pb}/_{238U}$	±	$^{207Pb}/_{235U}$	±	$^{207Pb}/_{206Pb}$	±	% disc.
(a)	(b)	(c)	(d)	(e)	(f)	(f)	(g)	(f)	(g)	(f)	(g)		(h)	(i)	(h)	(i)	(h)	(i)	(j)
AGC01-5																			
z1	204	3.46	0.29	10440	0.107	0.450925	0.31	14.17480	0.32	0.22799	0.06	0.984	2399.4	6.2	2761.5	3.0	3038.0	0.9	25.1
z2	24.0	11.09	0.10	1165	0.033	0.538850	0.21	20.10509	0.22	0.27061	0.06	0.960	2778.6	4.8	3096.4	2.2	3309.5	1.0	19.7
z3	279	1.80	0.34	13881	0.116	0.562468	0.07	24.68102	0.08	0.31825	0.04	0.847	2876.8	1.6	3295.7	0.8	3561.4	0.6	23.7
z4	604	1.79	0.21	31062	0.074	0.554743	0.12	24.13713	0.13	0.31557	0.04	0.941	2844.9	2.9	3273.9	1.3	3548.4	0.7	24.4
z5	11.5	8.73	0.22	583	0.069	0.550330	0.33	18.88570	0.35	0.24889	0.10	0.956	2826.5	7.6	3036.0	3.4	3177.7	1.6	13.6
z6	2.0	48.55	0.22	102	0.069	0.597180	0.34	25.52952	0.35	0.31005	0.10	0.958	3018.5	8.1	3328.7	3.4	3521.2	1.5	17.8
z7	9.5	12.51	0.41	436	0.120	0.679321	0.36	30.82818	0.35	0.32913	0.06	0.987	3341.8	9.3	3513.6	3.5	3613.1	0.9	9.6
z9	1.9	35.68	0.45	97	0.144	0.517326	0.46	16.55631	0.53	0.23211	0.22	0.907	2687.8	10.1	2909.5	5.1	3066.7	3.6	15.1
z12	57.7	2.28	0.47	2876	0.138	0.663712	0.19	29.62502	0.19	0.32373	0.06	0.950	3281.6	4.8	3474.5	1.9	3587.6	0.9	10.9
z13	22.3	3.86	0.10	1239	0.047	0.380437	0.38	15.17349	0.38	0.28927	0.05	0.991	2078.3	6.8	2826.2	3.6	3413.7	0.8	45.5
z14	34.0	3.90	0.51	1644	0.149	0.673054	0.24	30.58973	0.24	0.32963	0.06	0.973	3317.6	6.3	3505.9	2.4	3615.4	0.9	10.5
z15	3.3	16.59	0.05	177	0.045	0.185385	0.55	6.08416	0.57	0.23803	0.13	0.973	1096.3	5.5	1988.0	5.0	3106.8	2.1	70.1
za3	1425	0.19	0.32	74842	0.088	0.727255	0.22	33.31105	0.22	0.33220	0.04	0.980	3523.2	6.0	3589.9	2.2	3627.3	0.7	3.7
za4	1009	0.16	0.62	50100	0.166	0.740445	0.09	34.48300	0.10	0.33776	0.04	0.910	3572.2	2.6	3624.0	1.0	3652.7	0.6	2.9
za5	790	0.15	0.68	38878	0.178	0.764175	0.09	35.82602	0.10	0.34002	0.05	0.898	3659.5	2.6	3661.7	1.0	3662.9	0.7	0.1
za6	5.1	5.46	0.71	268	0.188	0.753344	0.85	35.32161	0.86	0.34005	0.12	0.991	3619.8	23.7	3647.7	8.5	3663.0	1.8	1.5
za11	729	0.33	0.70	34935	0.185	0.756952	0.06	35.44899	0.08	0.33965	0.04	0.823	3633.1	1.8	3651.2	0.8	3661.2	0.7	1.0
za12	593	0.28	0.18	32271	0.047	0.700790	0.08	28.70627	0.09	0.29709	0.05	0.862	3423.6	2.1	3443.5	0.9	3455.1	0.7	1.2
za13	70.8	0.58	0.72	3406	0.188	0.760919	0.21	35.66258	0.23	0.33992	0.07	0.950	3647.6	6.0	3657.2	2.2	3662.4	1.1	0.5
za14	86.4	0.37	0.74	4213	0.171	0.861727	0.12	39.75634	0.13	0.33461	0.06	0.907	4006.5	3.6	3764.6	1.3	3638.3	0.9	-13.6
za15	113	0.28	0.57	5505	0.158	0.722867	0.21	33.76065	0.22	0.33873	0.06	0.963	3506.8	5.7	3603.1	2.1	3657.0	0.9	5.3
za16	351	0.26	0.67	16919	0.179	0.746489	0.12	34.83201	0.14	0.33842	0.07	0.867	3594.6	3.4	3633.9	1.4	3655.6	1.1	2.2
EKC02-20																			
za1	81.5	0.49	0.60	4091	0.157	0.731375	0.17	31.76297	0.18	0.31498	0.05	0.968	3538.5	4.7	3543.0	1.8	3545.5	0.7	0.25
za2	290	1.13	0.52	14672	0.139	0.720883	0.06	30.97407	0.07	0.31162	0.04	0.810	3499.4	1.5	3518.2	0.7	3529.0	0.6	1.1
za3	146	1.01	0.40	7555	0.110	0.695423	0.09	29.96002	0.10	0.31246	0.04	0.892	3403.3	2.3	3485.5	0.9	3533.1	0.7	4.7
za5	8.4	0.95	0.40	459	0.104	0.733347	0.56	30.75034	0.59	0.30412	0.20	0.940	3545.9	15.1	3511.1	5.8	3491.3	3.1	-2.0
za6	23.9	0.75	0.64	1198	0.169	0.731036	0.27	31.77484	0.30	0.31524	0.13	0.904	3537.3	7.3	3543.3	2.9	3546.8	1.9	0.35
za7	150	0.44	0.68	7371	0.180	0.728553	0.21	31.63865	0.21	0.31496	0.05	0.971	3528.0	5.6	3539.1	2.1	3545.4	0.8	0.64
za9	16.9	0.27	0.59	870	0.144	0.790766	0.31	34.28191	0.33	0.31442	0.12	0.931	3756.0	8.8	3618.2	3.3	3542.8	1.9	-8.0

Table 1.(cont.)

				Isotopic ratios									Dates (Ma)						
Sample	$\frac{Pb^*}{Pb_c}$	Pb_c (pg)	$\frac{Th}{U}$	$\frac{^{206}Pb}{^{204}Pb}$	$\frac{^{208}Pb}{^{206}Pb}$	$\frac{^{206}Pb}{^{238}U}$	% err	$\frac{^{207}Pb}{^{235}U}$	% err	$\frac{^{207}Pb}{^{206}Pb}$	% err	corr. coef.	$\frac{^{206}Pb}{^{238}U}$	±	$\frac{^{207}Pb}{^{235}U}$	±	$\frac{^{207}Pb}{^{206}Pb}$	±	% disc.
(a)	(b)	(c)	(d)	(c)	(f)	(f)	(g)	(f)	(g)	(f)	(g)		(h)	(i)	(h)	(i)	(h)	(i)	(j)
EKC02-8																			
z1	7.9	6.51	0.21	465	0.063	0.540983	0.45	17.52591	0.47	0.23496	0.11	0.971	2787.6	10.2	2964.1	4.5	3086.2	1.8	11.9
z2	27.9	1.65	0.43	1501	0.123	0.607797	0.16	21.22943	0.17	0.25333	0.05	0.951	3061.2	4.0	3149.1	1.7	3205.7	0.8	5.7
z3	15.9	2.21	0.18	926	0.060	0.497303	0.58	15.37741	1.22	0.22426	1.08	0.475	2602.2	12.4	2838.9	11.7	3011.6	17.3	16.5
z4	6.7	5.46	0.10	407	0.057	0.270338	0.51	7.68933	0.55	0.20629	0.17	0.949	1542.5	7.0	2195.4	5.0	2876.6	2.8	51.9
z5	2.3	2.69	0.43	137	0.135	0.549035	1.70	19.27767	1.73	0.25466	0.22	0.992	2821.2	38.8	3055.8	16.7	3213.9	3.4	15.1
z6	10.2	1.09	0.15	569	0.123	0.198964	0.37	6.28737	0.38	0.22919	0.08	0.979	1169.8	3.9	2016.7	3.3	3046.4	1.3	67.1
z7	18.6	1.42	0.14	1072	0.063	0.373289	0.26	11.94476	0.28	0.23208	0.08	0.953	2044.9	4.6	2600.1	2.6	3066.4	1.3	38.7
za1	92.9	1.46	0.74	4676	0.205	0.628553	0.21	22.16294	0.22	0.25573	0.06	0.958	3143.9	5.3	3190.9	2.1	3220.6	1.0	3.0
za2	5.6	0.52	1.13	280	0.304	0.646913	0.78	22.86917	0.81	0.25639	0.20	0.969	3216.1	19.8	3221.4	7.9	3224.7	3.2	0.34
za3	15.5	0.85	0.46	841	0.125	0.647619	0.27	22.86508	0.32	0.25607	0.15	0.872	3218.9	6.9	3221.2	3.1	3222.7	2.4	0.15
za5	25.7	0.39	0.25	1445	0.066	0.657405	0.43	23.12099	0.44	0.25508	0.08	0.982	3257.1	10.9	3232.0	4.2	3216.6	1.3	-1.6
EKC02-10																			
z1	16.0	4.68	0.05	987	0.029	0.237751	0.23	6.08975	0.25	0.18577	0.10	0.923	1375.0	2.8	1988.8	2.2	2705.1	1.6	54.4
z2	26.1	1.98	0.11	1540	0.044	0.410224	0.17	12.07517	0.20	0.21349	0.10	0.864	2215.9	3.1	2610.3	1.8	2932.2	1.6	28.8
z3	8.6	2.88	0.19	512	0.096	0.280312	0.41	7.21213	0.46	0.18660	0.17	0.927	1592.9	5.8	2138.0	4.1	2712.5	2.9	46.4
z4	10.4	5.51	0.05	647	0.020	0.405893	0.32	10.89469	0.34	0.19467	0.10	0.957	2196.1	5.9	2514.2	3.2	2782.0	1.6	24.8
z5	9.8	2.65	0.05	608	0.020	0.346799	0.37	9.36667	0.41	0.19589	0.15	0.930	1919.3	6.2	2374.6	3.8	2792.2	2.5	36.0
z7	13.5	1.69	0.05	817	0.021	0.378784	0.24	11.41951	0.26	0.21865	0.05	0.979	2070.6	4.3	2558.0	2.4	2970.8	0.8	35.3
z8	10.4	3.42	0.05	639	0.022	0.388996	0.34	11.33120	0.40	0.21127	0.18	0.899	2118.2	6.1	2550.8	3.7	2915.3	2.8	32.0
za1	43.1	10.1	0.03	2602	0.025	0.170872	0.11	4.69925	0.12	0.19946	0.05	0.917	1016.9	1.0	1767.1	1.0	2821.8	0.8	68.9
za2	30.5	3.50	0.05	1790	0.049	0.172537	0.13	5.05462	0.14	0.21247	0.06	0.919	1026.1	1.2	1828.5	1.2	2924.5	0.9	69.9
za3	22.5	0.68	0.08	1322	0.029	0.464205	0.18	15.10745	0.20	0.23604	0.06	0.944	2458.1	3.7	2822.0	1.9	3093.4	1.0	24.6
EKC02-40																			
za1	22.1	0.49	0.40	1163	0.106	0.723215	0.82	30.84079	0.83	0.30928	0.10	0.993	3508.1	22.2	3514.0	8.1	3517.4	1.5	0.34
za2	131	0.47	0.41	6799	0.108	0.722945	0.12	30.81662	0.16	0.30916	0.11	0.730	3507.1	3.1	3513.2	1.6	3516.7	1.7	0.36
za3	0.5	0.33	0.46	42	0.129	0.679657	10.2	28.96572	10.0	0.30910	1.58	0.988	3343.0	265.3	3452.4	98.3	3516.4	24.5	6.31
za4	89.6	0.49	0.36	4688	0.095	0.725701	0.17	30.95870	0.18	0.30940	0.06	0.949	3517.4	4.7	3517.7	1.8	3517.9	0.9	0.02
a2	2.8	11.9	0.36	142	0.096	0.641935	0.30	21.96699	0.32	0.24819	0.08	0.969	3196.6	7.6	3182.3	3.1	3173.2	1.2	-0.93
a3	2.9	17.3	0.29	151	0.077	0.635578	0.22	21.59563	0.24	0.24643	0.10	0.914	3171.6	5.5	3165.7	2.3	3162.0	1.5	-0.39
a5	2.0	28.8	0.22	104	0.059	0.615920	0.18	20.24006	0.22	0.23833	0.11	0.876	3093.7	4.5	3102.9	2.1	3108.9	1.7	0.62
a4	1.1	19.1	0.16	65	0.043	0.639111	0.43	22.00366	0.47	0.24970	0.15	0.949	3185.5	10.9	3183.9	4.5	3182.9	2.3	-0.11
a7	2.9	42.8	0.43	139	0.116	0.641624	0.12	22.04500	0.15	0.24919	0.08	0.823	3195.4	3.0	3185.7	1.5	3179.6	1.3	-0.63
a8	4.0	73.9	0.29	195	0.078	0.641275	0.11	22.09136	0.13	0.24985	0.06	0.883	3194.0	2.9	3187.8	1.3	3183.8	1.0	-0.41
a9	2.5	52.6	0.25	128	0.068	0.634773	0.13	21.55123	0.16	0.24624	0.08	0.863	3168.4	3.2	3163.7	1.5	3160.7	1.3	-0.31
a10	1.1	54.0	0.28	63	0.074	0.649805	0.17	21.97970	0.22	0.24532	0.13	0.827	3227.4	4.4	3182.8	2.2	3154.8	2.0	-2.9

Table 1.(cont.)

				Isotopic ratios									Dates (Ma)						
Sample	$\frac{Pb^*}{Pb_c}$	Pb_c (pg)	$\frac{Th}{U}$	$\frac{^{206}Pb}{^{204}Pb}$	$\frac{^{208}Pb}{^{206}Pb}$	$\frac{^{206}Pb}{^{238}U}$	% err	$\frac{^{207}Pb}{^{235}U}$	% err	$\frac{^{207}Pb}{^{206}Pb}$	% err	corr. coef.	$\frac{^{206}Pb}{^{238}U}$	±	$\frac{^{207}Pb}{^{235}U}$	±	$\frac{^{207}Pb}{^{206}Pb}$	±	% disc.
(a)	(b)	(c)	(d)	(e)	(f)	(f)	(g)	(f)	(g)	(f)	(g)		(h)	(i)	(h)	(i)	(h)	(i)	(j)
EKC02-38																			
za1	49.1	0.76	1.00	2401	0.270	0.617367	0.12	20.22262	0.13	0.23757	0.05	0.924	3099.4	3.0	3102.1	1.3	3103.8	0.8	0.18
za2	166	0.67	0.51	8437	0.135	0.722225	0.08	30.76978	0.10	0.30899	0.06	0.801	3504.4	2.1	3511.7	0.9	3515.9	0.9	0.42
za3	45.6	0.62	0.46	2353	0.120	0.732260	0.1	31.24892	0.2	0.30951	0.07	0.879	3541.8	3.7	3526.9	1.5	3518.5	1.1	-0.86
za5	11.5	2.06	0.45	609	0.121	0.717598	0.45	30.59994	0.46	0.30927	0.06	0.991	3487.0	12.1	3506.3	4.5	3517.3	0.9	1.1
za6	3.0	3.05	0.45	174	0.125	0.696969	1.31	29.65453	1.32	0.30859	0.10	0.997	3409.1	34.7	3475.4	13.0	3513.9	1.5	3.8
EKC02-46																			
za1	49.0	0.90	0.33	2585	0.088	0.725926	0.12	30.88494	0.12	0.30857	0.04	0.932	3518.2	3.1	3515.4	1.2	3513.8	0.7	-0.16
za2	29.6	0.77	0.84	1496	0.227	0.618827	0.16	20.26994	0.18	0.23756	0.06	0.947	3105.2	4.1	3104.3	1.7	3103.7	0.9	-0.06
za3	39.4	0.62	0.27	2108	0.075	0.695726	0.2	29.33800	0.2	0.30584	0.05	0.964	3404.4	4.6	3464.9	1.8	3500.0	0.7	3.51
za7	4.6	1.86	0.54	252	0.143	0.720512	0.84	30.63854	0.84	0.30841	0.11	0.992	3498.0	22.8	3507.5	8.3	3513.0	1.7	0.55
za8	13.4	0.76	0.50	697	0.132	0.725141	0.30	30.90623	0.33	0.30912	0.12	0.930	3515.3	8.2	3516.1	3.2	3516.5	1.8	0.05
EKC02-47																			
za1	167	0.63	0.65	8645	0.175	0.616339	0.09	20.17211	0.10	0.23737	0.05	0.862	3095.3	2.1	3099.6	1.0	3102.4	0.8	0.29
za2	75.3	0.98	0.36	3944	0.096	0.720626	0.17	30.73152	0.17	0.30929	0.05	0.964	3498.4	4.5	3510.5	1.7	3517.4	0.7	0.70
za3	20.9	0.68	0.74	1070	0.199	0.643097	0.2	22.56710	0.2	0.25451	0.09	0.920	3201.2	5.2	3208.5	2.2	3213.0	1.4	0.47
za7	28.7	1.13	0.85	1431	0.233	0.630255	0.28	22.10376	0.47	0.25436	0.37	0.606	3150.6	7.0	3188.3	4.5	3212.1	5.9	2.4
za9	53.6	0.63	0.90	2627	0.249	0.630261	0.11	22.11925	0.13	0.25454	0.05	0.918	3150.6	2.9	3189.0	1.2	3213.2	0.8	2.5
za10	12.3	2.89	0.80	632	0.215	0.641573	0.36	22.49486	0.38	0.25429	0.07	0.983	3195.2	9.1	3205.3	3.7	3211.7	1.1	0.65
WKC00-88																			
za3	108	0.24	0.02	6295	0.006	0.648577	0.19	23.00773	0.19	0.25728	0.05	0.961	3222.6	4.7	3227.3	1.9	3230.1	0.8	0.29
za6	121	0.77	0.22	6691	0.059	0.664092	0.41	25.07061	0.41	0.27380	0.06	0.990	3283.0	10.4	3311.0	4.0	3327.9	0.9	1.7
za7	51.8	1.62	0.06	2834	0.017	0.647710	0.2	22.96638	0.2	0.25716	0.05	0.954	3219.3	3.8	3225.5	1.6	3229.4	0.8	0.40
za9	21.2	1.02	0.34	1143	0.090	0.689262	0.27	27.37265	0.27	0.28803	0.06	0.977	3379.8	7.0	3396.9	2.7	3407.0	0.9	1.0
za10	33.5	0.61	0.17	1883	0.046	0.661020	0.12	24.67230	0.13	0.27070	0.07	0.873	3271.1	3.0	3295.3	1.3	3310.1	1.0	1.5
za12	131	0.54	0.22	7228	0.061	0.663439	0.13	24.60122	0.14	0.26894	0.06	0.917	3280.5	3.4	3292.5	1.4	3299.9	0.9	0.75
za13	50.1	0.88	0.03	2918	0.009	0.641748	0.15	22.71191	0.16	0.25668	0.05	0.947	3195.9	3.8	3214.7	1.5	3226.4	0.8	1.2
a1	0.4	4.43	0.64	30.52	0.170	0.656050	4.85	22.99734	5.06	0.25424	1.08	0.977	3251.8	123.9	3226.8	49.2	3211.3	17.0	-1.6
a2	1.1	11.4	1.06	55.80	0.295	0.622346	0.90	21.82217	0.96	0.25431	0.29	0.955	3119.2	22.3	3175.8	9.4	3211.8	4.5	3.6
a3	0.9	19.3	0.86	49.34	0.275	0.532207	0.57	18.06676	0.66	0.24621	0.27	0.914	2750.7	12.8	2993.3	6.3	3160.5	4.3	15.9
a4	1.0	29.3	1.64	48.91	0.445	0.641107	0.40	22.68358	0.51	0.25661	0.27	0.851	3193.4	10.1	3213.5	5.0	3226.0	4.3	1.3
a5	0.6	64.6	1.29	33.85	0.405	0.549814	0.27	19.12424	0.44	0.25227	0.30	0.744	2824.4	6.1	3048.1	4.2	3199.1	4.7	14.4
a6	0.7	109.7	1.46	36.41	0.394	0.642739	0.26	22.49115	0.49	0.25379	0.37	0.683	3199.8	6.6	3205.2	4.8	3208.6	5.8	0.35

Table 1. (cont.)

				Isotopic ratios									Dates (Ma)						
Sample	$^{206}Pb^{*}/Pb_c$	Pb_c (pg)	Th/U	$^{206}Pb/^{204}Pb$	$^{208}Pb/^{206}Pb$	$^{206}Pb/^{238}U$	% err	$^{207}Pb/^{235}U$	% err	$^{207}Pb/^{206}Pb$	% err	corr. coef.	$^{206}Pb/^{238}U$	±	$^{207}Pb/^{235}U$	±	$^{207}Pb/^{206}Pb$	±	% disc.
(a)	(b)	(c)	(d)	(e)	(f)	(f)	(g)	(f)	(g)	(f)	(g)		(h)	(i)	(h)	(i)	(h)	(i)	(j)
KPV99-90																			
za1	1087	0.40	0.48	58409	0.129	0.655779	0.06	23.67575	0.07	0.26185	0.04	0.827	3250.7	1.5	3255.1	0.7	3257.8	0.6	0.28
za2	106	0.48	0.68	5483	0.184	0.652100	0.17	23.47309	0.18	0.26107	0.05	0.960	3236.4	4.3	3246.8	1.7	3253.2	0.8	0.65
za3	4.4	2.61	0.36	259	0.111	0.568351	0.9	19.93015	0.9	0.25433	0.09	0.995	2901.0	20.1	3088.0	8.3	3211.9	1.3	12.0
za4	19.5	2.62	0.58	873	0.160	0.639373	0.12	22.91041	0.13	0.25988	0.04	0.941	3186.6	3.0	3223.1	1.2	3246.0	0.7	2.3
za5	82.5	0.95	0.64	4318	0.172	0.656453	0.14	23.71432	0.15	0.26200	0.05	0.952	3253.4	3.6	3256.7	1.4	3258.8	0.7	0.21
za6	187	0.81	0.49	10022	0.133	0.648136	0.08	23.27437	0.09	0.26044	0.05	0.865	3220.9	2.0	3238.5	0.9	3249.4	0.7	1.1
za7	49.0	0.73	0.61	2585	0.163	0.656263	0.18	23.70145	0.19	0.26194	0.07	0.938	3252.6	4.5	3256.2	1.9	3258.4	1.0	0.22
za8	213	0.44	0.56	11248	0.151	0.656226	0.09	23.69946	0.10	0.26193	0.04	0.901	3252.5	2.4	3256.1	1.0	3258.3	0.7	0.23
za9	2307	0.20	0.47	123748	0.125	0.655302	0.10	23.66469	0.11	0.26191	0.04	0.910	3248.9	2.5	3254.7	1.1	3258.3	0.7	0.37
KPV99-89																			
za1	143	0.63	0.67	7380	0.181	0.617844	0.07	20.25897	0.09	0.23781	0.06	0.753	3101.3	1.6	3103.8	0.8	3105.4	0.9	0.16
za3	69.1	0.44	0.61	3575	0.165	0.648659	0.12	22.96859	0.13	0.25681	0.05	0.914	3223.0	3.1	3225.6	1.3	3227.3	0.9	0.17
za4	59.0	3.80	0.50	2707	0.136	0.643920	0.2	22.76928	0.2	0.25646	0.07	0.939	3204.4	5.0	3217.1	2.0	3225.1	1.1	0.81
za5	53.7	0.90	0.66	2799	0.178	0.617576	0.13	20.26008	0.14	0.23793	0.05	0.941	3100.3	3.2	3103.9	1.3	3106.2	0.7	0.24
za6	19.8	1.14	0.62	1037	0.167	0.647899	0.21	22.89463	0.22	0.25629	0.06	0.957	3220.0	5.4	3222.5	2.2	3224.0	1.0	0.16
za7	71.3	0.18	0.78	3614	0.211	0.617561	0.21	20.26114	0.22	0.23795	0.06	0.966	3100.2	5.2	3103.9	2.1	3106.3	0.9	0.25
za8	111	0.19	0.65	5754	0.179	0.607413	0.14	19.89861	0.17	0.23760	0.08	0.870	3059.6	3.5	3086.4	1.6	3103.9	1.3	1.8
BS04-1																			
za5	8.8	2.52	0.82	396	0.253	0.563891	0.58	19.97724	0.62	0.25694	0.21	0.939	2882.7	13.4	3090.3	6.0	3228.1	3.4	13.2
za6	110	0.44	0.58	5709	0.157	0.648305	0.21	22.94329	0.21	0.25667	0.05	0.974	3221.6	5.3	3224.5	2.1	3226.4	0.8	0.19
za7	33.5	1.48	0.59	1753	0.158	0.647150	0.2	22.85239	0.2	0.25611	0.07	0.941	3217.1	4.8	3220.7	2.0	3222.9	1.1	0.23
za8	65.9	0.38	0.77	3312	0.208	0.647139	0.15	22.87866	0.16	0.25641	0.06	0.934	3217.0	3.9	3221.8	1.6	3224.8	0.9	0.31
za9	17.2	1.57	0.60	905	0.161	0.647379	0.28	22.85529	0.30	0.25605	0.10	0.939	3218.0	7.0	3220.8	2.9	3222.6	1.6	0.18
za10	67.5	1.25	0.54	3518	0.144	0.648236	0.33	22.89715	0.34	0.25618	0.07	0.979	3221.3	8.4	3222.6	3.3	3223.4	1.1	0.08
BS04-2																			
za2	131	0.56	0.47	7075	0.126	0.647902	0.11	22.92069	0.13	0.25658	0.06	0.869	3220.0	2.8	3223.6	1.3	3225.8	1.0	0.23
za3	58.9	0.58	0.65	3085	0.174	0.654629	0.20	23.57747	0.20	0.26122	0.05	0.973	3246.3	5.0	3251.1	2.0	3254.1	0.7	0.30
za4	68.5	0.64	0.95	3437	0.258	0.617884	0.2	20.25058	0.2	0.23770	0.08	0.893	3101.5	4.1	3103.4	1.8	3104.6	1.3	0.13
za6	67.5	2.01	0.61	3557	0.165	0.649289	0.15	23.28084	0.15	0.26005	0.04	0.963	3225.4	3.7	3238.8	1.5	3247.0	0.6	0.85
za7	416	0.69	0.23	23888	0.066	0.587845	0.06	19.17204	0.07	0.23654	0.04	0.823	2980.7	1.4	3050.5	0.7	3096.8	0.7	4.7

Table 1. (cont.)

				Isotopic ratios									Dates (Ma)						
Sample	$^{206}Pb^{*}$ / Pb_c	Pb_c (pg)	Th / U	$^{206}Pb/^{204}Pb$	$^{208}Pb/^{206}Pb$	$^{206}Pb/^{238}U$	% err	$^{207}Pb/^{235}U$	% err	$^{207}Pb/^{206}Pb$	% err	corr. coef.	$^{206}Pb/^{238}U$	±	$^{207}Pb/^{235}U$	±	$^{207}Pb/^{206}Pb$	±	% disc.
(a)	(b)	(c)	(d)	(e)	(f)	(f)	(g)	(f)	(g)	(f)	(g)		(h)	(i)	(h)	(i)	(h)	(i)	(j)
EKC03-3																			
za1	82.7	0.40	0.30	4422	0.079	0.707287	0.16	28.90776	0.17	0.29643	0.07	0.920	3448.2	4.2	3450.4	1.7	3451.7	1.0	0.13
za2	242	0.59	0.36	12746	0.095	0.705930	0.11	28.94845	0.12	0.29741	0.05	0.921	3443.1	3.0	3451.8	1.2	3456.8	0.7	0.51
za3	58.6	0.47	0.31	3129	0.081	0.709184	0.3	29.06410	0.3	0.29723	0.06	0.982	3455.4	8.3	3455.7	3.1	3455.9	0.9	0.02
za4	106	0.45	0.34	5593	0.089	0.708225	0.21	29.02559	0.21	0.29724	0.04	0.978	3451.8	5.6	3454.4	2.1	3455.9	0.7	0.15
za6	97.3	0.21	0.31	5161	0.084	0.693877	0.15	28.40480	0.15	0.29690	0.05	0.945	3397.4	3.9	3433.2	1.5	3454.1	0.8	2.1
za7	260	0.35	0.31	13848	0.082	0.700485	0.15	28.73923	0.16	0.29756	0.05	0.943	3422.5	4.0	3444.7	1.6	3457.6	0.8	1.3
a1	2.1	31.5	1.43	74.8	0.666	0.441497	0.25	22.03384	0.30	0.36196	0.15	0.866	2357.3	4.9	3185.2	2.9	3758.1	2.3	44.2
a3	2.1	103.8	0.88	94.6	0.273	0.568156	0.12	20.58241	0.20	0.26274	0.13	0.762	2900.2	2.8	3119.1	1.9	3263.2	2.1	13.8
a4	0.7	4.31	1.74	37.8	0.527	0.594789	3.76	22.47647	3.88	0.27407	0.51	0.992	3008.8	90.4	3204.5	37.7	3329.5	7.9	12.0
a5	1.9	8.43	1.32	83.1	0.363	0.673317	0.81	26.64959	0.82	0.28706	0.11	0.990	3318.7	20.9	3370.7	8.0	3401.7	1.8	3.1
a6	1.0	12.0	1.86	44.9	0.569	0.583148	0.98	21.48723	1.04	0.26724	0.24	0.973	2961.6	23.3	3160.8	10.0	3289.9	3.8	12.4
a7	1.0	13.1	1.93	46.1	0.538	0.641919	0.86	23.83172	0.94	0.26926	0.27	0.957	3196.6	21.8	3261.5	9.1	3301.7	4.3	4.0
a8	1.9	42.3	1.68	73.3	0.440	0.774470	0.23	37.10445	0.25	0.34747	0.09	0.936	3697.0	6.4	3696.3	2.4	3695.9	1.3	-0.04
a9	0.9	17.3	2.34	42.2	0.550	0.774630	0.91	29.84664	0.96	0.27945	0.22	0.974	3697.6	25.6	3481.8	9.4	3359.8	3.4	-13.2
a10	1.9	7.54	1.27	83.0	0.369	0.609659	0.84	22.19798	0.87	0.26407	0.15	0.986	3068.6	20.5	3192.4	8.5	3271.2	2.3	7.8
a11	1.0	17.0	1.10	47.1	0.507	0.389125	0.65	14.60626	0.74	0.27224	0.27	0.931	2118.8	11.8	2789.9	7.0	3319.0	4.2	42.2
a12	1.2	15.8	2.47	50.8	0.547	0.898275	0.72	41.37459	0.84	0.33406	0.37	0.901	4131.8	21.9	3804.2	8.4	3635.8	5.6	-18.6
a13	0.9	24.6	0.77	46.8	0.271	0.508124	0.52	19.02946	0.66	0.27162	0.36	0.845	2648.6	11.3	3043.3	6.4	3315.4	5.6	24.4
KPV99-96																			
za1	135	0.23	0.38	7090	0.100	0.712099	0.12	29.40089	0.14	0.29945	0.07	0.861	3466.4	3.1	3467.0	1.3	3467.4	1.1	0.04
za2	23.6	0.27	0.29	1274	0.078	0.706854	0.26	28.95419	0.28	0.29708	0.09	0.942	3446.6	7.0	3452.0	2.7	3455.1	1.4	0.32
za3	99.4	0.37	0.30	5301	0.081	0.706727	0.2	28.95566	0.2	0.29715	0.05	0.967	3446.1	5.6	3452.0	2.1	3455.4	0.9	0.35
za4	124	0.34	0.32	6616	0.084	0.707309	0.15	28.98770	0.17	0.29724	0.06	0.920	3448.3	4.1	3453.1	1.6	3455.9	1.0	0.28
a1	0.8	10.1	0.67	46	0.165	0.675694	1.15	22.09333	1.39	0.23714	0.63	0.895	3327.8	29.8	3187.8	13.5	3100.9	10.0	-9.4
a2	0.5	8.5	0.77	33	0.209	0.612046	2.11	19.91016	2.51	0.23593	1.06	0.909	3078.2	51.6	3087.0	24.3	3092.7	16.9	0.59
a3	2.4	17.2	0.32	123.0	0.090	0.612525	0.45	20.85293	0.51	0.24691	0.21	0.912	3080.1	11.0	3131.8	4.9	3165.1	3.3	3.4
a4	0.6	34.7	0.54	37.5	0.223	0.403512	0.45	13.20198	0.98	0.23729	0.72	0.726	2185.2	8.4	2694.2	9.3	3101.9	11.5	34.7
a5	0.6	45.1	0.73	38.5	0.224	0.548006	0.31	17.88967	0.81	0.23676	0.64	0.684	2816.9	7.1	2983.8	7.8	3098.4	10.1	11.2
a6	0.9	32.2	0.69	49.6	0.266	0.426600	0.35	13.55560	0.58	0.23046	0.39	0.741	2290.4	6.8	2719.2	5.4	3055.2	6.3	29.6
EKC03-9																			
za1	69.5	0.54	0.60	3600.1	0.162	0.650360	0.21	23.15248	0.22	0.25819	0.06	0.957	3229.6	5.4	3233.4	2.2	3235.7	1.0	0.24
za2	16.1	3.96	0.46	764.4	0.123	0.649231	0.27	23.10457	0.28	0.25811	0.08	0.958	3225.2	6.9	3231.4	2.8	3235.2	1.3	0.39
za4	136	2.83	0.70	6899.8	0.188	0.649644	0.08	23.13623	0.09	0.25830	0.04	0.874	3226.8	1.9	3232.7	0.8	3236.3	0.7	0.37
za5	2.7	0.32	0.08	170.2	0.022	0.644488	1.34	22.93834	1.37	0.25813	0.23	0.986	3206.6	33.7	3224.3	13.3	3235.4	3.6	1.1
a1	1.3	10.8	0.25	73.1	0.067	0.642691	0.68	22.39054	0.72	0.25267	0.22	0.950	3199.6	17.0	3200.8	7.0	3201.6	3.5	0.08
a2	1.6	60.1	0.37	83.9	0.100	0.647535	0.15	22.90711	0.20	0.25657	0.11	0.835	3218.6	3.9	3223.0	1.9	3225.8	1.7	0.28
a3	0.7	7.17	1.22	38.9	0.331	0.636729	2.05	22.24850	2.20	0.25342	0.72	0.945	3176.1	51.4	3194.6	21.4	3206.3	11.4	1.2
a4	0.6	19.0	1.54	35.0	0.315	0.834288	1.55	28.47703	3.20	0.24756	2.28	0.751	3910.8	45.5	3435.7	31.4	3169.2	36.1	-31.4
a5	0.9	22.0	0.64	49.7	0.162	0.683558	0.48	23.93998	0.55	0.25401	0.22	0.916	3358.0	12.6	3266.0	5.3	3209.9	3.5	-5.9
a6	1.2	71.0	0.49	65.2	0.131	0.644432	0.19	22.57983	0.33	0.25412	0.24	0.686	3206.4	4.7	3209.0	3.2	3210.6	3.8	0.17

Table 1. (cont.)

				Isotopic ratios									Dates (Ma)						
Sample	$\frac{Pb^*}{Pb_c}$	Pb_c (pg)	$\frac{Th}{U}$	$\frac{^{206}Pb}{^{204}Pb}$	$\frac{^{208}Pb}{^{206}Pb}$	$\frac{^{206}Pb}{^{238}U}$	% err	$\frac{^{207}Pb}{^{235}U}$	% err	$\frac{^{207}Pb}{^{206}Pb}$	% err	corr. coef.	$\frac{^{206}Pb}{^{238}U}$	±	$\frac{^{207}Pb}{^{235}U}$	±	$\frac{^{207}Pb}{^{206}Pb}$	±	% disc.
(a)	(b)	(c)	(d)	(e)	(f)	(f)	(g)	(f)	(g)	(f)	(g)		(h)	(i)	(h)	(i)	(h)	(i)	(j)
EKC03-11																			
za1	2.5	1.91	0.51	127	0.136	0.644303	1.07	22.60126	1.09	0.25441	0.22	0.980	3205.9	27.0	3209.9	10.6	3212.4	3.4	0.26
za2	54.4	0.28	0.35	2966	0.094	0.641365	0.22	22.49067	0.23	0.25433	0.07	0.956	3194.4	5.4	3205.2	2.2	3211.9	1.0	0.69
za3	9.5	1.51	0.12	559	0.034	0.644515	0.4	22.62095	0.4	0.25455	0.08	0.984	3206.7	11.0	3210.8	4.3	3213.3	1.2	0.26
a1	0.7	26.3	0.98	40	0.247	0.644637	1.55	20.00882	1.91	0.22512	0.98	0.861	3207.2	39.1	3091.8	18.5	3017.6	15.7	-8.0
a2	3.8	23.5	0.14	197	0.038	0.608915	0.23	19.67511	0.25	0.23435	0.09	0.932	3065.7	5.6	3075.5	2.4	3082.0	1.5	0.66
a3	1.7	8.8	0.26	94	0.072	0.603009	0.64	19.60025	0.70	0.23574	0.23	0.945	3041.9	15.5	3071.8	6.7	3091.4	3.6	2.0
a4	1.2	21.6	0.47	65.1	0.168	0.464119	0.42	15.03640	0.54	0.23497	0.30	0.834	2457.7	8.5	2817.5	5.2	3086.2	4.8	24.4
a5	1.3	36.2	0.29	72.6	0.079	0.616041	0.25	20.13261	0.51	0.23702	0.37	0.736	3094.1	6.1	3097.7	4.9	3100.1	5.8	0.24
KPV99-94																			
za1	170	0.35	0.48	9157.2	0.130	0.650460	0.11	23.16372	0.13	0.25828	0.06	0.891	3230.0	2.8	3233.8	1.2	3236.2	0.9	0.24
za2	338	0.27	0.31	18861	0.083	0.650856	0.11	23.18030	0.12	0.25830	0.04	0.928	3231.5	2.8	3234.5	1.2	3236.4	0.7	0.19
za3	293	0.32	0.19	16727	0.052	0.650581	0.21	23.16739	0.22	0.25827	0.06	0.965	3230.5	5.3	3234.0	2.1	3236.2	0.9	0.22
za4	975	0.33	0.45	52785	0.123	0.647147	0.09	23.04619	0.10	0.25828	0.04	0.915	3217.0	2.4	3228.9	1.0	3236.3	0.7	0.75
a1	2.2	3.56	0.39	120.9	0.108	0.608856	1.46	20.74472	1.56	0.24711	0.44	0.959	3065.4	35.5	3126.7	15.1	3166.3	7.0	4.0
a3	2.2	20.7	0.57	109.6	0.167	0.578200	0.27	19.16862	0.31	0.24044	0.13	0.906	2941.4	6.4	3050.3	3.0	3122.9	2.1	7.2

(a) z1, z2, a1, a2, etc. are fractions composed of single grains of zircon and apatite, respectively
numbers in parantheses following apatite fractions are the number of grains, if not equal to one
za1, za2, etc. are zircon fractions that were subjected to the chemical abrasion technique

(b) Ratio of radiogenic Pb (including 208Pb) to common Pb.

(c) Total weight of common Pb.

(d) Model Th/U ratio calculated from radiogenic 208Pb/206Pb ratio and 207Pb/206Pb age.

(e) Measured ratio corrected for spike and fractionation only. Mass fractionation corrections were based on analysis of NBS-981 and NBS-983. Corrections of 0.25 ± 0.04%/amu (atomic mass unit) and 0.07 ± 0.04%/amu were applied to single-collector Daly analyses and dynamic Faraday-Daly analyses, respectively.

(f) Corrected for fractionation, spike, and blank. All common Pb was assumed to be procedural blank.

(g) Errors are 2 sigma, propagated using the algorithms of Ludwig (1980).

(h) Calculations are based on the decay constants of Jaffey et al. (1971).

(i) Errors are 2 sigma.

(j) % discordance = 100 - (100 x 206Pb/238U date / 207Pb/206Pb date).

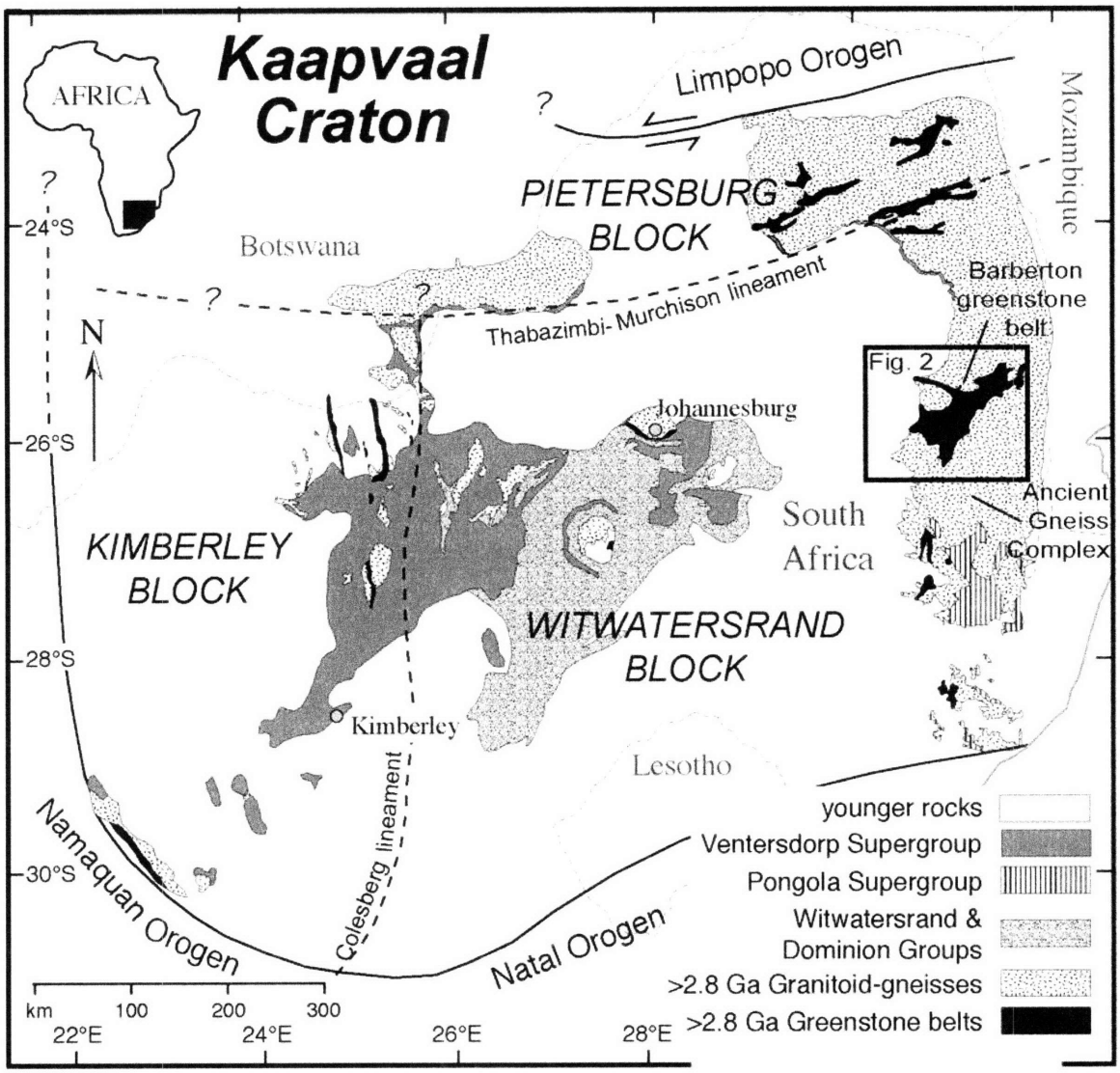

Fig. 1 Schoene et al.

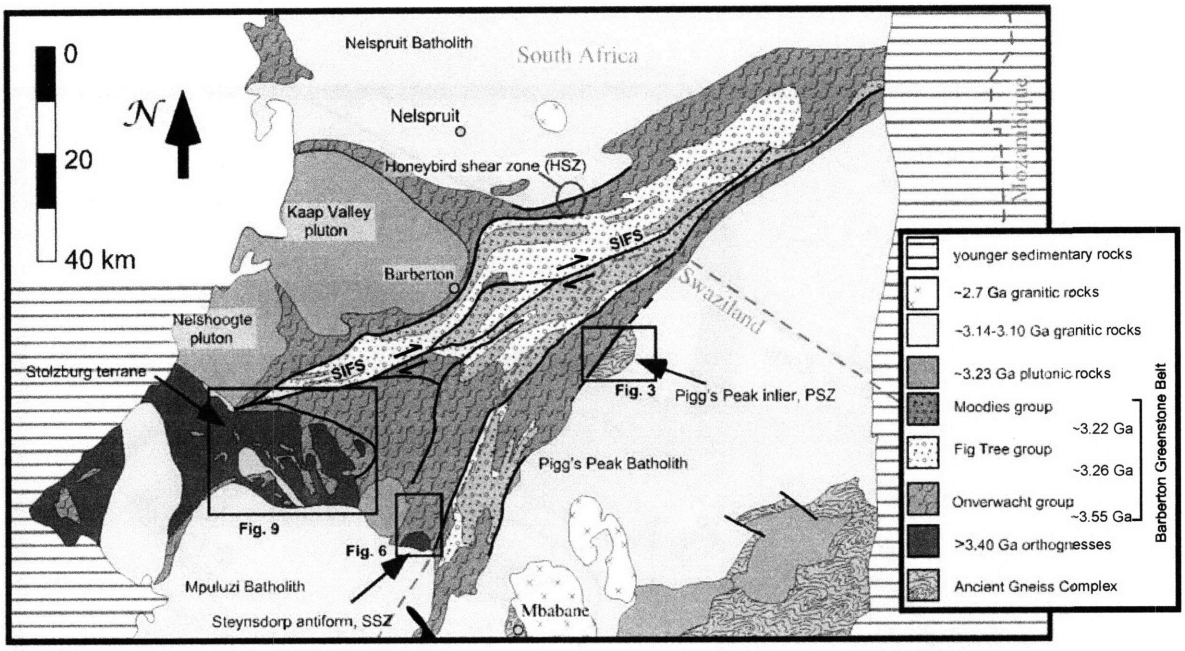

Fig. 2 Schoene et al.

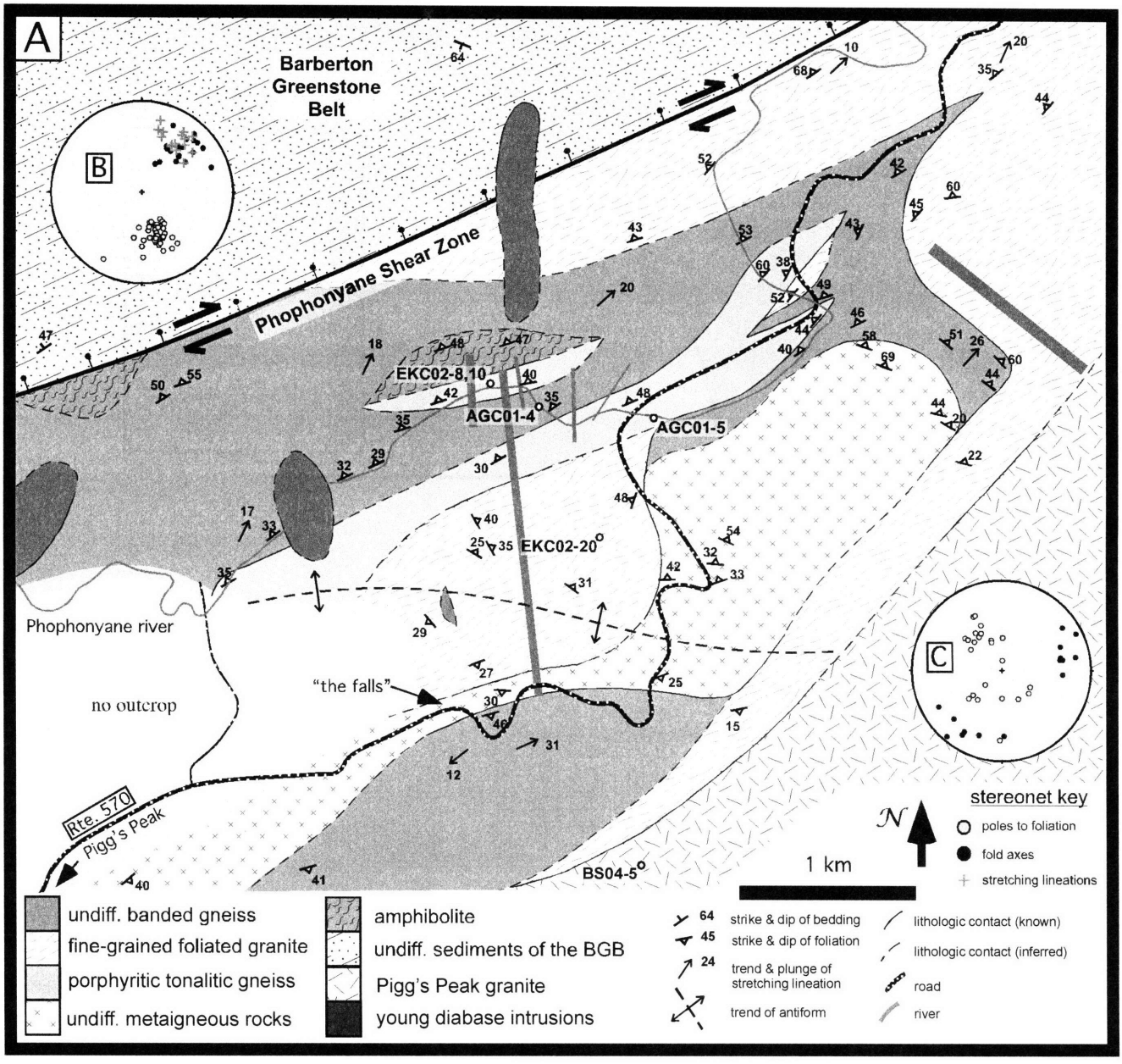

Fig. 3 Schoene et al.

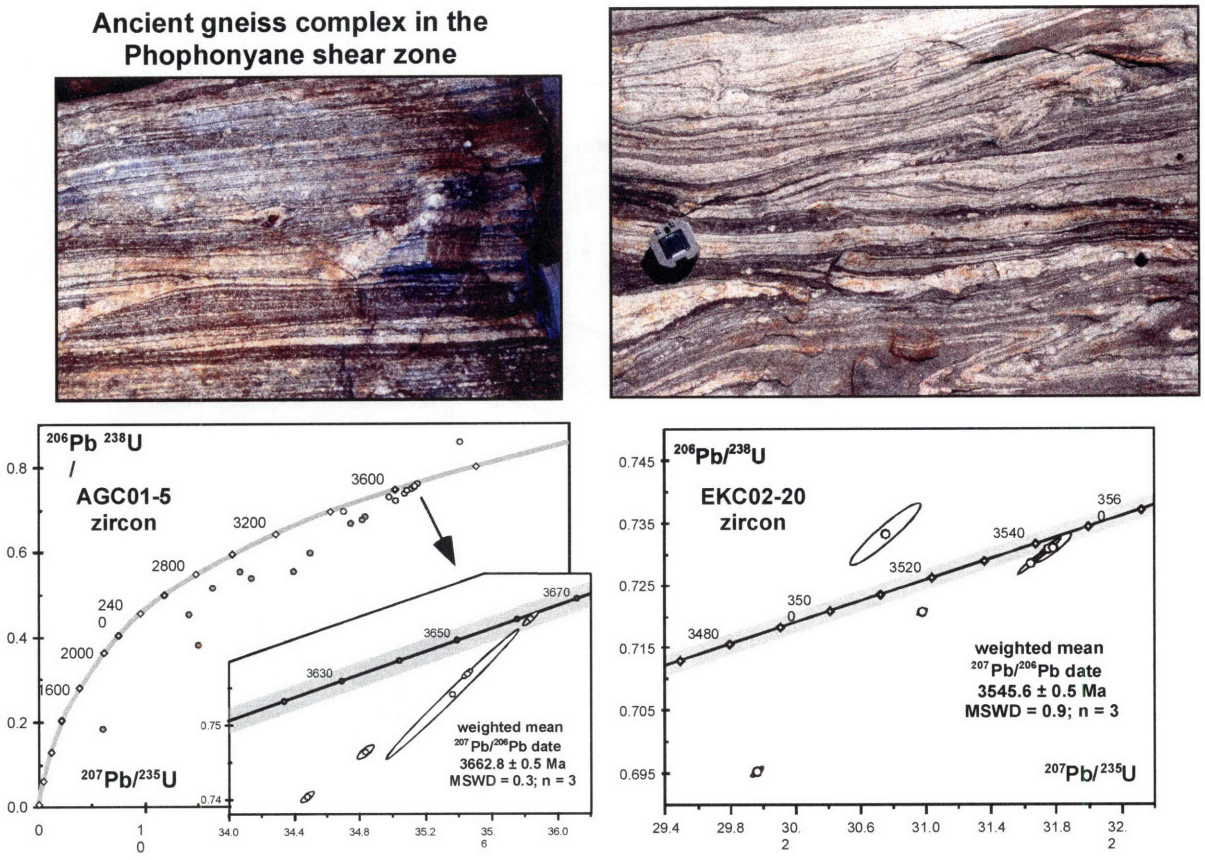

Fig. 4 Schoene et al.

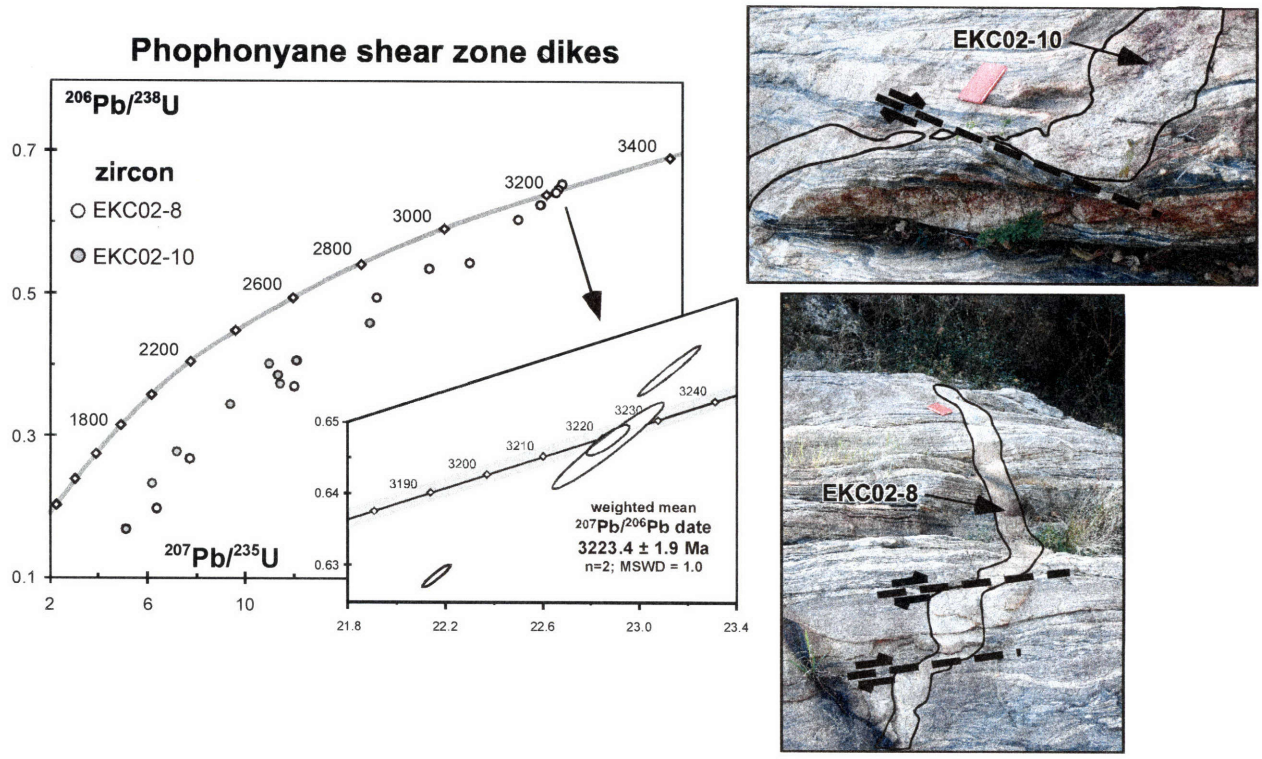

Fig. 5 Schoene et al.

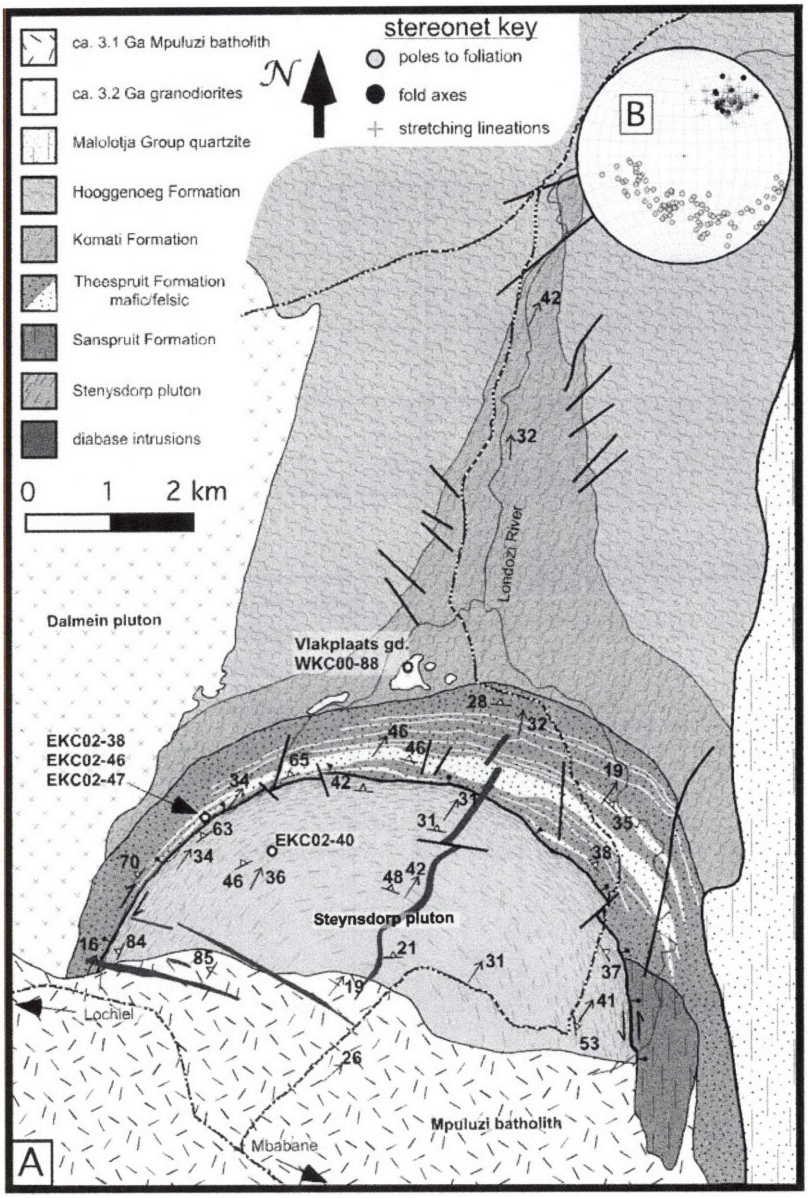

Fig. 6 Schoene et al.

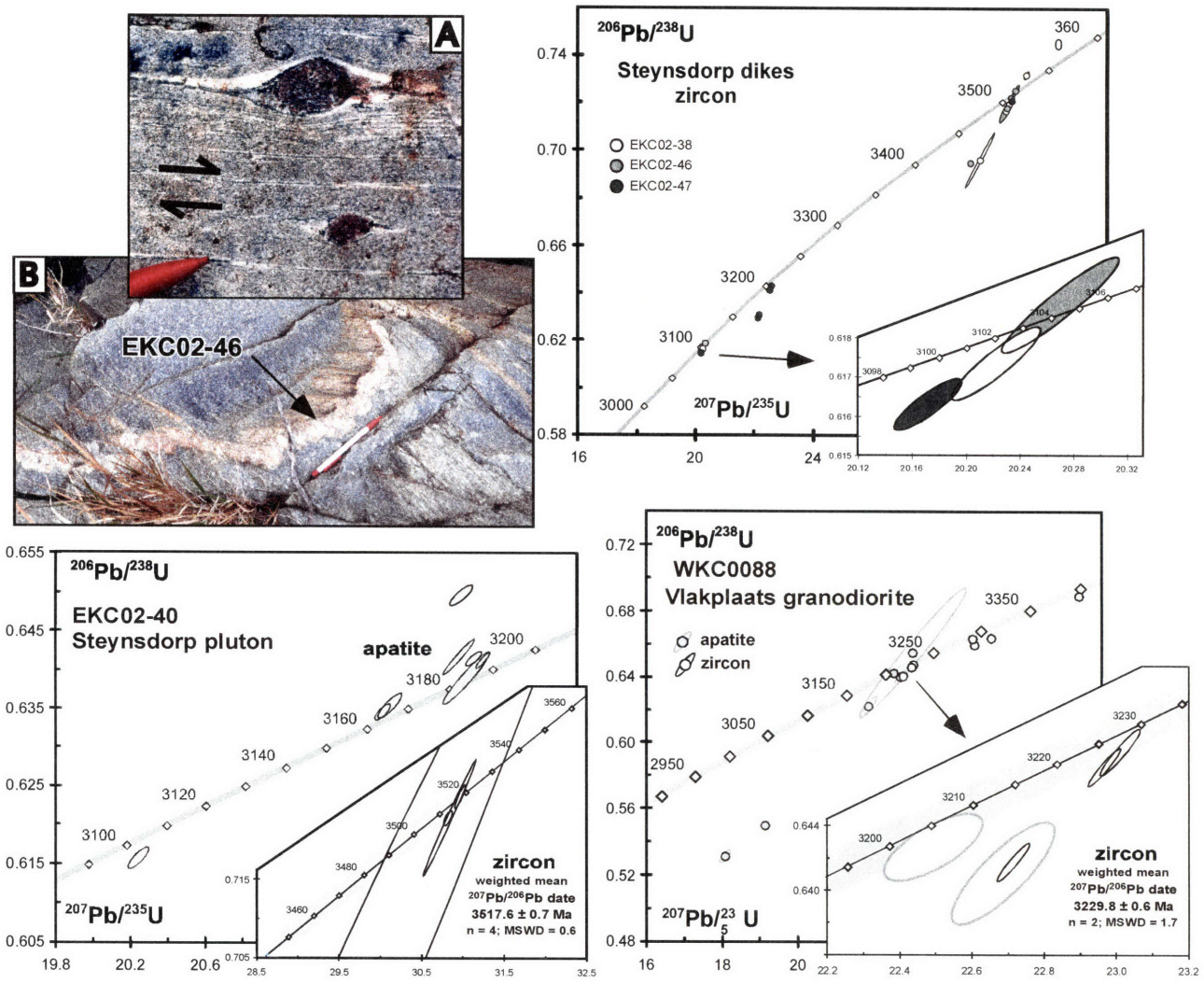

Fig. 7 Schoene et al.

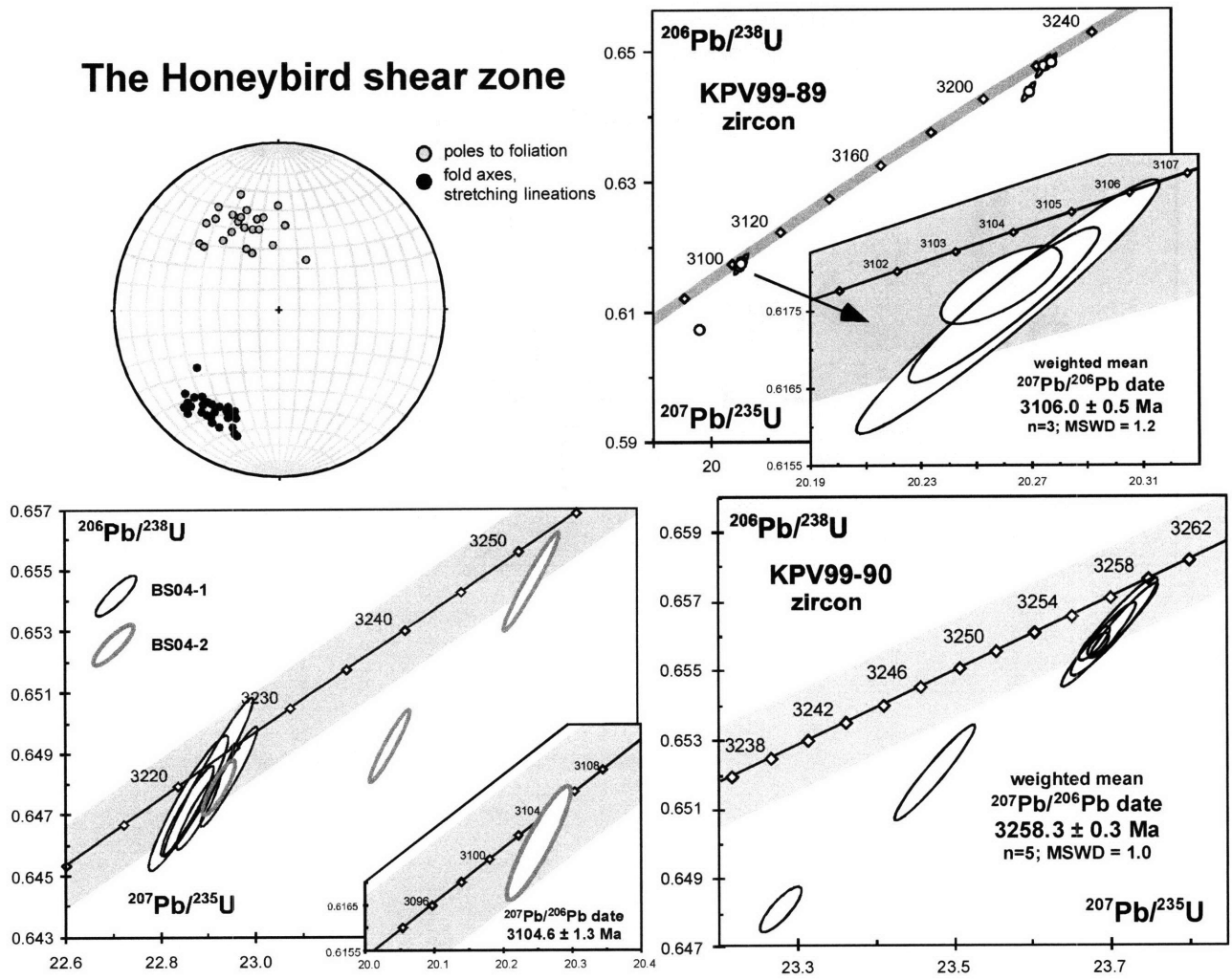

Fig. 8 Schoene et al.

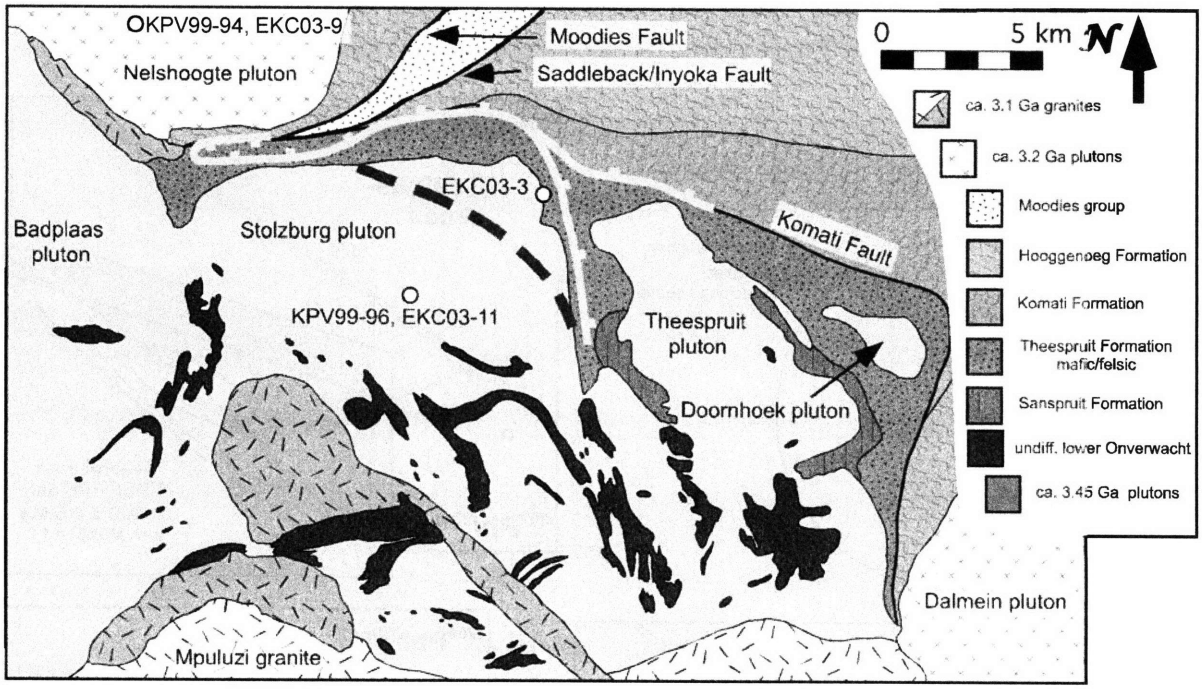

Fig. 9 Schoene et al.

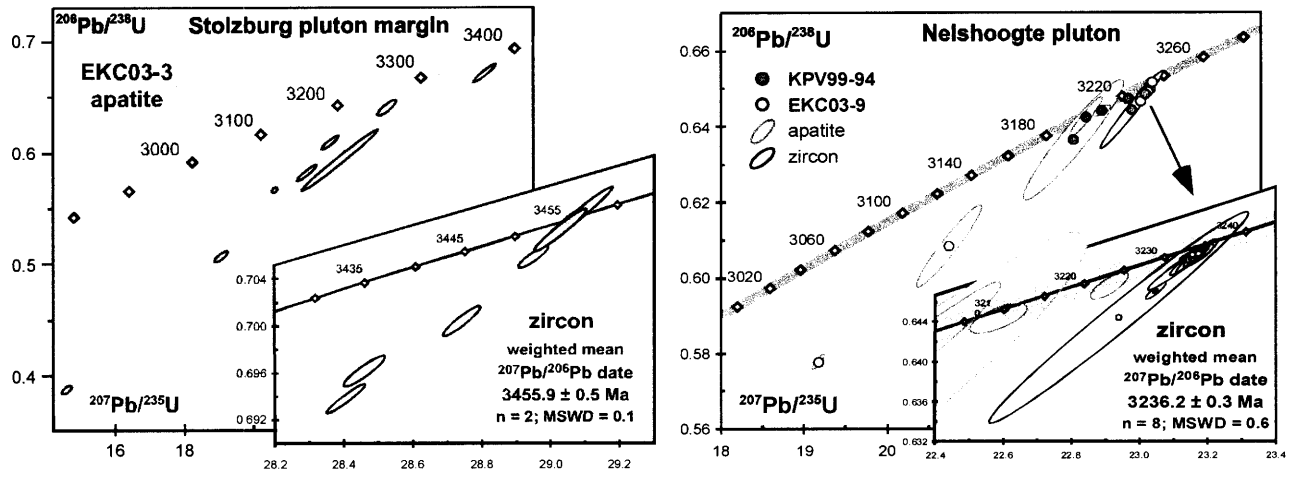

Fig. 10 Schoene et al.

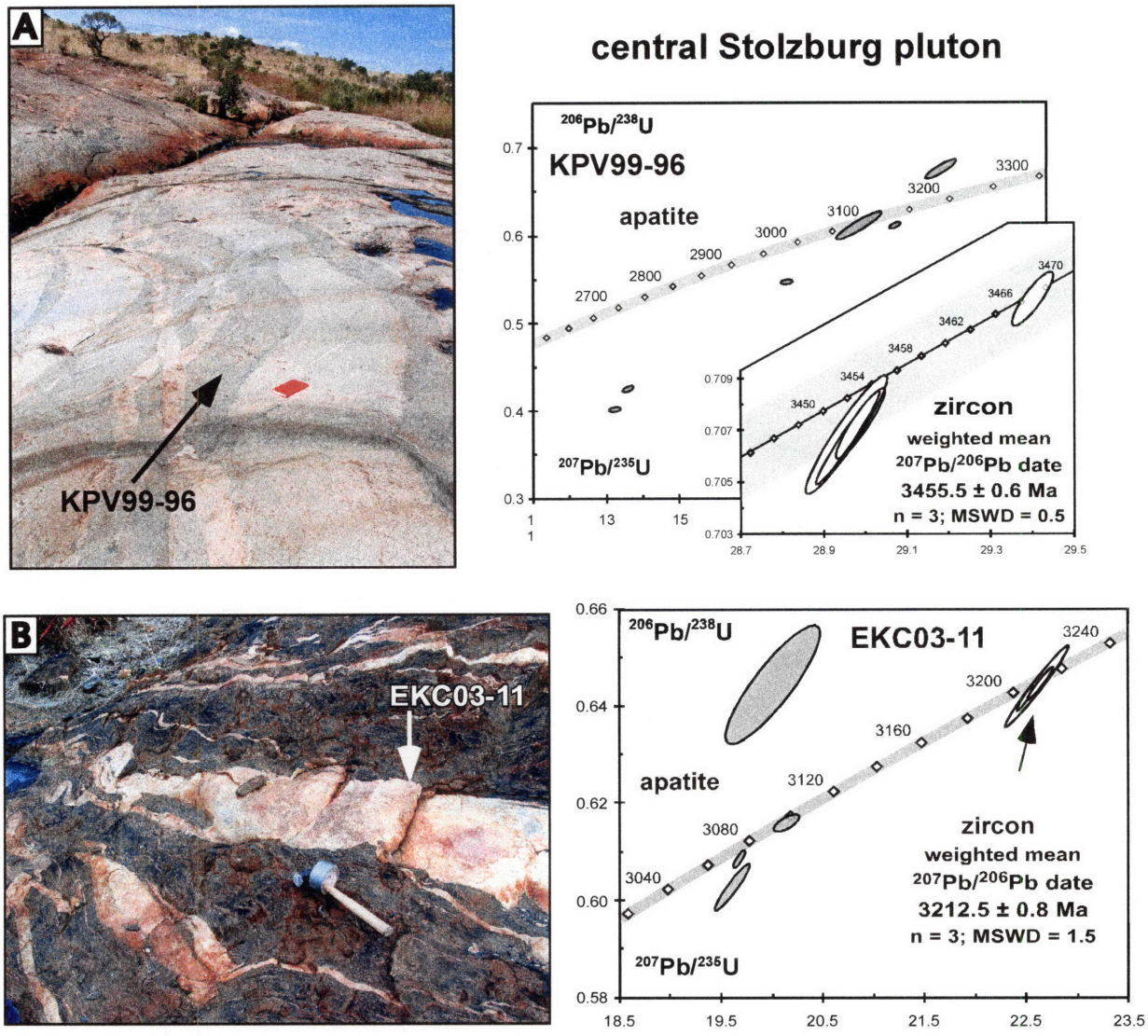

Fig. 11 Schoene et al.

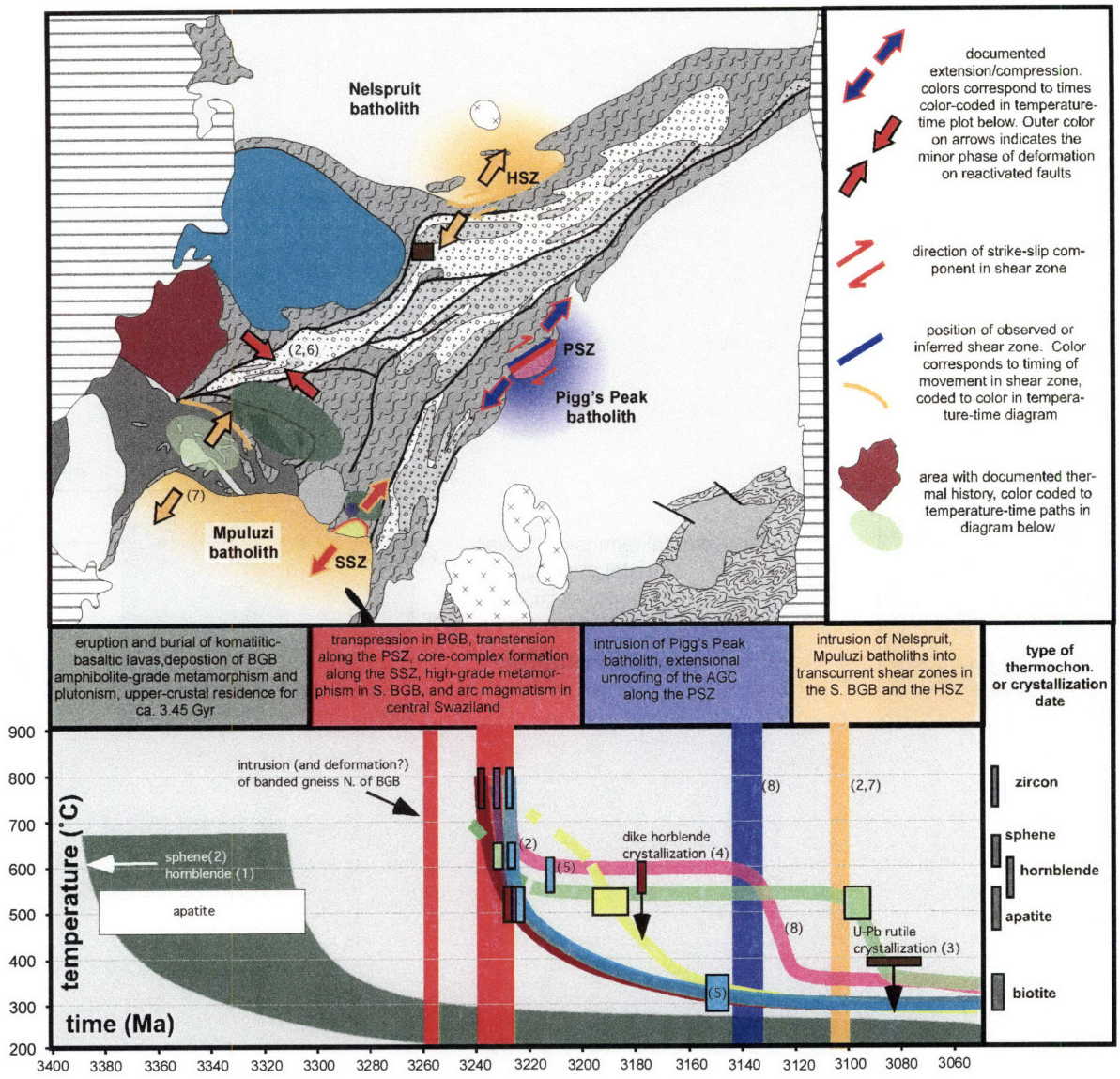

Fig. 12 Schoene et al.

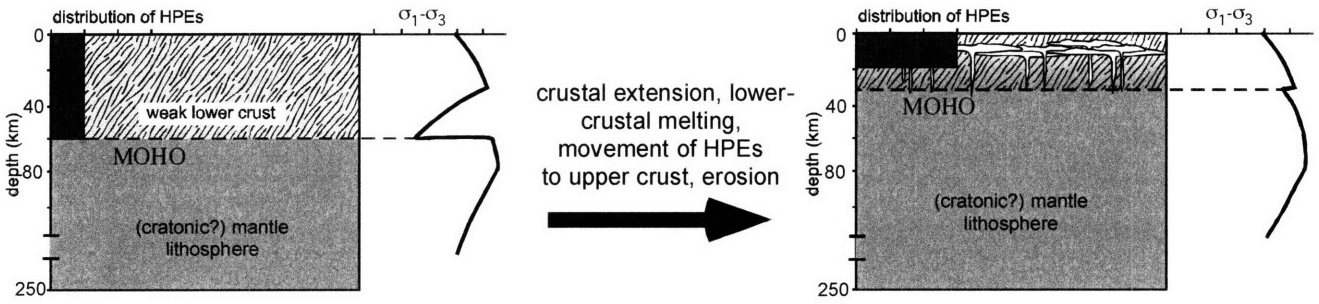

Fig. 13 Schoene et al.

CHAPTER 3

Rates and mechanisms of Mesoarchean magmatic arc construction, eastern Kaapvaal craton, Swaziland

Blair Schoene* and Samuel A. Bowring

Department of Earth, Atmospheric and Planetary Sciences; Room 54-1116; 77 Massachusetts Ave., Massachusetts Institute of Technology, Cambridge, MA 02139, USA.

**schoene@mit.edu*

To be submitted to *GSA Bulletin*

ABSTRACT

The timescales and mechanisms of magmatism and deformation during orogenesis are important for developing models of lithospheric growth. We investigate a well preserved Mesoarchean crustal section from the oldest portion of the Kaapvaal craton, southern Africa, that records the complex interactions between deformation and magmatism during craton assembly ca. 3.23 Ga. U-Pb ID-TIMS zircon geochronology and apatite thermochronology in conjunction with geological mapping show that the tonalitic to granodioritic Usutu magmatic suite intruded into the ca. 3.45-3.66 Ga Ancient Gneiss Complex over a period of ~16 Myr ca. 3236-3220 Ma as discrete pulses of magma with variable intrusive styles. Usutu rocks retain magmatic fabrics that preserve a history of NW-SE shortening, consistent with deformation recorded in the adjacent Barberton greenstone belt. It is shown in that in some cases, the magmatic fabrics form up to 2 Myr after zircon crystallization, suggesting prolonged residence of interstitial liquid before crystal mush reinvigoration by new magma injections. U-Pb zircon and apatite dates from basement gneisses (the Nhlangano gneiss) reveal that they represent exposed lower crust of the ca. 3.23 Ga orogenic belt, providing a view into different crustal levels during orogenesis. We suggest a simple ca. 3.2-3.3 Ga subduction model that accounts for the geology and geochronology of the eastern Kaapvaal craton, including the Barberton greenstone belt. Additionally, the preserved magmatic fabrics in the Usutu rocks compared to the highly deformed adjacent terranes of similar age suggest strain was partitioned into the margins of the Ancient Gneiss Complex to accommodate a rigid block of crust. Thus, it seems that the Ancient Gneiss Complex had attained cratonic strength by ca. 3.23 Ga and formed the nuclei upon which the rest of the craton was built and modified over the following 500 Myr.

1. INTRODUCTION

Studies of orogenic belts show that the generation, transport and emplacement of tonalitic to granodioritic magmas have been fundamental processes in building continental lithosphere since early in earth history. Therefore, understanding the relationship between magmatism and deformation as a function of time is fundamental in generating robust tectonic models for orogenic belts and lithosphere stabilization. This is difficult because complex strain partitioning between wall-rocks and magmas in addition to the complicated kinematic response of different crustal levels to applied regional stresses necessitates high-precision temporal constraints on all parts of an orogenic belt, which are not often available (e.g. Axen et al., 1998; Hollister and Crawford, 1986; Miller and Paterson, 2001; Pavlis, 1996). Fortunately, plutonic rocks often preserve fabrics that are formed while still in a magmatic state, evidenced in part by the alignment of elongate minerals or compositional heterogeneties (Hutton, 1988; Paterson et al., 1998). These features, often called magmatic fabrics, have potential to preserve strain induced by regional stress imposed on the magma or by fluid flow in a dynamic magma chamber or conduit (Mahan et al., 2003; Wiebe and Collins, 1998). In both cases, U-Pb zircon dates in such rocks can be used to constrain the timing of fabric formation and therefore paleostress environments if zircon crystallization and fabric generation were cogenetic. Comparing the timing of magmatism and fabric generation in some rocks to subsolidus deformation in other rocks can provide information about strain partitioning during deformation, which in turn can be used a proxy for gradients in lithospheric strength as a function of time (Axen et al., 1998; Klepeis et al., 2004; Klepeis et al., 2003). Such information is important in the study of Archean orogenic belts in particular because the

timescales and mechanisms by which cratons attained their apparent strength remains poorly understood (Schmitz et al., 2004; Schoene et al., in prep). Changes in magmatic regimes, deformational styles, or strain partitioning through the crust occur on sub-million year timescales and the efficacy of geochronology towards unravelling a sequence of tectonothermal events is therefore dependent on attaining absolute precision of similar magnitudes.

Complicated and protracted geologic histories result in increased opportunity for open-system behavior of different geochronometers, compromising the accuracy of calculated dates. Additionally, typical analytical precision of isotopic measurements in older rocks simply translates into larger absolute age uncertainties than in younger rocks. The U-Pb method is the most useful dating scheme for Archean rocks because it can overcome both of these problems. The dual decay of ^{238}U and ^{235}U to ^{206}Pb and ^{207}Pb, respectively, allows for an internal test of open-system behavior, thereby allowing one to validate the accuracy of the calculated dates (see review in Davis et al., 2003). If it can be established that a mineral behaved as a closed system (i.e. it is concordant), then it allows for the use of the $^{207}Pb/^{206}Pb$ date, whose uncertainty does not increase substantially with the age of the mineral for a constant analytical error, and is therefore the most precise approach for dating Archean rocks (e.g. Mattinson, 1987). In concordant minerals with high ratios of radiogenic to initial Pb (common Pb; Pb_c), the $^{207}Pb/^{206}Pb$ date is unarguably the most *accurate* for Archean rocks as well. Recent advances in sample preparation techniques, most notably the advent of the chemical abrasion technique for zircon analysis, have greatly improved our ability to isolate concordant domains of zircon (Mattinson, 2003, 2005). This in conjunction with

improved laboratory blanks to <0.5 pg level has allowed for the generation of data with precision well below the 0.1% level on low-Pb, closed-system domains of Archean zircon. Consequently, the calibration of magmatic, metamorphic, and deformational processes to better than 1 Myr is possible, allowing for a much richer understanding of tectonic events during the construction of Archean cratons.

We examine a spectacularly preserved section through a ca. 3.2 Ga magmatic arc in the oldest portion of the Kaapvaal craton, in the vicinity of the Barberon greenstone belt (BGB). This classic exposure of Archean crust has fueled debate on Archean Earth processes, from the evolution of life, the eruption of komatiitic lavas, the origin of oceans, synorogenic sediment transport, and concentration of the world's largest gold deposits. Nearly all of the studies focusing on the plate tectonic assembly of this cratonic nuclei come from within or directly adjacent to the supracrustal rocks preserved in the BGB, and thereby lack a larger regional context (de Ronde and de Wit, 1994; Kamo and Davis, 1994; Kisters et al., 2003; Lowe, 1994). For example, it is generally agreed that the NE-SW trending BGB represents a suture between two or more continental blocks that were assembled via subduction and terrane accretion ca. 3.23 Ga (de Wit et al., 1992; Dziggel et al., 2002; Lowe, 1994, 1999). However, few studies have tested this hypothesis by examining the basement complexes NW and SE of the belt, for example to test the vergence of the inferred subduction zone. Here, we investigate a several groups of rocks SE of the BGB called the Usutu intrusive suite and the Nhlangano orthogneiss. No detailed field description these rocks has been published, though there is some geochronologic data to suggest that their generation and emplacement may be temporally related to ca. 3.23 Ga craton assembly (Kröner et al., 1989; Kröner et al., 1991). The

contrast in intrusive and deformational styles between the Usutu suite and the basement orthogneisses offer valuable insight into strain and melt distribution in the lower crust during pre-cratonic orogeny.

This study uses a combination of mapping and U-Pb geo- and thermochronology to understand the tectonothermal evolution of the eastern Kaapvaal craton during ca. 3.23 Ga continental assembly. We summarize a preliminary investigation of outcrops of the Usutu intrusive suite that extend from NW Swaziland, where they are in contact with the BGB, to their southern extent in central Swaziland, where they intrude syntectonically into basement orthogneisses. High-precision U-Pb ID-TIMS geochronology of concordant zircon domains allows for the establishment of crystallization ages of individual intrusions with precision on weighted mean dates of $\geq$0.01%. Crystallization ages for the previously undated Nhlangano gneiss reveal this orthogneiss complex to represent compositionally diverse ca. 3.2-3.3 Ga lower crust. Finally, U-Pb apatite thermochronology (closure temperature ~450-550 °C; Chamberlain and Bowring, 2000; Cherniak et al., 1991; Schoene and Bowring, submitted) is used to place thermal constraints on the metamorphic and exhumation history of rocks. We use these data to test and refine comprehensive regional tectonic models for the early history of the Kaapvaal craton. An outgrowth of these models is that the crust behaved as anisotropically during orogenesis and arc magamtism, focusing strain along the boundaries of the oldest crustal block, indicating an early onset of cratonic rigidity and nucleation.

2. GEOLOGIC BACKGROUND

Rocks of the eastern Kaapvaal craton record a complex history during the Mesoarchean, culminating in its assembly and stabilization ca. 3.23-3.10 Ga in and around the Barberton greenstone belt (BGB; Fig. 1). A period of concomitant deformation, metamorphism, and magmatism ca. 3.23 Ga in the BGB has been inferred to be the result of the collision of two or more microcontinental blocks (de Ronde and de Wit, 1994; de Wit et al., 1992; Heubeck and Lowe, 1994a; Lowe, 1999). Evidence for the timing of this deformation in the BGB is provided by U-Pb dates of syn- and post-tectonic tonalitic dikes in synorogenic sedimentary rocks, and occurred between ca. 3229-3227 Ma (de Ronde and Kamo, 2000; Kamo and Davis, 1994). Deformation in supracrustal slivers included in the ca. 3.45 Ga basement orthogneiss complexes south of the BGB, such as the Stolzburg pluton (Fig. 1), is bracketed by a U-Pb date on a syntectonic dike of 3229±5 Ma (Dziggel et al., 2005), and the occurrence of a late synkinematic dike, dated by U-Pb at ca. 3213 Ma (Schoene et al., in prep). Amphibolite-grade metamorphism in this area occurred before the closure of metamorphic titanite, dated in two places at ca. 3229 Ma (Diener et al., 2005; Dziggel et al., 2005). Transtesional deformation in the Phophoyane shear zone, along the eastern margin of the BGB in the Pigg's Peak inlier (Fig. 1), was bracketed by U-Pb dating on syntectonic dikes to have occurred before ca. 3223 Ma (Schoene et al., in prep). Formation of the Steynsdorp core-complex in the southern BGB (Fig. 1) occurred soon before ca. 3230 Ma, bracketed by U-Pb dates of a cross-cutting granodioritic plug and also by U-Pb apatite thermochronology (Schoene et al., in prep). The synchronous occurrence of compressional and extensional tectonics during ca. 3.23 Ga deformation may be related to oblique convergence of lithospheric

blocks, resulting in flower-structure type transform boundary in the BGB (Schoene et al., in prep).

Despite a prolonged focus of research on the ca. 3.23 Ga history of the BGB, the location or age of the inferred microcontinents, and the vergence of inferred pre-assembly subduction are poorly understood. (de Ronde and de Wit, 1994; de Wit et al., 1992) suggested that the Saddleback-Inyoka fault system, which runs NE-SW though the north-central portion of the BGB, formed a major continental lithospheric suture between rocks north and south of the BGB. Lowe (1994) described a more complicated scenario involving no less than four microcontinental blocks that were sutured during thrusting along numerous belt-parallel faults. It is clear that numerous blocks retaining unique thermal histories are represented in the BGB, but major restructuring of the belt due to focused strain-partitioning, transtensional faulting, and granitic batholith intrusion ca. 3.2-3.1 Ga has partially obscured the ca. 3.23 Ga position of different lithotectonic blocks as well as the kinematic history of important faults (Schoene et al., in prep).

A more integrated view of craton assembly ca. 3.23 Ga will be accomplished by studies that stretch beyond the BGB into the neighboring basement rocks, whose tectonothermal histories are poorly known. The most prominent features north of the BGB are the Kaap Valley and Nelshoogte plutons, dated most precisely by U-Pb at 3227.2±0.2 Ma and 3236.2±0.3 Ma, respectively (Schoene et al., 2006; Schoene et al., in prep). A banded tonalitic orthogneiss from a transtensional shear zone bounding the northern margin of the BGB was dated by U-Pb at 3258.3±0.3 Ma, providing the only date of pre-3.23 Ga bedrock north of the BGB (Schoene et al., in prep). However, xenoliths of ca. 3.3 Ga crustal material were recovered from north of the BGB within the

ca. 3106 Ma Nelspruit batholith, which may represent the age of juvenile continental crust involved in a ca. 3.23 Ga collision (Kamo and Davis, 1994).

The Ancient Gneiss Complex (AGC), located south of the BGB in Swaziland, contains the oldest rocks in the Kaapvaal craton and is often invoked as one of the bounding blocks in a ca. 3.23 Ga continental collision (de Wit et al., 1992; Jackson et al., 1987; Lowe, 1994, 1999). The AGC is traditionally subdivided into three major units: the Ngwane gneiss, the Dwalile metamorphic suite, and the Tsawela gneiss (Hunter, 1970, 1979; Hunter et al., 1978; Jackson, 1984). The Ngwane gneiss comprises a series of multiply deformed tonalites, granodiorites, amphibolites, and pegmatites that are interlayered in heterogeneous bands and folds at the cm to dm scale (Jackson, 1984). U-Pb crystallization ages from these rocks and associated homogeneous granites are older than 3500 Ma; the oldest U-Pb dates of 3.64-3.66 Ga have come from the Pigg's Peak inlier in NW Swaziland (Compston, 1988; Kröner et al., 1989; Schoene et al., in prep). The Dwalile suite is a series of actinolite-chlorite metasediments and mafic to felsic metavolcanics that resemble the basal portions of the BGB both in rock-type and age, and have detrital and volcanic U-Pb zircon dates of ca. 3.55 Ga (Jackson, 1984; Kröner and Tegtmeyer, 1994). The Tsawela gneiss is a relatively homogeneous foliated hornblende tonalite for which no U-Pb dates have been published, but Pb-Pb dates are 3.43-3.45 Ga (Kröner et al., 1989; Kröner and Tegtmeyer, 1994). Throughout northern and central Swaziland, a series of younger tonalitic to granodioritic rocks called the Usutu intrusive suite cross-cut the AGC (Hunter, 1970; Hunter et al., 1978; Wilson, 1982). Though the Usutu suite has never been described in detail, preliminary Pb-Pb dates of ca. 3.23 Ga (Kröner et al., 1991) suggest that they may be related to deformation, magmatism and

inferred terrane assembly in the BGB. A strongly foliated granodiorite from the Phophonyane shear zone in the Pigg's Peak inlier, potentially correlative to the Usutu suite, crystallized ca. 3226 Ma (Schoene and Bowring, submitted).

In south-central and southern Swaziland, a series of mafic-silicic banded orthogneisses called the Nhlangano gneiss are similar in appearance to the Ngwane gneiss. Field relations, however, suggest these to be younger than the Ngwane gneiss (Jackson, 1984; Wilson, 1982), though only one ion microprobe U-Pb date of ca. 2745 Ma has been published (Kröner et al., 1989). Detrital zircon from granulite grade metapelites and quartzites from the Mahamba gneisses and Mkhondvo metamorphic suite, which are tectonically interwoven with the Nhlangano gneisses, give dates >3400 Ma (Condie et al., 1996; Kröner et al., 1991). Timing of metamorphism of these units is not well known, though Condie et al. (1996) suggested it to be ~2745 Ma based on a Pb-Pb zircon evaporation date from a melt leucosome from with in the Mkondvo metamorphic suite. This date corresponds roughly to wide-spread granitic magmatism in central and southern Swaziland.

This study focuses on the geology and geochronology of the Usutu intrusive suite and Nhlangano gneiss from nothern to south-central Swaziland. The history of these rocks in relation to the inferred terrane accretion ca. 3.23 Ga in the BGB is unconstrained but potentially important in generating regional scale geodynamic models for the growth and stabilization of this portion of the Kaapvaal craton.

3. GEOLOGY AND GEOCHRONOLOGY OF THE USUTU SUITE

The present study examines the Usutu intrusive suite and Nhlangano gneiss from the southern margin of the BGB through south-central Swaziland. In general, Usutu rocks range in composition from hornblende tonalite to granodiorite with associated gabbroic dikes. Similar to the AGC, the Usutu rocks are more easily eroded and make up the low-lying valleys of central Swaziland. Outcrop is therefore generally confined to rivers or areas of high relief formed by the resistant ca. 2.7 Ga granites or younger diabase dikes. For simplicity and descriptive purposes, we subdivide descriptions of the Usutu intrusive suite into three domains. This section summarizes the field observations, rock descriptions, and U-Pb geo- and thermochronology of the different lithologic units of the Usutu suite and Nhlangano gneiss. U-Pb data are presented in Table 1, and the description of the analytical procedure is in the Appendix.

3.1. The Malolotja inlier - NW Swaziland

3.1.1. Field description

Two exposures of Usutu-aged rocks crop out in NW Swaziland. One is an inlier of AGC located near Pigg's Peak (Fig. 1), described in detail by (Schoene et al., in prep), where they are highly deformed by the Phophonyane shear zone. This transtensional shear zone, active at ca. 3.23 Ga and reactived at ca. 3.14 Ga (Schoene and Bowring, submitted), was responsible for juxtaposing low-grade rocks of the BGB against amphibolite grade orthogneisses of the AGC and Usutu suite. A second exposure of Usutu rocks is located along the Komati river near the border of the Malolotja nature reserve, where the Usutu rocks are in contact with Malolotja group quartzites of the BGB

to the west (Lamb, 1984; Lamb and Paris, 1988) and are cross-cut by the Pigg's Peak batholith on the east (Fig. 2). We term this sequence of outcrops the Malolotja inlier. Several hundred meters east of the contact with the quartzites, the Usutu suite is very well exposed for several kilometers along the Komati river. These rocks record complex interactions of mafic and silicic magmas that is overprinted by strong shearing near the contact with the quartzites.

The main rock type present ~1.5 km east of the quartzite contact is a megacrystic biotite granodiorite. This rock contains phenocrysts of K-feldspar up to 6 cm long and 2 cm wide that are aligned within a fine- to medium-grained granodioritic matrix (Fig. 3). There is no evidence that the megacrysts were rotated into alignment and matrix quartz and feldspar show little or no stretching, suggesting the megacryst alignment defines a magmatic fabric striking ~020 and dipping 60-80° to the west (Fig. 2). However, in some places the alignment of biotite is strong and wraps around euhedral feldspar grains, which may have resulted from solid-state strain. The concentration of megacrysts varies between 0 and 50% of the rock, and this variability is sometimes gradational over tens of centimeters and sometimes megacrystic zones are truncated sharply by compositionally (granitic to gabbroic) or texturally (coarse- to fine-grained) distinct units. Distinct gabbroic bands or schlieren have soft contacts with the host granodiorite and often contain xenocrystic K-feldspar megacrysts (Fig. 3). Rare ovoid mafic enclaves with fine-grained margins are also present and further suggest that the amount of solid-state strain in the rock was low (Fig. 3). Also present are multiple generations of fine-grained granitic to aplitic dikes that obviously cross-cut the fabric in the rocks.

The amount of megacrystic material decreases towards the contact with the quartzites, and this transition correlates with an increase in the amount of mafic material present (Fig. 3). Also, solid-state strain in the rocks increases westward, and these rocks grade into S-L tectonites within ~200 m of the contact with a poorly exposed amphibolite unit that separates them from the quartzites. Mafic bands within the granodiorite compose >10% of the rock and are flattened with aspect ratios of ≤50/1. Larger bands of mafic material (1-10 m thick) occur as well. Megacrystic rock is also present, and K-feldpsar megacrysts record the solid-state strain particularly well, behaving as mantled porphyroclasts (Passchier and Trouw, 2005). Most K-feldspar porphyroclasts have symmetric mineral trails, though some have slight sigmoidal geometry interpreted to reflect normal shear sense (top to the NW), which is consistent with poorly developed but steeply dipping stretching lineations in the rock (Fig. 2). Younger aplitic dikes are aligned parallel to the foliation, are foliated themselves and are boudinaged in places (Fig. 2).

3.1.2. Sample descriptions and U-Pb geochronology

EKC03-33

This sample was collected from within a relatively homogeneous low-strain zone ~1.5 km from the contact with the quartzites. It contains 1-6 cm megacrysts of K-feldspar within a tonalitic to granodioritic matrix. This sample yielded abundant elongate euhedral prismatic zircons. Out of six zircon analyses, three were concordant, giving $^{207}Pb/^{206}Pb$ dates that range between ~3232 and 3227 Ma. It likely that these data represent mixing

between differently aged domains of zircon or inheritance of slightly older grains within a 3227 Ma rock. Pb-loss would result in discordant data, unless it happened at a single moment in time within ~300 Myr of crystallization (such that a Pb-loss trajectory parallels concordia), which is not likely in zircon given the difficulty of diffusing Pb within non-metamict zircon. So the date of the youngest zircon of 3227.2±1.0 Ma is interpreted to approximate the crystallization age of the rock (Fig. 3).

EKC03-23 and BS04-3

These samples were collected from one of the western-most exposures of Usutu rocks, where medium- to fine-grained tonalite is cut by a series of aplitic dikes. The dikes are oriented parallel to the host rock foliation and are foliated and boudinaged. A sample of the host rock (EKC03-23) and one dike (BS04-3) were collected. EKC03-23 yielded abundant euhedral elongate prismatic zircon. Seven zircon analyses from the host rock EKC03-23 yielded four near concordant analyses that yield a weighted mean $^{207}Pb/^{206}Pb$ date of 3230.3±0.4 Ma (MSWD = 0.4; Fig. 3). The dike, BS04-3, yielded <30 zircons <100 μm long ranging in morphology from elongate and euhedral to nearly spherical, and many of these dissolved after a short period of chemical abrasion. Nine grains were successfully analyzed, and only one is concordant. However, four near concordant grains yield identical $^{207}Pb/^{206}Pb$ dates, and the five together yield a weighted mean $^{207}Pb/^{206}Pb$ date of 3224.4±0.4 Ma (MSWD = 1.5; Fig. 2)). Two round grains yielded much younger $^{207}Pb/^{206}Pb$ dates of ca. 3160 Ma, and these were likely metamorphic. Therefore, shearing occurred at this outcrop after ca. 3224 Ma.

3.2. The Mbuluzi river section

3.2.1. Field Descriptions

The Usutu suite in central Swaziland north of Manzini outcrops sparsely in small river drainages or as highly weathered exposures in topographically steep areas. However, there is a good exposure along an 10 km stretch of the Mbuluzi river that can be accessed in two spots by a series of dirt roads north and west of Luve. The most continuous exposures occur within 1 km of the road crossings: in the east, along the road from Luve to Mbabane and in the west where a dirt road dead ends at the Mbuluzi river.

At the eastern crossing, two main lithologies of Usutu rocks are exposed, including megacrystic granodiorite (EKC02-23) and homogeneous medium-grained biotite tonalite (EKC02-24), though more mafic bands within the megacrystic unit and cross-cutting pegamatitic dikes are also present. The megacrystic unit records the interaction of mafic and silicic magmas during intrusion, evidenced by soft contacts with mafic material. K-feldspar megacrysts are ($\leq$3-4 cm long and $\leq$1-3 cm wide) and define a strong magmatic fabric that varies locally in strike and dip by $\pm$10-15° (Fig. 4). Megacrysts also occur as xenocrysts in the mafic units and both single megacrysts and magmatic fabrics cross-cut soft mafic-silicic contacts. Contacts between the tonalite and the megacrystic granodiorite in places are soft to gradational such that it is difficult to distinguish their relative age, though in other places the tonalite clearly cross-cuts the megacrystic unit. Magmatic fabrics are continuous across lithologic contacts that strike at high angles to it.

Usutu rocks at the western river crossing preserve intrusive relationships with the wall rocks as well as mixing and mingling relationships between different magmas. Wall

rocks are heterogeneously deformed and brecciated and both mafic and silicic in composition. Their protoliths are likely to be a series of bimodal volcaniclastic and volcanic rocks, but some may also be siliciclastic in origin. In places, these rocks are obviously xenoliths, though in others they may maintain continuity with wall rocks, perhaps as roof pendants. In sections with little intrusive material, the orientation of foliation in the metamorphic rocks strikes generally NW – at high angles to the magmatic fabrics observed in the Usutu rocks. Several magmatic phases crop out here, including medium grained leucotonalite (sample EKC02-32), megacrystic granodiorite, and fine-grained hornblende gabbro. These rocks are cut by a series of undeformed granitic dikes and plugs that appear similar to what is mapped as Pigg's Peak granite several kilometers north of the Mbuluzi river (Wilson, 1982; sample EKC03-18). Similar to other Usutu rocks, these different phases sometimes have distinct cross-cutting relationships and sometimes more diffuse contacts where magma mixing occurs. These outcrops have a much higher proportion of gabbroic rocks than elsewhere. In situ melting of fine-grained mafic material is also observed, and in places tonalitic leucosomes appears to form small dikes or veinlets that connect to larger magmatic bodies. The plutonic rocks here have a fabric that is interpreted to be primarily magmatic in origin based on the observation that textural bands defined by mineralogic and grain size variability occur with no observable strecthing in the grains. Also, foliation in xenolithic material is highly discordant to the fabric in some magmatic rocks. However, in several places there is mineral flattening and open folds develop. Boudinage is also observed in mafic dikes within the tonalitic rocks. These observations all point to a dynamic system involving the contemporaneous

intrusion of multiple batches of magmas and deformation controlled by contrasting rheological properties.

3.2.2. Sample Descriptions and U-Pb Geochronology

EKC02-23

This is a sample of very fresh megacrystic granodiorite from the eastern crossing of the Mbuluzi river. It contained abundant stubby euhedral zircons ranging in size from 50-150 μm. Six zircons from this rock were analyzed, of which three were concordant and yield a weighted mean $^{207}Pb/^{206}Pb$ date of 3229.8±0.5 Ma (MSWD = 1.9), which is interpreted to be the timing of crystallization of the rock.

EKC02-24

This is a sample of very fresh biotite tonalite from the eastern crossing of the Mbuluzi river. It contained abundant zircon, ranging in morphology from elongate and prismatic to tabular, though each morphology had sharp crystal terminations. Five of six zircon analyses were concordant and yield a weighted mean $^{207}Pb/^{206}Pb$ date of 3227.5±0.3 Ma (MSWD = 0.4), interpreted to be the crystallization age of the rock.

EKC02-32

This is a sample of homogeneous massive leucotonalite from the western outcrop. Biotite in this sample has been replaced by chlorite, though plagioclase remains largely extent unaltered. This rock yielded abundant euhedral elongate prismatic zircon. Of five

zircon analyses, three yielded a concordant cluster, one is slightly negative discordant, and one is slightly positively discordant. A weighted mean $^{207}Pb/^{206}Pb$ date of three analyses is 3231.3±0.5 Ma (MSWD = 0.7). This date represents the crystallization of at least a portion of the leucotonalite in the area.

EKC03-18

This is a sample of a fine-grained granitic plug that cross-cuts the other lithologies in the western outcrop. It may or may not be representative of the granite mapped as Mpuluzi batholith several kilometers north and west of this outcrop. It yielded abundant zircons that were either elongate euhedral prisms or rounded prisms. Four rounded grains were inherited, with $^{207}Pb/^{206}Pb$ dates of either ca. 3280 or 3224 Ma. Five grains with sharp crystal terminations were variably discordant with $^{207}Pb/^{206}Pb$ dates of ca. 3180-3190 Ma. A single concordant grain with <15 pg of Pb* gave a $^{207}Pb/^{206}Pb$ date of 3186.8±2.1 Ma. This most accurately represents the crystallizaion age of the rock and clearly post-dates the intrusion and deformation of other rocks in the area.

3.3. Central Swaziland

3.3.1. Field Geology

Exposure in the southern areas of the Usutu suite (here arbitrarily defined as outcrops generally south of Manzini) is also mainly confined to river outcrops, though the confluence of a number of major drainage systems makes for more continuous sections than in areas further north. Usutu rocks in the area can be generally divided into three lithotectonic terranes based on the style of intrusion, ratio of intrusive rocks to host

basement gneisses, and the amount of post-intrusion deformation (Fig. 6). We focus our geologic description of this domain to the areas near sample localities.

The northern portion of the map area in Fig. 6 is characterized by tonalite to granodiorite with variable amounts of hornblende. In the western side of the map area the Usutu river exposes coarse grained hornblende-rich tonalite (sample EKC02-35). In places a fabric defined by alignment of sub- to euhedral hornblende is well developed, striking NE-SW and dipping SE. A similar rock type occurs throughout central Swaziland but has a strong foliation; geochronology in the following section reveals that in at least one locality (sample EKC03-36), the foliated rock is >3.4 Ga and likely associated with the Tsawela gneiss (Jackson, 1984; Kröner and Tegtmeyer, 1994).

South of Matsapha along the Usushwana river, rocks contain a steeply-dipping magmatic fabric defined by variations in grain-size, modal distribution of major constituent minerals such as hornblende, biotite and plagioclase, and other igneous textures such as alignment of elongate minerals (sample EKC03-21; Fig. 7). Magmatic layering ranges in thickness from several centimeters to tens of meters. Mafic enclaves and xenoliths are concentrated within discreet layers several meters thick, suggesting magma intruded as steeply dipping dikes with slightly different composition or pre-intrusion crystallization history. In this scenario, a batch of magma would entrain mafic enclaves or xenoliths from a wall rock, and then migrate upward (Fig. 7).

Further south on the Usushwana river, the proportion of xenolithic material increases until older wall rock pendants that were intruded by younger magma dominate the outcrops (near samples BS04-6, -7, and -8). These bimodal basement orthogneisses (sample BS04-7) are multiply-deformed, evidenced by refolded folds in mafic-silicic

bands and have a strong resemblance to the Ngwane gneiss from northern Swaziland. Fold patterns in the orthogneiss are open to isoclinal with fold hinges that roughly parallel weak stretching lineations and boudinage trains. In places, hornblende leucotonalite (sample BS04-8) is observed intruding boudin necks in the orthogneiss, suggesting it intruded synchronous with deformation (Fig. 8). These observations, and that magmatic fabrics are warped around xenoliths in places, suggest that small scale heterogeneities in the fabric represent flow of magma. For the most part, the leucotonalite shows little or no solid-state deformation in these outcrops, and magmatic fabrics are consistent with the intrusion synchronous with NW-SE shortening and with the maximum stretching direction as NE-SW in the horizontal plane. An undeformed medium grained granodiorite cuts all fabrics in these outcrops (sample BS04-6), and this rock is similar to other massive granodiorite bodies in the map area, which were originally the only rocks within this southern area mapped as the Usutu granodiorite (Wilson, 1982).

Within several kilometers upstream of the confluence of the Usushwana and the Usutu rivers, a series of granodiorites and tonalites (±hornblende) are strongly deformed whether they are associated with the bimodal orthogneisses or not. In most outcrops, the deformation is characterized by a strong flattening fabric with subhorizontal lineations and open folds with moderately dipping axes. Foliation in bimodal gneisses near the confluence of the Ngwempisi and Usutu rivers is parallel to the foliation in the Usutu rocks and parallel to the magmatic fabrics exhibited further north. Bimodal gneiss in these outcrops (sample EKC02-64, presented in the Nhlangano gneiss samples) is difficult if not impossible to distinguish from Usutu-aged rocks, if present. One outcrop

examined along the Usutu river contained a granodioritic augen gneiss (sample BS04-12) with strong foliation that dips steeply to the south. This rock also has well developed mantled porphyroclasts that record dextral shear (Fig. 9). The foliation is cross-cut by a late aplitic dike that has a poorly developed foliation parallel to the host rock (sample BS04-11). The southern extent of the Usutu suite is marked by the northern boundary of the undeformed ca. 2.7 Ga Hlatikulu granite (sample EKC02-65). Those rocks and their significance will be discussed briefly below.

EKC02-35

This is a sample of coarse grained hornblende tonalite, collected along the Usutu river in the western portion of the map area (Fig. 6). It is undeformed and has no visible magmatic fabric, though rocks with weak magmatic fabrics occur nearby. This rock yielded abundant euhedral elongate to stubby prismatic zircons. Five zircons were analyzed and three near concordant grains yield a weighted mean $^{207}Pb/^{206}Pb$ date of 3236.1±0.5 Ma (MSWD = 0.6), interpreted to reflect crystallization of the rock (Fig. 8).

Two apatite grains were analyzed from this rock, and they are ≤1% discordant and give $^{207}Pb/^{206}Pb$ dates between ca. 2865 and 2790 Ma, likely reflecting partial resetting by the Ngwempisi pluton, which crops out <2 km to the SW (Fig. 10).

EKC02-36

This is a sample of medium to fine grained foliated hornblende biotite leucotonalite collected along the Usushwana river in the NW portion of the map area (Fig. 6). Foliation in this sample is defined by fine-grained elongated bands of hornblende and

biotite. Zircon from this sample is elongate and subhedral, with well-rounded crystal terminations, either indicative of metamorphic overgrowths or post-crystallization resorption. Three grains were analyzed and are nearly concordant with $^{207}Pb/^{206}Pb$ dates between ca. 3428 and 3436 Ma, with the most concordant giving the youngest date (Fig. 8). Thus, determining a precise crystallization age for this rock requires a more detailed investigation of zircon textures in addition to more U-Pb analyses. However, it is clear based on the geochronology and composition of this rock that it is associated with the Tsawela gneiss, whose type locality is in the Mankayane inlier in western Swaziland (Jackson, 1984; Jackson et al., 1987; Kröner and Tegtmeyer, 1994).

Two apatite grains were analyzed from this sample, and they are both >4% discordant and have $^{207}Pb/^{206}Pb$ dates between ca. 2893 and 2790 Ma, reflecting partial resetting by the intrusion of the Mbabane pluton, which crops out <2 km to the north (Fig. 10).

EKC03-21

This sample came from an outcrop of layered hornblende tonalite, tonalite, and granodiorite from the Usushwana river directly south of Matsapha (Fig. 6). EKC03-21 is a coarse grained biotite tonalite with minor hornblende. Zircon from this sample is elongate to stubby and prismatic with slightly rounded crystal terminations. Of five analyses, three were nearly concordant and give a weighted mean $^{207}Pb/^{206}Pb$ date of 3232.1±0.5 Ma (MSWD = 0.8), which is interpreted to be the crystallization age of the rock (Fig. 8). One grain is slightly younger, at ca. 3226 Ma, but is negatively discordant, and one positively discordant grian is ca. 3232 Ma.

One concordant apatite analysis gave a $^{207}Pb/^{206}Pb$ date of ca. 3190 Ma, which is interpreted to reflect cooling of the rock through the closure temperature of apatite (Fig. 8).

BS04-7

This sample is a fine-grained foliated tonalite with layering defined by amount of quartz and feldspar. It was sampled from a large body of banded tonalite along the Usushwana river where BS04-8 intrudes synchronous with deformation. Zircon from BS04-7 varies from tabular elipsoids to knobby subhedral elongate prisms to small euhedral elongate prisms. Seven zircons were successfully analyzed from a range of morphologies, though the most euhedral grains tended to dissolve during leaching and only two were recovered for analysis. Near concordant grains from the slightly rounded population of zircons give $^{207}Pb/^{206}Pb$ dates that range from 3411-3440 Ma (Fig. 8). One small euhedral grain is discordant and gives a $^{207}Pb/^{206}Pb$ date of ca. 3315 Ma. The youngest discordant grain is a minimum age for the crystallization age of the rock, though the ca. 3.4 dates are likely a more accurate respresentation of crystallization.

BS04-8

This sample is a medium-grained hornblende tonalite that was collected adjacent to BS04-7, where it is observed to intrude the banded gneiss during deformation. Biotite and hornblende occur in bands several cm in length that define a magmatic fabric whose orientation is highly dependent on its proximity to and geometry of the adjacent banded gneiss. Zircon from BS04-8 is euhedral and varies from elongate prisms at smaller grain

widths (<100 μm) to stubby prisms or elipsiods in large grains. All five zircons analyzed were concordant, and three yield weighted mean $^{207}Pb/^{206}Pb$ date of 3232.1±0.4 Ma (MSWD = 0.7), interpreted to be the crystallization age of the rock (Fig. 8). Two inherited grains give $^{207}Pb/^{206}Pb$ dates of ca. 3411 and 3541 Ma, the former of which was the only analysis from the ellipsoidal population of zircon.

BS04-6

This sample is an undeformed medium to coarse-grained granodiorite that cuts all the fabric in the outcrop where BS04-7 and BS04-8 were collected. It yielded abundant euhedral elongate to stubby prismatic zircon in addition to a large, very clear blocky population that is euhedral but often broken. Six zircon analyses were all concordant and three from the blocky population yield a weighted mean $^{207}Pb/^{206}Pb$ date of 3219.9±1.0 Ma (MSWD = 1.5), interpreted to be the crystallization age of the rock (Fig. 8). Three inherited prismatic grains give $^{207}Pb/^{206}Pb$ dates from ca. 3256-3260 Ma.

Five grains of apatite were also analyzed for U-Pb analysis. All analyses are concordant except for one, which is -1.1% discordant, though all give $^{207}Pb/^{206}Pb$ dates between ~3180-3200 Ma. In addition, there is a strong correlation between date and grain size, suggesting that these data record cooling through the closure of apatite 20-40 Myr after intrusion of BS04-6 (Fig. 8).

BSO4-11, BS04-12

These samples were collected from an exposure along the Usutu river, about two kilometers upstream from its confluence with the Ngwempisi river. BS04-12 is a foliated

granodioritic augen gneiss, with mantled porphyroclasts that give a dextral strike-slip shear sense (Fig. 9). BS04-11 is a sample of an ~0.5 m wide aplitic dike that cross-cuts the local foliation, and is lightly foliated itself, but shows no folding or offset, suggesting it post dates simple shear in the outcrop. Both samples yielded abundant large blocky to elongate zircons as well as a population of stubby to elongate prismatic zircons. Four of the large blocky grains from BS04-12 were analyzed, three of which are concordant and yield a weighted mean $^{207}Pb/^{206}Pb$ date of 3221.8±0.4 Ma (MSWD = 0.5), interpreted to be the crystallization age of the rock (Fig. 9). Two blocky grains and one small prismatic grain were analyzed from BS04-11. The two blocky grains are concordant and yield a weighted mean date of 3221.6±0.4 Ma (MSWD = 0.2), interpreted to represent crystallizaion of the dike (Fig. 9). The prismatic grain is concordant, but inherited with a $^{207}Pb/^{206}Pb$ date of ca. 3235 Ma. Because the two samples yield identical dates, it suggests that intrusion and shearing of sample BS04-12 occurred in a short period of time.

3.4. The Nhlangano Gneiss

3.4.1. Geology of Southern Swaziland Gneiss Terranes

The geology of south-central Swaziland is most adequately characterized by a series of ca. 2.7 Ga granites that cross cut a series of granulite grade ortho- and paragneisses grouped into three main units: the Nhlangano gneiss, the Mahamba gneiss, and the Mkhondvo metamorphic suite (Wilson, 1982). These units, as mapped, are very difficult to distinguish in places, and the interelationship between the paragneisses and orthogneisses is not well characterized. We tentatively suggest that the Mkhondvo suite

and Mahamba gneiss be grouped together in that both represent high-grade supracrustal rocks infolded with the more abundant Nhlangano orthogneiss.

Field observation concentrated on one spectacularly exposed locality along the Mkhondvo river near an inlier of the Mkhondvo metamorphic suite (here called the Mkhondvo suite inlier; Fig. 1), reported to contain granulite grade metamorphic assemblages (Condie et al., 1996). This area shows the Mkhondvo suite infolded synformally within Nhlangano orthogneiss. In general, the orthogneisses are similar to those intruded by the Usutu suite along the Usushwana and Usutu rivers (samples BS04-7, presented above, and EKC02-64; Fig. 10), though in places contain pink granodioritic augen orthogneiss (sample EKC03-36; Fig. 10) in addition to highly attenuated mafic-silicic banded gneisses (samples EKC02-66, EKC03-35, BS04-18; Fig. 10). In fact, the NE-SW foliation trend in the orthogneiss observed north of the Hlatikulu granite is likely continuous with N-S foliations observed near the Mkhondvo suite inlier, in that the change in strike is gradual.

The highly strained gneiss units in the Mkhondvo valley are cut abruptly by several plutonic rocks of unknown age. Some of these are mapped as the Usutu suite (sample BS04-20), presumably because of their granodioritic to tonalitic composition. Another cross-cutting unit, the Hlatikulu granite (samples EKC02-65, BS04-21), is present throughout the Mkhondvo valley and within the surrounding hills.

3.4.2. Nhlangano gneiss geochronology

Five samples of banded orthogneiss were collected for U-Pb geochronology. Sample EKC02-64 is a well foliated porphyritic granodioritic orthogneiss and was collected from

a good exposure along the Usutu river ~2 km downstream of the confluence with the Ngwempisi river. This outcrop contains several phases of deformed gneiss, of which EKC02-64 is the oldest. EKC02-66 is a well foliated tonalitic gneiss collected from an outcrop near the road along the Mkhondvo river (Fig. 10). Samples EKC03-35 and EKC03-36 were collected several hundred meters from each other, from outcrops in contact with the Mkondovo suite inlier (Fig. 1). EKC03-35 is a sample of an example of tonalitic gneiss from a section of banded gneisses (Fig. 10). EKC03-36 is a sample of highly attenuated banded granodioritic augen gneiss (Fig. 10).

Each of the samples yielded abundant euhedral elongate to stubby prismatic zircons, mostly with slightly rounded grain edges. Also present were rounded grains that are either metamorphic or resorbed igneous grains, though these were usually avoided for analysis. With the exception of EKC02-64, zircons from all of the samples were extremely difficult to analyze, in that they dissolved during chemical abrasion in only a few hours. Those zircons that were successfully analyzed were all discordant to some degree, such that determining a high-precision crystallization age for these rocks is not possible. Of those analyses that were <3% discordant, all but four give $^{207}Pb/^{206}Pb$ dates that fall between 3239 and 3265 Ma. One 1.2% discordant grain from EKC03-36 gives a $^{207}Pb/^{206}Pb$ date of ca. 3224 Ma. Two grains from EKC02-64 and EKC03-35 that were significantly rounded compared the others, gave $^{207}Pb/^{206}Pb$ dates of ca. 3329 and 3425 Ma, respectively, and these are likely inherited. Two concordant grains from EKC02-64 give a weighted mean $^{207}Pb/^{206}Pb$ date of 3265.6±0.5 Ma (MSWD = 0.1), interpreted to be the crystallization age of that rock (Fig. 10).

Despite the discordance of the Nhlangano gneiss zircons, it is observed that magmatic zircons from other samples in this and related studies (Schoene and Bowring, submitted; Schoene et al., in prep) that are <3% discordant are not more than 15 Myr younger than the true crystallization age. Therefore, we think that the various samples of Nhlangano gneiss in this study likely crystallized between about 3240 and 3280 Ma. Concordant data from EKC02-64 support this conjecture.

Single grains of apatite were measured from samples EKC03-35 and EKC03-36, which were collected about 400 and 800 m from the contact with the Hlatikulu granite, respectively. The apatite fractions are variably discordant and have $^{207}Pb/^{206}Pb$ dates between ca. 2.73 and 3.10 Ga, and on average, dates from EKC03-35 are younger than those from EKC03-36 (Fig. 10). This is interpreted to reflect partial resetting of apatite dates by the ca. 2.73 Ga granite (see below), the degree of which is a function of distance from the intrusion. The fact that the apatite was only partially reset ca. 2.7 Ga unambiguously means that these rocks and the Mkhondvo metamorphic suite, which crops out <500 m away, did not reach granulite grade metamorphic conditions ca. 2.7 Ga.

EKC02-65, BS04-21

These are both samples of the Hlatikulu granite, one collected near the northern boundary of the batholith (EKC02-65; Fig. 6), and one near the contact of the Nhalngano gneiss, west of the Mkhondvo metamorphic suite inlier (BS04-21; Fig. 1). Both rocks are medium to fine-grained biotite granites and clearly cross-cut the foliation patterns in local gneisses. Each yielded abundant pristine stubby prismatic zircon, and BS04-21 also had a population of rounded, botryoidal zircon that appear resorbed or overgrown. Three of

four analyses from BS04-21 yield a weighted mean $^{207}Pb/^{206}Pb$ date of 2729.8±0.4 Ma (MSWD = 1.3; Fig. 11). One analysis, picked from the rounded population of zircon gives a slightly younger $^{207}Pb/^{206}Pb$ date of ca. 2727.6 Ma, and therefore this grain represents zircon associated with late magmatic fluids. All three zircon analyses from EKC02-65 are concordant and yield a weighted mean $^{207}Pb/^{206}Pb$ date of 2728.9±0.5 Ma (MSWD = 0.5; Fig. 11). These two sample populations of zircon barely overlap within error, and likely represent phases of the batholith that crystallized at slightly different times.

BS04-20

This sample is a fine-grained, undeformed tonalite that cross-cuts the northern margin of the Mkondvo suite inlier and is cut by the Hlatikulu granite. This sample contained abundant euhedral stubby to elongate zircon, from which five were picked for analysis. Two inherited, highly discordant analyses from this sample give $^{207}Pb/^{206}Pb$ dates of ca. 3300 Ma. One near concordant grain gives a $^{207}Pb/^{206}Pb$ date of ca. 3206 Ma, and one concordant grain gives a $^{207}Pb/^{206}Pb$ date of ca. 2897 Ma. The youngest concordant grain has a $^{207}Pb/^{206}Pb$ date of 2733.9±0.7 Ma, and this date must closely approximate the timing of intrusion of this rock (Fig. 11).

4. DISCUSSION

4.1. Rates and mechanisms of magmatism in the Usutu suite

The Usutu suite intruded over a period of ~16 Myr between 3236 and 3220 Ma and recorded NE-SW striking magmatic fabrics of variable intensity, which can be used to

deduce the paleostress conditions during intrusion (Fig. 12). Generally speaking, a magmatic fabric is defined as the alignment of linear or planar minerals in the presence of melt (Hutton, 1988; Paterson et al., 1998). This definition purposely avoids any implications as to how the fabric formed. Important factors to consider in the generation of these fabrics are the contributions of internal flow of magma within the confines of a rigid host-rock versus the imposition of regional stress patterns on a potentially complicated crystal-rich/crystal-poor mush of variable composition and viscosity. One end member model suggests that fabrics are generated by the competing interaction between density- or mechanically-driven flow versus advective heat transfer, followed by a quenching of the magma to preserve snapshots of these dynamic processes (Abbot, 1989; Barriere, 1981; Wiebe, 1994, 1996). The other end member suggests that strain within the magma is imposed by regional stress fields, such that the orientation of elongate minerals, for example, may mimic the finite strain ellipsoid in the surrounding host rocks (Brown and Rushmer, 1997; Brown and Solar, 1998b; Hutton, 1988; Mahan et al., 2003; Neves et al., 1996). Evaluating magmatic fabrics is usually approached by examining the relationship between fabrics or foliations in host rocks at different scales of observation relative to those within the intrusive rock (Paterson et al., 1998). Though assessing the generation of magmatic fabrics in the Usutu suite is generally hindered because of limited outcrop, the combination of field observations and geochronology still provides unique insight to the geologic history of the region and the processes of magma emplacement.

Usutu rocks in the Malolotja inlier developed a strong magmatic fabric that is overprinted with subsolidus strain close to the contact with the fault contact with the

quartzites of the Malolotja group to the west (Figs. 2, 3). The magmatic fabric, defined by alignment of elongate minerals such as megacrystic K-feldspar and biotite, flattened mafic enclaves, and compositional contacts within the rock, is parallel to the fault zone and foliation in the quartzites and footwall orthogneisses (Fig. 2). These observations suggest that fabric generation is closely linked to strain in the shear zone, and therefore was a result of either flow of magma emplaced as sheets parallel to the shear zone, through suboriztonal shortening perpendicular to the shear zone during intrusion, or some combination of the two. Magmatism along this shear zone occurred for at least the time period between ca. 3230.3 and 3224.4 Ma, and E-W directed shortening and normal-sense shear affected the aplitic dike BS04-3 after 3224.4±0.4 Ma (Figs. 2, 3, 12). When the magmatic fabric formed is difficult to say, and requires assumptions about how long a magma can maintain a significant melt fraction (Glazner et al., 2004; Matzel et al., in press; Reid et al., 1997; Vazquez and Reid, 2002). If we assume the megacrystic sample EKC03-33 was solid soon after zircon crystallization at 3227.2±1.0 Ma, it requires the generation of the magmatic fabric at that time. Alternatively, the megacrystic unit could have intruded and contained some percent melt for millions of years, especially if it was continually heated by magma replenishment, and then inherited the magmatic fabric during a relatively short period of movement on the shear zone ca. 3224.4 Ma. Evidence from the east Mbuluzi river outcrop suggests this scenario is possible.

The east Mbuluzi river outcrop has two endmember units, the megacrystic granodiorite (EKC02-23) and the homogeneous tonalite (EKC02-24), which contain zircon that crystallized two million years apart, at 3229.8±0.5 and 3227.5±0.3 Ma, respectively (Fig. 4, 12). Contacts between the units are soft to gradational in spots and

sharp in others; both units contain a NE-SW striking magmatic fabric. This fabric may have resulted from flow through a subvertical NE-SW striking conduit or by NW-SE directed compression during intrusion. The timing of generation of the fabric could also be debated: either fabrics in both rock-types were generated at different times under similar conditions, or the older megacrystic unit was remobilized by the intrusion of the hotter tonalitic magma such that interstitial liquid accommodated supersolidus deformation. In the former scenario, soft contacts are generated through partial assimilation of the older unit, and in the latter they are generated through magma mixing. Evidence that regional stresses played a role in the generation of the fabrics comes from the observation that they are parallel to fabrics and foliations throughout central Swaziland and the BGB, and also that magmatic fabrics are continuous across the contacts between granodiorite and tonalite that are at high angles to the fabric. This latter observation is especially supportive of a model in which, despite a ~2 Myr difference in zircon crystallization between the different units, the fabric was generated ca. 3227 Ma during intrusion of the tonalite and NW-SE compression. Evidence from the west Mbuluzi outcrop suggests that NW-SE compressive strain was partitioned into the magma as opposed to the host rocks, given that foliation in host rocks are highly discordant to the magmatic fabric observed across Swaziland (Fig. 5). Magma-host rock interactions from central Swaziland, however, record different interactions.

The section exposed along the Usushwana river in central Swaziland, south of Manzini (Fig. 6), is characterized by a southward increase in the proportion of basement gneiss as xenoliths towards a dominance of roof or wall pendants. In the NW portion of this section, steeply dipping magmatic fabrics are evident as compositional and textural

layering, defined by features such as grain size, and the modal percentage and degree of alignment of hornblende (Fig. 7C). Additionally, horizons of mafic enclaves and xenoliths strike parallel to other magmatic fabrics, which suggests that these fabrics were generated when single batches of magma incorporated these inclusions and were then emplaced into their present position as steeply dipping dikes or sheets (e.g. Brown and Solar, 1998a; Snyder et al., 1997; Fig. 7A,B). An alternative model comes from similar observations in other magmatic systems, which are interpreted to reflect accumulation of material on the floor of a magma chamber through gravity driven transport of phenocrysts, mafic enclaves, or xenoliths (Wiebe, 1994, 1996; Wiebe et al., 2002; Wiebe and Collins, 1998). Tilting of layers then comes from subsidence or downwarping within the chamber during magma accumulation through subsequent magma injections and crystallization. These systems are recognizable by "way-up" indicators such as loadcasts or piping at mafic-silicic magma interfaces, unidirectional warping of enclaves or phenocryst or xenolith accumulation. Way-up indicators were not observed in the Usutu rocks, and the consistency of the strike of magmatic fabrics throughout Usutu rocks suggests the steeply dipping fabrics did not result from subsidence of, for example, an ellipsoidal magma chamber. The alternating and conjugate dip angles in the fabrics may indicate their orientation is being controlled at depth by host-rock foliation or shear zone orientation (Fig. 6). The host orthogneisses to the south contain a similar conjugate foliation pattern, suggesting its control on magma intrusion.

There is a transition southward along the Usushwana river such that outcrop is dominated by older orthogneisses, which preserve intrusive contacts with the Usutu rocks. Consistent dates of ca. 3232.1 Ma from Usutu rocks through this transition

(EKC03-21 and BS04-8; Figs. 8, 12) suggest the sequential intrusion of a relatively homogeneous batch of magma in a short period of time. The interaction between intrusive rocks and host rock, combined with deformation patterns in the host rock show that the Usutu rocks intruded during NW-SE shortening and NE-SW stretching. This is evidenced by foliations in orthogneisses parallel to magmatic fabrics in intruding Usutu rocks, and the observation that Usutu rocks intrude boudinaged orthogneiss (Fig. 8). Similar observations in other magmatic systems have been attributed to magma intrusion during active ballooning or diapiric emplacement of a magma chamber such that there is an overall compressional regime near the contacts between magma and host rock (Johnson et al., 2001; Miller and Paterson, 1999; Paterson and Vernon, 1995). Again, the mere consistency of the implied NW-SE compression from fabrics in Usutu rocks across Swaziland suggest that is not the primary cause of the magmatic fabrics or the deformation in the host rocks. The duration of NW-SE compressional deformation is bracketed in part by the date of the foliated megacrystic granodiorite of 3221.8 and the cross-cutting dike of identical age (Fig. 9). These rocks record oblique compression in that they also record dextral simple shear. Compressional stresses terminated entirely through this section of rocks by the time the massive granodiorite intruded at 3219.9±1.0 Ma (BS04-6; Fig. 8).

To summarize, the suite of magmatic fabrics observed in the Usutu rocks through north and central Swaziland are consistent with their intrusion into a NW-SE compressive regime between ca. 3236 and 3220 Ma, though the style of intrusion and post-intrusion history differs depending on the location. In NW Swaziland in the Malolotja inlier, the style of magmatism and generation of magmatic fabrics was strongly influenced by its

intrusion into a N-S trending normal-sense shear zone that juxtaposes hanging-wall quartzites of the BGB against Usutu rocks. In central Swaziland, on the Mbuluzi river, there is a temporal or kinematic decoupling between host rock deformation and magmatic fabric generation. Here, rejuvenation of crystal-rich mush 2 Myr after its formation resulted in a coupling of magmatic fabrics rocks with different zircon ages. In central Swaziland, a relatively large volume of magma intruded ca. 3232 Ma as steeply dipping sheets or dikes during penetrative deformation of host orthogneisses. Conjugate orientation of intrusive sheets, the kinematics of deformation, and the synchronous relationship of magmatism and deformation are consistent with magma intruding along steeply-dipping reverse faults. There is no apparent correlation between the style of intrusion or the composition of Usutu rocks and the timing of intrusion, suggesting that either mechanical heterogeneities in the crust or other factors such as strain rate during intrusion controlled intrusion style. The result is an apparently anisotropic strain distribution across the paleoarc, which wil be discussed further below.

4.2. Formation and high-grade metamorphism of the Nhlagano gneiss

The Nhlangano orthogneiss is nearly identical in its lithologic variation to the Usutu suite but is ≤40 Myr older and has undergone heterogeneous noncoaxial subsolidus deformation typical of lower crustal gneiss terranes. In south-central Swaziland, within the extent of the ca. 2.73 Ga granitic batholiths, the Nhlangano gneiss has a N-S foliation trend. Based on our observations and from previous mapping (Wilson, 1982), the change in foliation pattern appears to be a large wavelength secondary folding of the subvertical foliation such that in southern Swaziland, in the vicinity of the town of Nhlangano, the

foliation trends NW-SE. The apparent axial plane of this ~100 km wavelength fold strikes E-W and is subvertical. Placing this deformation pattern into a regional context requires more detailed structural analysis in southern Swaziland, but the timing of generation of the fabric is tractable within our study. Dates of granitic to tonalitic rocks cross-cutting these structures in central Swaziland are ca. 2.73 Ga (Fig. 11), which does not adequately resolve the issue, in that it leaves an ~500 Myr window of time between crystallization and deformation. However, the syntectonic intrusion and deformation of samples BS04-11 and BS04-12 at ca. 3222 Ma (Fig. 9) bracket deformation of the Nhlangano gneiss to have occurred before that, in that they contain the same foliation as the nearby outcrop of ca. 3265 Ma Nhlangano gneiss (EKC02-64; Fig. 6)). Additionally, U-Pb apatite thermochronology from Nhlangano gneiss samples (samples EKC03-35 and EKC03-36) show that granulite grade metamorphism in the Mkhondo metamorphic suite 500 m away did not occur ca. 2.7 Ga, as was concluded by Condie et al. (1996). These apatites, which have $^{207}Pb/^{206}Pb$ dates between ca. 2730 and 3100 Ma (Fig. 10), surely would have been reset fully during granulite grade metamorphism, and their dates would reflect post 2.73 Ga cooling. Given that older dates come from the sample that is further away from the Hlatikulu granite (sample BS04-21), located about 400 and 800 m to the west of samples EKC03-35 and EKC03-36, respectively, it seems more likely the data reflect partial resetting ca. 2.73 Ga. Therefore, it is also likely that granulite grade metamorphism in the Mkhondvo suite occurred synchronous with deformation ca. 3.2-3.3 Ga. If true, the original cooling path of the Nhlangano gneiss samples would be similar to that of sample BS04-6, which cooled through the closure temperature of apatite ca. 3180-3200 Ma (Fig. 8). Detrital zircon geochronology from samples of the Mkhondvo

suite near this locality is also more consistent with deposition and burial ca. 3.2-3.3 Ga, in that those grains are all >3460 Ma (Condie et al., 1996). Lastly, a model requiring ca. 2.7 Ga granulite grade metamorphism is difficult given that nearby Pongola supergroup sediments, deposited ca. 2985 Ma (Hegner et al., 1994), did not likely experience even moderate grade regional metamorphism after their deposition (e.g. Gold and von Veh, 1995; Wilson, 1982), suggesting the deformation occurred prior to its eruption and deposition. Therefore the conclusion that intrusion and deformation of the Nhlangano gneiss occurred concomitantly with granulite-grade metamorphism in the Mkhondvo suite ca. 3.70-3.23 Ga remains a robust and testable hypothesis to be pursued in future research.

4.3. crustal scale strain partitioning during arc magmatism and deformation

Tonalitic to granodioritic magmas of the Usutu suite intruded over a period of ~16 Myr, but only record significant solid state deformation in NW Swaziland along the boundary of the BGB and in central Swaziland, near the boundary with the Nhlangano gneiss. In other words, strain partitioning over this period of time was apparently focused along the boundaries of the AGC as currently mapped (Wilson, 1982). Thus, compressional strain throughout the AGC was partitioned into magmatic phases during 3.23 Ga deformation. Strain localization into felsic magmas should be a common phenomenon due to their lower strength (e.g. Brown and Solar, 1998b; Hollister and Crawford, 1986), so the more important question here is how stress was accommodated following crystallization. On one hand, strain localization may continue within the subsolidus plutonic rock because of

pre-existing or induced strength contrasts near the margins of the magma body that force shear zones through its interior (e.g. Davidson et al., 1992).

On the other hand, the relatively rigid behavior of the crystallized magma may force strain accumulation into the host rock, if a significant rheological contrast exists between the crystallized magma and its host (Pavlis, 1996). If the latter case prevailed, then subsolidus strain in the AGC may have gone undetected in this study such that bulk strain across the arc was homogeneous. However, due to the sheer volume of Usutu magmas and the compositional (and therefore rheological) similarities between the Usutu rocks and the host orthogneisses, it is unlikely that solid state strain occurred at the exposed crustal level(s) between ca. 3236 and 3220 Ma within the core of the AGC. Part of the solution to this problem may be obscured by the sampling bias in this study, in that we present little data from the AGC in central Swaziland to show whether or not younger, deformed rocks (perhaps similar in age to the Nhlangano gneisses) are included in the banded gneiss package. Even if that is the case, it remains that during the period from at least ca. 3236 to 3220 Ma, the AGC behaved as a rigid block of crust, despite regional NW-SE compression observed within the magmatic fabrics of the Usutu suite and evidenced in the BGB. Instead, stress was accommodated along shear zones at the NW margin of the AGC in the Malolotja inlier and Pigg's Peak inlier until ca. 3224 Ma (sample BS04-3; Schoene et al., in prep).

Focused deformation along the margins of the AGC ca. 3224 Ma may be due to preexisting lithospheric weaknesses in those locations. Transtensional reactivation of compressional structures from 3.2-3.1 Ga in the BGB is likely due to strain localization at that lithospheric boundary. Whether or not an important lithospheric boundary exists at

the southern margin of the AGC is difficult to assess. Xenocrystic zircons and isolated portions of crust > 3.5 Ga from within the Nhlangano gneiss (Kröner et al., 1989) suggest that intrusion and deformation of the Nhlangano gneiss was superimposed on older crust. Therefore, focused deformation on the southern margin of the AGC may simply be due to prolonged weaking of the crust from the injection of magma from 3280-3220 Ma. Lastly, the difference in deformation style across the orogen may be a result of vertical decoupling of the crust (Axen et al., 1998; Klepeis et al., 2003; Miller and Paterson, 2001; Royden, 1996), such that the zone beneath the AGC responsible for producing the melts that led to intrusion of the Usutu suite also soaked up most of the strain during that time. Given that the highest-grade rocks in the region occur within the Nhlangano gneiss, understanding the their relationship to the AGC and BGB could provide crucial constraints on the behavior of the ca. 3.23 Ga crustal column during orogenesis. Further insight into this necessitates additional detailed mapping and geochronology within the AGC to unravel its pre-3236 structural history and also more work in the Nhlangano gneiss to elucidate its importance in ca. 3.23 Ga crustal structure and rheology.

4.4. Towards a regional geodynamic model of craton assembly

The field and geochronologic data from this study greatly expands our ability to evaluate tectonic models for the ca. 3.23 Ga evolution of the BGB within a regional framework. In general, the styles of magmatism and lithologic variation in combination with previously published geochemistry (Hunter et al., 1978, 1984) are consistent with the generation of the Usutu rocks in a magmatic arc during subduction, in that they share many characteristics with well-studied Phanerozoic magmatic arcs (e.g. Pitcher, 1993).

In this regard, current models for subduction and terrane accretion in and around the BGB ca. 3.23 Ga seem robust (de Ronde and de Wit, 1994; de Ronde and Kamo, 2000; de Wit et al., 1992; Dziggel et al., 2002; Kamo and Davis, 1994; Lowe, 1999). However, this study presents several implications that must be reconciled by any tectonic model for the assembly of the eastern Kaapvaal craton: 1) the generation and deformation of the Nhlangano orthogneiss ca. 3.20-3.70 Ga, 2) the apparently synchronous formation of the Nhlangnao gneiss and the Stentor basement orthogneiss ca. 3258 Ma north of the BGB, and 3) the coincidence in timing between tonalitic magmatism in the Usutu suite with the Kaap Valley and Nelshoogte plutons ca. 3236 and 3227 Ma, north of the BGB (Fig. 13). The three criteria above cannot be reconciled with a singly-vergent ca. 3.23 Ga subduction zone using the BGB as a lithospheric suture (e.g. via the Saddleback-Inyoka fault system; Fig. 1).

Simultaneous ca. 3.23-3.27 Ga crust formation north and south of the BGB can be accommodated via a doubly-vergent subduction zone with the AGC as the overriding plate to the south and a more juvenile, perhaps island arc terrane, as the overriding plate to the north (Fig. 14). In this model, generation of the Nhlangano gneiss occurred in the deep crust via subduction zone magmatism and deep arc deformation, followed by collision of the two continental fragments north and south of the BGB. Continued NW-SE compression resulted in exhumation of the Nhlangano gneiss from the lower to middle crust; and partial to full delamination of the oceanic slab resulted in a migration of magmatism inwards toward the suture ca. 3236-3224 Ma. This model is convenient in that studies based on syntectonic deposition and folding of sedimentary strata and paleocurrent directions in the Moodies group from the BGB are consistent with both the

AGC and rocks north of the BGB as the overriding plates during subduction (Heubeck and Lowe, 1994a, 1994b; Jackson et al., 1987; Lamb, 1984). It is also consistent with previous documentation of crustal thickening, transension, and sedimentary basin formation ca. 3.23 Ga in the BGB, potentially along a transpressive margin (de Ronde and de Wit, 1994; de Ronde and Kamo, 2000; de Wit et al., 1992; Dziggel et al., 2002; Kamo and Davis, 1994; Lowe, 1999; Schoene et al., in prep). Finally, a long-lived (e.g. 50 Ma) subduction zone has potential to bring together more than two allocthonous terranes that potentially preserve their own history of magmatism, deformation and sediment accumulation (Lowe, 1994, 1999). In Fig. 14, the Stolzburg and Steynsdorp plutons (Fig. 1) are labeled as terranes to signify that they are likely complex amalagamations of plutonic and volcanosedimetnary material (de Wit et al., 1992; Lowe, 1994). Their affinity to the AGC is not well understood, though similarities in dates of the Stolzburg and associated plutons (Fig. 1) and the Tsawela gneiss from the AGC suggests a common origin. For that reason, we have placed the subduction zone to the NW of the Stolzburg terrane. In reality, the complicated 3D nature of the system introduced by potentially large strike-slip motions on all of the faults makes reconstruction difficult. The full complexity of the system is difficult to assess, in that the limited present exposures may have once been part of a larger cratonic block that was rifted during the Archean along its present eastern margin. Also, ca. 3.2-3.3 Ga plutonic rocks occur in the central portion of the craton, exposed in the Vredefort impact structure and the Johannesburg Dome (Barton Jr et al., 1999; Flowers et al., 2003; Hart et al., 1999; Poujol and Anhaeusser, 2001; Robb et al., 1992) may imply the plate boundaries inferred here within the eastern Kaapvaal craton can be extended further west (de Wit et

al., 1992). Further expanding and testing the model proposed here thus requires more high-precision geochronology in combination with structural investigation in the limited basement exposures north and west of the BGB.

Though the above model clearly oversimplifies the structural and thermal complexities involved in ca. 3.23 Ga deformation evidenced in the BGB, it is not contrary to them. For example, it was suggested that oblique collision occurred ca. 3.23 Ga, in order to account for the simultaneous occurrence of compressive and transtensional motion on faults within and on the boundary of the BGB (de Ronde and de Wit, 1994; Schoene et al., in prep). In reality, this behavior is predictable given the complex distribution of rheologies that results from amalgamating numerous geologic terranes composed of plutonic basement and volcanic and sedimentary supracrustal rocks. Of particular importance in this regard is the apparently rigid behavior of the AGC block during ca. 3.23 Ga deformation. Strain through the AGC was accommodated within magmatic phases from ca. 3236-3227 Ma, and translational and compressive movement along its boundaries occurred at the same time or shortly after, suggesting the AGC was too strong to sustain subsolidus deformation. The AGC as a rigid block during ca. 3.23 Ga convergence provides a convenient mechanism for generating complicated strain patterns across the eastern Kaapvaal craton during that time by forcing deformation of structurally weaker rocks to warp around a rigid crustal to lithospheric plug. The inevitable result is that translation, rotation, compression and extension occurred to accommodate regional stresses ca. 3.23 Ga. The AGC was again isolated from deformation during subsequent transtension within the BGB between 3.2 and 3.1 Ga that resulted in the stabilization of the eastern Kaapvaal craton (Schoene et al., in prep.). The

apparent cratonic rigidity of the AGC before 3.23 Ga implies that stabilization of the Kaapvaal craton was seeded within the AGC and subsequent stabilization of the rest of craton continued for over 500 Myr (de Wit et al., 1992; Schmitz et al., 2004).

APPENDIX: U-PB ANALYTICAL METHODS

Zircon and apatite were concentrated by standard crushing, Wilfley table, heavy-liquid and magnetic separation. Zircon was pre-treated with the chemical-abrasion technique (Mattinson, 2003, 2005). Zircons were placed in a muffle furnace at 900 ± 20°C for ~60 hours in quartz beakers before being transferred to 300 µl Teflon FEP microcapsules and leached in ~120 µl 29M HF + ~25 µl 30% HNO_3 for 12-14 hours at ~180 °C. The acid was removed from the capsules and the fractions were then rinsed in ultrapure H_2O, fluxed on a hotplate at ~80 °C for an hour in 6M HCl, ultrasonically cleaned for an hour, placed back on the hotplate for an additional 30 minutes, and rinsed in the capsults in ultrapure H_2O and 30% HNO_3. Fractions were spiked with a mixed ^{233}U-^{235}U-^{205}Pb tracer and fully dissolved in ~120 µl 29M HF with ~25 µl 30% HNO_3 at ~210°C for 48 hours, dried to fluorides, and then re-dissolved in 6M HCl at ~180°C overnight. Single grains of apatite were hand-picked from non-magnetic separates, rinsed and ultrasonically cleaned in ultrapure H_2O and acetone prior to loading into single 300 µl FEP teflon microcapsules. Apatite was then spiked with the mixed ^{233}U-^{235}U-^{205}Pb tracer and dissolved in 12N HCl overnight, dried down and redissolved in 6N HCl overnight.

U and Pb were separated using an HCl-based single-column (zircon) or an HBr-based two-column (apatite) anion exchange chemistry modified after (Krogh, 1973). U and Pb isotopic measurements were performed on a VG Sector-54 multi-collector thermal-ionization mass spectrometer at MIT. Pb and U were either loaded together (HCl-based chemistry) or on separate (HBr-based chemistry) Re filaments in a silica-gel/phosphoric acid mixture (Gerstenberger and Haase, 1997). Pb was measured by either 1) peak-hopping on a single Daly detector (for smaller beams), or 2) a dynamic Faraday-

Daly routine (F-D) that cycles between placing mass 204 in the axial Daly collector and masses 205-208 on the H1-H4 Faraday detectors to placing mass 205 in the axial Daly and masses 206-208 in the H1-H3 Faradays, providing real-time Daly gain correction. U isotopic measurements were made in static Faraday mode. Mass fractionation on the Daly detector was determined to be 0.25 ± 0.04 %/a.m.u. over a wide temperature range based on analysis of the NBS-981 common Pb standard and spiked aliquots of NBS-983. Mass fractionation and detector bias on the F-D routine was determined to be 0.07 ± 0.04 %/a.m.u. U mass fractionation is calculated in real-time using the ^{233}U-^{235}U tracer. All common Pb for the zircon analyses was attributed to procedural blank. Total procedural Pb blanks for the HBr-based chemistry were determined to be 1.2 ± 0.4 pg, which was used in the reduction of apatite data. U blanks are assigned a value of 0.10 ± 0.05 pg. All samples were spiked with a ^{205}Pb-^{233}U-^{235}U tracer, whose calibration is detailed in (Schoene et al., 2006), in which an error of ± 0.015% is assigned to the $^{205}Pb/^{235}U$ of the tracer.

REFERNCES CITED

Abbot, R. N. J., 1989, Internal structures in part of the South Mountain batholith, Nova Scotia, Canada: GSA Bull., v. 101, p. 1493-1506.

Armstrong, R. A., W. Compston, M. J. de Wit, and I. S. William, 1990, The stratigraphy of the 3.5-3.2 Ga Barberton Greenstone Belt revisited: a single zircon ion microprobe study: EPSL, v. 101, p. 90-106.

Axen, G. J., J. E. Selverstone, T. Byrne, and J. M. Fletcher, 1998, If the strong crust leads, will the weak crust follow? GSA Today, v. 8, p. 1-8.

Barriere, M., 1981, On curved laminae, graded layers, convection currents and dynamic crystal sorting in the Ploumanac'h (Brittany) subalkaline granite: Contrib. Miner. Petrol., v. 77, p. 214-224.

Barton Jr, J. M., E. S. Barton, and A. Kröner, 1999, Age and isotopic evidence for the origin of the Archean granitoid instrusives of the Johannesburg Dome, South Africa: J. Afr. Earth Sci., v. 28, p. 693-702.

Brown, M., and T. Rushmer, 1997, The role of deformation in the movement of granitic melt: views from the laboratory and the field, *in* M. B. Holness, ed., Deformation-Enhanced Fluid transport in the Earth's Crust and Mantle: London, Chapman & Hall, p. 111-144.

Brown, M., and G. S. Solar, 1998a, Granite ascent and emplacement during contractional deformation in convergent orogens: Jour. Struc. Geol., v. 20, p. 1365-1393.

Brown, M., and G. S. Solar, 1998b, Shear-zone systems and melts: feedback relations and self-organization in orogenic belts: Jour. Struc. Geol., v. 20, p. 211-227.

Chamberlain, K. R., and S. A. Bowring, 2000, Apatite-feldspar U-Pb thermochronometer: a reliable mid-range (~450°C), diffusion controlled system: Chem. Geol., v. 172, p. 173-200.

Cherniak, D. J., W. A. Lanford, and F. J. Ryerson, 1991, Lead diffusion in apatite and zircon using ion implantation and Rutherford Backscattering techniques: Geochim. Cosmochim. Acta, v. 55, p. 1663-1673.

Compston, W., Kröner, A., 1988, Multiple zircon growth within early Archean tonalitic gneiss from the Ancient Gneiss Complex, Swaziland: EPSL, v. 87, p. 13-28.

Condie, K. C., A. Kröner, and C. C. Milisenda, 1996, Geochemistry and geochronology of the Mkhondo suite, Swaziland: evidence for passive-margin deposition and granulite facies metamorphism in the Late Archean of Southern Africa: Jour. Afr. Earth Sci., v. 21, p. 483-506.

Davidson, C., L. S. Hollister, and S. M. Schmid, 1992, Role of melt in the formation of a deep-crustal compressive shear zone: The MacLaren Glacier metamorphic belt, South Central Alaska: Tectonics, v. 11.

Davis, D. W., I. S. Williams, and T. E. Krogh, 2003, Historical development of zircon geochronology, *in* J. M. Hanchar, and P. W. O. Hoskin, eds., Zircon: Reviews in Mineralogy and Geochemistry, v. 53: Washington, D.C., Mineralogical Society of America, p. 145-181.

de Ronde, C. E. J., and M. J. de Wit, 1994, Tectonic history of the Barberton Greenstone Belt, South Africa: 490 million years of Archean crustal evolution: Tectonics, v. 13, p. 983-1005.

de Ronde, C. E. J., M. J. de Wit, and E. T. C. Spooner, 1994, Early Archean (>3.2 Ga) Fe-oxide-rich, hydrothermal discharge veins in the barberton greenstone belt, South Africa: GSA Bull., v. 106, p. 86-104.

de Ronde, C. E. J., and S. Kamo, 2000, An Archean arc-arc collisional event: a short-lived (*ca.* 3 Myr) episode, Weltevreden area, Barberton greenstone belt, South Africa: Jour. Afr. Earth Sci., v. 30, p. 219-248.

de Wit, M. J., 1982, Gliding and overthrust nappe tectonics in the Barberton greenstone belt: Jour. Struc. Geol., v. 4, p. 117-136.

de Wit, M. J., C. Roering, R. J. Hart, R. A. Armstrong, C. E. J. de Ronde, R. W. E. Green, M. Tredoux, E. Peberdy, and R. A. Hart, 1992, Formation of an Archean continent: Nature, v. 357, p. 553-562.

Diener, J. F. A., G. Stevens, A. F. M. Kisters, and M. Poujol, 2005, Metamorphism and exhumation of the basal parts of the Barberton greenstone belt, South Africa: Constraining the rates of Mesoarchean tectonism: Precambrian Research, v. 143, p. 87-112.

Dziggel, A., R. A. Armstrong, G. Stevens, and L. Nasdala, 2005, Growth of zircon and titanite during metamorphism in the granitoid-gneiss terrane south fo the Barberton greenstone belt, South Africa: Mineral. Mag., v. 69, p. 1019-1036.

Dziggel, A., G. Stevens, M. Poujol, C. R. Anhaeusser, and R. A. Armstrong, 2002, Metamorphism of the granite-greenstone terrane south of the Barberton Greenstone Belt, South Africa: an insight into the tectono-thermal evolution of the 'lower' portions of the Onverwacht Group: Precambrian Research, v. 114, p. 221-247.

Flowers, R. M., D. E. Moser, and R. J. Hart, 2003, Evolution of the amphibolite-granulite facies transition exposed by the Vredefort impact structure, Kaapvaal Craton, South Africa: J. Geol., v. 111, p. 455-470.

Gerstenberger, H., and G. Haase, 1997, A highly effective emitter substance for mass spectrometric Pb isotope ratio determinations: Chem. Geol., v. 136, p. 309-312.

Glazner, A. F., J. M. Bartley, D. S. Coleman, W. Gray, and R. Z. Taylor, 2004, Are plutons assembled over millions of year by amalgamation from small magma chambers? GSA Today, v. 14, p. 4-11.

Gold, D. J. C., and M. W. von Veh, 1995, Tectonic evolution of the Late Archean Pongola-Mozaan basin, South Africa: J. African Earth Science, v. 21, p. 203-212.

Hart, R. A., D. Moser, and M. Andreoli, 1999, Archean age for the granulite facies metamorphism near the center of the Vredfort structure, South Africa: Geology, v. 27.

Hegner, E., A. Kröner, and A. W. Hofman, 1984, Age and isotope geochemistry of the Archean Pongola and Usushwana suites in Swasiland, southern Africa: a case for crustal contamination of mantle-derived magma: Earth Planet. Sci. Lett., v. 70, p. 267-279.

Hegner, E., A. Kröner, and P. Hunt, 1994, A precise U-P zircon age fort he Archean Pongola Supergroup volcanics in Swaziland: Journal of African Earth Sciences, v. 18, p. 339-341.

Heubeck, C., and D. R. Lowe, 1994a, Depositional and tectonic setting of the Archean Moodies Group, Barberton Greenstone Belt, South Africa: Precam. Res., v. 68, p. 257-290.

Heubeck, C., and D. R. Lowe, 1994b, Late syndepositional deformation and detachment tectonics in the barberton Greenstone Belt, South Africa.: Tectonics, v. 13, p. 1514-1536.
Hollister, L. S., and M. L. Crawford, 1986, Melt-enhanced deformation: A major tectonic process: Geology, v. 14, p. 558-561.
Hunter, D. R., 1954, 1:50,000 Geological series: Geological Survey of Swaziland.
Hunter, D. R., 1970, The Acient Gneiss complex in Swaziland: Trans. Geol. Soc. S. Africa, v. 73, p. 107-150.
Hunter, D. R., 1979, The role of tonalitic and trondhjemitic rocks in the crustal development of Swaziland and eastern Transvaal, South Africa, *in* F. Barker, ed., Trondhjemites, Dacites, and Related Rocks: Amsterdam, Elsevier, p. 301-322.
Hunter, D. R., F. Barker, and H. T. Millard, 1978, The geochemical nature of the Archean Ancient Gneiss Complex and granodiorite suite, Swaziland: a preliminary study: Precambrian Research, v. 7, p. 105-127.
Hunter, D. R., F. Barker, and H. T. Millard, 1984, Geochemical investigations of Archean bimodal and Dwalile metamorphic suites, Ancient Gneiss Complex, Swaziland: Precambrian Research, v. 24, p. 131-155.
Hutton, D. H. W., 1988, Granite emplacement mechanisms and tectonic controls: inferences from deformation studies: Trans. Royal Soc. Edinburgh: Earth Sci., v. 79, p. 245-255.
Jackson, M. P. A., 1984, Archean structural styles in the Ancient Gneiss Complex of Swaziland, southern Africa, *in* A. Kröner, and R. Greiling, eds., Precambrian Tectonics Illustrated: Stuttgart, Schweizerbart'sche Verlagsbuchhandlung, p. 1-18.
Jackson, M. P. A., K. A. Eriksson, and C. W. Harris, 1987, Early Archean foredeep sedimentation related to crustal shortening: a reinterpretation of the Barberton Sequence, southern Africa: Tectonophysics, v. 136, p. 197-221.
Johnson, S. E., M. Albertz, and S. R. Paterson, 2001, Growth rates of dike-fed plutons: Are they compatible with observations in the middle and upper crust? Geology, v. 29, p. 727-730.
Kamo, S., and D. W. Davis, 1994, Reassessment of Archean crustal development in the Barberton Mountain Land, South Africa, based on U-Pb dating: Tectonics, v. 13, p. 167-192.
Kisters, A. F. M., G. Stevens, A. Dziggel, and R. A. Armstrong, 2003, Extensional detachment faulting and core-complex formation in the southern Barberton granite-greenstone terrain, South Africa: evidence for a 3.2 Ga orogenic collapse: Precambrian Research, v. 127, p. 335-378.
Klepeis, K. A., G. L. Clarke, G. Gehrels, and J. D. Vervoort, 2004, Processes controlling vertical coupling and decoupling between the upper and lower crust of orogens: results from Fiordland, New Zealand: Jour. Struc. Geol., v. 26, p. 765-791.
Klepeis, K. A., G. L. Clarke, and T. Rushmer, 2003, Magma transport and coupling between deformation and magmatism in the continental lithosphere: GSA Today, v. Jan., p. 4-11.
Krogh, T. E., 1973, A low contamination method for hydrothermal decomposition of zircon and extraction of U and Pb for isotopic age determination: Geochim. Cosmochim. Acta, v. 37, p. 485-494.

Kröner, A., W. Compston, and I. S. William, 1989, Growth of early Archean crust in the Ancient Gneiss Complex of Swaziland as revealed by single zircon dating: Tectonophysics, v. 161, p. 271-298.

Kröner, A., and A. Tegtmeyer, 1994, Gneiss-greenstone relationships in the Ancient Gneiss Complex of southwestern Swaziland, southern Africa, and implications for early crustal evolution.: Precam. Res., v. 67, p. 109-139.

Kröner, A., J. I. Wendt, A. Tegtmeyer, C. C. Milisenda, and W. Compston, 1991, Geochronology of the Ancient Gneiss Complex, Swaziland, and implications for crustal evolution, *in* L. D. Ashwal, ed., Two cratons and an orogen–excursion guidebook and review articles for a field workshop through selected Archean terranes of Swaziland, South Africa and Zimbabwe: Johannesburg, Dept. of Geology, Univ. Witwatersrand, p. 8-31.

Lamb, S. H., 1984, Structures on the eastern margin of the Archaean Barberton greenstone belt, northwest Swaziland, *in* A. Kröner, and R. Greiling, eds., Precambrian Tectonics Illustrated: Stuttgart, Germany, E. Schweizerbart'sche Verlagbuchhandlung, p. 19-39.

Lamb, S. H., and I. Paris, 1988, Post-Onverwacth Group stratigraphy in the SE part of the Archean Barberton greenstone belt: J. Afr. Earth Sci., v. 7, p. 285-306.

Lowe, D. R., 1994, Accretionary history of the Archean Barberton greenstone belt (3.55-3.22 Ga), Southern Africa: Geology, v. 22, p. 1099-1102.

Lowe, D. R., 1999, Geologic evolution of the Barberton Greenstone Belt and vicinity, *in* D. R. Lowe, and G. R. Byerly, eds., Geologic evolution of the Barberton Greenstone Belt, South Africa, v. Special Paper 329: Boulder, Geol. Soc. Amer., p. 287-312.

Lowe, D. R., and G. R. Byerly, 1999, Geologic evolution of the Barberton Greenstone Belt, South Africa, v. Special Paper 329: Boulder, CO, Geol. Soc. Amer.

Mahan, K. H., J. M. Bartley, D. S. Coleman, A. F. Glazner, and B. S. Carl, 2003, Sheeted intrusion of the synkinematic McDoogle pluton, Sierra Nevada, California: GSA Bull., v. 115, p. 1570-1582.

Maphalala, R. M., and A. Kröner, 1993, Pb-Pb single zircon ages for the younger Archean granitoids of Swaziland, southern Africa: Extended abstracts 16th colloquium of African Geology, p. 201-206.

Mattinson, J. M., 1987, U-Pb ages of zircons: a basic examination of error propagation: Chemical Geology, v. 66, p. 151-162.

Mattinson, J. M., 2003, CA (chemical abrasion)-TIMS: high-resolution U-Pb zircon geochronology combining high-temperature annealing of radiation damage and multi-step partial dissolution analysis: Eos Trans. AGU, Fall Meet. Suppl., Abstract V22E-06.

Mattinson, J. M., 2005, Zircon U-Pb chemical-abrasion ("CA-TIMS") method: combined annealing and multi-step dissolution analysis for improved precision and accuracy of zircon ages: Chem. Geol., v. 220, p. 47-56.

Matzel, J. P., S. A. Bowring, and R. B. Miller, in press, Timescales of pluton construction at differing crustal levels: examples from the Mount Stuart and Tenpeak intrusions, North Cascades, WA: GSA Bull.

Miller, R. B., and S. R. Paterson, 1999, In defense of magmatic diapirs: Jour. Struc. Geol., v. 21, p. 1161-1173.

Miller, R. B., and S. R. Paterson, 2001, Influence of lithological heterogeneity, mechanical anisotropy, and magmatism on the rheology of an arc, North Cascades, Washington: Tectonophysics, v. 342, p. 351-370.
Neves, S. P., A. Vauchez, and C. J. Archanjo, 1996, Shear zone-controlled magma emplacement or magma-assisted nucleation of shear zones? Insights from northeast Brazil: Tectonophysics, v. 262, p. 349-364.
Passchier, C. W., and R. A. Trouw, 2005, Microtectonics: Berlin, Springer-Verlag, 366 p.
Paterson, S. R., T. K. J. Fowler, K. L. Schmidt, A. S. Yoshinobu, E. S. Yuan, and R. B. Miller, 1998, Interpreting magmatic fabric patterns in plutons: Lithos, v. 44, p. 53-82.
Paterson, S. R., and R. H. Vernon, 1995, Bursting the bubble of ballooning plutons: A return to nested diapirs emplaced by multiple processes: GSA Bull., v. 107, p. 1356-1380.
Pavlis, T. L., 1996, Fabric development in syn-tectonic intrusive sheets as a consequence fo melt-dominated flow and thermal softening of the crust: Tectonophysics, v. 253, p. 1-31.
Pitcher, W. S., 1993, The nature and origin of granite: London, Blackie Academic and Professional, 321 p.
Poujol, M., and C. R. Anhaeusser, 2001, The Johannesburg Dome, South Africa: new single zircon U-Pb isotopic evidence for early Archean granite-greenstone development within the central Kaapvaal Craton: Precam. Res., v. 108, p. 139-157.
Reid, M. R., C. D. Coath, T. M. Harrison, and K. M. McKeegan, 1997, Prolonged residence times for the youngest rhyolites associated with Long Valley caldera: Ion microprobe dating of young zircons: Earth Planet. Sci. Lett., v. 150, p. 27-38.
Robb, L. J., D. W. Davis, S. L. Kamo, and F. M. Meyer, 1992, Ages of altered granites adjoining the Witwatersrand Basin with implications for the origin of gold and uranium: Nature, v. 357, p. 677-680.
Royden, L., 1996, Coupling and decoupling of crust and mantle in convergent orogens; implications for strain partitioning in the crust: Journal of Geophysical Research, B, Solid Earth and Planets, v. 101, p. 17,679-17,705.
Schmitz, M. D., S. A. Bowring, M. J. de Wit, and V. Gartz, 2004, Subduction and terrane collision stabilized the western Kaapvaal craton tectosphere 2.9 billion years ago: Earth Planet. Sci. Lett., v. 222, p. 363-376.
Schoene, B., and S. A. Bowring, submitted, Determining accurate T-t paths in U-Pb thermochronology: an example from the SE Kaapvaal craton, Southern Africa: Geo. and Cosmo. Acta.
Schoene, B., J. L. Crowley, D. C. Condon, M. D. Schmitz, and S. A. Bowring, 2006, Reassessing the uranium decay constants for geochronology using ID-TIMS U-Pb data: Geochim. Cosmochim. Acta, v. 70, p. 426-445.
Schoene, B., M. J. de Wit, and S. A. Bowring, in prep, The importance and timing of transtension in the Barberton greenstone belt and the stabilization of the eastern Kaapvaal craton.
Snyder, D., C. Crambes, S. Tait, and R. A. Wiebe, 1997, Magma mingling in dikes and sills: Jour. Geol., v. 105, p. 75-86.

Vazquez, J. A., and M. R. Reid, 2002, Time scales of magma storage and differentiation of voluminous high-silica rhyolites at Yellowstone caldera, Wyoming: Contrib. Miner. Petrol., v. 144, p. 274-285.

Wiebe, R. A., 1994, Silicic magma chambers as traps for basaltic magmas: The Cadillac Mountain intrusive complex, Mount Desert Island, Maine: Jour. Geol., v. 102, p. 423-437.

Wiebe, R. A., 1996, Mafic-silicic layered intrusions: the role of basaltic injections on magmatic processes and the evolution of silicic magma chambers: Trans. Royal Soc. Edinburgh: Earth Sci., v. 87, p. 233-242.

Wiebe, R. A., K. D. Blair, D. P. Hawkins, and C. P. Sabine, 2002, Mafic injections, in situ hybridization, and crystal accumulation in the Pyramid Peak granite, California: GSA Bull., v. 114, p. 909-920.

Wiebe, R. A., and W. J. Collins, 1998, Depositional features and stratigraphic sections in granitic plutons: implications for the emplacement and crystallization of granitic magma: Jour. Struc. Geol., v. 20, p. 1273-1289.

Wilson, A. C., 1982, 1:250,000 Geological map of Swaziland: Geological Survey Mines Department.

Figure Captions:

Fig. 1: Geologic map of the eastern Kaapvaal craton, with important features from this study labeled. Black boxes denote areas of more detailed maps, in Figs. 2 and 6. Sample locations are labeled here or in Figs. 2 or 6. Map compiled from this study, (de Ronde et al., 1994; de Wit, 1982; Lowe and Byerly, 1999; Schoene et al., in prep; Wilson, 1982). Age information from this study, (Armstrong et al., 1990; Hegner et al., 1984; Hegner et al., 1994; Kamo and Davis, 1994; Kröner et al., 1989; Kröner and Tegtmeyer, 1994; Kröner et al., 1991; Maphalala and Kröner, 1993).

Fig. 2: The Usutu suite in the Malolotja inlier. A) Geologic map of the Malolotja inlier, with structural information in stereonet. Note that north in the stereonet is rotated into parallelism with the map north. B) Concordia plot for sample BS04-3. 3) Sample location of BS04-3, interpreted to represent aplitic dike that is stretched and boudinaged after intrusion.

Fig. 3: The Usutu suite in the Malolotja inlier. A) example of Usutu rocks with no subsolidus overprinting. Dark shape is mafic magma enclave included in megacrystic granodiorite with magmatic fabric defined by aligned K-feldspar. Photo take near sample EKC03-33, ~1.5 km east of faulted quartzite contact. B) Mafic-silicic banding within the Usutu suite, interpreted to reflect intrusion and interaction of multiple composition magmas, within the shear zone. Note that K-feldspar megacrysts exhibit little to no subsolidus deformation here, but develop mineral tails further west. Sample collected

~700 m from faulted quartzite contact. C) Concordia plot for zircon from samples EKC03-23 and EKC03-33. Uncertainties at the 95% confidence level.

Fig. 4: The Usutu suite at the Mbuluzi east river crossing. A) Photo of undeformed megacrystic granodiorite sample EKC02-23 with magmatic fabric defined by alignment of K-feldspar megacrysts. Late aplitic dike in upper portion of photo. Writing utensil for scale. B) Concordia plot for megacrystic granodiorite EKC02-23 and tonalite EKC02-24 from the Mbuluzi east outcrop. Uncertainties at the 95% confidence level.

Fig. 5: The Usutu suite at the Mbuluzi west river crossing. A) Concordia diagram for leucotonalite sample EKC02-32 and a cross-cutting granite EKC03-18. B) An example of a mafic host-rock intruded by the Usutu suite, with in situ melt generation. Goat feces are ~5 cm in diameter. C) Assimilation of mafic enclave into leucotonalite. D) Stereonet showing structural information from the Mbuluzi east and west river crossings. Uncertainties at the 95% confidence level.

Fig 6: Geologic map of central Swaziland; see Fig. 1 for location. Sample locations shown as white circles. Locations of cities, Matsapha and Manzini are also shown. Map information based on this study and (Hunter, 1954; Wilson, 1982).

Fig. 7: Igneous textures preserved in the Usutu suite along the Usushwana river, near sample locality EKC03-21 (Fig. 6). A) Composite dike recording the interaction of mafic magmatic enclaves within tonalitic magma, with no solid-state shearing evident. B)

Unstrained hornblende gabbro enclaves within hornblende tonalite magma. C) Magmatic layering in tonalite, defined by the modal proportion of hornblende versus plagioclase and variable grain size. This is a representative example of sample EKC03-21.

Fig. 8: Intrusive relationships of the Usutu suite and basement rocks in central Swaziland. See Fig. 6 for sample locations. A) Concordia plot summarizing zircon and apatite data from EKC03-21, BS04-6, and BS04-8. B) Concordia plots for two basement gneisses EKC02-36 and BS04-7, and one Usutu rock EKC02-35. C) Photograph illustrating the intrusive relationship between basement orthogneiss BS04-7 and hornblende tonalite BS04-8. The younger tonalite is interpreted to intrude syntectonically during boudinage of older banded gneiss. Black line drawn to denote contact between the two units. Uncertainties at the 95% confidence level.

Fig. 9: Example of deformed Usutu augen gneiss. A) Photograph of the texture of BS04-12, showing mantled pophyroclasts of K-feldspar, interpreted to indicate right-lateral simple shear and strong flatenning. Photo taken parallel to lineations and perpindicular to foliation. B) Concorida diagram of augen gneiss BS04-12 and cross-cutting syntectonic dike BS04-11. Uncertainties at the 95% confidence level.

Fig. 10: The Nhlangano gneiss. A) U-Pb apatite thermochronology from the Nhlangano gneiss EKC03-35, -36, and one Usutu rock EKC02-35 and an older orthogneiss EKC02-36 from central Swaziland. See Figs. 1 and 6 for sample locations. Date are interpreted

to reflect partial resetting by adjacent ca. 2.73 granites. B) U-Pb geochronology of the Nhlangano gneiss from magmatic zircons, indicating crystallization ages between ~3240 amd 3280, based on extrapolation of discordant data back to concordia. C) Field photograph of mafic-silicic banded Nhlangano orthogneiss, indicating sample lithology of EKC03-35; actual sample location several meters away. D) Field photograph of Nhlangano augen orthogneiss, from which sample EKC03-36 was collected. Note vertical white band in left of photo represents a single deformed K-feldspar megacryst. Uncertainties at the 95% confidence level.

Fig. 11: Concordia diagram for ca. 2.73 granites in south-central Swaziland. See Figs. 1 and 6 for sample localities. Uncertainties at the 95% confidence level.

Fig. 12: Diagram summarizing crystallization ages of Usutu rocks, catergorized by sample locations. See Figs. 1, 2 and 6 for sample locations. EKC02-8* from Schoene et al. (2006), and AGC01-4** from Schoene and Bowring (in review). Uncertainties at the 95% confidence level.

Fig. 13: Summary of age information from 3.27-3.22 Ga south and north of the BGB. Data from this study shown as a probability density function for visualization purposes, but likely holds little statistical meaning. Data for samples from Usutu suite are weighted means of crystallization ages, and data from Nhlangano gneiss are single zircon analyses.

Dates of plutonic rocks from north of the BGB are plotted as vertical bars with errors multiplied by three so they are easily seen. Age from the Kaap Valley pluton from (Schoene et al., 2006), and ages from the Nelshoogte pluton and the Stentor basement from (Schoene et al., in prep).

Fig. 14: idealized cartoon illustrating the geologic evolution of the eastern Kaapvaal craton ca. 3.30-3.22 Ga. Note that A and B are not to scale, though C is approximately to scale with no vertical exaggeration. White squares in C represent approximate levels of crust of rocks now seen at the surface; their juxtaposition was accommodated via 3.2-3.1 transtension (Schoene et al., in prep). See text for discussion.

Table 1. U-Pb isotopic data

				Isotopic ratios									Dates (Ma)						
Sample	$^{206}Pb^*$ / Pb_c	Pb_c (pg)	Th / U	$^{206}Pb/^{204}Pb$	$^{208}Pb/^{206}Pb$	$^{206}Pb/^{238}U$	% err	$^{207}Pb/^{235}U$	% err	$^{207}Pb/^{206}Pb$	% err	corr. coef.	$^{206}Pb/^{238}U$	±	$^{207}Pb/^{235}U$	±	$^{207}Pb/^{206}Pb$	±	% disc.
(a)	(b)	(c)	(d)	(e)	(f)	(f)	(g)	(f)	(g)	(f)	(g)		(h)	(i)	(h)	(i)	(h)	(i)	(j)
EKC03-33																			
za1	158	2.06	0.49	8357	0.133	0.640328	0.06	22.66600	0.07	0.25673	0.04	0.819	3190.3	1.5	3212.7	0.7	3226.7	0.7	1.4
za2	149	0.99	0.68	7577	0.183	0.647950	0.11	22.94236	0.13	0.25680	0.06	0.876	3220.2	2.8	3224.5	1.2	3227.2	1.0	0.3
za3	19	3.42	0.13	1084	0.036	0.643935	0.20	22.77134	0.21	0.25648	0.08	0.931	3204.5	5.0	3217.2	2.1	3225.2	1.2	0.8
za5	35	4.95	0.75	1512	0.201	0.651236	0.11	23.14377	0.12	0.25775	0.04	0.932	3233.0	2.9	3233.0	1.2	3233.0	0.7	0.0
za6	45	3.30	0.78	2267	0.208	0.649954	0.13	23.06746	0.14	0.25740	0.05	0.937	3228.0	3.2	3229.8	1.3	3230.9	0.7	0.1
za10	100	0.43	0.61	5173	0.166	0.640808	0.17	22.75386	0.19	0.25753	0.06	0.943	3192.2	4.4	3216.5	1.8	3231.7	1.0	1.5
EKC03-23																			
za1	267	0.89	0.54	12463	0.146	0.648127	0.07	22.96561	0.08	0.25699	0.05	0.819	3220.9	1.7	3225.5	0.8	3228.3	0.7	0.29
za2	450	0.58	0.48	22273	0.129	0.646029	0.08	22.90262	0.09	0.25712	0.04	0.880	3212.7	2.1	3222.8	0.9	3229.1	0.7	0.6
za3	399	0.49	0.55	19931	0.152	0.633685	0.08	22.36249	0.09	0.25594	0.06	0.802	3164.1	1.9	3199.6	0.9	3221.9	0.9	2.3
za4	198	0.63	0.54	9596	0.144	0.647845	0.09	22.98662	0.11	0.25734	0.05	0.883	3219.8	2.4	3226.4	1.0	3230.5	0.8	0.4
za6	385	0.56	1.06	17231	0.284	0.649095	0.10	23.03195	0.12	0.25735	0.07	0.841	3224.7	2.6	3228.3	1.2	3230.5	1.0	0.2
za8	206	0.90	0.18	10333	0.047	0.649736	0.06	23.04742	0.07	0.25727	0.04	0.808	3227.2	1.4	3228.9	0.7	3230.0	0.7	0.1
za9	61	0.62	0.24	3138	0.063	0.650487	0.22	23.07572	0.23	0.25729	0.07	0.946	3230.1	5.5	3230.1	2.2	3230.2	1.2	0.0
BS04-3																			
za1	3.6	1.19	0.55	206	0.148	0.646100	1.05	22.81694	1.08	0.25613	0.20	0.983	3212.9	26.7	3219.2	10.5	3223.0	3.1	0.4
za2	9.2	0.88	0.51	500	0.135	0.661636	0.42	23.45338	0.43	0.25709	0.09	0.980	3273.5	10.8	3245.9	4.2	3229.0	1.4	-1.8
za4	118	0.41	0.65	6050	0.179	0.621357	0.15	21.14940	0.18	0.24686	0.09	0.860	3115.3	3.8	3145.5	1.7	3164.8	1.4	2.0
za5	176	0.59	0.68	8980	0.187	0.623946	0.11	21.20527	0.12	0.24649	0.04	0.931	3125.6	2.7	3148.0	1.2	3162.4	0.7	1.5
za6	9.0	9.07	0.32	507	0.092	0.615914	0.48	21.59832	0.48	0.25433	0.07	0.990	3093.6	11.7	3165.8	4.7	3211.9	1.1	4.6
za8	172	0.70	0.29	9446	0.082	0.610397	0.15	21.56909	0.16	0.25628	0.05	0.957	3071.6	3.8	3164.5	1.6	3224.0	0.7	5.9
za9	49	0.86	0.90	2416	0.247	0.633518	0.14	22.39705	0.15	0.25641	0.06	0.927	3163.5	3.4	3201.1	1.4	3224.8	0.9	2.4
za10	395	0.70	0.56	20541	0.152	0.641493	0.10	22.68253	0.11	0.25645	0.05	0.895	3194.9	2.5	3213.4	1.1	3225.0	0.8	1.2
EKC02-23																			
za1	363	1.70	0.41	17816	0.113	0.628725	0.07	22.18403	0.08	0.25590	0.04	0.860	3144.5	1.7	3191.8	0.8	3221.7	0.6	3.0
za2	297	1.46	0.93	13474	0.255	0.632527	0.08	22.36934	0.09	0.25649	0.04	0.885	3159.6	2.0	3199.9	0.9	3225.3	0.7	2.6
za3	116	1.33	0.88	5376	0.239	0.644021	0.10	22.80293	0.12	0.25680	0.06	0.873	3204.8	2.6	3218.6	1.1	3227.2	0.9	0.9
za4	79	0.49	0.18	4461	0.048	0.647426	0.14	22.95164	0.15	0.25711	0.06	0.922	3218.1	3.5	3224.9	1.5	3229.1	0.9	0.4
za5	286	0.38	0.86	14054	0.232	0.647522	0.11	22.96889	0.12	0.25727	0.05	0.922	3218.5	2.8	3225.6	1.2	3230.0	0.7	0.5
za6	60	0.53	0.28	3339	0.075	0.648375	0.13	23.00213	0.14	0.25730	0.06	0.903	3221.9	3.2	3227.0	1.4	3230.3	1.0	0.3

Table 1.(cont.)

				Isotopic ratios									Dates (Ma)						
Sample	$\frac{Pb^*}{Pb_c}$	Pb_c (pg)	$\frac{Th}{U}$	$\frac{^{206}Pb}{^{204}Pb}$	$\frac{^{208}Pb}{^{206}Pb}$	$\frac{^{206}Pb}{^{238}U}$	% err	$\frac{^{207}Pb}{^{235}U}$	% err	$\frac{^{207}Pb}{^{206}Pb}$	% err	corr. coef.	$\frac{^{206}Pb}{^{238}U}$	±	$\frac{^{207}Pb}{^{235}U}$	±	$\frac{^{207}Pb}{^{206}Pb}$	±	% disc.
(a)	(b)	(c)	(d)	(e)	(f)	(f)	(g)	(f)	(g)	(f)	(g)		(h)	(i)	(h)	(i)	(h)	(i)	(j)
EKC02-24																			
za1	158	5.29	0.51	7052	0.138	0.640987	0.25	22.67971	0.25	0.25662	0.05	0.981	3192.9	6.3	3213.3	2.5	3226.1	0.8	1.30
za2	244	1.41	0.42	12294	0.114	0.648141	0.08	22.95173	0.09	0.25683	0.04	0.882	3220.9	2.0	3224.9	0.9	3227.4	0.7	0.25
za3	298	1.01	0.46	15829	0.123	0.647645	0.1	22.93653	0.1	0.25686	0.04	0.906	3219.0	2.3	3224.3	1.0	3227.5	0.7	0.34
za4	522	0.92	0.39	28117	0.105	0.648655	0.08	22.97330	0.09	0.25687	0.04	0.877	3222.9	2.0	3225.8	0.9	3227.6	0.7	0.18
za5	523	0.4	0.50	27509	0.135	0.648709	0.11	22.96981	0.12	0.25681	0.04	0.932	3223.2	2.9	3225.7	1.2	3227.2	0.7	0.16
za6	73	0.7	0.51	3852	0.138	0.650700	0.17	23.05023	0.18	0.25692	0.06	0.951	3230.9	4.4	3229.1	1.8	3227.9	0.9	-0.12
EKC02-32																			
za1	813	0.38	0.67	41355	0.181	0.646782	0.17	22.93444	0.18	0.25718	0.05	0.957	3215.6	4.4	3224.2	1.8	3229.5	0.8	0.55
za2	329	0.58	0.77	16474	0.206	0.649801	0.07	23.07298	0.09	0.25753	0.05	0.817	3227.4	1.8	3230.0	0.8	3231.6	0.8	0.17
za3	84	1.33	0.57	4161	0.153	0.649086	0.17	23.03476	0.19	0.25738	0.09	0.892	3224.6	4.4	3228.4	1.9	3230.8	1.4	0.24
za4	234	1.06	0.74	11664	0.198	0.649281	0.08	23.04677	0.09	0.25744	0.04	0.882	3225.4	2.1	3228.9	0.9	3231.1	0.7	0.22
za5	71	2.06	0.88	3149	0.237	0.651217	0.11	23.13505	0.12	0.25766	0.05	0.925	3233.0	2.8	3232.6	1.2	3232.4	0.7	-0.02
EKC03-18																			
za1	168	1.47	0.33	8602	0.089	0.635250	0.09	21.89261	0.10	0.24995	0.04	0.904	3170.3	2.3	3179.0	1.0	3184.4	0.7	0.56
za2	201	1.02	0.53	10777	0.142	0.647275	0.08	22.87535	0.09	0.25632	0.04	0.878	3217.5	2.1	3221.7	0.9	3224.2	0.7	0.26
za3	58	1.13	0.67	3056	0.179	0.647900	0.12	22.89320	0.13	0.25627	0.05	0.932	3220.0	3.0	3222.4	1.2	3223.9	0.7	0.15
za4	62	0.39	0.52	3326	0.147	0.610052	0.07	21.03869	0.08	0.25012	0.04	0.871	3070.2	1.8	3140.4	0.8	3185.5	0.6	4.55
za5	41	0.42	0.21	2333	0.059	0.622626	0.10	21.53464	0.10	0.25085	0.04	0.917	3120.4	2.4	3163.0	1.0	3190.1	0.7	2.76
za6	47	0.86	0.45	2550	0.123	0.633262	0.09	21.88420	0.10	0.25064	0.04	0.907	3162.5	2.2	3178.6	1.0	3188.8	0.7	1.04
za7	8.6	1.70	0.48	485	0.130	0.639214	0.49	22.06263	0.51	0.25033	0.13	0.965	3185.9	12.2	3186.5	5.0	3186.8	2.1	0.04
za8	90	0.56	0.55	4751	0.148	0.661031	0.12	24.18776	0.14	0.26538	0.06	0.906	3271.2	3.2	3276.0	1.3	3279.0	0.9	0.30
za9	151	0.78	0.95	7297	0.253	0.663830	0.07	24.33020	0.08	0.26582	0.05	0.829	3282.0	1.7	3281.7	0.8	3281.5	0.7	-0.02

Table 1.(cont.)

				Isotopic ratios									Dates (Ma)						
Sample	$^{Pb*}/_{Pb_c}$	Pb_c (pg)	$^{Th}/_{U}$	$^{206}Pb/^{204}Pb$	$^{208}Pb/^{206}Pb$	$^{206}Pb/^{238}U$	% err	$^{207}Pb/^{235}U$	% err	$^{207}Pb/^{206}Pb$	% err	corr. coef.	$^{206}Pb/^{238}U$	±	$^{207}Pb/^{235}U$	±	$^{207}Pb/^{206}Pb$	±	% disc.
(a)	(b)	(c)	(d)	(e)	(f)	(f)	(g)	(f)	(g)	(f)	(g)		(h)	(i)	(h)	(i)	(h)	(i)	(j)
EKC02-35																			
za1	998	0.63	0.31	54457	0.084	0.642547	0.06	22.82544	0.07	0.25764	0.04	0.834	3199.0	1.6	3219.5	0.7	3232.3	0.7	1.31
za2	488	0.44	0.46	25888	0.123	0.651484	0.07	23.20128	0.09	0.25829	0.05	0.804	3234.0	1.9	3235.4	0.9	3236.3	0.9	0.09
za3	260	0.57	0.69	13177	0.190	0.634383	0.06	22.38022	0.08	0.25587	0.05	0.787	3166.9	1.5	3200.4	0.8	3221.4	0.8	2.14
za4	82	0.43	0.33	4460	0.088	0.648080	0.14	23.07343	0.14	0.25822	0.05	0.945	3220.7	3.4	3230.0	1.4	3235.9	0.7	0.60
za5	265	0.35	0.38	14279	0.102	0.651244	0.18	23.19488	0.19	0.25831	0.07	0.937	3233.1	4.5	3235.2	1.8	3236.4	1.0	0.13
a1 (95)	1.1	11.41	2.77	47	0.767	0.554014	0.99	15.65022	1.15	0.20488	0.45	0.923	2841.8	22.7	2855.7	11.0	2865.5	7.3	1.02
a2 (135)	2.4	17.06	1.46	104	0.404	0.540211	0.3	14.56589	0.3	0.19556	0.13	0.927	2784.3	6.7	2787.3	3.2	2789.5	2.1	0.23
EKC02-36																			
za1	1119	0.47	0.54	56963	0.145	0.698353	0.06	28.22418	0.07	0.29312	0.04	0.818	3414.4	1.5	3426.9	0.7	3434.2	0.6	0.74
za2	878	0.68	0.53	44866	0.141	0.699788	0.07	28.18293	0.08	0.29209	0.04	0.845	3419.8	1.8	3425.5	0.8	3428.8	0.7	0.3
za3	369	0.49	0.45	19107	0.122	0.691326	0.4	27.98202	0.4	0.29356	0.04	0.994	3387.7	10.6	3418.5	4.0	3436.6	0.7	1.83
a3 (95)	1	5.00	0.23	55	0.065	0.541610	1.73	15.56971	1.84	0.20849	0.36	0.982	2790.2	39.2	2850.8	17.5	2893.9	5.8	4.4
a4 (150)	2	16.02	0.37	127	0.117	0.473944	0.29	12.78543	0.34	0.19565	0.14	0.910	2500.8	6.0	2664.0	3.2	2790.3	2.3	12.5
EKC03-21																			
za1	629	0.49	0.73	31662	0.196	0.650279	0.06	23.09430	0.07	0.25758	0.04	0.800	3229.3	1.4	3230.9	0.7	3231.9	0.7	0.10
za3	133	2.19	0.64	5777	0.171	0.649724	0.07	23.07645	0.08	0.25760	0.05	0.826	3227.1	1.7	3230.2	0.8	3232.1	0.7	0.19
za5	106	0.56	0.57	5524	0.154	0.648190	0.1	23.03382	0.1	0.25773	0.09	0.800	3221.1	2.9	3228.4	1.4	3232.9	1.3	0.5
za6	89	0.41	0.49	4697	0.135	0.638878	0.21	22.69538	0.21	0.25764	0.04	0.978	3184.6	5.3	3214.0	2.1	3232.4	0.7	1.9
a1 (55)	5.9	2.77	4.13	173	1.106	0.642698	0.94	22.17495	0.96	0.25024	0.13	0.990	3199.6	23.8	3191.4	9.3	3186.3	2.1	-0.53

Table 1. U-Pb isotopic data

				Isotopic ratios									Dates (Ma)						
Sample	$\frac{Pb^*}{Pb_c}$	Pb_c (pg)	$\frac{Th}{U}$	$\frac{^{206}Pb}{^{204}Pb}$	$\frac{^{208}Pb}{^{206}Pb}$	$\frac{^{206}Pb}{^{238}U}$	% err	$\frac{^{207}Pb}{^{235}U}$	% err	$\frac{^{207}Pb}{^{206}Pb}$	% err	corr. coef.	$\frac{^{206}Pb}{^{238}U}$	±	$\frac{^{207}Pb}{^{235}U}$	±	$\frac{^{207}Pb}{^{206}Pb}$	±	% disc.
(a)	(b)	(c)	(d)	(e)	(f)	(f)	(g)	(f)	(g)	(f)	(g)		(h)	(i)	(h)	(i)	(h)	(i)	(j)
BS04-7																			
za1	112	2.32	0.49	5796	0.131	0.703135	0.10	28.52495	0.11	0.29423	0.05	0.886	3432.5	2.7	3437.3	1.1	3440.1	0.8	0.28
za2	138	1.97	0.26	6747	0.070	0.694308	0.17	27.66153	0.18	0.28895	0.05	0.961	3399.0	4.5	3407.2	1.8	3412.0	0.8	0.49
za3	785	0.77	0.26	42260	0.068	0.702401	0.1	28.45518	0.1	0.29382	0.04	0.836	3429.7	1.6	3434.9	0.7	3437.9	0.6	0.31
za4	180	0.50	0.56	9268	0.151	0.665477	0.21	24.91872	0.22	0.27158	0.07	0.952	3288.4	5.4	3305.0	2.2	3315.2	1.1	1.03
za7	1110	0.19	0.27	59565	0.073	0.694396	0.17	27.78240	0.17	0.29018	0.05	0.960	3399.4	4.4	3411.4	1.7	3418.5	0.8	0.72
za8	136	10.44	0.29	6445	0.076	0.697804	0.07	27.89760	0.08	0.28996	0.04	0.871	3412.3	1.9	3415.5	0.8	3417.4	0.6	0.19
BS04-8																			
za1	2729	0.61	0.34	144966	0.090	0.695227	0.05	27.69521	0.06	0.28892	0.04	0.784	3402.5	1.3	3408.4	0.6	3411.8	0.6	0.3
za2	3133	0.69	0.68	159391	0.182	0.649825	0.07	23.07707	0.08	0.25756	0.04	0.851	3227.5	1.7	3230.2	0.7	3231.9	0.6	0.17
za3	580	0.60	0.60	29943	0.160	0.650089	0.09	23.09444	0.10	0.25765	0.04	0.894	3228.6	2.2	3230.9	1.0	3232.4	0.7	0.15
za4	600	0.56	0.71	29270	0.186	0.731132	0.07	31.66497	0.08	0.31411	0.04	0.846	3537.6	1.9	3539.9	0.8	3541.2	0.7	0.13
za5	178	0.40	0.61	9195	0.165	0.648247	0.16	23.02419	0.17	0.25760	0.07	0.920	3221.4	3.9	3228.0	1.6	3232.1	1.0	0.42
BS04-6																			
za2	231	0.54	0.52	12080	0.140	0.657275	0.21	23.76126	0.21	0.26219	0.04	0.978	3256.6	5.3	3258.6	2.0	3259.9	0.7	0.13
za3	164	0.68	0.39	8799	0.104	0.656805	0.09	23.68880	0.10	0.26158	0.05	0.902	3254.7	2.4	3255.7	1.0	3256.3	0.7	0.06
za4	159	0.76	0.46	8425	0.123	0.656046	0.11	23.65171	0.12	0.26147	0.06	0.879	3251.8	2.7	3254.1	1.2	3255.6	0.9	0.15
za6	743	1.14	0.63	38205	0.170	0.646775	0.07	22.79281	0.09	0.25559	0.04	0.876	3215.6	1.9	3218.1	0.8	3219.7	0.6	0.16
za7	1234	0.64	0.99	59380	0.265	0.646538	0.06	22.79307	0.07	0.25569	0.04	0.810	3214.7	1.5	3218.1	0.7	3220.3	0.7	0.22
za8	1095	0.27	0.54	57233	0.145	0.646147	0.08	22.76771	0.09	0.25556	0.04	0.888	3213.1	2.1	3217.1	0.9	3219.5	0.7	0.25
a1 (90)	3	23.28	3.54	95	0.953	0.636939	0.33	21.90784	0.63	0.24946	0.44	0.769	3177.0	8.2	3179.7	6.2	3181.3	6.9	0.17
a2 (145)	11	99.85	0.97	461	0.260	0.639883	0.06	22.16504	0.07	0.25123	0.05	0.781	3188.6	1.5	3191.0	0.7	3192.5	0.7	0.16
a4 (100)	7	11.40	1.23	288	0.328	0.646589	0.21	22.30274	0.23	0.25017	0.09	0.922	3214.9	5.4	3197.0	2.3	3185.8	1.4	-1.16
a5 (145)	6	18.26	1.25	253	0.337	0.640099	0.13	22.19352	0.15	0.25146	0.07	0.886	3189.4	3.3	3192.2	1.5	3194.0	1.1	0.18
a6 (170)	2	26.55	0.94	76	0.253	0.644193	0.30	22.44201	0.36	0.25266	0.19	0.856	3205.5	7.5	3203.1	3.5	3201.5	2.9	-0.16

Table 1. (cont.)

				Isotopic ratios									Dates (Ma)						
Sample	$\frac{Pb^*}{Pb_c}$	Pb_c (pg)	$\frac{Th}{U}$	$\frac{^{206}Pb}{^{204}Pb}$	$\frac{^{208}Pb}{^{206}Pb}$	$\frac{^{206}Pb}{^{238}U}$	% err	$\frac{^{207}Pb}{^{235}U}$	% err	$\frac{^{207}Pb}{^{206}Pb}$	% err	corr. coef.	$\frac{^{206}Pb}{^{238}U}$	±	$\frac{^{207}Pb}{^{235}U}$	±	$\frac{^{207}Pb}{^{206}Pb}$	±	% disc.
(a)	(b)	(c)	(d)	(e)	(f)	(f)	(g)	(f)	(g)	(f)	(g)		(h)	(i)	(h)	(i)	(h)	(i)	(j)
BS04-11																			
za1	5510	0.70	0.92	268112	0.248	0.647444	0.05	22.84301	0.06	0.25589	0.04	0.764	3218.2	1.2	3220.3	0.6	3221.6	0.6	0.13
za2	361	6.51	0.90	17645	0.242	0.647356	0.06	22.84259	0.07	0.25592	0.04	0.824	3217.9	1.5	3220.3	0.7	3221.8	0.6	0.15
za3	72	6.54	0.58	3756	0.154	0.651180	0.1	23.17491	0.1	0.25812	0.04	0.886	3232.8	2.0	3234.3	0.9	3235.2	0.7	0.10
BS04-12																			
za1	1256	0.34	0.89	61369	0.240	0.643876	0.09	22.69433	0.10	0.25563	0.04	0.905	3204.2	2.3	3213.9	1.0	3220.0	0.7	0.62
za2	2810	0.28	1.02	133952	0.276	0.646779	0.07	22.82349	0.09	0.25593	0.04	0.880	3215.6	1.9	3219.4	0.8	3221.8	0.6	0.25
za3	3742	0.40	1.10	176202	0.297	0.647034	0.1	22.82788	0.1	0.25588	0.04	0.881	3216.6	1.9	3219.6	0.8	3221.5	0.6	0.19
za4	5014	0.53	0.98	241146	0.265	0.647569	0.05	22.85273	0.06	0.25595	0.04	0.768	3218.7	1.2	3220.7	0.6	3221.9	0.6	0.13
EKC02-66																			
za1	77	0.69	0.36	4162.8	0.099	0.633011	0.14	22.58508	0.16	0.25877	0.07	0.887	3161.5	3.5	3209.2	1.6	3239.2	1.2	3.03
za2	63	1.09	0.32	3391.1	0.089	0.641958	0.16	23.10661	0.18	0.26105	0.07	0.925	3196.7	4.1	3231.4	1.7	3253.1	1.1	2.20
za3	49	0.85	0.14	2756.8	0.044	0.546016	0.08	19.19867	0.09	0.25501	0.04	0.891	2808.6	1.8	3051.9	0.9	3216.2	0.7	15.60
EKC02-64																			
za1	881	1.07	0.32	47223	0.085	0.657460	0.07	23.85223	0.08	0.26312	0.04	0.856	3257.3	1.8	3262.4	0.8	3265.5	0.7	0.32
za2	642	1.16	0.39	33383	0.105	0.657410	0.06	23.85243	0.08	0.26315	0.04	0.843	3257.1	1.7	3262.4	0.7	3265.6	0.7	0.33
za3	1570	0.12	0.34	82998	0.093	0.680006	0.1	27.32409	0.2	0.29143	0.22	0.299	3344.4	1.8	3395.1	2.3	3425.2	3.5	3.02
EKC03-35																			
za11	62	1.68	0.33	2958.0	0.090	0.668105	0.08	25.25509	0.12	0.27416	0.09	0.656	3298.6	2.1	3318.1	1.2	3330.0	1.4	1.21
a1 (72)	4.3	5.89	0.21	229.2	0.058	0.533515	0.51	13.96392	0.56	0.18983	0.15	0.963	2756.2	11.5	2747.3	5.3	2740.7	2.5	-0.70
a2 (190)	5.2	67.96	0.23	261.4	0.064	0.514442	0.07	13.38413	0.09	0.18869	0.06	0.763	2675.6	1.5	2707.1	0.9	2730.8	1.0	2.47
a4 (45)	1.5	7.39	0.23	94.1	0.063	0.536525	0.97	13.94658	1.06	0.18853	0.38	0.933	2768.9	21.8	2746.1	10.0	2729.4	6.3	-1.78
a5 (60)	1.5	6.85	0.39	84.5	0.105	0.558060	0.92	15.11220	0.99	0.19640	0.24	0.971	2858.6	21.3	2822.3	9.5	2796.5	3.9	-2.75
a6 (95)	1.9	13.59	0.36	101.9	0.100	0.535765	0.44	14.21527	0.48	0.19243	0.14	0.955	2765.7	10.0	2764.2	4.6	2763.1	2.4	-0.12
a7 (145)	4.3	29.51	0.28	227.9	0.078	0.523582	0.13	13.52635	0.16	0.18737	0.08	0.855	2714.4	3.0	2717.1	1.5	2719.2	1.4	0.22
a8 (120)	3.0	32.29	0.50	150.7	0.131	0.560401	0.15	14.79977	0.18	0.19154	0.09	0.855	2868.3	3.4	2802.5	1.7	2755.4	1.6	-5.08

Table 1. (cont.)

				Isotopic ratios									Dates (Ma)						
Sample	$\frac{Pb^*}{Pb_c}$	Pb_c (pg)	$\frac{Th}{U}$	$\frac{^{206}Pb}{^{204}Pb}$	$\frac{^{208}Pb}{^{206}Pb}$	$\frac{^{206}Pb}{^{238}U}$	% err	$\frac{^{207}Pb}{^{235}U}$	% err	$\frac{^{207}Pb}{^{206}Pb}$	% err	corr. coef.	$\frac{^{206}Pb}{^{238}U}$	±	$\frac{^{207}Pb}{^{235}U}$	±	$\frac{^{207}Pb}{^{206}Pb}$	±	% disc.
(a)	(b)	(c)	(d)	(e)	(f)	(f)	(g)	(f)	(g)	(f)	(g)		(h)	(i)	(h)	(i)	(h)	(i)	(j)
EKC03-36																			
za1	247	0.54	0.42	13179	0.116	0.627896	0.10	22.40673	0.11	0.25881	0.05	0.902	3141.3	2.5	3201.5	1.1	3239.5	0.8	3.83
za2	149	0.68	0.53	7803.0	0.144	0.642513	0.21	22.92516	0.21	0.25878	0.05	0.977	3198.9	5.2	3223.8	2.1	3239.3	0.7	1.58
za8	65	3.85	0.26	3158	0.070	0.647439	0.08	23.10843	0.09	0.25886	0.04	0.877	3218.2	2.1	3231.5	0.9	3239.8	0.7	0.85
za9	389	0.49	0.29	21320	0.080	0.641473	0.07	22.67624	0.09	0.25638	0.04	0.861	3194.8	1.9	3213.2	0.8	3224.6	0.7	1.17
za10	33	0.60	0.65	1677	0.180	0.639608	0.15	23.20469	0.16	0.26312	0.08	0.887	3187.5	3.7	3235.6	1.6	3265.5	1.2	3.03
za11	71	0.43	0.34	3839.9	0.092	0.640505	0.31	22.88323	0.31	0.25912	0.07	0.977	3191.0	7.7	3222.0	3.1	3241.3	1.1	2.0
a1 (60)	3.9	6.99	0.27	202.8	0.076	0.529824	0.53	13.88913	0.56	0.19013	0.12	0.979	2740.7	11.9	2742.2	5.3	2743.3	1.9	0.1
a4 (35)	1.5	3.53	0.58	83.5	0.173	0.562936	1.98	18.39225	2.03	0.23696	0.25	0.993	2878.8	46.0	3010.5	19.5	3099.7	4.0	8.8
a5 (55)	2.9	5.10	0.43	148.7	0.120	0.554933	0.74	15.61655	0.78	0.20410	0.15	0.981	2845.7	17.1	2853.6	7.4	2859.3	2.5	0.6
a6 (72)	3.7	8.44	0.20	197.2	0.056	0.538031	0.33	14.36576	0.36	0.19365	0.11	0.956	2775.2	7.5	2774.2	3.4	2773.4	1.8	-0.1
a7 (105)	4.5	25.85	0.29	226.4	0.086	0.503824	0.10	13.32873	0.13	0.19187	0.08	0.811	2630.2	2.2	2703.2	1.2	2758.3	1.3	5.6
a8 (140)	4.9	61.25	0.37	235.3	0.117	0.476877	0.10	13.04429	0.12	0.19839	0.07	0.838	2513.6	2.1	2682.9	1.1	2813.0	1.1	12.8
EKC02-64																			
za1	881	1.07	0.32	47223	0.085	0.657460	0.07	23.85223	0.08	0.26312	0.04	0.856	3257.3	1.8	3262.4	0.8	3265.5	0.7	0.32
za2	642	1.16	0.39	33383	0.105	0.657410	0.06	23.85243	0.08	0.26315	0.04	0.843	3257.1	1.7	3262.4	0.7	3265.6	0.7	0.33
za3	1570	0.12	0.34	82998	0.093	0.680006	0.1	27.32409	0.2	0.29143	0.22	0.299	3344.4	1.8	3395.1	2.3	3425.2	3.5	3.02
EKC02-65																			
za1	176	1.19	0.80	8944.9	0.223	0.525437	0.08	13.65228	0.11	0.18844	0.07	0.744	2722.2	1.8	2725.9	1.0	2728.6	1.2	0.29
za2	166	1.92	1.47	7093	0.408	0.525635	0.07	13.65889	0.08	0.18846	0.05	0.838	2723.0	1.6	2726.4	0.8	2728.8	0.8	0.26
za3	32	3.42	0.79	1493	0.218	0.525122	0.31	13.64960	0.32	0.18852	0.06	0.983	2720.9	7.0	2725.7	3.0	2729.3	1.0	0.38

Table 1. (cont.)

				Isotopic ratios									Dates (Ma)						
Sample	$^{Pb*}/_{Pb_c}$	Pb_c (pg)	$^{Th}/_{U}$	$^{206}Pb/^{204}Pb$	$^{208}Pb/^{206}Pb$	$^{206}Pb/^{238}U$	% err	$^{207}Pb/^{235}U$	% err	$^{207}Pb/^{206}Pb$	% err	corr. coef.	$^{206}Pb/^{238}U$	±	$^{207}Pb/^{235}U$	±	$^{207}Pb/^{206}Pb$	±	% disc.
(a)	(b)	(c)	(d)	(e)	(f)	(f)	(g)	(f)	(g)	(f)	(g)		(h)	(i)	(h)	(i)	(h)	(i)	(j)
BS04-20																			
za1	28	0.65	0.41	1488.4	0.115	0.644035	0.21	24.92600	0.23	0.28070	0.08	0.939	3204.9	5.4	3305.3	2.2	3366.8	1.2	6.10
za2	414	1.05	0.61	22353	0.168	0.528156	0.05	13.76746	0.07	0.18906	0.04	0.760	2733.7	1.1	2733.8	0.6	2734.0	0.7	0.01
za3	4.2	0.49	0.39	236.5	0.137	0.515480	0.95	19.80413	1.23	0.27864	0.78	0.773	2680.0	20.9	3081.8	11.9	3355.3	12.2	24.51
za4	1897	0.27	0.26	108360	0.072	0.564975	0.05	16.27296	0.07	0.20890	0.04	0.768	2887.2	1.2	2893.0	0.6	2897.0	0.7	0.42
za5	370	0.60	0.49	19535	0.133	0.640392	0.07	22.38542	0.09	0.25352	0.05	0.793	3190.6	1.7	3200.6	0.8	3206.9	0.8	0.65
BS04-21																			
za1	510	0.53	0.20	30051	0.056	0.524833	0.05	13.64586	0.07	0.18857	0.04	0.769	2719.6	1.1	2725.4	0.6	2729.8	0.7	0.5
za3	2.2	0.25	0.64	138.5	0.178	0.526586	1.68	13.67389	1.86	0.18833	0.52	0.963	2727.1	37.4	2727.4	17.6	2727.6	8.5	0.0
za4	108	0.29	0.14	6442.3	0.040	0.524939	0.10	13.64619	0.11	0.18854	0.05	0.903	2720.1	2.1	2725.5	1.0	2729.5	0.8	0.4
za5	122	1.09	0.20	7107.9	0.055	0.525893	0.11	13.67847	0.13	0.18864	0.05	0.912	2724.1	2.5	2727.7	1.2	2730.4	0.8	0.3

(a) za1, za2, a1, a2, etc. are fractions composed of single grains of zircon and apatite, respectively
numbers in parantheses following apatite fractions are the grain diameter, in μm

(b) Ratio of radiogenic Pb (including 208Pb) to common Pb.

(c) Total weight of common Pb.

(d) Model Th/U ratio calculated from radiogenic 208Pb/206Pb ratio and 207Pb/206Pb age.

(e) Measured ratio corrected for spike and fractionation only. Mass fractionation corrections were based on analysis of NBS-981 and NBS-983. Corrections of 0.25 ± 0.04%/amu (atomic mass unit) and 0.07 ± 0.04%/amu were applied to single-collector Daly analyses and dynamic Faraday-Daly analyses, respectively.

(f) Corrected for fractionation, spike, and blank. All common Pb was assumed to be procedural blank.

(g) Errors are 2 sigma, propagated using the algorithms of Ludwig (1980).

(h) Calculations are based on the decay constants of Jaffey et al. (1971).

(i) Errors are 2 sigma.

(j) % discordance = 100 - (100 x 206Pb/238U date / 207Pb/206Pb date).

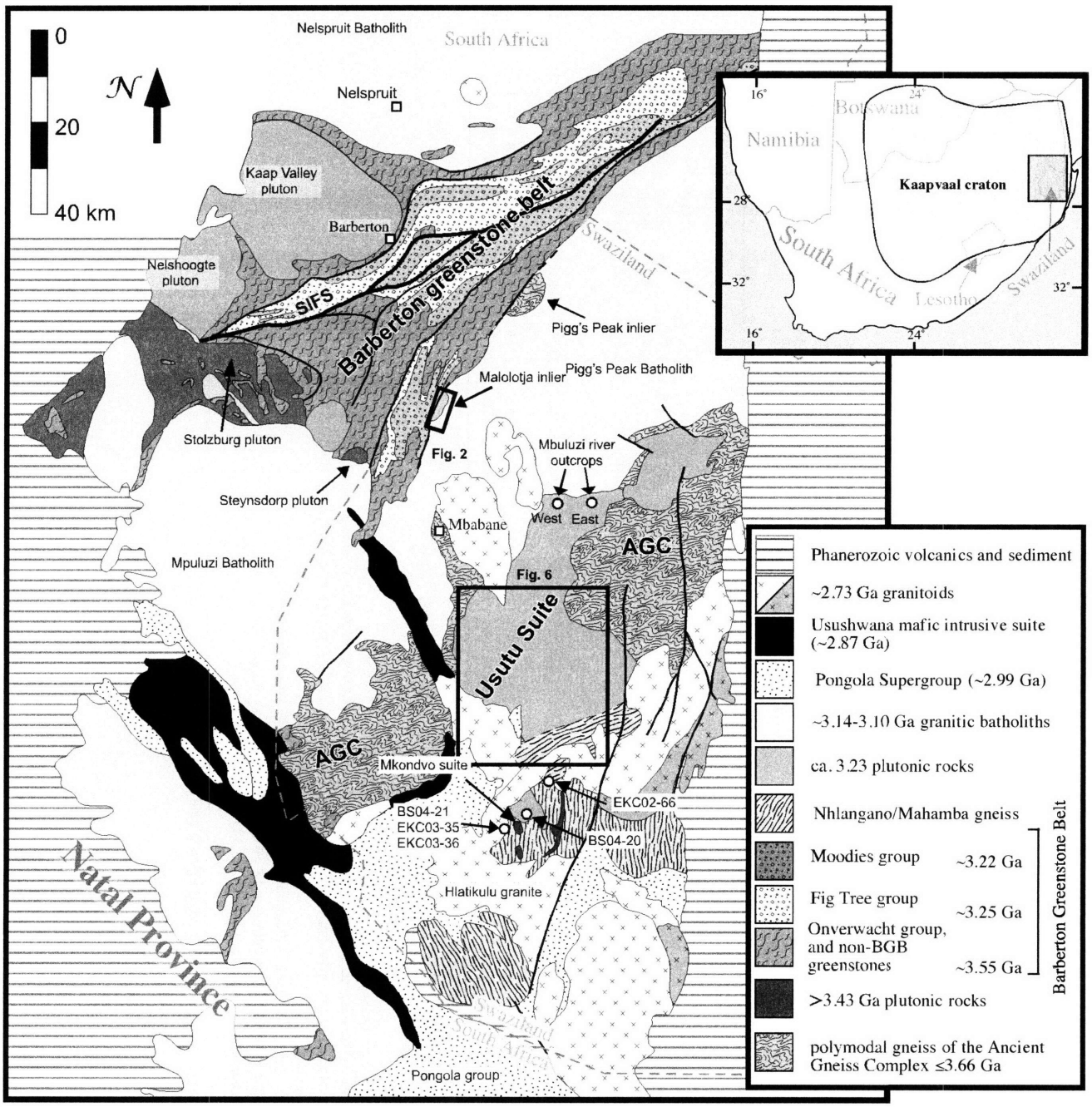

Fig1. Schoene and Bowring

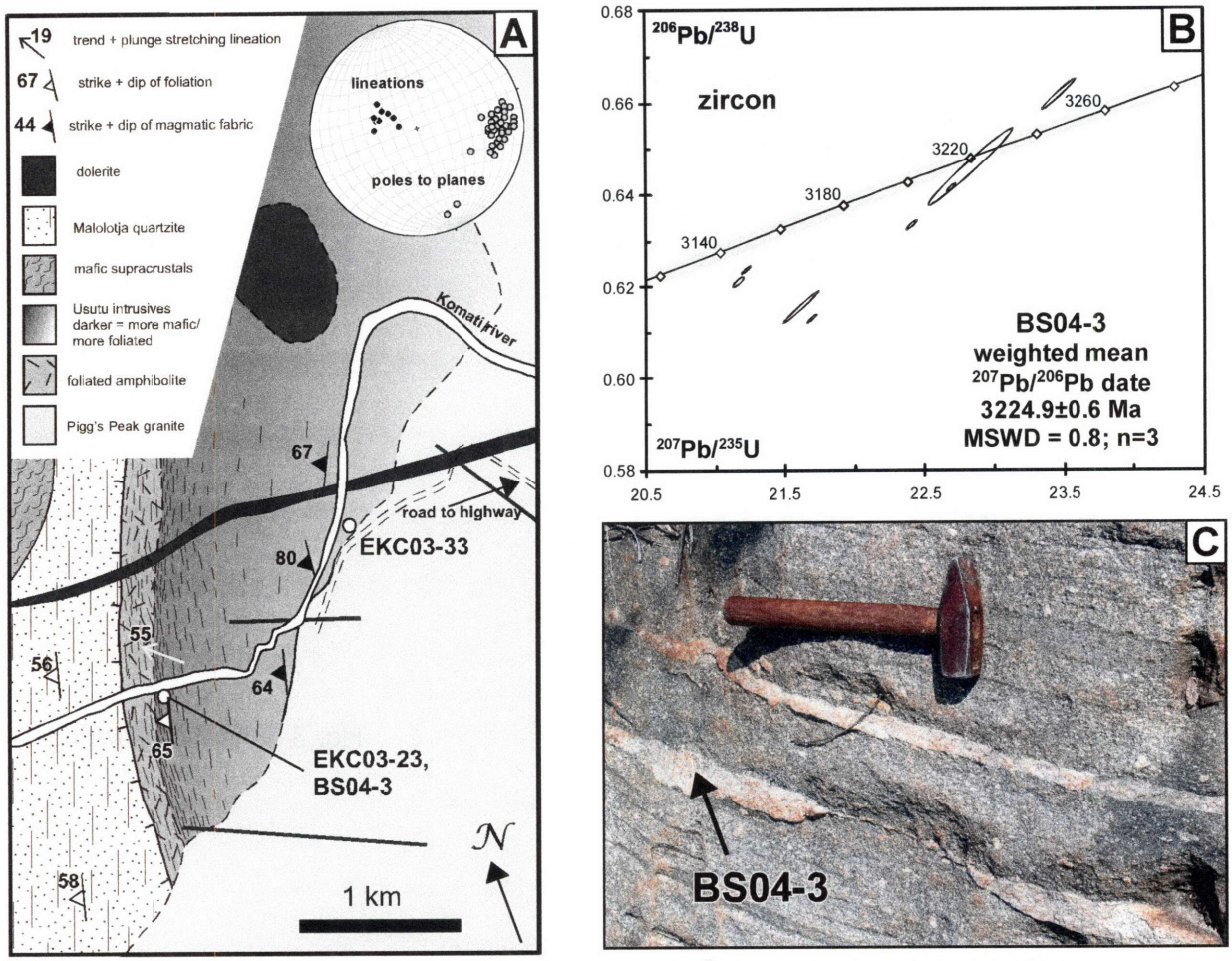

Fig. 2 Schoene&Bowring

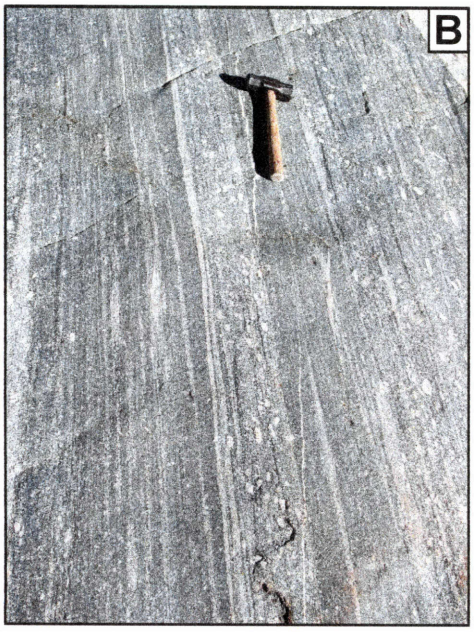

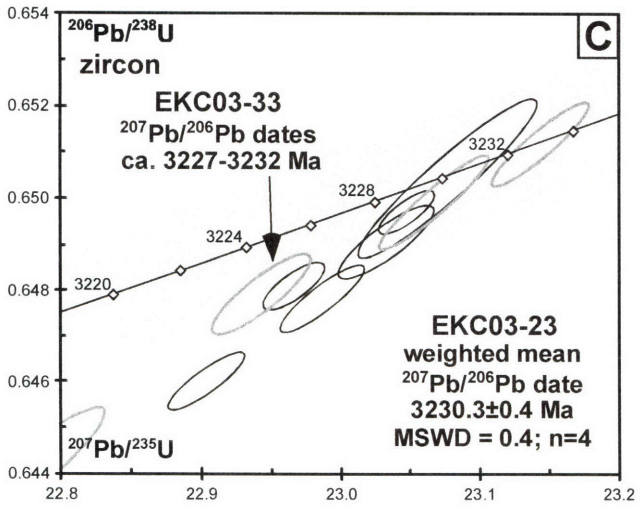

Fig. 3 Schoene&Bowring

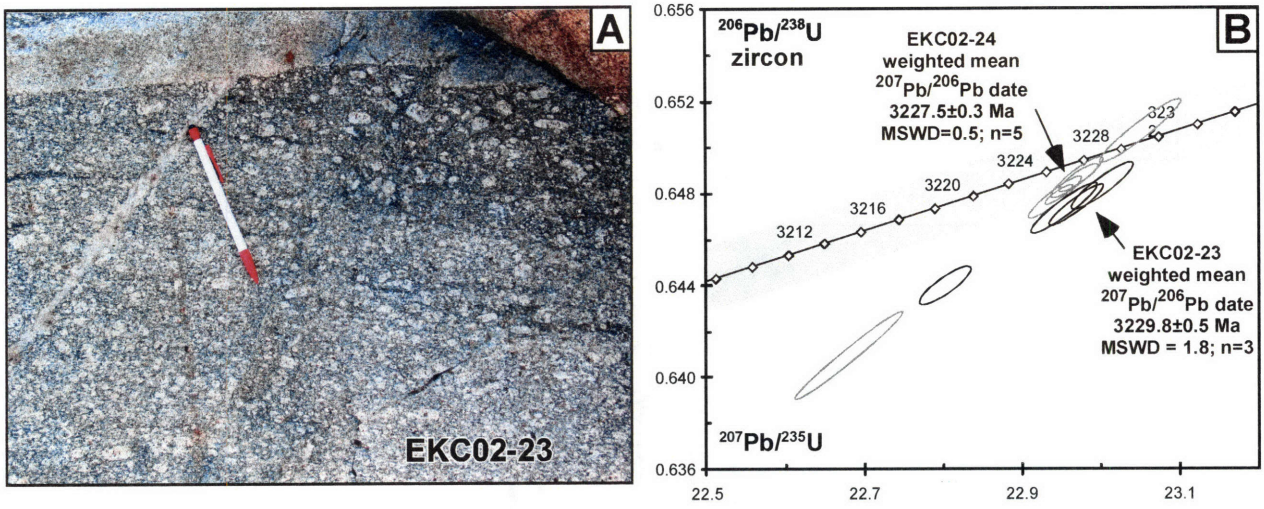

Fig. 4 Schoene&Bowring

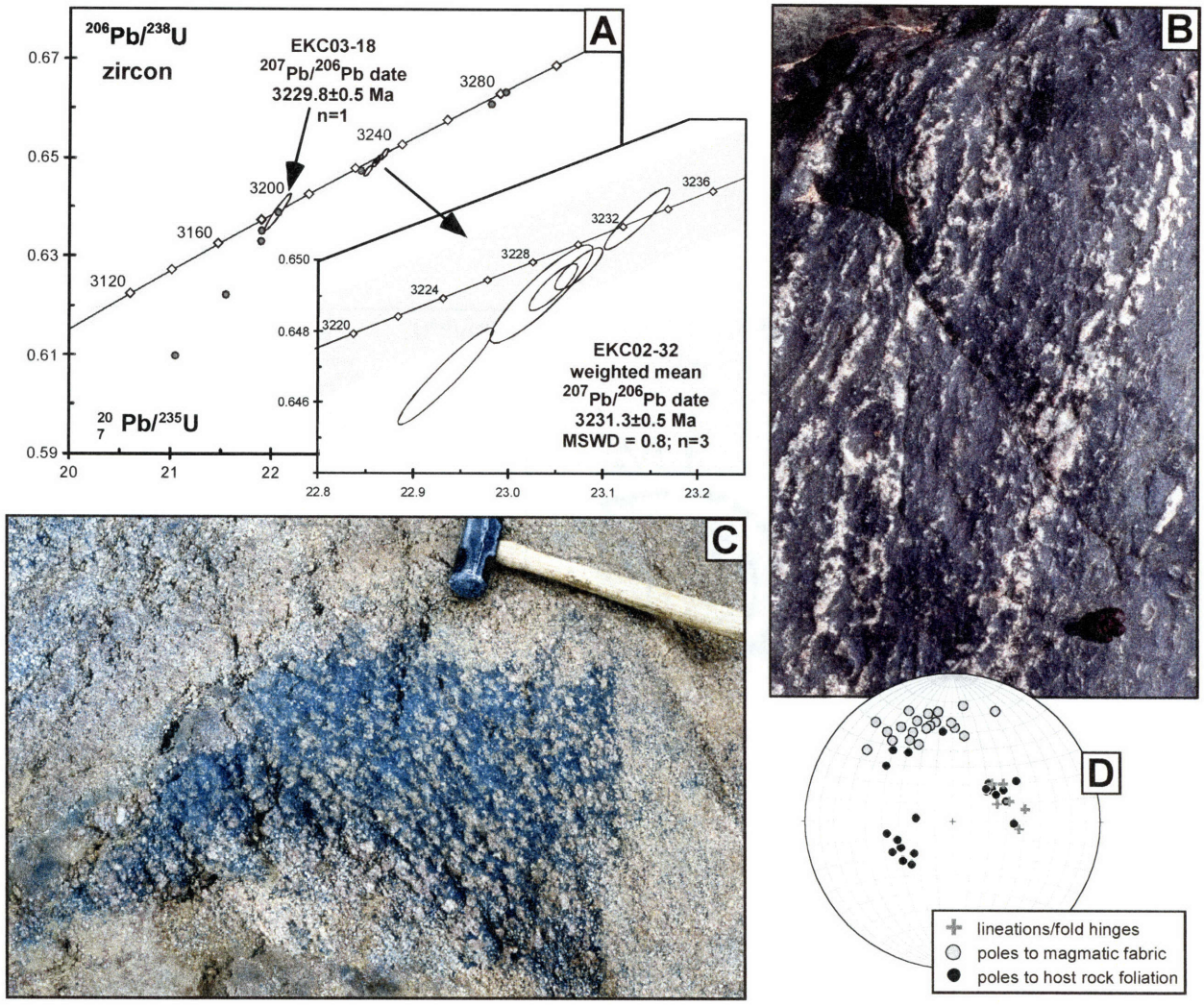

Fig. 5 Schoene&Bowring

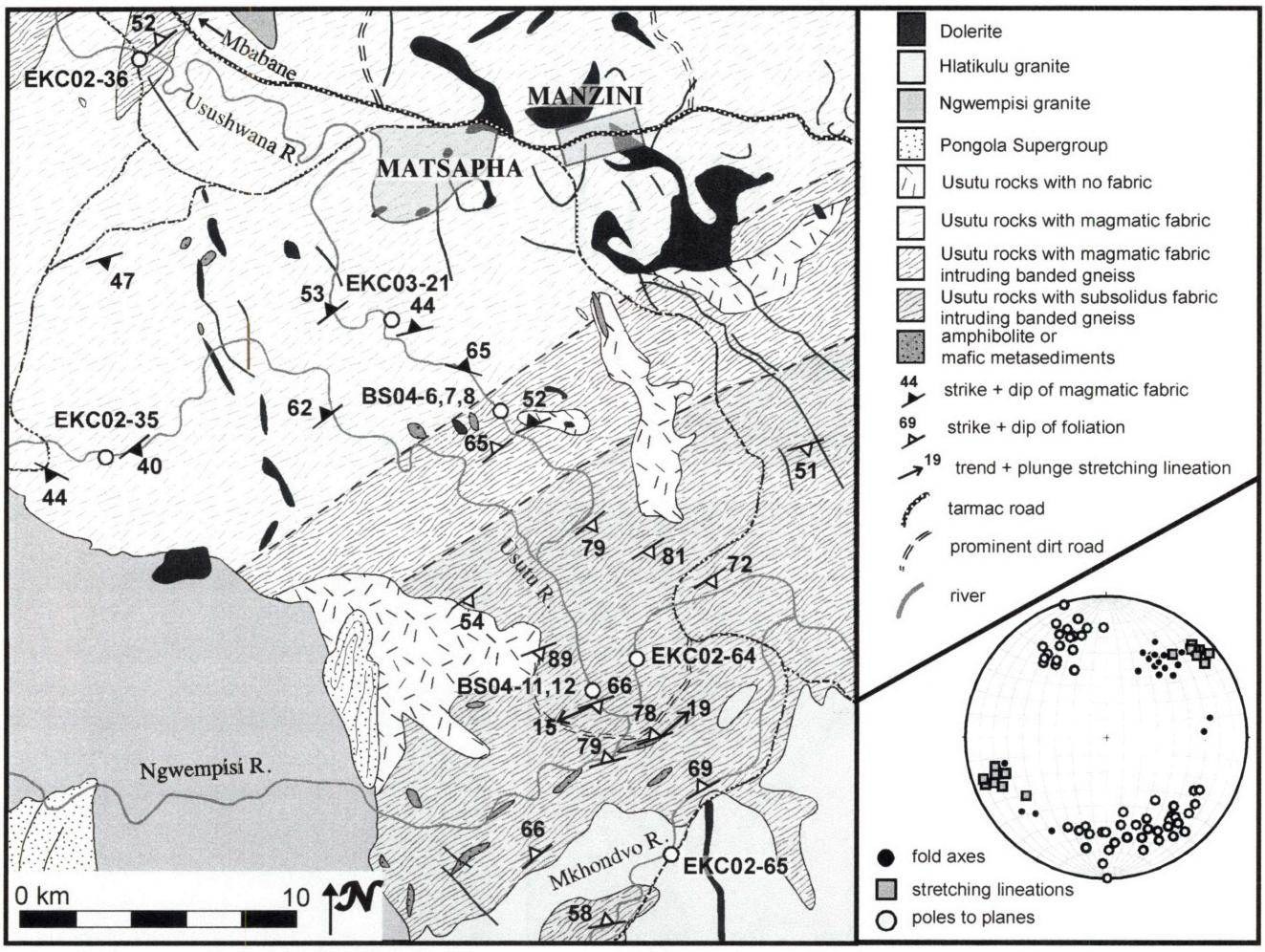

Fig. 6 Schoene&Bowring

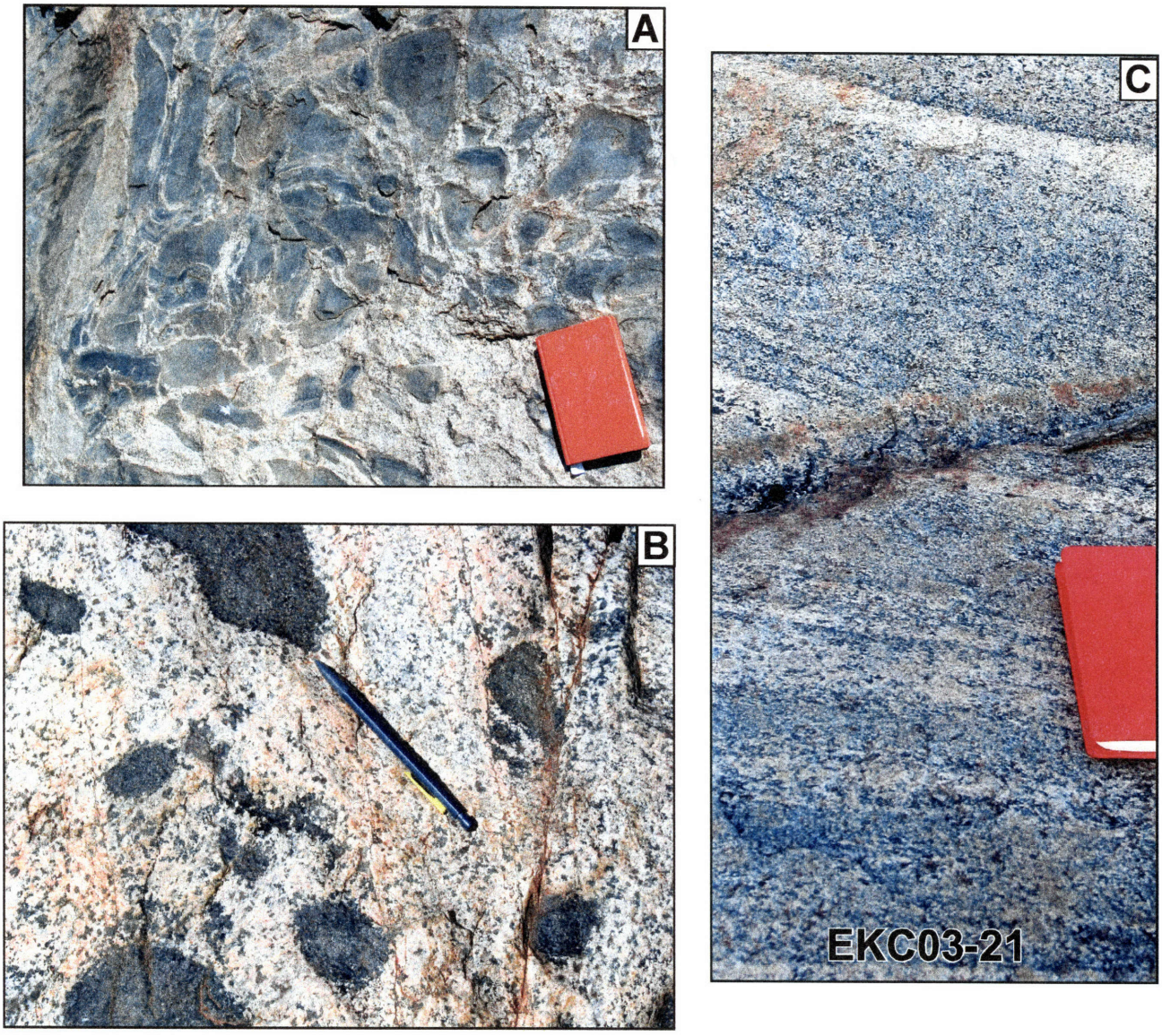

Fig 7 Schoene&Bowring

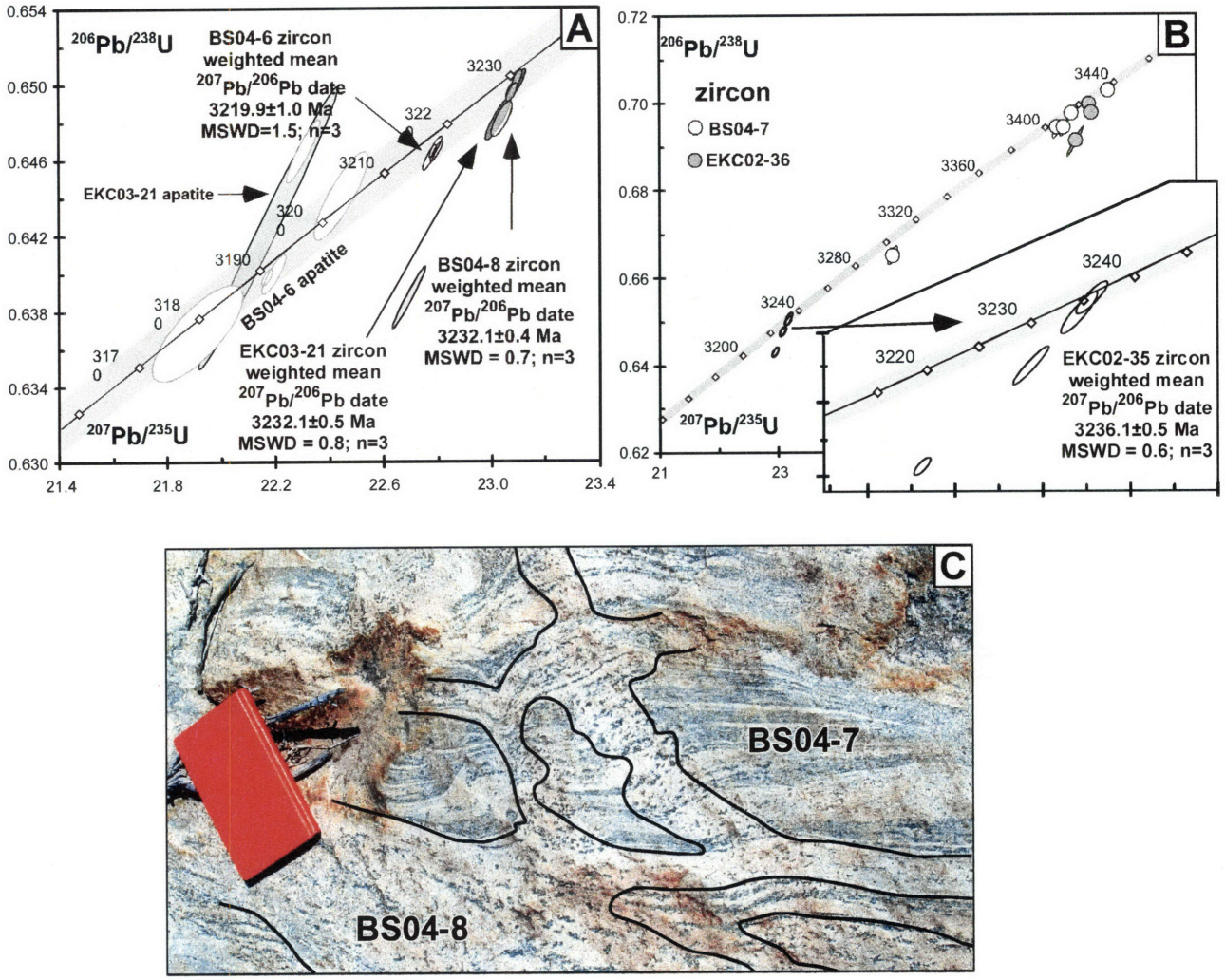

Fig. 8 Schoene&Bowring

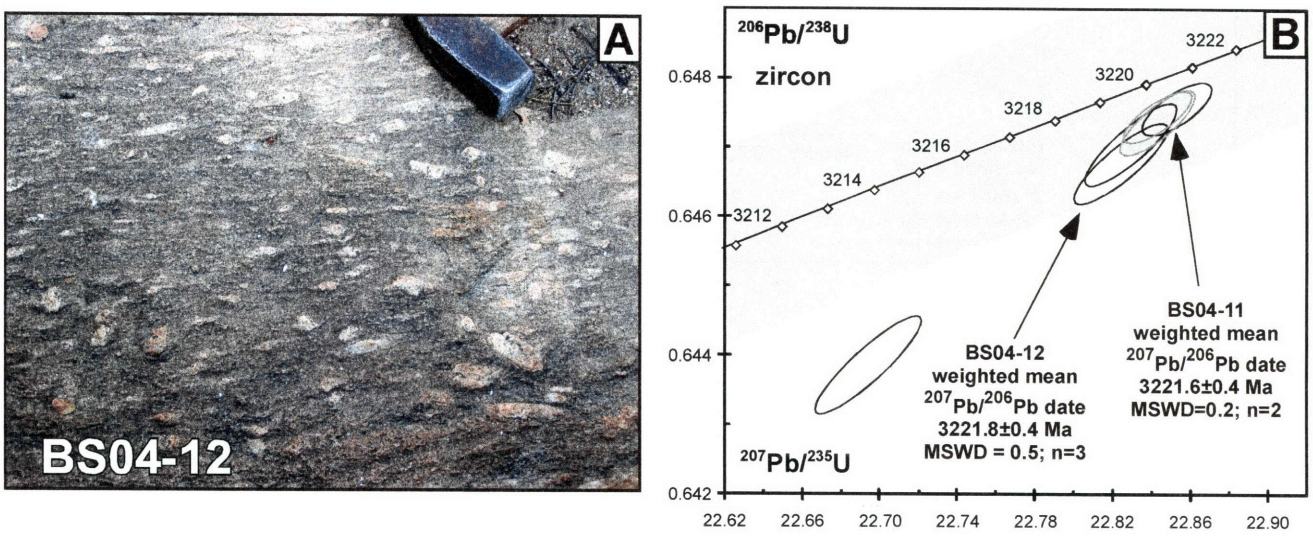

Fig. 9 Schoene&Bowring

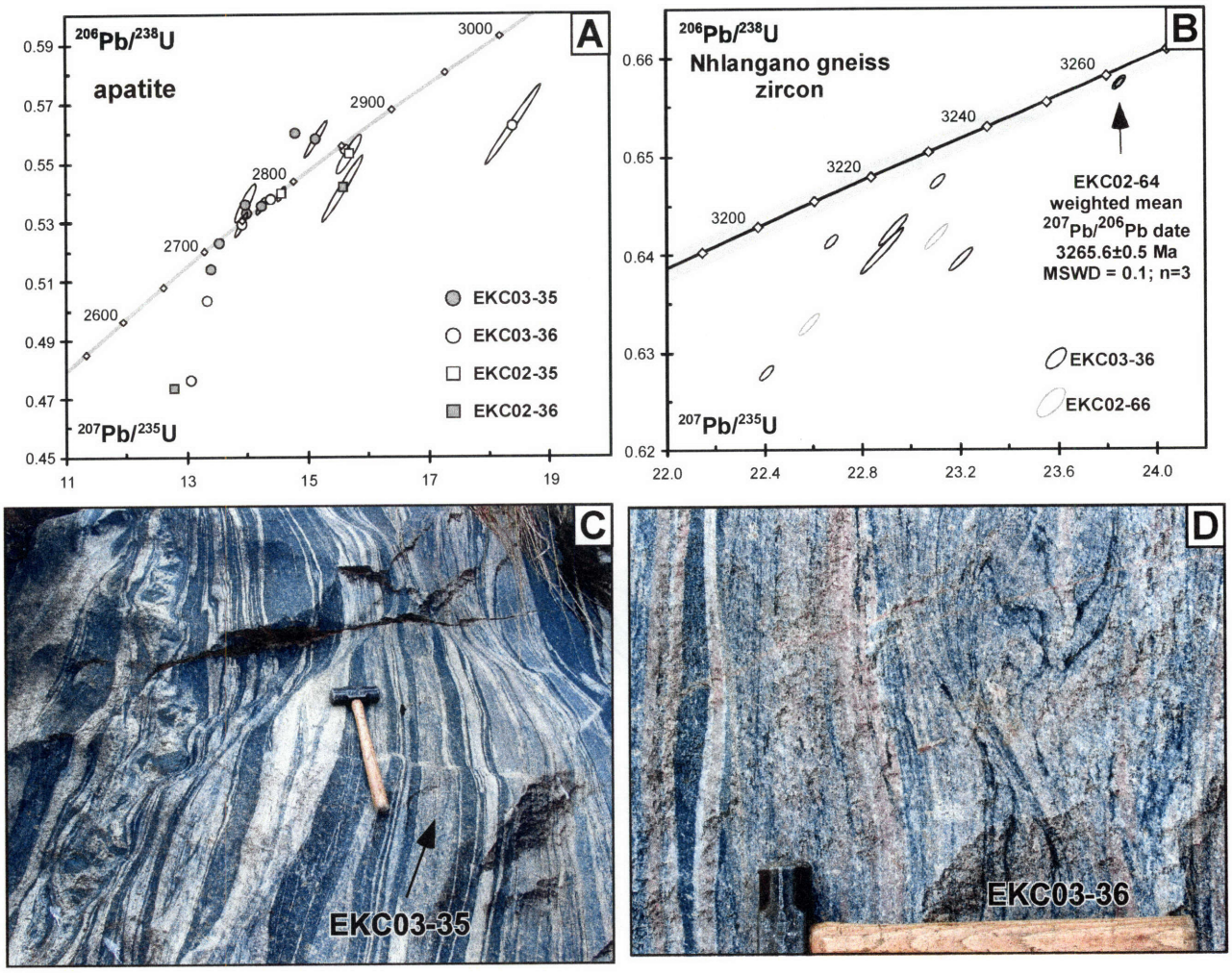

Fig. 10 Schoene&Bowring

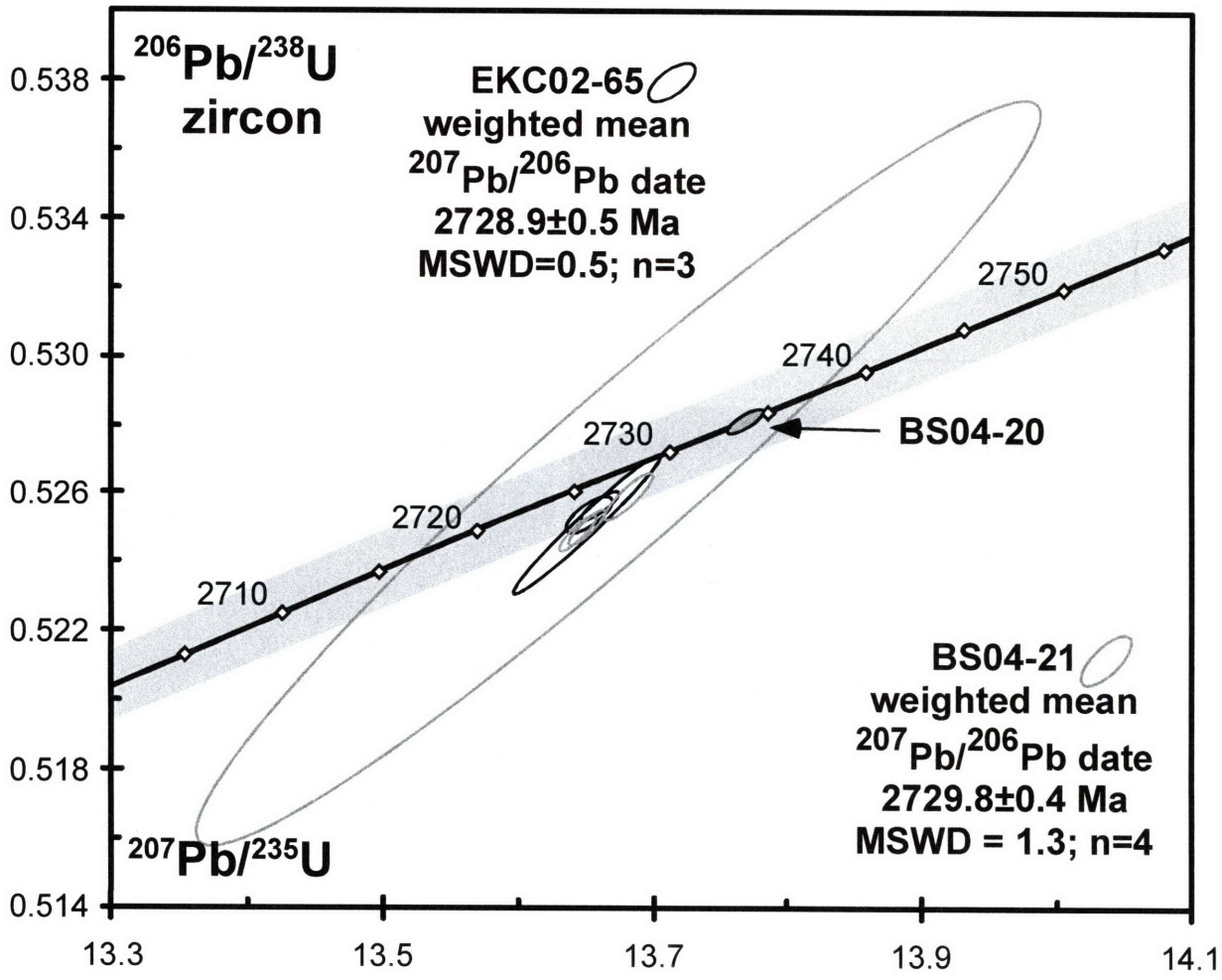

Fig. 11 Schoene&Bowring

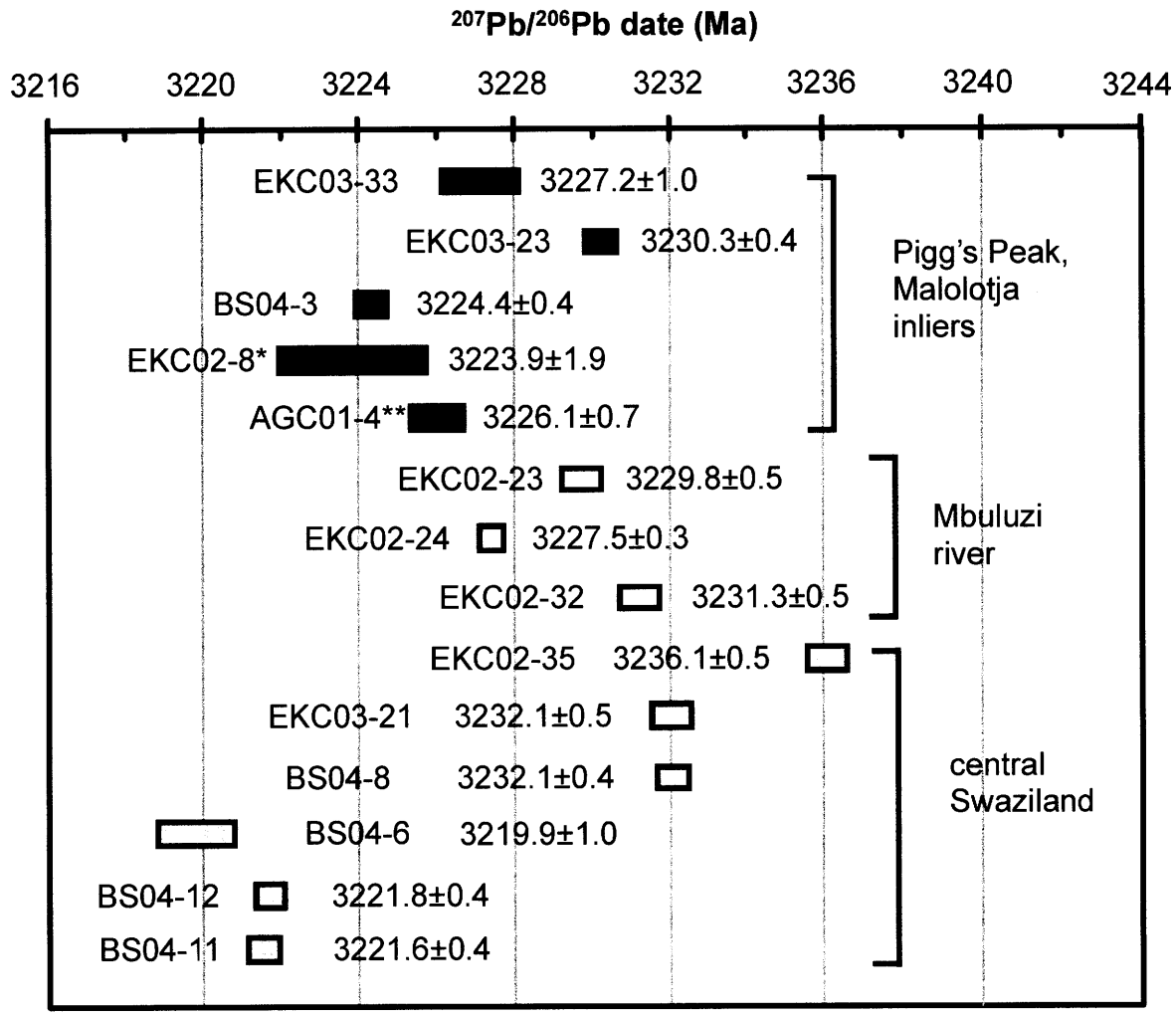

Fig. 12 Schoene&Bowring

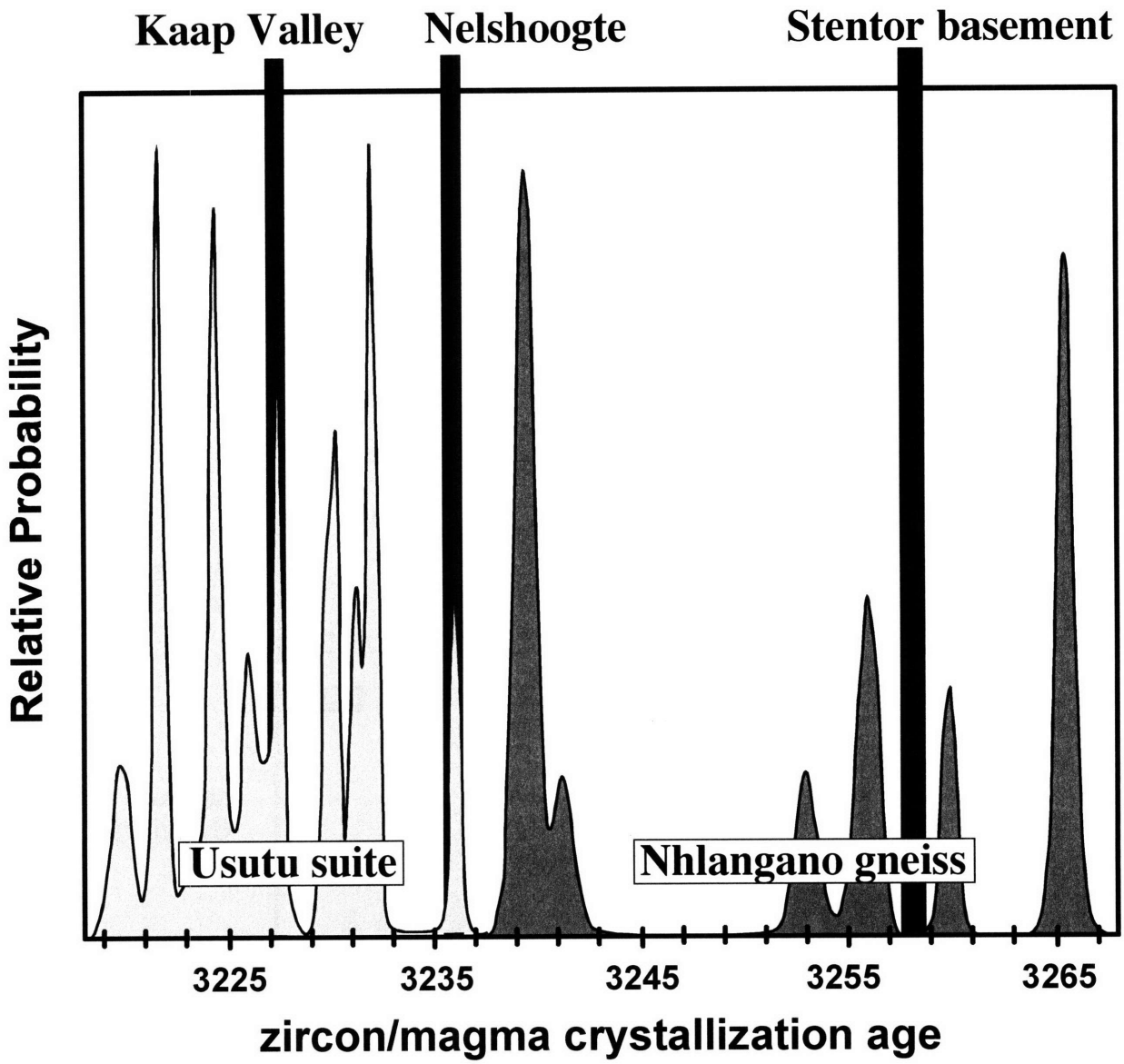

Fig. 13 Schoene&Bowring

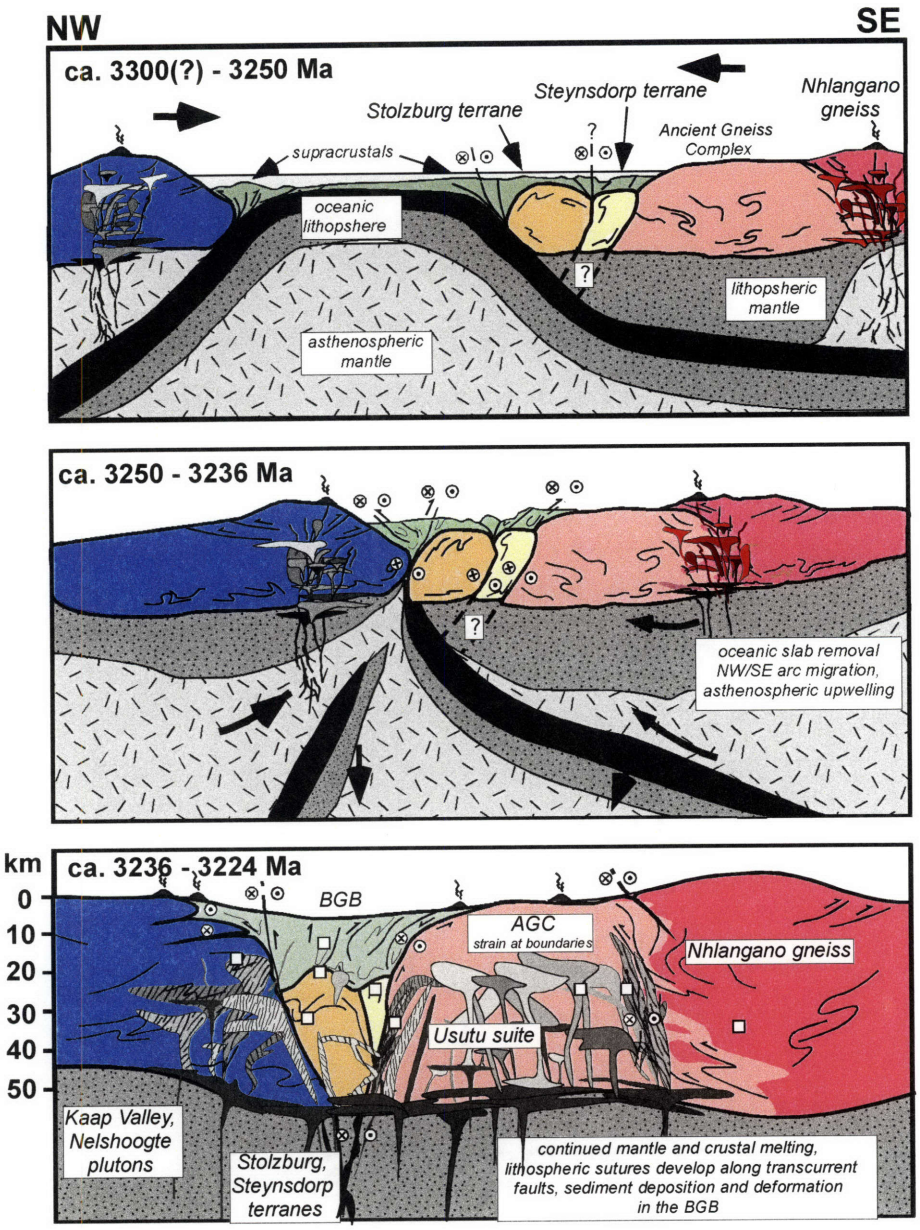

Fig 14. Schoene and Bowring

CHAPTER 4

Sm-Nd isotopic mapping of lithospheric growth and stabilization in the eastern Kaapvaal craton

Blair Schoene[1], Francis Ö.L. Dudás[1], Samuel A. Bowring[1], and Maarten de Wit[2]

1. Department of Earth, Atmospheric and Planetary Sciences, Massachusetts Institute of Technology, Cambridge, MA 02139, USA.

2. AEON, and Department of Geological Sciences, University of Cape Town, Rondebosch, 7701, South Africa.

For submission to *Geology*

ABSTRACT

We use the Sm-Nd isotope systematics of 79 Archean granitoids from the eastern Kaapvaal craton, southern Africa, to delineate important lithospheric boundaries and constrain the timescales of craton amalgamation and intracrustal geochemical differentiation. Offsets in ε_{Nd} values of 3.2-3.3 Ga granitoids across the NE-SW trending Barberton greenstone belt (BGB) are consistent with ca. 3.23 Ga accretion of newly formed lithosphere north of the belt onto pre-existing ca. 3.66 Ga lithosphere south of the belt along a doubly-verging subduction zone. Sm-Nd isotopic data show that the southern magmatic arc was constructed on pre-existing ca. 3.66 Ga lithosphere. When the new Sm-Nd data are combined with that from the literature to track the Nd isotopic systematics of magmas intruding the oldest lithospheric blocks between ca. 3.2 and 2.7 Ga, the Nd budget was controlled entirely by pre-existing enriched crust rather than addition from the mantle.

1. INTRODUCTION

The 3-dimensional physical and geochemical structure of continental lithosphere is constrained by the integration of geophysical and xenolith data, though the latter is dependent on the relatively rare occurrence of xenolith bearing volcanic rocks. Alternatively, the geochemistry and isotopic characteristics of igneous rocks now at the surface can be viewed as probes for their source regions, and therefore provide insight into magmatic processes as well as lithospheric structure. Utilizing the Sm-Nd isotope systematics of such rocks provides the benefit of constraining the time-scales of early crust-mantle segregation and subsequent magmatic and geochemical differentiation of the lithosphere (Albaréde et al., 2000; Bowring and Housh, 1995; DePaolo, 1980; DePaolo and Wasserburg, 1976a). Therefore, differences in the Nd signature of plutonic rocks can be used to identify important lithospheric discontinuities that may not be recorded in the ages of surface exposures (Bennett and DePaolo, 1987; Davis and Hegner, 1992; Dickin, 2000; Milisenda et al., 1988).

The Kaapvaal craton in southern Africa is one of the most extensively studied fragments of Archean lithosphere, but high-resolution seismic studies and the occurrence of xenolith bearing kimberlites are restricted to the mostly Neoarchean central and western craton, whereas the best exposed and oldest basement rocks occur in the eastern craton (Carlson et al., 2000; de Wit et al., 1992; Schmitz et al., 2004). To bridge this gap in knowledge of the 3-D petrologic and geochemical structure of the eastern Kaapvaal craton, we analyzed the Sm-Nd isotopic systematics of 79 dated ca. 3.7-2.7 Ga plutonic and orthogneiss samples from an ~200 km long transect across potential Mesoarchean lithospheric discontinuities. We use the Sm-Nd isotope data to refine and identify

lithospheric boundaries that are not obvious from the crystallization ages of exposed rocks, allowing for the development of improved tectonic models for the assembly and stabilization of the eastern Kaapvaal craton and evaluation of intracrustal geochemical differentiation within single lithospheric blocks as a function of time.

2. GEOLOGIC SETTING AND SAMPLING

Most of the present-day crustal architecture of the Kaapvaal craton flanking the Barberton Greenstone Belt (BGB) can be explained within the context of ca. 3.2-3.3 Ga arc magmatism and dominantly NW-SE compressional tectonics (de Ronde and de Wit, 1994; de Ronde and Kamo, 2000; de Wit et al., 1992; Kamo and Davis, 1994; Lowe, 1994, Dziggel, 2005 #657), followed by ~100 Myr of transtensional deformation, granitic magmatism and spatially diverse tectonic denudation (de Ronde and de Wit, 1994; Schoene and Bowring, submitted; Schoene et al., in prep; Westraat et al., 2005). It has been inferred that ca. 3.23 Ga deformation was the result of the amalgamation of at least two microcontinental blocks, with the Saddleback-Inyoka fault system (SIFS) within the BGB representing a lithospheric suture zone (Fig. 1; de Ronde and de Wit, 1994; de Wit et al., 1992; Heubeck and Lowe, 1994; Lowe and Byerly, 1999). However, there is considerable uncertainty about the identity of the two terranes and their amalgamation mechanism. The 3.66-3.45 Ga mafic-silicic banded gneiss of the Ancient Gneiss Complex (AGC) to the south of the BGB is one of the terranes (Jackson et al., 1987), and it was intruded by a suite of granodiorites to tonalites from 3236 to 3220 Ma that record NW-SE compression in magmatic fabrics (Schoene and Bowring, in prep). Further

south, a suite of complexly deformed orthogneisses called the Nhlangano gneiss (NG), gives slightly discordant U-Pb dates of ~3240-3280 Ma (Schoene and Bowring, in prep), though its relationship to the AGC is not well understood. The terrane to the north of the BGB has been suggested to represent a young island-arc type continental fragment that was accreted onto the AGC ca. 3.23 Ga along a NE-trending boundary (de Wit et al., 1992), consistent with zircon dates from two plutons of ca. 3236 and 3227 Ma, one banded gneiss sample dated at ca. 3258 Ma, and ca. 3.3 Ga basement xenoliths from within a ca. 3.1 Ga granitic batholith (Kamo and Davis, 1994; Schoene et al., in prep). Bordering the SW BGB, basement orthogneiss complexes (e.g. the ca. 3.45 Ga Stolzburg and the ca. 3.52 Ga Steynsdorp complexes) were also intruded by ca. 3.23 Ga syntectonic tonalitic to granodioritic magmas (Dziggel et al., 2005; Schoene et al., in prep). Schoene and Bowring (in prep) propose a NE-SW trending doubly-vergent subduction zone from ca. 3.3 to 3.23 Ga to account for the synchroneity of magmatism and deformation north and south of the BGB and the generation of the NG. The Neoarchean history of area is represent by the eruption and deposition of the Pongola Supergroup ca. 2.985 Ga and the intrusion of the undeformed Usushwana complex and associated mafic to ultramafic dikes ca. 2.850 Ga (Fig. 1; Hegner et al. 1984).

Based on the geochronology of surface geology, we divide the study area into four areas for the following discussion (Fig. 1): The NBGB (rocks on the NW side of the SIFS, NW of the BGB), the SST (consisting of the Stolzburg terrane and Steynsdorp complex), the AGC, and the NG. We collected plutonic and orthogneiss samples from these four areas that range in composition from granite to gabbro with crystallization ages between ca. 3.7 and 2.7 Ga (Fig. 1). Seventy-nine Sm-Nd analyses are presented in Table

1 along with their location, rock-type, and known or inferred crystallization age, which are also plotted in Fig. 1.

3. Sm-Nd RESULTS AND DISCUSSION

3.1. Nd isotopic map of the eastern Kaapvaal

To evaluate the distribution of old crust that may or may not be exposed at the surface, we examine the range of $\varepsilon_{Nd}(t)$ (the ε_{Nd} at the time of crystallization) across the crustal transect for rocks of similar age. Contemporaneous magmatism occurred across the entire study area ca. 3.2-3.3 Ga; ca. 3.1 Ga granitic magmatism also extends from the AGC across the SST into the NBGB. Magmatism at ca. 2.7 Ga occurs in the AGC and NG only (Fig. 1). Fig. 2 shows the position of the sample locations projected onto a line trending 325° (approximately perpendicular to the NE-SW regional structural grain; cross-section line shown in Fig. 1) plotted against the $\varepsilon_{Nd}(t)$ of the samples. Both ca. 3.2-3.3 and ca. 3.1 Ga rocks show higher $\varepsilon_{Nd}(t)$ values in the NBGB. Ca. 3.1 Ga samples in the NBGB have $\varepsilon_{Nd}(t) > -2$ and samples to the south have $\varepsilon_{Nd}(t) < -2$. For 3.2-3.3 rocks, there are no samples with $\varepsilon_{Nd}(t) < 0$ in the NBGB, whereas $\varepsilon_{Nd}(t)$ for samples in other areas range from 0 to -3 (with two exceptions), while there are no samples in the SST that have $\varepsilon_{Nd}(t) < -2$. However, there is no increase in $\varepsilon_{Nd}(t)$ in 3.2-3.3 Ga samples in southern Swaziland across the boundary between the AGC and NG, indicating a similar low ε_{Nd} reservoir contributing to those rocks. Similarly, for ca. 2.7 Ga granites, there is no difference in $\varepsilon_{Nd}(t)$ across that surface transition.

The marked offsets in $\varepsilon_{Nd}(t)$ between coeval magmas in the NBGB, SST, and AGC likely represent isotopically unique lithosphere in each terrane. Alternatively, the data may reflect similar crustal age but different magmatic processes across the boundaries. To test this, we also plotted the Sm/Nd ratios of rocks in Fig. 2 in each terrane. If elevated $\varepsilon_{Nd}(t)$ values in the NBGB are the result of a higher contribution of mantle-derived melt, there should be a correlation between high $\varepsilon_{Nd}(t)$ and high Sm/Nd. Though some of the ca. 3.1 Ga granite samples from the NBGB do show such a correlation, 3.2-3.3 Ga rocks show near identical Sm/Nd across the SIFS despite the offset in $\varepsilon_{Nd}(t)$ (Fig. 2). Thus, these older granodiorites to tonalites are likely derived by a similar set of processes and a similar bulk composition source, but inherited some component of older crust south of the SIFS. Though there is no offset in $\varepsilon_{Nd}(t)$ across the AGC-NG boundary, Sm/Nd values decrease southward from a low of 0.17 near the SST to a low value of 0.13 in the NG.

3.2. Intracrustal Nd isotopic evolution

Our Sm-Nd transect across the study area suggests that similarities in $\varepsilon_{Nd}(t)$ between the basement rocks south of the SIFS can be modeled as a single lithospheric block, allowing evaluation of Sm-Nd evolution for 1 Gyr of early craton evolution ca. 3.7-2.7 Ga. We have plotted $\varepsilon_{Nd}(t)$ and Sm/Nd as a function of time for the data from rocks south of the SIFS from this study combined with those from the literature in Fig. 3 (a total of 104 data points). In general, $\varepsilon_{Nd}(t)$ of basement rocks define a linear array between 2.7 and 3.3

Ga, while the $\varepsilon_{Nd}(t)$ of rocks >3.45 Ga are more variable and plot mostly below that array (Fig. 3B). Metavolcanics of the Neoarchean Pongola Supergroup and the predominantly gabbroic Usushwana complex (Fig. 1) plot well above this array. In an attempt to quantify these trends, we calculated the ε_{Nd} for each data point at five dates corresponding to periods of magmatism between ca. 2.73 to 3.25 Ga. We then calculated the average ε_{Nd} at those times for (1) all the magmas of that age, and (2) all the basement rocks present at that time, as a proxy for average crustal Nd (i.e. 'basement rocks' for ca. 3.1 Ga magmas include 3.2-3.3 Ga magmas in addition to >3.45 Ga magmas; Pongola and Usushwana rocks were not included as basement rocks; Fig. 4). We find that at 3.25 Ga, the $\varepsilon_{Nd}(t)$ values of rocks south of the SIFS are elevated relative to the average crustal ε_{Nd} in Fig. 4 and therefore require input from a high ε_{Nd} source such as the mantle (Fig. 4). The Nd isotopic signatures of granitic magmas at ca. 3.1 and 2.73 Ga can be entirely explained by in situ crustal melting with little or no extracrustal Nd input. Pongola volcanics and the Usushwana intrusives also have elevated $\varepsilon_{Nd}(t)$ relative to the average crustal value, but still well below a depleted mantle value (approx. +4; Fig. 3B; Bowring and Housh, 1995; DePaolo, 1981). Sm/Nd of Pongola and Usushwana magmas are also consistent with contribution from a non-crustal source (Fig. 3A), in that as a whole they plot above the ca. 3.1 and 2.73 Ga granites. The other data follow a trend of lower Sm/Nd with time that is consistent with progressive Sm/Nd fractionation by multiple periods of crustal melting (Fig. 3A). The $\varepsilon_{Nd}(t)$ values of the Pongola and Usushwana rocks were a result of mixed mantle and crustal contributions, but those

magmatic episodes had little effect on the bulk crustal Sm-Nd systematics because the $\varepsilon_{Nd}(t)$ of 2.73 Ga granites can be explained without their involvement.

The above analysis assumes that calculated $\varepsilon_{Nd}(t)$ of >3.45 Ga basement rocks in the AGC are accurate, despite previous skepticism that many Archean rocks can retain primary Sm/Nd (Gruau et al., 1996; Moorbath et al., 1997; Vervoort et al., 1996). In addition to primary heterogeneity in these oldest rocks, apparent scatter in $\varepsilon_{Nd}(t)$ and Sm/Nd values could be created by depletion to variable degrees caused by removal of partial melts or fractionation of Sm/Nd into metamorphic fluids. Partial melting was likely unimportant in the Sm-Nd evolution of the sampled rocks because in situ melt is rarely observed and because low-grade metavolcanics at the base of the BGB have a similar range in $\varepsilon_{Nd}(t)$ to plutonic rocks (Carlson et al., 1983; Kröner et al., 1996; Kröner and Tegtmeyer, 1994). Distinguishing between primary heterogeneity and the affects of metamorphism in >3.45 Ga rocks is difficult. By comparison, however, the consistency of $\varepsilon_{Nd}(t)$ values between 0 and -3 in the NG and pristine 3.2-3.3 Ga igneous rocks in central Swaziland shows that primary Sm/Nd and $\varepsilon_{Nd}(t)$ values can be retained through ca. 2.7 Ga reheating. In any case, if the Sm-Nd systematics of >3.45 Ga samples were slightly compromised by open system behavior, the *average* value used in the analysis above is less likely to be affected.

3.3. Tectonic implications

Sm-Nd isotopic mapping of the eastern Kaapvaal craton is consistent with the existence of at least three distinct lithospheric blocks that were involved in subduction–accretion tectonics ca. 3.3-3.2 Ga, represented in Fig. 1 as the NBGB, the SST and the AGC. Coeval magmatism north and south of the BGB from 3.3-3.2 Ma (Schoene and Bowring, in prep), combined with offset $\varepsilon_{Nd}(t)$ values across the SIFS (Fig. 2), are consistent with a model that involves a doubly-verging subduction zone that closed an ocean basin ca. 3.23 Ga along the BGB (Fig. 5). From ca. 3.30-3.24 Ga, the NBGB (Fig. 1) was formed and accreted onto pre-existing AGC and SST lithosphere, while the AGC hosted arc magmatism and deformation recorded in the exhumed NG. In addition to the geology and geochronology that support this model for the generation of the NG (Schoene and Bowring, in prep), low Sm/Nd values (Fig. 2) and evidence for mantle-derived Nd into the NG (Fig. 4) support the addition of arc magmas to the crust ca. 3.2-3.3 Ga. Thus, the AGC is, or once was, more expansive than is presently exposed. Inherited zircons in 3.2-3.3 Ga rocks within the NG support this hypothesis (Schoene and Bowring, in prep), as do the consistently low $\varepsilon_{Nd}(t)$ of ca. 2.7 Ga granites (approx. -5 to -8) across the trace of the AGC–NG boundary (Fig. 2).

The relationship between the SST and the AGC remains elusive, though slightly elevated $\varepsilon_{Nd}(t)$ values of 3.2-3.3 Ga magmas compared to the AGC suggest the SST may represent one or more distinct crustal slivers, as has been hypothesized based on sedimentary and structural studies from within the BGB (Heubeck and Lowe, 1994; Lowe, 1994). Despite this, an approximate mass balance based on Nd isotopic signature

(Fig. 4) suggests that geochemically the AGC, SST, and NG behaved as a semi-continuous lithospheric block since 3.2-3.3 Ga. For example, the observation that the average $\varepsilon_{Nd}(t)$ of 3.1 Ga magmas south of the SIFS corresponds to that of the bulk crust (Fig. 4) is consistent with a model in which magmatism was a result of crustal thinning and lower-crustal melting near the margin of the BGB with little extracrustal Nd input (Schoene et al., in prep). Though the geochemistry and Nd isotopes of the 2.73 granites is consistent with their derivation from crustal melting (Condie et al., 1996; Kleinhanns et al., 2003), no mechanism for providing heat to the base of the crust has been suggested. Given that the field area is immediately adjacent to a Mesozoic rifted margin on the east, and basement outcrops to the west are largely obscured by younger sedimentary sequences, identifying the geological evidence for the cause of ca. 2.73 Ga magmatism will be difficult. However, it is worth mentioning the potential correlation between the widespread Ventersdorp rifting event throughout the central craton (e.g. de Wit et al. 1992). In any case, the implication of the Sm-Nd data is that the cratonic nuclei south of the SIFS underwent periods of crustal growth through the addition of volumetrically significant mantle melts from ca. 3.7 to 3.2 Ga followed by periods of heating, crustal melting and stratification for ~500 Myr. During this period, ca. 3.2-3.1 Ga crustal extension and granite production in the lower crust of the BGB and 2.73 Ga granitic magmatism in the AGC and NG led to the piecewise stabilization of the eastern Kaapvaal craton. This post-assembly modification of the crust was an integral part of its stabilization because it transported heat producing elements to the upper crust while (at least in the BGB) simultaneously thinning it, resulting in a more rigid rheological profile (Ranalli and Murphy, 1987; Sandiford et al., 2002; Schoene et al., in prep).

APPENDIX: ANALYTICAL METHODS

Whole rock samples were powdered using standard shatterbox techniques. Approximately 50-100 mg of powder were spiked with a ^{149}Sm-^{150}Nd tracer and placed in an HF-HNO_3 mix in Teflon pressure vessels at 220°C for 4-5 days, converted to 6 M HCl and placed back in an 180°C oven for 24 h, which completely dissolved the sample. Separation of Sm and Nd was done using a standard two-stage HDEHP ion chromotography procedure. Isotopic measurements were made on the MIT Isoprobe-T mass spectrometer and both elements were analyzed as the metal. Nd was loaded on triple Re filaments in 1 μl of 0.1 M H_3PO_4 and analyzed using a three-sequence dynamic multicollector Faraday routine with an ~5 V signal of ^{144}Nd. Sm was loaded on single Ta filaments in 1 μl of 1 M H_3PO_4 using a static multicollector Faraday routine with an ~400 mV signal of ^{149}Sm. Sm and Nd were corrected for mass fractionation using an exponential law normalizing to $^{152}Sm/^{147}Sm = 1.783$ and $^{146}Nd/^{144}Nd = 0.7219$, respectively. Long-term reproducibility of Nd isotopic measurements of the Ames and Shinetsu Nd standards are ~20 ppm on the Isoprobe-T, corresponding to a conservative estimate of ±0.5 ε_{Nd} units in the Archean. Duplicate analyses from this study were reproducible to <0.1 ε_{Nd} units. ε_{Nd} is simply the $^{143}Nd/^{144}Nd$ value normalized to a condritic value, and was calculated based on the present day isotopic composition of chondritic uniform reservoir (CHUR) of $^{147}Sm/^{144}Nd = 0.1967$ and $^{143}Nd/^{144}Nd = 0.512638$ using the equation $\varepsilon_{Nd}(t) = [(^{143}Nd/^{144}Nd)_{sample}(t)/ (^{143}Nd/^{144}Nd)_{CHUR}(t)-1]x10^4$ (DePaolo and Wasserburg, 1976b).

REFERENCES CITED

Albaréde, F., J. Blichert-Toft, J. D. Vervoort, J. D. Gleason, and M. Rosing, 2000, Hf-Nd isotope evidence for a transient dynamic regime in the early terrestrial mantle: Nature, v. 404, p. 488-490.

Bennett, V. C., and D. J. DePaolo, 1987, Proterozoic crustal history of the western United States as determined by neodymiom isotopic mapping: GSA Bull., v. 99, p. 674-685.

Bowring, S. A., and T. Housh, 1995, The earth's early evolution: Science, v. 269, p. 1535-1540.

Carlson, R. W., F. R. Boyd, S. B. Shirey, P. E. Janney, T. L. Grove, S. A. Bowring, M. D. Schmitz, J. C. Dann, D. R. Bell, J. J. Gurney, S. H. Richardson, M. Tredoux, A. H. Menzies, D. G. Pearson, R. A. Hart, A. C. Wilson, and D. E. Moser, 2000, Continental growth, preservation, and modification in Southern Africa: GSA Today, v. 10, p. 1-8.

Carlson, R. W., D. R. Hunter, and F. Barker, 1983, Sm-Nd age and isotopic systematics of the bimodal suite, ancient gneiss complex, Swaziland: Nature, v. 305, p. 701-704.

Condie, K. C., A. Kröner, and C. C. Milisenda, 1996, Geochemistry and geochronology of the Mkhondo suite, Swaziland: evidence for passive-margin deposition and granulite facies metamorphism in the Late Archean of Southern Africa: Jour. Afr. Earth Sci., v. 21, p. 483-506.

Davis, W. J., and E. Hegner, 1992, Neodymium isotopic evidence for the tectonic assembly of Late Archan crust in the Slave province, northwest Canada: Contrib. Miner. Petrol., v. 111, p. 493-502.

de Ronde, C. E. J., and M. J. de Wit, 1994, Tectonic history of the Barberton Greenstone Belt, South Africa: 490 million years of Archean crustal evolution: Tectonics, v. 13, p. 983-1005.

de Ronde, C. E. J., M. J. de Wit, and E. T. C. Spooner, 1994, Early Archean (>3.2 Ga) Fe-oxide-rich, hydrothermal discharge veins in the barberton greenstone belt, South Africa: GSA Bull., v. 106, p. 86-104.

de Ronde, C. E. J., and S. Kamo, 2000, An Archean arc-arc collisional event: a short-lived (*ca.* 3 Myr) episode, Weltevreden area, Barberton greenstone belt, South Africa: Jour. Afr. Earth Sci., v. 30, p. 219-248.

de Wit, M. J., 1982, Gliding and overthrust nappe tectonics in the Barberton greenstone belt: Jour. Struc. Geol., v. 4, p. 117-136.

de Wit, M. J., C. Roering, R. J. Hart, R. A. Armstrong, C. E. J. de Ronde, R. W. E. Green, M. Tredoux, E. Peberdy, and R. A. Hart, 1992, Formation of an Archean continent: Nature, v. 357, p. 553-562.

DePaolo, D. J., 1980, Crustal growth and mantle evolution: inferences from models of element transport and Nd and Sr isotopes: Geo. and Cosmo. Acta, v. 44, p. 1185-1196.

DePaolo, D. J., 1981, Neodymium isotopes in the Colorado Front Range and implications for crust formation and mantle evolution in the Proterozoic: Nature, v. 291.

DePaolo, D. J., and G. J. Wasserburg, 1976a, Inferences about magma sources and mantle structure from variations of $^{143}Nd/^{144}Nd$: Geophysical Rsearch Letters, v. 3, p. 743-746.

DePaolo, D. J., and G. J. Wasserburg, 1976b, Nd isotopic variations and petrogenetic models: Geophys. Res. Lett., v. 3, p. 249-252.

Dickin, A. P., 2000, Crustal formation in the Grenville Province: Nd-isotope evidence: Can. Jour. of Ear. Sci., v. 37, p. 165-181.

Dziggel, A., R. A. Armstrong, G. Stevens, and L. Nasdala, 2005, Growth of zircon and titanite during metamorphism in the granitoid-gneiss terrane south fo the Barberton greenstone belt, South Africa: Mineral. Mag., v. 69, p. 1019-1036.

Gruau, G., M. Rosing, D. Bridgewater, and R. C. O. Gill, 1996, Resetting of Sm-Nd systematics during metamorphism of >3.7-Ga rocks: implications for isotopic models of early Earth differentiation: Chem. Geol., v. 133, p. 225-240.

Hegner, E., A. Kröner, and A. W. Hofman, 1984, Age and isotope geochemistry of the Archean Pongola and Usushwana suites in Swaziland, southern Africa: a case for crustal contamination of mantle-derived magma: Earth Planet. Sci. Lett., v. 70, p. 267-279.

Heubeck, C., and D. R. Lowe, 1994, Depositional and tectonic setting of the Archean Moodies Group, Barberton Greenstone Belt, South Africa: Precam. Res., v. 68, p. 257-290.

Jackson, M. P. A., K. A. Eriksson, and C. W. Harris, 1987, Early Archean foredeep sedimentation related to crustal shortening: a reinterpretation of the Barberton Sequence, southern Africa: Tectonophysics, v. 136, p. 197-221.

Kamo, S., and D. W. Davis, 1994, Reassessment of Archean crustal development in the Barberton Mountain Land, South Africa, based on U-Pb dating: Tectonics, v. 13, p. 167-192.

Kleinhanns, I. C., J. D. Kramers, and B. S. Kamber, 2003, Importance of water for Archean granitoid petrology: a comparative study of TTG and potassic granitoids from Barberton Mountain Land, South Africa: Contrib. Miner. Petrol., v. 145, p. 377-389.

Kröner, A., W. Compston, and I. S. William, 1989, Growth of early Archean crust in the Ancient Gneiss Complex of Swaziland as revealed by single zircon dating: Tectonophysics, v. 161, p. 271-298.

Kröner, A., E. Hegner, J. I. Wendt, and G. R. Byerly, 1996, The oldest part of the Barberton granitoid-greenstone terrain, South Africa: evidence for crust formation between 3.5 and 3.7 Ga: Precam. Res., v. 78, p. 105-124.

Kröner, A., and A. Tegtmeyer, 1994, Gneiss-greenstone relationships in the Ancient Gneiss Complex of southwestern Swaziland, southern Africa, and implications for early crustal evolution.: Precam. Res., v. 67, p. 109-139.

Layer, P. W., Kröner, A., McWilliams, M., York, D., 1989, Elements of the Archean thermal history and apparent polar wander of the eastern Kaapvaal Craton, Swaziland, from single grain dating and paleomagnetism: EPSL, v. 93, p. 23-24.

Lowe, D. R., 1994, Accretionary history of the Archean Barberton greenstone belt (3.55-3.22 Ga), Southern Africa: Geology, v. 22, p. 1099-1102.

Lowe, D. R., and G. R. Byerly, 1999, Geologic evolution of the Barberton Greenstone Belt, South Africa, v. Special Paper 329: Boulder, CO, Geol. Soc. Amer.

Milisenda, C. C., T. C. Liew, A. Hofmann, and A. Kröner, 1988, Isotopic mapping of age provinces in precambrian high-grade terrains: Sri Lanka: J. Geol., v. 96, p. 608-615.

Moorbath, S., M. J. Whitehouse, and B. S. Kamber, 1997, Extreme Nd-isotope heterogeneity in the early Archaean – fact of fiction? Case histories from northern Canada and West Greenland: Chem. Geol., v. 135, p. 213-231.

Ranalli, G., and D. C. Murphy, 1987, Rheological stratification of the lithosphere: Tectonophysics, v. 132, p. 281-295.

Sandiford, M., S. McLaren, and N. Neumann, 2002, Long-term thermal consequences of the redistribution of heat-producing elements associated with large-scale granitic complexes: J. Metamorphic Geol., v. 20, p. 87-98.

Schmitz, M. D., S. A. Bowring, M. J. de Wit, and V. Gartz, 2004, Subduction and terrane collision stabilized the western Kaapvaal craton tectosphere 2.9 billion years ago: Earth Planet. Sci. Lett., v. 222, p. 363-376.

Schoene, B., and S. A. Bowring, in prep, The Usutu suite.

Schoene, B., and S. A. Bowring, *in press*, Determining accurate T-t paths in U-Pb thermochronology: an example from the SE Kaapvaal craton, Southern Africa: Geo. and Cosmo. Acta.

Schoene, B., J. L. Crowley, D. C. Condon, M. D. Schmitz, and S. A. Bowring, 2006, Reassessing the uranium decay constants for geochronology using ID-TIMS U-Pb data: Geochim. Cosmochim. Acta, v. 70, p. 426-445.

Schoene, B., M. J. de Wit, and S. A. Bowring, in prep, The importance and timing of transtension in the Barberton greenstone belt and the stabilization of the eastern Kaapvaal craton.

Vervoort, J. D., P. J. Patchett, G. E. Gehrels, and A. P. Nutman, 1996, Constraints on early Earth differentiation from hafnium and neodymium isotopes: Nature, v. 379, p. 624-627.

Westraat, J. D., A. F. M. Kisters, M. Poujol, and G. Stevens, 2005, Transcurrent shearing, granite sheeting and the incremental construction of the tabular 3.1 Ga Mpuluzi batholith, Barberton granite-greenstone terrane, South Africa: Jour. Geol. Soc. London, v. 162, p. 373-388.

Wilson, A. C., 1982, 1:250,000 Geological map of Swaziland: Geological Survey Mines Department.

Figure captions:

Fig. 1: Geologic map of the eastern Kaapvaal craton, showing sample locations and crystallization ages from this study. Also shown are the extents of lithospheric blocks (NBGB, SST, AGC, NG) inferred from the surface geology discussed in text, whose boundaries are denoted by red dashed lines. Map compiled from (de Ronde et al., 1994; de Wit, 1982; Lowe and Byerly, 1999; Schoene and Bowring, in prep; Schoene et al., in prep; Wilson, 1982).

Fig. 2: Nd isotopic data and Sm/Nd plotted as a function of distance along the transect A-A', shown in Fig. 1, for magmatic rocks 2.73, 3.1, and 3.2-3.3 Ga. Lithospheric boundaries inferred from surface geology indicated by dashed lines. See text for abbreviations and Fig. 1 for terrane locations in map view. Error bars on ε_{Nd} are fixed at ±0.5 at the 2-sigma level, as discussed in the Appendix, and errors in Sm/Nd are smaller than symbol.

Fig. 3: Sm/Nd (A) and ε_{Nd} (B) values from this study and from the literature plotted as a function of crystallization age, for samples south of the SIFS. gray circles = this study; black cirles = (Carlson et al., 1983); white squares = (Kröner et al., 1996); gray diamonds = (Kröner and Tegtmeyer, 1994); white diamonds = (Hegner et al., 1984). Shaded areas outline the majority of the evolution curves for rocks of the age that corresponds to the oldest portion of a given trajectory. Depleted mantle curve was estimated by drawing a line between 0 and +10 at 4500 and 0 Ma, respectively.

Fig. 4: ε_{Nd} mass-balance for rocks south of the SIFS. Points and 2-sigma errors correspond to weighted mean values of ε_{Nd} for magmas of a given age and the basement rocks present at the time of crystallization. If the magma value is higher, it requires input from a depleted reservoir, if magma and basement rocks values are equal, then $\varepsilon_{Nd}(t)$ can be accounted for by intracrustal Nd recycling.

Fig. 5: Cartoon illustrating the ca. 3.3-3.2 Ga tectonic evolution for basement rocks from the eastern Kaapvaal craton. Arrows in top panel show relative plate motions of the NBGB, and the AGC/SST, while arrows in the bottom panel indicate advection of asthenospheric mantle after final sinking of the oceanic slab, accounting for ca. 3220-3240 Ma magmatism north and south of the BGB. See text for abbreviations and Fig. 1 for surface extent of lithospheric blocks.

Table 1: Sample summary and Sm-Nd data

sample description							analytical data						
Name (a)	Rock unit (b)	Lithology (c)	Latitude (d)	Longitude (d)	age (e)	ref. (e)	[Sm] (f)	[Nd] (f)	147Sm 144Nd (g)	143Nd 144Nd (g)	± (h)	εNd(o) (i)	εNd(t) (i)
ca. 2.73 Ga granites													
WKC0066	Mbabane pluton	co. grained granite	26.3046	31.1551	2690	*1	9.66	59.52	0.09815	0.510563	6	-40.47	-6.38
WKC0071	Hlatikulu granite	med. grained granite	26.7484	31.3851	2730	2	7.25	41.76	0.10493	0.510639	6	-39.00	-6.56
WKC0078	Hlatikulu granite	med. grained granite	26.7556	31.4540	2730	2	9.56	59.28	0.09753	0.510499	6	-41.73	-6.67
WKC0081	Ngwempisi granite	co. grained granite	26.6000	31.1614	2730	**3	16.44	105.68	0.09404	0.510499	8	-41.72	-5.48
EKC02-25	Malendela pluton	co. grained granite	26.2029	31.3340	2730	**3	13.63	94.27	0.08739	0.510235	8	-46.87	-8.23
EKC02-30	Mbabane pluton	co. grained granite	26.3302	31.2626	2690	*1	14.77	96.72	0.09230	0.510356	6	-44.51	-8.41
EKC02-34	Ngwempisi granite	co. grained granite	26.5985	31.1524	2730	**3	22.32	136.33	0.09899	0.510445	6	-42.77	-8.24
EKC02-65	Hlatikulu granite	med. grained granite	26.7349	31.4008	2729	2	16.62	94.46	0.10640	0.510609	6	-39.58	-7.90
EKC02-68	Sinceni pluton	co. grained granite	26.6667	31.5505	2730	**3	10.10	48.56	0.12577	0.511032	6	-31.32	-6.26
BS04-13	Hlatikulu granite	fi. grained granite	26.8651	31.2911	2730	*2	28.39	161.93	0.10599	0.510575	4	-40.24	-8.18
BS04-20	Hlatikulu granite	med. grained granite	26.8543	31.2933	2733	2	19.29	112.78	0.10341	0.510573	6	-40.29	-7.37
BS04-21	Hlatikulu granite	med. grained granite	26.8726	31.2727	2730	2	22.08	149.10	0.08954	0.510309	6	-45.42	-7.61
ca. 3.1 Ga rocks													
KPV99-78	Nelspruit batholith	med. grained granite	25.0772	30.1304	3106	*4,5	15.92	91.07	0.10568	0.510758	12	-36.67	-0.23
KPV99-79	Nelspruit batholith	porphyritic granite	25.3599	30.9937	3106	*4,5	2.77	10.85	0.15456	0.512098	8	-10.53	6.39
KPV99-80	Nelspruit batholith	med. grained granite	25.3599	30.9937	3106	*4,5	6.67	42.10	0.09584	0.510581	8	-40.13	0.24
KPV99-83	Nelspruit batholith	med. grained granite	25.4739	30.9640	3106	*4,5	14.39	86.60	0.10049	0.510523	6	-41.25	-2.76
KPV99-84	Nelspruit batholith	peg. dike	25.4739	30.9640	3106	*4,5	13.46	87.60	0.09292	0.510478	8	-42.14	-0.59
KPV99-86	Stentor pluton	homo. granodiorite	25.6174	31.3064	3106	*4,5	6.34	40.61	0.09441	0.510489	8	-41.91	-0.96
KPV99-87	Stentor pluton	fol. granodiorite	25.6174	31.3064	3106	*4,5	4.93	22.02	0.13539	0.511520	22	-21.80	2.80
KPV99-88	Stentor pluton	pegamtitic granite	25.6174	31.3064	3107	*4,5	2.48	6.96	0.21529	0.513043	6	7.90	0.46
KPV99-89	Stentor pluton	fol. granodiorite	25.6497	31.2426	3107	5	6.69	42.85	0.09437	0.510527	6	-41.18	-0.21
KPV99-91	Stentor pluton	late peg. dike	25.6497	31.2426	3104	5	2.76	11.59	0.14406	0.511504	28	-22.12	-1.10
KPV99-91*	Stentor pluton	late peg. dike	25.6497	31.2426	3104	5	2.13	8.89	0.14516	0.511504	16	-22.12	-1.49
KPV99-102	Mpuluzi batholith	med. grained granite	26.0834	30.7348	3107	*4	1.25	8.52	0.08895	0.510190	8	-47.75	-4.64
WKC0045	Mpuluzi batholith	med. grained granite	26.1565	30.7532	3107	*4	15.15	81.39	0.11254	0.510754	6	-36.76	-3.08
WKC0055	Pigg's Peak batholith	med. grained granite	26.0674	31.1830	3140	*6	5.63	35.18	0.09667	0.510474	6	-42.22	-2.09
EKC02-49	Mpuluzi batholith	fi. grained granite	26.1898	30.9604	3107	*4	5.91	33.97	0.10510	0.510625	6	-39.27	-2.61
EKC02-55	Mpuluzi batholith	med. grained granite	26.4645	31.0050	3107	*4	5.57	30.68	0.10970	0.510699	6	-37.83	-3.01
EKC03-1	Pigg's Peak batholith	med. grained granite	26.0333	31.1667	3140	*6	5.35	29.42	0.11003	0.510780	6	-36.23	-1.54
3.2-3.3 Ga rocks													
KPV 99-81	Nelspruit batholith	amphibolite xenolith	25.3599	30.9937	3250	**	11.17	62.06	0.10880	0.511127	14	-29.47	7.72
KPV 99-82	Nelspruit basement	banded gneiss	25.4739	30.9640	3258	*5	11.28	70.57	0.09665	0.510514	8	-41.43	0.60
KPV99-85	Kaap Valley pluton	fol. grained tonalite	25.7688	31.0613	3227	*4,7	2.96	15.35	0.11668	0.510976	8	-32.43	0.88
KPV 99-90	Stentor basment	banded gneiss	25.6497	31.2426	3258	5	4.33	23.84	0.10992	0.510821	8	-35.44	1.02
KPV 99-90*	Stentor basment	banded gneiss	25.6497	31.2426	3258	5	4.30	23.83	0.10906	0.510801	8	-35.83	1.00
KPV99-92	Kaap Valley pluton	fol. tonalite	25.7570	30.8452	3227	*4,7	3.33	16.73	0.12020	0.511078	6	-30.42	1.43
KPV99-94	Nelshoogte Pluton	fol. granoriorite	25.8912	30.6235	3236	5	0.70	3.97	0.10584	0.510763	10	-36.57	1.35
KPV99-95	Stolzburg pluton - young	aplitic dike	26.0218	30.7442	3213	*4,5	3.07	18.82	0.09859	0.510550	6	-40.73	-0.09
KPV99-97	Stolzburg pluton - young	fi. grained granodiorite	26.0218	30.7442	3213	*4,5	2.71	15.53	0.10558	0.510645	8	-38.87	-1.14
KPV99-98	Stolzburg pluton - young	fi. grained granodiorite	26.0218	30.7442	3213	*4,5	2.16	11.73	0.11133	0.510767	6	-36.50	-1.14
KPV99-101	Dalmein pluton	med. grain granodiorite	26.0733	30.9007	3216	*4	6.47	34.80	0.11250	0.510800	6	-35.86	-0.95
KPV99-103	Mpuluzi batholith	mafic tonalite xenolith	26.0834	30.7348	3200	**	5.45	25.46	0.12937	0.511202	8	-28.01	-0.10
WKC0068	Ancient Gneiss Complex	late pegmatitic dike	26.3455	31.1453	3200	**	2.13	11.13	0.11587	0.510874	6	-34.41	-1.08
WKC0079	Usutu suite	med. grain granodiorite	26.5216	31.2529	3227	*2	0.73	4.96	0.08919	0.510242	6	-46.73	-1.98
WKC0088	Vlakplaats plug	med. grain granodiorite	26.1403	30.9809	3230	5	3.47	19.97	0.10515	0.510651	8	-38.77	-0.65

Name (a)	Rock unit (b)	Lithology (c)	Latitude (d)	Longitude (d)	age (e)	ref. (e)	[Sm] (f)	[Nd] (f)	147Sm/144Nd (g)	143Nd/144Nd (g)	± (h)	εNd(o) (i)	εNd(t) (i)
EKC02-1	Dalmein pluton	med. grain granodiorite	26.0884	30.9373	3216	*4	8.02	52.03	0.09319	0.510413	6	-43.41	-0.49
EKC02-51	Kaap Valley pluton	fol. tonalite	25.7578	30.8455	3227	7	2.49	13.60	0.11081	0.510825	8	-35.36	0.38
EKC03-18	Usutu suite	med. grain granodiorite	26.2841	31.3904	3186	2	2.37	14.13	0.10151	0.510611	6	-39.54	-0.32
AGC01-4	Usutu suite	fol. tonalite	25.8952	31.3069	3226	6	7.62	41.98	0.10978	0.510716	6	-37.50	-1.36
EKC02-23	Usutu suite	megacryst. granodiorite	26.2657	31.4450	3230	2	5.06	31.24	0.09796	0.510734	4	-37.15	4.00
EKC02-24	Usutu suite	med. grained tonalite	26.2657	31.4450	3227	2	8.97	44.72	0.12123	0.510971	6	-32.52	-1.13
EKC02-32	Usutu suite	med. grained tonalite	26.2841	31.3904	3232	2	8.87	60.36	0.08882	0.510217	6	-47.22	-2.28
EKC02-35	Usutu suite	med. grain leucotonalite	26.6010	31.1666	3236	2	3.30	20.12	0.09923	0.510454	6	-42.61	-2.04
EKC03-21	Usutu suite	med. grained tonalite	26.5533	31.3096	3232	2	2.65	16.33	0.09806	0.510482	4	-42.06	-1.00
EKC03-23	Usutu suite	fol. tonalite	26.0547	31.1472	3230	2	8.27	41.80	0.11959	0.511074	6	-30.50	1.62
EKC03-33	Usutu suite	megacryst. granodiorite	26.0540	31.1529	3227	2	10.61	60.24	0.10648	0.510587	6	-40.00	-2.46
EKC02-64	Nhlangano gneiss	porph. banded gneiss	26.6675	31.3977	3266	2	2.68	20.87	0.07762	0.509969	6	-52.06	-1.92
EKC02-66	Nhlangano gneiss	tonalitic banded gneiss	26.8003	31.3371	3266	2	1.68	10.22	0.09970	0.510542	6	-40.88	-0.03
EKC03-35	Nhlangano gneiss	tonalitic banded gneiss	26.8760	31.2805	3300	2	5.89	37.81	0.09418	0.510358	6	-44.47	-0.84
EKC03-36	Nhlangano gneiss	megacryst grano. gneiss	26.8764	31.2819	3300	2	3.99	22.40	0.10762	0.510689	6	-38.01	-0.10
EKC03-37	Nhlangano gneiss	mphibolite banded gneis	26.8763	31.2834	3300	2	4.93	19.61	0.15188	0.511574	6	-20.76	-1.70
BS04-6	Usutu suite	med. grain granodiorite	26.5766	31.3455	3219	2	0.84	6.49	0.07788	0.510098	8	-49.54	-0.23
BS04-8	Usutu suite	med. grain leucotonalite	26.5766	31.3455	3232	2	2.42	17.71	0.08256	0.510077	6	-49.96	-2.42
BS04-18	Nhlangano gneiss	aplitic banded gneiss	26.8540	31.2987	3300	*2	6.91	38.56	0.10835	0.510715	6	-37.51	0.09
>3.45 Ga rocks													
KPV 99-96	Stolzburg pluton	ton./grano. banded gneiss	26.0218	30.7442	3445	5	3.16	16.76	0.11402	0.510788	8	-36.08	0.67
WKC0048	Ancient Gneiss Complex	tonalitic banded gneiss	25.9098	31.3030	3664	*5,8	19.60	143.33	0.08268	0.510192	6	-47.71	6.29
WKC0049	Ancient Gneiss Complex	tonalitic banded gneiss	25.9098	31.3030	3550	*5,8	6.18	22.70	0.16460	0.511676	6	-18.77	-4.10
WKC0056	Ancient Gneiss Complex	tonalitic banded gneiss	26.0642	31.1831	3550	*5,8	5.31	24.60	0.13047	0.511074	6	-30.51	-1.81
WKC0067	Ancient Gneiss Complex	tonalitic banded gneiss	26.3455	31.1453	3500	*5,8	14.01	72.84	0.11631	0.510815	6	-35.56	0.75
WKC0082	Ancient Gneiss Complex	mphibolite banded gneis	26.6747	31.1266	3550	*5,8	6.60	24.72	0.16152	0.511757	6	-17.18	-1.07
WKC0083	Ancient Gneiss Complex	peg. banded gneiss	26.6747	31.1266	3550	*5,8	3.15	12.31	0.15466	0.511585	6	-20.53	-1.28
WKC0084	Ancient Gneiss Complex	tonalitic banded gneiss	26.6747	31.1266	3550	*5,8	2.52	12.71	0.11969	0.510879	4	-34.31	0.98
WKC0087	Steynsdorp pluton	fol. tonalite-granodiorite	26.1779	30.9871	3517	*4,5	3.06	14.34	0.12905	0.511316	8	-25.79	4.96
AGC01-1	Tsawela gneiss	tonalitic banded gneiss	26.7558	30.9794	3450	*9	3.22	16.38	0.11879	0.510850	6	-34.88	-0.20
AGC01-2	Ancient Gneiss Complex	tonalitic banded gneiss	26.7141	31.0448	3550	*5,8	1.06	7.57	0.08457	0.510182	8	-47.91	3.49
AGC01-5	Ancient Gneiss Complex	tonalitic banded gneiss	25.8961	31.3104	3662	5	7.59	37.98	0.12073	0.510790	6	-36.05	-0.11
EKC02-20	phophonyane granite	fi. grained fol. granite	25.8961	31.3104	3545	5	2.82	15.22	0.11188	0.510533	6	-41.06	-2.27
EKC02-40	Steynsdorp pluton	fol. tonalite-granodiorite	26.1779	30.9604	3517	5	2.56	13.99	0.11051	0.510709	6	-37.63	1.50
EKC03-3	Stolzburg pluton	homo. granodiorite	25.9740	30.7630	3445	5	0.78	4.08	0.11639	0.510813	10	-35.61	0.09
BS04-7	Tsawela gneiss	tonalitic banded gneiss	26.5766	31.3455	3411	2	3.86	22.96	0.10168	0.510433	6	-43.02	-1.21

sample description | **analytical data**

(a) sample name, grouped by approximate age. * indicates duplicate analysis
(b) name of rock unit or locality for rocks whose association is difficult
(c) lithology of rock based on hand-sample description
(d) latitude and longitdue derived by hand-held global positioning system
(e) approximate U-Pb crystallization age in Ma, with references.
No symbol, # = exact rock sample dated; *,# = same unit dated, but different sample in this study
**,# = inferred same unit dated, based on rock type or map correlation; **, no number = poor age constraints
1) Layer et al. (1989); 2) Schoene and Bowring (in prep.); 3) Wilson (1982); 4) Kamo and Davis (1994); 5) Schoene et al. (in prep.); 6) Schoene and Bowring (in review); 7) Schoene et al. (2006); 8) Kröner et al. (1989); 9) Kröner and Tegtmeyer (1994)
(f) concentrations in ppm, as determined by isotope dilution
(g) isotopic ratios corrected for mass fractionation (see text) and 100 pg Sm and Nd blank. Precision on Sm/Nd ratios ≤0.1%
(h) 2-sigma standard error of fractionation-corrected ratio
(i) Epsilon Nd value at the present day (0) and the time of crystallization (t), calculated as follows: $[(^{143}Nd/^{144}Nd)_{sample}(^{143}Nd/^{144}Nd)_{(CHUR)}-1] * 10^4$
see text for CHUR values used.

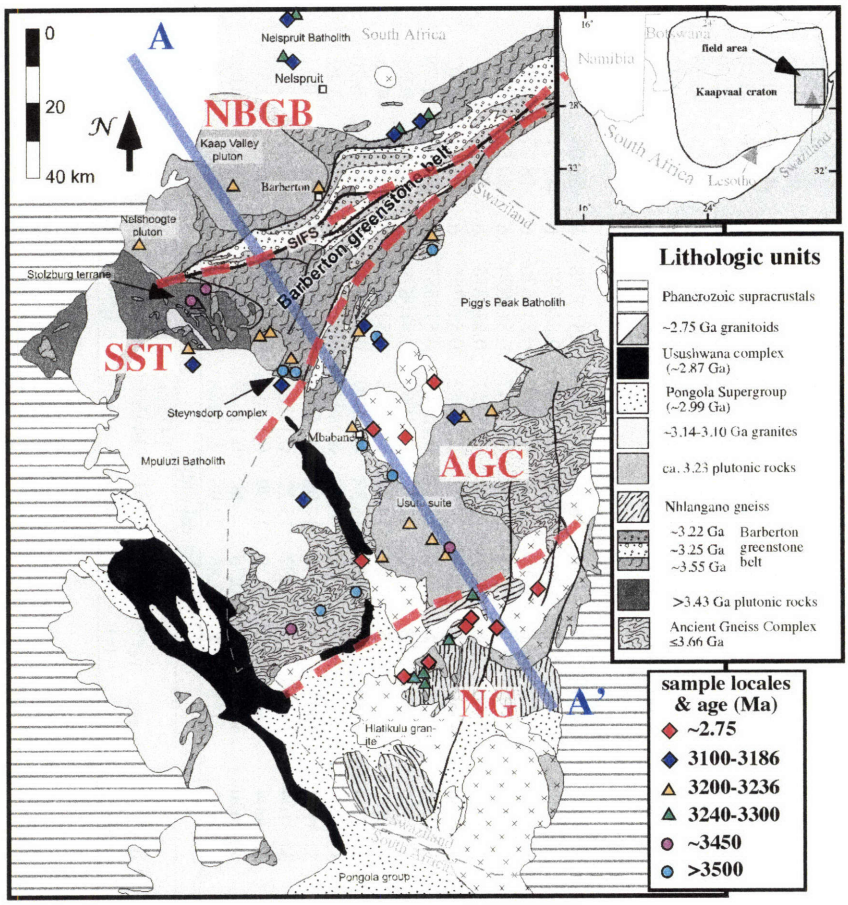

Fig1. Schoene et al.

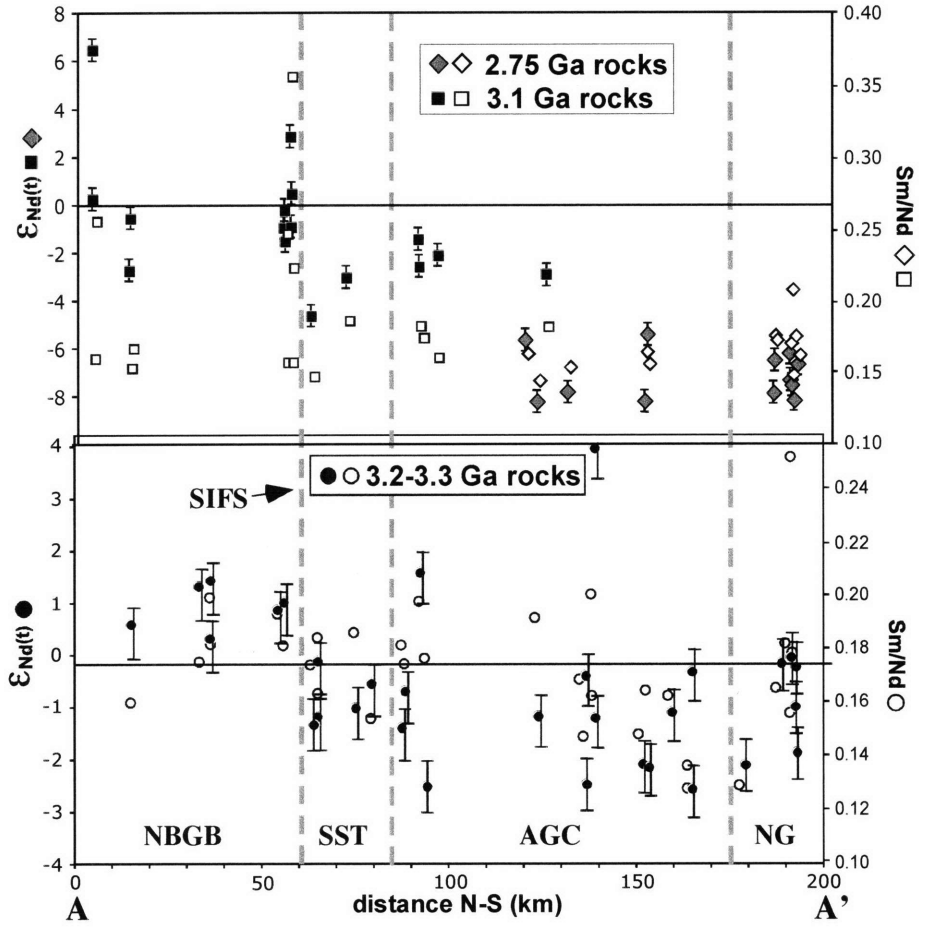

Fig. 2 Schoene et al.

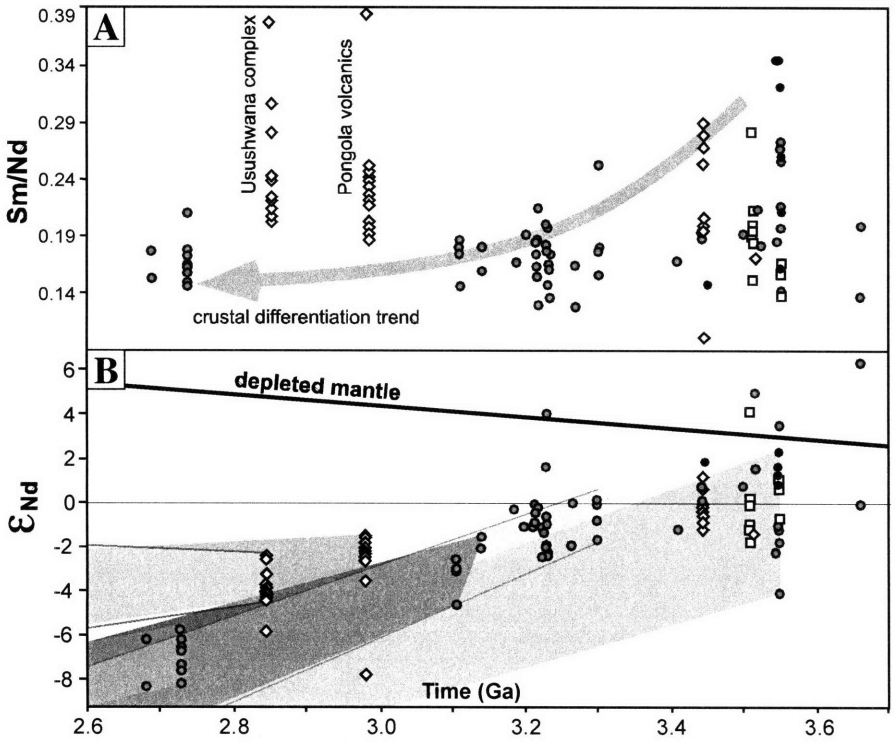

Fig. 3 Schoene et al.

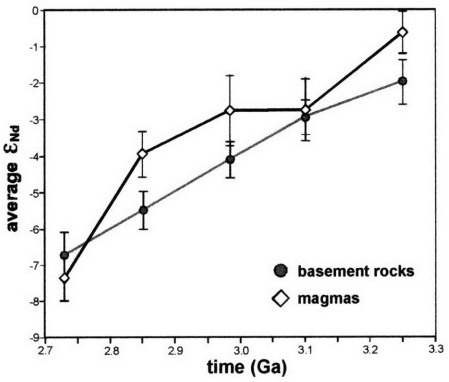

Fig. 4 Schoene et al.

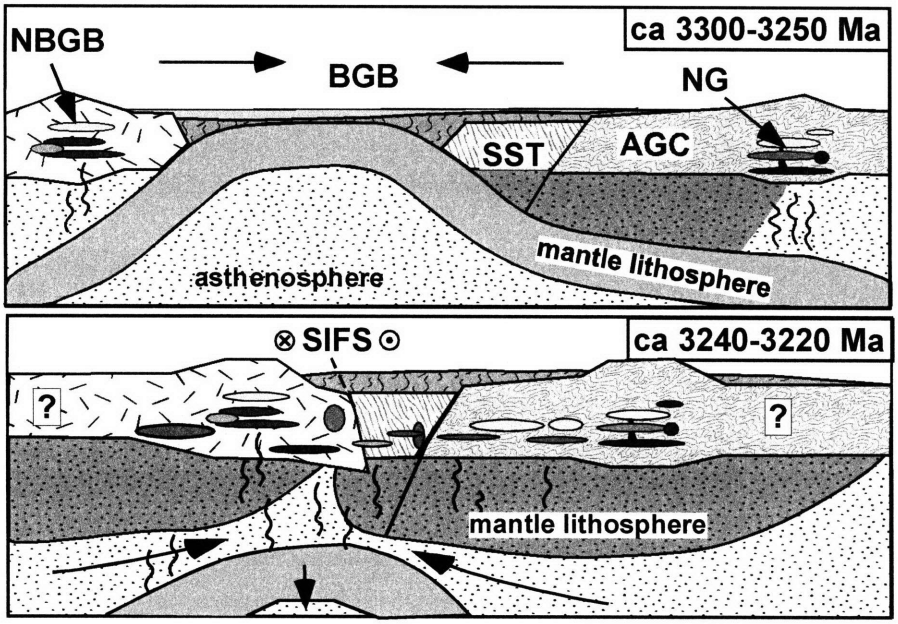

Fig. 5 Schoene et al.

CHAPTER 5

Reassessing the Uranium decay constants for geochronology using ID-TIMS U-Pb data.

Blair Schoene[1], James L. Crowley[1], Daniel J. Condon[1], Mark D. Schmitz[2], Samuel A. Bowring[1].

1. Department of Earth, Atmospheric and Planetary Sciences, Massachusetts Institute of Technology, Cambridge, MA 02139, USA.
2. Department of Geosciences, Boise State University, Boise, ID 83725, USA.

Published in *Geochimica et Cosmochimica Acta 70: 426-445, 2006*

ABSTRACT

As the internal precision of radiometric dates approaches the 0.1% level, systematic biases between different methods have become apparent. Many workers have suggested that calibrating other decay constants against the U-Pb system is a viable solution to this problem. We test this assertion empirically and quantitatively by analyzing U-Pb systematics of zircon and xenotime on the single- to sub-grain scale by high-precision ID-TIMS geochronology on eleven rock samples ranging from 0.1 to 3.3 Ga. Large statistically equivalent datasets give $^{207}Pb/^{206}Pb$ dates that are systematically older than $^{206}Pb/^{238}U$ dates by ~0.15% in Precambrian samples to as much as ~3.3% in Mesozoic samples, suggesting inaccuracies in the mean values of one or both of the U decay constants. These data are used to calculate a ratio of the U decay constants that is lower than the accepted ratio by 0.09% and is a factor of five more precise. Four of the samples are used to augment existing data from which the U-Pb and $^{40}Ar/^{39}Ar$ systems can be compared. The new data support most previous observations that U-Pb and $^{207}Pb/^{206}Pb$ dates are older than $^{40}Ar/^{39}Ar$ by $\leq$ 1%, though scatter in the amount of offset in samples as a function of age suggests that the bias is not entirely systematic, and may incorporate interlaboratory biases and/or geologic complexities. Studies that calibrate other decay schemes against U-Pb should include an assessment of inaccuracies in the U decay constants in addition to other systematic biases and non-systematic geologic uncertainty.

1. INTRODUCTION

Since the discovery of radioactivity and the birth of geochronology at the turn of the last century, increasingly precise dates for minerals and rocks have been used to establish a time-line for the history of the planet. In the past two decades, improvements in analytical techniques and instrument design have led to an explosion of high-precision dates using many different chronometers, such that it is now possible to explore the rates and durations of events and processes from planetary accretion to human history at the 0.1-0.2% level. However, such unparalleled precision has also revealed that systematic biases between different methods often exceed internal analytical precision, stressing the need to reevaluate the currently accepted values and associated errors for long-lived radionuclide decay constants (Begemann et al., 2001; Min et al., 2000; Renne et al., 1998a; Steiger and Jäger, 1977).

It is useful to examine this intersystem bias using the U-Pb and $^{40}Ar/^{39}Ar$ methods because they are the most widely applicable, precise, and broadly utilized geochronologic techniques, primarily due to the high concentrations of U and K in many commonly dated accessory and modal minerals, and the relatively long half-lives of the parent isotopes ($t_{1/2}$: $^{40}K \sim 1.25$ Gyr; $^{238}U \sim 4.46$ Gyr; $^{235}U \sim 0.70$ Gyr). Numerous studies (Min et al., 2000; Min et al., 2001; Nomade et al., 2004; Renne, 2000; Renne et al., 1998a; Schmitz and Bowring, 2001; Villeneuve et al., 2000) have noted that $^{40}Ar/^{39}Ar$ dates are systematically younger than U-Pb dates from rapidly cooled rocks and do not overlap with U-Pb dates if one ignores systematic uncertainties. Min et al. (2000), Renne (2000), and Renne et al. (1998a) suggest that much of the bias can be accounted for by inaccuracies in the ^{40}K decay constant and physical constants, which differ by ~2% from

those used in other scientific communities. Due to the high precision of the U decay constant measurements (0.11 and 0.14% for ^{238}U and ^{235}U, respectively; Jaffey et al., 1971) and because of the internal check of their accuracy provided by the dual decay of ^{238}U to ^{206}Pb and ^{235}U to ^{207}Pb, it has been suggested that the $^{40}Ar/^{39}Ar$ system may be calibrated against the U-Pb system (Begemann et al., 2001; Renne et al., 1998a; Villeneuve et al., 2000). Similarly, decay constants for several other lower-precision decay schemes (e.g. Lu-Hf, Re-Os and Th-Pb) have been in part derived or tuned by comparison with U-Pb dates (e.g. Amelin and Zaitsev, 2002; Begemann et al., 2001; Chen et al., 2002; Scherer et al., 2001; Söderlund et al., 2004). Complicating this practice, however, are studies suggesting that the U decay constants of Jaffey et al. (1971) may be slightly inaccurate (though within the reported errors), based on high-precision U-Pb multigrain zircon data from Phanerozoic samples that have $^{207}Pb/^{206}Pb$ dates that are systematically older than the $^{206}Pb/^{238}U$ dates (Mattinson, 1994a; Mattinson, 1994b; Mattinson, 2000). Given that Pb-loss, inheritance, intermediate daughter product disequilibria, or small inaccuracies in tracer calibration could also produce this effect, it is crucial to generate additional high-precision U-Pb data in order to assess the accuracy of the U decay constants. Inaccuracies in the U decay constants not only limit the power of the U-Pb system to resolve absolute time, but also complicate high-precision intercalibration with other decay schemes.

The purpose of this contribution is to present high-precision U-Pb zircon and xenotime data from eleven rocks whose crystallization ages span over three billion years in order to 1) check for systematic internal bias in the U-Pb system by evaluating concordance of high-*n* statistically equivalent datasets, and 2) to compare U-Pb results

from this study and from the literature with existing $^{40}Ar/^{39}Ar$ or K-Ar data. We have purposely chosen samples in which we have resolved or eliminated the ubiquitous effects of Pb-loss and inheritance through zircon preparation methods such as the air-abrasion (Krogh, 1982) and chemical-abrasion (i.e. CA-TIMS; Mattinson, 2003; Mattinson, 2005) techniques, and analytical precision on single analyses are comparable to the quoted errors on the U decay constants; only such datasets provide the means to evaluate the accuracy of the U decay constants quantitatively (Mattinson, 2000; Schmitz et al., 2003). Because these samples represent over three billion years of geologic time, systematic biases in the U-Pb and $^{40}Ar/^{39}Ar$ dating techniques, which propagate as a function of age, are more readily evaluated.

2. ANALYTICAL METHODS

2.1. Sample preparation

Minerals were extracted from rock samples by standard crushing, Wilfley table, heavy-liquid and magnetic separation. Fragments from large crystals and single zircons were broken into smaller fragments with a fine-tipped steel tool. Analyzed zircon was selected from the least magnetic fraction and selected based on the absence of cracks, inclusions, and surface contamination.

In order to minimize Pb-loss and increase the probability of concordance, zircon was subjected to one or both of the following techniques: 1) standard air-abrasion (Krogh, 1982) and total dissolution, and 2) a modified version of the chemical-abrasion technique (Mattinson, 2003; Mattinson, 2005). Zircon that was only abraded was ultrasonically cleaned in 30% HNO_3 for an hour, fluxed in 30% HNO_3 at ~80°C for an

hour, and rinsed in ultrapure acetone and H_2O before being loaded into 300 μl Teflon FEP microcapsules and spiked with a mixed ^{233}U-^{235}U-^{205}Pb tracer. Zircon was dissolved in Parr vessels in ~120 μl 29M HF with ~25 μl 30% HNO_3 at ~210°C for 48 hours, dried to fluorides, and then re-dissolved in 6M HCl at ~180°C overnight. For the CA-TIMS technique, zircon was placed in a muffle furnace at 900 ± 20°C for ~60 hours in quartz beakers before being transferred to 300 μl Teflon FEP microcapsules, placed in a Parr vessel and leached in ~120 μl 29M HF + ~25 μl 30% HNO_3 for 12-14 hours at ~180 °C. The acid solution was removed, and fractions were rinsed in ultrapure H_2O, fluxed on a hotplate at ~80 °C for an hour in 6M HCl, ultrasonically cleaned for an hour, and then placed back on the hotplate for an additional 30 minutes. The HCl solution was removed and the fractions were again rinsed in ultrapure acetone and H_2O, spiked, and fully dissolved using the procedure described above.

Xenotime was ultrasonically cleaned for an hour in H_2O, washed in 30% HNO_3 at ~50 °C for 10 minutes, and rinsed in ultrapure acetone and H_2O before being loaded into 300 μl Teflon FEP microcapsules and spiked with a mixed ^{233}U-^{235}U-^{205}Pb tracer. Xenotime was dissolved in 12M HCl at ~180 °C for 48 hours in a Parr vessel, dried down, and then re-dissolved in 6M HCl at ~180 °C overnight. U and Pb for all minerals were separated using an HCl based anion-exchange chromatographic procedure (Krogh, 1973).

2.2. Mass spectrometry and blank estimation

Most U and Pb isotopic measurements were performed on a VG Sector-54 multi-collector thermal-ionization mass spectrometer at MIT, but a few were analyzed with the Isoprobe-

T multi-collector thermal-ionization mass spectrometer at MIT. Pb and U were loaded together on a single Re filament in a silica-gel/phosphoric acid mixture (Gerstenberger and Haase, 1997). Pb was measured by either peak-hopping on a single Daly detector (for smaller beams) or a dynamic Faraday-Daly routine (F-D) that cycles between placing mass 204 in the axial Daly collector and masses 205-208 on the H1-H4 Faraday detectors to placing mass 205 in the axial Daly and masses 206-208 in the H1-H3 Faradays, providing real-time Daly gain correction. U isotopic measurements were made in static Faraday mode or, in very low-U samples, on the Daly detector. Mass discrimination for Pb on the Daly detector was determined to be 0.25 ± 0.04 %/a.m.u. over a wide temperature range based on analysis of the NBS-981 common Pb standard and spiked aliquots of NBS-983. Mass fractionation and detector bias on the F-D routine was determined to be 0.07 ± 0.04 %/a.m.u. for the VG Sector-54 mass spectrometer and 0.09 ± 0.04 %/a.m.u. for the Isoprobe-T mass spectrometer based on cross-calibration with the single Daly detector runs on numerous samples and spiked aliquots of NBS-983. U mass fractionation is calculated in real-time using a ^{233}U-^{235}U double spike. All common Pb for the zircon and xenotime analyses was attributed to procedural blank based on frequent total analytical blank determinations. A sensitivity test shows that the composition of the common Pb in all minerals had no effect on the calculated dates. U blanks are difficult to precisely measure, but are <0.1 pg. The $^{207}Pb/^{206}Pb$ dates are insensitive to the U blank, but variability in the U blank on low U samples in this study can affect discordance. Therefore, a value of 0.1 pg ± 50% was used in all data reduction, and the consistency of the discordance in the results suggests this is accurate.

2.3. Tracer Calibration

Improvements in analytical protocols (e.g. reduction in Pb and U blanks, improved ionization, measurement of U isotopes as oxide species) in routine U-Pb analysis has led to the interpretation of high-*n* datasets at unprecedented precision, and precipitated the recalibration of the MIT mixed ^{233}U-^{235}U-^{205}Pb tracer solution to ensure the accuracy of U-Pb dates. This recalibration was conducted from September to December of 2004. The tracer isotopic composition of U was redetermined using improved methods to control mass fractionation, including analysis as the oxide, critical mixture methods (Hofmann, 1971; Roddick et al., 1992). The isotopic composition of Pb in the tracer was determined by a combination of Daly and F-D analyses on large tracer aliquots and the same fractionation corrections made for geologic samples were used to correct these data. The calibration was carried out using standard isotope dilution methods against three mixed U-Pb gravimetric solutions prepared in independent laboratories (J. Mattinson, UCSB, pers. comm. 2004; R. Parrish, NIGL, pers. comm. 2004; and one mixed at MIT in Sept. 2004; these solutions are freely available for distribution through the EARTHTIME Network - visit www.earth-time.org). The gravimetric solutions were prepared by dissolving and quantitatively mixing different Pb and U metals of certified composition (UCSB and NIGL) and also by mixing separate Pb and U solutions of certified composition (MIT). Mass discrimination was calculated using internal U and Pb corrections (the MIT solution contained only enriched ^{206}Pb, providing no reference isotope for the internal fractionation correction. For these solutions, the 2σ standard deviation of the fractionation determinations from the other solutions, found to be 0.12 ± 0.03 %/a.m.u., was used). Errors on the calibration were propagated using standard

techniques, and incorporate the uncertainties in the measured isotopic ratios of calibration solutions (and the calculated Pb and U mass fractionation values) and the Pb and U isotopic compositions of the tracer and the gravimetric solutions. The standard error from a total of 11 experimental mixtures from the three gravimetric solutions was calculated in two ways: 1) by taking the weighted mean of the calculated $^{205}Pb/^{235}U$ from the 11 experiments (2SE = 0.015%; MSWD = 0.3; MSWD = mean square of the weighted deviates; York, 1966; York, 1967), or 2) by taking the weighted mean of the weighted means of the three solution determinations (2SE = 0.015%; MSWD = 0.2). We prefer the latter method in theory, because it would robustly account for any systematic errors arising from the weighing and mixing of the different gravimetric solutions (those errors were not propagated into the calculations because they were difficult to accurately determine for all three solutions). The low MSWDs of weighted means from these determinations suggest that systematic errors between the solutions do not exist and that we are likely overestimating one source of error. It is important to note that the new tracer composition used in this study differs from that used in previous contributions from the MIT laboratory, and the implications of this will be discussed later in the text.

2.4. Determination of reported ages and errors

Rigorous and transparent error propagation is important for intercalibrating geochronologic data between different laboratories and different methods. Quantitative discussions of error propagation and statistical analysis for the U-Pb and $^{40}Ar/^{39}Ar$ methods are presented elsewhere (Ludwig, 1980; Ludwig, 1998; Ludwig, 2000; Mattinson, 1987; Min et al., 2000; Renne et al., 1998a; Renne et al., 1998b). We

highlight aspects of random versus systematic errors in geochronology below. Sample-specific errors (often referred to as internal errors) are those that result from random fluctuations in the experimental conditions, and define the precision of the resulting measurements. For the U-Pb method internal errors include counting statistics, uncertainties in correcting for mass discrimination, and the uncertainty in the assignment of a composition for various sources of common Pb (e.g. laboratory blank versus initial Pb in the crystal; in this study the contribution of common Pb to the overall uncertainty is negligible). Internal errors for $^{40}Ar/^{39}Ar$ include analytical uncertainties and a variable neutron flux within an individual irradiation package. One must incorporate internal errors when testing for the equivalency of a given dataset, in turn allowing the quantitative comparison of dates relative to one another from a given laboratory.

Systematic, or "external," errors are those that affect the accuracy of measurements, and must be evaluated and applied depending on the specific situation. For example, the uncertainties in the ages of standards used in $^{40}Ar/^{39}Ar$ geochronology only need to be incorporated when comparing dates between unknowns that use a different set of flux monitors or a different primary standard (e.g. Renne et al., 1998b). A fundamental source of systematic error in ID-TIMS geochronology is the Pb/U ratio of the mixed Pb-U tracer used in isotope dilution calculations; this source of error should be incorporated when comparing dates measured with differing isotopic spike mixtures, for example in different laboratories. Other systematic errors that are necessary when comparing data from different geochronologic methods include uncertainties in the decay constants of ^{235}U, ^{238}U and ^{40}K, and physical constants such as the $^{40}K/K$ ratio and the branching ratio of ^{40}K (Min et al., 2000; Renne et al., 1998b).

For our purposes, it is beneficial to present data at each level of error propagation. Data reduction, age calculation and the generation of concordia plots use the algorithms of Ludwig (1980), and/or the statistical reduction and plotting program ISOPLOT (Ludwig, 1991). For efficiency, U-Pb errors on analyses from this study are reported in the following manner, unless otherwise noted: ± X/Y/Z, where X is the internal error in absence of all systematic errors, Y includes the tracer calibration error, and Z includes both tracer calibration and decay constant errors of Jaffey et al. (1971). For $^{207}Pb/^{206}Pb$ dates, tracer errors are negligible and Y is not reported (so it reads ± X/Z). The MSWD (mean square of the weighted deviates; York, 1966; York, 1967) of equivalence refers to the probability that a weighted-mean population of isotopic ratios is statistically equivalent and is calculated prior to the addition of systematic errors (Ludwig, 1998). Concordia diagrams for the eleven samples analyzed in this study are shown in figure 1, data are presented in table 1, and U-Pb dates of weighted mean clusters are summarized in figure 2. Errors in K-Ar and $^{40}Ar/^{39}Ar$ data considered in this paper are calculated using the methods of Karner and Renne (1998) and Renne et al. (1998b) when not provided by the original authors. All errors for U-Pb data are standard errors of the mean, unless otherwise noted, and U-Pb, K-Ar, and $^{40}Ar/^{39}Ar$ age uncertainties are presented at the 95% confidence level.

3. SAMPLE DESCRIPTION, PREVIOUS GEOCHRONOLOGY AND U-Pb RESULTS

3.1. Narryer complex granite (JCA-62-02)

Homogeneous, weakly foliated biotite granite in the Narryer gneiss complex, northwestern Yilgarn Craton, was collected immediately north of the Jack Hills adjacent to the Sharpe bore well. Cathodoluminescence (CL) imaging shows that most zircons are dominated by concentric oscillatory zoning and some have narrow weakly zoned rims. After CL imaging, three grains that lacked obvious rims were removed from the epoxy mount, annealed, air-abraded, and broken into 10-20 fragments, some of which were chemical-abraded and analyzed. Four fragments from one grain and one fragment from another grain form a statistically significant cluster (MSWD of equivalence = 0.9). They yield a weighted mean $^{207}Pb/^{206}Pb$ date of 3313.7 ± 0.3/7.6 Ma (MSWD = 0.7), a weighted mean $^{207}Pb/^{235}U$ date of 3312.2 ± 0.3/0.5/1.8 Ma (MSWD = 0.6), and a weighted mean $^{206}Pb/^{238}U$ date of 3309.7 ± 0.7/1.1/3.8 Ma (MSWD = 1.1).

3.2. Kaap Valley Pluton (EKC02-51)

The Kaap Valley pluton is a tonalitic multi-phase intrusion from the southeast Kaapvaal craton, southern Africa. Kamo and Davis (1994) dated six zircon and titanite fractions from two compositionally distinct phases of the pluton, giving a weighted mean $^{207}Pb/^{206}Pb$ date of 3227 ± 1 Ma (excluding systematic errors). The equivalence of titanite and zircon dates, in combination with $^{207}Pb/^{206}Pb$ apatite dates of ~3225.6 Ma (Schoene and Bowring, 2003), indicate a very rapid post intrusion cooling history for the Kaap Valley pluton, assuming a closure temperature of ~600 °C for titanite (Cherniak, 1993; Corfu and Stone, 1998; Frost et al., 2000) and ~500 °C for apatite (Chamberlain and Bowring, 2000; Cherniak et al., 1991). Single-grain step-heating experiments on hornblende yield a weighted mean $^{40}Ar/^{39}Ar$ date of 3213.4 ± 4.3 (MSWD = 0.4; internal

errors, excluding 2 of 6 analyses whose plateaus comprise <60% of total Ar released; Layer et al., 1992) relative to the primary K-Ar standard 3GR (a.k.a. Hb3gr) at 1071 Ma (Zartman, 1964).

Our sample was collected from a roadcut located several kilometers east of the pass on R61 between Badplaas and Barberton, Mpumalanga, South Africa. This phase of the pluton is a fine-grained biotite tonalite containing abundant zircon and apatite. Thirteen air-abraded zircons, one multi-grain zircon fraction, and four chemical-abraded grains were analyzed. All analyses except for one form a statistically significant cluster (MSWD of equivalence = 0.5). They yield a weighted mean $^{207}Pb/^{206}Pb$ date of 3227.2 ± 0.2/7.4 Ma (MSWD = 0.5), a weighted mean $^{207}Pb/^{235}U$ date of 3224.9 ± 0.4/0.5/1.8 Ma (MSWD = 0.6), and a weighted mean $^{206}Pb/^{238}U$ date of 3221.4 ± 0.8/1.2/3.6 Ma (MSWD = 0.5).

3.3. Eglab Porphyry (EGB-032)

EGB-032 is an unmetamorphosed hornblende-biotite dacite porphyry derived from the Eglab region of the Requibath massif, west Africa (Peucat et al., 2005). Hornblende gives a weighted mean step-heating $^{40}Ar/^{39}Ar$ date of 2054.6 ± 2.4 (external sources of error excluded), based on an age of 28.02 Ma for the Fish Canyon sanidine (P. Renne, personal comm. 2005). Of fourteen analyses, four air-abraded and seven chemical-abraded analyses form a single discordant cluster (MSWD of equivalence = 0.2). They yield a weighted mean $^{207}Pb/^{206}Pb$ date of 2071.6 ± 0.4/6.1 (MSWD = 0.2), a weighted mean $^{207}Pb/^{235}U$ date of 2069.5 ± 0.4/0.5/1.7 Ma (MSWD = 0.3), and a weighted mean $^{206}Pb/^{238}U$ date of 2067.5 ± 0.7/0.9/2.8 (MSWD = 0.2).

3.4. QGNG

The QGNG zircon standard is derived from a quartz-gabbro/norite gneiss from the Eyre peninsula, southern Australia. Black et al. (2003b) assigned a weighted mean $^{207}Pb/^{206}Pb$ date of 1851.6 ± 0.6 Ma (MSWD = 0.6) and a weighted mean $^{206}Pb/^{238}U$ date of 1842.0 ± 3.1 Ma (both exclude decay constant errors) using a subset of the most precise, least discordant analyses that were obtained from a single laboratory. In their dataset, the $^{206}Pb/^{238}U$ dates show more variability (0.4%) than the $^{207}Pb/^{206}Pb$ dates, and the $^{206}Pb/^{238}U$ date was taken as the most reliable value based on the inference that the volumetrically dominant interior parts of the grains had lost ~0.5% of their radiogenic Pb. Our dataset includes seven chemical-abraded grains that form a discordant cluster (MSWD of equivalence = 1.5). They yield a weighted mean $^{207}Pb/^{206}Pb$ date of 1851.5 ± 0.3/5.8 Ma (MSWD = 1.2), a weighted mean $^{207}Pb/^{235}U$ date of 1850.0 ± 0.5/0.6/1.7 Ma (MSWD = 1.9), and a weighted mean $^{206}Pb/^{238}U$ date of 1848.7 ± 0.7/0.9/2.7 Ma (MSWD = 2.1).

3.5. Duluth Complex anorthisitic series (AS3)

AS3 is from the Duluth Complex anorthositic series, northern Minnesota, USA (Paces and Miller, 1993; Schmitz et al., 2003). Schmitz et al. (2003) assigned a U-Pb concordia age of 1099.1 ± 0.2 Ma (± 1.2 Ma including tracer calibration and decay constant errors) using a subset of concordant analyses, which agrees with a $^{207}Pb/^{206}Pb$ date of 1099.1 ± 0.5/5.0 Ma (without/with decay constant errors) obtained by Paces and Miller (1993). Eight grains from the same population utilized by Schmitz and Bowring (2003) were chemical-abraded and the results form a statistically significant discordant cluster

(MSWD of equivalence = 0.4). They yield a weighted mean $^{207}Pb/^{206}Pb$ date of 1098.6 ± 0.3/5.0 Ma (MSWD = 0.4), a weighted mean $^{207}Pb/^{235}U$ date of 1096.8 ± 0.2/0.3/1.2 Ma (MSWD = 0.6), and a weighted mean $^{206}Pb/^{238}U$ date of 1095.9 ± 0.2/0.3/1.4 Ma (MSWD = 0.5).

3.6. Palisade Rhyolite (MS99-30)

The Palisade rhyolite is part of the North Shore Volcanic group, associated with the failed Mesoproterozoic Midcontinent rift of central North America (Davis and Green, 1997; Green, 1977; Green et al., 1993). Min et al. (2000) reported nine concordant single grain sanidine incremental heating experiments that gave a weighted mean $^{40}Ar/^{39}Ar$ date of 1088.4 ± 4.0 Ma (internal errors only) relative to an age of 28.02 Ma for the Fish Canyon sanidine, which they interpreted as the eruption age for the Palisade rhyolite. They also augmented a previous discordant zircon dataset (Davis and Green, 1997) by reporting a weighted mean $^{207}Pb/^{206}Pb$ date of 1097.6 ± 2.1 Ma (external errors excluded) for the 14 analyses from both datasets.

Densely welded rhyolite was collected from a roadcut near the junction of highways 61 and 1, a few kilometers north of Palisade Head, Minnesota. 21 zircon grains were analyzed including fifteen air-abraded grains and six chemical-abraded grains. Nineteen analyses define a single discordant cluster (MSWD of equivalence = 0.5). They yield a weighted mean $^{207}Pb/^{206}Pb$ date of 1096.1 ± 0.4/5.0 (MSWD = 0.3), a weighted mean $^{207}Pb/^{235}U$ date of 1094.8 ± 0.2/0.3/1.2 (MSWD = 0.8) and a weighted mean $^{206}Pb/^{238}U$ date of 1094.2 ± 0.2/0.4/1.5 Ma (MSWD = 0.7).

3.7. Zircon 91500

Zircon crystal 91500 is from a syenite pegmatite in Ontario, Canada (Hewitt, 1953; Wiedenbeck et al., 1995). Wiedenbeck et al. (1995) assigned a weighted mean $^{207}Pb/^{206}Pb$ date of 1065.4 ± 0.6 Ma (MSWD = 1.3) and a weighted mean $^{206}Pb/^{238}U$ date of 1062.4 ± 0.8 Ma (MSWD = 2.1) based on data from three laboratories. Similar $^{207}Pb/^{206}Pb$ dates were more recently reported, but some of the analyses are more discordant (Amelin and Zaitsev, 2002; Paquette and Pin, 2001). Large fragments that we obtained were broken and air-abraded. Seven fragments form a statistically significant cluster (MSWD of equivalence = 0.5). They yield a weighted mean $^{207}Pb/^{206}Pb$ date of 1066.4 ± 0.3/5.0 Ma (MSWD = 0.4), a weighted mean $^{207}Pb/^{235}U$ date of 1064.5 ± 0.2/0.3/1.2 Ma (MSWD = 0.3), and a weighted mean $^{206}Pb/^{238}U$ date of 1063.6 ± 0.2/0.3/1.4 Ma (MSWD = 0.7).

3.8. Xenotime z6413

z6413 is derived from a granite which contains megacrysts of xenotime, originally collected from within the Purdy #3 Mine, Mattawan Township, Ontario, Canada (see Stern and Rayner (2003) for detailed description). Stern and Rayner (2003) assigned a weighted mean $^{207}Pb/^{206}Pb$ date of 996.7 ± 0.8 Ma (MSWD = 0.7) and a weighted mean $^{206}Pb/^{238}U$ date of 993.8 ± 0.7 Ma (MSWD = 0.3). Seven small fragments that we analyzed form a statistically significant cluster (MSWD of equivalence = 0.2). They yield a weighted mean $^{207}Pb/^{206}Pb$ date of 999.7 ± 0.3/5.0 Ma (MSWD = 0.2), a weighted mean $^{207}Pb/^{235}U$ date of 998.5 ± 0.2/0.2/1.1 Ma (MSWD = 0.4), and a weighted mean $^{206}Pb/^{238}U$ date of 997.9 ± 0.2/0.3/1.3 Ma (MSWD = 0.3).

3.9. Zircon z6266

z6266 is a zircon megacryst from Sri Lanka (Stern, 2001; Stern and Amelin, 2003) for which Stern and Amelin (2003) assigned a weighted mean $^{207}Pb/^{206}Pb$ date of 562.6 ± 0.4 Ma (MSWD = 1.2) and a weighted mean $^{206}Pb/^{238}U$ date of 559.0 ± 0.2 Ma (MSWD = 1.1). Five chemical-abraded and two air-abraded grains that we analyzed form a discordant cluster (MSWD of equivalence = 0.8). They yield a weighted mean $^{207}Pb/^{206}Pb$ date of 562.00 ± 0.50/4.59 Ma (MSWD = 0.9), a weighted mean $^{207}Pb/^{235}U$ date of 559.80 ± 0.13/0.18/0.76 Ma (MSWD = 1.0), and a weighted mean $^{206}Pb/^{238}U$ date of 559.27 ± 0.11/0.19/0.79 Ma (MSWD = 0.7).

3.10. North Mountain basalt (NMB-03-1)

The North Mountain basalt was erupted in association with the rifting of North America in the early Jurassic, and is part of the Newark Supergroup, Nova Scotia, Canada (Hodych and Dunning, 1992). Pegmatitic lenses within the basalt contain abundant zircon which Hodych and Dunning (1992) assigned a $^{206}Pb/^{238}U$ date of 202 ± 1 Ma based on two multi-grain analyses. Ten air-abraded zircon grains (collected from the same locality) that we analyzed form a statistically significant cluster (MSWD of equivalence = 0.8). They yield a weighted mean $^{207}Pb/^{206}Pb$ date of 203.97 ± 0.45/4.32 Ma (MSWD = 0.9), a weighted mean $^{207}Pb/^{235}U$ date of 201.48 ± 0.05/0.07/0.32 Ma (MSWD 0.7), and a weighted mean $^{206}Pb/^{238}U$ date of 201.27 ± 0.03/0.06/0.27 Ma (MSWD = 0.7).

3.11. GA-1550 monzonite (RSES01-98)

The GA-1550 biotite, derived from Mount Dromedary complex, south of Narooma, New

South Wales, Australia, is one of the few primary K-Ar standards for which an age has been determined based on a direct calibration of its $^{40}Ar^*$ concentration against a known volume of air. Three K-Ar age determinations or recalibrations have been published: 97.9 ± 1.8 (McDougall and Roksandic, 1974), 98.8 ± 1.0 (Renne et al., 1998b), and 98.5 ± 1.6 (Spell and McDougall, 2003) (decay constant uncertainties excluded). Sample RSES01-98 is a recollection of the monzonite from the original quarry that yielded GA-1550 (McDougall and Roksandic, 1974, Spell and McDougall, 2003).

Twenty zircons were analyzed, including three chemical-abraded grains, and all analyses except one give $^{206}Pb/^{238}U$ dates of ca. 99.1 Ma. Although they define a clear cluster, the nineteen analyses are not equivalent. In addition to Pb-loss and inheritance, intermermediate daughter product disequilibria can explain scatter in the $^{207}Pb/^{235}U$ (i.e. z6, z10, z11, z12, z10.5, and z16) and $^{206}Pb/^{238}U$ (z5, z15, z17aa, z18aa) ratios, and these possibilities for zircon discordance will be discussed in detail in the following section. Regardless of the cause of the scatter, the ten analyses that form a statistically significant cluster (MSWD of equivalence = 0.7) and are closest to concordia are likely to represent the crystallization age of the rock. While analytical inaccuracies could also create the observed scatter in the results, the consistency of the analyses from other samples in this study suggest otherwise. The ten equivalent analyses yield a weighted mean $^{207}Pb/^{206}Pb$ date of 102.14 ± 0.47/4.26 Ma (MSWD = 0.5), a weighted mean $^{207}Pb/^{235}U$ date of 99.24 ± 0.03/0.04/0.17 Ma (MSWD = 0.8), and a weighted mean $^{206}Pb/^{238}U$ date of 99.12 ± 0.02/0.03/0.14 Ma (MSWD = 1.0).

4. DISCUSSION

4.1. Interpretation of systematic discordance of U-Pb data

Assigning high-precision absolute crystallization ages to the samples is complicated because the $^{207}Pb/^{206}Pb$ dates do not agree within internal error of the $^{206}Pb/^{238}U$ dates (Figs. 1 and 2). Explanations for the data include: 1) intermediate daughter product disequilibria, 2) Pb-loss, 3) systematic analytical inaccuracies, and 4) decay constant inaccuracies.

The incorporation of ^{231}Pa and ^{230}Th outside of secular equilibrium during mineral crystallization results in either an excess of ^{207}Pb or deficiency of ^{206}Pb, respectively (Anczkiewicz et al., 2001; Mattinson, 1973; Mortensen et al., 1992; Parrish, 1990; Schärer, 1984). If this phenomenon is important in shifting minerals dates below concordia, as is observed in this study, it necessitates a preferential exclusion of Th or a preferential inclusion of Pa in the crystal lattice compared to the magma. Evaluating the magnitude of such effects is difficult because it requires some knowledge of the ratio of the Th/U (or Pa/U) in the crystal to the Th/U (or Pa/U) in the host magma. ^{230}Th disequilibrium is more easily dealt with in this case because there is a limit of ~108 kyr in the $^{206}Pb/^{238}U$ date caused by Th deficiency (Parrish, 1990). Therefore, the potential effect of ^{230}Th disequilibrium is a strong function of the age of the sample compared to the amount of discordance observed. For example, in the youngest sample, RSES01-98, the discordance of the weighted mean dates is 2.96 ± 0.45% and with a maximum correction for ^{206}Pb deficiency, the discordance becomes 0.27 ± 0.47% and is concordant within errors. For the second youngest sample, the North Mountain Basalt, the discordance shifts from 1.32 ± 0.22 to 0.68 ± 0.22% discordant, which is significant but

not enough to explain the discordance. The effect becomes increasingly insignificant, such that for the oldest sample, JCA-62-02, the discordance only shifts from 0.121 ± 0.023 to 0.117 ± 0.023%. ^{231}Pa excess is more difficult to quantify because there is no theoretical limit to its magnitude, very little is known about the distribution coefficient of Pa between minerals and magmas, and the oxidation state of the magma and therefore the valence of Pa may play a large role in its compatibility in zircon and xenotime. Qualitative arguments for compatibility of Pa into zircon show that in the tetravalent state, Pa^{4+} is likely to be less compatible that Zr^{4+}, and would cause a small deficiency in ^{207}Pb and therefore cannot explain our datasets (Barth et al., 1989; Mattinson, 1973; Schmitz and Bowring, 2001). In the pentavalent state, Pa^{5+} is likely to be more compatible in zircon and may be responsible for documented examples of excess ^{207}Pb (Anczkiewicz et al., 2001; Mattinson, 1973; Mortensen et al., 1992) and may also be the cause for subtle scatter in many U-Pb datasets (Amelin and Zaitsev, 2002). While we speculate that excess ^{207}Pb may be partially responsible for the observed scatter in ^{207}Pb/^{235}U dates in sample RSES01-98, we find it exceedingly unlikely that it would affect each analyzed zircon from a sample equally and as a function of age such that older samples show systematically larger absolute offset. Such systematic discordance is likely derived from a systematic source.

Numerous studies have shown that U-Pb systematics in zircon are usually complicated by an obvious or subtle combination of multi-stage Pb-loss and inheritance, which results in discordant data (e.g. Corfu et al., 2003; Pidgeon and Aftalion, 1978; Wetherill, 1956). In fact, discordance is observed so frequently in zircons from both young and old igneous and metamorphic rocks such that seeking out concordant zircons

based on geologic context is nearly impossible. However, nearly all processes that produce discordance are highly unlikely to affect all grains from a sample equally. In the case of Pb-loss, a common interpretation is that the upper intercept of a discordia or a weighted mean $^{207}Pb/^{206}Pb$ date (for samples with recent Pb-loss) is the best approximation of a crystallization age (see reviews in Davis et al., 2003; Ireland and Williams, 2003; Parrish and Noble, 2003). Either interpretation hinges on zircon discordance being a result of a single stage of Pb-loss and the observation that such open-system behavior is unlikely to affect every zircon from a population equally. Discordant data produced from a mixture of two or more domains of different ages is also unlikely to affect every zircon from a sample equally. Because our data consist of statistically equivalent, high-*n*, datasets from samples of various ages, neither open-system behavior nor inheritance is a viable explanation for the systematic discordance observed. Instead, these data suggest that such factors, if present, were eliminated through rigorous grain pre-treatment including air-abrasion and/or chemical-abrasion.

The most important sources of systematic experimental inaccuracies involve Pb mass-fractionation and the calibration of the ^{205}Pb-^{233}U-^{235}U tracer solution. We are confident that Pb mass-fractionation is accurate to within the quoted errors (± 0.04%/a.m.u.), and a sensitivity test shows that reasonable changes in those values change all U-Pb and $^{207}Pb/^{206}Pb$ dates of a given sample, but do not significantly change the amount of discordance. The best way to address any inaccuracies in Pb mass-fractionation for geochronology, which will become increasingly important in high-precision U-Pb geochronology, is through the use of a ^{202}Pb-^{205}Pb double spike (Todt et al. 1996).

The ^{205}Pb-^{233}U-^{235}U tracer solution used in this study was recently calibrated through a total of eleven experimental isotope dilution mixtures (see analytical details). We note that the new tracer calibration used in this study differs from previous calibrations, and a notable example is that the $^{206}Pb/^{238}U$ date from sample AS3 in this study differs from that of Schmitz et al., (2003) by ~0.25%, largely from differences in tracer calibration. Schmitz et al. (2003) suggest based on concordant zircon data from that study, that the U decay constants need no revision, but note that because the magnitude of systematic uncertainties of the tracer calibration approach that of the reported errors in the U decay constants, their ability to quantitatively evaluate the accuracy of the U decay constants is limited. The present tracer calibration is more precise than previous calibrations and we also believe it to be more accurate for several reasons: 1) decreased U blank in tracer calibration experiments through oxide analysis of U; 2) the isotopic composition of U in the tracer was determined by multiple methods including critical mixtures (Hofmann, 1971; Roddick et al., 1992) and standard isotope dilution with mass fractionation corrected by referencing multiple standard U solutions; 3) measurement of the Pb/U ratio in the tracer was conducted against three mixed U-Pb gravimetric solutions that were prepared in independent laboratories (see description in the analytical methods). The high level of internal agreement of the resulting Pb/U ratio of the tracer (2SE = 0.015%) ensures that any systematic errors that resulted from mixing, weighing, dilution, distribution, or the initial isotopic composition and concentrations of the gravimetric solutions were very small relative to the magnitude of observed discrepancies between U-Pb and $^{207}Pb/^{206}Pb$ dates.

Multiple recent ID-TIMS U-Pb studies from other laboratories with independent mixed Pb-U tracers also observe slight discordance in weighted mean clusters of zircons with $^{207}Pb/^{206}Pb$ dates that are older than $^{206}Pb/^{238}U$ dates by ~0.3-0.6%. Datasets acquired at the Royal Ontario Museum from samples Temora 1 (Black et al., 2003a), QGNG (Black et al., 2003b), R33 (Black et al., 2004), and z6266 (Stern and Amelin, 2003) all plot slightly below the concordia curve. Data from z6266 acquired at the Geological Survey of Canada show similar results (Stern and Amelin, 2003). We stress that continued high-precision analysis of zircon standards by multiple laboratories is the best way to provide an external check for tracer calibration and other resolvable analytical problems that result in interlaboratory variability.

Given that we rule out geological and analytical explanations for the discordance in our datasets, the only viable explanation for our data is that there is a systematic inaccuracy, albeit within the stated uncertainties, in the presently accepted values of the U decay constants.

4.2. Assessing inaccuracies of the U decay constants

The ^{238}U and ^{235}U decay constants are the most precisely known of those used in geochronology, with assigned 95% confidence interval uncertainties of 0.107 and 0.136%, respectively, based on the alpha-counting experiments of Jaffey et al. (1971). That study included four experiments on two separate batches of high-purity ^{238}U and two experiments on one batch of high-purity ^{235}U. All four experiments on ^{238}U produced results that agree within error and showed no indication of systematic errors or drift in the experiments. The ^{235}U experiments were more precise than the ^{238}U experiments, but were

shown to have an unknown source of systematic drift over the course of the measurements, such that the two sequential experiments did not agree within error. To account for this, Jaffey et al. (1971) multiplied the counting errors of the ^{235}U activity results by 1.5 and propagated those into the quoted errors for the study. Finally, Jaffey et al. (1971) concluded that if further systematic errors exist, they "will no more than double the quoted errors." Because of this, Mattinson (1987) suggested that the stated errors of the ^{238}U and ^{235}U decay constants should be inflated by a further 50% for realistic use in geochronology.

Because individual U-Pb analyses of zircons in this study approach the precision of the decay constants and weighted means of equivalent populations are well within those errors, it is possible to validate the accuracy of the Jaffey et al. (1971) counting experiments empirically and quantitatively (Begemann et al., 2001; Mattinson, 1994a; Mattinson, 1994b; Mattinson, 2000). We believe that the analyses presented in this study, which consistently plot below the concordia curve (Fig. 1), are indicative of a systematic inaccuracy in one or both of the U decay constants. Mattinson (2000) reached a similar conclusion based on multigrain analyses of <200 Ma zircon that yield $^{207}Pb/^{206}Pb$ dates that are systematically older than the $^{206}Pb/^{238}U$ dates by 2 Myr (with uncertainties of <1 Myr). Based on the assumption that the ^{238}U decay constant is correct, Mattinson (2000) calculated a ^{235}U decay constant of 9.857×10^{-10} yr^{-1} that is within the error of the Jaffey et al. (1971) value but 0.09% higher than the mean value.

We are now in a better position to quantitatively evaluate the accuracy of the U decay constants using large datasets of single grains or grain fragments that span over three billion years. The discrepancy between $^{207}Pb/^{206}Pb$ and $^{206}Pb/^{238}U$ in our data is, in

fact, identical within errors to that documented by Mattinson (2000) (Fig. 3), and if we make the assumption that the ^{238}U decay constant is correct, we calculate a ^{235}U decay constant of $9.8569 \pm 0.0017/0.0110 \times 10^{-10}$ yr^{-1} (without/with error of λ_{238}; Fig. 3). On the other hand, if we make the assumption that the ^{235}U decay constant is correct, we calculate a ^{238}U decay constant of $1.54993 \pm 0.00026/0.00219 \times 10^{-10}$ yr^{-1} (without/with error of λ_{235}; Fig. 3). Both numbers are within error of the Jaffey et al. (1971) values, but 0.09% different than the mean value. The most robust and precise calculation provided by our data, and the number that determines whether or not a datum is concordant, is the ratio between the ^{238}U and the ^{235}U decay constants (0.15738 ± 0.00003; Fig. 3), because it involves no assumption about the absolute values of either decay constant and therefore we need not propagate their errors. We should note that the equivalence of the different datasets as shown in figure 3 further supports the assertion that factors such as intermediate daughter product disequilibrium or Pb-loss are not likely to be an important cause for the discordance. The error in the calculated decay constants without incorporating uncertainties of the counting experiments from Jaffey et al. (1971) (but with tracer uncertainties) is 0.017%, but increases to 0.110% and 0.138% for the calculated ^{235}U and ^{238}U decay constant, respectively, with the systematic addition of those errors. Therefore, the precision of the ratio of the decay constants can be increased with additional U-Pb data, but the ultimate precision of either decay constant individually cannot be better than the error of most precise counting experiment.

The thorough discussion of the potential errors and sources of those errors in Jaffey et al (1971) suggests that if only one of the decay constants is inaccurate, it is most likely ^{235}U. For this reason, some workers have suggested recalibrating the ^{235}U decay

constant to that of ^{238}U (e.g. Mattinson, 2000), with the goal of improving its accuracy and precision. Although this intercalibration reduces the uncertainty on the ^{235}U decay constant by ~20%, further refinement through intercalibration is limited by the precision of the ^{238}U decay constant. Therefore, we join others (Begemann et al., 2001; Schön et al., 2004) in suggesting that for the purposes of high-precision geochronology and the attainment of a highly robust, internally consistent geologic time-scale calibrated by multiple dating methods, the best way to address the issue of decay constant inaccuracies is to repeat the alpha-counting experiments of Jaffey et al. (1971). Without this, high-precision *intercomparative* geochronology from multiple dating methods beyond the 0.1% level is precluded.

Acceptance of inaccuracy in one or both of the U decay constants raises the question of which date(s) should be used to for establishing high-precision benchmarks in the geological time-scale. $^{206}Pb/^{238}U$, $^{207}Pb/^{235}U$, and $^{207}Pb/^{206}Pb$ cannot be compared accurately without propagating decay constant errors, and in fact, the concept of an "absolute age" is difficult to defend. For problems that calculate durations of events or depositional sequences, however, it is the relative differences in dates that are most crucial. In these cases, the most precise of the three systems is the best date to use, given the sample-specific caveats of Pb-loss and intermediate daughter product disequilibria.

4.4. Comparison of U-Pb dates with $^{40}Ar/^{39}Ar$ dates

Several recent studies have pointed out the systematic offset between U-Pb and $^{40}Ar/^{39}Ar$ dates (Chambers et al., 2005; Kamo et al., 2003; Min et al., 2000; Min et al., 2001; Nomade et al., 2004; Renne, 2000; Renne et al., 1998a; Schmitz and Bowring, 2001).

Table 2 and figure 4 summarize the data discussed in those papers, other pertinent data from the literature, and also the data from the four samples that we analyzed. The assumption underlying each of these comparisons, which is often discussed in the original studies, is that both the U-Pb dates and $^{40}Ar/^{39}Ar$ dates record the same geologic event (e.g. crystallization from a magma). Magma residence time in young plutonic and volcanic systems may invalidate that assumption, and possibly affects the U-Pb data from the Fish Canyon Tuff (Reid and Coath, 2000; Reid et al., 1997; Schmitz and Bowring, 2001) and other young igneous rocks. Intermediate daughter product disequilibria in zircon is difficult to address but may be significant in U-Pb dates from rocks <100 Ma (see previous discussion). Problems associated with magma residence time and intermediate daughter product disequilibria are more easily overcome in older rocks, because their absolute effects likely become negligible as a percentage of the age and associated uncertainty. Another source of complication arises from the post-crystallization thermal histories of the rocks in question and the fact that the different phases analyzed for U-Pb and $^{40}Ar/^{39}Ar$ have different closure temperatures and are involved in a suite of different metamorphic reactions. For example, it is unclear whether currently published $^{40}Ar/^{39}Ar$ and U-Pb titanite, and Pb-Pb dates from the Bushveld Complex and the Acapulco meteorite represent cooling or metamorphic ages (Table 2, Figs. 4 and 5; Buick et al., 2001; Nomade et al., 2004; Renne, 2000), though (U-Th)/He data from the meteorite are consistent with rapid cooling (Min et al., 2003). The data from the Kaap Valley pluton is difficult to compare because of a complicated low-temperature thermal history and the potential for alteration in hornblende and apatite over three billion years (Layer et al., 1992, Schoene and Bowring, 2003). When comparing U-

Pb and $^{40}Ar/^{39}Ar$ dates, these problems are heightened by potential inaccuracies in the U decay constants (discussed above), and also in comparing $^{40}Ar/^{39}Ar$ dates determined by total fusion and step-heating experiments (e.g. McDougall and Harrison, 1999). In many examples from the literature (Table 2, Fig. 4), certain geologic or laboratory biases may have been negligible for the goals of those studies, but may be important for the purposes of high-precision intercomparative geochronology. We choose to include all the available data in the following discussion to examine the problem as it exists now, with hopes that it will emphasize the importance of examining those concerns in future studies that compare U-Pb and $^{40}Ar/^{39}Ar$ data.

The intercalibration efforts cited from the literature and presented in this study have two important things in common: 1) mean $^{40}Ar/^{39}Ar$ dates are within internal errors or systematically younger than $^{207}Pb/^{206}Pb$, $^{207}Pb/^{235}U$ and $^{206}Pb/^{238}U$ dates (Table 2, Figs. 4 and 5), and 2) if external sources of error are included in the age estimates, dates from both isotopic schemes are statistically indistinguishable (with the exception of the Acapulco meteorite; Fig. 4). U-Pb data from this study suggest that inaccuracies in the U decay constants introduce a small bias between the two dating techniques, which will change as a function of age (Fig. 5A). Other important potential sources of bias include the decay constants and physical constants of ^{40}K, the K-Ar age calibration of primary standards, and the intercalibration of other $^{40}Ar/^{39}Ar$ secondary standards with primary standards. Figure 5A shows the contribution of various sources of systematic errors in $^{40}Ar/^{39}Ar$ dates as a function of the age of the sample, calculated using the techniques of Karner and Renne (1998), Min et al. (2000), and Renne et al. (1998b). Plotted in figure 5B are the offsets between U-Pb and $^{40}Ar/^{39}Ar$ or K-Ar dates, which show that in samples

< 2 Ga, U-Pb and $^{40}Ar/^{39}Ar$ dates are indistinguishable if one ignores decay constant errors but includes the error of the primary K-Ar standard (the data are relative to GA1550 of Renne et al. (1998b) and the Fish Canyon sanidine (FCs) at 28.02 Ma, and using the ^{40}K decay constants of Steiger and Jäger (1997)), in that all of the data plot within the extent of the GA1550 primary standard uncertainties (black dashed line in Fig. 5B is the 2σ upper bounds of that calibration). The offset between U-Pb and $^{40}Ar/^{39}Ar$ dates for the Bushveld Complex, the Eglab porphyry, and the Acapulco meteorite are likely to be outside the error-bounds introduced by the Ar*/K calibration of GA1550 from Renne et al. (1998b), and therefore some of the bias must lie in the ^{40}K decay constant or physical constants (Fig. 5B). Figure 5B also shows the effect on $^{40}Ar/^{39}Ar$ dates if the data is re-normalized to the GA1550 K-Ar date and GA1550/FCs values of Spell and McDougall (2003); note that the reported errors on the K-Ar date are ~60% larger than those from Renne et al. (1998b).

Min et al. (2000) critically evaluated the selection criteria for the ^{40}K decay constants and physical constants (and associated errors) used in geochronology (Beckinsale and Gale, 1969), and concluded that the values suggested in Steiger and Jäger (1977) need to be revised. They recommended new values that more closely coincide with those from the nuclear physics and chemistry literature (Audi et al., 1997; Endt and Van der Leun, 1973) and indicated that larger associated errors are more realistic. Min et al. (2000) and Renne (2000) show that using the new recommended values, the bias between $^{207}Pb/^{206}Pb$ and $^{40}Ar/^{39}Ar$ dates for the Palisade rhyolite and Acapulco meteorite disappears (black solid curve in Fig. 5B; includes new values for the ^{40}K total decay constant, the branching ratio of the ^{40}K decay, and the $^{40}K/K$ value; we

also fix the value of GA1550 to our $^{206}Pb/^{238}U$ date). Kwon et al. (2002) use a statistical regression approach to solve for the values of the total decay constant of ^{40}K and the age of the FCs (holding other variables constant), using a subset of data from the literature for which U-Pb or historical dates are available (gray solid curve in Fig. 5B; FCs = 28.269 Ma and λ_{40} less than Steiger and Jäger (1977) by ~1.22%). Finally, different combinations of variations of the primary K-Ar standard, primary standard/secondary standard intercalibration, and decay constant and physical constant uncertainties are able to produce similar offsets of U-Pb and $^{40}Ar/^{39}Ar$ dates, implying that there is no unique solution to this problem if one accounts for all the available variables from first principles. For geochronology, however, this final point is unimportant because if some combination of those variables produces accurate dates, then our purposes are served. Several aspects of figure 5 suggest that U-Pb and $^{40}Ar/^{39}Ar$ intercalibration is best done with older samples, if additional fresh samples can be obtained: 1) systematic errors in $^{40}Ar/^{39}Ar$ dates decrease as a percentage of age (Fig. 5A), and 2) the choice of primary standard in $^{40}Ar/^{39}Ar$ dating is less important for older samples (Fig. 5B).

High-precision intercalibration between $^{40}Ar/^{39}Ar$ and U-Pb data is precluded with the current dataset, as the large errors and absolute scatter in the offset between the two dating schemes suggest that the bias between those data is not created by systematic errors alone (Fig. 5). The scatter may arise from unexplored open-system behavior in either method or from interlaboratory variability. This observation highlights the importance of generating $^{40}Ar/^{39}Ar$ and U-Pb data from the same rocks from multiple laboratories and over a wide range of geologic time, such that systematic interlaboratory

errors and geologic complexities can be distinguished from inaccuracies in the U and ^{40}K decay constants and physical constants.

5. CONCLUSIONS

– High-precision statistically equivalent U-Pb datasets from this study systematically plot below the mean value of concordia, but within its reported errors. We believe this is indicative of inaccuracies in one or both of the mean values of the U decay constants and concur with previous literature that the bias likely resides in the currently used decay constant value for ^{235}U. Using U-Pb data alone, we recalculate the *ratio* of the decay constants with very high precision (± ~0.02%). Recalibrating the ^{235}U decay constant against that of ^{238}U can increase the precision of the former (from 0.14% to 0.11%), but a further increase in precision can only be accomplished through additional alpha-counting experiments (Begemann et al., 2001; Mattinson, 1994a; Mattinson, 1994b; Mattinson, 2000).

– Given tangible uncertainty in the U decay constants, comparison of $^{207}Pb/^{206}Pb$, $^{207}Pb/^{235}U$, and $^{206}Pb/^{238}U$ dates cannot be done accurately without incorporating decay constant errors. High-precision relative chronology within any one system need not incorporate decay constant errors, and the most appropriate system to use depends on which is the most precise and accurate. The accuracy of a given system for a specific sample depends on the importance of open system behavior such as Pb-loss and intermediate daughter product disequilibria.

– We compared U-Pb, $^{40}Ar/^{39}Ar$ and K-Ar dates from samples spanning a wide range of geologic time. Although external sources of error are too large to statistically distinguish between high-precision U-Pb and $^{40}Ar/^{39}Ar$ dates from any one sample, K-Ar and $^{40}Ar/^{39}Ar$ dates are systematically younger or within internal error of U-Pb dates, which is unlikely explained by geologic phenomena alone. However, these data do not form a trend that can be explained by only systematic errors, suggesting that interlaboratory biases or geologic complications are important in some or all of the samples examined.

– High-precision intercalibration between the U-Pb and $^{40}Ar/^{39}Ar$ geochronology is hampered until 1) further experiments are carried out on determination of the U decay constants and 2) more datasets are generated from which we can compare and contrast data from a wide range of geologic time generated in a large number of laboratories. This must include the selection, documentation, and distribution of high quality accessory minerals to all labs involved in high-precision geochronology.

–Studies that rely on the determination or tuning of decay constants for other chronometers such as Re-Os (Chen et al., 2002) and Lu-Hf (Scherer et al., 2001; Söderlund et al., 2004) by comparison to the U-Pb system must incorporate the effects resulting from uncertainty in the U decay constants.

Acknowledgements. This manuscript was greatly improved by reviews from J. Mattinson, R. Parrish and J. Lee. Comments made on an early version of the manuscript by K. Hodges are much appreciated. This work was supported in part by NSF grant EAR

0451802 (The EARTHTIME Network: Developing an infrastructure for high-resolution calibration of Earth History) to S. Bowring. Additional support was provided to B. Schoene by a subaward from NSF grant EAR 031521 (CHRONOS to C. Cervato). We also thank C. Allen for providing zircon separates from GA-1550, N. Rayner for xenotime z6413, and S. Kamo for zircons QGNG and z6266.

REFERENCES

Amelin Y. and Zaitsev A. N. (2002) Precise geochronology of phoscorites and carbonatites: The critical role of U-series disequilibrium in age interpretations. *Geo. and Cosmo. Acta* **66**(13), 2399-2419.

Anczkiewicz R., Oberli F., Burg J. P., Villa I. M., Gunther D., and Meier M. (2001) Timing of normal faulting along the Indus Suture in Pakistan Himalaya and a case of major $^{231}Pa/^{235}U$ initial disquilibrium in zircon. *Earth and Planetary Science Letters* **191**, 101-114.

Audi G., Bersillon O., Blanchot J., and Wapstra A. H. (1997) The NUBASE evaluation of nuclear and ecay properties. *Nuclear Physics* **A624**, 1-124.

Barth, S. Oberli, F. and Meier M. (1989) U-Th-Pb systematics of morphologically characterized zircon and allanite: a high-resolution isotopic study of the Alpine Rensen pluton (northern Italy). *Earth Planet. Sci. Lett.* **95**, 235-254

Beckinsale R. D. and Gale N. H. (1969) A reappraisal of the decay constants and branching ratio of ^{40}K. *EPSL* **6**, 289-294.

Begemann F., Ludwig K. R., Lugmair G. W., Min K., Nyquist L. E., Patchett P. J., Renne P. R., Shih C.-Y., Villa I. M., and Walker R. J. (2001) Call for an improved set of decay constants for geochronological use. *Geochemica and Cosmochinica Acta* **65**(1), 111-121.

Black, L.P., Kamo, S.L., Allen, C.M., Aleinikoff, J.N., Davis, D.W., Korsch, R.J., Foudoulis, C. (2003a) TEMORA 1: a new zircon standard for Phanerozoic U-Pb geochronology. *Chemical Geology* **200**, 155-170.

Black L. P., Kamo S. L., Williams I. S., Mundil R., Davis D. A., Korsch R. J., and Foudoulis C. (2003b) The application of SHRIMP to Phanerozoic geochronology; a critical appraisal of four zircon standards. *Chemical Geology* **200**, 171-188.

Black, L.P., Kamo, S.L., Allen, C.M., Davis, D.W., Aleinikoff, J.N., Valley, J.W., Mundil, R., Campbell, I.H., Korsch, R.J., WIlliams, I.S., Foudoulis, C. (2004) Improved $^{206}Pb/^{238}U$ microprobe geochronology by the monitoring of a trace-element-related matrix effect; SHRIMP, ID-TIMS, ELA-ICP-MS and oxygen isotope documentation for a series of zircon standards. *Chemical Geology* **205**, 115-140.

Buick I. S., Maas R., and Gibson R. (2001) Precise U-Pb titanite age constrains on the emplacement of the Bushveld Complex, South Africa. *Jour. Geol. Soc. London* **158**, 3-6.

Chamberlain K. R. and Bowring S. A. (2000) Apatite-feldspar U-Pb thermochronometer: a reliable mid-range (~450°C), diffusion controlled system. *Chemical Geology* **172**, 173-200.

Chambers L. M., Pringle M. S., and Parrish R. R. (2005) Rapid formation of the Small Isles Tertiary centre constrained by precise $^{40}Ar/^{39}Ar$ and U-Pb ages. *Lithos* **79**, 367-384.

Chen J. H., Papanastassiou D. A., and Wasserburg G. J. (2002) Re-Os and Pd-Ag systematics in Group IIIAB irons and in pallasites. *Geo. and Cosmo. Acta* **66**(21), 3793-3810.

Cherniak D. J. (1993) Lead diffusion in titanite and preliminary results on the effects of radiation damage on Pb transport. *Chemical Geology* **110**, 177-194.

Cherniak D. J., Lanford W. A., and Ryerson F. J. (1991) Lead diffusion in apatite and zircon using ion implantation and Rutherford Backscattering techniques. *Geochemica and Cosmochinica Acta* **55**, 1663-1673.

Corfu F., Hanchar J. M., Hoskin P. W. O., and Kinny P. (2003) Atlas of zircon textures. In *Zircon*, Vol. 53 (ed. J. M. Hanchar and P. W. O. Hoskin), pp. 468-500. Mineralogical Society of America.

Corfu F. and Stone D. (1998) The significance of titanite and apatite U-Pb ages: Constraints for the post-magmatic thermal-hydrothermal evolution of a batholithic complex, Berens River area, northwestern Superiod Province, Canada. *Geochimica et Cosmochimica Acta* **62**(17), 2979-2995.

Davis D. W. and Green J. C. (1997) Geochronology of the North American Midcontinent rift in western Lake Superior and implications for its geodynamic evolution. *Can. Jour. of Ear. Sci.* **34**, 476-488.

Davis D. W., Williams I. S., and Krogh T. E. (2003) Historical development of zircon geochronology. In *Zircon*, Vol. 53 (ed. J. M. Hanchar and P. W. O. Hoskin), pp. 145-181. Mineralogical Society of America.

Endt P. M. and Van der Leun C. (1973) Energy levels of A = 21-44 nuclei (V). *Nuclear Physics* **A214**, 1-625.

Frost B. R., Chamberlain K. R., and Schumacher J. C. (2000) Sphene (titanite): phase relations and role as a geochronometer. *Chemical Geology* **172**, 131-148.

Gerstenberger H. and Haase G. (1997) A highly effective emitter substance for mass spectrometric Pb isotope ratio determinations. *Chemical Geology* **136**, 309-312.

Göpel C., Manhés G. and Allégre C. (1992) U-Pb study of the Acapulco meteorite. *Meteoritics* **27**, 226.

Green J. C. (1977) Keweenawan plateau volcanism in the Lake Superior region. In *Volcanic Regimes in Canada*, Vol. 16 (ed. W. R. A. Baragar, L. C. Coleman, and J. M. Hall), pp. 407-422. Geological Association of Canada, Special Paper.

Green J. C., Fitz T. J., and Iii. (1993) Extensive felsic lavas and rheoignimbrites in the Keweenawan Midcontinent Rift plateau volcanics, Minnesota: petrographic and field recognition. *Journal of Volcanology and Geothermal Research* **54**, 177-196.

Hamilton M.A., Pearson D.G., Thompson R.N., Kelley S.P., and Emeleus C.H. (1998) Rapid eruption of Skye lavas inferred from precise U-Pb and Ar-Ar dating of the Rum and Cuillin plutonic complexes. *Nature* **394**, 260-263.

Hewitt, D.F. (1953) Geology of the Brudenell-Raglan Area. *Annual report of the Ontatario Department of Mines* **62**, part 5: 85-86

Hodych J. P. and Dunning G. R. (1992) Did the Manicouagan impact trigger end-of-Triassic mass extinction? *Geology* **20**, 21-54.

Hofmann A. (1971) Fractionation corrections for mixed-isotope spikes of Sr, K, and Pb. *Earth and Planetary Science Letters* **10**, 397-402.

Ireland T. R. and Williams I. S. (2003) Considerations in zircon geochronology by SIMS. In *Zircon*, Vol. 53 (ed. J. M. Hanchar and P. W. O. Hoskin), pp. 215-241. Mineralogical Society of America.

Jaffey A. H., Flynn K. F., Glendenin L. E., Bentley W. C., and Essling A. M. (1971) Precision measurement of half-lives and specific activities of ^{235}U and ^{238}U. *Phys. Rev.* **C4**, 1889-1906.

Kamo S.L., Czamanske G.K., Krogh T.E. (1996) A minimum U-Pb age for Siberian flood-basalt volcanism. *Geo. et Cosmo. Acta* **60**, 3505-3511

Kamo S., Czamanske G. K., Amelin Y., Fedorenko V. A., Davis D. W., and Trofimov V. R. (2003) Rapid eruption of Siberian flood-volcanic rocks and evidence for coincidence with the Permian-Triassic boundary and mass extinction at 251 Ma. *Earth and Planetary Science Letters* **214**, 75-91.

Kamo S. and Davis D. W. (1994) Reassessment of Archean crustal development in the Barberton Mountain Land, South Africa, based on U-Pb dating. *Tectonics* **13**(1), 167-192.

Karner D. B. and Renne P. R. (1998) $^{40}Ar/^{39}Ar$ geochronology of Roman volcanic province tephra in the Tiber River valley: Age calibration of middle Pleistocene sea-level changes. *GSA Bull.* **110**(6), 740-747.

Krogh T. E. (1973) A low contamination method for hydrothermal decomposition of zircon and extraction of U and Pb for isotopic age determination. *Geo. and Cosmo. Acta* **37**, 485-494.

Krogh T. E. (1982) Improved accuracy of U-Pb zircon ages by the creation of more concordant systems using an air abrasion technique. *Geochimica et Cosmochimica Acta* **46**, 637-649.

Kwon J., Min K., Bickel P. J., and Renne P. R. (2002) Statistical methods for jointly estimating the decay constant of ^{40}K and the age of a dating standard. *Mathematical Geology* **34**(4), 457-474.

Layer P. W., Kröner A., and York D. (1992) Pre-3000 Ma thermal history of the Archean Kaap Valley pluton, South Africa. *Geology* **20**, 717-720.

Ludwig K. R. (1980) Calculation of uncertainties of U-Pb isotope data. *EPSL* **46**, 212-220.

Ludwig K. R. (1991) Isoplot–a plotting and regression program for radiogenic isotope data. *USGS Open-File report* **91-445**.

Ludwig K. R. (1998) On the treatment of concordant uranium-lead ages. *Geo. and Cosmo. Acta* **62**(4), 665-676.

Ludwig K. R. (2000) Decay constant errors in U-Pb concordia-intercept ages. *Chemical Geology* **166**, 315-318.

Mattinson J. M. (1973) Anomolous isotopic composition of lead in young zircons. *Carnegie Inst. Yearbook* **72**, 613-616.

Mattinson J. M. (1987) U-Pb ages of zircons: a basic examination of error propagation. *Chemical Geology* **66**, 151-162.

Mattinson J. M. (1994a) Real and apparent concordance and discordance in the U-Pb systematics of zircons: limitations of "high-precision" U/Pb and Pb/Pb ages. *Eos* **75**, 691.

Mattinson J. M. (1994b) Uranium decay constant uncertainties and their implications for high-resolution U-Pb geochronology. *GSA Abst. with Prog.* **77; A-221**.

Mattinson J. M. (2000) Revising the "gold standard" – the uranium decay constants of Jaffey et al., 1971. *Eos Trans. AGU, Spring Meet. Suppl., Abstract V61A-02.*

Mattinson J. M. (2003) CA (chemical abrasion)-TIMS: high-resolution U-Pb zircon geochronology combining high-temperature annealing of radiation damage and multi-step partial dissolution analysis. *Eos Trans. AGU, Fall Meet. Suppl., Abstract V22E-06.*

Mattinson J. M. (2005) Zircon U-Pb chemical-abrasion ("CA-TIMS") method: combined annealing and multi-step dissolution analysis for improved precision and accuracy of zircon ages. *Chemical Geology* **220** (1-2), 47-56.

McDougall I. and Harrison T. M. (1999) *Geochronology and Thermochronology by the $^{40}Ar/^{39}Ar$ method.* Oxford University Press.

McDougall I. and Roksandic Z. (1974) Total fusion $^{40}Ar/^{39}Ar$ ages using HIFAR reactor. *J. Geol. Soc. Aust.* **21**, 81-89.

Min K., Farley K. A., Renne P. R., and Marti K. (2003) Single grain (U-Th)/He ages from phosphates in Acapulco meteorite and implications for thermal history. *Earth and Planetary Science Letters* **209**, 323-336.

Min K., Mundil R., Renne P. R., and Ludwig K. R. (2000) A test for systematic errors in $^{40}Ar/^{39}Ar$ geochronology through comparison with U-Pb analysis of a 1.1 Ga rhyolite. *Geochimica et Cosmochimica Acta* **64**, 73-98.

Min K., Renne P. R., and Huff W. D. (2001) $^{40}Ar/^{39}Ar$ dating of Ordovician K-bentonites in laurentia and Baltoscandia. *Earth and Planetary Science Letters* **185**, 121-134.

Mortensen J. K., Roddick J. C., and Parrish R. R. (1992) Evidence for high levels of unsupported radiogenic ^{207}Pb in zircon from a granitic pegmatite: implications for interpretation of discordant U-Pb data. *EOS, Transactions of the America Geophysical Union* **73**, 370.

Mundil R., Ludwig K.R., Metcalfe I., and Renne P.R. (2004) Age and timing of the Permian mass extinctions: U/Pb dating of closed-system zircons. *Science* **305**, 1760-1763.

Nomade S., Renne P. R., and Merkle R. K. W. (2004) $^{40}Ar/^{39}Ar$ age constraints on ore deposition and cooling of the Bushveld Complex, South Africa. *Jour. Geol. Soc. London* **161**, 411-420.

Paces J. B. and Miller J. D. J. (1993) Precise U-Pb ages of Duluth Complex and related mafic intrusions, northeastern Minnesota: Geochronological insights to physical, petrogenetic, paleomagnetic, and tectonomagmatic processes associtaed with the 1.1 Ga Midcontinent Rift System. *J. Geophys. Res.* **98**, 13997-14013.

Paquette J.-L. and Pin C. (2001) A new miniaturized extraction chromatography method for precise U-Pb zircon geochronology. *Chemical Geology* **176**(1-4), 311-319.

Parrish R. R. (1990) U-Pb dating of monazite and its application to geological problems. *Can. Jour. of Ear. Sci.* **27**, 1431-1450.

Parrish R. R. and Noble S. R. (2003) Zircon U-Th-Pb geochronology by isotope dilution – thermal ionization mass spectrometry (ID-TIMS). In *Zircon*, Vol. 53 (ed. J. M. Hanchar and P. W. O. Hoskin), pp. 183-213. Mineralogical Society of America.

Peucat J.-J., Capdevila R., Drareni A., Mahdjoub Y., and Kahoui M. (2005) The Eglab massif in the West African Craton (Algeria), an original segment of the Eburnean orogenic belt: petrology, geochemistry and geochronology. *Precambrian Research* **136**, 309-352.

Pidgeon R. T. and Aftalion M. (1978) Cogenetic and inherited zircon U-Pb systems in granites: Palaeozoic granites of Scotland and England. In *Geological Journal Special issue No. 10* (ed. D. R. Bowes and B. E. Leake). Seel House Press.

Reid M. R. and Coath C. D. (2000) In situ U-Pb ages of zircons from the Bishop Tuff: no evidence for long crystal residence times. *Geology* **28**, 443-446.

Reid M. R., Coath C. D., Harrison T. M., and McKeegan K. M. (1997) Prolonged residence times for the youngest rhyolites associated with Long Valley caldera: Ion microprobe dating of young zircons. *EPSL* **150**, 27-38.

Renne P. R. (2000) $^{40}Ar/^{39}Ar$ age of plagioclase from Acapulco meteorite and the problem of systematic errors in cosmochronology. *Earth and Planetary Science Letters* **175**, 13-26.

Renne P.R. and Basu A.R. (1991) Rapid eruption of the Siberian Traps flood basalts at the Permo-Triassic boundary. *Science* **253**, 176-179

Renne P. R., Karner D. B., and Ludwig K. R. (1998a) Absolute ages aren't exactly. *Science* **282**, 1840-1841.

Renne P. R., Swisher C. C., Deino A. L., Karner D. B., Owens T. L., and DePaolo D. J. (1998b) Intercalibration of standards, absolute ages and uncertainties in 40Ar/39Ar dating. *Chemical Geology* **145**, 117-152.

Renne P.R., Zichao Z., Richards M.A., Black M.T., and Basu A.R. (1995) Synchrony and causal relations between Permian-Triassic boundary crises and Siberian flood volcanism. *Science* **269**, 1413-1416.

Roddick J. C., Sullivan R. W., and Dudäs F. O. (1992) Precise calibration of Nd tracer isotopic compositions for Sm-Nd studies. *Chemical Geology* **97**, 1-8.

Schärer U. (1984) The effect of initial ^{230}Th disequilibrium on young U-Pb ages: the Makalu case, Himalaya. *Earth and Planetary Science Letters* **67**, 191-204.

Scherer E., Münker C., and Mezger K. (2001) Calibration of the Lutetium-Hafnium clock. *Science* **293**, 683-687.

Schmitz M. D. and Bowring S. A. (2001) U-Pb zircon and titanite sytematics of the Fish Canyon Tuff: an assessment of high-precision U-Pb geochronology and its application to young volcanic rocks. *Geo. and Cosmo. Acta* **65**(15), 2571-2587.

Schmitz M. D., Bowring S. A., and Ireland T. R. (2003) Evaluation of Duluth Complex anorthositic series (AS3) zircon as a U-Pb geochronological standard: New high-precision isotope dilution thermal ionization mass spectrometry results. *Geo. and Cosmo. Acta* **67**(19), 3665-3672.

Schoene B. and Bowring S. A. (2003) U-Pb apatite and sphene thermochronology documenting mid-crustal temperature gradients during Archean lithospheric stabilization, Kaapvaal craton, southern Africa. *GSA Abst. with Prog.* **35**(6), 594.

Schön R., WInkler G., and Kutschera W. (2004) A critical review of experimental data for the half-lives of the uranium isotopes ^{238}U and ^{235}U. *Applied Radiation and Isotopes* **60**, 263-273.

Söderlund U., Patchett P. J., Vervoort J. D., and Isachsen C. E. (2004) The ^{176}Lu decay constant determined by Lu-Hf and U-Pb isotope systematics of Precambrian mafic intrusions. *Earth and Planetary Science Letters* **219**, 311-324.

Spell T. L. and McDougall I. (2003) Characterization and calibration of $^{40}Ar/^{39}Ar$ dating standards. *Chemical Geology* **198**, 189-211.

Steiger R. H. and Jäger E. (1977) Subcommission on Geochronology: Convention on the use of decay constants in geo- and cosmochronology. *EPSL* **36**, 359-362.

Stern, R.A. (2001) A new isotopic and trace element standard for the ion microprobe: preliminary TIMS U-Pb and electron microprobe data, current research. *Radiogenic Age and Isotopic Studies: Report 14.* Geological Survey of Canada, Ottawa, Canada.

Stern R. A. and Amelin Y. (2003) Assessment of errors in SIMS zircon U-Pb gechronology using a natural zircon standard and NIST SRM 610 glass. *Chemical Geology* **197**, 111-142.

Stern R. A. and Rayner N. (2003) Ages of several xenotime megacrysts by ID-TIMS: potential reference materials for ion microprobe U-Pb geochronology. *in Radiogenic Age and Isotopic Studies: Report 16, Geological Survey of Canada*, Vol. Current Research 2003-F1, pp. 7 p.

Todt, W., Cliff, R.A., Hanser A., and Hofmann, A.W. (1996) Evaluation of a ^{202}Pb-^{205}Pb double spike for high-precision lead isotope analysis. *AGU Geophysical Monograph* **95**, *Earth Processes: Reading the isotopic Code.* pp. 29-37

Tucker R.D. (1992) U-Pb dating of plinian-eruption ashfalls by the isotopic dilution method: a reliable and precise tool for time-scale calibration and biostratigraphic correlation. *Geol. Soc. Am. Abst. with Prog.* **24**, A198.

Tucker R.D. and McKerrow W.S. (1995) Early Paleozoic chronology: a review in light of new U-Pb zircon ages from Newfoundland and Britain. *Can. Jour. Earth Sci.* **32**, 368-379

Villeneuve M., Sandeman H. A., and Davis W. J. (2000) A method for intercalibration of U-Th-Pb and ^{40}Ar-^{39}Ar ages in the Phanerozoic. *Geochimica et Cosmochimica Acta* **64**(23), 4017-4030.

Wetherill G. W. (1956) Discordant uranium-lead ages. *Trans. Amer. Geophys. Union* **37**, 320-326.

Wiedenbeck M., Allé P., Corfu F., Griffin W. L., Meier M., Oberli F., Von Quadt A., Roddick J. C., and Spiegel W. (1995) Three natural zircon standards for U-Th-Pb, Lu-Hf, trace element and REE analyses. *Geostandards Newsletter* **19**, 1-23.

York D. (1966) Least-squares fitting of a straight line. *Can. Jour. Phys.* **44**, 1079-1086.

York D. (1967) The best isochron. *Earth and Planetary Science Letters* **2**, 479-482.

Zartman R. E. (1964) A geochronologic study of the Long Grove Pluton from the Llano uplift, Texas. *Journal of Petrology* **5**(3), 359-408.

Figure captions:

Figure 1: U-Pb concordia diagrams. Gray band is the concordia curve error envelope using U decay constants and 95% confidence intervals from Jaffey et al. (1971). Plotted with ISOPLOT (Ludwig, 1991). Error ellipses are 2SE of internal errors only.

Figure 2: Weighted mean U-Pb dates (in Ma) for equivalent data clusters. Analyses included in the weighted mean calculations are shown in Table 1 and Figure 1. Errors are 2SE.

Figure 3: U decay constants calculated from our U-Pb data (sample numbers shown across the top), compared against values of Jaffey et al. (1971) and Mattinson (2000) (the latter does not include errors in λ_{238}). (A) Calculated ^{235}U decay constant, assuming the value ^{238}U decay constant is correct. (B) Calculated ^{238}U decay constant, assuming the value ^{235}U decay constant is correct. (C) Calculated ratio of the U decay constants, making no assumptions about their absolute values. Errors are at the 95% confidence interval and are calculated using standard error-propagation techniques and by assuming concordance of weighted mean $^{206}Pb/^{238}U$ and $^{207}Pb/^{235}U$ ratios of statistically significant clusters and calculating the weighted mean decay constant values and errors. Decay constant errors of ^{235}U and ^{238}U from Jaffey et al. (1971) are propagated after weighted mean decay constants of ^{238}U and ^{235}U, respectively, are calculated.

Figure 4: Summary diagram for U-Pb and $^{40}Ar/^{39}Ar$ dates (in Ma). $^{40}Ar/^{39}Ar$ data are normalized to Fish Canyon sanidine = 28.02 Ma and the primary standard GA1550

Ar*/K values of Renne et al. (1998b). Tracer calibration errors for data from this study are negligible at the shown scale and those from other studies are not reported. References are given in Table 2. Errors are at the 95% confidence level.

Figure 5: Sensitivity analysis of systematic errors used in $^{40}Ar/^{39}Ar$ dates. The Y-axis in both diagrams is the % of the age, and the curves and U-Pb data in (B) are plotted as % offset from $^{40}Ar/^{39}Ar$ data in table 2 and figure 4. (A) The magnitude of systematic errors from various sources in calculated $^{40}Ar/^{39}Ar$ dates as a function of age. Also plotted is the % discordance of the weighted mean dates of U-Pb data from this study. (B) The effects of varying parameters important in calculating $^{40}Ar/^{39}Ar$ dates. Curves are plotted as % difference from $^{40}Ar/^{39}Ar$ dates calculated using FCs = 28.02 Ma and the primary standard GA1550 Ar*/K values of Renne et al. (1998b). Black solid curve: effect of using the ^{40}K decay constants and physical constants (including $^{40}K/K$) recommended by Min et al. (2000) and fixing the GA1550 age to our $^{206}Pb/^{238}U$ date. Gray solid curve: effect of using the age of the FCs and the ^{40}K decay constant of Kwon et al. (2002). Black dashed curve: effect of increasing the age of the K-Ar primary standard to its maximum error-bounds. Gray dashed curve: using the GA1550 Ar*/K and GA1550/FCs data from Spell and McDougall (2003), without showing the error-bounds, which are ~60% larger than those in the Renne et al. (1998b) calibration. Errors are at the 95% confidence level.

Table 1. U-Pb isotopic data.

				Isotopic ratios									Dates (Ma)						
	^{206}Pb	^{208}Pb	^{206}Pb		^{207}Pb		^{207}Pb		corr.	^{206}Pb		^{207}Pb		^{207}Pb			
Sample	Pb^*	Pb_c	(pg)	Th	^{204}Pb	^{206}Pb	^{238}U	% err	^{235}U	% err	^{206}Pb	% err	coef.	^{238}U	±	^{235}U	±	^{206}Pb	±	% disc.
(a)	(b)	(c)	(d)	(e)	(f)	(f)	(g)	(f)	(g)	(f)	(g)		(h)	(i)	(h)	(i)	(h)	(i)	(j)
JCA-62-02 Granite in Narryer gneiss complex																			
z1a*	2597	0.29	0.34	139617	0.091	0.670922	0.05	25.10333	0.07	0.27137	0.04	0.787	3309.43	1.33	3312.24	0.64	3313.94	0.63	0.14
z1b*	903	0.53	0.37	48314	0.098	0.670656	0.07	25.09321	0.08	0.27137	0.04	0.863	3308.40	1.84	3311.85	0.81	3313.94	0.65	0.17
z1c*	1201	0.44	0.36	64274	0.097	0.671097	0.05	25.10611	0.07	0.27133	0.04	0.789	3310.11	1.35	3312.35	0.64	3313.71	0.63	0.11
z1d*	943	0.32	0.35	50630	0.093	0.671272	0.06	25.11060	0.08	0.27130	0.04	0.834	3310.78	1.63	3312.53	0.74	3313.58	0.65	0.08
z2a*	232	0.39	0.36	12420	0.097	0.670902	0.12	25.08919	0.13	0.27122	0.06	0.889	3309.35	3.09	3311.69	1.31	3313.11	0.96	0.11
z2b*	109	0.27	0.35	5876	0.093	0.663882	0.11	24.68440	0.13	0.26967	0.07	0.820	3282.21	2.73	3295.82	1.27	3304.10	1.17	0.66
z3*	114	0.36	0.33	6172	0.087	0.668920	0.13	24.98632	0.15	0.27091	0.08	0.850	3301.70	3.29	3307.68	1.47	3311.31	1.24	0.29
EKC02-51_1L Kaap Valley pluton																			
z1	66	1.79	0.54	3508	0.144	0.648392	0.16	22.96112	0.16	0.25683	0.05	0.958	3221.92	3.98	3225.30	1.60	3227.39	0.74	0.17
z5	148	0.79	0.54	7806	0.145	0.648467	0.09	22.96530	0.10	0.25685	0.05	0.871	3222.21	2.23	3225.47	0.98	3227.50	0.78	0.16
z7	53	1.06	0.46	2819	0.125	0.648074	0.16	22.94685	0.18	0.25680	0.07	0.920	3220.68	4.12	3224.69	1.72	3227.18	1.10	0.20
z8	18	1.98	0.56	959	0.149	0.648473	0.27	22.95927	0.29	0.25678	0.11	0.928	3222.24	6.74	3225.22	2.79	3227.07	1.68	0.15
z9	48	1.71	0.54	2530	0.145	0.648570	0.18	22.97234	0.19	0.25689	0.06	0.952	3222.62	4.64	3225.77	1.88	3227.73	0.93	0.16
z10	45	1.65	0.50	2399	0.135	0.644285	0.34	22.77233	0.35	0.25635	0.06	0.984	3205.84	8.58	3217.264	3.36	3224.40	0.98	0.58
z11	54	1.52	0.67	2796	0.179	0.648177	0.16	22.95640	0.17	0.25687	0.05	0.951	3221.08	4.13	3225.10	1.67	3227.60	0.83	0.20
z12	135	0.80	0.66	6953	0.176	0.648418	0.08	22.95658	0.09	0.25677	0.05	0.844	3222.02	2.03	3225.10	0.92	3227.02	0.80	0.15
z13	100	1.02	0.50	5301	0.134	0.647344	0.15	22.91348	0.16	0.25672	0.05	0.949	3217.82	3.85	3223.27	1.56	3226.67	0.80	0.27
z14	25	0.95	0.45	1356	0.120	0.648286	0.25	22.95805	0.26	0.25684	0.06	0.970	3221.51	6.34	3225.17	2.51	3227.44	1.00	0.18
z16	174	0.77	0.47	9278	0.127	0.647780	0.22	22.93461	0.22	0.25678	0.05	0.974	3219.53	5.55	3224.17	2.19	3227.06	0.80	0.23
z17	64	0.74	0.26	3571	0.070	0.648292	0.12	22.95085	0.13	0.25676	0.05	0.927	3221.53	3.08	3224.86	1.28	3226.94	0.78	0.17
z18	98	1.10	0.53	5159	0.143	0.647710	0.18	22.93388	0.21	0.25680	0.11	0.854	3219.25	4.54	3224.14	2.04	3227.18	1.73	0.25
z19a	698	1.32	0.49	37067	0.131	0.645508	0.07	22.85424	0.08	0.25678	0.04	0.867	3210.63	1.78	3220.76	0.79	3227.06	0.64	0.51
z19b	656	1.40	0.49	34848	0.131	0.645607	0.10	22.85362	0.10	0.25674	0.04	0.920	3211.02	2.41	3220.73	1.01	3226.78	0.64	0.49
za1*	83	1.28	0.34	4548	0.092	0.648511	0.12	22.95610	0.13	0.25673	0.07	0.853	3222.38	2.92	3225.08	1.31	3226.77	1.11	0.14
za3*	43	1.49	0.37	2347	0.100	0.648273	0.15	22.95005	0.17	0.25676	0.06	0.929	3221.45	3.88	3224.83	1.61	3226.92	0.96	0.17
za4*	161	1.03	0.39	8720	0.106	0.648258	0.20	22.94795	0.21	0.25674	0.07	0.951	3221.40	5.10	3224.74	2.06	3226.81	1.03	0.17
za5*	98	1.06	0.32	5405	0.086	0.648202	0.10	22.94780	0.11	0.25676	0.05	0.909	3221.17	2.55	3224.73	1.08	3226.94	0.73	0.18
EGB-032 Eglab porphyry																			
z1	50	0.56	0.68	2774	0.198	0.375949	0.22	6.63698	0.23	0.12804	0.07	0.946	2057.33	3.80	2064.28	2.02	2071.23	1.31	0.67
z2	55	0.55	0.83	2985	0.239	0.378150	0.11	6.67659	0.14	0.12805	0.08	0.841	2067.64	2.03	2069.53	1.22	2071.41	1.32	0.18
z3	62	0.61	0.51	3630	0.145	0.378797	0.12	6.70051	0.14	0.12829	0.06	0.893	2070.66	2.15	2072.69	1.20	2074.71	1.08	0.19
z4	24	0.65	0.90	1310	0.259	0.378265	0.19	6.68110	0.24	0.12810	0.15	0.801	2068.17	3.41	2070.12	2.15	2072.07	2.57	0.19
z5	23	0.72	0.75	1268	0.217	0.377682	0.25	6.66810	0.28	0.12805	0.12	0.907	2065.45	4.49	2068.40	2.49	2071.37	2.10	0.29
z8	50	0.62	0.76	2744	0.224	0.368262	0.22	6.50328	0.23	0.12808	0.08	0.942	2021.22	3.79	2046.34	2.05	2071.75	1.38	2.44
z9	16	0.47	0.77	900	0.222	0.378309	0.28	6.67986	0.33	0.12806	0.16	0.866	2068.38	4.96	2069.96	2.90	2071.55	2.90	0.15
za1*	244	0.72	0.75	13410	0.215	0.378087	0.09	6.67574	0.11	0.12806	0.05	0.870	2067.34	1.64	2069.42	0.94	2071.48	0.93	0.20
za2*	83	1.20	0.74	4596	0.212	0.378056	0.10	6.67449	0.11	0.12804	0.05	0.882	2067.20	1.76	2069.25	1.00	2071.30	0.94	0.20
za3*	143	0.58	0.55	8194	0.159	0.378089	0.10	6.67645	0.11	0.12807	0.06	0.869	2067.35	1.76	2069.51	1.01	2071.66	1.00	0.21
za4*	67	0.58	0.74	3681	0.213	0.378271	0.10	6.68083	0.12	0.12809	0.06	0.884	2068.20	1.84	2070.09	1.05	2071.96	0.97	0.18
za5*	130	0.52	0.77	7117	0.222	0.378062	0.16	6.67546	0.16	0.12806	0.05	0.949	2067.22	2.76	2069.38	1.45	2071.53	0.92	0.21
za6*	32	1.08	0.77	1768	0.221	0.378236	0.20	6.67927	0.21	0.12807	0.07	0.936	2068.04	3.49	2069.88	1.86	2071.71	1.30	0.18
za7*	80	0.51	0.79	4371	0.227	0.378060	0.21	6.67451	0.22	0.12804	0.07	0.955	2067.21	3.70	2069.25	1.94	2071.27	1.15	0.20
QGNG																			
z1*	484	1.25	0.97	25374	0.283	0.331978	0.05	5.18061	0.07	0.11318	0.04	0.750	1847.96	0.81	1849.44	0.57	1851.10	0.81	0.17
z2*	454	0.94	1.03	23564	0.299	0.332255	0.07	5.18714	0.09	0.11323	0.05	0.845	1849.30	1.18	1850.51	0.74	1851.86	0.84	0.14
z3*	377	2.17	0.89	20179	0.258	0.332009	0.07	5.18396	0.08	0.11324	0.04	0.846	1848.11	1.14	1849.99	0.72	1852.10	0.81	0.22
z4*	256	1.83	1.00	13358	0.290	0.332171	0.10	5.18437	0.12	0.11320	0.06	0.866	1848.90	1.64	1850.05	1.01	1851.37	1.07	0.13
z5*	111	4.67	1.02	5780	0.297	0.331893	0.09	5.17929	0.10	0.11318	0.05	0.889	1847.55	1.48	1849.22	0.88	1851.10	0.86	0.19
z6.1*	759	0.47	1.00	39559	0.292	0.332313	0.05	5.18675	0.07	0.11320	0.04	0.781	1849.58	0.85	1850.44	0.58	1851.42	0.76	0.10
z7.1*	276	1.12	1.04	14305	0.303	0.332176	0.06	5.18380	0.08	0.11318	0.06	0.723	1848.92	0.98	1849.96	0.72	1851.12	1.05	0.12

Table 1. U-Pb isotopic data.

				Isotopic ratios									Dates (Ma)						
	Pb*	Pb_c	Th	^{206}Pb	^{208}Pb	^{206}Pb		^{207}Pb		^{207}Pb		corr.	^{206}Pb		^{207}Pb		^{207}Pb		
Sample	Pb_c	(pg)	U	^{204}Pb	^{206}Pb	^{238}U	% err	^{235}U	% err	^{206}Pb	% err	coef.	^{238}U	±	^{235}U	±	^{206}Pb	±	% disc.
(a)	(b)	(c)	(d)	(e)	(f)	(f)	(g)	(f)	(g)	(f)	(g)		(h)	(i)	(h)	(i)	(h)	(i)	(j)
AS3 Duluth Complex anorthitic series																			
za2*	330	0.89	0.61	19172	0.185	0.185287	0.05	1.94545	0.07	0.07615	0.05	0.681	1095.79	0.49	1096.88	0.48	1099.02	1.04	0.29
za4*	823	0.40	0.71	46658	0.217	0.185288	0.05	1.94505	0.07	0.07613	0.05	0.731	1095.80	0.49	1096.74	0.44	1098.60	0.90	0.26
za5*	2445	0.40	0.66	140356	0.200	0.185287	0.05	1.94462	0.06	0.07612	0.04	0.747	1095.80	0.46	1096.59	0.41	1098.18	0.82	0.22
za6*	213	1.28	0.62	12347	0.187	0.185319	0.05	1.94543	0.07	0.07614	0.05	0.734	1095.97	0.50	1096.87	0.46	1098.65	0.92	0.24
za7*	195	1.11	0.56	11487	0.169	0.185367	0.09	1.94590	0.11	0.07614	0.07	0.763	1096.23	0.88	1097.03	0.77	1098.65	1.48	0.22
za8*	775	0.76	0.65	44570	0.198	0.185342	0.06	1.94598	0.07	0.07615	0.05	0.788	1096.09	0.58	1097.06	0.49	1098.98	0.90	0.26
za9*	635	0.91	0.61	36929	0.185	0.185313	0.05	1.94519	0.07	0.07613	0.04	0.743	1095.94	0.49	1096.79	0.44	1098.51	0.89	0.23
za10*	987	0.74	0.62	57263	0.187	0.185236	0.06	1.94438	0.07	0.07613	0.04	0.797	1095.52	0.57	1096.51	0.47	1098.51	0.85	0.27
MS99-30 Palisade rhyolite																			
za2*	100	0.96	0.83	5545	0.252	0.184970	0.07	1.93859	0.10	0.07601	0.07	0.735	1094.07	0.72	1094.51	0.65	1095.40	0.72	0.12
za3*	79	1.25	0.89	4295	0.270	0.184947	0.16	1.93919	0.20	0.07605	0.12	0.791	1093.94	1.58	1094.72	1.33	1096.25	1.33	0.21
za4*	48	0.92	0.89	2609	0.269	0.185036	0.11	1.94024	0.14	0.07605	0.08	0.806	1094.43	1.13	1095.08	0.94	1096.37	0.91	0.18
za6*	36	1.20	0.81	2029	0.245	0.184909	0.14	1.93815	0.17	0.07602	0.09	0.837	1093.74	1.43	1094.36	1.15	1095.63	1.03	0.17
za7*	26	4.91	0.85	1435	0.259	0.185003	0.16	1.93958	0.21	0.07604	0.12	0.804	1094.25	1.65	1094.85	1.37	1096.07	1.34	0.17
za10*	204	1.15	0.82	11341	0.250	0.184910	0.07	1.93813	0.09	0.07602	0.06	0.775	1093.74	0.73	1094.35	0.63	1095.58	0.65	0.17
z1	43	3.69	0.78	2396	0.240	0.183121	0.10	1.92213	0.13	0.07613	0.08	0.779	1084.00	1.02	1088.81	0.88	1098.42	0.90	1.31
z1.1	34	0.90	0.68	1948	0.207	0.184877	0.12	1.93883	0.21	0.07606	0.16	0.634	1093.56	1.22	1094.59	1.40	1096.65	1.78	0.28
z2	19	3.32	0.89	1035	0.269	0.184966	0.19	1.93941	0.27	0.07605	0.18	0.743	1094.05	1.95	1094.80	1.79	1096.28	1.96	0.20
z2.1	59	0.94	0.76	3323	0.231	0.184958	0.09	1.93930	0.14	0.07605	0.11	0.650	1094.00	0.86	1094.76	0.93	1096.28	1.16	0.21
z3	77	1.51	0.85	4257	0.259	0.184996	0.07	1.93955	0.11	0.07604	0.08	0.698	1094.21	0.73	1094.84	0.72	1096.09	0.84	0.17
z4	61	1.20	0.88	3340	0.266	0.185009	0.27	1.93968	0.29	0.07604	0.08	0.955	1094.28	2.76	1094.89	1.92	1096.09	0.93	0.16
z4.1	55	1.37	0.83	3044	0.253	0.184936	0.08	1.93934	0.13	0.07606	0.10	0.620	1093.89	0.77	1094.77	0.86	1096.56	1.10	0.24
z5	23	2.52	0.84	1286	0.254	0.185072	0.17	1.93971	0.21	0.07601	0.13	0.790	1094.62	1.68	1094.90	1.42	1095.44	1.42	0.07
z5.1	27	1.27	0.86	1485	0.262	0.185096	0.17	1.94045	0.21	0.07603	0.13	0.788	1094.76	1.67	1095.16	1.43	1095.95	1.44	0.11
z6.1	37	1.87	0.87	2036	0.265	0.184898	0.10	1.93856	0.14	0.07604	0.10	0.734	1093.68	1.03	1094.50	0.94	1096.14	1.04	0.22
z6	115	1.49	0.77	6421	0.236	0.182514	0.05	1.91220	0.08	0.07599	0.06	0.658	1080.70	0.53	1085.35	0.55	1094.69	0.68	1.28
z7	98	11.89	0.78	5407	0.236	0.185114	0.06	1.94145	0.09	0.07606	0.06	0.713	1094.85	0.61	1095.50	0.58	1096.79	0.66	0.18
z9	14	4.05	0.79	818	0.239	0.184908	0.29	1.93870	0.35	0.07604	0.20	0.816	1093.73	2.87	1094.55	2.37	1096.18	2.24	0.22
z10	39	1.70	0.82	2174	0.250	0.185107	0.41	1.94068	0.44	0.07604	0.15	0.944	1094.82	4.16	1095.23	2.95	1096.04	1.59	0.11
z11	36	2.03	0.85	1978	0.258	0.185173	0.16	1.94262	0.19	0.07609	0.09	0.862	1095.17	1.62	1095.90	1.25	1097.35	1.04	0.20
91500																			
z2	227	2.47	0.36	14093	0.108	0.179343	0.05	1.85250	0.07	0.07492	0.04	0.760	1063.38	0.49	1064.32	0.44	1066.26	0.87	0.27
z12	1654	0.96	0.35	102639	0.106	0.179348	0.06	1.85281	0.07	0.07493	0.04	0.805	1063.41	0.58	1064.43	0.48	1066.53	0.87	0.29
z13	1058	0.84	0.36	65582	0.108	0.179354	0.05	1.85272	0.06	0.07492	0.04	0.764	1063.44	0.48	1064.40	0.42	1066.39	0.84	0.28
z14	1073	0.83	0.35	66606	0.107	0.179364	0.07	1.85251	0.08	0.07491	0.05	0.828	1063.50	0.66	1064.32	0.54	1066.02	0.92	0.24
z15	389	1.72	0.34	24213	0.105	0.179388	0.06	1.85331	0.07	0.07493	0.04	0.789	1063.63	0.54	1064.61	0.46	1066.62	0.87	0.28
z18	372	0.61	0.35	23079	0.107	0.179444	0.05	1.85335	0.07	0.07491	0.05	0.688	1063.94	0.45	1064.62	0.44	1066.02	0.97	0.20
z20	210	0.87	0.35	13016	0.107	0.179364	0.05	1.85330	0.08	0.07494	0.06	0.615	1063.50	0.48	1064.60	0.52	1066.85	1.26	0.31
z6413																			
x1k	11286	0.49	0.16	738065	0.049	0.167425	0.05	1.67321	0.07	0.07248	0.04	0.789	997.91	0.48	998.41	0.42	999.50	0.82	0.16
x1m	5476	0.30	0.15	359189	0.045	0.167455	0.06	1.67389	0.07	0.07250	0.04	0.826	998.08	0.56	998.66	0.47	999.95	0.85	0.19
x1n	5158	0.13	0.17	336515	0.050	0.167439	0.05	1.67358	0.07	0.07249	0.05	0.736	997.99	0.48	998.55	0.45	999.77	0.97	0.18
x1p	4623	0.16	0.17	301712	0.050	0.167422	0.04	1.67329	0.06	0.07249	0.04	0.716	997.89	0.39	998.44	0.37	999.63	0.83	0.17
x1q	2622	0.21	0.17	171135	0.051	0.167379	0.05	1.67275	0.07	0.07248	0.05	0.723	997.65	0.44	998.23	0.42	999.50	0.92	0.18
x1r	2478	0.23	0.17	161766	0.051	0.167410	0.04	1.67331	0.06	0.07249	0.04	0.716	997.83	0.42	998.44	0.40	999.82	0.89	0.20
x1u	2494	0.21	0.16	162828	0.050	0.167436	0.04	1.67344	0.06	0.07249	0.04	0.702	997.97	0.40	998.49	0.39	999.63	0.88	0.17
z6266																			
z1	88	0.62	0.22	5736	0.068	0.090650	0.07	0.73602	0.11	0.05889	0.09	0.610	559.38	0.36	560.08	0.48	562.91	1.94	0.63
z3	83	2.02	0.22	5426	0.069	0.090634	0.07	0.73566	0.10	0.05887	0.07	0.698	559.28	0.36	559.87	0.42	562.24	1.54	0.52
z7a*	165	0.55	0.22	10733	0.069	0.090652	0.05	0.73565	0.07	0.05886	0.06	0.639	559.39	0.25	559.86	0.32	561.76	1.25	0.42
z9a*	105	0.71	0.22	6821	0.069	0.090621	0.05	0.73559	0.08	0.05887	0.06	0.707	559.21	0.29	559.83	0.34	562.37	1.21	0.56
z10a*	76	0.72	0.22	4972	0.069	0.090633	0.06	0.73593	0.10	0.05889	0.07	0.667	559.28	0.34	560.03	0.43	563.12	1.63	0.68
z12a*	288	0.39	0.22	18719	0.069	0.090641	0.05	0.73539	0.08	0.05884	0.06	0.648	559.32	0.26	559.71	0.32	561.31	1.25	0.35
z13a*	263	0.67	0.22	17098	0.069	0.090597	0.05	0.73512	0.07	0.05885	0.05	0.701	559.07	0.26	559.56	0.30	561.52	1.07	0.44

Table 1. U-Pb isotopic data.

				Isotopic ratios									Dates (Ma)						
	Pb*	Pb_c	Th	^{206}Pb	^{208}Pb	^{206}Pb		^{207}Pb		^{207}Pb		corr.	^{206}Pb		^{207}Pb		^{207}Pb		
Sample	Pb_c	(pg)	U	^{204}Pb	^{206}Pb	^{238}U	% err	^{235}U	% err	^{206}Pb	% err	coef.	^{238}U	±	^{235}U	±	^{206}Pb	±	% disc.
(a)	(b)	(c)	(d)	(e)	(f)	(f)	(g)	(f)	(g)	(f)	(g)		(h)	(i)	(h)	(i)	(h)	(i)	(j)
NMB-03-1 North Mountain basalt																			
z3	156	1.10	2.23	6468	0.720	0.031713	0.06	0.21948	0.10	0.05020	0.08	0.625	201.26	0.12	201.48	0.18	204.10	1.83	1.39
z4	195	1.13	2.00	8459	0.642	0.031711	0.05	0.21939	0.08	0.05018	0.07	0.596	201.25	0.10	201.40	0.15	203.22	1.57	0.97
z5	131	0.77	1.63	6078	0.526	0.031718	0.05	0.21955	0.09	0.05020	0.07	0.607	201.29	0.11	201.54	0.17	204.47	1.68	1.55
z8	187	0.56	2.23	7788	0.714	0.031713	0.06	0.21939	0.11	0.05017	0.09	0.618	201.26	0.13	201.40	0.20	203.08	1.98	0.89
z11	155	0.92	1.85	6899	0.596	0.031703	0.05	0.21944	0.09	0.05020	0.07	0.618	201.20	0.11	201.45	0.17	204.32	1.67	1.53
z12	136	0.80	2.29	5612	0.733	0.031718	0.06	0.21944	0.11	0.05018	0.09	0.597	201.29	0.12	201.44	0.20	203.22	2.03	0.95
z18	1658	0.44	2.50	65403	0.804	0.031728	0.05	0.21959	0.07	0.05019	0.05	0.712	201.36	0.09	201.56	0.12	204.03	1.07	1.31
z19	1967	0.38	2.36	79326	0.764	0.031710	0.05	0.21956	0.07	0.05022	0.05	0.696	201.24	0.09	201.54	0.12	205.05	1.11	1.86
z20	283	1.34	1.86	12607	0.597	0.031719	0.07	0.21950	0.09	0.05019	0.06	0.796	201.30	0.14	201.49	0.17	203.81	1.29	1.23
z21	345	1.41	2.42	13836	0.776	0.031713	0.04	0.21941	0.07	0.05018	0.06	0.624	201.26	0.09	201.42	0.13	203.22	1.30	0.96
RSES01-98 (GA-1550)																			
z1	185	1.22	0.38	11716	0.121	0.015496	0.05	0.10266	0.07	0.04805	0.05	0.669	99.12	0.05	99.23	0.07	101.72	1.29	2.55
z2	205	0.64	0.70	11944	0.222	0.015499	0.05	0.10268	0.08	0.04805	0.06	0.640	99.14	0.05	99.25	0.07	101.80	1.40	2.61
z3	72	0.85	0.34	4645	0.109	0.015501	0.06	0.10273	0.10	0.04807	0.08	0.649	99.16	0.06	99.30	0.10	102.62	1.81	3.37
z4	154	0.83	0.67	9017	0.215	0.015499	0.05	0.10271	0.08	0.04806	0.06	0.633	99.15	0.05	99.27	0.08	102.24	1.50	3.03
z5	106	1.25	0.50	6530	0.159	0.015484	0.06	0.10261	0.09	0.04806	0.07	0.621	99.05	0.06	99.18	0.09	102.24	1.75	3.12
z6	298	0.99	0.56	17994	0.178	0.015577	0.05	0.10320	0.08	0.04805	0.06	0.633	99.64	0.05	99.73	0.08	101.79	1.49	2.12
z7	447	1.02	0.46	27591	0.148	0.015488	0.05	0.10262	0.07	0.04805	0.05	0.680	99.08	0.05	99.19	0.07	101.87	1.20	2.74
z9	154	0.71	0.45	9523	0.145	0.015491	0.05	0.10262	0.08	0.04805	0.06	0.599	99.09	0.05	99.19	0.08	101.50	1.52	2.37
z10	103	0.50	0.65	6051	0.209	0.015498	0.05	0.10306	0.10	0.04823	0.08	0.569	99.14	0.05	99.59	0.09	110.47	1.88	10.25
z10.5	332	0.94	0.76	19001	0.245	0.015504	0.06	0.10283	0.08	0.04810	0.06	0.697	99.18	0.05	99.38	0.08	104.34	1.36	4.94
z11	326	0.93	0.63	19253	0.203	0.015491	0.05	0.10273	0.08	0.04810	0.06	0.693	99.09	0.05	99.29	0.07	104.04	1.32	4.75
z12	96	1.17	0.49	5911	0.158	0.015496	0.06	0.10279	0.09	0.04811	0.07	0.648	99.13	0.06	99.35	0.09	104.71	1.71	5.33
z13	98	2.64	0.52	5955	0.166	0.015494	0.06	0.10267	0.09	0.04806	0.06	0.704	99.12	0.06	99.23	0.08	102.09	1.45	2.92
z15	173	0.92	0.79	9822	0.254	0.015481	0.05	0.10258	0.07	0.04806	0.05	0.654	99.03	0.05	99.15	0.07	102.02	1.27	2.93
z16	35	3.93	0.47	2174	0.151	0.015489	0.10	0.10284	0.16	0.04816	0.12	0.637	99.08	0.10	99.40	0.15	106.88	2.89	7.29
z17aa	55	1.33	0.58	3317	0.187	0.015456	0.10	0.10252	0.15	0.04810	0.11	0.697	98.88	0.10	99.10	0.14	104.34	2.53	5.23
z18aa	137	1.27	0.53	8328	0.171	0.015481	0.05	0.10266	0.08	0.04809	0.06	0.639	99.03	0.05	99.23	0.07	103.89	1.40	4.67
z21a*	65	0.71	0.57	3923	0.182	0.015494	0.07	0.10271	0.13	0.04808	0.11	0.547	99.11	0.07	99.28	0.13	103.22	2.66	3.98
z23a*	84	0.61	0.46	5177	0.148	0.015491	0.06	0.10269	0.10	0.04808	0.08	0.601	99.10	0.06	99.26	0.09	103.14	1.82	3.92
z24a*	195	1.02	0.59	11667	0.190	0.015492	0.06	0.10268	0.09	0.04807	0.06	0.725	99.10	0.06	99.25	0.08	102.69	1.44	3.49

(a) z1, z2 etc. are labels for fractions composed of single grains or fragments of grains; x = xenotime, z = zircon; * denotes zircon fractions that were subjected to the chemical abrasion technique (all others, except the xenotime, underwent mechanical abrasion); Labels with bold text denote fractions used in the weighted mean calculations (see text and Figure 2).

(b) Ratio of radiogenic Pb to common Pb.

(c) Total weight of common Pb.

(d) Model Th/U ratio calculated from radiogenic 208Pb/206Pb ratio and 207Pb/206Pb age.

(e) Measured ratio corrected for spike and fractionation only. Mass fractionation corrections were based on analysis of NBS-981 and NBS-983. Corrections of 0.25 ± 0.04%/amu (atomic mass unit) and 0.07 ± 0.04%/amu were applied to single-collector Daly analyses and dynamic Faraday-Daly analyses, respectively, performed on the Sector-54 mass spectrometer. Correction of 0.09 ± 0.04%/amu was applied to dynamic Faraday-Daly analyses performed on the Isoprobe-T mass spectrometer.

(f) Corrected for fractionation, spike, blank, and initial common Pb. All common Pb was assumed to be procedural blank.

(g) Errors are 2 sigma, propagated using the algorithms of Ludwig (1980).

(h) Calculations are based on the decay constants of Jaffey et al. (1971).

(i) Errors are 2 sigma.

(j) % discordance = 100 - (100 x 206Pb/238U date / 207Pb/206Pb date).

Table 2: Summary of U-Pb and $^{40}Ar/^{39}Ar$ comparison from geologic samples

	$^{40}Ar/^{39}Ar$ date[a]					U-Pb date[c]					
	(Ma)	±[b]	mineral	reference	interpretation	(Ma)	±[b]	type	reference	% difference[d]	±[b]
Fish Canyon	28.02	0.06	sanidine	Renne et al. (1998b)	timing of eruption	28.478	0.024	$^{206}Pb/^{238}U$	Schmitz and Bowring (2001)	1.62	0.23
	28.12	*0.08*	sanidine	Spell and McDougall (2003)	timing of eruption						
MAC-83 Tuff	24.25	0.10	biotite	Villineuve et al. (2000)	timing of eruption	24.22	0.08	$^{207}Pb/^{235}U$	Villineuve et al. (2000) *monazite*	-0.14	0.53
Rum complex	60.60	1.0	phlogopite	Hamilton et al. (1998)	timing of crystallization	60.53	0.08	$^{206}Pb/^{238}U$	Hamilton et al. (1998)	-0.21	1.67
Cuillin complex	58.10	1.2	biotite	Hamilton et al. (1998)	timing of crystallization	58.91	0.07	$^{206}Pb/^{238}U$	Hamilton et al. (1998)	1.34	2.11
Muck Tuff	61.54	0.19	sanidine	Chambers et al. (2005)	timing ot eruption	61.08	0.27	$^{206}Pb/^{238}U$	Chambers et al. (2005)	-0.75	0.53
GA1550 (K-Ar)	98.8	1.1	biotite	Renne et al. (1998b)	crystallization/cooling	102.14	0.47	$^{207}Pb/^{206}Pb$	this study	3.38	1.23
	98.5	1.6	biotite	Spell and McDougall (2003)		99.12	0.02	$^{206}Pb/^{238}U$	this study	0.32	1.10
	97.9	1.8	biotite	McDougall and Roksandik (1974)							
Siberian Traps	250.0	0.2	sanidine	Renne and Basu (1991)	timing of eruption	251.7	0.4	$^{206}Pb/^{238}U$	Kamo et al. (2003)	0.67	0.18
						251.1	0.3	$^{206}Pb/^{238}U$	Kamo et al. (2003)	0.43	0.14
						251.3	0.2	$^{206}Pb/^{238}U$	Kamo et al. (1996)	0.51	0.11
P-T boundary	249.9	0.2	sanidine, plagioclase	Renne et al. (1995)	bracket provided by eruption ages above and below the boundary	252.2	0.4	$^{206}Pb/^{238}U$	Mundil et al. (2004)	0.91	0.18
Deicke	449.8	2.3	sanidine	Min et al. (2001)	timing of eruption	454.5	0.5	$^{206}Pb/^{238}U$	Tucker (1992)	1.03	0.53
Millbrig	448.0	2.0	sanidine	Min et al. (2001)	timing of eruption	453.1	1.3	$^{206}Pb/^{238}U$	Tucker (1992)	1.13	0.54
Kinnekulle	454.8	2.0	sanidine	Min et al. (2001)	timing of eruption	456.9	1.8	U-Pb	Tucker and McKerrow (1995)	0.45	0.59
Bushveld Complex	2042.4	3.2	biotite	Nomade et al. (2004)	post-intrusion metasomatic growth	2058.9	0.8	$^{207}Pb/^{206}Pb$	Buick et al. (2001) *titanite metamorphic/cooling date*	0.81	0.16
Acapulco meteorite	4507	18	plagioclase	Renne (2000)	cooling date	4557	2	$^{207}Pb/^{206}Pb$	Göpel et al. (1992)	1.10	0.41
Palisade rhyolite	1088.4	3.6	sanidine	Min et al. (2000)	timing of eruption	1097.6	2.1	$^{207}Pb/^{206}Pb$	Min et al. (2000)	0.84	0.38
						1096.1	0.4	$^{207}Pb/^{206}Pb$	this study	0.71	0.33
						1094.2	0.2	$^{206}Pb/^{238}U$	this study	0.54	0.33
Eglab porphyry	2054.8	2.4	hornblende	P. Renne, Pers. Comm.	timing of eruption	2071.6	0.4	$^{207}Pb/^{206}Pb$	this study	0.81	0.12
						2067.5	0.7	$^{206}Pb/^{238}U$	this study	0.62	0.12
Kaap Valley pluton	3218.3	6.7	hornblende	Layer et al. (1992)	cooling date	3227	1	$^{207}Pb/^{206}Pb$	Kamo and Davis (1994)	0.27	0.21
						3227.2	0.2	$^{207}Pb/^{206}Pb$	this study	0.28	0.21
						3221.4	0.8	$^{206}Pb/^{238}U$	this study	0.10	0.21

(a) dates not in italics are normalized to FCs = 28.02 using the GA1550/FCs calibration of Renne et al. (1998b). Kaap Valley pluton data were renormalized to FCs = 28.02 using the Hb3gr/FCs calibration of Renne (2000). Muck Tuff renormalized using TCs/Taylor Creek of Renne et al. (1998b). Date in italics is normalized using primary GA 1550 calibration and GA1550/FCs calibration of Spell and McDougall (2003). GA-1550 dates are K-Ar primary calibrations.

(b) errors are at the 95% confidence interval and exclude errors for the age of GA1550, the GA1550/FCs calibration, and external errors.

(c) U-Pb dates are all interpreted to be zircon crystallization dates except for the Acapulco meteorite, which is a Pb-Pb isochron cooling date from phosphates, the sphene metamorphic cooling date from Buick et al. (2001) from the Bushveld complex, and the monazite date from Villineuve et al. (2000).

(d) % difference is calculated relative to the uppermost $^{40}Ar/^{39}Ar$ or K-Ar date

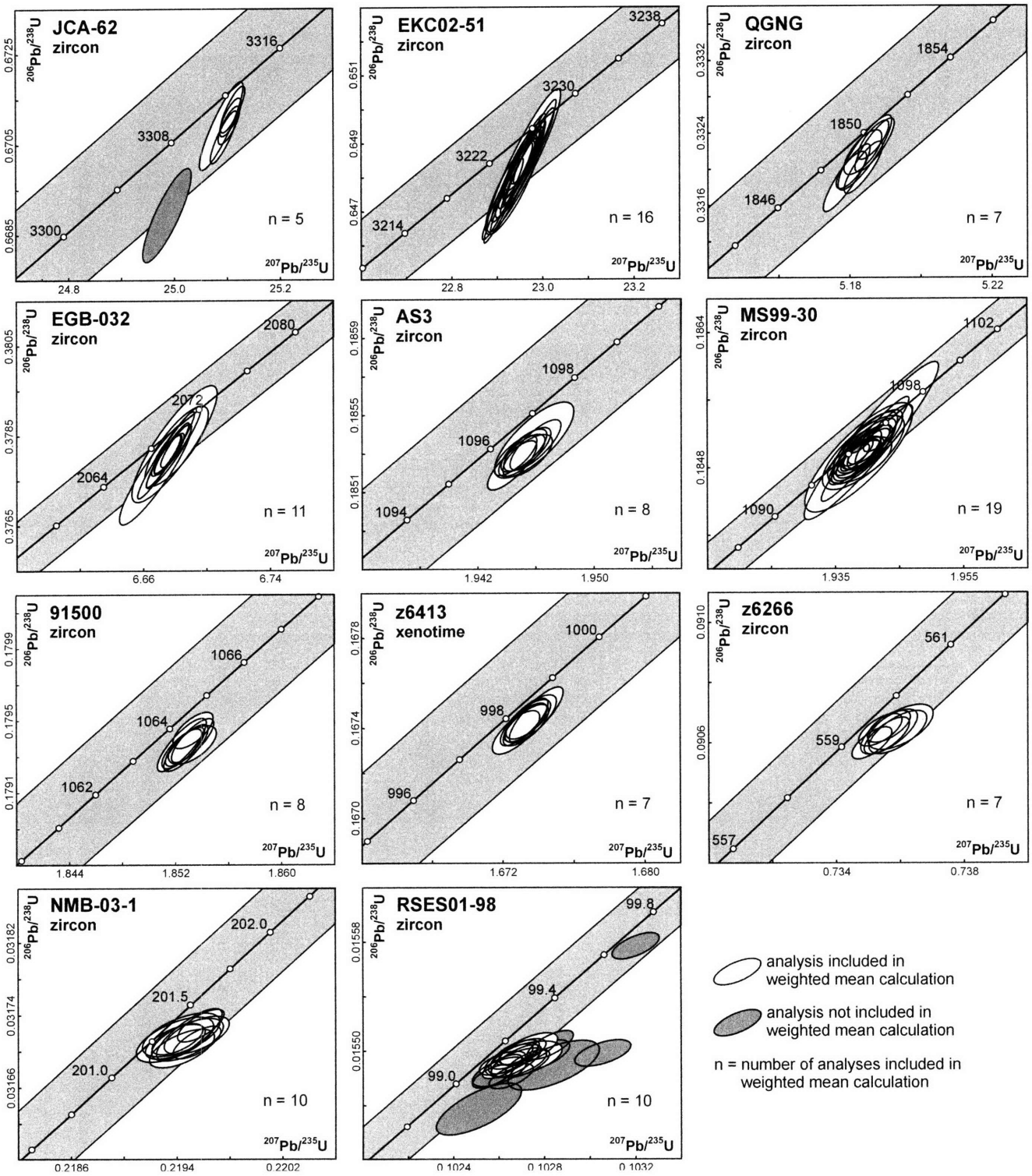

Fig. 1. Schoene et al.

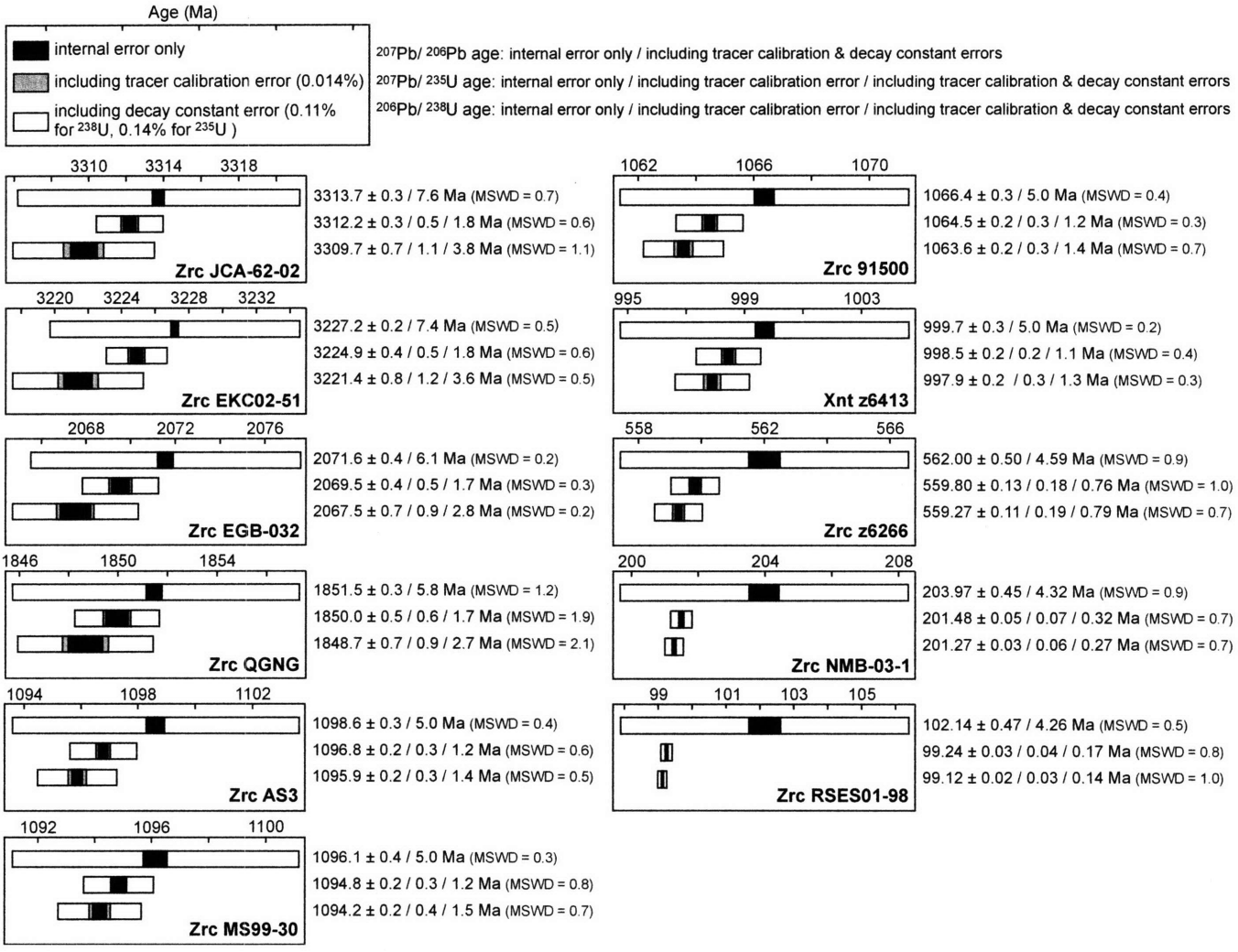

Fig. 2. Schoene et al.

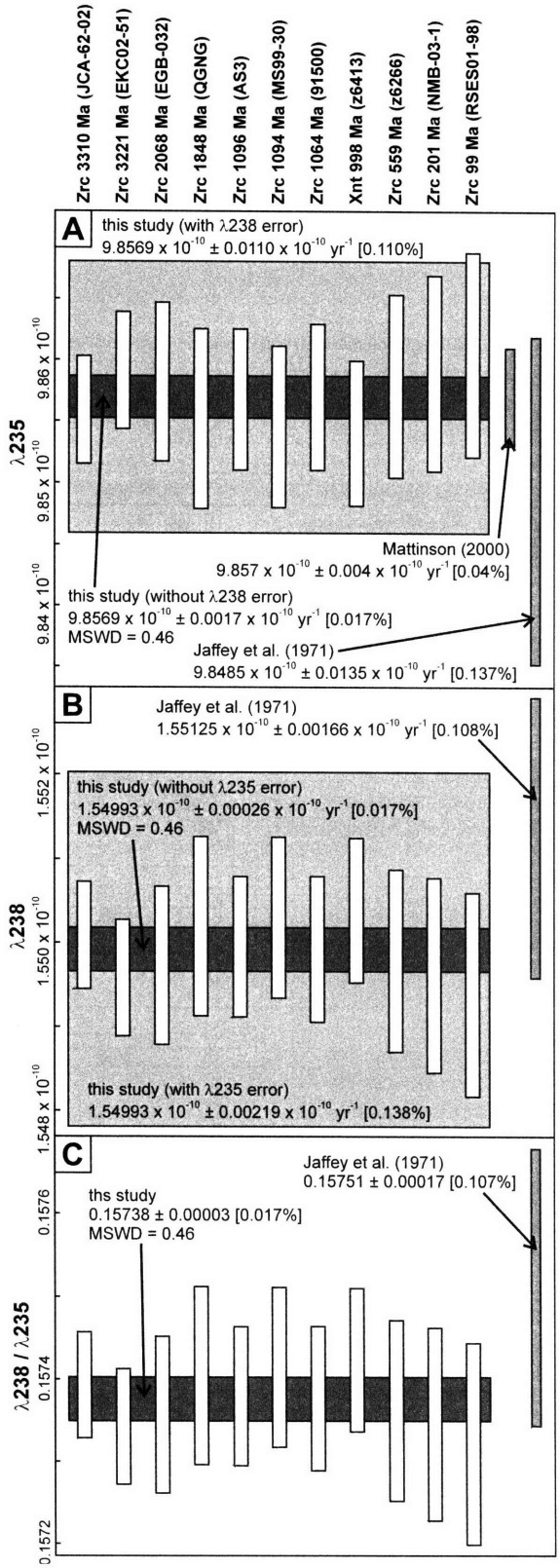

Fig. 3. Schoene et al.

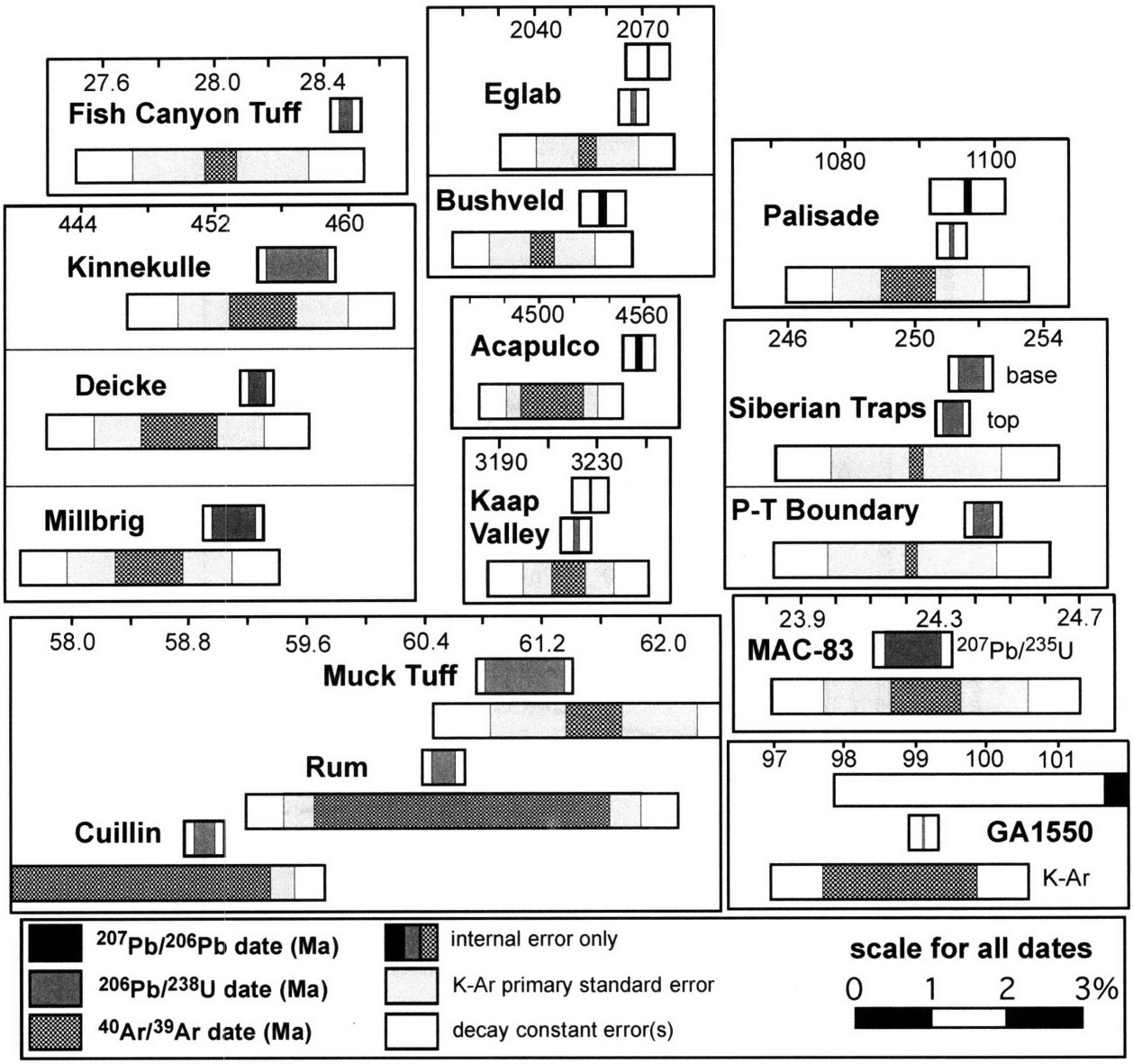

Fig. 4. Schoene et al.

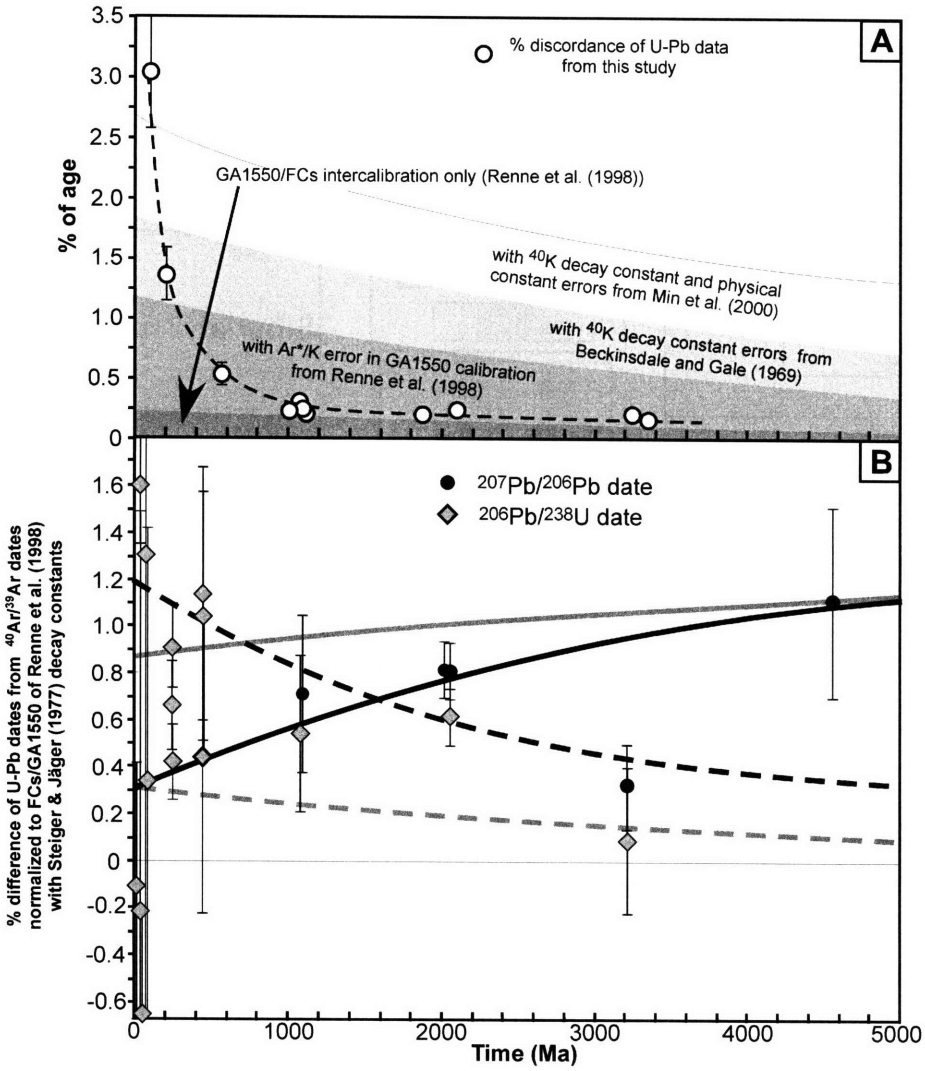

Fig. 5. Schoene et al.

CHAPTER 6

U-Pb systematics of the McClure Mountain syenite: thermochronological constraints on the age of the $^{40}Ar/^{39}Ar$ standard MMhb

Blair Schoene[1]* and Samuel A. Bowring[1]

[1] Department of Earth, Atmospheric and Planetary Sciences; Room 54-1116; 77 Massachusetts Ave., Massachusetts Institute of Technology, Cambridge, MA 02139, USA.

**schoene@mit.edu*

published in *Contributions to Mineralogy and Petrology 151: 615-630, 2006*

ABSTRACT

Recent advances in U-Pb geochronology allow unprecedented levels of precision in the determination of geological ages. However, increased precision has also illuminated the importance of understanding subtle sources of open-system behavior such as Pb-loss, inheritance, intermediate daughter product disequilibria, and the accuracy of the model assumptions for initial Pb (Pb_c). Deconvolution of these effects allows a much richer understanding of the power and limitations of U-Pb geochronology and thermochronology. In this study, we report high-precision ID-TIMS U-Pb data from zircon, baddelleyite, titanite and apatite from the McClure Mountain syenite, from which the $^{40}Ar/^{39}Ar$ hornblende standard MMhb is derived. We find that excess ^{206}Pb in zircon due to inclusions of high-Th minerals and elevated Th/U in titanite and apatite jeopardize the utility of the ^{238}U-^{206}Pb system in this rock. Strongly air-abraded zircons give dates that are younger than chemical-abraded zircons, which yield a statistically robust $^{207}Pb/^{235}U$ date of 523.98 ± 0.12 Ma that is interpreted as the crystallization age. We explore the best method of Pb_c correction in titanite and apatite by analyzing the U-Pb isotopes of K-feldspar and using 2-D and 3-D regression methods – the latter of which yields the best results in each case. However, the calculated compositions of Pb_c for titanite, apatite and K-feldspar are different, implying that using a single Pb_c correction for multiple U-Pb thermochronometers may be inaccurate. The U-Pb thermochronological results are used to predict a closure time for Ar in hornblende of 522.98 ± 1.00 Ma. Widely cited K-Ar and $^{40}Ar/^{39}Ar$ dates overlap with the U-Pb date, and relatively large errors make it impossible to verify whether U-Pb dates are systematically ≤ 1% older than K-Ar and $^{40}Ar/^{39}Ar$ dates.

1. INTRODUCTION

U-Pb geochronology is one of the most precise methods for placing temporal constraints on igneous and metamorphic processes and for establishing benchmarks for the stratigraphic time scale. Because of the high closure temperature ($T_c \geq 1000$ °C) for diffusion of Pb and the high U (and negligible initial Pb) concentrations in zircon, this mineral is ideal for dating the timing of crystallization under igneous and metamorphic conditions. In addition, minerals with lower T_c such as titanite ($T_c \approx 550$-650 °C; Cherniak 1993; Corfu 1988; Frost et al. 2000), apatite ($T_c \approx 450$-550 °C; Chamberlain and Bowring 2000; Cherniak et al. 1991; Nemchin and Pidgeon 1999), and rutile ($T_c \approx 400$-500 °C; Cherniak and Watson 2000; Mezger et al. 1991; Schmitz and Bowring 2003) have allowed the determination of thermal histories of rocks in the lower to middle crust. Over the past fifteen years, improvements in isotope dilution thermal ionization mass-spectrometry (ID-TIMS), sample preparation, and laboratory blanks have resulted in internal precision on individual dates to below the 0.1% level, allowing for the calibration of geologic time at an unprecedented level. However, such precision has also revealed the importance of quantitatively addressing what are often subtle sources of open-system behavior in U-Pb systematics such as intermediate daughter product disequilibria, Pb-loss, and inheritance (see reviews in Hanchar and Hoskin 2003). These issues are also important in U-Pb thermochronology, though precision is often limited by relatively low ratios of radiogenic lead to initial (a.k.a. common) lead (Pb^*/Pb_c), introducing significant error in the correction for the isotopic composition of Pb_c (Ludwig 1980, 1998). In fact, the Pb_c correction is arguably the most prominent source of inaccuracy in U-Pb thermochronology and is a critical aspect to calculating dates which are as accurate as

they are precise (Chamberlain and Bowring 2000; Corfu 1988; Verts et al. 1996). But because the isotopic signature of Pb in rocks or magmas may vary widely as a function of time and space during crystallization and cooling, each approach to the correction involves a set of assumptions that are difficult to address in detail.

Improvements in both the precision and accuracy of U-Pb geo- and thermochronology is important both for a better understanding of the geologic record but also for the purposes of intercalibrating the U-Pb system with other geochronologic methods. For example, Renne et al. (1998a) pointed out that many $^{40}Ar/^{39}Ar$ dates are systematically younger than U-Pb dates by $\leq 1\%$, and Min et al. (2000) suggested – based on a re-evalution of the experimental data – that this is because the values of the ^{40}K decay constant used by the geochronologic community (Steiger and Jäger 1977) should be ~2% lower and that larger associated uncertainties are more realistic. Because high-precision experimental redetermination of the ^{40}K decay constant is a very difficult task, it has been suggested that it be calibrated against the U decay constants, whose values are the most precisely known in geochronology (Jaffey et al. 1971). However, Mattinson (2000) and Schoene et al. (2006) use systematic discordance of high-precision ID-TIMS U-Pb dates to show that one or both of the mean values of the U decay constants are inaccurate (but within the reported errors), which will adversely affect the approach of calibrating other decay schemes against U-Pb. Intercalibration of the two methods therefore requires both the generation of a large set of mineral pairs dated with high-precision by both methods that unambiguously record the same event, and ultimately repeated experiments to redetermine the U and K decay constants.

Intercalibrating the U-Pb and $^{40}Ar/^{39}Ar$ systems is complicated in part by the contrasting closure temperatures of diffusion of the respective daughter products (Dodson 1973). High-K minerals used in $^{40}Ar/^{39}Ar$ geochronology such as hornblende ($T_c \approx 550$-500 °C; Harrison 1981) or micas ($T_c < 350$ °C; Grove and Harrison 1996; Harrison et al. 1985) record cooling through their closure temperatures and therefore cannot be compared with zircon U-Pb dates that record crystallization. This problem may be overcome by using $^{40}Ar/^{39}Ar$ geochronology in sanidine from young volcanic rocks, whose $^{40}Ar/^{39}Ar$ systematics likely record the timing of eruption because the T_c is below that of magmatic temperatures. However, U-Pb dates from zircons in young magmatic systems are sometimes complicated by pre-eruptive crystallization of unknown duration (Reid and Coath 2000; Reid et al. 1997; Schmitz and Bowring 2001). This problem becomes less important as the age of the sample increases because reasonable estimates of magma residence time (Reid and Coath 2000; Reid et al. 1997) are likely to be smaller than the individual errors of high-precision U-Pb dates. On the other hand, older volcanic rocks pose difficulty for $^{40}Ar/^{39}Ar$ dating because mineralogically pure sanidine is unstable at surface conditions and may not record the timing of eruption (e.g. Min et al. 2000). Quickly-cooled plutonic rocks provide another option for intercalibration, though assessing systematic biases between U-Pb and $^{40}Ar/^{39}Ar$ dates introduced by ^{40}K decay constant inaccuracies is necessarily based on an assumed cooling rate, unless U-Pb thermochronology can be used to establish a thermal context for the $^{40}Ar/^{39}Ar$ data (Schmitz and Bowring 2001; Schoene et al. 2006).

In this contribution, we address the issues of precision versus accuracy in U-Pb dating and systematic biases between the U-Pb and $^{40}Ar/^{39}Ar$ dating methods. We present

data from the McClure Mountain syenite, the source of a widely used standard in $^{40}Ar/^{39}Ar$ dating, the McClure Mountain hornblende (MMhb; Alexander et al. 1978; Samson and Alexander 1987). Ample K-Ar and $^{40}Ar/^{39}Ar$ data for this hornblende allow for the assessment of interlaboratory bias and sample heterogeneity. In addition, the abundance of high-U minerals, such as zircon, baddeleyite, titanite, and apatite allow us to characterize the thermal history of this rock in the U-Pb system alone. Back-scattered electron (BSE) and cathodoluminesence (CL) imaging in combination with ID-TIMS U-Pb dating of zircon provide a high-precision date for crystallization of the rock. Careful assessment of the compositions of Pb_c in titanite, apatite and K-feldspar in relation to their petrographic context allows us to calculate a temperature-time curve with high confidence, providing a framework for comparison with $^{40}Ar/^{39}Ar$ dates. In addition, assessment of Pb isotopic systematics as a function of time allows for the construction of petrologic models for the McClure Mountain magmatic system.

2. METHODS

2.1 Electron microprobe analysis

The MIT JEOL 733 Superprobe electron microprobe (EMP) facility was used for both imaging and energy dispersive spectrometry (EDS) of zircon separates and thin sections. Zircons were hand-picked based on varying morphology, color, clarity, and degree of metamictization and were mounted in epoxy resin and polished to reveal the crystal centers. Both grain-mounts and thin sections were polished, cleaned, and carbon-coated. BSE and CL images were collected using a 15 keV accelerating voltage with a beam current between 4 and 50 nA depending on the individual mineral. EDS analysis was

conducted using a 1 μm beam size, and this technique was used for mineral identification and qualitative major element analysis.

2.2 U-Pb analytical procedure

Minerals were extracted from the rock sample by standard crushing, Wilfley table, heavy-liquid, and magnetic separation. Zircon fractions were pre-treated with either the air-abrasion (Krogh 1982) or chemical-abrasion (Mattinson 2003, 2005) technique. Air-abraded zircons were ultrasonically cleaned in 30% HNO_3 for one hour, fluxed in 30% HNO_3 at ~80°C for one hour, and rinsed in ultrapure acetone and H_2O before being loaded into 300 μl Teflon FEP microcapsules and spiked with a mixed ^{233}U-^{235}U-^{205}Pb tracer. Zircon was dissolved in ~120 μl 29M HF with ~25 μl 30% HNO_3 at ~210°C for 48 hours, dried to fluorides, and then re-dissolved in 6M HCl at ~180°C overnight. For the chemical-abrasion technique, zircons were placed in a muffle furnace at 900 ± 20°C for ~60 hours in quartz beakers before being transferred to 300 μl Teflon FEP microcapsules and leached in ~120 μl 29M HF + ~25 μl 30% HNO_3 for 12-14 hours at ~180 °C. Fractions were then rinsed in ultrapure H_2O, fluxed on a hotplate at ~80 °C for an hour in 6M HCl, ultrasonically cleaned for one hour, placed back on the hotplate for an additional 30 minutes, and rinsed in ultrapure H_2O and 30% HNO_3. Fractions were then spiked and fully dissolved using the procedure described above. Cleaning and dissolution of baddeleyite, titanite, and feldspar follow that of air-abraded zircons; apatite was rinsed only in water and dissolved in 12N HCl overnight. Step-wise leaching of feldspar followed the procedure of Housh and Bowring (1991), modified to account for smaller sample size. U and Pb were separated using an HCl-based single-column (zircon

and baddeleyite) or an HBr-based two-column (titanite, apatite, feldspar, and feldspar leachates) anion exchange chemistry modified after Krogh (1973).

U and Pb isotopic measurements were done on a VG Sector-54 multi-collector thermal-ionization mass spectrometer at MIT. Pb and U were either loaded together (HCl-based chemistry) or separate (HBr-based chemistry) on Re filaments in a silica-gel/phosphoric acid mixture (Gerstenberger and Haase 1997). Pb was measured by either: 1) peak-hopping on a single Daly detector (for smaller beams); 2) a dynamic Faraday-Daly routine (F-D) that cycles between placing mass 204 in the axial Daly collector and masses 205-208 on the H1-H4 Faraday detectors to placing mass 205 in the axial Daly and masses 206-208 in the H1-H3 Faradays, providing real-time Daly gain correction; or 3) for samples with large 204 peaks, in static Faraday mode. U isotopic measurements were made as the oxide in static Faraday mode. Mass fractionation and detector bias on the Daly detector were determined to be 0.25 ± 0.04 %/a.m.u. over a wide temperature range based on analysis of the NBS-981 common Pb standard and spiked aliquots of NBS-983. Mass fractionation on the F-D and static Faraday routines was determined to be 0.07 ± 0.04 %/a.m.u. U mass fractionation was calculated in real-time using a ^{233}U-^{235}U double spike. All common Pb for the zircon and baddeleyite analyses was attributed to procedural blank. A sensitivity test shows that the composition the common Pb in zircon and baddeleyite has little or no effect on the calculated dates. Total procedural Pb blanks for the HBr-based chemistry were determined to be 1.5 ± 0.4 pg, which was used in the reduction of titanite, apatite, and total dissolution K-feldspar data. K-feldspar leachates were assigned a Pb blank of 10 pg based on the amount of reagent used in the procedure, and the blank is a negligible proportion of the total Pb in those analyses. U

blanks are difficult to measure, but are ≤0.1 pg, and only in feldspar analyses is the blank a significant portion of the total U, but in no cases are the blank-corrected isotopic ratios sensitive to the U blank. All samples were spiked with a ^{205}Pb-^{233}U-^{235}U tracer, whose calibration is detailed in Schoene et al. (2006), in which an error of ± 0.015% is assigned to the Pb/U of the tracer.

Isotopic ratios and associated errors were reduced using the algorithms of Ludwig (1980) and are presented at the 95% confidence level. Tracer and decay constant errors are considered systematic errors and are added to the error of weighted mean data clusters (Ludwig 1998; Mattinson 1987; Renne et al. 1998b; Schmitz and Bowring 2001; Schmitz et al. 2003). Values and errors for the uranium decay constants are from Jaffey et al. (1971). Concordia plots, isochron regressions and weighted mean calculations and associated MSWD (mean square of weighted deviates; York 1969) calculations were generated in ISOPLOT (Ludwig 1991).

3. SAMPLE DESCRIPTION

The sample used in this study is from the McClure Mountain complex, a series of ultramafic to low-Si alkalic igneous intrusions in the Wet Mountains region of Colorado, USA. The complex is composed of early crystallized mafic-ultramafic layered intrusions such as olivine gabbro, pyroxenite, anorthosite, and dunite, which are in turn intruded by massive hornblende-biotite syenite and then by nepheline syenite (Parker and Hildebrand 1963; Shawe and Parker 1967). A series of carbonatites, lamprophyres, and quartz-barite-thorite dikes and veins cross-cuts these older units (Olson et al. 1977).

This study focuses on the hornblende-biotite syenite from which MMhb was extracted (Alexander et al. 1978). A re-collection of the syenite (D. Hawkins, pers. comm. 1998) attempted to sample the same quarry-derived boulders as were described in (Alexander et al. 1978). Major constituent minerals include K-feldspar, plagioclase, hornblende, biotite, and clinopyroxene. Titanite and apatite make up several percent of the rock. Nepheline, magnetite, ilmenite, zircon, baddeleyite, zirconolite, calcite, iron-sulfides, and alteration products such as sericite and chlorite constitute < 2 percent of the rock. Hornblende, pyroxene, biotite, titanite, and apatite occur as ~2-8 mm diameter clusters of intergrown crystals encased in a matrix of microperthitic K-feldspar and plagioclase crystals <1-10 mm in diameter (Fig. 1A). The rock description of Alexander et al. (1978) did not identify pyroxene in their sample, but instead describes the hornblende as zoned with olive-green cores and brown-green exteriors. Our thin sections show similar zonation, through the olive-green cores are Mg-rich clinopyroxene (Fig. 1A). In addition to pyroxene cores, hornblende is ubiquitously filled with inclusions of all other phases in the rock, which sometimes occur as euhedral crystals and sometimes filling cracks and cleavages (esp. with respect to biotite). In each thin section, there are discrete sub-linear zones several millimeters in length containing calcite, nepheline, baddelleyite, and symplectitic plagioclase/K-feldspar intergrowths in addition to other major phases (Fig. 1B). These low-Si, high-CO_2 zones are not located along cracks or in zones of obvious alteration, but instead appear to be concentrated in-between major phase minerals.

Apatite occurs as euhedral crystals ~50-200 μm in diameter and is included in every major phase in the rock, indicating it was an early liquidus phase (Fig. 1A). CL

images of apatite in thin section are generally featureless, though some show weak concentric zoning (Fig. 2A). Titanite occurs with hornblende, oxides, and/or biotite as both anhedral and euhedral phenocrysts up to 300 μm in diameter (Figs. 1A, 2B). Zircon ($ZrSiO_4$), baddeleyite (ZrO_2), and zirconolite ($CaZrTi_2O_7$) are rare in thin section, though all were identified in at least one section using EDS. Several ~20 μm zircon grains were identified in thin section by EDS and were located both in clusters with titanite and apatite and also within the feldspar matrix. Traditional mineral separation provided a large amount of zircon, whose textures and geochronology are described in the results section. Baddeleyite is found in both the calcite-rich zones described above (Fig. 2C) and also intergrown with zircon and zirconolite. Zirconolite is also found as microcrystic intergrowths with ilmenite, magnetite and titanite. Though zirconolite has proved useful as a U-Pb geochronometer (Rasmussen and Fletcher 2004), grains found in thin section are <20 μm in diameter and were not recovered in minerals separates.

4. U-Pb ISOTOPIC RESULTS

4.1. Zircon

Zircon from this sample forms two end-member populations, both of which range in grain-size from 30-500 μm. Group 1: magnetic, euhedral, brown-gray dipyramids that are cloudy to opaque due to inclusions and/or metamictization. Group 2: non-magnetic, sub- to anhedral, pink to colorless, translucent grains. These two populations are equally easy to distinguish by CL images (Fig. 3). Note that zircons located in thin section are too small to make generalizations about the petrogrpahic context of the endmember populations identified in mineral separates. Group 1 exhibits both oscillatory growth

zoning, typical of magmatic zircons, and "convolute" zoning – a texture that has been interpreted to reflect subsolidus remobilization of trace elements – creating chaotically patchy zones of bright and dim luminesence (Fig. 3D-I; Corfu et al. 2003; Pidgeon et al. 1998). Also, this group of zircons has a higher concentration of inclusions, including anorthite, K-feldspar, magnetite, allanite, and thorite (Fig. 3E,G). Allanite inclusions typically contain weight-percent U and Th, and form radiation halos of dim CL about 10-20 μm in radius in the surrounding zircon (Fig. 3G,H). Group 2 zircons are dominated by oscillatory growth zoning, though thin zones of bright or dark luminescence cross-cutting this zonation occur as well; zircon resorption during periods of undersaturation either in the magma or during subsolidus fluid migration may explain the truncated zonation (Fig. 3A-D).

Seventeen single-grain zircon fractions were analyzed for U-Pb systematics including six group 2 air-abraded grains, one unabraded group 2 zircon, five chemical-abraded group 1 zircons, and five chemical-abraded group 2 zircons. U-Pb isotopic data are presented in Table 1 and a concordia diagram is shown in Fig. 4. All air-abraded zircons are positively discordant, and yield $^{206}Pb/^{238}U$ and $^{207}Pb/^{235}U$ ratios that are lower than those of the chemical-abraded grains, consistent with Pb-loss in domains that were not totally removed by the air-abrasion technique. The ten chemical-abraded zircons give a range of $^{206}Pb/^{238}U$ dates, and those with the highest Th/U ratios (between 14 and 211; Table 1) are negatively discordant. The dispersion in those data is most likely due to ^{230}Th disequilbrium resulting in excess ^{206}Pb derived from variably abundant inclusions of thorite and allanite in group 1 zircons, as seen in BSE images (Fig. 3E,G). Though previously documented examples of ^{230}Th disequilibrium are interpreted to result from

magmatic growth (Mattinson 1973; Parrish 1990; Schärer 1984) – as opposed to Th-rich inclusions – the resulting negative discordance is expected to be similar. Indeed, some group 2 zircons have Th/U above 1 as well, which may be derived from unseen micro-inclusions of high Th minerals or from within the zircon crystal structure. $^{207}Pb/^{235}U$ ratios from all ten of the chemical-abraded zircons are statistically indistinguishable and yield a weighted-mean date of 523.98 ± 0.12/0.18/0.74 Ma (MSWD = 1.4; internal errors/with tracer calibration errors/with tracer calibration and decay constant errors). We consider this to represent most accurately the crystallization age of the rock.

4.2. Baddeleyite

Baddeleyite grains are brown to colorless and range in size from <20-200 μm. Three clear baddeleyite grains were analyzed (b12, b14, and b15), and these all have low Pb^*/Pb_c (<15) and two of them are greater than 14% negatively discordant and one plots near concordia (b12). Eleven brown baddeleyites were analyzed, and five are between 3 and 28% negatively discordant while the other fractions span a range of time slightly below concordia from ~520 to 525 Ma (Table 1; Fig. 5). Fraction b8 is more discordant and has an older $^{207}Pb/^{206}Pb$ date than the other five brown grains, which may be due to inheritance (though inheritance is not commonly reported in baddelleyite) or to its relatively low Pb^*/Pb_c (~14). The dispersion of the six grains near concordia is consistent both with continuous growth of baddeleyite and with open-system behavior with respect to U and/or Pb after a single-stage of crystallization. The observed negative discordance in numerous grains provides ample evidence that open-system behavior was important in these grains, and therefore we question whether any of the grains record

accurate age information. Four fractions, however, are equivalent (MSWD of equivalence = 1.2) and yield a $^{207}Pb/^{235}U$ date of 522.41 ± 0.27/0.34/1.03 Ma (MSWD = 0.9; internal errors/with tracer calibration error/with tracer calibration and decay constant error), though whether or not this date represents crystallization of all or any of the baddeleyite is questionable.

4.3. Titanite and apatite

Nine titanite fractions were analyzed, including six single-grain fractions and three fractions with 2-3 grains each (Table 2). Grain diameter ranged from ~50 to 500 μm and grains were subhedral, bottle-brown to dark orange in color and free of visible inclusions. The seven apatite fractions each comprised between 4-7 sub- to euhedral grains that were clear, colorless, and free of inclusions and ranged from ~50 to 300 μm in diameter (Table 2). Two outliers in $^{207}Pb/^{206}Pb$ - $^{238}U/^{206}Pb$ space (a4 and s6; determined to be outside 2SD of the population; figure not shown) are plotted on concordia diagrams, but are excluded from weighted mean dates and linear regressions. Age calculations from these data are sensitive to the choice of common Pb, due to the relatively low Pb^*/Pb_c ratios in both titanite (1.5-11) and apatite (1.3-2.1). The implications and methodology of deriving an adequate Pb_c correction is discussed below.

4.4. Feldspar

Single feldspar crystals ranging from 100-400 μm in diameter were hand-picked from non-magnetic separates and were free of inclusions or alteration. A random-sample of ten of these grains was selected for EDS analysis and each was high-K feldspar. Five

single-grain K-feldspar crystals were dissolved and analyzed by ID-TIMS for U-Pb isotopic composition (Table 2). These have low but variable U contents, and show significant scatter in isotope correlation diagrams (Fig. 6). One fraction of ~20 grains was subjected to a modified version of the step-wise leaching procedure of Housh and Bowring (1991) and analyzed for U/Pb isotopic compositions (Table 2; Fig. 6). The first two leaching steps were not analyzed and the fraction was completely dissolved by the sixth leaching step. The first analyzed leach step (Fsp2a) gives the least radiogenic Pb isotope composition ($^{206}Pb/^{204}Pb = 17.369 \pm 0.017$ and $^{207}Pb/^{204}Pb = 15.425 \pm 0.020$; Fig. 7), and is used as the closest approximation of initial Pb in feldspar for Pb_c corrections in titanite and apatite (as discussed below). The poor linear fit of these data on U-Pb isotope correlation diagrams (Fig. 6) indicates either that not all feldspar crystals had the same initial lead composition or that post-crystallization open-system behavior with respect to uranium and/or lead affected the grains.

5. DISCUSSION

5.1. Inaccuracies due to U decay constants and ^{230}Th disequilibria

Several studies (Mattinson 1994 2000; Schoene et al. 2006) have suggested that the mean values of one or both of the U decay constants may be inaccurate, as evidenced by normally discordant high-precision U-Pb datasets spanning a wide range of time. Those studies imply that the real values of the decay constants are within the errors reported in the original alpha-counting experiments (Jaffey et al. 1971), but many authors note that the value of the ^{238}U decay constant is likely the more accurate of the two based on

evaluation of the quality of the experiments (Begemann et al. 2001; Mattinson 1994, 2000; Schoene et al. 2006; Schön et al. 2004). Our zircon data are consistent with those conclusions, in that the chemical-abraded zircon analyses with Th/U of <20 are also slightly normally discordant. In this regard, it may be more accurate in an absolute sense to rely solely on the ^{238}U-^{206}Pb system for age calculations while using the $^{207}Pb/^{235}U$ date for evaluation of concordance/discordance only.

On the other hand, any mineral that has a Th/U ratio that differs from the magma or fluid from which it crystallized should be expected to have either an excess or deficiency in ^{206}Pb, which will affect the accuracy of the calculated $^{206}Pb/^{238}U$ date. While this phenomenon is most pronounced in monazite (Parrish 1990; Schärer 1984), it has previously been inferred to affect zircon systematics as well (Amelin and Zaitsev 2002; Oberli et al. 2004; Schmitz and Bowring 2001). Excess ^{206}Pb is a controlling factor in our zircon $^{206}Pb/^{238}U$ data, due in part to the variable abundance of high-Th mineral inclusions such as thorite and allanite, and possibly because of elevated Th levels in the zircon grains themselves. Correcting $^{206}Pb/^{238}U$ dates for excess ^{206}Pb requires either some knowledge of the Th/U of the melt from which the minerals crystallized (Parrish 1990; Schärer 1984) or by making the assumption that all minerals crystallized from a fluid with identical Th/U values, forcing data to converge upon a single $^{206}Pb/^{238}U$. Our data show that no single assumed value for the Th/U of the magma can cause the data to converge, proving that assumption to be incorrect in this case. The apatite and titanite populations are also likely affected by this problem, in that these minerals have model Th/U ratios of ~7-8 and 4-6 (Table 2), respectively, while that of the crystallizing magma is unconstrained. Several studies have also argued that excess ^{207}Pb in zircon, derived

from non-equilibrium values of ^{231}Pa, can jeopardize $^{207}Pb/^{235}U$ dates (Amelin and Zaitsev 2002; Anczkiewicz, et al. 2001 Mattinson 1973; Mortensen, et al. 1992). However, these cases are relatively rare and the consistency of our $^{207}Pb/^{235}U$ dates from chemical-abraded zircons suggest that this is not an issue for the data reported in the present study.

Therefore, we choose to focus on the $^{207}Pb/^{235}U$ dates from zircon, titanite and apatite rather than the more precise $^{206}Pb/^{238}U$ dates. The trade-off in precision between the two methods is minimal compared to the potential inaccuracies introduced by excess ^{206}Pb. Any inaccuracy in the ^{235}U decay constant will introduce a systematic error, but will not affect the relative offset between the closure dates of the different minerals (for example, the data in Schoene et al. (2006) would predict an offset of 0.1% between $^{206}Pb/^{238}U$ and $^{207}Pb/^{235}U$ dates). Therefore, the cooling history of the rock and any potential bias with the $^{40}Ar/^{39}Ar$ method may still be addressed accurately. If future work results in refinement of the ^{235}U decay constant, correcting these dates to be more accurate in absolute time is a trivial issue.

5.2. Common Pb correction

The apatite and titanite dates are heavily dependent on the correction used for the initial isotopic composition of lead (a.k.a. common lead; Pb_c), which can be chosen using several methods: 1) selecting a composition based on a bulk Pb evolution model, such as that in Stacey and Kramers (1975); 2) determining and applying the Pb isotopic composition of cogenetic low-U minerals; or 3) employing two- and three-dimensional isochron regression techniques, in which the intercept of a line with one of the axes

describes the best-fit Pb_c composition. Several studies have investigated the effects of using a Pb_c correction derived from the Stacey and Kramers (1975) two-stage Pb-evolution model in comparison to those extracted from coexisting low-U minerals such as K-feldspar (e.g. Chamberlain and Bowring 2000; Corfu 1988; Mezger and Cosca 1999; Schmitz and Bowring 2001; Verts et al. 1996). The latter methods are deemed to yield more accurate dates because, in general, the data are sensitive enough to the choice of Pb_c that it is difficult to justify an ad-hoc correction using a model Pb_c composition; in some cases the U-Pb dates reduced with feldspar Pb also plot closer to concordia. However, Chamberlain and Bowring (2000) note that in one sample, a poor linear fit of apatite and feldspar in $^{207}Pb/^{204}Pb$-$^{206}Pb/^{204}Pb$ space suggest that the two minerals do not meet one of the required assumptions: that the minerals were in isotopic equilibrium at a mutual time of crystallization and that each phase has remained closed with respect to U and Pb since that time. We attempt here to test those assumptions further by measuring U-Pb systematics of K-feldspar and using 2-D U-Pb isochrons or the 3-D total Pb-U isochron (Ludwig 1998) to constrain whether those assumptions are met.

We have calculated the $^{206}Pb/^{204}Pb$ and $^{207}Pb/^{204}Pb$ values for Pb_c in titanite and apatite using each of the techniques described above. The results are shown in Fig. 7 and the data reduced with those compositions are plotted in concordia space in Fig. 8. It is easy to distinguish the K-feldspar Pb isotopic values from the Stacey and Kramers (1975) values at 520 Ma (Fig. 7). The calculated $^{206}Pb/^{204}Pb$ and $^{207}Pb/^{204}Pb$ values from the 2-D isochron regressions overlap with the feldspar data, though the apatite data are discernibly less radiogenic than the Stacey and Kramers (1975) estimate and the calculated initials are relatively imprecise. The least radiogenic feldspar datum

(corresponding to the first leach step which contained minimal U; Fsp2a) lies outside the Pb_c compositions calculated from the 3-D total Pb-U isochron regressions of titanite and apatite (Fig. 7). The added precision of regressing titanite and apatite together on the 3-D isochron yields a result with higher precision than with each phase individually, but gives an unacceptably high MSWD of linearity (~3-10; isochrons are not shown). This is also true for regressions involving apatite, titanite, and K-feldspar (MSWDs are ~3-10), suggesting these minerals were not in isotopic equilibrium at any moment in time or that open-system behavior was important.

It should be noted that the 3-D total Pb-U isochron utilizes both U decay schemes, and therefore the result may be affected by ^{230}Th disequilibrium. As a sensitivity test, the ratios uncorrected for non-blank Pb_c (Table 1) were corrected for excess ^{206}Pb using methods similar to those in Schärer (1984) and Parrish (1990) for various magmatic Th/U ratios. This test shows that while the calculated dates can vary significantly (e.g. can lower apatite dates by 1-2 Myr for Th/U of the magma between 5 and 1), the calculated initial Pb isotopic compositions are insensitive. Therefore, for all dates calculated using isochron Pb_c estimates, the Pb_c compositions and the associated errors are used to reduce the raw U-Pb data and the resulting $^{206}Pb/^{238}U$ and $^{207}Pb/^{235}U$ ratios are plotted in concordia space and used to calculate weighted-mean dates (Fig. 8; the resulting dates are summarized in Fig. 9).

A further caveat lies in that titanite fractions have less total Pb than either apatite or feldspar, and are therefore potentially more sensitive to the effect of Pb blank on the resulting 3-D isochron solution. A sensitivity test shows that using blank values of 0-10 pg has a negligible effect on the calculated initial $^{207}Pb/^{204}Pb$, but using blank values of >5

pg has considerable affect on the calculated initial $^{206}Pb/^{204}Pb$ and on the U-Pb date calculated with the 3-D regression (for example, a 5 pg blank returns a U-Pb date of 523.2 ± 3.9 Ma and an initial $^{206}Pb/^{204}Pb$ of 17.7 ± 1.4 and $^{207}Pb/^{204}Pb$ of 15.5 ± 0.4 with an MSWD = 0.1 and a 10 pg blank returns a U-Pb date of 532.9 ± 3.7 Ma and an initial $^{206}Pb/^{204}Pb$ of 13.9 ± 3.6 and $^{207}Pb/^{204}Pb$ of 15.5 ± 3.5 with an MSWD = 9.4). However, a Pb blank of > 5 pg is unreasonable for these data because of the consistency of total procedural blanks (which fall between 1 and 2 pg), the fact that low-Pb single grain fractions have ≤ 10 pg total Pb_c, and an increasingly poor linear fit of the data and correspondingly large errors of the resulting Pb_c values. Therefore, we consider the Pb blank of 1.5 ± 0.4 pg to be robust, and the resulting initial Pb_c values and U-Pb dates to be accurate.

Picking the best Pb_c composition is easily done in concordia space (Fig. 8) if we assume that the titanite and apatite data are most likely within error of concordia or normally discordant and that the cooling dates must be less than or equal to the zircon crystallization age. The apatite dataset is especially sensitive to the choice of Pb_c because these data overall have lower and more variable Pb^*/Pb_c. These data show substantial scatter and are negatively discordant when using the Stacey and Kramers (1975) Pb_c correction, and the amount of offset from concordia correlates roughly with the Pb^*/Pb_c of the individual analyses. Using the less radiogenic estimates shifts the data closer to concordia, though both the 2-D isochron solution and the feldspar Pb_c values shift the data to values that are normally discordant and older than the zircon date. The titanite data are less sensitive to the choice of Pb_c composition, though feldspar-corrected data also fall normally discordant with a weighted mean $^{207}Pb/^{235}U$ date that is substantially

older than with other Pb_c estimates (Fig. 9). The total Pb-U isochron solutions for titanite and apatite yield concordant results with weighted-mean $^{207}Pb/^{235}U$ dates that overlap with the zircon $^{207}Pb/^{235}U$ date (Figs. 8,9).

We conclude that the best composition of Pb_c for both titanite and apatite are the values determined by the total Pb-U isochron, and that these values are different from one another (Figs. 7,8,9; best-fit compositions are as follows: titanite $^{206}Pb/^{204}Pb = 17.79 \pm 0.34$, $^{207}Pb/^{204}Pb = 15.564 \pm 0.10$; apatite $^{206}Pb/^{204}Pb = 17.54 \pm 0.27$, $^{207}Pb/^{204}Pb = 15.47 \pm 0.04$). Additionally, neither thermochronometer is amenable to the feldspar Pb_c and therefore all three phases have different average Pb_c compositions. The best estimate weighted-mean $^{207}Pb/^{235}U$ closure dates for titanite and apatite are 523.26 ± 0.65/0.72/1.27 Ma (MSWD = 0.7) and 523.51 ± 1.47/1.53/2.09 Ma (MSWD = 2.1; internal errors/with tracer calibration errors/with tracer calibration and decay constant errors), respectively (Fig. 9).

5.3. Thermal and petrologic history of the rock

Given that the best estimates for Pb_c differ for titanite, apatite, and K-feldspar, we must conclude that the minerals were not in isotopic equilibrium at the time of their respective crystallization or that subsequent open-system behavior affected the U-Pb systematics. There are several end-member explanations for the observed variations in Pb isotope systematics: 1) that the minerals incorporated Pb with variable isotopic compositions at the time of crystallization; 2) that the isotopic signatures changed as a function of time during cooling due to interaction with reservoirs of variable Pb_c composition; or 3) that mineral alteration and recent weathering compromised closed-system behavior. Option 3

is unlikely both because of the freshness of the rock and the minerals analyzed and because such processes would also substantially disturb the age information recorded in titanite and apatite, which is not observed. If the first option is true, it requires that on average, the three phases crystallized from reservoirs of Pb with distinct isotopic signatures. Given that petrographically, titanite, apatite and feldspar likely have significant overlap in the timing of crystallization and are often in contact with one another, this option seems unlikely to be entirely responsible for the observed variation. In addition, this option would require that the minerals were able to retain a distinct isotopic signature above their respective closure temperatures in an environment that had magmas/fluids with fluctuating or evolving Pb isotopic values.

The best explanation for the observed differences in initial Pb_c composition in titanite, apatite and K-feldspar is that the average isotopic composition of the lead incorporated in each mineral is a function of differing closure temperatures and therefore reflects a changing composition of lead in the system during cooling. Mineralogical and textural features in our sample show that the composition of the magma and associated fluids changed with respect to major and trace element chemistry as a function of space (e.g. within the scale of a thin-section) and/or time. This is evidenced by the presence of calcite, baddeleyite and nepheline, which are not distributed homogeneously throughout the rock, but instead occur together in discrete millimeter-sized zones (Figs. 1B, 2C). K-feldspar and plagioclase symplectite texture (Fig. 1B) also occur in these zones, and this texture is often interpreted to reflect subsolidus quenching perhaps following the removal of a fluid-rich component (Fenn 1986; Lofgren 1980). Therefore, we infer that intercumulus or late-stage fluid became CO_2-rich and Si-undersaturated late in the rock's

crystallization history. It seems reasonable then that the Pb isotopic composition of the fluids may have changed with time and/or space as well; therefore minerals with different closure temperatures would retain different isotopic compositions of Pb_c at their time of closure to diffusion. Evidence consistent with this interpretation comes from Armbrustmacher and Hedge (1982), who conducted a trace element and Sr-isotope study of the McClure Mountain complex and showed that the main body of the nepheline syenite, which post-dates the hornblende-biotite syenite, has distinctly less-radiogenic Sr isotopic values. They concluded that this is indicative of multiple distinct source regions for the different magmatic compositions of the complex. We should note also that the U-Pb data from baddeleyite are consistent with this model. Though the potential for open-system behavior in these data complicates their interpretation, the weighted mean $^{207}Pb/^{235}U$ date of three equivalent points (Fig. 5) is ~1-1.5 Ma younger than the zircon date; if this date is robust, it is consistent with their crystallization being concurrent with a late-stage fluid evolving towards Si-undersaturation.

Whether or not titanite, apatite and K-feldspar could equilibrate with the Pb isotopic characteristics of a host fluid during cooling is dependent on the balance between the rates of fluid advection through the rock and volume diffusion of Pb within individual minerals. Typical values for nominal closure temperatures for diffusion of Pb in titanite and apatite (T_c = ~600-650 °C and ~450-550 °C, respectively) are derived from a combination of diffusion experiments (Cherniak 1993; Cherniak et al. 1991), crystal-chemical theory based on ionic porosity (Dahl 1997), and the consistency of numerous geologic studies (e.g. Chamberlain and Bowring 2000; Corfu 1988; e.g. Corfu and Stone 1998; Mezger et al. 1991; Nemchin and Pidgeon 1999). A simple calculation using the

diffusion parameters for apatite from Cherniak et al. (1991) shows that if the rock remained at a constant temperature of 575 °C for 1-2 Myr (the maximum offset in closure dates between apatite and titanite), one would expect diffusion of Pb to be important in apatite on length-scales of 100-150 μm. Given that the radii of apatite cylinders analyzed in this study vary between 50 and 150 μm, and that the rates of grain boundary diffusion are far greater than volume diffusion (e.g. Joesten 1992), it is reasonable that apatite could equilibrate with a fluid that is temporally variable with respect to the Pb isotopic composition over those time scales.

The closure temperature of Pb in K-feldspar is not well constrained, though the diffusion experiments of Cherniak (1995) suggest that under anhydrous conditions Pb is less mobile than in apatite. Because feldspar lacks sufficient U to be a good U-Pb thermochronometer, there are no field-based tests to verify the diffusion experiments and the effect of hydrous conditions are unknown but potentially important. If the closure temperature of feldspar with respect to Pb is higher than apatite, then the evolution of the Pb isotopic values of the interacting fluid would have to fluctuate up and down as a function of time because the feldspar Pb_c estimates are less radiogenic than the apatite total Pb-U isochron estimate (Fig. 7). If the closure temperature for Pb in K-feldspar is in fact lower than apatite (Chamberlain and Bowring 2000), a simpler single-stage model is more appropriate where the isotopic composition of Pb in the fluid evolves towards less radiogenic values with time. The excess scatter in U-Pb data from titanite, apatite and feldspar, evidenced by high MSWDs and outliers in isotope correlation diagrams (e.g. Figs. 6,9) may be suggestive of more complicated interaction of mineral growth, volume and grain boundary diffusion of Pb, and transport of Pb of different compositions by

magmatic fluids during cooling. It may also be a reflection of the grain-size dependency on closure temperature (Dodson 1973, 1986), partial equilibration of Pb_c composition, or armoring of mineral-inclusions that prevents fluid-mineral interaction entirely (Loferski and Ayuso 1995; Meurer and Boudreau 1996; Willmore et al. 2000).

The implications of our observations of variable Pb_c compositions in different phases in the rock go beyond a petrologic model and are applicable more generally to U-Pb thermochronology. The accuracy of some studies relies on correctly assigning a Pb_c composition to the data and in slowly cooled rocks, typical of Archean and Proterozoic terranes, the methods used here may not be applicable. The grain-size dependence on closure temperature of thermochronometers means that neither 2-D nor 3-D isochrons are valid methods of Pb_c composition determination in slowly-cooled rocks. Making a correction with the isotopic composition of cogenetic low-U minerals such as K-feldspar may also be inaccurate. The importance of this point to a given study is of course dependent on the sensitivity of an interpretation to a Pb_c correction. For example, in minerals that are periodically or permanently open to diffusion for hundreds of millions or billions of years (e.g. Schmitz and Bowring 2003), there is a far greater time period in which different fluids may act as reservoirs for Pb_c, but any inaccuracy introduced with that correction may be unimportant compared to the magnitude of the spread in U-Pb dates. Fort studies that pursue relatively short-duration, high-precision cooling histories or intermethod comparison, the Pb_c correction is of utmost importance.

5.4. Intercalibration of U-Pb and $^{40}Ar/^{39}Ar$ from MMhb

Because K-Ar and $^{40}Ar/^{39}Ar$ hornblende dates from MMhb are cooling dates, we have established a context within the U-Pb system to which dates can be compared. Given the high-precision, relatively fast, cooling path constrained by the ^{235}U-^{207}Pb system, and that the closure temperature of Ar in hornblende is between titanite and apatite (T_c = 500-550 °C; McDougall and Harrison 1999), the $^{40}Ar/^{39}Ar$ cooling date should fall, within internal errors, between the lower-bound $^{207}Pb/^{235}U$ date of apatite and the upper-bound $^{207}Pb/^{235}U$ date of titanite, or 522.98 ± 1.00 Ma (including tracer calibration errors, but not decay constant errors) if no bias existed between the two systems (Fig. 10).

MMhb ranks among the most-dated minerals by the K-Ar and $^{40}Ar/^{39}Ar$ methods, despite the fact that its homogeneity and quality as a standard are often questioned. Baksi et al. (1996) showed that unpurified 15 mg splits of MMhb show isotopic inhomogeneity, giving $^{40}Ar/^{39}Ar$ dates ranging from 513.5 ± 1.4 to 520.4 ± 1.8 Ma with respect to the SB-3 biotite at 162.9 Ma, and concluded that MMhb is unsuitable as a fluence monitor in $^{40}Ar/^{39}Ar$ geochronology. This concern is supported by previous work summarized in Baksi et al. (1996) and also in subsequent intercalibration studies by Renne et al. (1998b) and Spell and McDougall (2003), who find inhomogeneity in total-fusion analyses relative to the Fish Canyon sanidine and GA-1550 biotite. Inhomogeneity in dates for MMhb is likely derived from impure separates or inclusions of high-K minerals such as biotite and K-feldspar (Lee et al. 1991; Villa et al. 1996). Incremental heating experiments on MMhb support this inference in that early heating steps show anomalously low apparent ages, though resulting plateau dates yield highly consistent results (Lee et al. 1991; Rex et al. 1993; Villa et al. 1996). Despite evidence for

inhomogeneity in MMhb, continued work to re-collect and proliferate this standard is being carried out (Kunk et al. 1994; Kunk and Miller 2002), emphasizing the importance of attaining an accurate reference date and further characterizing under what conditions this standard can be considered homogeneous.

The most widely cited reference dates for MMhb are the K-Ar compilation date from Samson and Alexander (1987) of 520.4 ± 3.4 Ma and the total-fusion $^{40}Ar/^{39}Ar$ dates from Renne et al., (1998b) and Spell and McDougall (2003) of 523.1 ± 5.2 and 523.3 ± 1.8 Ma, referenced to the primary biotite standard GA-1550 using K-Ar ages of 98.8 ± 1.9 and 98.5 ± 1.6, respectively ($^{40}Ar/^{39}Ar$ dates include intercalibration errors, but not decay constant errors). These K-Ar and $^{40}Ar/^{39}Ar$ dates return apparent biases of 0.5 ± 0.7, 0.0 ± 1.0, and 0.0 ± 0.4% with respect to the ^{235}U-^{207}Pb system (excluding decay constant errors; Fig. 10). A robust $^{206}Pb/^{238}U$ date would likely be younger than the $^{207}Pb/^{235}U$ date by ~0.1% (ca. 0.5 Myr) given tangible inaccuracies in the U decay constants (Mattinson 2000; Schoene et al. 2006). Though each date overlaps within internal error of the predicted $^{207}Pb/^{235}U$ date, the K-Ar date has a high probability of being different than the $^{207}Pb/^{235}U$ date. The offsets between the U-Pb and $^{40}Ar/^{39}Ar$ dates are consistent with previous observations that U-Pb dates are often systematically older than $^{40}Ar/^{39}Ar$ dates by ≤1.0% (Min et al. 2000; Min et al. 2001; Renne 2000; Renne et al. 1998a; Schoene et al. 2006) if only internal errors are considered. However, these data are also consistent with their being no bias between the two methods. Assessing more precisely any bias with respect to MMhb would be aided by higher-precision $^{40}Ar/^{39}Ar$ dates. This goal may be realized through the intercalibration of MMhb against other $^{40}Ar/^{39}Ar$ standards using purified separates and the step-heating method both because of

the potential for greater precision and the added benefit of evaluating concordancy. Such a study – in combination with our U-Pb age – may further reveal whether MMhb is a suitable standard for geochronology or whether it should be abandoned for a more suitable reference material.

6. CONCLUSIONS

The McClure Mountain syenite yields two populations of zircon, and the abundance of high-Th inclusions in one population and sporadically high Th contents in the other negate the use of the $^{206}Pb/^{238}U$ date. A weighted mean $^{207}Pb/^{235}U$ date from ten chemical-abraded zircon fractions of 523.98 ± 0.12/0.18/0.74 Ma (MSWD = 1.4; internal errors/with tracer calibration errors/with tracer calibration and decay constant errors) is our best estimate for the crystallization age of the syenite.

We explore the best correction for the isotopic composition of initial Pb (Pb_c) in titanite and apatite and K-feldspar, and show that the composition is different for each mineral. This implies that using a single Pb_c correction for multiple U-Pb thermochronometers may be inaccurate, especially in rocks that have complicated late-stage magmatic or hydrothermal histories or in slowly-cooled rocks.

A possible model to explain this involves a late stage magmatic fluid, whose Pb isotopic composition changed as a function of time, controlled the composition of Pb_c in each mineral phase at the time of its respective closure to diffusion of Pb.

The $^{207}Pb/^{235}U$ cooling dates for titanite and apatite are 523.26 ± 0.65/0.72/1.27 Ma (MSWD = 0.7) and 523.51 ± 1.47/1.53/2.09 Ma (MSWD = 2.1; internal errors/with tracer calibration errors/with tracer calibration and decay constant errors), respectively.

U-Pb thermochronologic data yield a best estimate closure date for Ar in hornblende of 522.98 ± 1.00 Ma with respect to the ^{235}U-^{207}Pb system, from which intermethod biases may be assessed. While these data are consistent with previous studies that show K-Ar and $^{40}Ar/^{39}Ar$ dates to be younger than U-Pb dates by ≤ 1%, they are also consistent with there being no bias. The ambiguity is primarily a result of large errors in the K-Ar and $^{40}Ar/^{39}Ar$ dates, which may be a result of the inhomogeneity in MMhb pointed out by other workers.

Acknowledgments

Helpful reviews by J. Hanchar and an anonymous reviewer made this an overall better paper. This work was supported in part by NSF grant EAR 0451802 (The EARTHTIME Network: Developing an infrastructure for high-resolution calibration of Earth History) to S. Bowring. Additional support was provided to B. Schoene by a subaward from NSF grant EAR 031521 (CHRONOS to C. Cervato).

REFERENCES CITED

Alexander JEC, Mickelson GM, Lanphere MA (1978) MMhb-1: A new ^{40}Ar-^{39}Ar dating standard. In: Zartman RE (ed) Short Papers of the Fourth International Conference, Geochronology, Cosmochronology, and Isotope Geology, vol 78-701. U.S. Geological Survey, Open-File report, pp 6-8

Amelin Y, Zaitsev AN (2002) Precise geochronology of phoscorites and carbonatites: The critical role of U-series disequilibrium in age interpretations. Geohcim. et Cosmochim. Acta 66(13):2399-2419

Armbrustmacher TJ, Hedge CE (1982) Genetic implications of minor-element and Sr-isotope geochemistry of alkaline rock complexes in the Wet Mountains area, Fremont and Custer counties, Colorado. Contrib. Miner. Petrol. 79:424-435

Baksi AK, Archibald DA, Farrar E (1996) Intercalibration of $^{40}Ar/^{39}Ar$ dating standards. Chem. Geol. 129:307-324

Begemann F, Ludwig KR, Lugmair GW, Min K, Nyquist LE, Patchett PJ, Renne PR, Shih C-Y, Villa IM, Walker RJ (2001) Call for an improved set of decay constants for geochronological use. Geochim. Cosmochim. Acta 65(1):111-121

Chamberlain KR, Bowring SA (2000) Apatite-feldspar U-Pb thermochronometer: a reliable mid-range (~450°C), diffusion controlled system. Chem. Geol. 172:173-200

Cherniak DJ (1993) Lead diffusion in titanite and preliminary results on the effects of radiation damage on Pb transport. Chem. Geol. 110:177-194

Cherniak DJ (1995) diffusion of Pb in plagioclase and K-feldspar investigated using Rutherford backscatter and resonant nuclear reaction analysis. Contrib. Miner. Petrol. 120:358-371

Cherniak DJ, Lanford WA, Ryerson FJ (1991) Lead diffusion in apatite and zircon using ion implantation and Rutherford Backscattering techniques. Geochim. Cosmochim. Acta 55:1663-1673

Cherniak DJ, Watson EB (2000) Pb diffusion in rutile. Contrib. Miner. Petrol. 139:198-207

Corfu F (1988) Differential response of U-Pb systems in coexisting accessory minerals, Winnepeg River Subprovince, Canadian Shield: implications for Archean crustal growth and stabilization. Contrib. Mineral. Petrol. 98:312-325

Corfu F, Hanchar JM, Hoskin PWO, Kinny P (2003) Atlas of zircon textures. In: Hanchar JM, Hoskin PWO (eds) Zircon, vol 53. Mineralogical Society of America, Washington, D.C., pp 468-500

Corfu F, Stone D (1998) The significance of titanite and apatite U-Pb ages: Constraints for the post-magmatic thermal-hydrothermal evolution of a batholithic complex, Berens River area, northwestern Superior Province, Canada. Geochim. Cosmochim. Acta 62(17):2979-2995

Dahl PS (1997) A crystal-chemical basis for Pb retention and fission-track annealing systematics in U-bearing minerals, with implications for geochronology. Earth Planet. Sci. Lett. 150:277-290

Dodson MH (1973) Closure temperature in cooling geochronological and petrological systems. Contrib. Mineral. Petrol. 40:259-274

Dodson MH (1986) Closure profiles in cooling systems. Materials Science Forum 7:145-154

Fenn PM (1986) On the origin of graphic granite. Amer. Min. 71:325-330
Frost BR, Chamberlain KR, Schumacher JC (2000) Sphene (titanite): phase relations and role as a geochronometer. Chemical Geology 172:131-148
Gerstenberger H, Haase G (1997) A highly effective emitter substance for mass spectrometric Pb isotope ratio determinations. Chem. Geol. 136:309-312
Grove M, Harrison TM (1996) $^{40}Ar^*$ diffusion in Fe-rich biotite. Amer. Mineral. 81:940-951
Hanchar JM, Hoskin PWO (2003) Reviews in Mineralogy and geochemistry: Zircon, vol 53. The Mineralogical Society of America, Washington, D.C.
Harrison TM (1981) Diffusion of ^{40}Ar in hornblende. Contrib. Miner. Petrol. 78:324-331
Harrison TM, Duncan I, McDougall I (1985) Diffusion of ^{40}Ar in biotite; temperature, pressure and compositional effects. Geochim. Cosmochim. Acta 49:2461-2468
Housh T, Bowring SA (1991) Lead isotopic heterogeneities within alkali feldspars: implications for the determination of initial lead isotopic compositions. Geochim. Cosmochim. Acta 55:2309-2316
Jaffey AH, Flynn KF, Glendenin LE, Bentley WC, Essling AM (1971) Precision measurement of half-lives and specific activities of ^{235}U and ^{238}U. Phys. Rev. C4:1889-1906
Joesten R (1992) Grain-boundary diffusion kinetics in silicate and oxide minerals. In: Ganguly J (ed) Diffusion, Atomic Ordering, and Mass Transport, vol 8. Springer-Verlag, pp 345-395
Krogh TE (1973) A low contamination method for hydrothermal decomposition of zircon and extraction of U and Pb for isotopic age determination. Geochim. Cosmochim. Acta 37:485-494
Krogh TE (1982) Improved accuracy of U-Pb zircon ages by the creation of more concordant systems using an air abrasion technique. Geochim. Cosmochim. Acta 46:637-649
Kunk MJ, Dalrymple GB, Snee LW (1994) Progress on the preparation of the proposed $^{40}Ar/^{39}Ar$ standard MMhb-1, plans for its calibration, and interlaboratory calibration of argon facilities. USGS Circ. (Abst. of the 8th International Conference on Geochronology, Cosmochronology and Isotope Geology) 1107:183
Kunk MJ, Miller AP (2002) Completion of NIST calibration of argon spikes, and plans for interlaboratory calibration of MMhb-2. Geol. Soc. Amer. Abs. w/ Prog. 34:340
Lee JKW, Onstott TC, Cashman KV, Cumbest RJ, Johnson D (1991) Incremental heating of hornblende in vacuo: implications for $^{40}Ar/^{39}Ar$ geochronology and the interpretation of thermal histories. Geology 19:872-876
Loferski PJ, Ayuso RA (1995) Petrography and mineral chemistry of the composite Deboullie pluton, northern Maine, U.S.A.: Implications for the genesis of Cu-Mo mineralization. Chem. Geol. 123:89-105
Lofgren G (1980) Experimental studies on the dynamic crystallisation of silicate melts. In: Hargraves RB (ed) Physics of magmatic processes, vol. Princeton University Press, New Jersey, pp 487-551
Ludwig KR (1980) Calculation of uncertainties of U-Pb isotope data. Earth Planet. Sci. Lett. 46:212-220
Ludwig KR (1991) Isoplot–a plotting and regression program for radiogenic isotope data. USGS Open-File report 91-445

Ludwig KR (1998) On the treatment of concordant uranium-lead ages. Geochim. Cosmochim. Acta 62(4):665-676
Mattinson JM (1973) Anomalous isotopic composition of lead in young zircons. Carnegie Inst. Yearbook 72:613-616
Mattinson JM (1987) U-Pb ages of zircons: a basic examination of error propagation. Chemical Geology 66:151-162
Mattinson JM (1994) Uranium decay constant uncertainties and their implications for high-resolution U-Pb geochronology. GSA Abst. with Prog. 77; A-221
Mattinson JM (2000) Revising the "gold standard" – the uranium decay constants of Jaffey et al. 1971. Eos Trans. AGU, Spring Meet. Suppl., Abstract V61A-02
Mattinson JM (2003) CA (chemical abrasion)-TIMS: high-resolution U-Pb zircon geochronology combining high-temperature annealing of radiation damage and multi-step partial dissolution analysis. Eos Trans. AGU, Fall Meet. Suppl., Abstract V22E-06
Mattinson JM (2005) Zircon U-Pb chemical-abrasion ("CA-TIMS") method: combined annealing and multi-step dissolution analysis for improved precision and accuracy of zircon ages. Chem. Geol. 220(1-2):47-56
McDougall I, Harrison TM (1999) Geochronology and Thermochronology by the $^{40}Ar/^{39}Ar$ method, vol. Oxford University Press, New York, NY
Meurer WP, Boudreau AE (1996) An evaluation of models of apatite compositional variability using apatite from the Middle Banded series of the Stillwater Complex, Montana. Contrib. Miner. Petrol. 125:225-236
Mezger K, Cosca MA (1999) The thermal history of the Eastern Ghats Belt (India) as revealed by U-Pb and $^{40}Ar/^{39}Ar$ dating of metamorphic and magmatic minerals: implications for the SWEAT correlation. Precam. Res. 1999:251-271
Mezger K, Rawnsley CM, Bohlen SR, Hanson GN (1991) U-Pb garnet, sphene, monazite, and rutile ages: implications for the duration of high-grade metamorphism and cooling histories, Adirondack, Mts., New York. Jour. Geol. 99:415-428
Min K, Mundil R, Renne PR, Ludwig KR (2000) A test for systematic errors in $^{40}Ar/^{39}Ar$ geochronology through comparison with U-Pb analysis of a 1.1 Ga rhyolite. Geochim. Cosmochim. Acta 64:73-98
Min K, Renne PR, Huff WD (2001) $^{40}Ar/^{39}Ar$ dating of Ordovician K-bentonites in Laurentia and Baltoscandia. Earth Planet. Sci. Lett. 185:121-134
Nemchin AA, Pidgeon RT (1999) U-Pb ages on titanite and apatite from the Darling Range granite: implications for Late Archean history of the southwestern Yilgarn Craton. Precam. Res. 96:125-139
Oberli F, Meier M, Berger A, Rosenburg CL, Giere R (2004) U-Th-Pb and $^{230}Th/^{238}U$ disequliibrium isotope systematics: precise accessory mineral chronology and melt evolution tracing in the Apline Bergell intrusion. Geochim. Cosmochim. Acta 68:2543-2560
Olson JC, Marvin RF, Parker RL, Mehnert HH (1977) Age and tectonic setting of lower Paleozoic alkalic and mafic rocks, carbonatites and thorium veins in south-central Colorado. Jour. Res. U.S. Geol. Survey Bull. 5(6):673-687
Parker RL, Hildebrand FA (1963) Preliminary report on alkalic intrusive rocks in the northern Wet Mountains, Colorado. U.S. Geol. Survey Prof. Paper 450-E:E8-E10

Parrish RR (1990) U-Pb dating of monazite and its application to geological problems. Can. Jour. of Earth Sci. 27:1431-1450
Pidgeon RT, Nemchin AA, Hitchen GJ (1998) Internal structures of zircons from Archean granites from teh Darling Range batholith: Implications for zircon stability and the interpretation of zircon U-Pb ages. Contrib. Miner. Petrol. 132:288-299
Rasmussen B, Fletcher IR (2004) Zirconolite: A new U-Pb chronometer for mafic igneous rocks. Geology 32(9):785-788
Reid MR, Coath CD (2000) In situ U-Pb ages of zircons from the Bishop Tuff: no evidence for long crystal residence times. Geology 28:443-446
Reid MR, Coath CD, Harrison TM, McKeegan KM (1997) Prolonged residence times for the youngest rhyolites associated with Long Valley caldera: Ion microprobe dating of young zircons. Earth Planet. Sci. Lett. 150:27-38
Renne PR (2000) $^{40}Ar/^{39}Ar$ age of plagioclase from Acapulco meteorite and the problem of systematic errors in cosmochronology. Earth Planet. Sci. Lett. 175:13-26
Renne PR, Karner DB, Ludwig KR (1998a) Absolute ages aren't exactly. Science 282:1840-1841
Renne PR, Swisher CC, Deino AL, Karner DB, Owens TL, DePaolo DJ (1998b) Intercalibration of standards, absolute ages and uncertainties in $^{40}Ar/^{39}Ar$ dating. Chem. Geol. 145:117-152
Rex DC, Guise PG, Wartho J-A (1993) Disturbed ^{40}Ar-^{39}Ar spectra from hornblendes: Thermal loss or contamination. Chem. Geol. 103:271-281
Samson SD, Alexander J, E.C. (1987) Calibration of the interlaboratory ^{40}Ar-^{39}Ar dating standard, MMhb-1. Chemical Geology 66:27-34
Schmitz MD, Bowring SA (2001) U-Pb zircon and titanite sytematics of the Fish Canyon Tuff: an assessment of high-precision U-Pb geochronology and its application to young volcanic rocks. Geochim. Cosmochim. Acta 65(15):2571-2587
Schmitz MD, Bowring SA (2003) constraints on the thermal evolution of continental lithosphere from U-Pb accessory mineral thermochronometry of lower crustal xenoliths, southern Africa. Contrib. Miner. Petrol. 144:592-618
Schmitz MD, Bowring SA, Ireland TR (2003) Evaluation of Duluth Complex anorthositic series (AS3) zircon as a U-Pb geochronological standard: New high-precision isotope dilution thermal ionization mass spectrometry results. Geochim. Cosmochim. Acta 67(19):3665-3672
Schoene B, Crowley JL, Condon DC, Schmitz MD, Bowring SA (2006) Reassessing the Uranium decay constants for geochronology using ID-TIMS U-Pb data. Geochim. Cosmochim. Acta 70:426-445
Schärer U (1984) The effect of initial ^{230}Th disequilibrium on young U-Pb ages: the Makalu case, Himalaya. Earth Planet. Sci. Lett. 67:191-204
Schön R, Winkler G, Kutschera W (2004) A critical review of experimental data for the half-lives of the uranium isotopes ^{238}U and ^{235}U. Applied Radiation and Isotopes 60:263-273
Shawe DR, Parker RL (1967) Mafic-ultramafic layered intrusion at Iron Mountain, Fremont County, Colorado. U.S. Geol. Survey Bull. 1251-A:A1-A20
Spell TL, McDougall I (2003) Characterization and calibration of $^{40}Ar/^{39}Ar$ dating standards. Chem. Geol. 198:189-211

Stacey JC, Kramers JD (1975) Approximation of terrestrial lead isotope evolution by a two-stage model. Earth Planet. Sci. Lett. 26:207-221
Steiger RH, Jäger E (1977) Subcommission on Geochronology: Convention on the use of decay constants in geo- and cosmochronology. Earth Planet. Sci. Lett. 36:359-362
Verts LA, Chamberlain KR, Frost CD (1996) U-Pb sphene dating of metamorphism: the importance of sphene growth in the contact aureole of the Red Mountain pluton, Laramie Mountains, Wyoming. Contrib. Miner. Petrol. 125:186-199
Villa IM, Grobéty B, Kelley SP, Trigila R, Wieler R (1996) Assessing Ar transport paths and mechanisms in the McClure Mountains hornblende. Contrib. Miner. Petrol. 126:67-80
Willmore CC, Boudreau AE, Kruger FJ (2000) The halogen geochemistry of the Bushveld Complex, Republic of South Africa: Implications for chalcophile element distribution in the lower and critical zones. Jour. Petrol. 41:1517-1539
York D (1969) Least-squares fitting of a straight line with correlated errors. Earth Planet. Sci. Lett. 5:320-324

Figure captions:

Figure 1: photomicrographs from the McClure Mountain syenite. Abbreviations are as follows: ap = apatite; bt = biotite; cc = calcite; cpx = high-Mg clinopyroxene; hbd = hornblende; ksp = K-feldspar; mg = magnetite; nph = nepheline; pl = plagioclase; tt = titanite. A) textural relationship between major constituent minerals. See text for discussion. Scale bar is 500 μm. B) example of carbonate-rich zone featuring symplectitic intergrowth of plagioclase and K-feldspar, as well as nepheline and calcite. See text for discussion. Scale bar is 200 μm.

Figure 2: BSE and CL images. Scale bar in each image is 100 μm. All abbreviations are the same as in figure 1 with the addition of: bd = baddelleyite; ilm = ilmenite; zl = zirconolite A) CL image of sub- to euhedral apatite in K-feldpsar matrix in polished thin section. Note weak concentric zoning in the right-hand grain. B) BSE image depicting typical setting of an inclusion-rich subhedral titanite. Note intergrowths of magnetite, ilmenite, titanite and zirconolite along grain boundaries. C) BSE image showing baddeleyite spatially associated with calcite. See text for discussion

Figure 3: BSE and CL images of type 1 (E-I) and type 2 (A-C) zircons from the McClure Mountain syenite. E and G are BSE images of the same zircons shown in CL in F and H, respectively. All other images are CL. pl = plagioclase, th = thorite, aln = allanite, ksp = K-feldspar. Scale bars are 100 μm. See text for discussion.

Figure 4: Concordia diagram for zircon. Data are in table 1. Gray band indicates error limits of the concordia curve. Calculated $^{207}Pb/^{235}U$ date includes all chemical-abraded grains. Errors are at the 95% confidence level.

Figure 5: Concordia diagram for baddeleyite. Gray band indicates the error limits of the concordia curve. Data are in table 1. Errors are at the 95% confidence level.

Figure 6: U-Pb isotope correlation diagram for K-feldspar. Data are in table 2. See text for discussion. Errors are at the 95% confidence level.

Figure 7: Pb isotope correlation diagram depicting the Pb_c values derived by different methods for correcting U-Pb titanite and apatite data. See text for discussion. Errors are at the 95% confidence level.

Figure 8: Concordia diagrams for titanite and apatite depicting the affect of different Pb_c corrections on the data. See text for discussion. Uncorrected data are in table 2, and a summary of the weighted mean $^{207}Pb/^{235}U$ dates, errors, and MSWDs are in figure 9. Gray band indicates error limits of the concordia curve. Errors are at the 95% confidence level.

Figure 9: Summary diagram for the Pb_c correction in titanite and apatite. Numbers in parentheses indicate the MSWD of the linear regressions (for multi-phase U-Pb dates) or weighted mean dates (single phase $^{207}Pb/^{235}U$ dates - method of calculation described in

text). Values of Pb_c are depicted in figure 7 and concordia diagrams with each Pb_c composition are in figure 8. Errors are at the 95% confidence level.

Figure 10: Summary comparing popular K-Ar and $^{40}Ar/^{39}Ar$ dates from the literature with $^{207}Pb/^{235}U$ dates from this study. Gray band marks the expected closure time of hornblende based on the maximum and minimum closure times of titanite and apatite, respectively. Errors on U-Pb dates include tracer calibration errors but not decay constant errors. Error-bars for zircon date are smaller than the symbol. Errors on $^{40}Ar/^{39}Ar$ dates include intercalibration errors but not errors for the primary standard used or for the decay constants or physical constants of ^{40}K. All errors are at the 95% confidence level.

Table 1. U-Pb isotopic data for zircon and baddelleyite.

				Isotopic ratios										Dates (Ma)						
Sample	$^{Pb*}/_{Pb_c}$	Pb_c (pg)	$^{Th}/_{U}$	$^{206}Pb/^{204}Pb$	$^{208}Pb/^{206}Pb$	$^{206}Pb/^{238}U$	% err	$^{207}Pb/^{235}U$	% err	$^{207}Pb/^{206}Pb$	% err	corr. coef.	$^{206}Pb/^{238}U$	±	$^{207}Pb/^{235}U$	±	$^{207}Pb/^{206}Pb$	±	% disc.
(a)	(b)	(c)	(d)	(e)	(f)	(f)	(g)	(f)	(g)	(f)	(g)		(h)	(i)	(h)	(i)	(h)	(i)	(j)
Zircon																			
z1	49	1.40	0.88	2707	0.277	0.084285	0.11	0.67209	0.15	0.05783	0.10	0.728	521.65	0.55	521.98	0.62	523.42	2.29	0.35
z2	31	1.87	0.89	1756	0.278	0.084444	0.11	0.67378	0.16	0.05787	0.12	0.707	522.59	0.58	523.01	0.67	524.79	2.53	0.43
z3	26	1.24	0.56	1589	0.175	0.084472	0.13	0.67444	0.19	0.05791	0.14	0.701	522.76	0.66	523.41	0.78	526.29	2.96	0.70
z12	29	0.98	0.74	1676	0.231	0.084435	0.12	0.67339	0.20	0.05784	0.15	0.631	522.54	0.61	522.77	0.81	523.76	3.36	0.24
z13	34	1.03	0.81	1952	0.255	0.084454	0.11	0.67330	0.16	0.05782	0.12	0.680	522.66	0.54	522.72	0.66	523.01	2.61	0.07
z14	29	2.57	0.75	1666	0.240	0.083544	0.13	0.66695	0.18	0.05790	0.13	0.703	517.24	0.63	518.86	0.74	526.02	2.85	1.74
z1.13	29	2.20	1.05	1559	0.331	0.084059	0.13	0.67131	0.19	0.05792	0.13	0.705	520.31	0.64	521.51	0.76	526.77	2.88	1.28
za1	508	1.18	21.39	4874	6.609	0.084789	0.07	0.67478	0.11	0.05772	0.09	0.602	524.65	0.33	523.61	0.46	519.07	1.96	-1.12
za2	414	0.57	20.63	4083	6.398	0.084752	0.08	0.67494	0.12	0.05776	0.08	0.699	524.43	0.41	523.71	0.48	520.62	1.84	-0.76
za3	1207	0.62	0.79	68209	0.247	0.084671	0.07	0.67588	0.10	0.05789	0.07	0.702	523.94	0.36	524.28	0.42	525.74	1.59	0.36
za4	473	0.46	0.90	26053	0.281	0.084665	0.05	0.67558	0.08	0.05787	0.06	0.671	523.91	0.26	524.10	0.32	524.92	1.28	0.20
za5	1987	0.43	1.53	95093	0.481	0.084591	0.05	0.67524	0.07	0.05789	0.05	0.768	523.47	0.27	523.89	0.29	525.74	0.99	0.45
za6	547	0.44	15.50	6774	4.878	0.084570	0.06	0.67554	0.09	0.05793	0.07	0.698	523.35	0.33	524.07	0.38	527.25	1.47	0.77
za7	3039	0.72	211.39	3470	63.366	0.085356	0.08	0.67556	0.14	0.05740	0.12	0.587	528.02	0.41	524.09	0.59	507.03	2.58	-4.31
za8	92	1.68	1.25	4701	0.391	0.084583	0.06	0.67503	0.10	0.05788	0.07	0.664	523.42	0.32	523.76	0.40	525.26	1.59	0.37
za9	539	0.26	13.54	7459	4.248	0.084558	0.08	0.67491	0.12	0.05789	0.09	0.683	523.27	0.40	523.70	0.48	525.53	1.89	0.45
za10	746	0.29	0.75	42552	0.235	0.084587	0.05	0.67580	0.07	0.05794	0.06	0.640	523.44	0.24	524.23	0.31	527.66	1.26	0.83
Baddelleyite																			
b1	28	2.59	0.55	1672	0.167	0.086533	0.13	0.68915	0.20	0.05776	0.14	0.681	535.00	0.64	532.29	0.82	520.68	3.17	-2.87
b2	25	1.67	0.52	1577	0.127	0.096993	0.19	0.75509	0.25	0.05646	0.15	0.801	596.76	1.10	571.17	1.07	470.56	3.26	-28.09
b3	103	1.44	0.06	6792	0.019	0.084332	0.07	0.67300	0.10	0.05788	0.07	0.728	521.93	0.35	522.54	0.39	525.20	1.44	0.65
b4	48	17.22	0.01	3269	0.004	0.084333	0.11	0.67299	0.15	0.05788	0.10	0.747	521.94	0.57	522.53	0.63	525.13	2.24	0.63
b5	22	3.18	0.10	1466	0.033	0.084322	0.11	0.67209	0.14	0.05781	0.09	0.764	521.87	0.55	521.98	0.59	522.46	2.05	0.12
b7	121	1.31	0.09	7965	0.029	0.084666	0.06	0.67577	0.09	0.05789	0.07	0.694	523.91	0.31	524.22	0.37	525.54	1.43	0.32
b8	14	1.13	1.58	747	0.501	0.084896	0.59	0.68056	0.64	0.05814	0.25	0.923	525.28	2.99	527.11	2.64	535.04	5.39	1.90
b9	34	1.71	0.56	2069	0.159	0.088754	0.14	0.69858	0.17	0.05709	0.10	0.808	548.16	0.72	537.94	0.72	494.82	2.24	-11.25
b10	21	1.31	0.20	1406	0.061	0.085515	0.26	0.67737	0.33	0.05745	0.19	0.810	528.96	1.34	525.18	1.36	508.80	4.28	-4.13
b11	31	2.19	0.28	2012	0.089	0.083933	0.12	0.66862	0.15	0.05778	0.10	0.777	519.55	0.59	519.88	0.63	521.30	2.14	0.35
b12	6.8	5.36	0.07	494	0.021	0.084426	0.20	0.67298	0.27	0.05781	0.18	0.751	522.49	0.99	522.52	1.10	522.67	3.89	0.03
b13	2.4	5.70	0.22	186	0.066	0.084779	0.48	0.67137	0.97	0.05743	0.79	0.579	524.59	2.44	521.55	3.95	508.21	17.5	-3.36
b14	14	4.38	0.13	981	0.033	0.106350	0.12	0.84630	0.20	0.05771	0.15	0.659	651.51	0.77	622.61	0.92	518.91	3.27	-26.88
b15	4.7	1.01	1.52	328	0.414	0.104385	1.93	0.84719	2.10	0.05886	0.83	0.919	640.06	11.79	623.11	9.78	562.04	18.0	-14.58

(a) z1, z2, b1, b2, etc. are fractions composed of single grains
za1, za2, etc. are zircon fractions that were subjected to the chemical abrasion technique
zircon fractions in italics are group 1 zircons and those in plain text are group 2 zircons
(b) Ratio of radiogenic Pb (including 208Pb) to common Pb.
(c) Total weight of common Pb.
(d) Model Th/U ratio calculated from radiogenic 208Pb/206Pb ratio and 207Pb/206Pb age.
(e) Measured ratio corrected for spike and fractionation only. Mass fractionation corrections were based on analysis of NBS-981 and NBS-983. Corrections of 0.25 ± 0.04%/amu (atomic mass unit) and 0.07 ± 0.04%/amu were applied to single-collector Daly analyses and dynamic Faraday-Daly analyses, respectively.
(f) Corrected for fractionation, spike, and blank. All common Pb was assumed to be procedural blank.
(g) Errors are 2 sigma, propagated using the algorithms of Ludwig (1980).
(h) Calculations are based on the decay constants of Jaffey et al. (1971).
(i) Errors are 2 sigma.
(j) % discordance = 100 - (100 x 206Pb/238U date / 207Pb/206Pb date).

Table 2. U-Pb isotopic data for titanite, apatite, and K-feldspar

					Isotopic ratios							corr. coef.		
Sample	# grains	$\frac{Pb^*}{Pb_c}$	Pb_c (pg)	$\frac{Th}{U}$	$\frac{^{208}Pb}{^{206}Pb}$	$\frac{^{238}U}{^{206}Pb}$	% err	$\frac{^{207}Pb}{^{206}Pb}$	% err	$\frac{^{204}Pb}{^{206}Pb}$	% err	238/206-207/206	238/206-204/206	207/206-204/206
(a)	(b)	(c)	(d)	(e)	(f)	(f)	(g)	(f)	(g)	(f)	(g)			
Titanite														
t1	1	4.4	34.3	4.9	1.55	10.38763	0.16	0.15790	0.62	0.00689	0.98	-0.21	0.00	-0.44
t3	3	6.3	46.7	5.0	1.58	10.74977	0.10	0.13262	0.41	0.00515	0.74	-0.25	0.00	-0.59
t5	4	5.8	28.2	5.2	1.62	10.64344	0.15	0.13862	0.71	0.00555	1.23	-0.19	0.00	-0.35
t6*	3	4.1	54.5	5.0	1.61	10.20520	0.12	0.16816	0.39	0.00758	0.60	-0.32	0.00	-0.63
t7	2	4.8	32.1	5.6	1.73	10.40264	0.17	0.15698	0.66	0.00682	1.05	-0.20	0.00	-0.41
t8	1	1.5	19.6	4.2	1.30	8.74440	0.58	0.26999	1.16	0.01461	1.52	-0.26	0.00	-0.16
t9	1	11.2	8.2	5.9	1.79	11.22827	0.29	0.09914	2.14	0.00284	5.15	-0.04	0.00	-0.17
t10	1	4.2	10.3	4.2	1.31	10.56132	0.47	0.14577	2.21	0.00605	3.71	-0.13	0.00	-0.11
t11	1	6.4	6.9	4.6	1.34	10.99103	0.51	0.11642	3.13	0.00402	6.26	-0.04	0.00	-0.22
Apatite														
a1	4	2.1	184.0	8.1	2.35	8.33778	0.15	0.29907	0.12	0.01669	0.17	-0.34	0.00	-0.746
a2	7	1.8	374.3	7.0	2.20	8.16325	0.16	0.31300	0.07	0.01763	0.12	-0.37	0.00	-0.785
a3	4	1.3	309.4	7.0	2.08	7.47699	0.21	0.36058	0.07	0.02097	0.15	-0.43	0.00	-0.591
a4 *	7	1.3	83.3	7.2	2.22	7.11610	0.28	0.38104	0.23	0.02229	0.28	-0.30	0.00	-0.716
a5	5	1.7	242.8	8.2	2.36	7.80379	0.18	0.33653	0.09	0.01929	0.14	-0.36	0.00	-0.794
a6	4	1.9	524.4	8.1	2.37	8.07804	0.15	0.31969	0.06	0.01812	0.10	-0.37	0.00	-0.885
a7	7	1.4	188.6	8.0	2.26	7.21837	0.22	0.37785	0.11	0.02215	0.15	-0.37	0.00	-0.744
K-feldspar														
total dissolution														
F1	1	0.07	293.4	NA	2.04	0.00968	2.51	0.88715	0.04	0.05753	0.10	-0.66	0.00	-0.730
F2	1	0.07	187.2	NA	1.98	0.03749	2.34	0.88467	0.04	0.05708	0.09	-0.61	0.00	-0.861
F3	1	0.07	708.7	NA	2.08	0.00016	2.45	0.88780	0.04	0.05747	0.09	-0.65	0.00	-0.897
F4	1	0.31	141.6	NA	1.99	0.00892	0.74	0.88781	0.05	0.05734	0.13	0.11	0.00	-0.515
F5	1	0.31	184.0	NA	2.02	0.00213	0.66	0.88808	0.05	0.05731	0.13	0.12	0.00	-0.512
step-leaching														
Fsp2.a	~20	0.00	10675.8	NA	2.12	0.00396	1.50	0.88806	0.04	0.05757	0.10	-0.90	0.00	-0.819
Fsp2.b	~20	0.31	439.4	NA	2.07	0.00916	0.55	0.88815	0.04	0.05752	0.11	0.22	0.00	-0.706
Fsp2.c	~20	0.31	353.5	NA	2.05	0.01724	0.55	0.88791	0.05	0.05749	0.10	0.24	0.00	-0.697
Fsp2.d	~20	0.31	113.8	NA	2.01	0.00813	0.76	0.88744	0.19	0.05738	0.09	0.09	0.00	-0.200

(a) t1, a1, F1 refer to mineral fraction analyzed. Fsp2.a, .b, .c, .d refer to sequential leaching step.
(*) indicates fractions that were not used in regressions or weighted-means
(b) Number of grains dissolved in fraction. For step-leaching, ~20 grains total were used and progressively leached.
(c) Ratio of radiogenic Pb (including 208Pb) to common Pb.
(d) Total weight of common Pb.
(e) Model Th/U ratio calculated from radiogenic 208Pb/206Pb ratio, reduced using the common Pb values determined by the total Pb-U isochron. NA = not applicable, because feldspar are not radiogenic enough to perform that calculation.
(f) Measured ratio corrected for spike, fractionation, and blank only. Mass fractionation corrections were based on analysis of NBS-981 and NBS-983. Corrections of 0.25 ± 0.04%/amu (atomic mass unit) and 0.07 ± 0.04%/amu were applied to single-collector Daly analyses and dynamic Faraday-Daly analyses, respectively.
A Pb blank of 1.5 ± 0.4 pg and a U blank of 0.10 ± 0.05 pg were applied to all data.
(g) Errors are 2 sigma, propagated using the algorithms of Ludwig (1980).

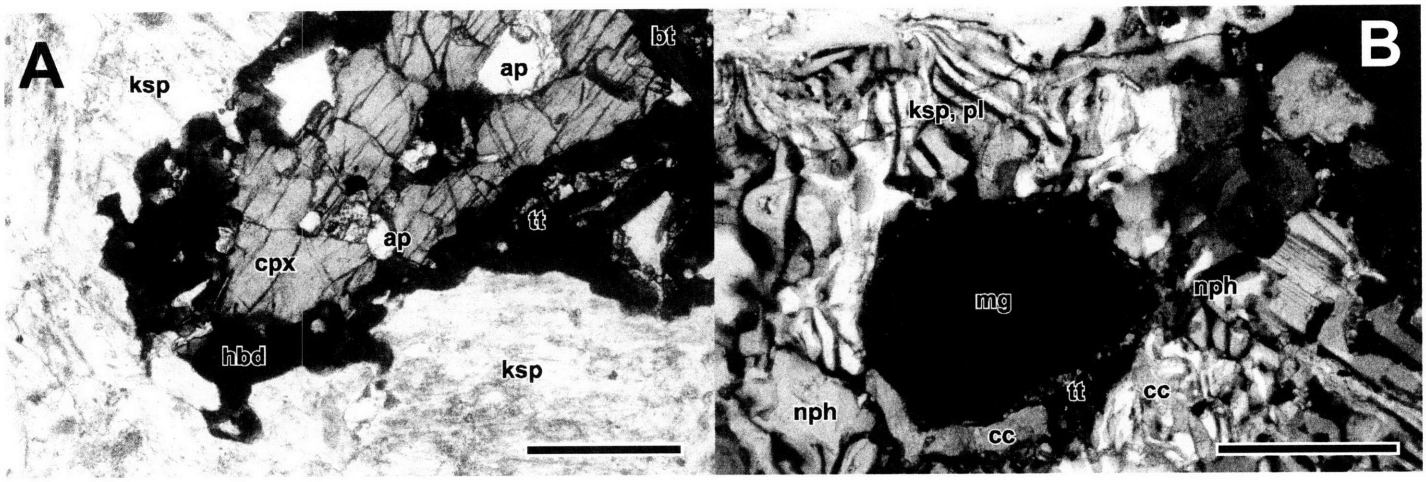

Schoene and Bowring_Fig 1.

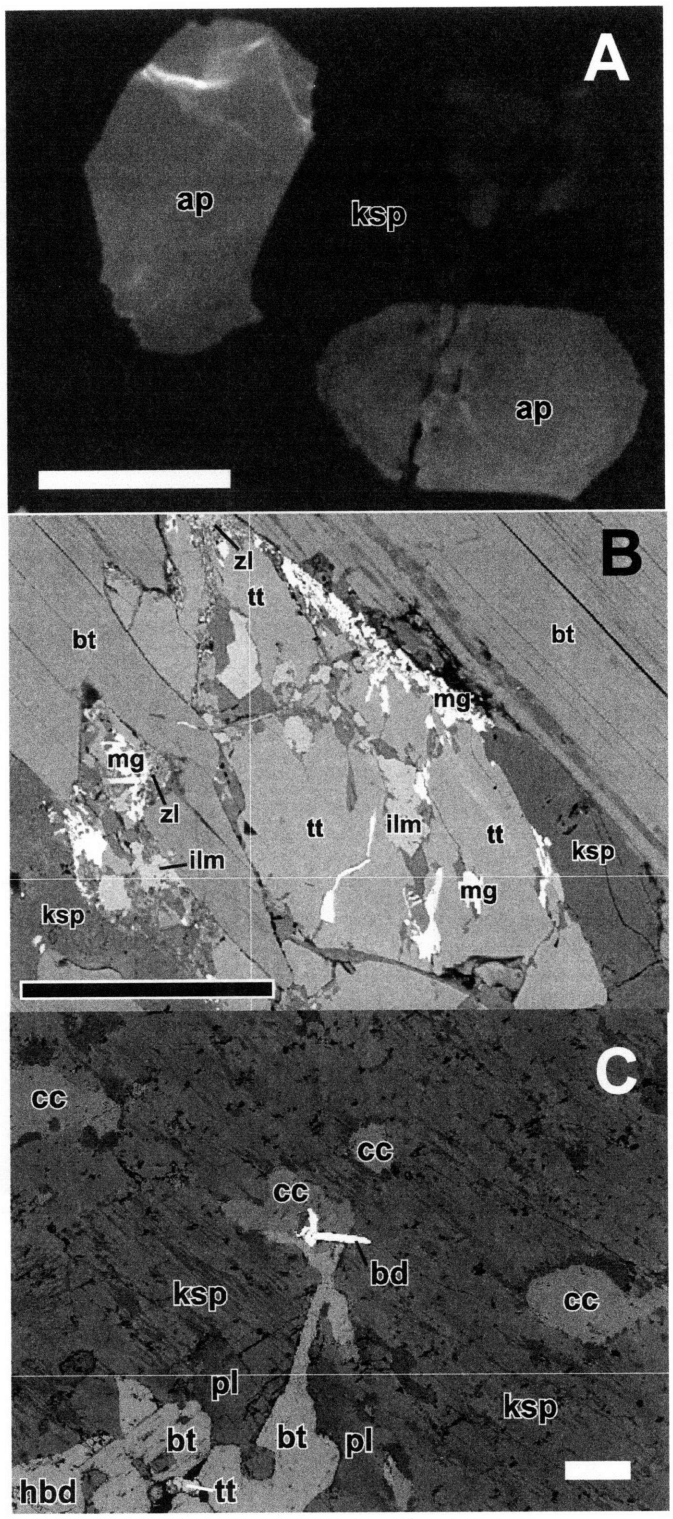

Schoene and Bowring_fig. 2

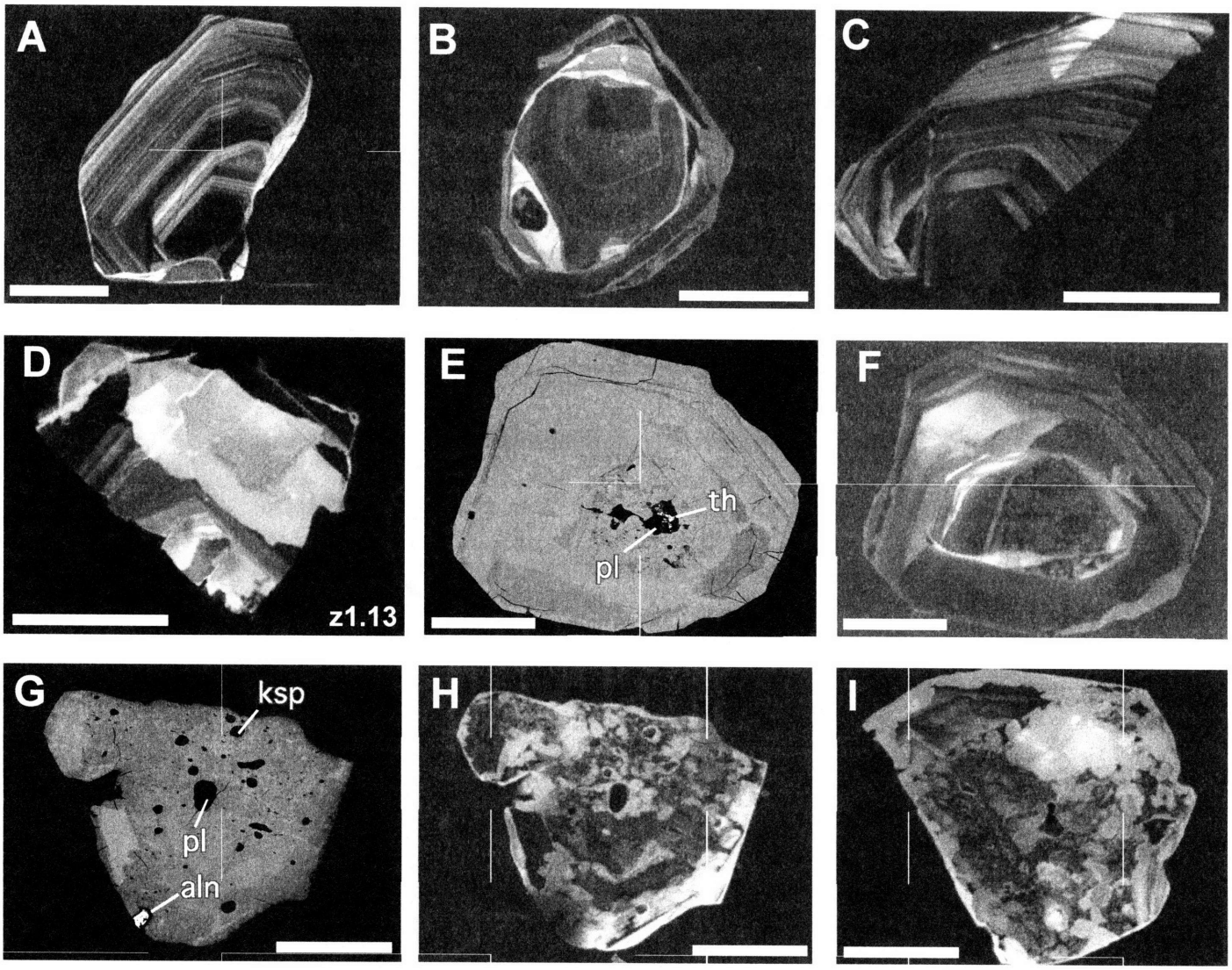

Schoene and Bowring_Fig 3.

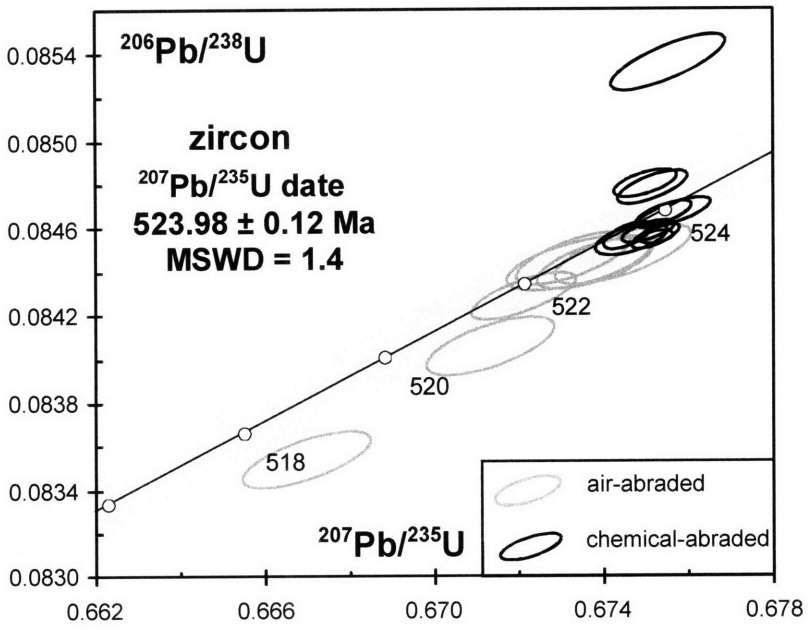

Schoene and Bowring_Fig. 4

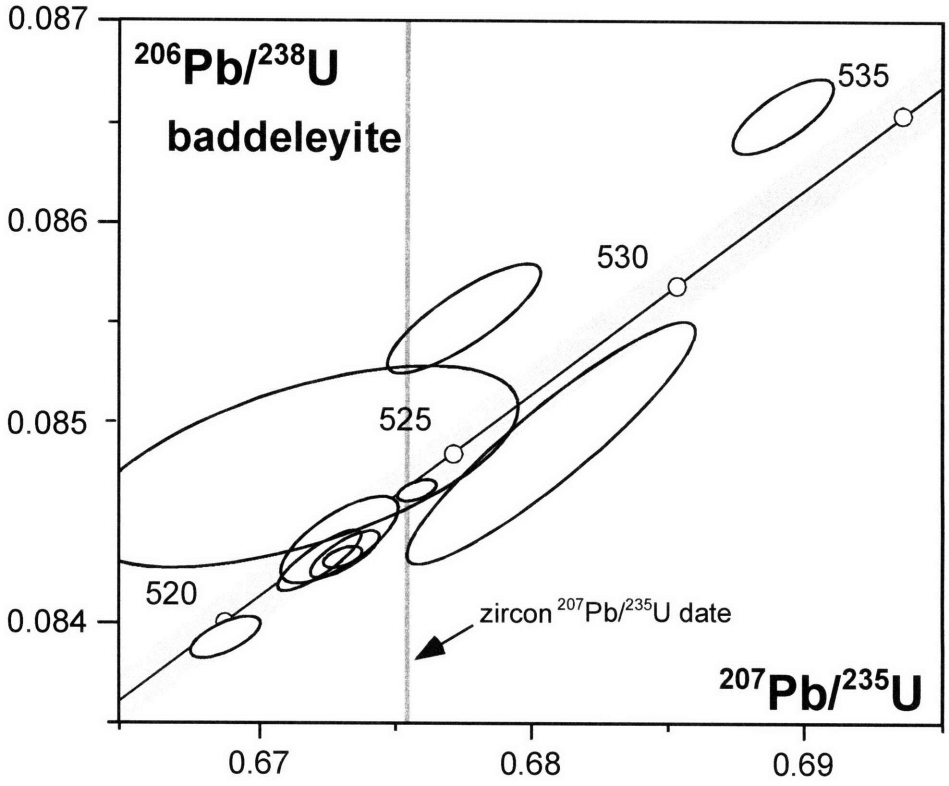

Schoene and Bowring_Fig. 5

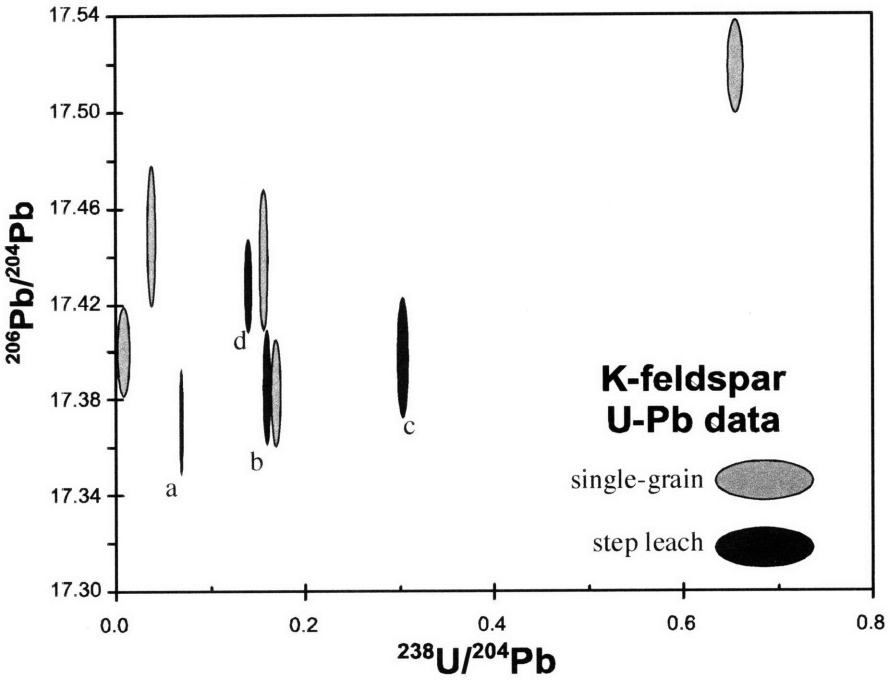

Schoene and Bowring_Fig. 6

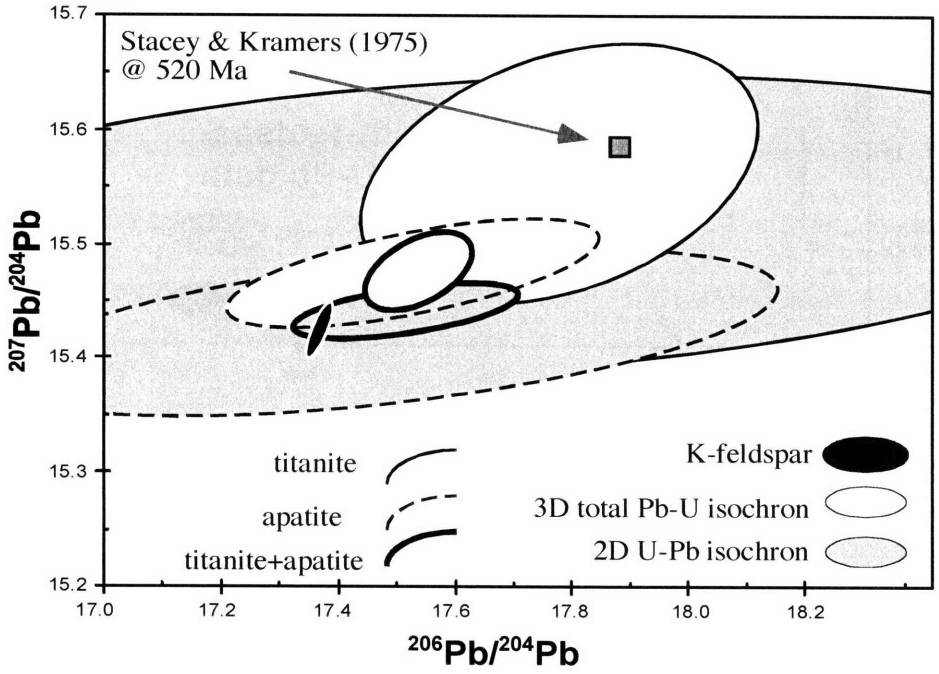

Schoene and Bowring_Fig. 7

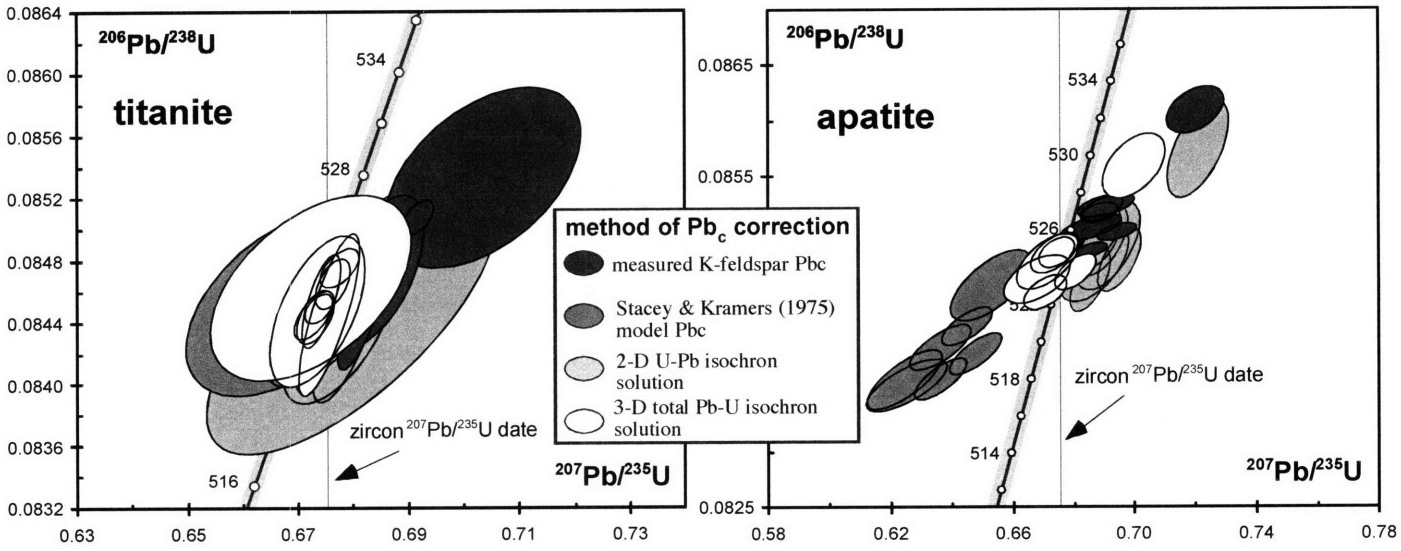

Schoene and Bowring_Fig. 8

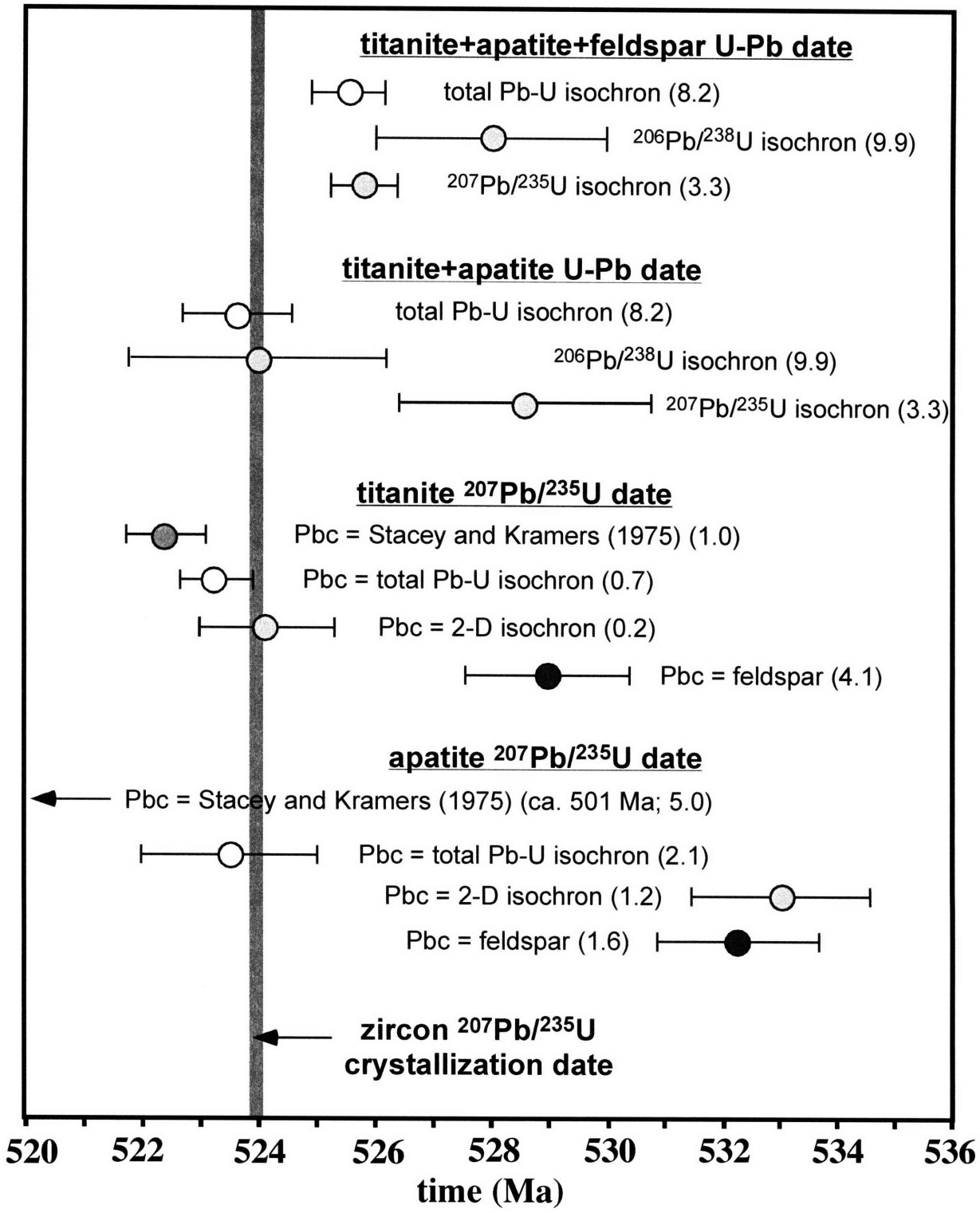

Schoene and Bowring_Fig. 9

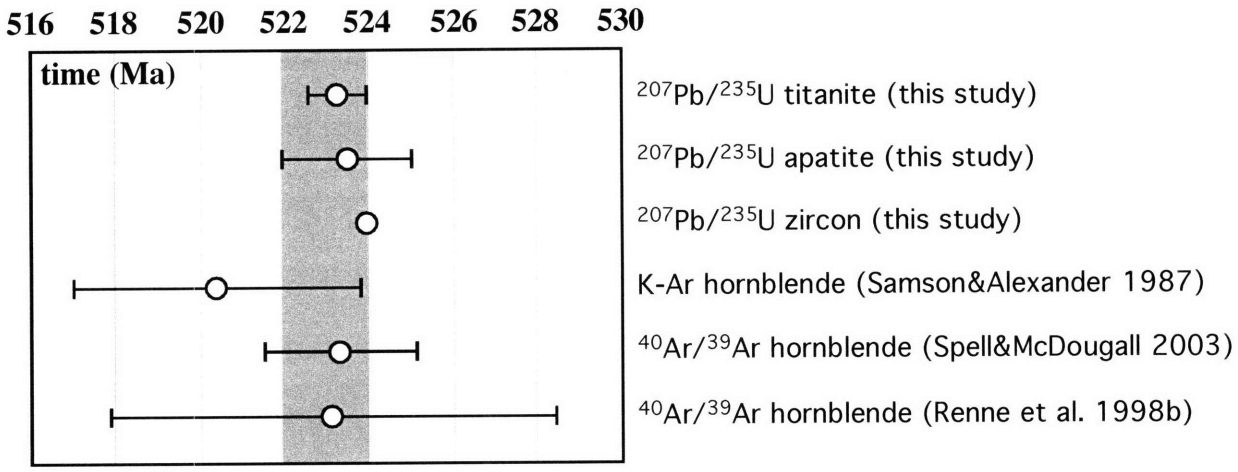

Schoene and Bowring_Fig. 10